aperture to find N_θ, N_ϕ, L_θ, and L_ϕ of (12-12a)–(12-12d) should also be done in cylindrical coordinates. It is then desirable to reformulate $r' \cos\psi$ and ds', as given by (12-15a)–(12-16c).

The most convenient position for placing the aperture is that shown in Figure 12.16 (aperture on x-y plane). The transformation between the rectangular and cylindrical components of $\mathbf{J}_s$ is given by (see Appendix VII)

$$\begin{bmatrix} J_x \\ J_y \\ J_z \end{bmatrix} = \begin{bmatrix} \cos\phi' & -\sin\phi' & 0 \\ \sin\phi' & \cos\phi' & 0 \\ 0 & 0 & 1 \end{bmatrix} \begin{bmatrix} J_\rho \\ J_\phi \\ J_z \end{bmatrix} \tag{12-41a}$$

A similar transformation exists for the components of $\mathbf{M}_s$. The rectangular and cylindrical coordinates are related by (see Appendix VII)

$$\begin{aligned} x' &= \rho' \cos\phi' \\ y' &= \rho' \sin\phi' \\ z' &= z' \end{aligned} \tag{12-41b}$$

Using (12-41a), (12-12a)–(12-12d) can be written as

$$N_\theta = \iint_S [J_\rho \cos\theta \cos(\phi - \phi') + J_\phi \cos\theta \sin(\phi - \phi') - J_z \sin\theta] \times e^{+jkr'\cos\psi}\, ds' \tag{12-42a}$$

$$N_\phi = \iint_S [-J_\rho \sin(\phi - \phi') + J_\phi \cos(\phi - \phi')]\, e^{+jkr'\cos\psi}\, ds' \tag{12-42b}$$

$$L_\theta = \iint_S [M_\rho \cos\theta \cos(\phi - \phi') + M_\phi \cos\theta \sin(\phi - \phi') - M_z \sin\theta] \times e^{+jkr'\cos\psi}\, ds' \tag{12-42c}$$

$$L_\phi = \iint_S [-M_\rho \sin(\phi - \phi') + M_\phi \cos(\phi - \phi')]\, e^{+jkr'\cos\psi}\, ds' \tag{12-42d}$$

where $r' \cos\psi$ and ds' can be written, using (12-15c) and (12-41b), as

$$r' \cos\psi = x' \sin\theta \cos\phi + y' \sin\theta \sin\phi = \rho' \sin\theta \cos(\phi - \phi') \tag{12-43a}$$

$$ds' = dx'\, dy' = \rho'\, d\rho'\, d\phi' \tag{12-43b}$$

In summary, for a circular aperture antenna the fields radiated can be obtained by *either* of the following:

1. If the fields over the aperture are known in *rectangular components*, use the same procedure as for the rectangular aperture with (12-43a) and (12-43b) substituted in (12-12a)–(12-12d).
2. If the fields over the aperture are known in *cylindrical components*, use the same procedure as for the rectangular aperture with (12-42a)–(12-42d), along with (12-43a) and (12-43b), taking the place of (12-12a)–(12-12d).

INTEL-1045
U.S. Patent 7,151,430

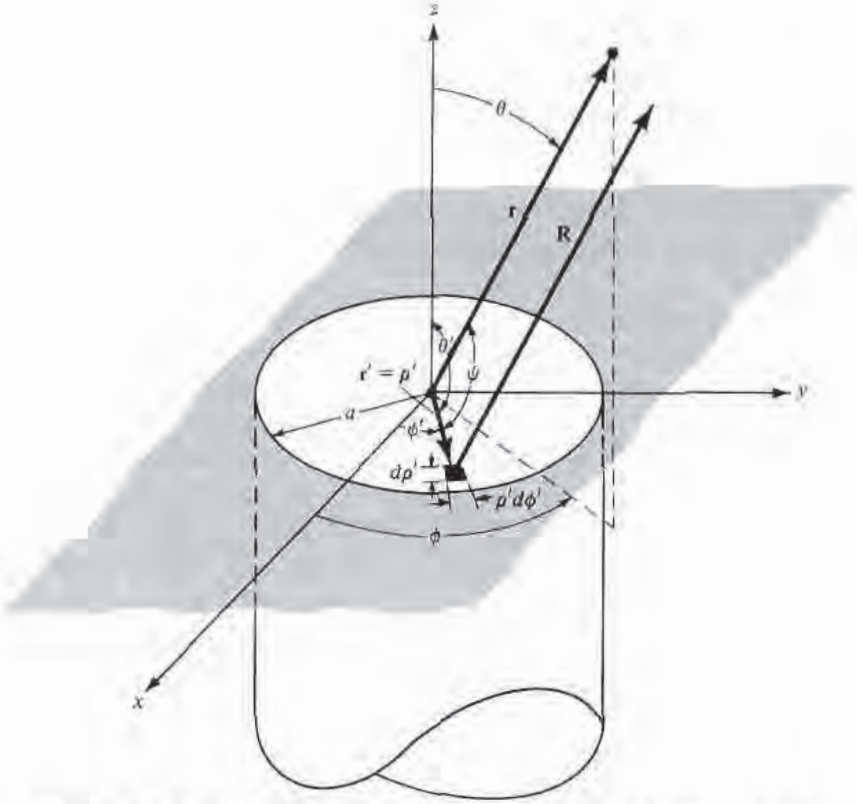


Figure 12.16 Circular aperture mounted on an infinite ground plane.

12.6.1 Uniform Distribution on an Infinite Ground Plane

To demonstrate the methods, the field radiated by a circular aperture mounted on an infinite ground plane will be formulated. To simplify the mathematical details, the field over the aperture is assumed to be constant and given by

$$\mathbf{E}_a = \hat{\mathbf{a}}_y E_0 \qquad \rho' \le a \tag{12-44}$$

where E_0 is a constant.

A. Equivalent and Radiation Fields

The equivalent problem of this is identical to that of Figure 12.7. That is,

$$\left.\begin{aligned} \mathbf{M}_s &= \begin{cases} -2\hat{\mathbf{n}} \times \mathbf{E}_a = \hat{\mathbf{a}}_x 2E_0 & \rho' \le a \\ 0 & \text{elsewhere} \end{cases} \\ \mathbf{J}_s &= 0 \qquad\qquad\qquad\quad \text{everywhere} \end{aligned}\right\} \tag{12-45}$$

Thus,

$$N_\theta = N_\phi = 0 \tag{12-46}$$

$$L_\theta = 2E_0 \cos\theta \cos\phi \int_0^a \rho' \left[\int_0^{2\pi} e^{+jk\rho' \sin\theta \cos(\phi - \phi')} d\phi' \right] d\rho' \tag{12-47}$$

INTEL-1045
U.S. Patent 7,151,430

Because

$$\int_0^{2\pi} e^{+jk\rho' \sin\theta\cos(\phi-\phi')}\,d\phi' = 2\pi J_0(k\rho' \sin\theta) \tag{12-48}$$

(12-47) can be written as

$$L_\theta = 4\pi E_0 \cos\theta \cos\phi \int_0^a J_0(k\rho' \sin\theta)\rho'\,d\rho' \tag{12-49}$$

where $J_0(t)$ is the Bessel function of the first kind of order zero. Making the substitution

$$\begin{aligned} t &= k\rho' \sin\theta \\ dt &= k \sin\theta\, d\rho' \end{aligned} \tag{12-49a}$$

reduces (12-49) to

$$L_\theta = \frac{4\pi E_0 \cos\theta \cos\phi}{(k \sin\theta)^2} \int_0^{ka\sin\theta} tJ_0(t)\,dt \tag{12-49b}$$

Since

$$\int_0^\beta zJ_0(z)\,dz = zJ_1(z)\Big|_0^\beta = \beta J_1(\beta) \tag{12-50}$$

where $J_1(\beta)$ is the Bessel function of order one, (12-49b) takes the form of

$$L_\theta = 4\pi a^2 E_0 \left\{ \cos\theta \cos\phi \left[\frac{J_1(ka \sin\theta)}{ka \sin\theta} \right] \right\} \tag{12-51}$$

Similarly

$$L_\phi = -4\pi a^2 E_0 \sin\phi \left[\frac{J_1(ka \sin\theta)}{ka \sin\theta} \right] \tag{12-52}$$

Using (12-46), (12-51), and (12-52), the electric field components of (12-10a)–(12-10c) can be written as

$$E_r = 0 \tag{12-53a}$$

$$E_\theta = j \frac{ka^2 E_0 e^{-jkr}}{r} \left\{ \sin\phi \left[\frac{J_1(ka \sin\theta)}{ka \sin\theta} \right] \right\} \tag{12-53b}$$

$$E_\phi = j \frac{ka^2 E_0 e^{-jkr}}{r} \left\{ \cos\theta \cos\phi \left[\frac{J_1(ka \sin\theta)}{ka \sin\theta} \right] \right\} \tag{12-53c}$$

In the principal E- and H-planes, the electric field components simplify to

E-Plane ($\phi = \pi/2$)

$$E_r = E_\phi = 0 \tag{12-54a}$$

$$E_\theta = j \frac{ka^2 E_0 e^{-jkr}}{r} \left[\frac{J_1(ka \sin\theta)}{ka \sin\theta} \right] \tag{12-54b}$$

H-Plane ($\phi = 0$)

$$E_r = E_\theta = 0 \tag{12-55a}$$

INTEL-1045
U.S. Patent 7,151,430

$$E_\phi = j\frac{ka^2E_0e^{-jkr}}{r}\left\{\cos\theta\left[\frac{J_1(ka\sin\theta)}{ka\sin\theta}\right]\right\} \tag{12-55b}$$

A three-dimensional pattern has been computed for the constant field circular aperture of $a = 1.5\lambda$, and it is shown in Figure 12.17. The pattern of Figure 12.17 seems to be symmetrical. However closer observation, especially through the two-dimensional E- and H-plane patterns, will reveal that not to be the case. It does, however, possess characteristics that are almost symmetrical.

B. Beamwidth, Side Lobe Level, and Directivity

Exact expressions for the beamwidths and side lobe levels cannot be obtained easily. However approximate expressions are available, and they are shown tabulated in Table 12.2. More exact data can be obtained by numerical methods.

Since the field distribution over the aperture is constant, the directivity is given by

$$\boxed{D_0 = \frac{4\pi}{\lambda^2}A_{em} = \frac{4\pi}{\lambda^2}A_p = \frac{4\pi}{\lambda^2}(\pi a^2) = \left(\frac{2\pi a}{\lambda}\right)^2 = \left(\frac{C}{\lambda}\right)^2} \tag{12-56}$$

since the maximum effective area A_{em} is equal to the physical area A_p of the aperture [as shown for the rectangular aperture in (12-37)].

A summary of the radiation parameters of this aperture is included in Table 12.2.

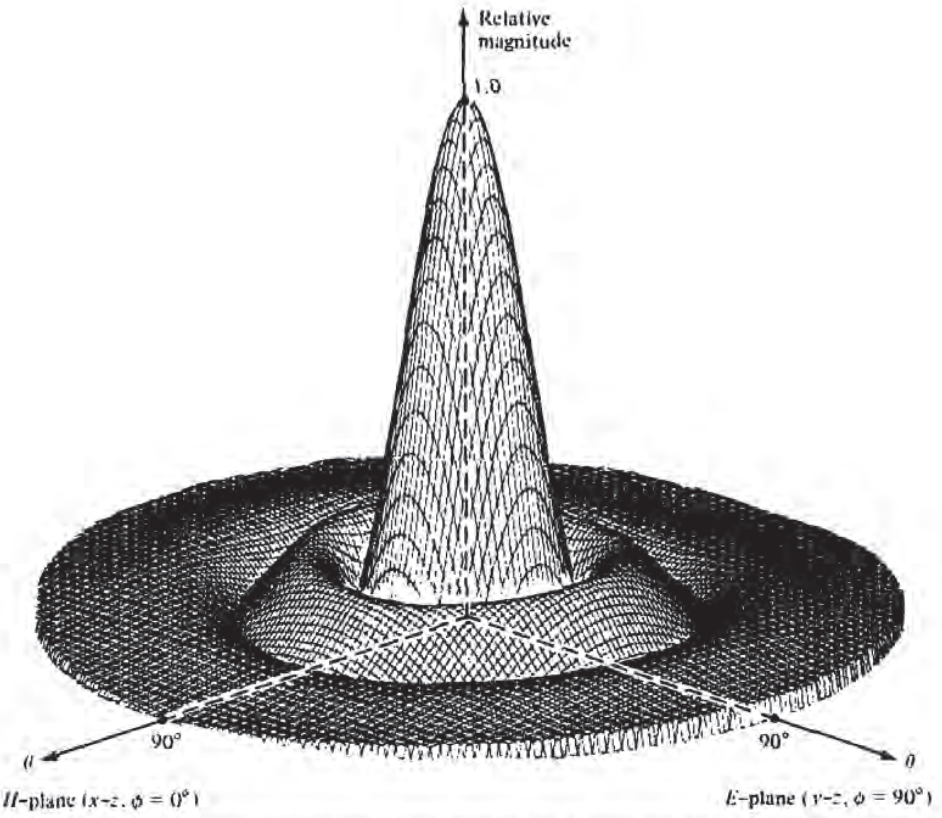
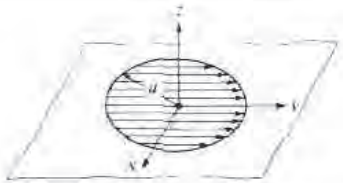
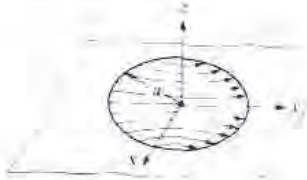


Figure 12.17 Three-dimensional field pattern of a constant field circular aperture mounted on an infinite ground plane ($a = 1.5\lambda$).

INTEL-1045
U.S. Patent 7,151,430

Table 12.2 EQUIVALENTS, FIELDS, BEAMWIDTHS, SIDE LOBE LEVELS, AND DIRECTIVITIES OF CIRCULAR APERTURES

	Uniform Distribution Aperture on Ground Plane	TE_{11}-Mode Distribution Aperture on Ground Plane
Aperture distribution of tangential components (*analytical*)	$\mathbf{E}_a = \hat{\mathbf{a}}_x E_0 \qquad \rho' \le a$	$\mathbf{E}_a = \hat{\mathbf{a}}_\rho E_\rho + \hat{\mathbf{a}}_\phi E_\phi$ $E_\rho = E_0 J_1(\chi'_{11}\rho'/a)\sin\phi'/\rho'$ $E_\phi = E_0 J_1'(\chi'_{11}\rho'/a)\cos\phi'$ $\rho' \le a$ $\chi'_{11} = 1.841$ $' = \dfrac{\partial}{\partial\rho'}$
Aperture distribution of tangential components (graphical)		
Equivalent	$\mathbf{M}_s = \begin{cases} -2\hat{\mathbf{n}} \times \mathbf{E}_a & \rho' \le a \\ 0 & \text{elsewhere} \end{cases}$ $\mathbf{J}_s = 0 \qquad \text{everywhere}$	$\mathbf{M}_s = \begin{cases} -2\hat{\mathbf{n}} \times \mathbf{E}_a & \rho' \le a \\ 0 & \text{elsewhere} \end{cases}$ $\mathbf{J}_s = 0 \qquad \text{everywhere}$
Far-zone fields $Z = ka\sin\theta$ $C_1 = j\dfrac{ka^2E_0e^{-jkr}}{r}$ $C_2 = j\dfrac{kaE_0J_1(\chi'_{11})e^{-jkr}}{r}$ $\chi'_{11} = 1.841$	$E_r = H_r = 0$ $E_\theta = jC_1\sin\phi\dfrac{J_1(Z)}{Z}$ $E_\phi = jC_1\cos\theta\cos\phi\dfrac{J_1(Z)}{Z}$ $H_\theta = -E_\phi/\eta$ $H_\phi = E_\theta/\eta$	$E_r = H_r = 0$ $E_\theta = C_2\sin\phi\dfrac{J_1(Z)}{Z}$ $E_\phi = C_2\cos\theta\cos\phi\dfrac{J_1'(Z)}{1-(Z/\chi'_{11})^2}$ $H_\theta = -E_\phi/\eta$ $H_\phi = E_\theta/\eta$ $J_1'(Z) = J_0(Z) - J_1(Z)/Z$

INTEL-1045
U.S. Patent 7,151,430

Table 12.2 (Continued)

Half-power beamwidth (degrees)	*E*-plane $a \gg \lambda$	$\frac{29.2}{a/\lambda}$	$\frac{29.2}{a/\lambda}$	$\frac{29.2}{a/\lambda}$
	H-plane $a \gg \lambda$	$\frac{29.2}{a/\lambda}$	$\frac{37.0}{a/\lambda}$	$\frac{37.0}{a/\lambda}$
First null beamwidth (degrees)	*E*-plane $a \gg \lambda$	$\frac{69.9}{a/\lambda}$	$\frac{69.9}{a/\lambda}$	$\frac{69.9}{a/\lambda}$
	H-plane $a \gg \lambda$	$\frac{69.9}{a/\lambda}$	$\frac{98.0}{a/\lambda}$	$\frac{98.0}{a/\lambda}$
First side lobe max. (to main max.) (dB)	*E*-plane	-17.6	-17.6	-17.6
	H-plane	-17.6	-26.2	-26.2
Directivity D_0 (dimensionless)		$\frac{4\pi}{\lambda^2}(\text{area}) = \frac{4\pi}{\lambda^2}(\pi a^2) = \left(\frac{2\pi a}{\lambda}\right)^2$		$0.836\left(\frac{2\pi a}{\lambda}\right)^2 = 10.5\pi\left(\frac{a}{\lambda}\right)^2$

INTEL-1045
U.S. Patent 7,151,430

12.6.2 TE_{11}-Mode Distribution on an Infinite Ground Plane

A very practical antenna is a circular waveguide of radius a mounted on an infinite ground plane, as shown in Figure 12.16. However, the field distribution over the aperture is usually that of the dominant TE_{11}-mode for a circular waveguide given by

$$\left.\begin{aligned} E_{\rho'} &= \frac{E_0}{\rho'} J_1\left(\frac{\chi'_{11}}{a}\rho'\right)\sin\phi' \\ E_{\phi} &= E_0 \frac{\partial}{\partial\rho'}\left[J_1\left(\frac{\chi'_{11}}{a}\rho'\right)\right]\cos\phi' \\ E_z &= 0 \\ \chi'_{11} &= 1.841 \end{aligned}\right\} \tag{12-57}$$

The analysis of this problem is assigned, at the end of this chapter, as an exercise to the reader (Problem 12.33). However, a three-dimensional pattern for $a = 1.5\lambda$ was calculated, and it is shown in Figure 12.18. This pattern should be compared with that of Figure 12.17 for the constant aperture field distribution.

The beamwidths and the side lobe levels in the E- and H-planes are different, and exact closed form expressions cannot be obtained. However, they can be calculated using iterative methods, and the data are shown in Figures 12.19 and 12.20 for the E- and H-planes, respectively.

A summary of all the radiation characteristics is included in Table 12.2.

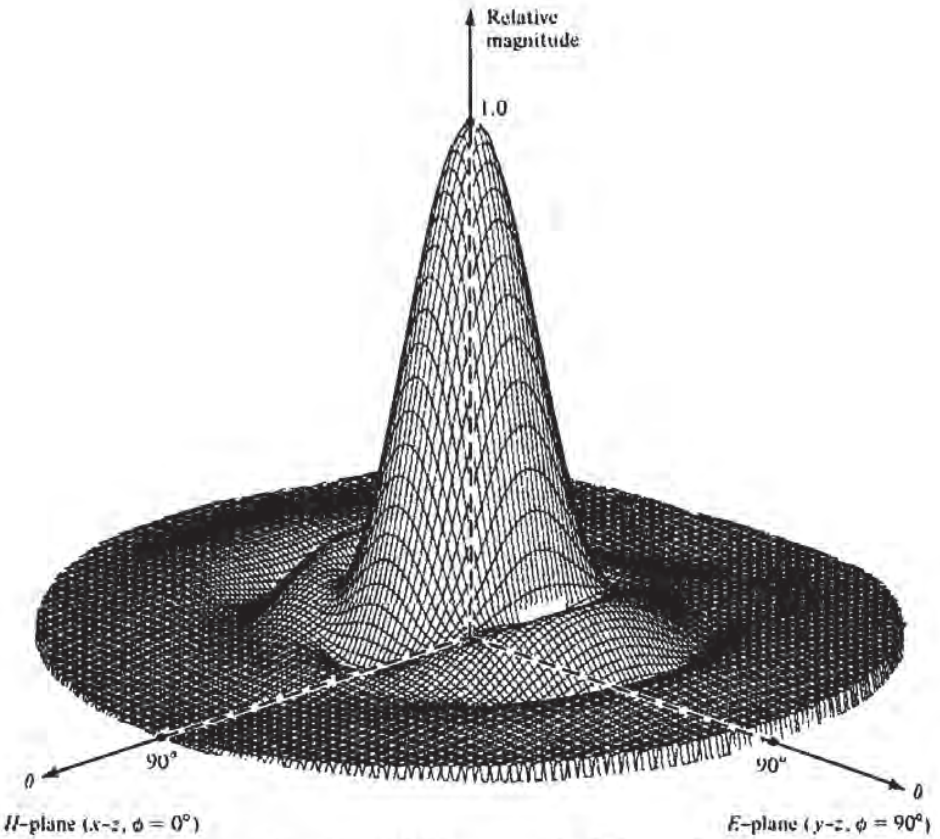


Figure 12.18 Three-dimensional field pattern of a TE_{11}-mode circular waveguide mounted on an infinite ground plane ($a = 1.5\lambda$).

INTEL-1045
U.S. Patent 7,151,430

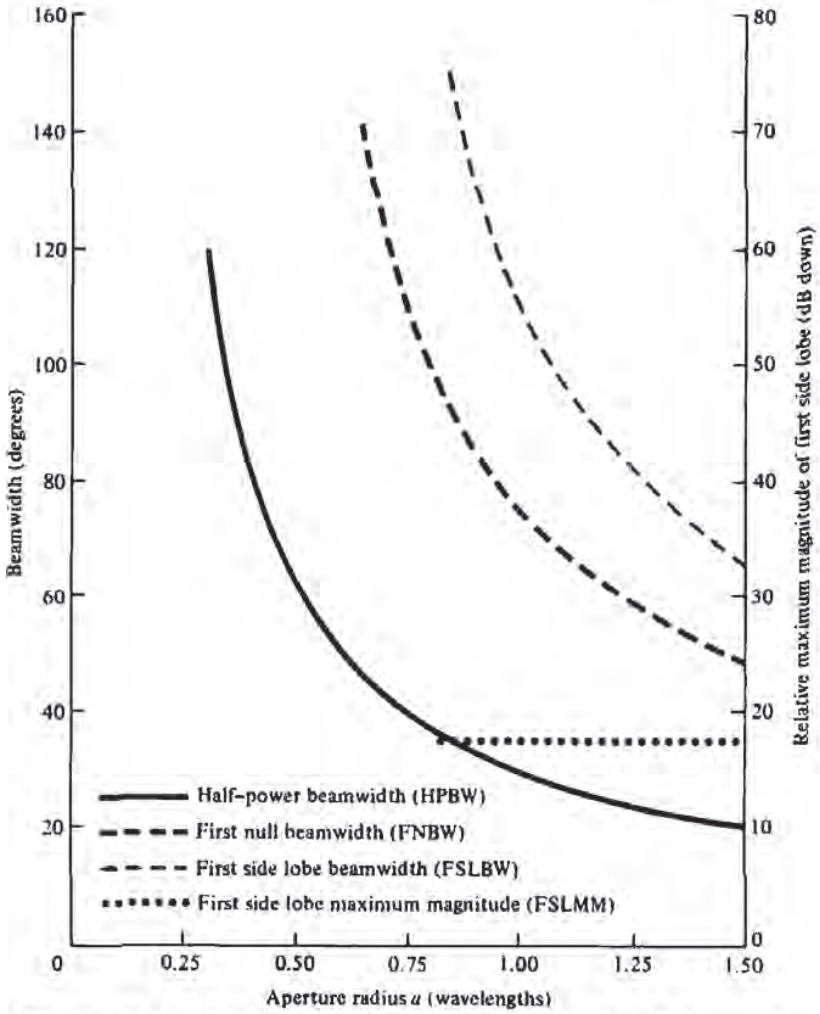


Figure 12.19 *E*-plane beamwidths and first side lobe relative maximum magnitude for TE_{11}-mode circular aperture mounted on an infinite ground plane.

12.6.3 Beam Efficiency

Beam efficiency, as defined by (2-53) and calculated by (2-54), for circular apertures not mounted on infinite ground planes is shown in Figure 12.21 [11]. The lower abscissa scale (in degrees) is in terms of the half-cone angle θ_1 (in degrees), and it should be used only when the radius of the aperture is 20λ ($a = 20\lambda$). The upper abscissa scale is in terms of u ($u = ka \sin \theta_1$), and it should be used for any radius circular aperture.

The procedure for finding the beam efficiency of a circular aperture is similar to that of a rectangular aperture as discussed in Section 12.5.4, illustrated in Figure 12.15, and demonstrated by Example 12.4.

12.7 DESIGN CONSIDERATIONS

As is the case for arrays, aperture antennas can be designed to control their radiation characteristics. Typically the level of the minor lobes can be controlled by tapering the distribution across the aperture: the smoother the taper from the center of the

INTEL-1045
U.S. Patent 7,151,430

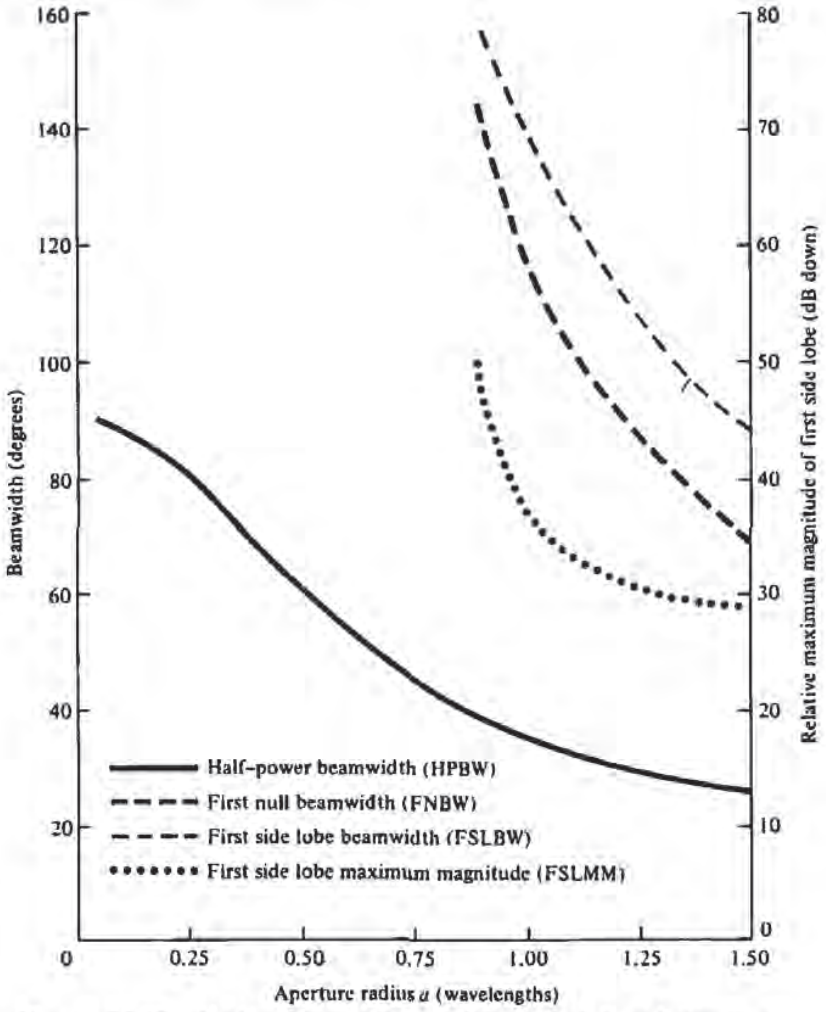


Figure 12.20 H-plane beamwidths and first side lobe relative maximum magnitude for TE_{11}-mode circular waveguide mounted on an infinite ground plane.

aperture toward the edge, the lower the side lobe level and the larger the half-power beamwidth, and conversely. Therefore a very smooth taper, such as that represented by a binomial distribution or others, would result in very low sidelobes but larger half-power beamwidths. In contrast, an abrupt distribution, such as that of uniform illumination, exhibits the smaller half-power beamwidth but the highest side lobe level (about -13.5 dB). Therefore if it is desired to achieve simultaneously both a very low sidelobe level, as well as a small half-power beamwidth, a compromise has to be made. Typically an intermediate taper, such as that of a Tschebyscheff distribution or any other similar one, will have to be selected. This has been discussed in detail both in Chapter 6 for arrays and in Chapter 7 for continuous sources. These can be used to design continuous distributions for apertures.

Aperture antennas, both rectangular and circular, can also be designed for satellite applications where the beamwidth can be used to determine the "footprint" area of the coverage. In such designs, it is important to relate the beamwidth to the size of the aperture. In addition, it is also important to maximize the directivity of the antennas within a desired angular sector defined by the beamwidth, especially at the edge-of-

INTEL-1045
U.S. Patent 7,151,430

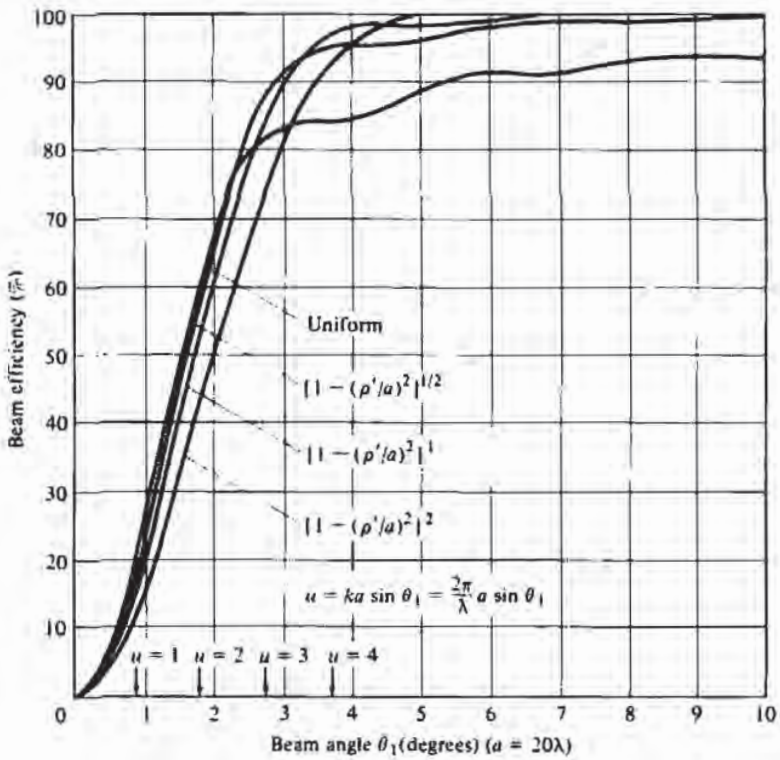


Figure 12.21 Beam efficiency versus half-cone angle θ_1, for a circular aperture with different field distributions. The aperture is not mounted on an infinite ground plane. (SOURCE: D. G. Fink (ed.), *Electronics Engineers' Handbook*, Section 18 (by W. F. Croswell), McGraw-Hill, New York, 1975)

coverage (EOC) [12]. This can be accomplished, using approximate closed-form expressions, as outlined in [12]. This procedure was used in Section 6.11 of Chapter 6 for arrays, and it is applicable for apertures, both rectangular and circular.

12.7.1 Rectangular Aperture

For a rectangular aperture, of dimensions a and b, with a uniform distribution the procedure to determine the optimum aperture dimensions a,b to maximize the directivity at an edge angle θ_e of a given angular sector ($0 \le \theta \le \theta_e$) is identical to that outlined in Section 6.11. Thus to determine the optimum dimension b of the aperture so that the directivity is maximum at an edge-of-coverage angle θ_{ec} of an angular sector $0 \le \theta \le \theta_{ec}$ in the E-plane is given by (6-105a), or

$$E\text{-Plane:} \qquad b = \frac{\lambda}{2 \sin \theta_{ec}} \tag{12-58a}$$

Similarly for the H-plane, the optimum dimension b is determined by

$$H\text{-Plane:} \qquad a = \frac{\lambda}{2 \sin \theta_{ch}} \tag{12-58b}$$

where θ_{ch} is the angle, in the H-plane, at the edge-of-coverage (EOC) angular sector where the directivity needs to be maximized.

INTEL-1045
U.S. Patent 7,151,430

Since the aperture antenna is uniformly illuminated, the directivity of (6-103) based on the optimum dimensions of (12-58a) and (12-58b) is

$$D_0 = \frac{4\pi}{\lambda^2} A_{em} = \frac{4\pi}{\lambda^2} A_p = \frac{4\pi}{\lambda^2} \left(\frac{\lambda}{2 \sin \theta_{ce}}\right)\left(\frac{\lambda}{2 \sin \theta_{ch}}\right) \tag{12-59}$$

12.7.2 Circular Aperture

A procedure similar to that for the rectangular aperture can be used for the circular aperture. In fact, it can be used for circular apertures with uniform distributions as well as tapered (parabolic or parabolic with a pedestal) [12].

For a circular aperture with uniform distribution, the normalized power pattern multiplied by the maximum directivity can be written as

$$P(\theta) = (2\pi a)^2 \left\{\frac{2J_1(ka \sin \theta)}{ka \sin \theta}\right\}^2 \tag{12-60}$$

The maximum value of (12-60) occurs when $\theta = 0$. However, for any other angle $\theta = \theta_c$, the maximum of the pattern occurs when

$$ka \sin \theta_c = 1.841 \tag{12-61}$$

or

$$a = \frac{1.841\lambda}{2\pi \sin \theta_c} = \frac{\lambda}{3.413 \sin \theta_c} \tag{12-61a}$$

Therefore to maximize the directivity at the edge $\theta = \theta_c$ of a given angular sector $0 \le \theta \le \theta_c$, the optimum radius of the uniformly illuminated circular aperture must be chosen according to (12-61a).

The maximum value of (12-60), which occurs at $\theta = 0$, is equal to

$$P(\theta = 0)|_{\max} = (2\pi a)^2 \tag{12-62}$$

while at the edge of the angular sector ($\theta = \theta_c$) is equal to

$$P(\theta = \theta_c) = (2\pi a)^2 \left\{\frac{2(0.5818)}{1.841}\right\}^2 = (2\pi a)^2(0.3995) \tag{12-63}$$

Therefore the value of the directivity at the edge of the desired coverage ($\theta = \theta_c$), relative to its maximum value at $\theta = 0$, is

$$\frac{P(\theta = \theta_c)}{P(\theta = 0)} = 0.3995 = -3.985 \text{ dB} \tag{12-64}$$

Since the aperture is uniformly illuminated, the directivity based on the optimum radius of (12-61a) is

$$D_0 = \frac{4\pi}{\lambda^2} A_p = \frac{4\pi}{\lambda^2} \pi \left(\frac{1.841}{2\pi \sin \theta_c}\right)^2 = \frac{3.4129}{\sin^2 \theta_c} = \frac{1.086\pi}{\sin^2 \theta_c} \tag{12-65}$$

A similar procedure can be followed for circular apertures with radial taper (parabolic) and radial taper squared of Table 7.2, as well as radial taper (parabolic) with pedestal. The characteristics of these, along with those of the uniform, are listed in Table 12.3.

INTEL-1045
U.S. Patent 7,151,430

Table 12.3 EDGE-OF-COVERAGE (EOC) DESIGNS FOR SQUARE AND CIRCULAR APERTURES

Aperture	Distribution	Size Square: Side Circular: Radius	Directivity	EOC Directivity (relative to peak)
Square	Uniform	$\frac{\lambda}{2\sin(\theta_c)}$	$\frac{\pi}{\sin^2(\theta_c)}$	−3.920 dB
Circular	Uniform	$\frac{\lambda}{3.413\sin(\theta_c)}$	$\frac{1.086\pi}{\sin^2(\theta_c)}$	−3.985 dB
Circular	Parabolic taper	$\frac{\lambda}{2.732\sin(\theta_c)}$	$\frac{1.263\pi}{\sin^2(\theta_c)}$	−4.069 dB
Circular	Parabolic taper with −10 dB pedestal	$\frac{\lambda}{3.064\sin(\theta_c)}$	$\frac{1.227\pi}{\sin^2(\theta_c)}$	−4.034 dB

(SOURCE: K. Praba, "Optimal Aperture for Maximum Edge-of-Coverage (EOC) Directivity," *IEEE Antennas & Propagation Magazine*, Vol. 36, No. 3, pp. 72–74, June 1994. © (1994) IEEE)

Example 12.5:

It is desired to design an aperture antenna, with uniform illumination, so that the directivity is maximized at an angle 30° from the normal to the aperture. Determine the optimum dimension and its associated directivity when the aperture is

(a) Square
(b) Circular

SOLUTION

For a square aperture $\theta_{ec} = \theta_{eh}$. Therefore the optimum dimension, according to (12-58a) or (12-58b), is

$$a = b = \frac{\lambda}{2\sin(30°)} = \lambda$$

while the directivity, according to (12-59), is

$$D_0 = \frac{\pi}{\sin^2\theta_c} = \frac{\pi}{\sin^2(30°)} = 12.5664 = 10.992 \text{ dB}$$

The directivity at $\theta = 30°$ is −3.920 dB from the maximum at $\theta = 0°$, or 7.072 dB.

For a circular aperture the optimum radius, according to (12-61a), is

$$a = \frac{\lambda}{3.413\sin(30°)} = \frac{\lambda}{3.413(0.5)} = 0.586\lambda$$

INTEL-1045
U.S. Patent 7,151,430

while the directivity, according to (12-65), is

$$D_0 = \frac{1.086\pi}{\sin^2 \theta_c} = \frac{1.086\pi}{\sin^2(30°)} = 13.647 = 11.35 \text{ dB}$$

The directivity at $\theta = 30°$ is -3.985 dB from the maximum at $\theta = 0°$, or 7.365 dB.

12.8 BABINET'S PRINCIPLE

Now that wire and aperture antennas have been analyzed, one may inquire as to whether there is any relationship between them. This can be answered better by first introducing *Babinet's principle* which in optics states that *when the field behind a screen with an opening is added to the field of a complementary structure, the sum is equal to the field when there is no screen.* Babinet's principle in optics does not consider polarization, which is so vital in antenna theory; it deals primarily with absorbing screens. An extension of Babinet's principle, which includes polarization and the more practical conducting screens, was introduced by Booker [13], [14]. Referring to Figure 12.22(a), let us assume that an electric source $\mathbf{J}$ radiates into an unbounded medium of intrinsic impedance $\eta = (\mu/\epsilon)^{1/2}$ and produces at point P the fields $\mathbf{E}_0$, $\mathbf{H}_0$. The same fields can be obtained by combining the fields when the electric source radiates in a medium with intrinsic impedance $\eta = (\mu/\epsilon)^{1/2}$ in the presence of

1. an infinite, planar, very thin, perfect electric conductor with an opening S_a, which produces at P the fields $\mathbf{E}_e$, $\mathbf{H}_e$ [Figure 12.22(b)]
2. a flat, very thin, perfect magnetic conductor S_a, which produces at P the fields $\mathbf{E}_m$, $\mathbf{H}_m$ [Figure 12.22(c)].

That is,

$$\begin{aligned} \mathbf{E}_0 &= \mathbf{E}_e + \mathbf{E}_m \\ \mathbf{H}_0 &= \mathbf{H}_e + \mathbf{H}_m \end{aligned} \tag{12-66a}$$

The field produced by the source in Figure 12.22(a) can also be obtained by combining the fields of

1. an electric source $\mathbf{J}$ radiating in a medium with intrinsic impedance $\eta = (\mu/\epsilon)^{1/2}$ in the presence of an infinite, planar, very thin, perfect electric conductor S_a, which produces at P the fields $\mathbf{E}_e$, $\mathbf{H}_e$ [Figure 12.22(b)]
2. a magnetic source $\mathbf{M}$ radiating in a medium with intrinsic impedance $\eta_d = (\epsilon/\mu)^{1/2}$ in the presence of a flat, very thin, perfect electric conductor S_a, which produces at P the fields $\mathbf{E}_d$, $\mathbf{H}_d$ [Figure 12.22(d)]

That is,

$$\begin{aligned} \mathbf{E}_0 &= \mathbf{E}_e + \mathbf{H}_d \\ \mathbf{H}_0 &= \mathbf{H}_e - \mathbf{E}_d \end{aligned} \tag{12-66b}$$

The dual of Figure 12.22(d) is more easily realized in practice than that of Figure 12.22(c).

To obtain Figure 12.22(d) from Figure 12.22(c), $\mathbf{J}$ is replaced by $\mathbf{M}$, $\mathbf{E}_m$ by $\mathbf{H}_d$, $\mathbf{H}_m$ by $-\mathbf{E}_d$, ϵ by μ, and μ by ϵ. This is a form of duality so often used in electromagnetics (see Section 3.7, Table 3.2). The electric screen with the opening in Figure

INTEL-1045
U.S. Patent 7,151,430

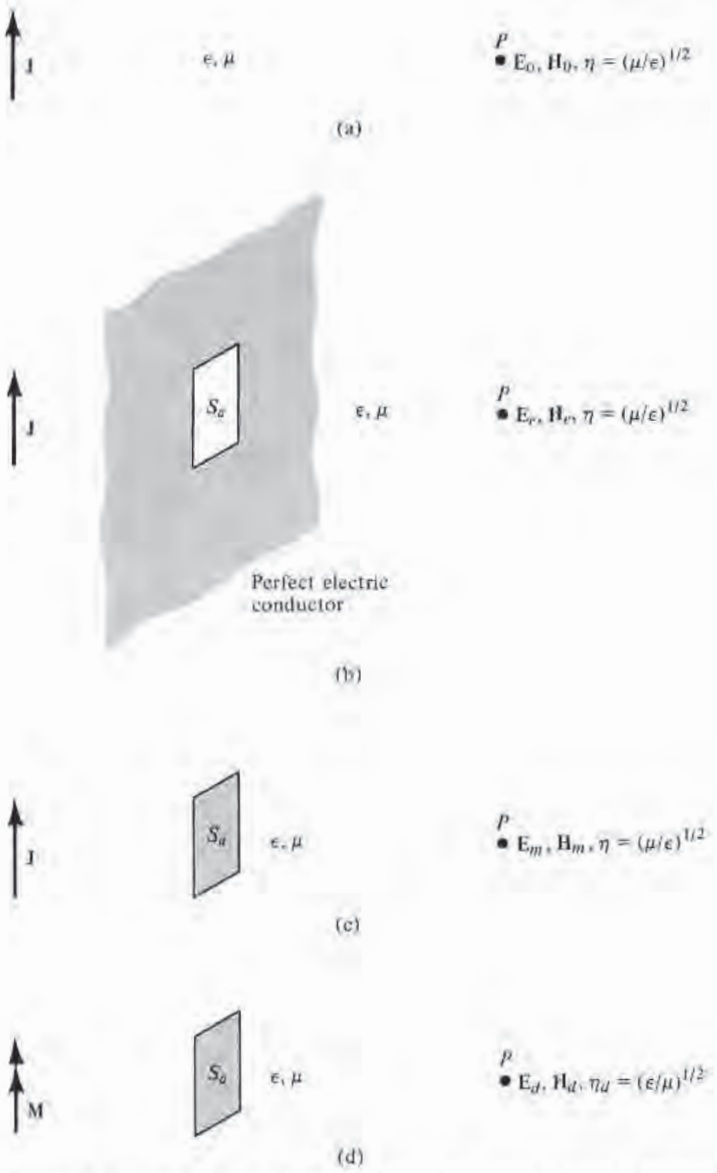


Figure 12.22 Electric source in an unbounded medium and Babinet's principle equivalents.

12.22(b) and the electric conductor of Figure 12.22(d) are also dual. They are usually referred to as *complementary structures*, because when combined they form a single solid screen with no overlaps. A proof of Babinet's principle and its extension can be found in the literature [5].

Using Booker's extension it can be shown [13], [14] by referring to Figure 12.23, that if a screen and its complement are immersed in a medium with an intrinsic impedance η and have terminal impedances of Z_s and Z_c, respectively, the impedances are related by

$$\boxed{Z_s Z_c = \frac{\eta^2}{4}} \tag{12-67}$$

INTEL-1045
U.S. Patent 7,151,430

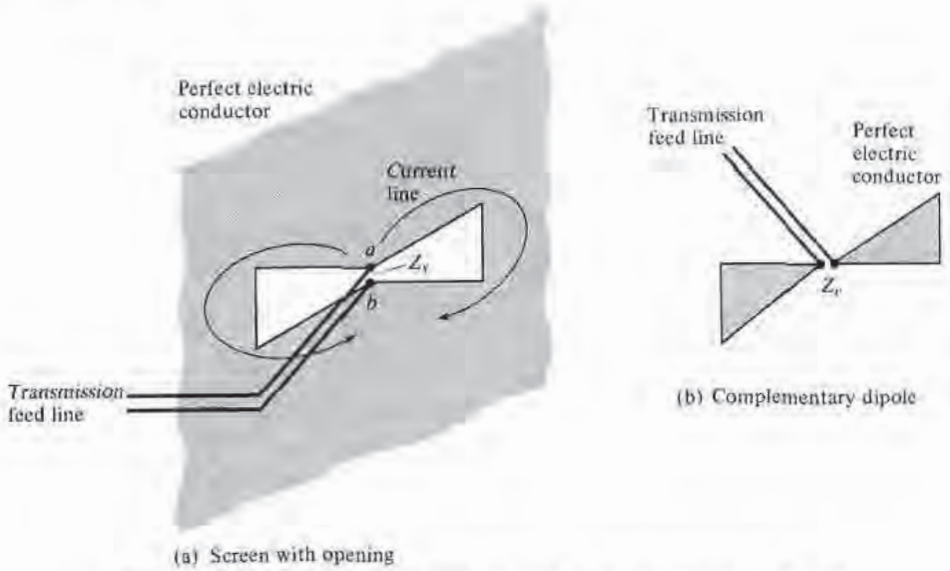


Figure 12.23 Opening on a screen and its complementary dipole.

To obtain the impedance Z_c of the complement (dipole) in a practical arrangement, a gap must be introduced to represent the feed points. In addition, the far-zone fields radiated by the opening on the screen ($E_{\theta s}$, $E_{\phi s}$, $H_{\theta s}$, $H_{\phi s}$) are related to the far-zone fields of the complement ($E_{\theta c}$, $E_{\phi c}$, $H_{\theta c}$, $H_{\phi c}$) by

$$E_{\theta s} = H_{\theta c}, \quad E_{\phi s} = H_{\phi c}, \quad H_{\theta s} = -\frac{E_{\theta c}}{\eta_0^2}, \quad H_{\phi s} = -\frac{E_{\phi c}}{\eta_0^2} \tag{12-68}$$

Infinite, flat, very thin conductors are not realizable in practice but can be closely approximated. If a slot is cut into a plane conductor that is large compared to the wavelength and the dimensions of the slot, the behavior predicted by Babinet's principle can be realized to a high degree. The impedance properties of the slot may not be affected as much by the finite dimensions of the plane as would be its pattern. The slot of Figure 12.23(a) will also radiate on both sides of the screen. Unidirectional radiation can be obtained by placing a backing (box or cavity) behind the slot, forming a so-called *cavity-backed slot* whose radiation properties (impedance and pattern) are determined by the dimensions of the cavity.

To demonstrate the application of Babinet's principle, an example is considered.

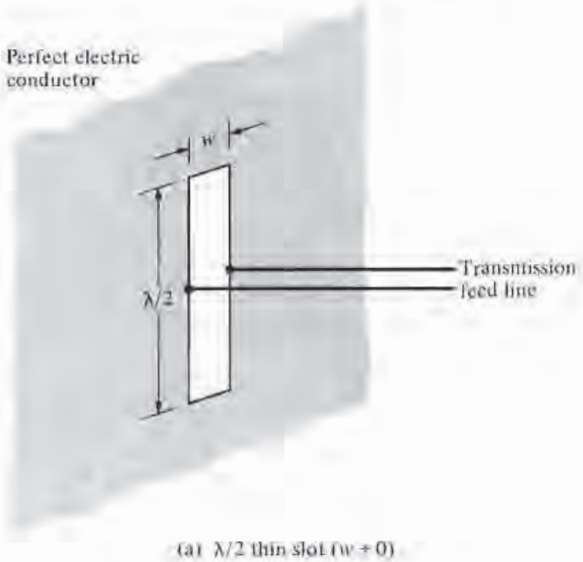
Example 12.6

A very thin half-wavelength slot is cut on an infinite, planar, very thin, perfectly conducting electric screen as shown in Figure 12.24(a). Find its input impedance. Assume it is radiating into free-space.

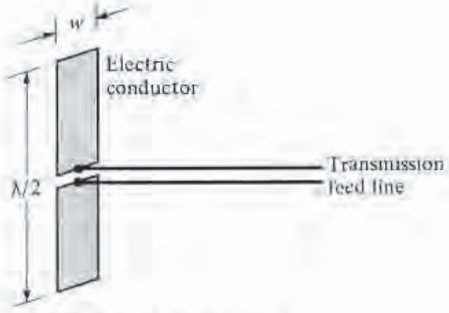
SOLUTION

From Babinet's principle and its extension we know that a very thin half-wavelength dipole, shown in Figure 12.24(b), is the complementary structure to the slot. From

INTEL-1045
U.S. Patent 7,151,430



(a) λ/2 thin slot ($w \to 0$)



(b) λ/2 flat thin dipole ($w \to 0$)

Figure 12.24 Half-wavelength thin slot on an electric screen and its complement.

Chapter 4, the terminal (input) impedance of the dipole is $Z_c = 73 + j42.5$. Thus the terminal (input) impedance of the slot, using (12-67), is given by

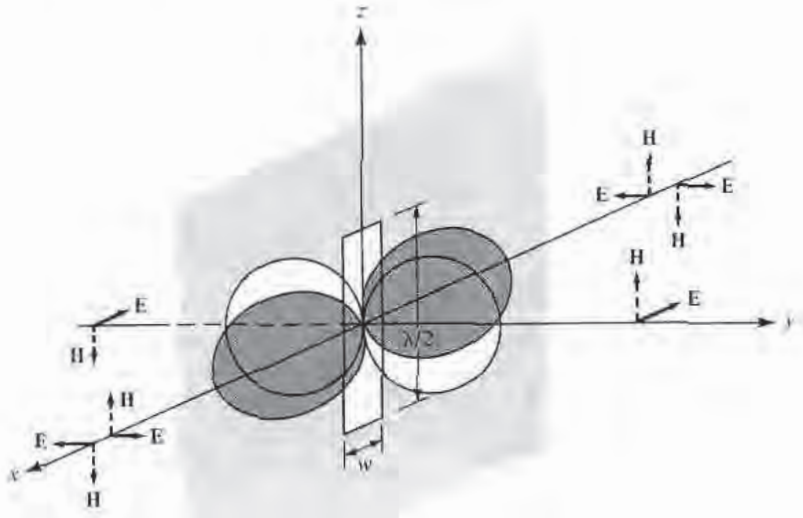
$$Z_s = \frac{\eta_0^2}{4Z_c} \simeq \frac{(376.7)^2}{4(73 + j42.5)} \simeq \frac{35{,}475.72}{73 + j42.5}$$

$$Z_s \simeq 362.95 - j211.31$$

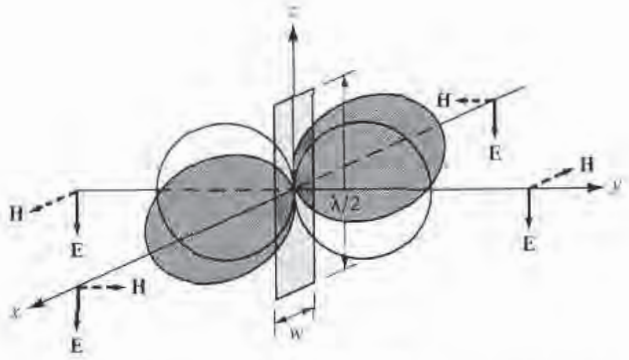
The slot of Figure 12.24(a) can be made to resonate by choosing the dimensions of its complement (dipole) so that it is also resonant. The pattern of the slot is identical in shape to that of the dipole except that the **E**- and **H**-fields are interchanged. When a vertical slot is mounted on a vertical screen, as shown in Figure 12.25(a), its electric field is horizontally polarized while that of the dipole is vertically polarized [Fig. 12.25(b)]. Changing the angular orientation of the slot or screen will change the polarization.

The slot antenna, as a cavity-backed design, has been utilized in a variety of law enforcement applications. Its main advantage is that it can be fabricated and concealed within metallic objects, and with a small transmitter it can provide covert communications. There are various methods of feeding a slot antenna [15]. For proper operation,

INTEL-1045
U.S. Patent 7,151,430



(a) λ/2 slot on a screen



(b) λ/2 flat dipole

Figure 12.25 Radiation fields of a λ/2 slot on a screen and of a λ/2 flat dipole. (SOURCE: J. D. Kraus, *Antennas*, McGraw-Hill, New York, 1988, Chapter 13)

the cavity depth must be equal to odd multiples of $\lambda_g/4$, where λ_g is the guide wavelength.

12.9 FOURIER TRANSFORMS IN APERTURE ANTENNA THEORY

Previously the spatial domain analysis of aperture antennas was introduced, and it was applied to rectangular and circular apertures radiating in an infinite, homogeneous, lossless medium. The analysis of aperture antennas mounted on infinite ground planes, covered with lossless and/or lossy dielectric media, becomes too complex when it is attempted in the spatial domain. Considerable simplification can result with the utility of the frequency (*spectral*) domain.

INTEL-1045
U.S. Patent 7,151,430

12.9.1 Fourier Transforms-Spectral Domain

From Fourier series analysis, any periodic function $f(x)$ with a period T can be represented by a Fourier series of cosine and sine terms. If the function $f(x)$ is aperiodic and exists only in the interval of $0 < x < T$, a Fourier series can be formed by constructing, in a number of ways, a periodic function. The Fourier series for the constructed periodic function represents the actual aperiodic function $f(x)$ only in the interval $0 < x < T$. Outside this space, the aperiodic function $f(x)$ is zero and the series representation is not needed. A Fourier series for $f(x)$ converges to the values of $f(x)$ at each point of continuity and to the midpoint of its values at each discontinuity.

In addition, $f(x)$ can also be represented as a superposition of discrete complex exponentials of the form

$$f(x) = \sum_{n=-\infty}^{+\infty} c_n e^{-j(2n\pi/T)x} \tag{12-69}$$

$$c_n = \frac{1}{T}\int_0^T f(x)e^{+j(2n\pi/T)x}dx \tag{12-69a}$$

or of continuous complex exponentials of the form

$$f(x) = \frac{1}{2\pi}\int_{-\infty}^{+\infty} \mathcal{F}(\omega)e^{-jx\omega}\,d\omega \qquad -\infty < \omega < +\infty \tag{12-70a}$$

whose inverse is given by

$$\mathcal{F}(\omega) = \int_{-\infty}^{+\infty} f(x)e^{+j\omega x}\,dx \qquad -\infty < x < +\infty \tag{12-70b}$$

The integral operation in (12-70a) is referred to as the *direct transformation* and that of (12-70b) as the *inverse transformation* and both form a *transform pair.*

Another useful identity is *Parseval's theorem,* which for the transform pair, can be written as

$$\int_{-\infty}^{+\infty} f(x)g^*(x)\,dx = \frac{1}{2\pi}\int_{-\infty}^{+\infty} \mathcal{F}(\omega)\,\mathcal{G}^*(\omega)\,d\omega \tag{12-71}$$

where * indicates complex conjugate.

From the definitions of (12-70a), (12-70b) and (12-71), the Fourier transforms can be expanded to two dimensions and can be written as

$$f(x,y) = \frac{1}{4\pi^2}\int_{-\infty}^{+\infty}\int_{-\infty}^{+\infty} \mathcal{F}(\omega_1, \omega_2)e^{-j(\omega_1 x + \omega_2 y)}\,d\omega_1\,d\omega_2 \tag{12-72a}$$

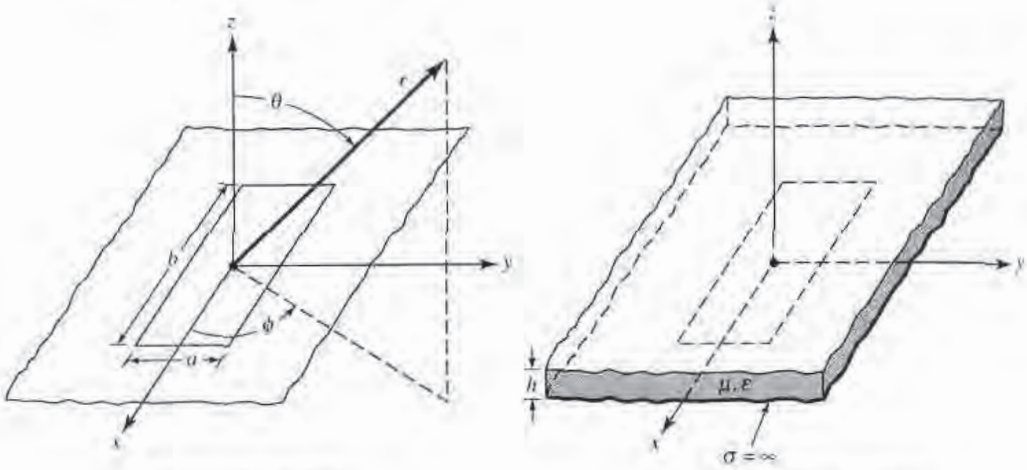
$$\mathcal{F}(\omega_1,\omega_2) = \int_{-\infty}^{+\infty}\int_{-\infty}^{+\infty} f(x, y)e^{+j(\omega_1 x + \omega_2 y)}\,dx\,dy \tag{12-72b}$$

$$\int_{-\infty}^{+\infty}\int_{-\infty}^{+\infty} f(x, y)\,g^*(x, y)\,dx\,dy = \frac{1}{4\pi^2}\int_{-\infty}^{+\infty}\int_{-\infty}^{+\infty} \mathcal{F}(\omega_1, \omega_2)\,\mathcal{G}^*(\omega_1, \omega_2)\,d\omega_1\,d\omega_2 \tag{12-72c}$$

The process can be continued to n dimensions.

The definitions, theorems, and principles introduced will be utilized in the sections that follow to analyze the radiation characteristics of aperture antennas mounted on infinite ground planes.

INTEL-1045
U.S. Patent 7,151,430



(a) Uncovered aperture (b) Dielectric-covered aperture

Figure 12.26 Rectangular apertures mounted on infinite ground planes.

12.9.2 Radiated Fields

To apply Fourier transforms (*spectral techniques*) to the analysis of aperture antennas, let us consider a rectangular aperture of dimensions a and b mounted on an infinite ground plane, as shown in Figure 12.26. In the source-free region ($z > 0$), the field $\mathbf{E}(x, y, z)$ of a monochromatic wave radiated by the aperture can be written as a superposition of plane waves (all of the same frequency, different amplitudes, and traveling in different directions) of the form $\mathbf{f}(k_x, k_y)e^{-j\mathbf{k}\cdot\mathbf{r}}$ [16], [17]. The function $\mathbf{f}(k_x, k_y)$ is the vector amplitude of the wave, and k_x and k_y are the spectral frequencies which extend over the entire frequency spectrum ($-\infty \le k_x, k_y \le \infty$). Thus the field $\mathbf{E}(x, y, z)$ can be written as

$$\mathbf{E}(x, y, z) = \frac{1}{4\pi^2}\int_{-\infty}^{+\infty}\int_{-\infty}^{+\infty}\mathbf{f}(k_x, k_y)e^{-j\mathbf{k}\cdot\mathbf{r}}\,dk_x\,dk_y \tag{12-73}$$

according to the definition of (12-72a). The object of a plane wave expansion is to determine the unknown amplitudes $\mathbf{f}(k_x, k_y)$ and the direction of propagation of the plane waves. Since

$$\mathbf{r} = \hat{\mathbf{a}}_x x + \hat{\mathbf{a}}_y y + \hat{\mathbf{a}}_z z \tag{12-74}$$

and the propagation factor $\mathbf{k}$ (often referred to as the *vector wavenumber*) can be defined as

$$\mathbf{k} = \hat{\mathbf{a}}_x k_x + \hat{\mathbf{a}}_y k_y + \hat{\mathbf{a}}_z k_z \tag{12-75}$$

(12-73) can be written as

$$\mathbf{E}(x, y, z) = \frac{1}{4\pi^2}\int_{-\infty}^{+\infty}\int_{-\infty}^{+\infty}[\mathbf{f}(k_x, k_y)e^{-jk_z z}]e^{-j(k_x x + k_y y)}\,dk_x\,dk_y. \tag{12-76}$$

The part of the integrand within the brackets can be regarded as the transform of $\mathbf{E}(x, y, z)$. This allows us to write the transform pair as

$$\boxed{\mathbf{E}(x, y, z) = \frac{1}{4\pi^2}\int_{-\infty}^{+\infty}\int_{-\infty}^{+\infty}\mathcal{E}(k_x, k_y, z)e^{-j(k_x x + k_y y)}\,dk_x\,dk_y} \tag{12-77a}$$

INTEL-1045
U.S. Patent 7,151,430

$$\boxed{\mathscr{E}(k_x, k_y, z) = \int_{-\infty}^{+\infty} \int_{-\infty}^{+\infty} \mathbf{E}(x, y, z) e^{+j(k_x x + k_y y)}\, dx\, dy} \tag{12-77b}$$

where

$$\boxed{\mathscr{E}(k_x, k_y, z) = \mathbf{f}(k_x, k_y) e^{-jk_z z}} \tag{12-77c}$$

In principle then, according to (12-77a) and (12-77b) the fields radiated by an aperture $\mathbf{E}(x, y, z)$ can be found provided its transform $\mathscr{E}(k_x, k_y, z)$ is known. To this point the transform field $\mathscr{E}(k_x, k_y, z)$ can only be found provided the actual field $\mathbf{E}(x, y, z)$ is known *a priori*. In other words, the answer must be known beforehand! However, as it will be seen from what follows, if the transform field at $z = 0$

$$\mathscr{E}(k_x, k_y, z = 0) = \mathbf{f}(k_x, k_y) \tag{12-78}$$

is formed, it will be sufficient to determine $\mathbf{E}(x, y, z)$. To form the transform $\mathscr{E}(k_x, k_y, z = 0) = \mathbf{f}(k_x, k_y)$, it will be necessary and sufficient to know only the tangential components of the **E**-field at $z = 0$. For the problem of Figure 12.26(a), the tangential components of the **E**-field at $z = 0$ exist only over the bounds of the aperture (they vanish outside it because of the presence of the infinite ground plane).

In general

$$\mathbf{f}(k_x, k_y) = \hat{\mathbf{a}}_x f_x(k_x, k_y) + \hat{\mathbf{a}}_y f_y(k_x, k_y) + \hat{\mathbf{a}}_z f_z(k_x, k_y) \tag{12-79}$$

which can also be written as

$$\mathbf{f}(k_x, k_y) = \mathbf{f}_t(k_x, k_y) + \hat{\mathbf{a}}_z f_z(k_x, k_y) \tag{12-79a}$$

$$\mathbf{f}_t(k_x, k_y) = \hat{\mathbf{a}}_x f_x(k_x, k_y) + \hat{\mathbf{a}}_y f_y(k_x, k_y) \tag{12-79b}$$

For aperture antennas positioned along the xy-plane, the only components of $\mathbf{f}(k_x, k_y)$ that need to be found are f_x and f_y. As will be shown in what follows, f_z can be found once f_x and f_y are known. This is a further simplification of the problem. The functions f_x and f_y are found, using (12-77a) and (12-77b), provided the tangential components of the **E**-field over the aperture (E_{xa} and E_{ya}) are specified. The solution of (12-77c) is valid provided the z variations of $\mathbf{E}(k_x, k_y, z)$ are separable. In addition, in the source-free region the field $\mathbf{E}(x, y, z)$ of (12-77a) must satisfy the homogeneous vector wave equation. These allow us to relate the propagation constant k_z to k_x, k_y and $k = (\omega\sqrt{\mu\epsilon})$, by

$$k_z^2 = k^2 - (k_x^2 + k_y^2) \tag{12-80}$$

or

$$k_z = \begin{cases} +[k^2 - (k_x^2 + k_y^2)]^{1/2} & \text{when } k^2 \geq k_x^2 + k_y^2 \quad (12\text{-}80a) \\ -j[(k_x^2 + k_y^2) - k^2]^{1/2} & \text{when } k^2 < k_x^2 + k_y^2 \quad (12\text{-}80b) \end{cases}$$

This is left as an exercise to the reader. The form of k_z as given by (12-80a) contributes to the propagating waves (radiation field) of (12-76) and (12-77a) whereas that of (12-80b) contributes to the evanescent waves. Since the field in the far-zone of the antenna is of the radiation type, its contribution comes from the part of the k_x, k_y spectrum which satisfies (12-80a). The values of k_x and k_y in (12-80)-(12-80b) are analogous to the eigenvalues for the fields inside a rectangular waveguide [12]. In

INTEL-1045
U.S. Patent 7,151,430

addition, k_z is analogous to the propagation constant for waveguides which is used to define cutoff.

To find the relation between f_z and f_x, f_y, we proceed as follows. In the source-free region ($z > 0$) the field $\mathbf{E}(x, y, z)$, in addition to satisfying the vector wave equation, must also be solenoidal so that

$$\nabla \cdot \mathbf{E}(x, y, z) = \nabla \cdot \left\{ \frac{1}{4\pi^2} \int_{-\infty}^{+\infty} \int_{-\infty}^{+\infty} \mathbf{f}(k_x, k_y) e^{-j\mathbf{k}\cdot\mathbf{r}}\, dk_x\, dk_y \right\} = 0 \quad (12\text{-}81)$$

Interchanging differentiation with integration and using the vector identity

$$\nabla \cdot (\alpha \mathbf{A}) = \alpha \nabla \cdot \mathbf{A} + \mathbf{A} \cdot \nabla \alpha \quad (12\text{-}82)$$

reduces (12-81) to

$$\frac{1}{4\pi^2} \int_{-\infty}^{+\infty} \int_{-\infty}^{+\infty} [\mathbf{f} \cdot \nabla (e^{-j\mathbf{k}\cdot\mathbf{r}})]\, dk_x\, dk_y = 0 \quad (12\text{-}83)$$

since $\nabla \cdot \mathbf{f}(k_x, k_y) = 0$. Equation (12-83) is satisfied provided that

$$\mathbf{f} \cdot \nabla e^{-j\mathbf{k}\cdot\mathbf{r}} = -j\mathbf{f} \cdot \mathbf{k} e^{-j\mathbf{k}\cdot\mathbf{r}} = 0 \quad (12\text{-}84)$$

or

$$\mathbf{f} \cdot \mathbf{k} = (\mathbf{f}_t + \hat{\mathbf{a}}_z f_z) \cdot \mathbf{k} = 0 \quad (12\text{-}84a)$$

or

$$f_z = -\frac{\mathbf{f}_t \cdot \mathbf{k}}{k_z} = -\frac{(f_x k_x + f_y k_y)}{k_z} \quad (12\text{-}84b)$$

From (12-84b) it is evident that f_z can be formed once f_x and f_y are known.

All three components of $\mathbf{f}$ (f_x, f_y and f_z) can be found, using (12-77b) and (12-78), provided the two components of $\mathbf{E}$ (E_x, E_y) at $z = 0$, which is the plane of the aperture and ground plane of Figure 12.26(a), are known. Because E_x and E_y along the $z = 0$ plane are zero outside the bounds of the aperture ($|x| > a/2$, $|y| > b/2$), (12-77b) and (12-78) reduce for f_x and f_y to

$$\boxed{f_x(k_x, k_y) = \int_{-b/2}^{+b/2} \int_{-a/2}^{+a/2} E_{xa}(x', y', z' = 0) e^{+j(k_x x' + k_y y')}\, dx'\, dy'} \quad (12\text{-}85a)$$

$$\boxed{f_y(k_x, k_y) = \int_{-b/2}^{+b/2} \int_{-a/2}^{+a/2} E_{ya}(x', y', z' = 0) e^{+j(k_x x' + k_y y')}\, dx'\, dy'} \quad (12\text{-}85b)$$

where primes indicate source points. $E_{xa}(x', y', z' = 0)$ and $E_{ya}(x', y', z' = 0)$, which represent the tangential components of the electric field over the aperture, are the only fields that need to be known. Once f_x and f_y are found by using (12-85a) and (12-85b), f_z and $\mathscr{C}(k_x, k_y, z)$ can be formed using (12-84a) and (12-77c), respectively. Thus, the solution for $\mathbf{E}(x, y, z)$ for the aperture in Figure 12.26(a) is given by

$$\mathbf{E}(x, y, z) = \frac{1}{4\pi^2} \left\{ \iint_{k_z = [k^2 - (k_x^2 + k_y^2)]^{1/2}}^{k_x^2 + k_y^2 \le k^2} \mathscr{C}(k_x, k_y, z) e^{-j(k_x x + k_y y)}\, dk_x\, dk_y \right.$$

(Equation continues on top of page 625)

INTEL-1045
U.S. Patent 7,151,430

$$+ \iint_{\substack{k_x^2+k_y^2 > k^2 \\ k_z=-j\sqrt{(k_x^2+k_y^2)-k^2}}} \mathscr{C}(k_x, k_y, z) e^{-j(k_x x + k_y y)}\, dk_x\, dk_y \Bigg\} \tag{12-86}$$

$$\boxed{\mathscr{C}(k_x, k_y, z) = \left[\hat{\mathbf{a}}_x f_x + \hat{\mathbf{a}}_y f_y - \hat{\mathbf{a}}_z \left(\frac{f_x k_x + f_y k_y}{k_z}\right)\right] e^{-jk_z z}} \tag{12-86a}$$

where f_x and f_y are given by (12-85a) and (12-85b).

In summary, the field radiated by the aperture of Figure 12.26(a) can be found by the following procedure:

1. Specify the tangential components of the **E**-field (E_{xa} and E_{ya}) over the bounds of the aperture.
2. Find f_x and f_y using (12-85a) and (12-85b), respectively.
3. Find f_z using (12-85b).
4. Find $\mathscr{C}(k_x, k_y, z)$ using (12-86a).
5. Formulate $\mathbf{E}(x, y, z)$ using (12-86).

This completes the solution for $\mathbf{E}(x, y, z)$. However, as is evident from (12-86), the integration is quite difficult even for the simplest of problems. However, if the observations are restricted in the far-field region, many simplifications in performing the integrations can result. This was apparent in Chapters 4, 5 and in others. In many practical problems, the far-zone is usually the region of greatest importance. Since it is also known that for all antennas the fields in the far-zone are primarily of the radiated type (*propagating waves*), then only the first integral in (12-86) contributes in that region.

In the next section, our attention is directed toward the evaluation of (12-86a) or (12-73) in the far-zone region (large values of kr). This is accomplished by evaluating (12-73) asymptotically for large values of kr by the method of *Stationary Phase* [18], [19].

To complete the formulation of the radiated fields in all regions, let us outline the procedure to find $\mathbf{H}(x, y, z)$. From Maxwell's equations

$$\begin{aligned}\mathbf{H}(x, y, z) &= -\frac{1}{j\omega\mu} \nabla \times \mathbf{E}(x, y, z) \\ &= -\frac{1}{j\omega\mu} \nabla \times \left[\frac{1}{4\pi^2} \int_{-\infty}^{+\infty} \int_{-\infty}^{+\infty} \mathbf{f}(k_x, k_y) e^{-j\mathbf{k}\cdot\mathbf{r}}\, dk_x\, dk_y\right]\end{aligned} \tag{12-87}$$

Interchanging integration with differentiation and using the vector identity

$$\nabla \times (\alpha \mathbf{A}) = \alpha \nabla \times \mathbf{A} + (\nabla\alpha) \times \mathbf{A} \tag{12-88}$$

reduces (12-87) to

$$\mathbf{H}(x, y, z) = -\frac{1}{4\pi^2 k\eta} \int_{-\infty}^{+\infty} \int_{-\infty}^{+\infty} (\mathbf{f} \times \mathbf{k}) e^{-j\mathbf{k}\cdot\mathbf{r}} dk_x\, dk_y \tag{12-89}$$

since $\nabla \times \mathbf{f}(k_x, k_y) = 0$ and $\nabla(e^{-j\mathbf{k}\cdot\mathbf{r}}) = -j\mathbf{k}e^{-j\mathbf{k}\cdot\mathbf{r}}$ from (12-84).

12.9.3 Asymptotic Evaluation of Radiated Field

The main objective in this section is the evaluation of (12-73) or (12-86a) for observations made in the far-field. For most practical antennas, the field distribution on the

INTEL-1045
U.S. Patent 7,151,430

aperture is such that an exact evaluation of (12-73) in closed form is not possible. However, if the observations are restricted to the far-field region (large kr), the integral evaluation becomes less complex. This was apparent in Chapters 4, 5, and others. The integral of (12-73) will be evaluated asymptotically for large values of kr using the method of *Stationary Phase* (Appendix VIII) [18], [19].

The stationary phase method assumes that the main contribution to the integral of (12-73) comes from values of k_x and k_y where $\mathbf{k} \cdot \mathbf{r}$ does not change for first order changes in k_x and k_y. That is to say $\mathbf{k} \cdot \mathbf{r}$ remains stationary at those points. For the other values of k_x and k_y, $\mathbf{k} \cdot \mathbf{r}$ changes very rapidly and the function $e^{-j\mathbf{k}\cdot\mathbf{r}}$ oscillates very rapidly between the values of $+1$ and -1. Assuming that $\mathbf{f}(k_x, k_y)$ is a slowly varying function of k_x and k_y, the integrand of (12-73) oscillates very rapidly outside the stationary points so that the contribution to the integral from that region is negligible. As the observation point approaches infinity, the contributions to the integral from the region outside the stationary points is zero. For practical applications, the observation point cannot be at infinity. However, it will be assumed to be far enough *such that the major contributions come from the stationary points.*

The first task in the asymptotic evaluation of (12-73) is to find the stationary points of $\mathbf{k} \cdot \mathbf{r}$. For that $\mathbf{k} \cdot \mathbf{r}$ is written as

$$\mathbf{k} \cdot \mathbf{r} = (\hat{\mathbf{a}}_x k_x + \hat{\mathbf{a}}_y k_y + \hat{\mathbf{a}}_z k_z) \cdot \hat{\mathbf{a}}_r r \tag{12-90}$$

Using the inverse transformation of (4-5), (12-90) can be written as

$$\mathbf{k} \cdot \mathbf{r} = r(k_x \sin\theta\cos\phi + k_y \sin\theta\sin\phi + k_z \cos\theta) \tag{12-91}$$

which reduces, using (12-80a) to

$$\mathbf{k} \cdot \mathbf{r} = r[k_x \sin\theta\cos\phi + k_y \sin\theta\sin\phi + \sqrt{k^2 - k_x^2 - k_y^2}\cos\theta] \tag{12-92}$$

The stationary points can be found by

$$\frac{\partial(\mathbf{k} \cdot \mathbf{r})}{\partial k_x} = 0 \tag{12-93a}$$

$$\frac{\partial(\mathbf{k} \cdot \mathbf{r})}{\partial k_y} = 0 \tag{12-93b}$$

Using (12-92) and (12-80), (12-93a) and (12-93b) reduce to

$$\frac{\partial(\mathbf{k} \cdot \mathbf{r})}{\partial k_x} = r\left(\sin\theta\cos\phi - \frac{k_x}{k_z}\cos\theta\right) = 0 \tag{12-94a}$$

$$\frac{\partial(\mathbf{k} \cdot \mathbf{r})}{\partial k_y} = r\left(\sin\theta\sin\phi - \frac{k_y}{k_z}\cos\theta\right) = 0 \tag{12-94b}$$

whose solutions are given, respectively, by

$$k_x = k_z \frac{\sin\theta\cos\phi}{\cos\theta} \tag{12-95a}$$

$$k_y = k_z \frac{\sin\theta\sin\phi}{\cos\theta} \tag{12-95b}$$

Using (12-95a) and (12-95b), (12-80) can be written as

$$k^2 = k_z^2 + k_x^2 + k_y^2 = k_z^2\left(1 + \frac{\sin^2\theta}{\cos^2\theta}\right) \tag{12-96}$$

INTEL-1045
U.S. Patent 7,151,430

which reduces for k_z to

$$k_z = k\cos\theta \tag{12-97}$$

With the aid of (12-97), the stationary point of (12-95a) and (12-95b) simplify to

$$k_x = k\sin\theta\cos\phi = k_1 \tag{12-98a}$$

$$k_y = k\sin\theta\sin\phi = k_2 \tag{12-98b}$$

The function $\mathbf{k}\cdot\mathbf{r}$ can be expanded into a Taylor series, about the stationary point k_1, k_2, and it can be approximated by the zero, first, and second order terms. That is,

$$\begin{aligned}\mathbf{k}\cdot\mathbf{r} \simeq \mathbf{k}\cdot\mathbf{r}\Big|_{k_1,k_2} &+ \frac{\partial(\mathbf{k}\cdot\mathbf{r})}{\partial k_x}\Big|_{k_1,k_2}(k_x - k_1) + \frac{\partial(\mathbf{k}\cdot\mathbf{r})}{\partial k_y}\Big|_{k_1,k_2}(k_y - k_2)\\ &+ \frac{1}{2}\frac{\partial^2(\mathbf{k}\cdot\mathbf{r})}{\partial k_x^2}\Big|_{k_1,k_2}(k_x - k_1)^2 + \frac{1}{2}\frac{\partial^2(\mathbf{k}\cdot\mathbf{r})}{\partial k_y^2}\Big|_{k_1,k_2}(k_y - k_2)^2\\ &+ \frac{\partial^2(\mathbf{k}\cdot\mathbf{r})}{\partial k_x\partial k_y}\Big|_{k_1,k_2}(k_x - k_1)(k_y - k_2)\end{aligned} \tag{12-99}$$

Since the second and third terms vanish at the stationary point $k_x = k_1$ and $k_y = k_2$, (12-99) can be expressed as

$$\mathbf{k}\cdot\mathbf{r} = \mathbf{k}\cdot\mathbf{r}\Big|_{k_1,k_2} - A\xi^2 - B\eta^2 - C\xi\eta \tag{12-100}$$

where

$$A = -\frac{1}{2}\frac{\partial^2(\mathbf{k}\cdot\mathbf{r})}{\partial k_x^2}\Big|_{k_1,k_2} \tag{12-100a}$$

$$B = -\frac{1}{2}\frac{\partial^2(\mathbf{k}\cdot\mathbf{r})}{\partial k_y^2}\Big|_{k_1,k_2} \tag{12-100b}$$

$$C = -\frac{\partial^2(\mathbf{k}\cdot\mathbf{r})}{\partial k_x\partial k_y}\Big|_{k_1,k_2} \tag{12-100c}$$

$$\xi = (k_x - k_1) \tag{12-100d}$$

$$\eta = (k_y - k_2) \tag{12-100e}$$

Using (12-97)-(12-98b), (12-90) reduces to

$$\mathbf{k}\cdot\mathbf{r}\Big|_{k_1,k_2} = kr \tag{12-101}$$

Similarly, with the aid of (12-92), A, B, and C can be written, after a few manipulations, as

$$A = -\frac{1}{2}\frac{\partial^2(\mathbf{k}\cdot\mathbf{r})}{\partial k_x^2}\Big|_{k_1,k_2} = \frac{r}{2k}\left(1 + \frac{\sin^2\theta\cos^2\phi}{\cos^2\theta}\right) \tag{12-102a}$$

$$B = -\frac{1}{2}\frac{\partial^2(\mathbf{k}\cdot\mathbf{r})}{\partial k_y^2}\Big|_{k_1,k_2} = \frac{r}{2k}\left(1 + \frac{\sin^2\theta\sin^2\phi}{\cos^2\theta}\right) \tag{12-102b}$$

$$C = -\frac{\partial^2(\mathbf{k}\cdot\mathbf{r})}{\partial k_x\partial k_y}\Big|_{k_1,k_2} = \frac{r}{k}\frac{\sin^2\theta}{\cos^2\theta}\cos\phi\sin\phi \tag{12-102c}$$

INTEL-1045
U.S. Patent 7,151,430

Thus (12-73) can be approximated around the stationary point $k_x = k_1$ and $k_y = k_2$, which contributes mostly to the integral, by

$$\mathbf{E}(x, y, z) \simeq \frac{1}{4\pi^2}\iint_{S_{1,2}} \mathbf{f}(k_x = k_1, k_y = k_2) e^{-j(kr - A\xi^2 - B\eta^2 - C\xi\eta)}\, d\xi\, d\eta \quad (12\text{-}103)$$

or

$$\mathbf{E}(x, y, z) \simeq \frac{1}{4\pi^2}\mathbf{f}(k_1, k_2) e^{-jkr}\iint_{S_{1,2}} e^{+j(A\xi^2 + B\eta^2 + C\xi\eta)}\, d\xi\, d\eta \quad (12\text{-}103a)$$

where $S_{1,2}$ is the surface near the stationary point.

The integral of (12-103a) can be evaluated with the method of *Stationary Phase*. That is, (see Appendix VIII)

$$\boxed{\iint_{S_{1,2}} e^{j(A\xi^2 + B\eta^2 + C\xi\eta)}\, d\xi\, d\eta = j\frac{2\pi\delta}{\sqrt{|4AB - C^2|}}} \quad (12\text{-}104)$$

$$\boxed{\delta = \begin{cases} +1 & \text{if } 4AB > C^2 \text{ and } A > 0 \\ -1 & \text{if } 4AB > C^2 \text{ and } A < 0 \\ -j & \text{if } 4AB < C^2 \end{cases}} \quad (12\text{-}104a)$$

With the aid of (12-102a)-(12-102c), the factor $4AB - C^2$ is

$$4AB - C^2 = \left(\frac{r}{k\cos\theta}\right)^2 \quad (12\text{-}105)$$

Since $4AB > C^2$ and $A > 0$, (12-103) reduces to

$$\iint_{S_{1,2}} e^{j(A\xi^2 + B\eta^2 + C\xi\eta)}\, d\xi\, d\eta = j\frac{2\pi k}{r}\cos\theta \quad (12\text{-}106)$$

and (12-103a) to

$$\mathbf{E}(r, \theta, \phi) = j\frac{ke^{-jkr}}{2\pi r}[\cos\theta\, \mathbf{f}(k_1 = k\sin\theta\cos\phi, k_2 = k\sin\theta\sin\phi)] \quad (12\text{-}107)$$

In the far-field region, only the θ and ϕ components of the electric and magnetic fields are dominant. Therefore, the E_θ and E_ϕ components of (12-107) can be written in terms of f_x and f_y. With the aid of (12-84b), $\mathbf{f}$ can be expressed as

$$\mathbf{f} = \hat{\mathbf{a}}_x f_x + \hat{\mathbf{a}}_y f_y + \hat{\mathbf{a}}_z f_z = \left[\hat{\mathbf{a}}_x f_x + \hat{\mathbf{a}}_y f_y - \hat{\mathbf{a}}_z \frac{(f_x k_x + f_y k_y)}{k_z}\right] \quad (12\text{-}108)$$

At the stationary point ($k_x = k_1 = k\sin\theta\cos\phi$, $k_y = k_2 = k\sin\theta\sin\phi$, $k_z = k\cos\theta$), (12-108) reduces to

$$\mathbf{f}(k_1, k_2) = \left[\hat{\mathbf{a}}_x f_x + \hat{\mathbf{a}}_y f_y - \hat{\mathbf{a}}_z \frac{\sin\theta}{\cos\theta}(f_x\cos\phi + f_y\sin\phi)\right] \quad (12\text{-}109)$$

Using the inverse transformation of (4-5), the θ and ϕ components of $\mathbf{f}$ can be written as

$$\boxed{f_\theta = \frac{f_x\cos\phi + f_y\sin\phi}{\cos\theta}} \quad (12\text{-}110a)$$

INTEL-1045
U.S. Patent 7,151,430

$$\boxed{f_\phi = -f_x \sin\phi + f_y \cos\phi} \tag{12-110b}$$

The **E**-field of (12-107) reduces, for the θ and ϕ components, to

$$\boxed{\mathbf{E}(r, \theta, \phi) \simeq j\frac{ke^{-jkr}}{2\pi r}[\hat{\mathbf{a}}_\theta(f_x \cos\phi + f_y \sin\phi) + \hat{\mathbf{a}}_\phi \cos\theta(-f_x \sin\phi + f_y \cos\phi)]} \tag{12-111}$$

and the **H**-field to

$$\mathbf{H}(r, \theta, \phi) = \sqrt{\frac{\epsilon}{\mu}}[\hat{\mathbf{a}}_r \times \mathbf{E}(r, \theta, \phi)] \tag{12-112}$$

where from (12-85a) and (12-85b)

$$\boxed{\begin{aligned} &f_x(k_x = k_1, k_y = k_2) \\ &= \int_{-b/2}^{+b/2}\int_{-a/2}^{+a/2} E_{xa}(x', y', z' = 0)\, e^{jk(x' \sin\theta\cos\phi + y' \sin\theta\sin\phi)}\, dx'\, dy' \end{aligned}} \tag{12-113a}$$

$$\boxed{\begin{aligned} &f_y(k_x = k_1, k_y = k_2) \\ &= \int_{-b/2}^{+b/2}\int_{-a/2}^{+a/2} E_{ya}(x', y', z' = 0)\, e^{jk(x' \sin\theta\cos\phi + y' \sin\theta\sin\phi)}\, dx'\, dy' \end{aligned}} \tag{12-113b}$$

To illustrate the frequency domain (*spectral*) techniques, the problem of a uniform illuminated aperture, which was previously analyzed in Section 12.5.1 using spatial methods, will be solved again using transform methods.

Example 12.7

A rectangular aperture of dimensions a and b is mounted on an infinite ground plane, as shown in Figure 12.26(a). Find the field radiated by it assuming that over the opening the electric field is given by

$$\mathbf{E}_a = \hat{\mathbf{a}}_y E_0, \qquad \begin{aligned} -a/2 \le x' \le a/2 \\ -b/2 \le y' \le b/2 \end{aligned}$$

where E_0 is a constant.

SOLUTION

From (12-113a) and (12-113b)

$$f_x = 0$$
$$f_y = E_0 \int_{-b/2}^{+b/2} e^{jky' \sin\theta\sin\phi}\, dy' \int_{-a/2}^{+a/2} e^{jkx' \sin\theta\cos\phi}\, dx'$$

which, when integrated, reduces to

$$f_y = abE_0\left(\frac{\sin X}{X}\right)\left(\frac{\sin Y}{Y}\right)$$

INTEL-1045
U.S. Patent 7,151,430

$$X = \frac{ka}{2} \sin\theta \cos\phi$$

$$Y = \frac{kb}{2} \sin\theta \sin\phi$$

The θ and ϕ components of (12-111) can be written as

$$E_\theta = j\frac{abkE_0 e^{-jkr}}{2\pi r}\left\{ \sin\phi \left[\frac{\sin X}{X}\right]\left[\frac{\sin Y}{Y}\right]\right\}$$

$$E_\phi = j\frac{abkE_0 e^{-jkr}}{2\pi r}\left\{ \cos\theta\cos\phi \left[\frac{\sin X}{X}\right]\left[\frac{\sin Y}{Y}\right]\right\}$$

which are identical to those of (12-23b) and (12-23c), respectively.

12.9.4 Dielectric Covered Apertures

The transform (*spectral*) technique can easily be extended to determine the field radiated by dielectric-covered apertures [20], [21]. For the sake of brevity, the details will not be included here. However, it can be shown that for a single lossless dielectric sheet cover of thickness h, dielectric constant ϵ_r, unity relative permeability, and free-space phase constant k_0, the far-zone radiated field E_θ, E_ϕ of the covered aperture of Figure 12.26(b) are related to E_θ^0, E_ϕ^0 of the uncovered aperture of Figure 12.26(a) by

$$\boxed{E_\theta(r, \theta, \phi) = f(\theta)\, E_\theta^0(r, \theta, \phi)} \qquad (12\text{-}114a)$$

$$\boxed{E_\phi(r, \theta, \phi) = g(\theta)\, E_\phi^0(r, \theta, \phi)} \qquad (12\text{-}114b)$$

where

E_θ, E_ϕ = field components of dielectric covered aperture [Fig. 12.26(b)]

E_θ^0, E_ϕ^0 = field components of uncovered aperture [Fig. 12.26(a)]

$$\boxed{f(\theta) = \frac{e^{jk_0 h\cos\theta}}{\cos\psi + jZ_h \sin\psi}} \qquad (12\text{-}114c)$$

$$\boxed{g(\theta) = \frac{e^{jk_0 h\cos\theta}}{\cos\psi + jZ_e \sin\psi}} \qquad (12\text{-}114d)$$

$$\boxed{\psi = k_0 h\sqrt{\epsilon_r - \sin^2\theta}} \qquad (12\text{-}114e)$$

$$\boxed{Z_e = \frac{\cos\theta}{\sqrt{\epsilon_r - \sin^2\theta}}} \qquad (12\text{-}114f)$$

INTEL-1045
U.S. Patent 7,151,430

$$\boxed{Z_h = \frac{\sqrt{\epsilon_r - \sin^2\theta}}{\epsilon_r \cos\theta}} \tag{12-114g}$$

The above relations do not include surface wave contributions which can be taken into account but are beyond the scope of this section [20].

To investigate the effect of the dielectric sheet, far-zone principal E- and H-plane patterns were computed for a rectangular waveguide shown in Figure 12.26(b). The waveguide was covered with a single dielectric sheet, was operating in the dominant TE_{10} mode, and was mounted on an infinite ground plane. The E- and H-plane patterns are shown in Figure 12.27(a) and 12.27(b), respectively. In the E-plane patterns, it is evident that the surface impedance of the modified ground plane forces the normal electric field component to vanish along the surface ($\theta = \pi/2$). This is similar to the effects experienced by the patterns of the vertical dipole above ground shown in Figure 4.28. Since the H-plane patterns have vanishing characteristics when the aperture is radiating in free-space, the presence of the dielectric sheet has a very small overall effect. This is similar to the effects experienced by the patterns of a horizontal dipole above ground shown in Figure 4.30. However, both the E- and H-plane patterns become more broad near the surface, and more narrow elsewhere, as the thickness increases.

12.9.5 Aperture Admittance

Another parameter of interest, especially when the antenna is used as a diagnostic tool, is its terminating impedance or admittance. In this section, using Fourier transform (*spectral*) techniques, the admittance of an aperture antenna mounted on an infinite ground plane and radiating into free-space will be formulated. Computations will be presented for a parallel-plate waveguide. The techniques can best be presented by considering a specific antenna configuration and field distribution. Similar steps can be used for any other geometry and field distribution.

The geometrical arrangement of the aperture antenna under consideration is shown in Figure 12.26(a). It consists of a rectangular waveguide mounted on an infinite ground plane. It is assumed that the field distribution, *above cutoff*, is that given by the TE_{10} mode, or

$$\mathbf{E}_a = \hat{\mathbf{a}}_y E_0 \cos\left(\frac{\pi}{a}x'\right) \qquad \begin{matrix} -a/2 \le x' \le a/2 \\ -b/2 \le y' \le b/2 \end{matrix} \tag{12-115}$$

where E_0 is a constant. The aperture admittance is defined as

$$Y_a = \frac{2P^*}{|V|^2} \tag{12-116}$$

where

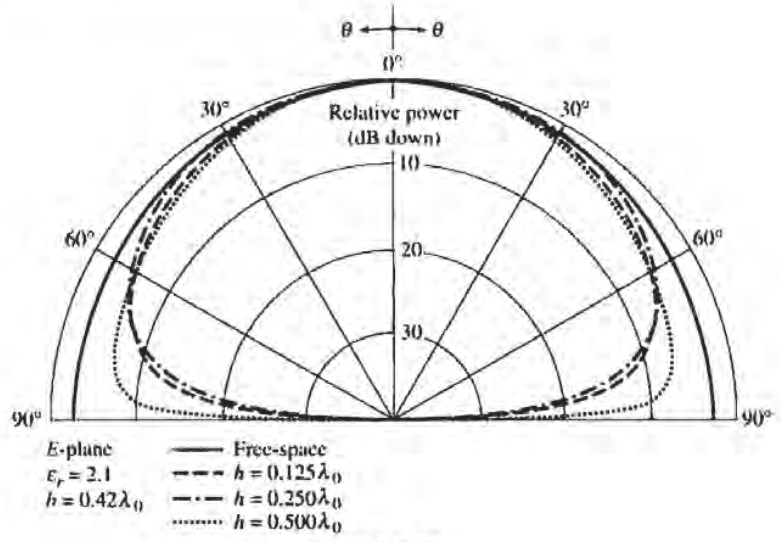
P^* = conjugate of complex power transmitted by the aperture

V = aperture reference voltage.

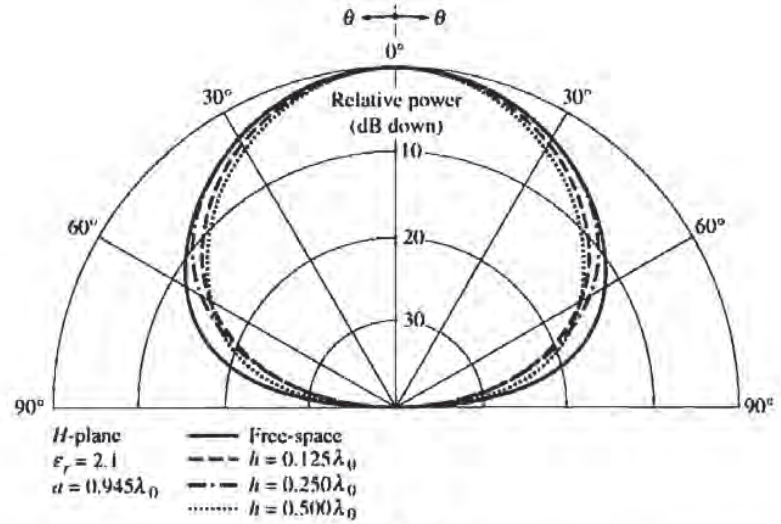
The complex power transmitted by the aperture can be written as

$$P = \frac{1}{2}\int_{S_a}\int [\mathbf{E}(x', y', z' = 0) \times \mathbf{H}^*(x', y', z' = 0)] \cdot \hat{\mathbf{a}}_z \, dx' \, dy' \tag{12-117}$$

INTEL-1045
U.S. Patent 7,151,430



(a) E-plane



(b) H-plane

Figure 12.27 Amplitude radiation patterns of a dielectric covered waveguide mounted on an infinite ground plane and with a TE_{10} mode aperture field distribution.

where S_a is the aperture of the antenna. $\mathbf{E}(x', y', z' = 0)$ and $\mathbf{H}(x', y', z' = 0)$ represent the total electric and magnetic fields at the aperture including those of the modes which operate below cutoff and contribute to the imaginary power. For the field distribution given by (12-115), (12-117) reduces to

$$P = -\frac{1}{2}\int_{S_a}\int [E_y(x', y', z' = 0)H_x^*(x', y', z' = 0)]\, dx'\, dy' \quad (12\text{-}117a)$$

The amplitude coefficients of all modes that can exist within the waveguide, propagating and nonpropagating, can be evaluated provided the total tangential **E**- and/or **H**-field at any point within the waveguide is known. Assuming that (12-115)

INTEL-1045
U.S. Patent 7,151,430

represents the total tangential E-field, it allows the determination of all mode coefficients. Even though this can be accomplished, the formulation of (12-117a) in the spatial domain becomes rather complex [22].

An alternate and simpler method in the formulation of the aperture admittance is to use Fourier transforms. By Parseval's theorem of (12-72c), (12-117a) can be written as

$$P = -\frac{1}{2}\int_{-\infty}^{+\infty}\int_{-\infty}^{+\infty} E_y(x', y', z' = 0)\, H_x^*(x', y', z' = 0)\, dx'\, dy'$$

$$= -\frac{1}{8\pi^2}\int_{-\infty}^{+\infty}\int_{-\infty}^{+\infty} \mathscr{E}_y(k_x, k_y)\, \mathscr{H}_x^*(k_x, k_y)\, dk_x\, dk_y \tag{12-118}$$

where the limits of the first integral have been extended to infinity since $E_y(x', y', z' = 0)$ vanishes outside the physical bounds of the aperture. $\mathscr{E}_y(k_x, k_y)$ and $\mathscr{H}_x(k_x, k_y)$ are the Fourier transforms of the aperture E- and H-fields, respectively.

The transform $\mathscr{E}(k_x, k_y, z = 0)$ is obtained from (12-78) while $\mathscr{H}(k_x, k_y, z = 0)$ can be written, by referring to (12-89), as

$$\mathscr{H}(k_x, k_y, z = 0) = -\frac{1}{k\eta}(\mathbf{f} \times \mathbf{k}) \tag{12-119}$$

For the problem at hand, the transforms $\mathscr{E}_y$ and $\mathscr{H}_x$ are given by

$$\mathscr{E}_y(k_x, k_y) = f_y(k_x, k_y) \tag{12-120}$$

$$\mathscr{H}_x(k_x, k_y) = -\frac{1}{k\eta}\left(k_z + \frac{k_y^2}{k_z}\right) f_y = -\frac{1}{k\eta}\left(\frac{k^2 - k_x^2}{k_z}\right) f_y \tag{12-121}$$

Using (12-77b) and (12-115), (12-120) reduces to

$$f_y(k_x, k_y) = E_0 \int_{-b/2}^{+b/2}\int_{-a/2}^{+a/2} \cos\left(\frac{\pi}{a}x'\right) e^{j(k_x x' + k_y y')}\, dx'\, dy'$$

$$f_y(k_x, k_y) = \left(\frac{\pi ab}{2}\right) E_0 \left[\frac{\cos X}{(\pi/2)^2 - (X)^2}\right]\left[\frac{\sin Y}{Y}\right] \tag{12-122}$$

where

$$X = \frac{k_x a}{2} \tag{12-122a}$$

$$Y = \frac{k_y b}{2} \tag{12-122b}$$

Substituting (12-120)–(12-122b) into (12-118) leads to

$$P = \frac{(\pi ab E_0)^2}{32\pi^2 k\eta}\int_{-\infty}^{+\infty}\int_{-\infty}^{+\infty}\left\{\frac{(k^2 - k_x^2)}{k_z^*}\left[\frac{\cos X}{(\pi/2)^2 - (X)^2}\right]^2\left[\frac{\sin Y}{Y}\right]^2\right\} dk_x\, dk_y \tag{12-123}$$

If the reference aperture voltage is given by

$$V = \frac{ab}{\sqrt{2}} E_0 \tag{12-124}$$

the aperture admittance can be written as

INTEL-1045
U.S. Patent 7,151,430

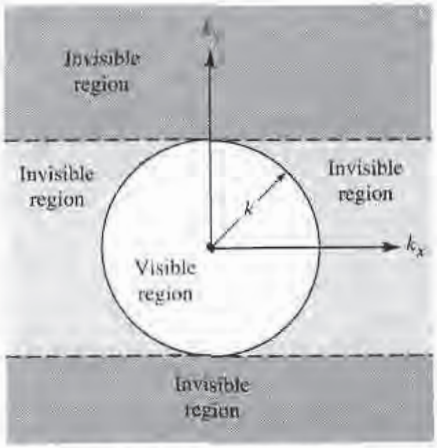


Figure 12.28 Visible and invisible regions in k-space.

$$Y_a = \frac{2P^*}{|V|^2} = \frac{1}{8k\eta}\int_{-\infty}^{+\infty}\left\{\left[\frac{\sin\left(\frac{k_y b}{2}\right)}{\frac{k_y b}{2}}\right]^2 \int_{-\infty}^{+\infty}\frac{(k^2 - k_x^2)}{k_z} \times \left[\frac{\cos\left(\frac{k_x a}{2}\right)}{\left(\frac{\pi}{2}\right)^2 - \left(\frac{k_x a}{2}\right)^2}\right]^2 dk_x\right\} dk_y \tag{12-125}$$

where k_z is given by (12-80a) and (12-80b). As stated before, the values of k_z as given by (12-80a) contribute to the radiated (real) power and those of (12-80b) contribute to the reactive (imaginary) power. Referring to Figure 12.28, values of k_x and k_y within the circle contribute to the aperture conductance, and the space is referred to as the *visible region*. Values of k_x and k_y outside the circle contribute to the aperture susceptance and constitute the *invisible region*. Thus (12-125) can be separated into its real and imaginary parts, and it can be written as

$$Y_a = G_a + jB_a \tag{12-126}$$

$$G_a = \frac{1}{4k\eta}\int_0^k \left[\frac{\sin\left(\frac{k_y b}{2}\right)}{\frac{k_y b}{2}}\right]^2 \left\{\int_0^{\sqrt{k^2 - k_y^2}} \frac{(k^2 - k_x^2)}{[k^2 - (k_x^2 + k_y^2)]^{1/2}} \times \left[\frac{\cos\left(\frac{k_x a}{2}\right)}{\left(\frac{\pi}{2}\right)^2 - \left(\frac{k_x a}{2}\right)^2}\right]^2 dk_x\right\} dk_y \tag{12-126a}$$

INTEL-1045
U.S. Patent 7,151,430

$$
\begin{aligned}
B_a = -\frac{1}{4k\eta}\Bigg\{ & \int_0^k \left[\frac{\sin\left(\frac{k_y b}{2}\right)}{\frac{k_y b}{2}}\right]^2 \left\{ \int_{\sqrt{k^2-k_y^2}}^{\infty} \frac{(k_x^2 - k^2)}{[(k_x^2 + k_y^2) - k^2]^{1/2}} \right. \\
& \left. \times \left[\frac{\cos\left(\frac{k_x a}{2}\right)}{\left(\frac{\pi}{2}\right)^2 - \left(\frac{k_x a}{2}\right)^2}\right]^2 dk_x \right\} dk_y \\
& + \int_k^{\infty} \left[\frac{\sin\left(\frac{k_y b}{2}\right)}{\frac{k_y b}{2}}\right]^2 \left\{ \int_0^{\infty} \frac{(k_x^2 - k^2)}{[(k_x^2 + k_y^2) - k^2]^{1/2}} \right. \\
& \left. \left. \times \left[\frac{\cos\left(\frac{k_x a}{2}\right)}{\left(\frac{\pi}{2}\right)^2 - \left(\frac{k_x a}{2}\right)^2}\right]^2 dk_x \right\} \right\} dk_y
\end{aligned}
\tag{12-126b}
$$

The first term in (12-126b) takes into account the contributions from the strip outside the circle for which $k_y < k$, and the second term includes the remaining space outside the circle.

The numerical evaluation of (12-126a) and (12-126b) is complex and will not be attempted here. Computations for the admittance of rectangular apertures radiating into lossless and lossy half-spaces have been carried out and appear in the literature [23]–[27]. Various ingenious techniques have been used to evaluate these integrals.

Because of the complicated nature of (12-126a) and (12-126b) to obtain numerical data, a simpler configuration will be considered as an example.

Example 12.8

A parallel plate waveguide is mounted on an infinite ground plane, as shown in Figure 12.29. Assuming the total electric field at the aperture is given by

$$\mathbf{E}_a = \hat{\mathbf{a}}_y E_0 \qquad -b/2 \le y' \le b/2$$

where E_0 is a constant, find the aperture admittance assuming the aperture voltage is given by $V = bE_0$.

SOLUTION

This problem bears a very close similarity to that of Figure 12.26(a), and most of the results of this example can be obtained almost directly from the previous formulation. Since the problem is two-dimensional, (12-120)–(12-122) reduce to

INTEL-1045
U.S. Patent 7,151,430

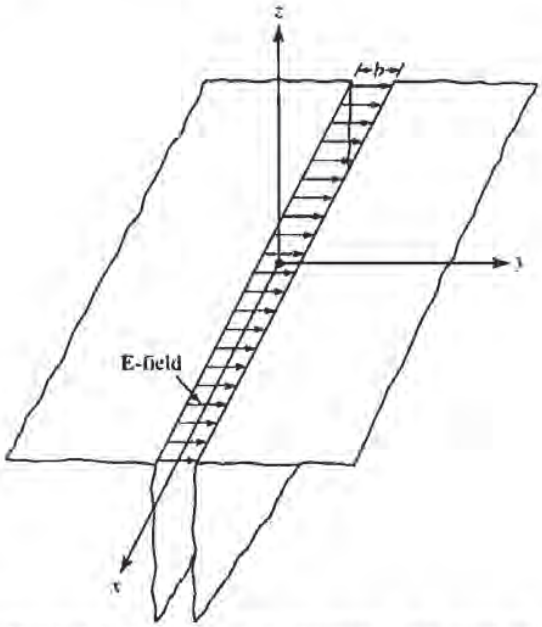


Figure 12.29 Parallel plate waveguide geometry and aperture field distribution.

$$\mathscr{E}_y(k_y) = f_y(k_y) = bE_0 \frac{\sin\left(\frac{k_y b}{2}\right)}{\frac{k_y b}{2}}$$

$$\mathscr{H}_x(k_y) = \frac{k}{\eta}\frac{f_y}{k_z} = \frac{kbE_0}{\eta k_z}\frac{\sin\left(\frac{k_y b}{2}\right)}{\frac{k_y b}{2}}$$

and (12-123) to

$$P = \frac{(bE_0)^2 k}{4\pi\eta}\int_{-\infty}^{+\infty}\frac{1}{k_z^*}\left[\frac{\sin\left(\frac{k_y b}{2}\right)}{\frac{k_y b}{2}}\right]^2 dk_y$$

Since the aperture voltage is given by $V = bE_0$, the aperture slot admittance (*per unit length along the x direction*) of (12-125) can be written as

$$Y_a = \frac{k}{2\pi\eta}\int_{-\infty}^{+\infty}\frac{1}{k_z}\left[\frac{\sin\left(\frac{k_y b}{2}\right)}{\frac{k_y b}{2}}\right]^2 dk_y$$

and the aperture slot conductance and susceptance of (12-126a) and (12-126b) as

INTEL-1045
U.S. Patent 7,151,430

$$G_a = \frac{k}{2\pi\eta}\int_{-k}^{k}\frac{1}{\sqrt{k^2 - k_y^2}}\left[\frac{\sin\left(\frac{k_y b}{2}\right)}{\frac{k_y b}{2}}\right]^2 dk_y$$

$$= \frac{k}{\pi\eta}\int_{0}^{k}\frac{1}{\sqrt{k^2 - k_y^2}}\left[\frac{\sin\left(\frac{k_y b}{2}\right)}{\frac{k_y b}{2}}\right]^2 dk_y$$

$$B_a = \frac{k}{2\pi\eta}\left\{\int_{-\infty}^{k}\frac{1}{\sqrt{k_y^2 - k^2}}\left[\frac{\sin\left(\frac{k_y b}{2}\right)}{\frac{k_y b}{2}}\right]^2 dk_y + \int_{k}^{\infty}\frac{1}{\sqrt{k_y^2 - k^2}}\left[\frac{\sin\left(\frac{k_y b}{2}\right)}{\frac{k_y b}{2}}\right]^2 dk_y\right\}$$

$$B_a = \frac{k}{\pi\eta}\int_{k}^{\infty}\frac{1}{\sqrt{k_y^2 - k^2}}\left[\frac{\sin\left(\frac{k_y b}{2}\right)}{\frac{k_y b}{2}}\right]^2 dk_y$$

If

$$w = \frac{b}{2}k_y$$

the expressions for the slot conductance and susceptance reduce to

$$G_a = \frac{2}{\eta\lambda}\int_{0}^{kb/2}\frac{1}{\sqrt{(kb/2)^2 - w^2}}\left(\frac{\sin w}{w}\right)^2 dw$$

$$B_a = \frac{2}{\eta\lambda}\int_{kb/2}^{\infty}\frac{1}{\sqrt{w^2 - (kb/2)^2}}\left(\frac{\sin w}{w}\right)^2 dw$$

The admittance will always be capacitive since B_a is positive.

The expressions for the slot conductance and susceptance (*per unit length along the x direction*) reduce for small values of kb to [5]

$$\left.\begin{aligned} G_a &\simeq \frac{\pi}{\eta\lambda}\left[1 - \frac{(kb)^2}{24}\right] \\ B_a &\simeq \frac{\pi}{\eta\lambda}\left[1 - 0.636\ln(kb)\right] \end{aligned}\right\} \quad \frac{b}{\lambda} < \frac{1}{10}$$

and for large values of kb to

INTEL-1045
U.S. Patent 7,151,430

$$\left.\begin{aligned} G_a &\simeq \frac{1}{\eta b} \\ B_a &\simeq \frac{\lambda}{\eta}\left(\frac{1}{\pi b}\right)^2\left[1-\frac{1}{2}\sqrt{\frac{\lambda}{b}}\cos\left(\frac{2b}{\lambda}+\frac{1}{4}\right)\pi\right] \end{aligned}\right\} \quad \frac{b}{\lambda}>1$$

Normalized values of λG_a and λB_a as a function of b/λ for an aperture radiating into free space are shown plotted in Figure 12.30.

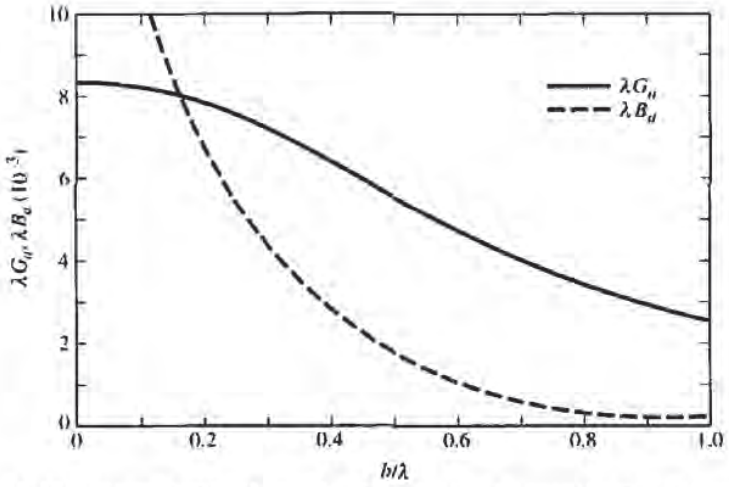


Figure 12.30 Normalized values of conductance and susceptance of narrow slot.

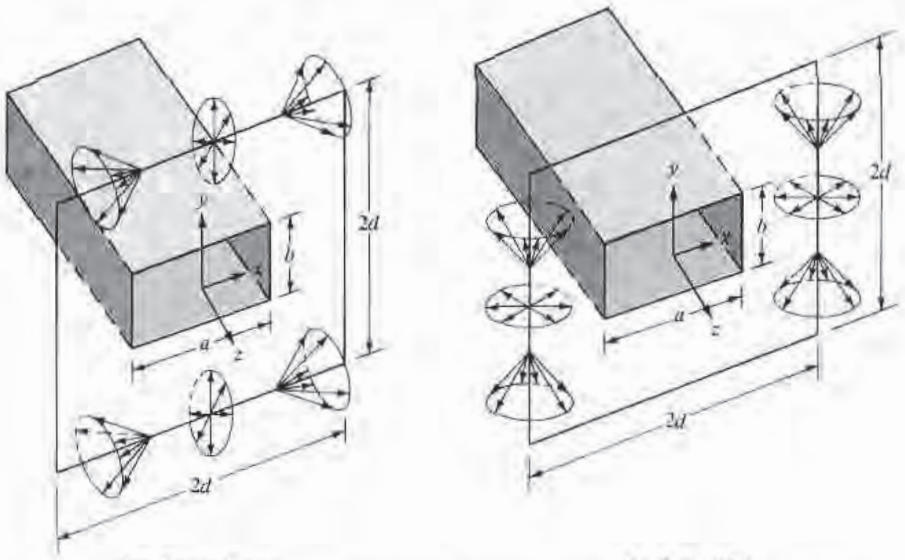
12.10 GROUND PLANE EDGE EFFECTS: THE GEOMETRICAL THEORY OF DIFFRACTION

Infinite size (physically and/or electrically) ground planes are not realizable in practice, but they can be approximated closely by very large structures. The radiation characteristics of antennas (current distribution, pattern, impedance, etc.) mounted on finite size ground planes can be modified considerably, especially in regions of very low intensity, by the effects of the edges. The ground plane edge diffractions for an aperture antenna are illustrated graphically in Figure 12.31. For these problems, rigorous solutions do not exist unless the object's surface can be described by curvilinear coordinates. Presently there are two methods that can be used conveniently to account for the edge effects. One technique is the *Moment Method* (MM) [28] discussed in Chapter 8 and the other is the *Geometrical Theory of Diffraction* (GTD) [29].

The Moment Method describes the solution in the form of an integral, and it can be used to handle arbitrary shapes. It mostly requires the use of a digital computer for numerical computations and, because of capacity limitations of computers, it is most computationally efficient for objects that are small electrically. Therefore, it is usually referred to as a *low-frequency asymptotic method.*

When the dimensions of the radiating object are large compared to the wavelength, *high-frequency asymptotic techniques* can be used to analyze many otherwise not mathematically tractable problems. One such technique, which has received consid-

INTEL-1045
U.S. Patent 7,151,430



(a) Upper-lower (b) Left-right

Figure 12.31 Diffraction mechanisms for an aperture mounted on a finite size ground plane (diffractions at upper-lower and left-right edges of the ground plane).

erable attention in the past few years, is the *G*eometrical *T*heory of *D*iffraction (GTD) which was originally developed by Keller [29]. The GTD is an extension of the classical *G*eometrical *O*ptics (GO; direct, reflected, and refracted rays), and it overcomes some of the limitations of GO by introducing a diffraction mechanism [2].

The diffracted field, which is determined by a generalization of Fermat's principle [2], [30], is initiated at points on the surface of the object where there is a discontinuity in the incident GO field (incident and reflected shadow boundaries). The phase of the field on a diffracted ray is assumed to be equal to the product of the optical length of the ray (from some reference point) and the phase constant of the medium. Appropriate phase jumps must be added as a ray passes through caustics.* The amplitude is assumed to vary in accordance with the principle of conservation of energy in a narrow tube of rays. The initial value of the field on a diffracted ray is determined from the incident field with the aid of an appropriate diffraction coefficient (which, in general, is a dyadic for electromagnetic fields). The diffraction coefficient is usually determined from the asymptotic solutions of the simplest boundary-value problems which have the same local geometry at the points of diffraction as the object(s) of investigation. Geometries of this type are referred to as *canonical* problems. One of the simplest geometries is a conducting wedge [31], [32]. Another is that of a conducting, smooth and convex, surface [33]–[35].

The primary objective in using the GTD to solve complicated geometries is to resolve each such problem into smaller components [8]–[10], [35]. The partitioning is made so that each smaller component represents a canonical geometry of a known solution. These techniques have also been applied for the modeling and analysis of antennas on airplanes [36], and they have combined both wedge and smooth con-

*A caustic is a point or a line through which all the rays of a wave pass. Examples of it are the focal point of a paraboloid (parabola of revolution) and the focal line of a parabolic cylinder. The field at the caustic is infinite because, in principle, an infinite number of rays pass through it.

INTEL-1045
U.S. Patent 7,151,430

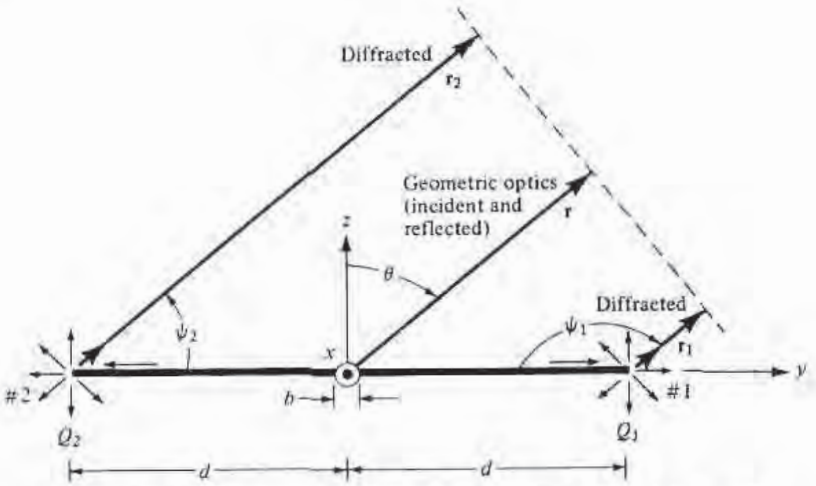


Figure 12.32 Aperture geometry in principal E-plane ($\phi = \pi/2$).

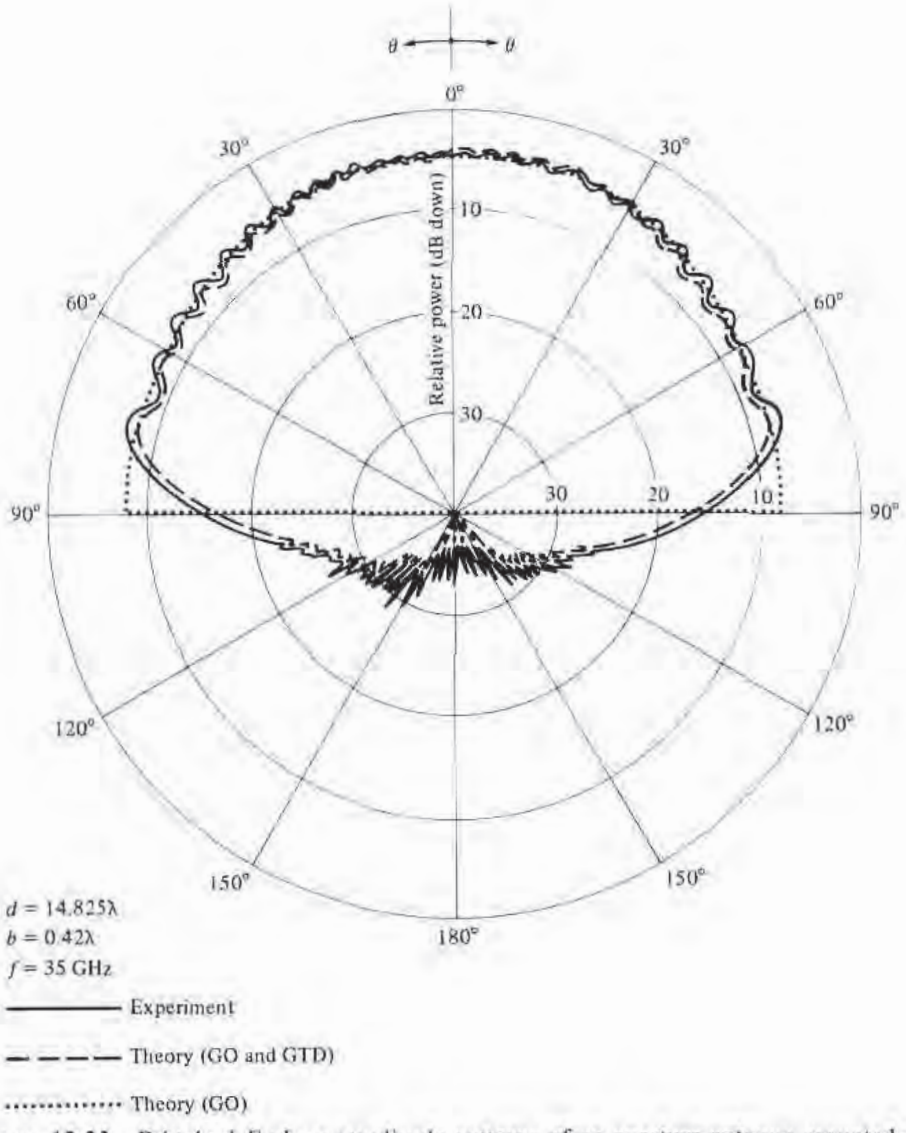


Figure 12.33 Principal E-plane amplitude patterns of an aperture antenna mounted on a finite size ground plane.

INTEL-1045
U.S. Patent 7,151,430

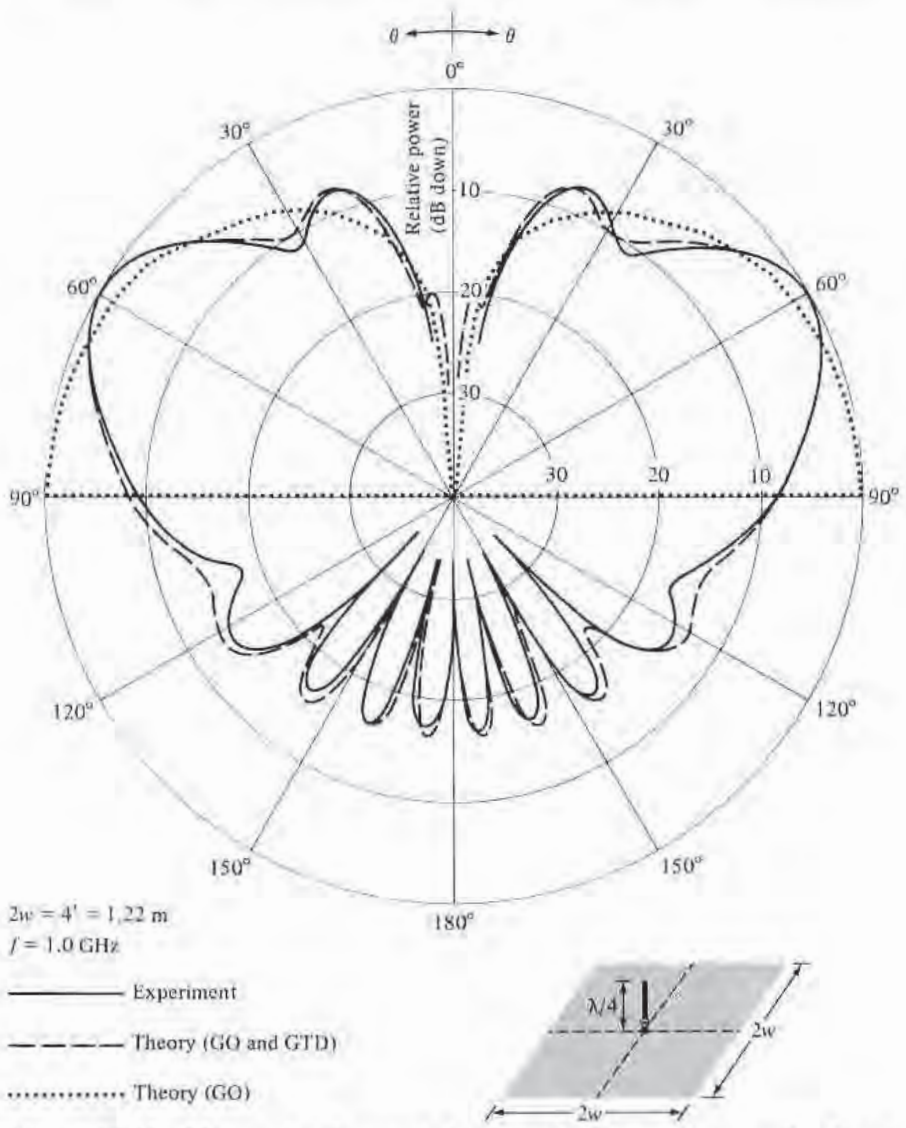


Figure 12.34 Measured and computed principal elevation plane amplitude patterns of a $\lambda/4$ monopole above infinite and finite square ground planes.

ducting surface diffractions [33], [35]. The ultimate solution is a superposition of the contributions from each canonical problem.

Some of the advantages of GTD are

1. It is simple to use.
2. It can be used to solve complicated problems that do not have exact solutions.
3. It provides physical insight into the radiation and scattering mechanisms from the various parts of the structure.
4. It yields accurate results which compare extremely well with experiments and other methods.
5. It can be combined with other techniques such as the Moment Method [37].

The derivation of the diffraction coefficients for a conducting wedge and their application are lengthy, and will not be repeated here. An extensive and detailed

INTEL-1045
U.S. Patent 7,151,430

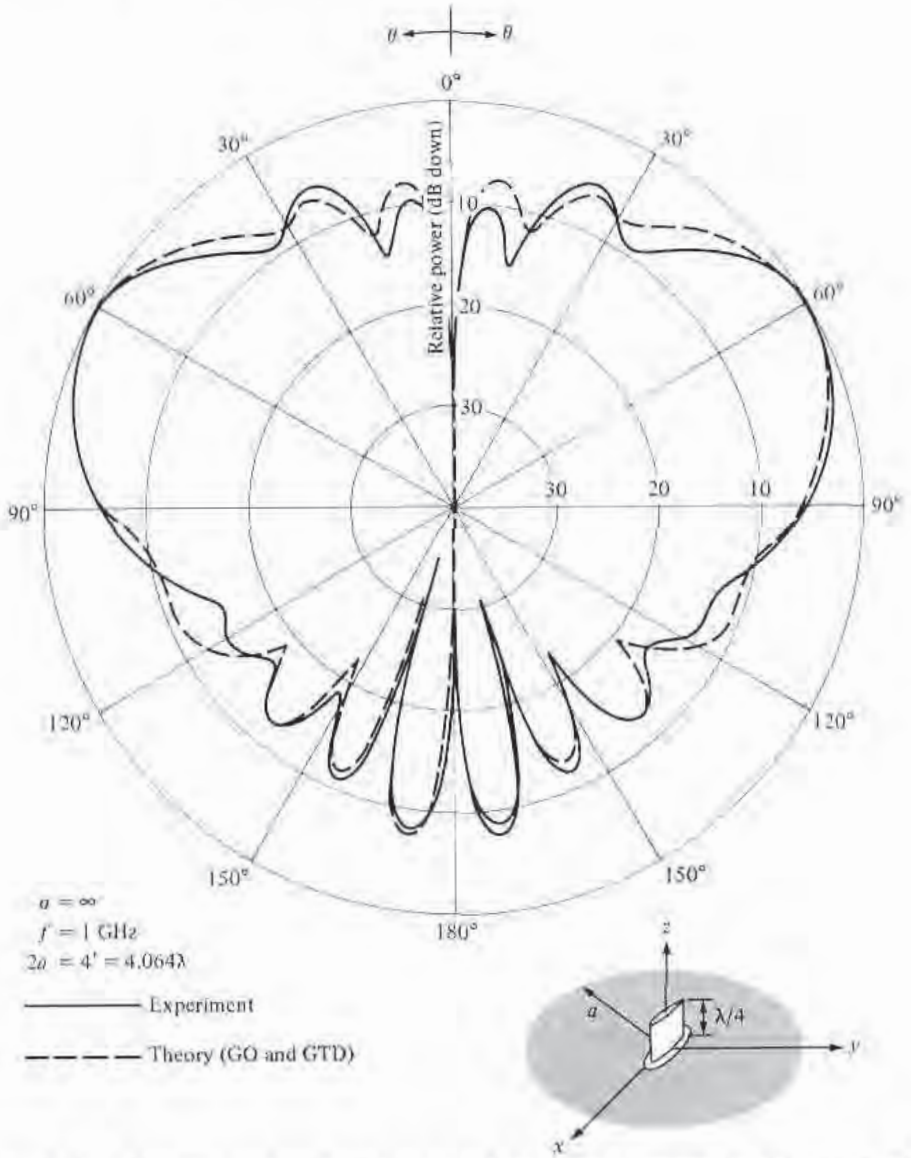


Figure 12.35 Measured and computed principal elevation plane amplitude patterns of a $\lambda/4$ monopole (blade) above a circular ground plane.

treatment of over 100 pages, for both antennas and scattering, can be found in [2]. However, to demonstrate the versatility and potential of the GTD, three examples are considered. The first is the *E*-plane pattern of a rectangular aperture of dimensions *a*,*b* mounted on a finite size ground plane, as shown in Figure 12.31. The GTD formulation along the *E*-plane includes the direct radiation and the fields diffracted by the two edges of the ground plane, as shown in Figure 12.32. The computed *E*-plane pattern along with the measured one are shown in Figure 12.33; an excellent agreement is indicated.

The two other examples considered here are the elevation pattern of a $\lambda/4$ monopole mounted on square and circular ground planes. The diffraction mechanism on the principal planes for these is the same as that of the aperture, which is shown in Figure 12.32. The corresponding principal elevation plane pattern of the monopole on the square ground plane is displayed in Figure 12.34 while that on the circular one is exhibited in Figure 12.35. For each case an excellent agreement is indicated with the measurements. It should be noted that the minor lobes near the symmetry axis

INTEL-1045
U.S. Patent 7,151,430

($\theta = 0°$ and $\theta = 180°$) for the circular ground plane of Figure 12.35 are more intense than the corresponding ones for the square ground plane of Figure 12.34. These effects are due to the ring-source radiation by the rim of the circular ground plane toward the symmetry axis [2], [10].

References

1. S. A. Schelkunoff, "Some Equivalence Theorems of Electromagnetics and Their Application to Radiation Problems," *Bell System Tech. J.* Vol. 15, pp. 92–112, 1936.
2. C. A. Balanis, *Advanced Engineering Electromagnetics*, John Wiley and Sons, New York, 1989.
3. C. Huygens, *Traite de la Lumiere*, Leyeden, 1690. Translated into English by S. P. Thompson, London, 1912, reprinted by The University of Chicago Press.
4. J. D. Kraus and K. R. Carver, *Electromagnetics* (second edition), McGraw-Hill, New York, 1973, pp. 464–467.
5. R. F. Harrington, *Time-Harmonic Electromagnetic Fields*, McGraw-Hill, New York, 1961, pp. 100–103, 143–263, 365–367.
6. A. E. H. Love, "The Integration of the Equations of Propagation of Electric Waves," *Phil. Trans. Roy. Soc. London, Ser. A*, Vol. 197, 1901, pp. 1–45.
7. R. Mittra (ed.), *Computer Techniques for Electromagnetics*, Pergamon Press, New York, 1973, pp. 9–13.
8. C. A. Balanis and L. Peters, Jr., "Equatorial Plane Pattern of an Axial-TEM Slot on a Finite Size Ground Plane," *IEEE Trans. Antennas Propagat.*, Vol. AP-17, No. 3, pp. 351–353, May 1969.
9. C. A. Balanis, "Pattern Distortion Due to Edge Diffractions," *IEEE Trans. Antennas Propagat.*, Vol. AP-18, No. 4, pp. 561–563, July 1970.
10. C. R. Cockrell and P. H. Pathak, "Diffraction Theory Techniques Applied to Aperture Antennas on Finite Circular and Square Ground Planes," *IEEE Trans. Antennas Propagat.*, Vol. AP-22, No. 3, pp. 443–448, May 1974.
11. D. G. Fink (ed.), *Electronics Engineers' Handbook*, Section 18 (Antennas by W. F. Croswell), McGraw-Hill, New York, 1975.
12. K. Praba, "Optimal Aperture for Maximum Edge-of-Coverage (EOC) Directivity," *IEEE Antennas and Propagatation Magazine*, Vol. 36, No. 3, pp. 72–74, June 1994.
13. H. G. Booker, "Slot Aerials and Their Relation to Complementary Wire Aerials," *J. Inst. Elec. Engrs.*, pt III A, 1946, pp. 620–626.
14. E. C. Jordan and K. G. Balmain, *Electromagnetic Waves and Radiating Systems*, Prentice-Hall, Inc., Englewood Cliffs, NJ, 1968.
15. J. D. Kraus, *Antennas*, McGraw-Hill, New York, 1988, Chapter 13.
16. H. G. Booker and P. C. Clemmow, "The Concept of an Angular Spectrum of Plane Waves, and its Relation to that of Polar Diagram and Aperture Distribution," *Proc. IEE* (London), Vol. 97, part III, January 1950, pp. 11–17.
17. G. Borgiotti, "Fourier Transforms Method of Aperture Antennas," *Alta Freq.*, Vol. 32, November 1963, pp. 196–204.
18. L. B. Felsen and N. Marcuvitz, *Radiation and Scattering of Waves*, Prentice-Hall, Englewood Cliffs, NJ, 1973.
19. R. E. Collin and F. J. Zucker, *Antenna Theory: Part 1*, Chapter 3, McGraw-Hill Book Co., New York, 1969.
20. C. M. Knop and G. I. Cohn, "Radiation from an Aperture in a Coated Plane," *Radio Science Journal of Research*, Vol. 68D, No. 4, April 1964, pp. 363–378.
21. F. L. Whetten, "Dielectric Coated Meandering Leaky-Wave Long Slot Antennas," Ph.D. Dissertation, Arizona State University, May 1993.
22. M. H. Cohen, T. H. Crowley, and C. A. Lewis, "The Aperture Admittance of a Rectangular Waveguide Radiating Into Half-Space," Antenna Lab., Ohio State University, Rept. 339-22, Contract W 33-038 ac21114, November 14, 1951.
23. R. T. Compton, "The Admittance of Aperture Antennas Radiating Into Lossy Media," Antenna Lab., Ohio State University Research Foundation, Rept. 1691-5, March 15, 1964.

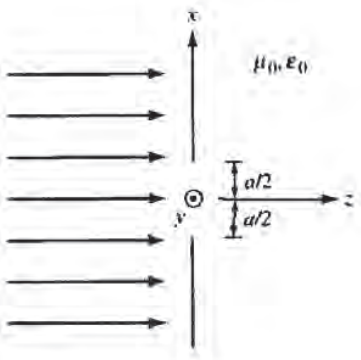
INTEL-1045
U.S. Patent 7,151,430

24. A. T. Villeneuve, "Admittance of a Waveguide Radiating into a Plasma Environment," *IEEE Trans. Antennas Propagat.*, Vol. AP-13, No. 1, January 1965, pp. 115–121.
25. J. Galejs, "Admittance of a Waveguide Radiating Into a Stratified Plasma," *IEEE Trans. Antennas Propagat.*, Vol. AP-13, No. 1, January 1965, pp. 64–70.
26. M. C. Bailey and C. T. Swift, "Input Admittance of a Circular Waveguide Aperture Covered by a Dielectric Slab," *IEEE Trans. Antennas Propagat.*, Vol. AP-16, No. 4, July 1968, pp. 386–391.
27. W. F. Croswell, W. C. Taylor, C. T. Swift, and C. R. Cockrell, "The Input Admittance of a Rectangular Waveguide-Fed Aperture Under an Inhomogeneous Plasma: Theory and Experiment," *IEEE Trans. Antennas Propagat.*, Vol. AP-16, No. 4, July 1968, pp. 475–487.
28. R. F. Harrington, *Field Computation by Moment Methods*, Macmillan Co., New York, 1968.
29. J. B. Keller, "Geometrical Theory of Diffraction," *Journal Optical Society of America*, Vol. 52, No. 2, pp. 116–130, February 1962.
30. R. G. Kouyoumjian, "The Geometrical Theory of Diffraction and Its Applications," in *Numerical and Asymptotic Techniques in Electromagnetics* (R. Mittra, ed.), Springer-Verlag, New York, 1975.
31. R. G. Kouyoumjian and P. H. Pathak, "A Uniform Geometrical Theory of Diffraction for an Edge in a Perfectly Conducting Surface," *Proc. IEEE*, Vol. 62, No. 11, pp. 1448–1461, November 1974.
32. D. L. Hutchins, "Asymptotic Series Describing the Diffraction of a Plane Wave by a Two-Dimensional Wedge of Arbitrary Angle," Ph.D. Dissertation, The Ohio State University, Dept. of Electrical Engineering, 1967.
33. P. H. Pathak and R. G. Kouyoumjian, "An Analysis of the Radiation from Apertures on Curved Surfaces by the Geometrical Theory of Diffraction, *Proc. IEEE*, Vol. 62, No. 11, pp. 1438–1447, November 1974.
34. G. L. James, *Geometrical Theory of Diffraction for Electromagnetic Waves*, Peter Peregrinus, Ltd., Stevenage, Herts., England, 1976.
35. C. A. Balanis and L. Peters, Jr., "Analysis of Aperture Radiation from an Axially Slotted Circular Conducting Cylinder Using GTD," *IEEE Trans. Antennas Propagat.*, Vol. AP-17, No. 1, pp. 93–97, January 1969.
36. C. A. Balanis and Y.-B. Cheng, "Antenna Radiation and Modeling for Microwave Landing System," *IEEE Trans. Antennas Propagat.*, Vol. AP-24, No. 4, pp. 490–497, July 1976.
37. W. D. Burnside, C. L. Yu, and R. J. Marhefka, "A Technique to Combine the Geometrical Theory of Diffraction and the Moment Method," *IEEE Trans. Antennas Propagat.*, Vol. AP-23, No. 4, pp. 551–558, July 1975.

PROBLEMS

12.1. A uniform plane wave traveling in the $+z$ direction, whose magnetic field is expressed as

$$\mathbf{H}^i = \hat{\mathbf{a}}_y H_0 e^{-jkz} \qquad z \leq 0$$



INTEL-1045
U.S. Patent 7,151,430

impinges upon an aperture on an infinite, flat, perfect electric conductor whose cross section is indicated in the figure.

(a) State the equivalent that must be used to determine the field radiated by the aperture to the right of the conductor ($z > 0$).

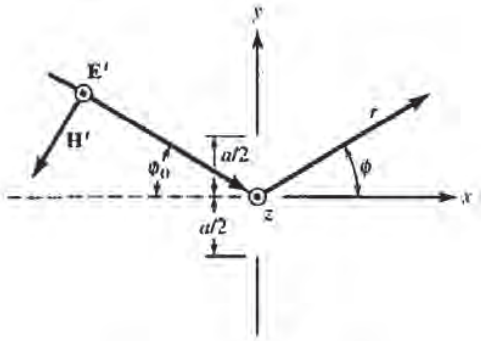
(b) Assuming the aperture dimension in the y direction is b, determine the far-zone fields for $z > 0$.

12.2. Repeat Problem 12.1 when the incident magnetic field is polarized in the x direction.

12.3. Repeat Problem 12.1 when the incident electric field is polarized in the y direction.

12.4. Repeat Problem 12.1 when the incident electric field is polarized in the x direction.

12.5. A perpendicularly polarized plane wave is obliquely incident upon an aperture, with dimension a and b, on a perfectly electric conducting ground plane of infinite extent, as shown in the figure. Assuming the field over the aperture is given by the incident field (ignore diffractions from the edges of the aperture), find the far-zone spherical components of the fields for $x > 0$.



12.6. Repeat Problem 12.5 for a parallelly polarized plane wave (when the incident magnetic field is polarized in the z direction, i.e., the incident magnetic field is perpendicular to the x-y plane while the incident electric field is parallel to the x-y plane).

12.7. A narrow rectangular slot of size L by W is mounted on an infinite ground plane that covers the x-y plane. The tangential field over the aperture is given by

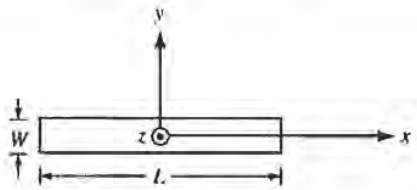
$$\mathbf{E}_a = \hat{\mathbf{a}}_y E_0 e^{-jk_0 x'\sqrt{2}/2}$$

Using the equivalence principle and image theory, we can replace the aperture and infinite ground plane with an equivalent magnetic current radiating in free space. Determine the

(a) appropriate equivalent

(b) far-zone spherical electric field components for $z > 0$

(c) direction (θ, ϕ) in which the radiation intensity is maximum



12.8. A rectangular aperture, of dimensions a and b, is mounted on an infinite ground plane, as shown in Figure 12.6(a). Assuming the tangential field over the aperture is given by

$$\mathbf{E}_a = \hat{\mathbf{a}}_z E_0 \qquad -a/2 \le y' \le a/2, \qquad -b/2 \le z' \le b/2$$

find the far-zone spherical electric and magnetic field components radiated by the aperture.

INTEL-1045
U.S. Patent 7,151,430

12.9. Repeat Problem 12.8 when the same aperture is analyzed using the coordinate system of Figure 12.6(b). The tangential aperture field distribution is given by

$$\mathbf{E}_a = \hat{\mathbf{a}}_x E_0 \qquad -b/2 \le x' \le b/2, \qquad -a/2 \le z' \le a/2$$

12.10. Repeat Problem 12.8 when the aperture field is given by

$$\mathbf{E}_a = \hat{\mathbf{a}}_x E_0 \cos\left(\frac{\pi}{a} y'\right) \qquad -a/2 \le y' \le a/2, \qquad -b/2 \le z' \le b/2$$

12.11. Repeat Problem 12.9 when the aperture field distribution is given by

$$\mathbf{E}_a = \hat{\mathbf{a}}_x E_0 \cos\left(\frac{\pi}{a} z'\right) \qquad -b/2 \le x' \le b/2 \qquad -a/2 \le z' \le a/2$$

12.12. Find the fields radiated by the apertures of Problems
(a) 12.8 (b) 12.9
(c) 12.10 (d) 12.11
when each of the apertures with their associated field distributions are *not* mounted on a ground plane. Assume the tangential **H**-field at the aperture is related to the **E**-field by the intrinsic impedance.

12.13. Find the fields radiated by the rectangular aperture of Section 12.5.3 when it is not mounted on an infinite ground plane.

12.14. For the rectangular aperture of Section 12.5.3 (with $a = 4\lambda$, $b = 3\lambda$), compute the
(a) *E*-plane beamwidth (*in degrees*) between the maxima of the *second* minor lobe
(b) *E*-plane amplitude (*in dB*) of the maximum of the second minor lobe (relative to the maximum of the major lobe)
(c) approximate directivity of the antenna using Kraus' formula. Compare it with the value obtained using the expression in Table 12.1.

12.15. For the rectangular aperture of Section 12.5.1 with $a = b = 3\lambda$, compute the directivity using (12-37) and the DIRECTIVITY computer program at the end of Chapter 2.

12.16. For the rectangular aperture of Section 12.5.2 with $a = b = 3\lambda$, compute the directivity using (12-37) and the DIRECTIVITY computer program at the end of Chapter 2.

12.17. Compute the directivity of the aperture of Section 12.5.3, using the DIRECTIVITY computer program at the end of Chapter 2, when
(a) $a = 3\lambda$, $b = 2\lambda$
(b) $a = b = 3\lambda$

12.18. Repeat Problem 12.17 when the aperture is not mounted on an infinite ground plane.

12.19. For the rectangular aperture of Section 12.5.3 with $a = 3\lambda$, $b = 2\lambda$, compute the
(a) *E*-plane half-power beamwidth
(b) *H*-plane half-power beamwidth
(c) *E*-plane first-null beamwidth
(d) *H*-plane first-null beamwidth
(e) *E*-plane first side lobe maximum (relative to main maximum)
(f) *H*-plane first side lobe maximum (relative to main maximum)
using the formulas of Table 12.1. Compare the results with the data from Figures 12.13 and 12.14.

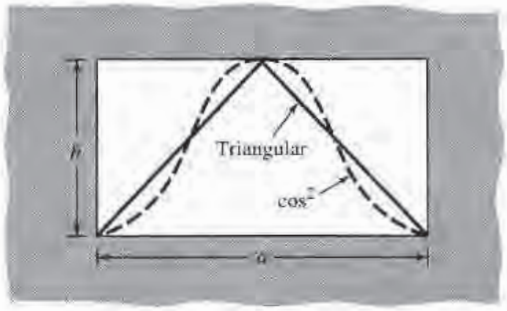
12.20. A square waveguide aperture, of dimensions $a = b$ and lying on the x-y plane, is radiating into free-space. Assuming a $\cos(\pi x'/a)$ by $\cos(\pi y'/b)$ distribution over the aperture, find the dimensions of the aperture (in wavelengths) so that the beam efficiency within a 37° total included angle cone is 90%.

12.21. Verify (12-39a), (12-39b), (12-39c), and (12-40).

12.22. A rectangular aperture mounted on an infinite ground plane has aperture electric field distributions and corresponding efficiencies of

INTEL-1045
U.S. Patent 7,151,430

FIELD DISTRIBUTION	APERTURE EFFICIENCY
(a) Triangular	75%
(b) Cosine square	66.67%



What are the corresponding directives (in dB) if the dimensions of the aperture are $a = \lambda/2$ and $b = \lambda/4$?

12.23. The physical area of an aperture antenna operating at 10 GHz is 200 cm^2 while its directivity is 23 dB. Assuming the antenna has an overall radiation efficiency of 90% and it is perfectly matched to the input transmission line, find the aperture efficiency of the antenna.

12.24. Two *X*-band (8.2–12.4 GHz) rectangular waveguides, each operating in the dominant TE_{10}-mode, are used, respectively, as transmitting and receiving antennas in a long distance communication system. The dimensions of each waveguide are $a = 2.286$ cm (0.9 in.) and $b = 1.016$ cm (0.4 in.) and the center frequency of operation is 10 GHz. Assuming the waveguides are separated by 10 kilometers and they are positioned for maximum radiation and reception toward each other, and the radiated power is 1 watt, find the:

(a) Incident power density at the receiving antenna

(b) Maximum power that can be delivered to a matched load

Assume the antennas are lossless, are polarization matched, and each is mounted on an infinite ground plane.

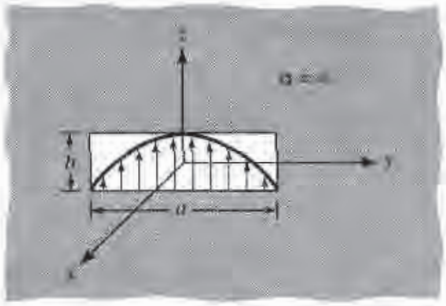
12.25. The normalized far-zone electric field radiated in the *E*-plane (*x*-*z* plane; $\phi = 0°$) by a waveguide aperture antenna of dimensions a and b, mounted on an infinite ground plane as shown in the figure, is given by

$$\mathbf{E} = -\hat{\mathbf{a}}_\theta j \frac{\omega\mu b I_0 e^{-jkr}}{4\pi r} \frac{\sin\left(\frac{kb}{2}\cos\theta\right)}{\frac{kb}{2}\cos\theta}$$

Determine in the *E*-plane the:

(a) Vector effective length of the antenna.

(b) Maximum value of the effective length.



INTEL-1045
U.S. Patent 7,151,430

State the value of θ (in degrees) which maximizes the effective length.

12.26. A uniform plane wave is incident upon an X-band rectangular waveguide, with dimensions of 2.286 cm and 1.016 cm, mounted on an infinite ground plane. Assuming the waveguide is operating in the dominant TE_{10} mode, determine the maximum power that can be delivered to a matched load. The frequency is 10 GHz and the power density of the incident plane wave is 10^{-4} watts/m^2.

12.27. Compute the aperture efficiency of a rectangular aperture, mounted on an infinite ground plane as shown in Figure 12.7, with an E-field aperture distribution directed toward y but with variations
(a) triangular in the x and uniform in the y
(b) cosine-squared in the x and uniform in the y
(c) cosine in the x and cosine in the y
(d) cosine-squared in both the x and y directions.
How do they compare with those of a cosine distribution?

12.28. An X-band (8.2–12.4 GHz) WR 90 rectangular waveguide, with inner dimensions of 0.9 in. (2.286 cm) and 0.4 in. (1.016 cm), is mounted on an infinite ground plane. *Assuming the waveguide is operating in the dominant* TE_{10}*-mode, find its directivity* at $f = 10$ GHz using the
(a) computer program DIRECTIVITY at the end of Chapter 2
(b) formula in Table 12.1
Compare the answers.

12.29. Repeat Problem 12.28 at $f = 20$ GHz for a K-band (18–26.5 GHz) WR 42 rectangular waveguide with inner dimensions of 0.42 in. (1.067 cm) and 0.17 in. (0.432 cm).

12.30. Four rectangular X-band waveguides of dimensions $a = 0.9$ in. (2.286 cm) and $b = 0.4$ in. (1.016 cm) and each operating on the dominant TE_{10}-mode, are mounted on an infinite ground plane so that their apertures and the ground plane coincide with the x-y plane. The apertures form a linear array, are placed along the x-axis with a center-to-center separation of $d = 0.85\lambda$ apart, and they are fed so that they form a broadside Dolph-Tschebyscheff array of -30 dB minor lobes. Assuming a center frequency of 10 GHz, determine the overall directivity of the array in decibels.

12.31. Sixty-four (64) X-band rectangular waveguides are mounted so that the aperture of each is mounted on an infinite ground plane that coincides with the x-y plane, and all together form an $8 \times 8 = 64$ planar array. Each waveguide has dimensions of $a = 0.9$ in. (2.286 cm), $b = 0.4$ in. (1.086 cm) and the center-to-center spacing between the waveguides is $d_x = d_y = 0.85\lambda$. Assuming a TE_{10}-mode operation for each waveguide, a center frequency of 10 GHz, and the waveguides are fed to form a *uniform* broadside planar array, find the directivity of the total array.

12.32. Find the far-zone fields radiated when the circular aperture of Section 12.6.1 is not mounted on an infinite ground plane.

12.33. Derive the far-zone fields when the circular aperture of Section 12.6.2
(a) is
(b) is not
mounted on an infinite ground plane.

12.34. A circular waveguide (not mounted on a ground plane), operating in the dominant TE_{11} mode, is used as an antenna radiating in free space. Write in simplified form the normalized far-zone electric field components radiated by the waveguide antenna. You do not have to derive them.

12.35. For the circular aperture of Section 12.6.1, compute its directivity, using the DIRECTIVITY computer program at the end of Chapter 2, when its radius is
(a) $a = 0.5\lambda$
(b) $a = 1.5\lambda$
(c) $a = 3.0\lambda$
Compare the results with data from Table 12.2.

12.36. Repeat Problem 12.35 when the circular aperture of Section 12.6.1 is not mounted on an infinite ground plane. Compare the results with those of Problem 12.35.

INTEL-1045
U.S. Patent 7,151,430

12.37. For the circular aperture of Problem 12.33, compute the directivity, using the DIRECTIVITY computer program at the end of Chapter 2, when its radius is
(a) $a = 0.5\lambda$
(b) $a = 1.5\lambda$
(c) $a = 3.0\lambda$
Compare the results with data from Table 12.2.

12.38. For the circular aperture of Section 12.6.2 with $a = 1.5\lambda$, compute the
(a) E-plane half-power beamwidth
(b) H-plane half-power beamwidth
(c) E-plane first-null beamwidth
(d) H-plane first-null beamwidth
(e) E-plane first side lobe maximum (relative to main maximum)
(f) H-plane first side lobe maximum (relative to main maximum)
using the formulas of Table 12.2. Compare the results with the data from Figures 12.19 and 12.20.

12.39. A circular aperture of radius a is mounted on an infinite electric ground plane. Assuming the opening is on the x-y plane and its field distribution is given by

(a) $\mathbf{E}_a = \hat{\mathbf{a}}_y E_0 \left[1 - \left(\frac{\rho'}{a}\right)^2\right], \qquad \rho' \leq a$

(b) $\mathbf{E}_a = \hat{\mathbf{a}}_y E_0 \left[1 - \left(\frac{\rho'}{a}\right)^2\right]^2, \qquad \rho' \leq a$

find the far-zone electric and magnetic field components radiated by the antenna.

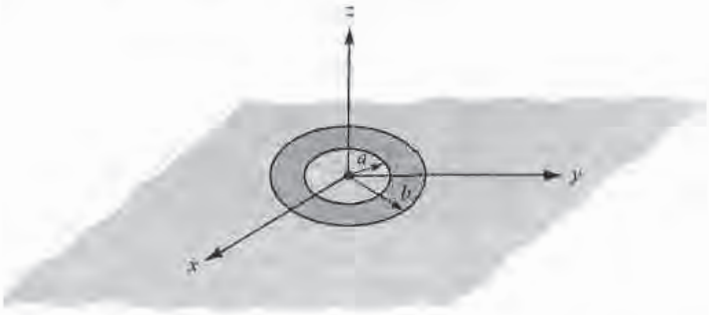
12.40. Repeat Problem 12.39 when the electric field is given by

$$\mathbf{E}_a = \hat{\mathbf{a}}_y E_0 [1 - (\rho'/a)], \qquad \rho' \leq a$$

Find only the radiation vectors $\mathbf{L}$ and $\mathbf{N}$. Work as far as you can. If you find you cannot complete the solution in closed form, state clearly why you cannot. Simplify as much as possible.

12.41. A coaxial line of inner and outer radii a and b, respectively, is mounted on an infinite electric ground plane. Assuming that the electric field over the aperture of the coax is

$$\mathbf{E}_a = -\hat{\mathbf{a}}_\rho \frac{V}{\epsilon \ln(b/a)} \frac{1}{\rho'}, \qquad a \leq \rho' \leq b$$



where V is the applied voltage and ϵ is the permittivity of the coax medium, find the far-zone spherical electric and magnetic field components radiated by the antenna.

12.42. It is desired to design a circular aperture antenna with a field distribution over its opening of

$$E = C[1 - (\rho'/a)^2]$$

where C is a constant, a its radius, and ρ' any point on the aperture, such that its beam efficiency within a 60° total included angle cone is 90%. Find its radius in wavelengths.

INTEL-1045
U.S. Patent 7,151,430

12.43. For the antenna of Problem 12.42, find its efficiency within a 40° total included angle cone when its radius is 2λ.

12.44. Design square apertures with uniform illumination so that the directivity at 60° from the normal is maximized relative to that at $\theta = 0°$. Determine the:
(a) Dimensions of the aperture (in λ)
(b) Maximum directivity (in dB)
(c) Directivity (in dB) at 60° from the maximum

12.45. Design a circular aperture with uniform illumination so that the directivity at 60° from the normal is maximized relative to that at $\theta = 0°$. Determine the
(a) Radius of the aperture (in λ)
(b) Maximum directivity (in dB)
(c) Directivity (in dB) at 60° from the maximum

12.46. Repeat Problem 12.45 for a circular aperture with a parabolic distribution.

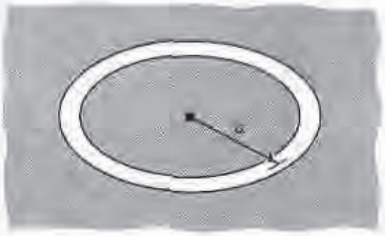
12.47. Repeat Problem 12.45 for a circular aperture with a parabolic taper on -10 dB pedestal.

12.48. Derive the edge-of-coverage (EOC) design characteristics for a circular aperture with a parabolic taper.

12.49. A vertical dipole is radiating into a free-space medium and produces fields $\mathbf{E}_0$ and $\mathbf{H}_0$. Illustrate alternate methods for obtaining the same fields using Babinet's principle and extensions of it.

12.50. (a) (1) Sketch the six principal plane patterns, and (2) define the direction of **E** and **H** along the three principal axes and at 45° to the axes, for a thin slot one-half wavelength long, cut in a conducting sheet which has infinite conductivity and extending to infinity, and open on both sides. Inside dimensions of the slot are approximately 0.5λ by 0.1λ. Assume that the width (0.1λ) of the slot is small compared to a wavelength. Assume a coordinate system such that the conducting plane lies on the x-y plane with the larger dimension of the slot parallel to the y-axis.
(b) Sketch the six approximate principal plane patterns $E_\theta(\phi = 0°)$, $E_\phi(\phi = 0°)$, $E_\theta(\phi = 90°)$, $E_\phi(\phi = 90°)$, $E_\theta(\theta = 90°)$, $E_\phi(\theta = 90°)$.

12.51. A very thin circular annular slot with circumference of one wavelength is cut on a very thin, infinite, flat, perfectly electric conducting plate. The slot is radiating into free space. What is the impedance (real and imaginary parts) of the slot?



12.52. Repeat Example 12.7 for a rectangular aperture with an electric field distribution of

$$\mathbf{E}_a = \hat{\mathbf{a}}_y E_0 \cos\left(\frac{\pi}{a} x'\right), \qquad \begin{matrix} -a/2 \le x' \le a/2 \\ -b/2 \le y' \le b/2 \end{matrix}$$

INTEL-1045
U.S. Patent 7,151,430

CHAPTER

13

HORN ANTENNAS

13.1 INTRODUCTION

One of the simplest and probably the most widely used microwave antenna is the horn. Its existence and early use dates back to the late 1800s. Although neglected somewhat in the early 1900s, its revival began in the late 1930s from the interest in microwaves and waveguide transmission lines during the period of World War II. Since that time a number of articles have been written describing its radiation mechanism, optimization design methods, and applications. Many of the articles published since 1939 which deal with the fundamental theory, operating principles, and designs of a horn as a radiator can be found in a book of reprinted papers [1] and chapters in handbooks [2], [3].

The horn is widely used as a feed element for large radio astronomy, satellite tracking, and communication dishes found installed throughout the world. In addition to its utility as a feed for reflectors and lenses, it is a common element of phased arrays and serves as a universal standard for calibration and gain measurements of other high-gain antennas. Its widespread applicability stems from its simplicity in construction, ease of excitation, versatility, large gain, and preferred overall performance.

An electromagnetic horn can take many different forms, four of which are shown in Figure 13.1. The horn is nothing more than a hollow pipe of different cross sections which has been tapered (flared) to a larger opening. The type, direction, and amount of taper (flare) can have a profound effect on the overall performance of the element as a radiator. In this chapter, the fundamental theory of horn antennas will be examined. In addition, data will be presented that can be used to understand better the operation of a horn and its design as an efficient radiator.

13.2 *E*-PLANE SECTORAL HORN

The *E*-plane sectoral horn is one whose opening is flared in the direction of the *E*-field, and it is shown in Figure 13.2(a). A more detailed geometry is shown in Figure 13.2(b).

*Portions of this chapter on aperture matched horns, multimode horns, and dielectric-loaded horns were first published by the author in [2], Copyright 1988, reprinted by permission of Van Nostrand Reinhold Co.

INTEL-1045
U.S. Patent 7,151,430

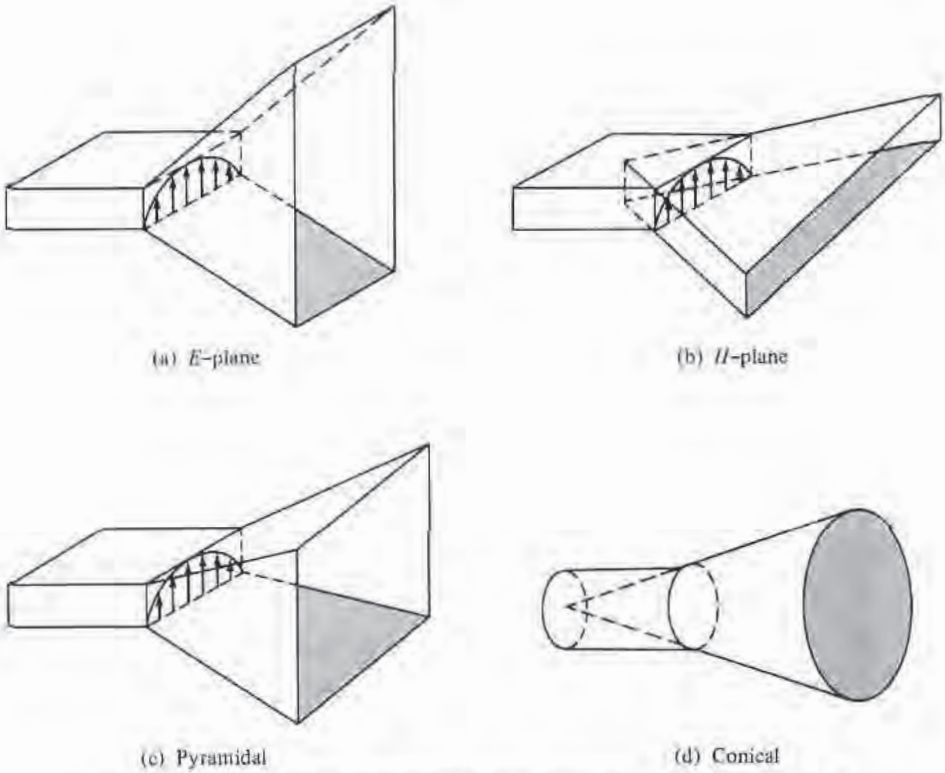


Figure 13.1 Typical electromagnetic horn antenna configurations.

13.2.1 Aperture Fields

The horn can be treated as an aperture antenna. To find its radiation characteristics, the equivalent principle techniques developed in Chapter 12 can be utilized. To develop an exact equivalent of it, it is necessary that the tangential electric and magnetic field components over a closed surface are known. The closed surface that is usually selected is an infinite plane that coincides with the aperture of the horn. When the horn is not mounted on an infinite ground plane, the fields outside the aperture are not known and an exact equivalent cannot be formed. However, the usual approximation is to assume that the fields outside the aperture are zero, as was done for the aperture of Section 12.5.2.

The fields at the aperture of the horn can be found by treating the horn as a radial waveguide [4]–[6]. The fields within the horn can be expressed in terms of cylindrical TE and TM wave functions which include Hankel functions. This method finds the fields not only at the aperture of the horn but also within the horn. The process is straightforward but laborious, and it will not be included here. However, it is assigned as an exercise at the end of the chapter (Problem 13.1).

It can be shown that if the (1) fields of the feed waveguide are those of its dominant TE_{10} mode and (2) horn length is large compared to the aperture dimensions, the lowest order mode fields at the aperture of the horn are given by

$$E_z' = E_x' = H_y' = 0 \tag{13-1a}$$

$$E_y'(x', y') \simeq E_1 \cos\left(\frac{\pi}{a}x'\right) e^{-j[ky'^2/(2\rho_1)]} \tag{13-1b}$$

INTEL-1045
U.S. Patent 7,151,430

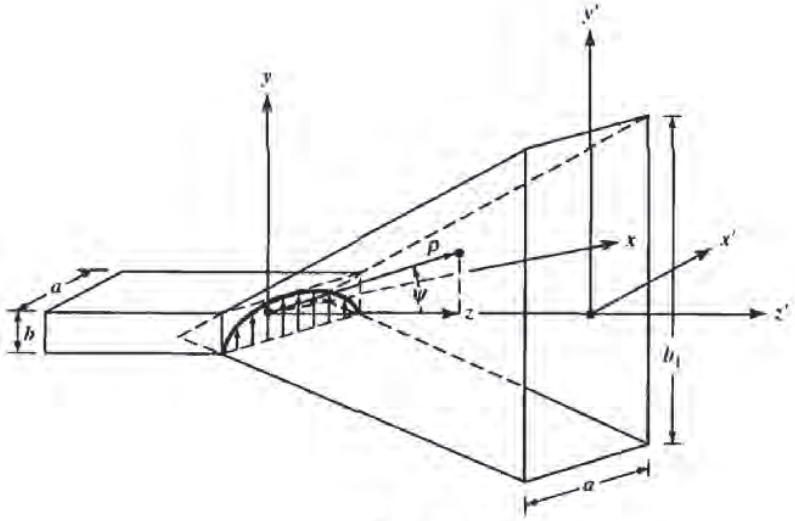
$$H_z'(x', y') \simeq jE_1\left(\frac{\pi}{ka\eta}\right)\sin\left(\frac{\pi}{a}x'\right)e^{-j[ky'^2/(2\rho_1)]} \tag{13-1c}$$

$$H_x'(x', y') \simeq -\frac{E_1}{\eta}\cos\left(\frac{\pi}{a}x'\right)e^{-j[ky'^2/(2\rho_1)]} \tag{13-1d}$$

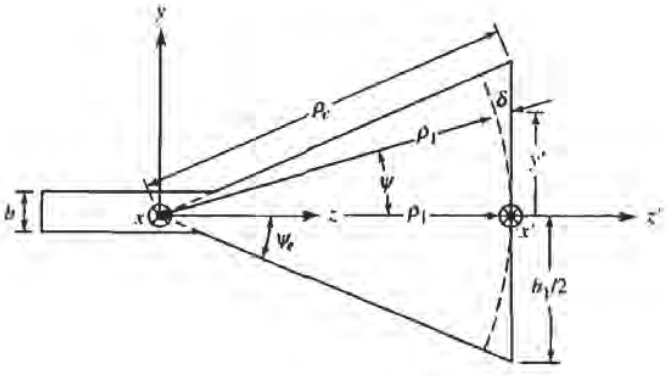
$$\rho_1 = \rho_e \cos\psi_e \tag{13-1e}$$

where E_1 is a constant. The primes are used to indicate the fields at the aperture of the horn. The expressions are similar to the fields of a TE_{10}-mode for a rectangular waveguide with aperture dimensions of a and $b_1(b_1 > a)$. The only difference is the complex exponential term which is used here to represent the quadratic phase variations of the fields over the aperture of the horn.

The necessity of the quadratic phase term in (13-1b)–(13-1d) can be illustrated geometrically. Referring to Figure 13.2(b), let us assume that at the imaginary apex of the horn (shown dashed) there exists a line source radiating cylindrical waves. As the waves travel in the outward radial direction, the constant phase fronts are cylin-



(a) E-plane horn



(b) E-plane view

Figure 13.2 E-plane horn and coordinate system.

INTEL-1045
U.S. Patent 7,151,430

drical. At any point y' at the aperture of the horn, the phase of the field will not be the same as that at the origin ($y' = 0$). The phase is different because the wave has traveled different distances from the apex to the aperture. The difference in path of travel, designated as $\delta(y')$, can be obtained by referring to Figure 13.2(b). For any point y'

$$[\rho_1 + \delta(y')]^2 = \rho_1^2 + (y')^2 \tag{13-2}$$

or

$$\delta(y') = -\rho_1 + [\rho_1^2 + (y')^2]^{1/2} = -\rho_1 + \rho_1\left[1 + \left(\frac{y'}{\rho_1}\right)^2\right]^{1/2} \tag{13-2a}$$

Using the binomial expansion and retaining only the first two terms of it, (13-2a) reduces to

$$\boxed{\delta(y') \simeq -\rho_1 + \rho_1\left[1 + \frac{1}{2}\left(\frac{y'}{\rho_1}\right)^2\right] = \frac{1}{2}\left(\frac{y'^2}{\rho_1}\right)} \tag{13-2b}$$

When (13-2b) is multiplied by the phase factor k, the result is identical to the quadratic phase term in (13-1b)–(13-1d).

The quadratic phase variation for the fields of the dominant mode at the aperture of a horn antenna has been a standard for many years, and it has been chosen because it yields in most practical cases very good results. Because of its simplicity, it leads to closed form expressions, in terms of sine and cosine Fresnel integrals, for the radiation characteristics (far-zone fields, directivity, etc.) of the horn. It has been shown recently [7] that using the more accurate expression of (13-2a) for the phase, error variations and numerical integration yield basically the same directivities as using the approximate expression of (13-2b) for large aperture horns (b_1 of Figures 13.2 or a_1 of Figure 13.10 greater than 50λ) or small peak aperture phase error ($S = \rho_e - \rho_1$ of Figure 13.2 or $T = \rho_{h_1} - \rho_2$ of Figure 13.10 less than 0.2λ). However, for intermediate aperture sizes ($5\lambda \leq b_1$ or $a_1 \leq 8\lambda$) or intermediate peak aperture phase errors ($0.2\lambda \leq S$ or $T \leq 0.6\lambda$) the more accurate expression of (13-2a) for the phase variation yields directivities which are somewhat higher (by as much as a few tenths of a decibel) than those obtained using (13-2b). Also it has been shown using a full-wave Moment Method analysis of the horn [8] that as the horn dimensions become large the amplitude distribution at the aperture of the horn contains higher order modes than the TE_{10} mode and the phase distribution at the aperture approaches the parabolic phase front.

Example 13.1

Design an E-plane sectoral horn so that the maximum phase deviation at the aperture of the horn is 56.72°. The dimensions of the horn are $a = 0.5\lambda$, $b = 0.25\lambda$, $b_1 = 2.75\lambda$.

SOLUTION

Using (13-2b)

$$\Delta\phi|_{\max} = k\delta(y')|_{y' = b_1/2} = \frac{k\,(b_1/2)^2}{2\rho_1} = 56.72\left(\frac{\pi}{180}\right)$$

INTEL-1045
U.S. Patent 7,151,430

or

$$\rho_1 = \left(\frac{2.75}{2}\right)^2 \frac{180}{56.72}\lambda = 6\lambda$$

The total flare angle of the horn should be equal to

$$2\psi_e = 2\tan^{-1}\left(\frac{b_1/2}{\rho_1}\right) = 2\tan^{-1}\left(\frac{2.75/2}{6}\right) = 25.81^\circ$$

13.2.2 Radiated Fields

To find the fields radiated by the horn, only the tangential components of the **E**- and/or **H**-fields over a closed surface must be known. The closed surface is chosen to coincide with an infinite plane passing through the mouth of the horn. To solve for the fields, the approximate equivalent of Section 12.5.2 is used. That is,

$$\left.\begin{aligned} J_y &= -\frac{E_1}{\eta}\cos\left(\frac{\pi}{a}x'\right)e^{-jk\delta(y')} \\ M_x &= E_1\cos\left(\frac{\pi}{a}x'\right)e^{-jk\delta(y')} \end{aligned}\right\} \begin{aligned} &-a/2 \le x' \le a/2 \\ &-b_1/2 \le y' \le b_1/2 \end{aligned} \tag{13-3}$$

and

$$\mathbf{J}_s = \mathbf{M}_s = 0 \qquad \text{elsewhere} \tag{13-3a}$$

Using (12-12a)

$$N_\theta = -\frac{E_1}{\eta}\cos\theta\sin\phi\, I_1 I_2 \tag{13-4}$$

where

$$\begin{aligned} I_1 &= \int_{-a/2}^{+a/2}\cos\left(\frac{\pi}{a}x'\right)e^{jkx'\sin\theta\cos\phi}\,dx' \\ &= -\left(\frac{\pi a}{2}\right)\left[\frac{\cos\left(\frac{ka}{2}\sin\theta\cos\phi\right)}{\left(\frac{ka}{2}\sin\theta\cos\phi\right)^2 - \left(\frac{\pi}{2}\right)^2}\right] \end{aligned} \tag{13-4a}$$

$$I_2 = \int_{-b_1/2}^{+b_1/2} e^{-jk[\delta(y')-y'\sin\theta\sin\phi]}\,dy' \tag{13-4b}$$

The integral of (13-4b) can also be evaluated in terms of cosine and sine Fresnel integrals. To do this, I_2 can be written, by completing the square, as

$$\begin{aligned} I_2 &= \int_{-b_1/2}^{+b_1/2} e^{-j[ky'^2/(2\rho_1)-k_y y']}\,dy' \\ &= e^{j(k_y^2\rho_1/2k)}\int_{-b_1/2}^{+b_1/2} e^{-j[(ky'-k_y\rho_1)^2/2k\rho_1]}\,dy' \end{aligned} \tag{13-5}$$

INTEL-1045
U.S. Patent 7,151,430

where

$$k_y = k \sin\theta \sin\phi \tag{13-5a}$$

Making a change of variable

$$\sqrt{\frac{\pi}{2}}\, t = \sqrt{\frac{1}{2k\rho_1}}\,(ky' - k_y\rho_1) \tag{13-6a}$$

$$t = \sqrt{\frac{1}{\pi k\rho_1}}\,(ky' - k_y\rho_1) \tag{13-6b}$$

$$dt = \sqrt{\frac{k}{\pi\rho_1}}\, dy' \tag{13-6c}$$

reduces (13-5) to

$$I_2 = \sqrt{\frac{\pi\rho_1}{k}}\, e^{j(k_y^2\rho_1/2k)} \int_{t_1}^{t_2} e^{-j(\pi/2)t^2}\, dt$$

$$= \sqrt{\frac{\pi\rho_1}{k}}\, e^{j(k_y^2\rho_1/2k)} \int_{t_1}^{t_2} \left[\cos\left(\frac{\pi}{2}t^2\right) - j\sin\left(\frac{\pi}{2}t^2\right)\right] dt \tag{13-7}$$

and takes the form of

$$I_2 = \sqrt{\frac{\pi\rho_1}{k}}\, e^{j(k_y^2\rho_1/2k)} \{[C(t_2) - C(t_1)] - j[S(t_2) - S(t_1)]\} \tag{13-8}$$

where

$$\boxed{t_1 = \sqrt{\frac{1}{\pi k\rho_1}}\left(-\frac{kb_1}{2} - k_y\rho_1\right)} \tag{13-8a}$$

$$\boxed{t_2 = \sqrt{\frac{1}{\pi k\rho_1}}\left(\frac{kb_1}{2} - k_y\rho_1\right)} \tag{13-8b}$$

$$C(x) = \int_0^x \cos\left(\frac{\pi}{2}t^2\right) dt \tag{13-8c}$$

$$S(x) = \int_0^x \sin\left(\frac{\pi}{2}t^2\right) dt \tag{13-8d}$$

$C(x)$ and $S(x)$ are known as the cosine and sine Fresnel integrals and are well tabulated [9] (see Appendix IV). Computer subroutines are also available for efficient numerical evaluation of each [10], [11].

Using (13-4a) and (13-8), (13-4) can be written as

$$N_\theta = E_1 \frac{\pi a}{2} \sqrt{\frac{\pi\rho_1}{k}} e^{j(k_y^2\rho_1/2k)} \times \left\{ \frac{\cos\theta\sin\phi}{\eta} \left[\frac{\cos\left(\frac{k_x a}{2}\right)}{\left(\frac{k_x a}{2}\right)^2 - \left(\frac{\pi}{2}\right)^2} \right] F(t_1, t_2) \right\} \tag{13-9}$$

INTEL-1045
U.S. Patent 7,151,430

where

$$\boxed{k_x = k \sin\theta \cos\phi} \tag{13-9a}$$

$$\boxed{k_y = k \sin\theta \sin\phi} \tag{13-9b}$$

$$\boxed{F(t_1, t_2) = [C(t_2) - C(t_1)] - j[S(t_2) - S(t_1)]} \tag{13-9c}$$

In a similar manner, N_ϕ, L_θ, L_ϕ of (12-12b)–(12-12d) reduce to

$$N_\phi = E_1 \frac{\pi a}{2}\sqrt{\frac{\pi\rho_1}{k}}e^{j(k_z^2\rho_1/2k)}\left\{\frac{\cos\phi}{\eta}\left[\frac{\cos\left(\frac{k_x a}{2}\right)}{\left(\frac{k_x a}{2}\right)^2 - \left(\frac{\pi}{2}\right)^2}\right]F(t_1, t_2)\right\} \tag{13-10a}$$

$$L_\theta = E_1 \frac{\pi a}{2}\sqrt{\frac{\pi\rho_1}{k}}e^{j(k_z^2\rho_1/2k)} \times \left\{-\cos\theta\cos\phi\left[\frac{\cos\left(\frac{k_x a}{2}\right)}{\left(\frac{k_x a}{2}\right)^2 - \left(\frac{\pi}{2}\right)^2}\right]F(t_1, t_2)\right\} \tag{13-10b}$$

$$L_\phi = E_1 \frac{\pi a}{2}\sqrt{\frac{\pi\rho_1}{k}}e^{j(k_z^2\rho_1/2k)}\left\{\sin\phi\left[\frac{\cos\left(\frac{k_x a}{2}\right)}{\left(\frac{k_x a}{2}\right)^2 - \left(\frac{\pi}{2}\right)^2}\right]F(t_1, t_2)\right\} \tag{13-10c}$$

The electric field components radiated by the horn can be obtained by using (12-10a)–(12-10c), and (13-9)–(13-10c). Thus,

$$\boxed{E_r = 0} \tag{13-11a}$$

$$\boxed{E_\theta = -j\frac{a\sqrt{\pi k\rho_1}\,E_1 e^{-jkr}}{8r} \times \left\{e^{j(k_z^2\rho_1/2k)}\sin\phi(1 + \cos\theta)\left[\frac{\cos\left(\frac{k_x a}{2}\right)}{\left(\frac{k_x a}{2}\right)^2 - \left(\frac{\pi}{2}\right)^2}\right]F(t_1, t_2)\right\}} \tag{13-11b}$$

$$\boxed{E_\phi = -j\frac{a\sqrt{\pi k\rho_1}\,E_1 e^{-jkr}}{8r} \times \left\{e^{j(k_z^2\rho_1/2k)}\cos\phi(\cos\theta + 1)\left[\frac{\cos\left(\frac{k_x a}{2}\right)}{\left(\frac{k_x a}{2}\right)^2 - \left(\frac{\pi}{2}\right)^2}\right]F(t_1, t_2)\right\}} \tag{13-11c}$$

INTEL-1045
U.S. Patent 7,151,430

where t_1, t_2, k_x, k_y, and $F(t_1, t_2)$ are given, respectively, by (13-8a), (13-8b), (13-9a), (13-9b), and (13-9c). The corresponding **H**-field components are obtained using (12-10d)–(12-10f).

In the principal E- and H-planes, the electric field reduces to

E-Plane ($\phi = \pi/2$)

$$E_r = E_\phi = 0 \tag{13-12a}$$

$$E_\theta = -j\frac{a\sqrt{\pi k\rho_1}E_1 e^{-jkr}}{8r}\left\{-e^{j(k\rho_1\sin^2\theta/2)}\left(\frac{2}{\pi}\right)^2(1+\cos\theta)F(t_1', t_2')\right\} \tag{13-12b}$$

$$t_1' = \sqrt{\frac{k}{\pi\rho_1}}\left(-\frac{b_1}{2} - \rho_1\sin\theta\right) \tag{13-12c}$$

$$t_2' = \sqrt{\frac{k}{\pi\rho_1}}\left(+\frac{b_1}{2} - \rho_1\sin\theta\right) \tag{13-12d}$$

H-Plane ($\phi = 0$)

$$E_r = E_\theta = 0 \tag{13-13a}$$

$$E_\phi = -j\frac{a\sqrt{\pi k\rho_1}E_1 e^{-jkr}}{8r}\left\{(1+\cos\theta)\left[\frac{\cos\left(\frac{ka}{2}\sin\theta\right)}{\left(\frac{ka}{2}\sin\theta\right)^2 - \left(\frac{\pi}{2}\right)^2}\right]F(t_1'', t_2'')\right\} \tag{13-13b}$$

$$t_1'' = -\frac{b_1}{2}\sqrt{\frac{k}{\pi\rho_1}} \tag{13-13c}$$

$$t_2'' = +\frac{b_1}{2}\sqrt{\frac{k}{\pi\rho_1}} \tag{13-13d}$$

To better understand the performance of an E-plane sectoral horn and gain some insight into its performance as an efficient radiator, a three-dimensional normalized field pattern has been plotted in Figure 13.3 utilizing (13-11a)–(13-11c). As expected, the E-plane pattern is much narrower than the H-plane because of the flaring and larger dimensions of the horn in that direction. Figure 13.3 provides an excellent visual view of the overall radiation performance of the horn. To display additional details, the corresponding normalized E- and H-plane patterns (in dB) are illustrated in Figure 13.4. These patterns also illustrate the narrowness of the E-plane and provide information on the relative levels of the pattern in those two planes.

To examine the behavior of the pattern as a function of flaring, the E-plane patterns for a horn antenna with $\rho_1 = 15\lambda$ and with flare angles of $20° \le 2\psi_e \le 35°$ are plotted in Figure 13.5. A total of four patterns is illustrated. Since each pattern is *symmetrical, only half of each pattern is displayed. For small included angles,* the pattern becomes narrower as the flare increases. Eventually the pattern begins to widen, becomes flatter around the main lobe, and the phase tapering at the aperture is such that even the main maximum does not occur on axis. This is illustrated in Figure 13.5 by the pattern with $2\psi_e = 35°$. As the flaring is extended beyond that point, the flatness (with certain allowable ripple) increases and eventually the main

INTEL-1045
U.S. Patent 7,151,430

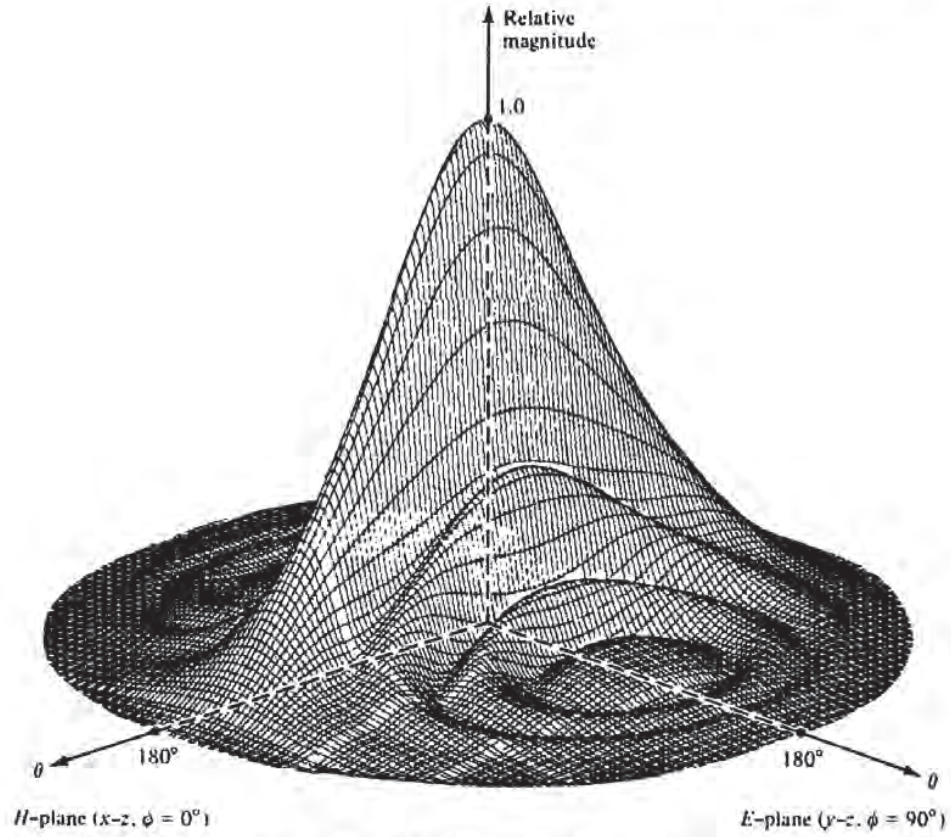


Figure 13.3 Three-dimensional field pattern of *E*-plane sectoral horn ($\rho_1 = 6\lambda$, $b_1 = 2.75\lambda$, $a = 0.5\lambda$).

maximum returns again on axis. It is also observed that as the flaring increases, the pattern exhibits much sharper cutoff characteristics. In practice, to compensate for the phase taper at the opening, a lens is usually placed at the aperture making the pattern of the horn always narrower as its flare increases.

Similar pattern variations occur as the length of the horn is varied while the flare angle is held constant. As the length increases, the pattern begins to broaden and eventually becomes flatter (with a ripple). Beyond a certain length, the main maximum does not even occur on axis, and the pattern continues to broaden and to become flatter (within an allowable ripple) until the maximum returns on axis. The process continues indefinitely.

An observation of the *E*-plane pattern, as given by (13-12a)–(13-12d), indicates that the *magnitude of the normalized pattern, excluding the factor* $(1 + \cos\theta)$, can be written as

$$E_{\theta n} = F(t_1', t_2') = [C(t_2') - C(t_1')] - j[S(t_2') - S(t_1')] \qquad (13\text{-}14a)$$

$$t_1' = \sqrt{\frac{k}{\pi\rho_1}}\left(-\frac{b_1}{2} - \rho_1 \sin\theta\right)$$

$$= 2\sqrt{\frac{b_1^2}{8\lambda\rho_1}}\left[-1 - \frac{1}{4}\left(\frac{8\rho_1\lambda}{b_1^2}\right)\left(\frac{b_1}{\lambda}\sin\theta\right)\right]$$

$$= 2\sqrt{s}\left[-1 - \frac{1}{4}\left(\frac{1}{s}\right)\left(\frac{b_1}{\lambda}\sin\theta\right)\right] \qquad (13\text{-}14b)$$

INTEL-1045
U.S. Patent 7,151,430

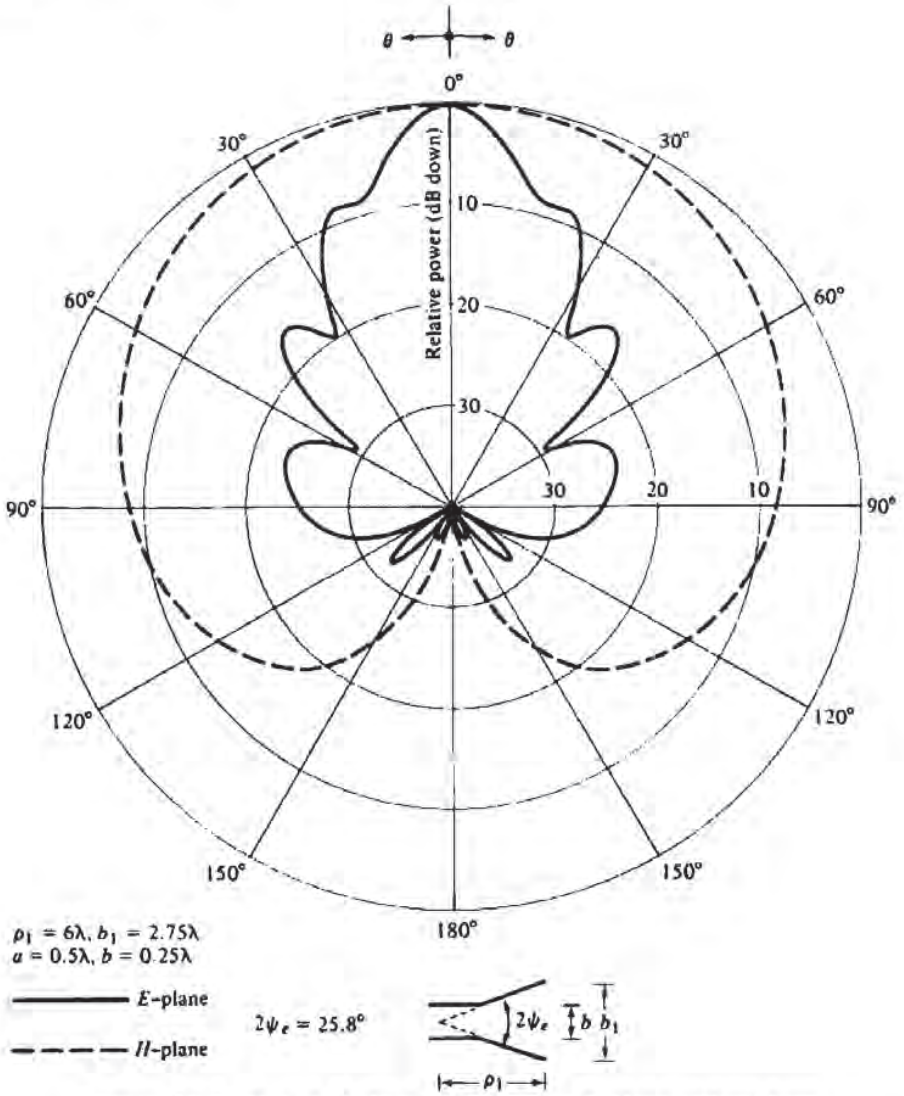


Figure 13.4 *E*- and *H*-plane patterns of an *E*-plane sectoral horn.

$$t_2' = \sqrt{\frac{k}{\pi\rho_1}}\left(\frac{b_1}{2} - \rho_1 \sin\theta\right)$$

$$= 2\sqrt{\frac{{b_1}^2}{8\lambda\rho_1}}\left[1 - \frac{1}{4}\left(\frac{8\rho_1\lambda}{{b_1}^2}\right)\left(\frac{b_1}{\lambda}\sin\theta\right)\right]$$

$$= 2\sqrt{s}\left[1 - \frac{1}{4}\left(\frac{1}{s}\right)\left(\frac{b_1}{\lambda}\sin\theta\right)\right] \tag{13-14c}$$

$$s = \frac{{b_1}^2}{8\lambda\rho_1} \tag{13-14d}$$

INTEL-1045
U.S. Patent 7,151,430

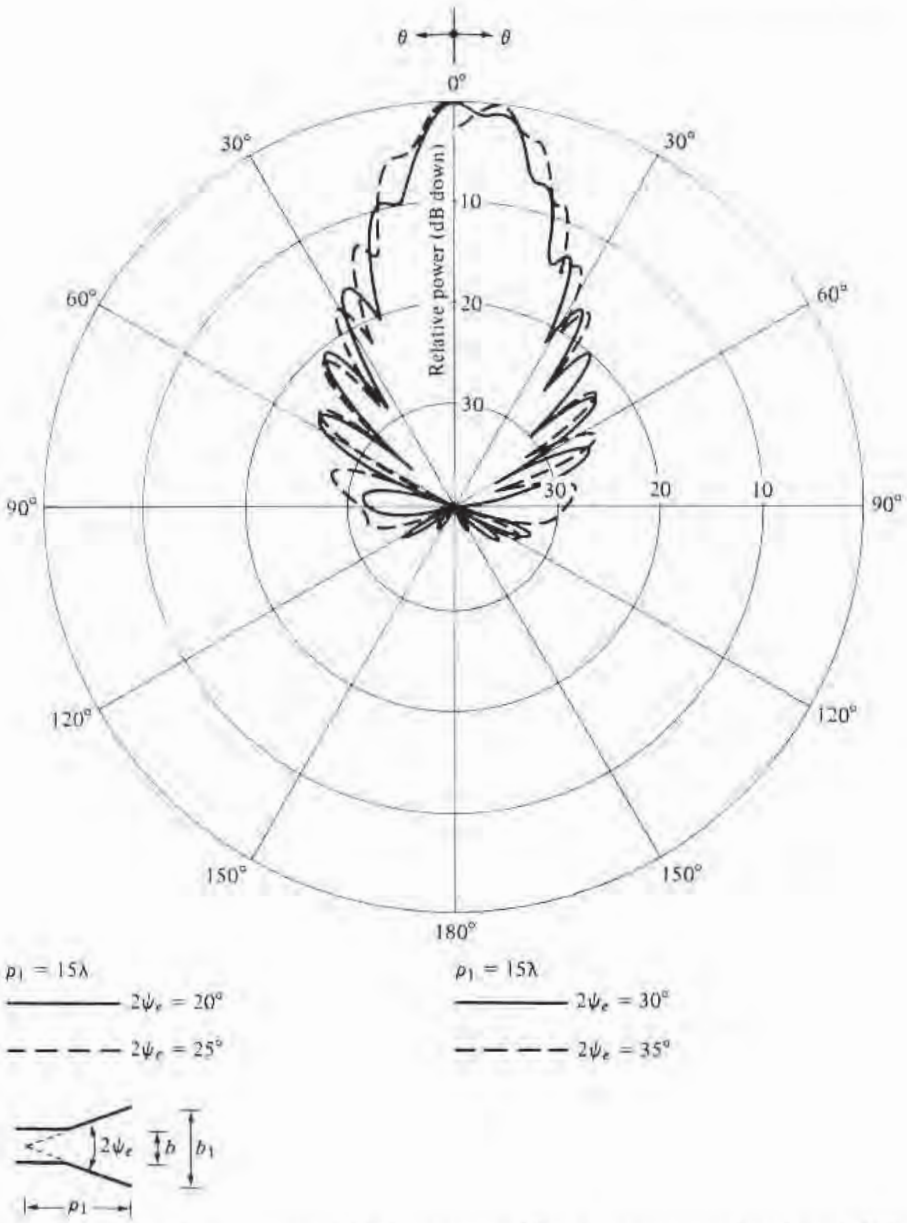


Figure 13.5 *E*-plane patterns of *E*-plane sectoral horn for constant length and different included angles.

For a given value of s, the field of (13-14a) can be plotted as a function of $b_1/\lambda \sin\theta$, as shown in Figure 13.6 for $s = \frac{1}{64}, \frac{1}{8}, \frac{1}{4}, \frac{1}{2}, \frac{3}{4}$, and 1. These plots are usually referred to as *universal curves*, because from them the normalized *E*-plane pattern of any *E*-plane sectoral horn can be obtained. This is accomplished by first determining the value of s from a given b_1 and ρ_1 by using (13-14d). For that value of s, the field strength (in dB) as a function of $(b_1/\lambda)\sin\theta$ (or as a function of θ for a given b_1) is obtained from Figure 13.6. Finally the value of $(1 + \cos\theta)$, normalized to 0 dB and written as $20 \log_{10}[(1 + \cos\theta)/2]$, is added to that number to arrive at the required field strength.

INTEL-1045
U.S. Patent 7,151,430

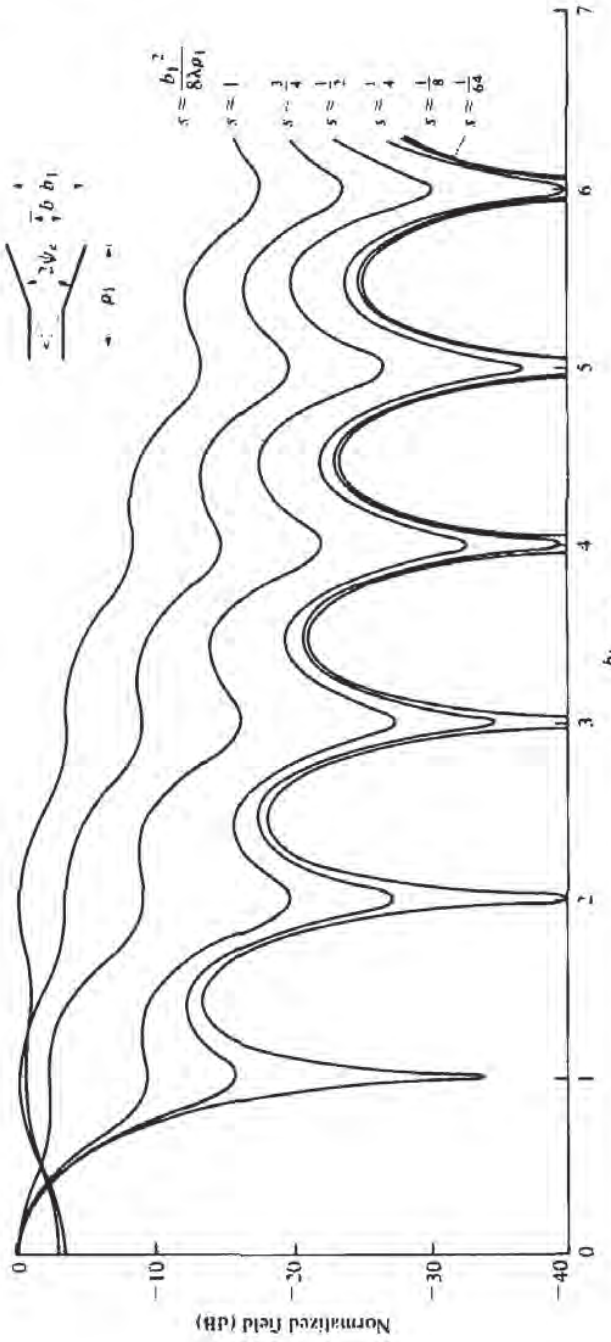


Figure 13.6 *E*-plane universal patterns for *E*-plane sectoral and pyramidal horns.

Example 13.2

An E-plane horn has dimensions of $a = 0.5\lambda$, $b = 0.25\lambda$, $b_1 = 2.75\lambda$, and $\rho_1 = 6\lambda$. Find its E-plane normalized field intensity (in dB *and* as a voltage ratio) at an angle of $\theta = 90°$ using the universal curves of Figure 13.6.

SOLUTION

Using (13-14d)

$$s = \frac{b_1^2}{8\lambda\rho_1} = \frac{(2.75)^2}{8(6)} = 0.1575 \approx \frac{1}{6.3}$$

None of the curves in Figure 13.6 represents $s = \frac{1}{6.3}$. Therefore interpolation will be used between the $s = \frac{1}{4}$ and $s = \frac{1}{8}$ curves.

At $\theta = 90°$

$$\frac{b_1}{\lambda}\sin(\theta) = 2.75\sin(90°) = 2.75$$

and at that point the field intensity between the $s = \frac{1}{4}$ and $s = \frac{1}{8}$ curves is about -20 dB. Therefore the total field intensity at $\theta = 90°$ is equal to

$$E_\theta = -20 + 20\log_{10}\left(\frac{1 + \cos 90°}{2}\right) = -20 - 6 = -26 \text{ dB}$$

or as a normalized voltage ratio of

$$E_\theta = 0.05$$

which closely agrees with the results of Figure 13.4.

13.2.3 Directivity

The directivity is one of the parameters that is often used as a figure-of-merit to describe the performance of an antenna. To find the directivity, the maximum radiation is formed. That is,

$$U_{\max} = U(\theta, \phi)|_{\max} = \frac{r^2}{2\eta}|\mathbf{E}|^2_{\max} \tag{13-15}$$

For most horn antennas $|\mathbf{E}|_{\max}$ is directed nearly along the z-axis ($\theta = 0°$). Thus,

$$|\mathbf{E}|_{\max} = \sqrt{|E_\theta|^2_{\max} + |E_\phi|^2_{\max}} = \frac{2a\sqrt{\pi k\rho_1}}{\pi^2 r}|E_1||F(t)| \tag{13-16}$$

Using (13-11b), (13-11c), and (13-9c)

$$|E_\theta|_{\max} = \frac{2a\sqrt{\pi k\rho_1}}{\pi^2 r}|E_1 \sin\phi\, F(t)| \tag{13-16a}$$

$$|E_\phi|_{\max} = \frac{2a\sqrt{\pi k\rho_1}}{\pi^2 r}|E_1 \cos\phi\, F(t)| \tag{13-16b}$$

INTEL-1045
U.S. Patent 7,151,430

$$F(t) = [C(t) - jS(t)] \tag{13-16c}$$

$$t = \frac{b_1}{2}\sqrt{\frac{k}{\pi\rho_1}} = \frac{b_1}{\sqrt{2\lambda\rho_1}} \tag{13-16d}$$

since

$$k_x = k_y = 0 \tag{13-16e}$$

$$t_1 = -t = -\frac{b_1}{2}\sqrt{\frac{k}{\pi\rho_1}} = -\frac{b_1}{\sqrt{2\lambda\rho_1}} \tag{13-16f}$$

$$t_2 = +t = +\frac{b_1}{2}\sqrt{\frac{k}{\pi\rho_1}} = \frac{b_1}{\sqrt{2\lambda\rho_1}} \tag{13-16g}$$

$$C(-t) = -C(t) \tag{13-16h}$$

$$S(-t) = -S(t) \tag{13-16i}$$

Thus

$$U_{\max} = \frac{r^2}{2\eta}|\mathbf{E}|^2_{\max} = \frac{2a^2k\rho_1}{\eta\pi^3}|E_1|^2|F(t)|^2$$

$$= \frac{4a^2\rho_1|E_1|^2}{\eta\lambda\pi^2}|F(t)|^2 \tag{13-17}$$

where

$$|F(t)|^2 = \left[C^2\left(\frac{b_1}{\sqrt{2\lambda\rho_1}}\right) + S^2\left(\frac{b_1}{\sqrt{2\lambda\rho_1}}\right)\right] \tag{13-17a}$$

The total power radiated can be found by simply integrating the average power density over the aperture of the horn. Using (13-1a)–(13-1d)

$$P_{\text{rad}} = \frac{1}{2}\iint_{S_0}\text{Re}(\mathbf{E}' \times \mathbf{H}'^*)\cdot d\mathbf{s} = \frac{1}{2\eta}\int_{-b_1/2}^{+b_1/2}\int_{-a/2}^{+a/2}|E_1|^2\cos^2\left(\frac{\pi}{a}x'\right)dx'\,dy' \tag{13-18}$$

which reduces to

$$P_{\text{rad}} = |E_1|^2\frac{b_1 a}{4\eta} \tag{13-18a}$$

Using (13-17) and (13-18a), the directivity for the E-plane horn can be written as

$$\boxed{D_E = \frac{4\pi U_{\max}}{P_{\text{rad}}} = \frac{64a\rho_1}{\pi\lambda b_1}|F(t)|^2 = \frac{64a\rho_1}{\pi\lambda b_1}\left[C^2\left(\frac{b_1}{\sqrt{2\lambda\rho_1}}\right) + S^2\left(\frac{b_1}{\sqrt{2\lambda\rho_1}}\right)\right]} \tag{13-19}$$

The overall performance of an antenna system can often be judged by its beamwidth and/or its directivity. The half-power beamwidth (HPBW), as a function of flare angle, for different horn lengths is shown in Figure 13.7. In addition, the directivity (normalized with respect to the constant aperture dimension a) is displayed in Figure 13.8. For a given length, the horn exhibits a monotonic decrease in half-power beam-

INTEL-1045
U.S. Patent 7,151,430

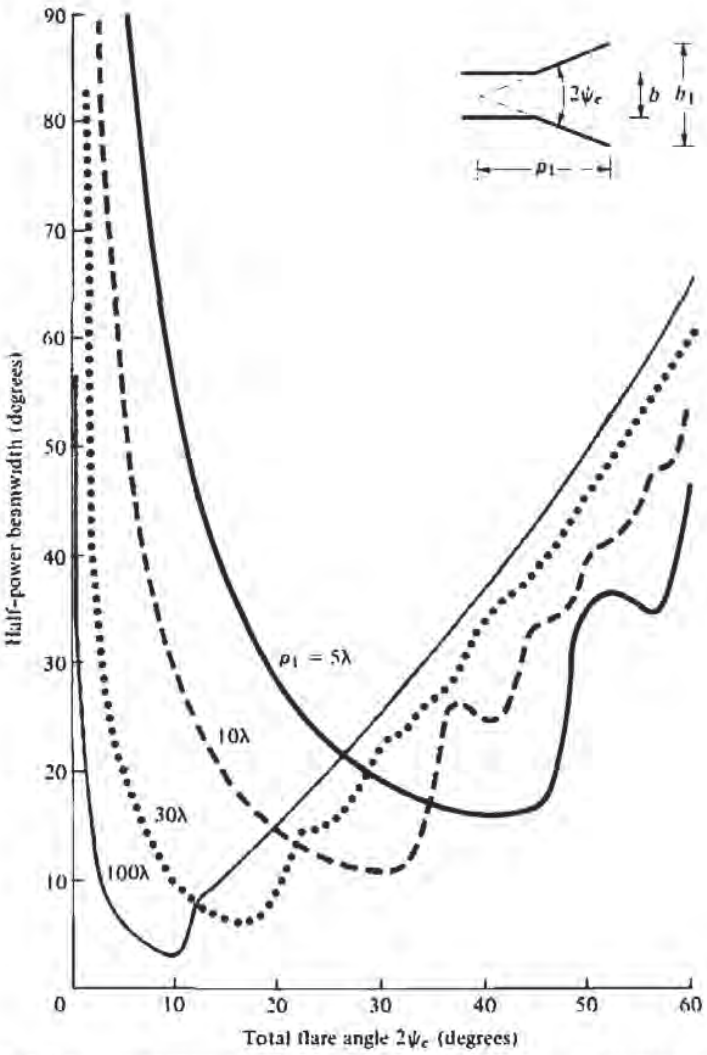


Figure 13.7 Half-power beamwidth of E-plane sectoral horn as a function of included angle and for different lengths.

width and an increase in directivity up to a certain flare. Beyond that point a monotonic increase in beamwidth and decrease in directivity is indicated followed by rises and falls. The increase in beamwidth and decrease in directivity beyond a certain flare indicate the broadening of the main beam.

If the values of b_1 (in λ), which correspond to the maximum directivities in Figure 13.8, are plotted versus their corresponding values of ρ_1 (in λ), it can be shown that each optimum directivity occurs when

$$\boxed{b_1 \simeq \sqrt{2\lambda\rho_1}} \tag{13-19a}$$

with a corresponding value of s equal to

$$\boxed{s|_{b_1=\sqrt{2\lambda\rho_1}} = s_{op} = \left.\frac{b_1^2}{8\lambda\rho_1}\right|_{b_1=\sqrt{2\lambda\rho_1}} = \frac{1}{4}} \tag{13-19b}$$

INTEL-1045
U.S. Patent 7,151,430

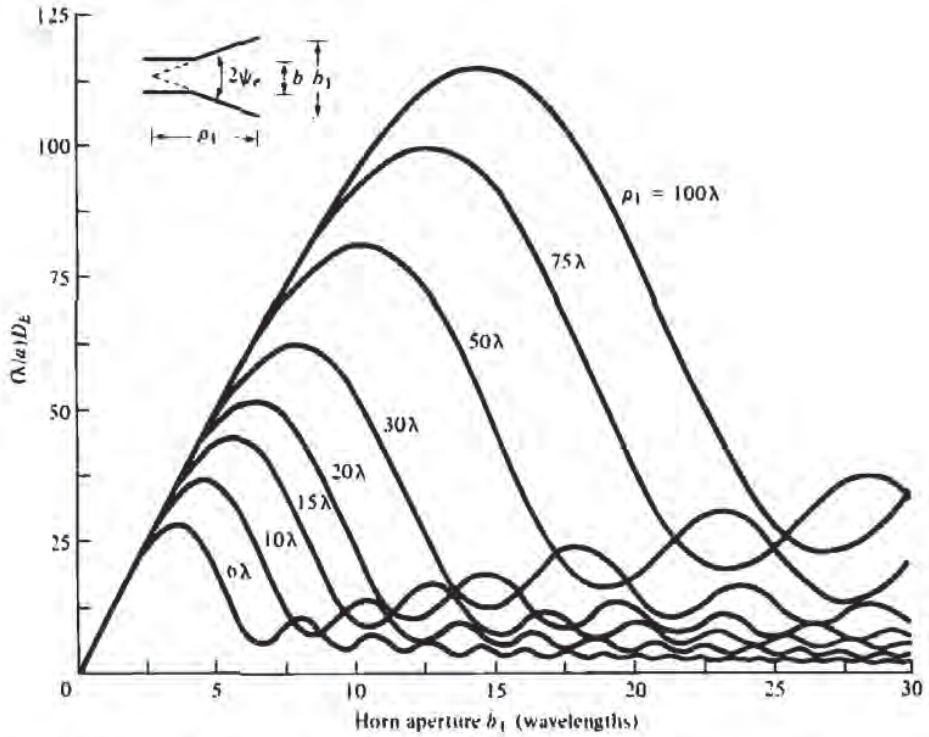


Figure 13.8 Normalized directivity of *E*-plane sectoral horn as a function of aperture size and for different lengths.

The classic expression of (13-19) for the directivity of an *E*-plane horn has been the standard for many years. However, it has been shown that this expression may not always yield very accurate values for the on-axis directivity. A more accurate expression for the maximum on-axis directivity based on an exact open-ended parallel-plate waveguide analysis has been derived, and it yields a modification to the on-axis value of (13-19), which provides sufficient accuracy for most designs [12], [13]. Using (13-19a), the modified formula for the on-axis value of (13-19) can be written as [12], [13]

$$D_E(\max) = \frac{16ab_1}{\lambda^2(1 + \lambda_g/\lambda)}\left[C^2\left(\frac{b_1}{\sqrt{2\lambda\rho_1}}\right) + S^2\left(\frac{b_1}{\sqrt{2\lambda\rho_1}}\right)\right]e^{\frac{\pi a}{\lambda}\left(1 - \frac{\lambda}{\lambda_g}\right)} \quad (13\text{-}19c)$$

where λ_g is the guide wavelength in the feed waveguide for the dominant TE_{10} mode. Predicted values based on (13-19) and (13-19c) have been compared with measurements and it was found that (13-19c) yielded results which were closer to the measured values [12].

The directivity of an *E*-plane sectoral horn can also be computed by using the following procedure [14].

1. Calculate B by

$$B = \frac{b_1}{\lambda}\sqrt{\frac{50}{\rho_e/\lambda}} \quad (13\text{-}20a)$$

INTEL-1045
U.S. Patent 7,151,430

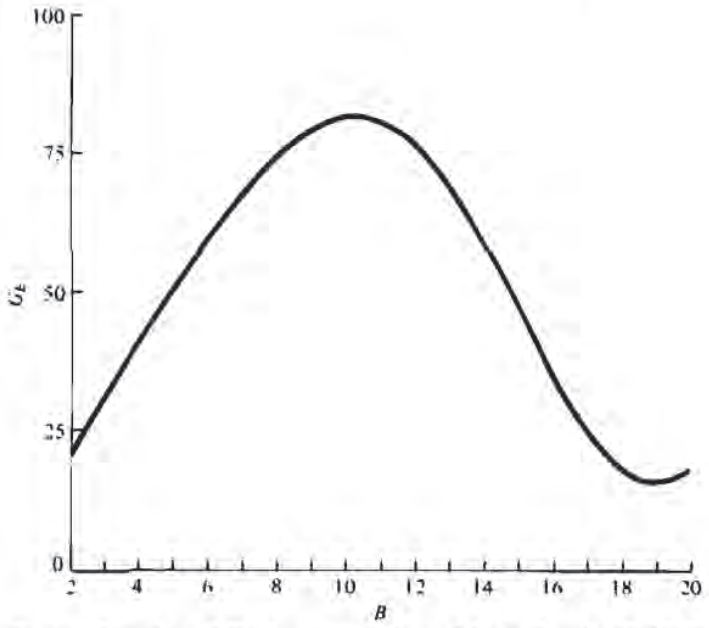


Figure 13.9 G_E as a function of B. (SOURCE: Adopted from data by E. H. Braun, "Some Data for the Design of Electromagnetic Horns," *IRE Trans. Antennas Propagat.*, Vol. AP-4, No. 1, January 1956. © (1956) IEEE)

2. Using this value of B, find the corresponding value of G_E from Figure 13.9. If, however, the value of B is smaller than 2, compute G_E using

$$G_E = \frac{32}{\pi} B \tag{13-20b}$$

3. Calculate D_E by using the value of G_E from Figure 13.9 or from (13-20b). Thus

$$\boxed{D_E = \frac{a}{\lambda} \frac{G_E}{\sqrt{\frac{50}{\rho_1/\lambda}}}} \tag{13-20c}$$

Example 13.3

An E-plane sectoral horn has dimensions of $a = 0.5\lambda$, $b = 0.25\lambda$, $b_1 = 2.75\lambda$, and $\rho_1 = 6\lambda$. Compute the directivity using (13-19) and (13-20c). Compare the answers.

SOLUTION

For this horn

$$\frac{b_1}{\sqrt{2\lambda\rho_1}} = \frac{2.75}{\sqrt{2(6)}} = 0.794$$

INTEL-1045
U.S. Patent 7,151,430

Therefore (from Appendix IV)

$$|C(0.794)|^2 = (0.72)^2 = 0.518$$
$$|S(0.794)|^2 = (0.24)^2 = 0.0576$$

Using (13-19)

$$D_E = \frac{64(0.5)6}{2.75\pi}(0.518 + 0.0576) = 12.79 = 11.07 \text{ dB}$$

To compute the directivity using (13-20c), the following parameters are evaluated:

$$\rho_e = \lambda\sqrt{(6)^2 + \left(\frac{2.75}{2}\right)^2} = 6.1555\lambda$$

$$\sqrt{\frac{50}{\rho_e/\lambda}} = \sqrt{\frac{50}{6.1555}} = 2.85$$

$$B = 2.75(2.85) = 7.84$$

For $B = 7.84$, $G_E = 73.5$ from Figure 13.9. Thus, using (13-20c)

$$D_E = \frac{0.5(73.5)}{2.85} = 12.89 = 11.10 \text{ dB}$$

Obviously an excellent agreement between the results of (13-19) and (13-20c).

13.3 *H*-PLANE SECTORAL HORN

Flaring the dimensions of a rectangular waveguide in the direction of the **H**-field, while keeping the other constant, forms an *H*-plane sectoral horn shown in Figure 13.1(b). A more detailed geometry is shown in Figure 13.10.

The analysis procedure for this horn is similar to that for the *E*-plane horn, which was outlined in the previous section. Instead of including all the details of the formulation, a summary of each radiation characteristic will be given.

13.3.1 Aperture Fields

The fields at the aperture of the horn can be found by treating the horn as a radial waveguide forming an imaginary apex shown dashed in Figure 13.10. Using this method, it can be shown that at the aperture of the horn

$$E_{x'} = H_{y'} = 0 \tag{13-21a}$$

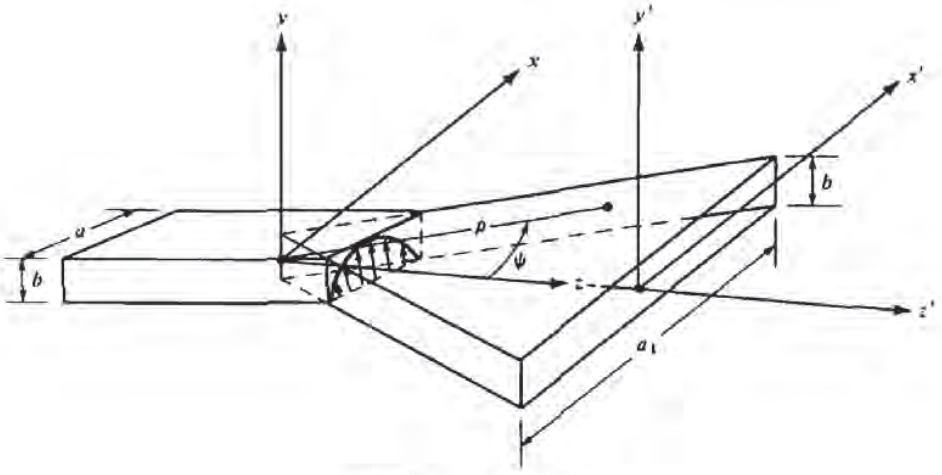
$$E_{y'}(x') = E_2 \cos\left(\frac{\pi}{a_1}x'\right) e^{-jk\delta(x')} \tag{13-21b}$$

$$H_{x'}(x') = -\frac{E_2}{\eta}\cos\left(\frac{\pi}{a_1}x'\right) e^{-jk\delta(x')} \tag{13-21c}$$

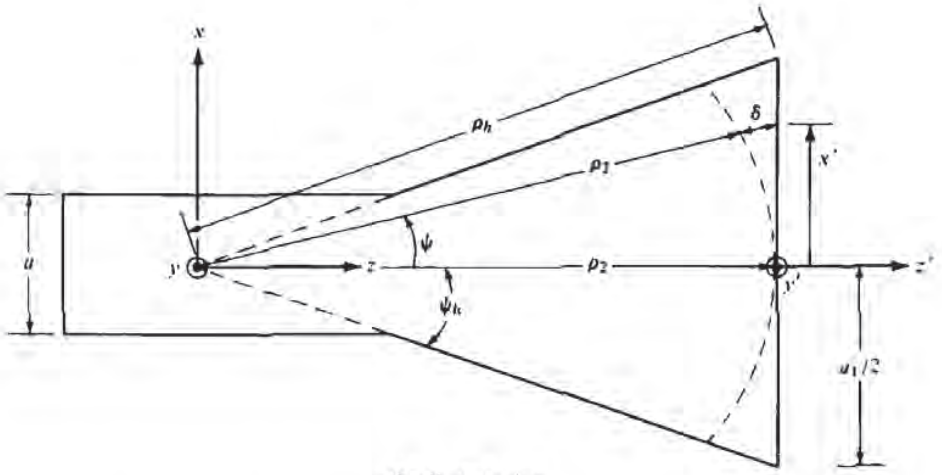
$$\delta(x') = \frac{1}{2}\left(\frac{x'^2}{\rho_2}\right) \tag{13-21d}$$

$$\rho_2 = \rho_h \cos\psi_h \tag{13-21e}$$

INTEL-1045
U.S. Patent 7,151,430



(a) *H*-plane sectoral horn



(b) *H*-plane view

Figure 13.10 *H*-plane sectoral horn and coordinate system.

13.3.2 Radiated Fields

The fields radiated by the horn can be found by first formulating the equivalent current densities $\mathbf{J}_s$ and $\mathbf{M}_s$. Using (13-21a)–(13-21c), it can be shown that over the aperture of the horn

$$J_x = J_z = M_y = M_z = 0 \tag{13-22a}$$

$$J_y = -\frac{E_2}{\eta}\cos\left(\frac{\pi}{a_1}x'\right)e^{-jk\delta(x')} \tag{13-22b}$$

$$M_x = E_2\cos\left(\frac{\pi}{a_1}x'\right)e^{-jk\delta(x')} \tag{13-22c}$$

and they are assumed to be zero elsewhere. Thus (12-12a) can be expressed as

$$N_\theta = \iint_S J_y\cos\theta\cos\phi\, e^{-jkr'\cos\psi}\,ds' = -\frac{E_2}{\eta}\cos\theta\sin\phi\, I_1 I_2 \tag{13-23}$$

INTEL-1045
U.S. Patent 7,151,430

where

$$I_1 = \int_{-b/2}^{+b/2} e^{+jky' \sin\theta\sin\phi}\, dy' = b\left[\frac{\sin\left(\frac{kb}{2}\sin\theta\sin\phi\right)}{\frac{kb}{2}\sin\theta\sin\phi}\right] \tag{13-23a}$$

$$I_2 = \int_{-a_1/2}^{+a_1/2} \cos\left(\frac{\pi}{a_1}x'\right) e^{-jk[\delta(x')-x'\sin\theta\cos\phi]}\, dx' \tag{13-23b}$$

By rewriting $\cos[(\pi/a_1)x']$ as

$$\cos\left(\frac{\pi}{a_1}x'\right) = \left[\frac{e^{j(\pi/a_1)x'} + e^{-j(\pi/a_1)x'}}{2}\right] \tag{13-24}$$

(13-23b) can be expressed as

$$I_2 = I_2' + I_2'' \tag{13-25}$$

where

$$I_2' = \frac{1}{2}\sqrt{\frac{\pi\rho_2}{k}}\, e^{j(k_x'^2\rho_2/2k)}\{[C(t_2') - C(t_1')] - j[S(t_2') - S(t_1')]\} \tag{13-26}$$

$$\boxed{t_1' = \sqrt{\frac{1}{\pi k\rho_2}}\left(-\frac{ka_1}{2} - k_x'\rho_2\right)} \tag{13-26a}$$

$$\boxed{t_2' = \sqrt{\frac{1}{\pi k\rho_2}}\left(+\frac{ka_1}{2} - k_x'\rho_2\right)} \tag{13-26b}$$

$$\boxed{k_x' = k\sin\theta\cos\phi + \frac{\pi}{a_1}} \tag{13-26c}$$

$$I_2'' = \frac{1}{2}\sqrt{\frac{\pi\rho_2}{k}}\, e^{j(k_x''^2\rho_2/2k)}\{[C(t_2'') - C(t_1'')] - j[S(t_2'') - S(t_1'')]\} \tag{13-27}$$

$$\boxed{t_1'' = \sqrt{\frac{1}{\pi k\rho_2}}\left(-\frac{ka_1}{2} - k_x''\rho_2\right)} \tag{13-27a}$$

$$\boxed{t_2'' = \sqrt{\frac{1}{\pi k\rho_2}}\left(+\frac{ka_1}{2} - k_x''\rho_2\right)} \tag{13-27b}$$

$$\boxed{k_x'' = k\sin\theta\cos\phi - \frac{\pi}{a_1}} \tag{13-27c}$$

$C(x)$ and $S(x)$ are the cosine and sine Fresnel integrals of (13-8c) and (13-8d), and they are well tabulated (see Appendix IV).

INTEL-1045
U.S. Patent 7,151,430

With the aid of (13-23a), (13-25), (13-26), and (13-27), (13-23) reduces to

$$N_\theta = -E_2 \frac{b}{2}\sqrt{\frac{\pi\rho_2}{k}} \times \left\{\frac{\cos\theta\sin\phi}{\eta}\frac{\sin Y}{Y}\left[e^{jf_1}F(t_1', t_2') + e^{jf_2}F(t_1'', t_2'')\right]\right\} \tag{13-28}$$

$$\boxed{F(t_1, t_2) = [C(t_2) - C(t_1)] - j[S(t_2) - S(t_1)]} \tag{13-28a}$$

$$\boxed{f_1 = \frac{k_x'^2\rho_2}{2k}} \tag{13-28b}$$

$$\boxed{f_2 = \frac{k_x''^2\rho_2}{2k}} \tag{13-28c}$$

$$\boxed{Y = \frac{kb}{2}\sin\theta\sin\phi} \tag{13-28d}$$

In a similar manner, N_ϕ, L_θ, and L_ϕ of (12-12b)–(12-12d) can be written as

$$N_\phi = -E_2 \frac{b}{2}\sqrt{\frac{\pi\rho_2}{k}} \times \left\{\frac{\cos\phi}{\eta}\frac{\sin Y}{Y}\left[e^{jf_1}F(t_1', t_2') + e^{jf_2}F(t_1'', t_2'')\right]\right\} \tag{13-29a}$$

$$L_\theta = E_2 \frac{b}{2}\sqrt{\frac{\pi\rho_2}{k}} \times \left\{\cos\theta\cos\phi\frac{\sin Y}{Y}\left[e^{jf_1}F(t_1', t_2') + e^{jf_2}F(t_1'', t_2'')\right]\right\} \tag{13-29b}$$

$$L_\phi = -E_2 \frac{b}{2}\sqrt{\frac{\pi\rho_2}{k}} \times \left\{\sin\phi\frac{\sin Y}{Y}\left[e^{jf_1}F(t_1', t_2') + e^{jf_2}F(t_1'', t_2'')\right]\right\} \tag{13-29c}$$

The far-zone electric field components of (12-10a)–(12-10c) can then be expressed as

$$\boxed{E_r = 0} \tag{13-30a}$$

$$\boxed{E_\theta = jE_2\frac{b}{8}\sqrt{\frac{k\rho_2}{\pi}}\frac{e^{-jkr}}{r} \times \left\{\sin\phi(1 + \cos\theta)\frac{\sin Y}{Y}\left[e^{jf_1}F(t_1', t_2') + e^{jf_2}F(t_1'', t_2'')\right]\right\}} \tag{13-30b}$$

INTEL-1045
U.S. Patent 7,151,430

$$E_\phi = jE_2\frac{b}{8}\sqrt{\frac{k\rho_2}{\pi}}\frac{e^{-jkr}}{r} \times \left\{\cos\phi(\cos\theta + 1)\frac{\sin Y}{Y}\left[e^{jf_1}F(t_1', t_2') + e^{jf_2}F(t_1'', t_2'')\right]\right\} \tag{13-30c}$$

The electric field in the principal E- and H-planes reduces to

E-Plane ($\phi = \pi/2$)

$$E_r = E_\phi = 0 \tag{13-31a}$$

$$E_\theta = jE_2\frac{b}{8}\sqrt{\frac{k\rho_2}{\pi}}\frac{e^{-jkr}}{r} \times \left\{(1 + \cos\theta)\frac{\sin Y}{Y}\left[e^{jf_1}F(t_1', t_2') + e^{jf_2}F(t_1'', t_2'')\right]\right\} \tag{13-31b}$$

$$Y = \frac{kb}{2}\sin\theta \tag{13-31c}$$

$$k_x' = \frac{\pi}{a_1} \tag{13-31d}$$

$$k_x'' = -\frac{\pi}{a_1} \tag{13-31e}$$

H-Plane ($\phi = 0$)

$$E_r = E_\theta = 0 \tag{13-32a}$$

$$E_\phi = jE_2\frac{b}{8}\sqrt{\frac{k\rho_2}{\pi}}\frac{e^{-jkr}}{r} \times \left\{(\cos\theta + 1)\left[e^{jf_1}F(t_1', t_2') + e^{jf_2}F(t_1'', t_2'')\right]\right\} \tag{13-32b}$$

$$k_x' = k\sin\theta + \frac{\pi}{a_1} \tag{13-32c}$$

$$k_x'' = k\sin\theta - \frac{\pi}{a_1} \tag{13-32d}$$

with f_1, f_2, $F(t_1', t_2')$, $F(t_1'', t_2'')$, t_1', t_2', t_1'', and t_2'' as defined previously.

Computations similar to those for the E-plane sectoral horn were also performed for the H-plane sectoral horn. A three-dimensional field pattern of an H-plane sectoral horn is shown in Figure 13.11. Its corresponding E- and H-plane patterns are displayed in Figure 13.12. This horn exhibits narrow pattern characteristics in the flared H-plane.

Normalized H-plane patterns for a given length horn ($\rho_2 = 12\lambda$) and different flare angles are shown in Figure 13.13. A total of four patterns is illustrated. Since each pattern is symmetrical, only half of each pattern is displayed. As the included angle is increased, the pattern begins to become narrower up to a given flare. Beyond that point the pattern begins to broaden, attributed primarily to the phase taper (phase

INTEL-1045
U.S. Patent 7,151,430

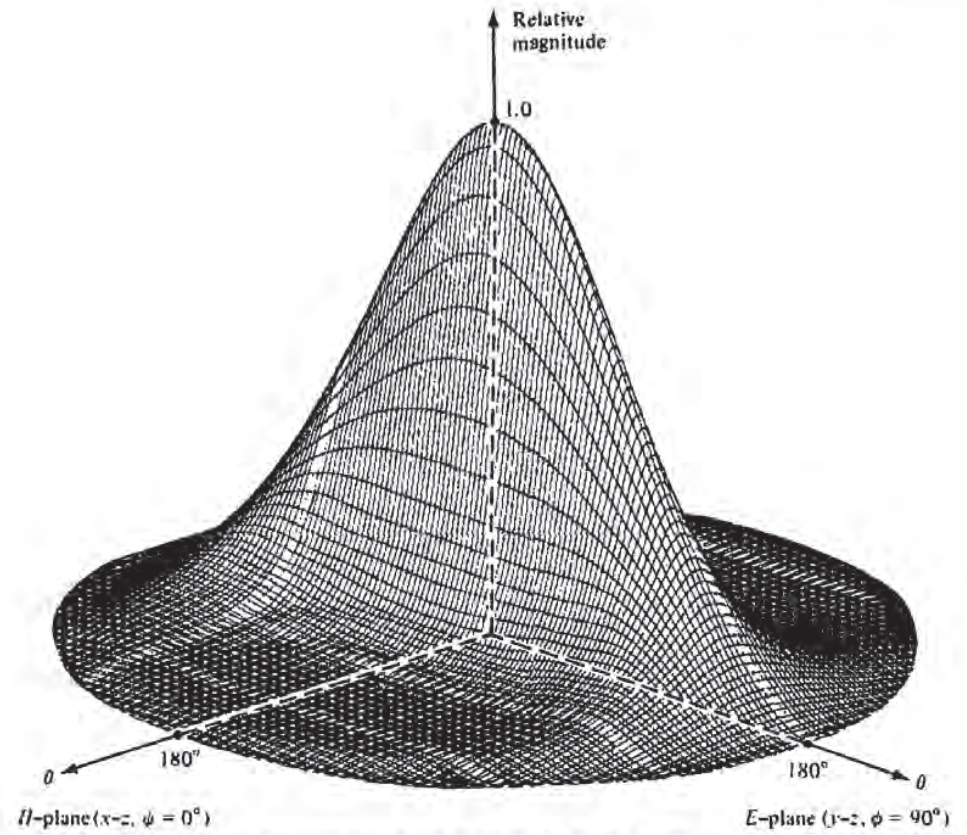


Figure 13.11 Three-dimensional field pattern of an *H*-plane sectoral horn ($\rho_2 = 6\lambda$, $a_1 = 5.5\lambda$, $b = 0.25\lambda$).

error) across the aperture of the horn. To correct this, a lens is usually placed at the horn aperture which would yield narrower patterns as the flare angle is increased. Similar pattern variations are evident when the flare angle of the horn is maintained fixed while its length is varied.

The *universal curves* for the *H*-plane sectoral horn are based on (13-32b), in the absence of the factor $(1 + \cos\theta)$. Neglecting the $(1 + \cos\theta)$ factor, the normalized *H*-plane electric field of the *H*-plane sectoral horn can be written as

$$E_{nhn} = [e^{jf_1}F(t_1', t_2') + e^{jf_2}F(t_1'', t_2'')] \tag{13-33}$$

$$F(t_1, t_2) = [C(t_2) - C(t_1)] - j[S(t_2) - S(t_1)] \tag{13-33a}$$

$$f_1 = \frac{k_x'^2\rho_2}{2k} = \frac{\rho_2}{2k}\left(k\sin\theta + \frac{\pi}{a_1}\right)^2$$

$$= \frac{\pi}{8}\left(\frac{1}{t}\right)\left(\frac{a_1}{\lambda}\sin\theta\right)^2\left[1 + \frac{1}{2}\left(\frac{\lambda}{a_1\sin\theta}\right)\right]^2 \tag{13-33b}$$

$$f_2 = \frac{k_x''^2\rho_2}{2k} = \frac{\rho_2}{2k}\left(k\sin\theta - \frac{\pi}{a_1}\right)^2$$

$$= \frac{\pi}{8}\left(\frac{1}{t}\right)\left(\frac{a_1}{\lambda}\sin\theta\right)^2\left[1 - \frac{1}{2}\left(\frac{\lambda}{a_1\sin\theta}\right)\right]^2 \tag{13-33c}$$

INTEL-1045
U.S. Patent 7,151,430

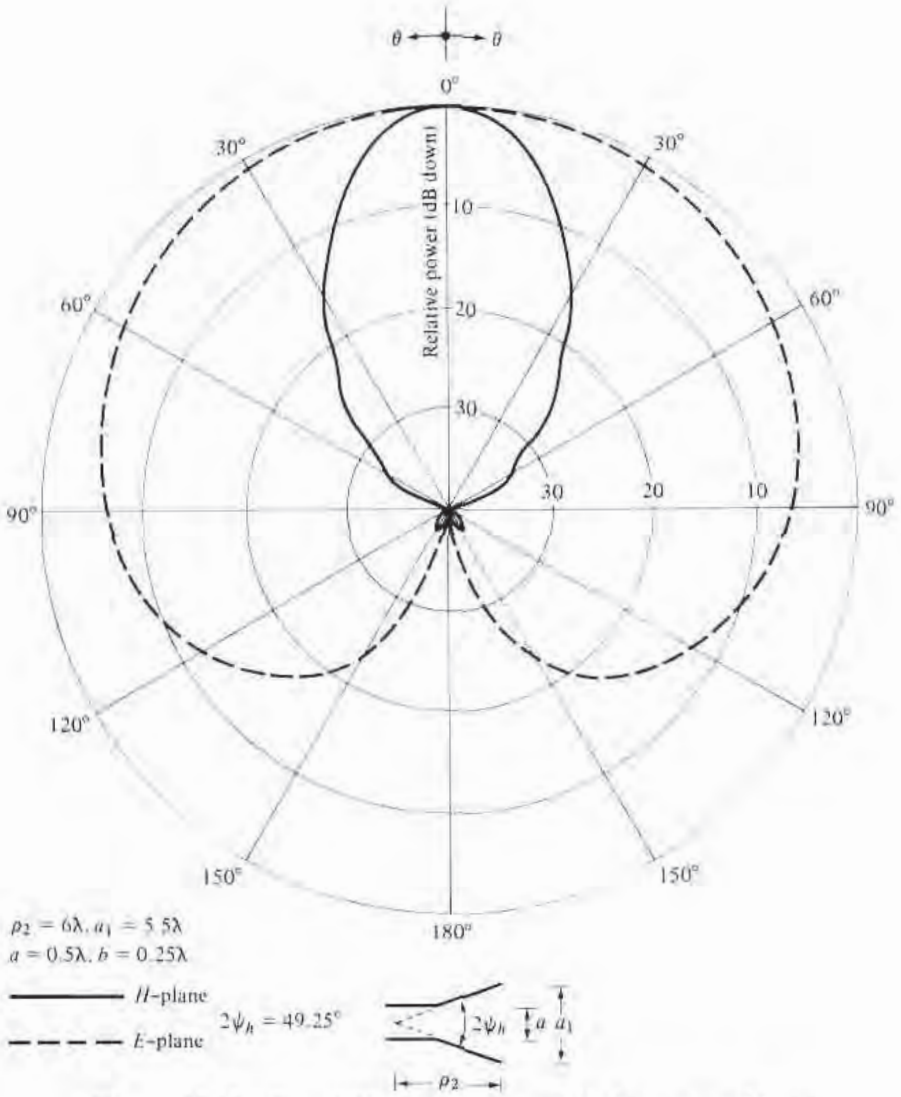


Figure 13.12 *E*- and *H*-plane patterns of *H*-plane sectoral horn.

$$t_1' = \sqrt{\frac{1}{\pi k \rho_2}}\left(-\frac{ka_1}{2} - k_x'\rho_2\right)$$

$$= 2\sqrt{t}\left[-1 - \frac{1}{4}\left(\frac{1}{t}\right)\left(\frac{a_1}{\lambda}\sin\theta\right) - \frac{1}{8}\left(\frac{1}{t}\right)\right] \tag{13-33d}$$

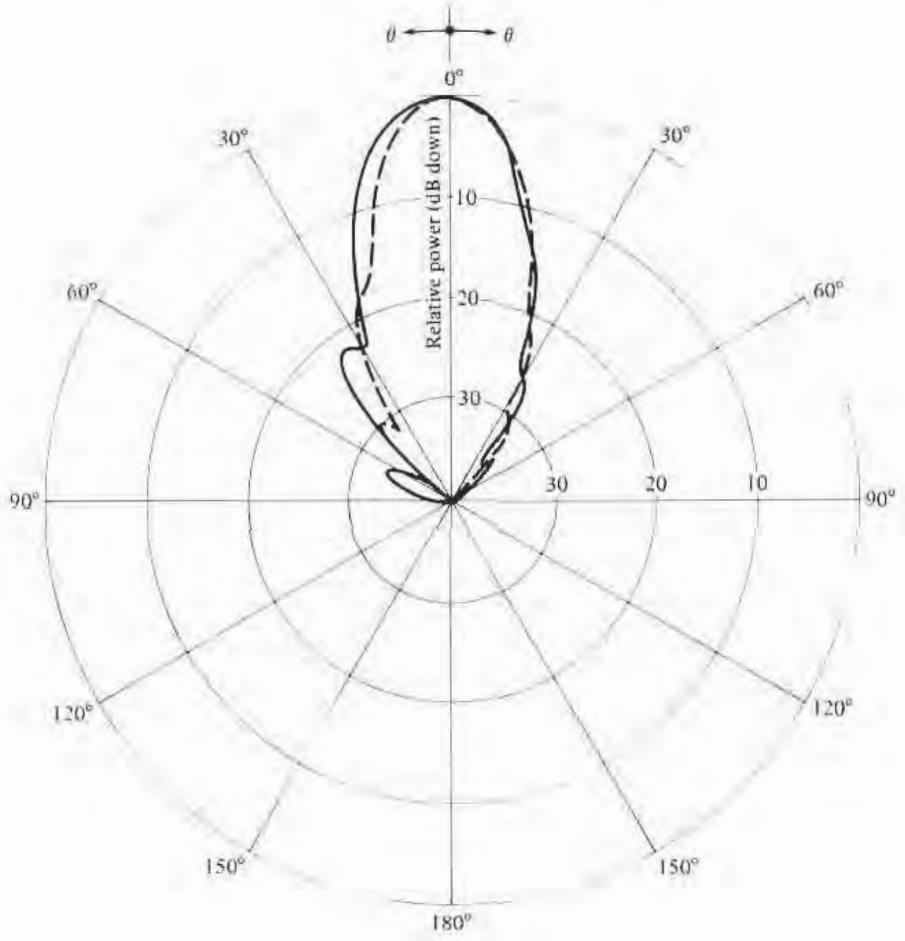
$$t_2' = \sqrt{\frac{1}{\pi k \rho_2}}\left(+\frac{ka_1}{2} - k_x'\rho_2\right)$$

$$= 2\sqrt{t}\left[+1 - \frac{1}{4}\left(\frac{1}{t}\right)\left(\frac{a_1}{\lambda}\sin\theta\right) - \frac{1}{8}\left(\frac{1}{t}\right)\right] \tag{13-33e}$$

$$t_1'' = \sqrt{\frac{1}{\pi k \rho_2}}\left(-\frac{ka_1}{2} - k_x''\rho_2\right)$$

$$= 2\sqrt{t}\left[-1 - \frac{1}{4}\left(\frac{1}{t}\right)\left(\frac{a_1}{\lambda}\sin\theta\right) + \frac{1}{8}\left(\frac{1}{t}\right)\right] \tag{13-33f}$$

INTEL-1045
U.S. Patent 7,151,430



$\rho_2 = 12\lambda$
$2\psi_h = 15°$
$2\psi_h = 20°$

$\rho_2 = 12\lambda$
$2\psi_h = 25°$
$2\psi_h = 30°$

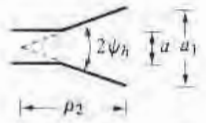


Figure 13.13 *H*-plane patterns of *H*-plane sectoral horn for constant length and different included angles.

$$t_2'' = \sqrt{\frac{1}{\pi k \rho_2}}\left(+\frac{ka_1}{2} - k_x''\rho_2\right)$$

$$= 2\sqrt{t}\left[+1 - \frac{1}{4}\left(\frac{1}{t}\right)\left(\frac{a_1}{\lambda}\sin\theta\right) + \frac{1}{8}\left(\frac{1}{t}\right)\right] \qquad (13\text{-}33g)$$

$$t = \frac{a_1^2}{8\lambda\rho_2} \qquad (13\text{-}33h)$$

INTEL-1045
U.S. Patent 7,151,430

For a given value of t, as given by (13-33h), the normalized field of (13-33) is plotted in Figure 13.14 as a function of $(a_1/\lambda)\sin\theta$ for $t = \frac{1}{\sqrt{3}}, \frac{1}{\sqrt{8}}, \frac{1}{3}, \frac{1}{2}, \frac{3}{5}$ and 1. Following a procedure identical to that for the E-plane sectoral horn, the H-plane pattern of any H-plane sectoral horn can be obtained from these curves. The normalized value of the $(1 + \cos\theta)$ factor in dB, written as $20\log_{10}[(1 + \cos\theta)/2]$, must also be included.

13.3.3 Directivity

To find the directivity of the H-plane sectoral horn, a procedure similar to that for the E-plane is used. As for the E-plane sectoral horn, the maximum radiation is directed nearly along the z-axis ($\theta = 0°$). Thus

$$|E_\theta|_{\max} = |E_2|\frac{b}{4r}\sqrt{\frac{2\rho_2}{\lambda}}\left|\sin\phi\{|C(t_2') + C(t_2'') - C(t_1') - C(t_1'')| - j[S(t_2') + S(t_2'') - S(t_1') - S(t_1'')]\}\right| \quad (13\text{-}34)$$

$$t_1' = \sqrt{\frac{1}{\pi k\rho_2}}\left(-\frac{ka_1}{2} - \frac{\pi}{a_1}\rho_2\right) \quad (13\text{-}34a)$$

$$t_2' = \sqrt{\frac{1}{\pi k\rho_2}}\left(+\frac{ka_1}{2} - \frac{\pi}{a_1}\rho_2\right) \quad (13\text{-}34b)$$

$$t_1'' = \sqrt{\frac{1}{\pi k\rho_2}}\left(-\frac{ka_1}{2} + \frac{\pi}{a_1}\rho_2\right) = -t_2' = v \quad (13\text{-}34c)$$

$$t_2'' = \sqrt{\frac{1}{\pi k\rho_2}}\left(+\frac{ka_1}{2} + \frac{\pi}{a_1}\rho_2\right) = -t_1' = u \quad (13\text{-}34d)$$

Since

$$C(-x) = -C(x) \quad (13\text{-}35a)$$

$$S(-x) = -S(x) \quad (13\text{-}35b)$$

$$|E_\theta|_{\max} = |E_2|\frac{b}{r}\sqrt{\frac{\rho_2}{2\lambda}}\left|\sin\phi\{|C(u) - C(v)| - j[S(u) - S(v)]\}\right| \quad (13\text{-}36)$$

$$u = t_2'' = -t_1' = \sqrt{\frac{1}{\pi k\rho_2}}\left(+\frac{ka_1}{2} + \frac{\pi}{a_1}\rho_2\right) = \frac{1}{\sqrt{2}}\left(\frac{\sqrt{\lambda\rho_2}}{a_1} + \frac{a_1}{\sqrt{\lambda\rho_2}}\right) \quad (13\text{-}36a)$$

$$v = t_1'' = -t_2' = \sqrt{\frac{1}{\pi k\rho_2}}\left(-\frac{ka_1}{2} + \frac{\pi}{a_1}\rho_2\right) = \frac{1}{\sqrt{2}}\left(\frac{\sqrt{\lambda\rho_2}}{a_1} - \frac{a_1}{\sqrt{\lambda\rho_2}}\right) \quad (13\text{-}36b)$$

Similarly

$$|E_\phi|_{\max} = |E_2|\frac{b}{r}\sqrt{\frac{\rho_2}{2\lambda}}\left|\cos\phi\{|C(u) - C(v)| - j[S(u) - S(v)]\}\right| \quad (13\text{-}37)$$

INTEL-1045
U.S. Patent 7,151,430

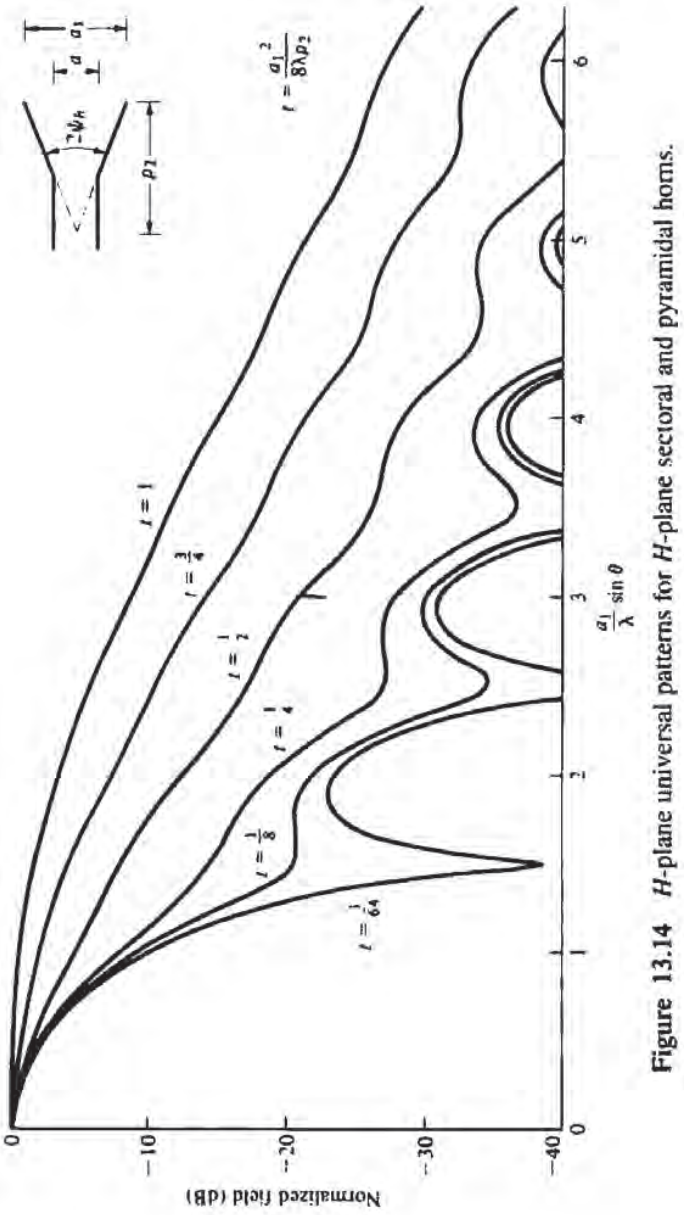


Figure 13.14 *H*-plane universal patterns for *H*-plane sectoral and pyramidal horns.

Thus

$$|\mathbf{E}|_{\max} = \sqrt{|E_\theta|^2_{\max} + |E_\phi|^2_{\max}} = |E_2|\frac{b}{r}\sqrt{\frac{\rho_2}{2\lambda}}\{[C(u) - C(v)]^2 + [S(u) - S(v)]^2\}^{1/2} \tag{13-38}$$

$$U_{\max} = |E_2|^2\frac{b^2\rho_2}{4\eta\lambda}\{[C(u) - C(v)]^2 + [S(u) - S(v)]^2\} \tag{13-39}$$

The total power radiated can be obtained by simply integrating the average power density over the mouth of the horn, and it is given by

$$P_{\text{rad}} = |E_2|^2\frac{ba_1}{4\eta} \tag{13-40}$$

Using (13-39) and (13-40), the directivity for the H-plane sectoral horn can be written as

$$\boxed{D_H = \frac{4\pi U_{\max}}{P_{\text{rad}}} = \frac{4\pi b\rho_2}{a_1\lambda} \times \{[C(u) - C(v)]^2 + [S(u) - S(v)]^2\}} \tag{13-41}$$

where

$$\boxed{u = \frac{1}{\sqrt{2}}\left(\frac{\sqrt{\lambda\rho_2}}{a_1} + \frac{a_1}{\sqrt{\lambda\rho_2}}\right)} \tag{13-41a}$$

$$\boxed{v = \frac{1}{\sqrt{2}}\left(\frac{\sqrt{\lambda\rho_2}}{a_1} - \frac{a_1}{\sqrt{\lambda\rho_2}}\right)} \tag{13-41b}$$

The half-power beamwidth (HPBW) as a function of flare angle is plotted in Figure 13.15. The normalized directivity (relative to the constant aperture dimension b) for different horn lengths, as a function of aperture dimension a_1, is displayed in Figure 13.16. As for the E-plane sectoral horn, the HPBW exhibits a monotonic decrease and the directivity a monotonic increase up to a given flare; beyond that, the trends are reversed.

If the values of a_1 (in λ), which correspond to the maximum directivities in Figure 13.16, are plotted versus their corresponding values of ρ_2 (in λ), it can be shown that each optimum directivity occurs when

$$\boxed{a_1 \simeq \sqrt{3\lambda\rho_2}} \tag{13-41c}$$

with a corresponding value of t equal to

$$\boxed{t|_{a_1=\sqrt{3\lambda\rho_2}} = t_{op} = \frac{a_1^2}{8\lambda\rho_2}\bigg|_{a_1=\sqrt{3\lambda\rho_2}} = \frac{3}{8}} \tag{13-41d}$$

The directivity of an H-plane sectoral horn can also be computed by using the following procedure [14].

1. Calculate A by

$$A = \frac{a_1}{\lambda}\sqrt{\frac{50}{\rho_1/\lambda}} \tag{13-42a}$$

INTEL-1045
U.S. Patent 7,151,430

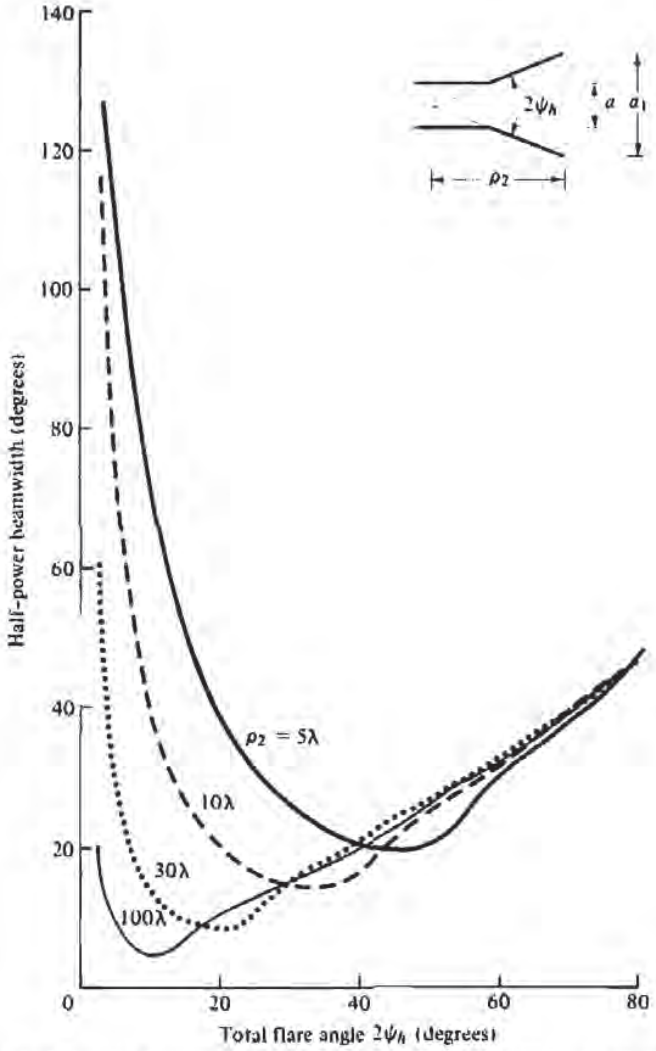


Figure 13.15 Half-power beamwidth of *H*-plane sectoral horn as a function of included angle and for different lengths.

2. Using this value of A, find the corresponding value of G_H from Figure 13.17. If the value of A is smaller than 2, then compute G_H using

$$G_H = \frac{32}{\pi} A \tag{13-42b}$$

3. Calculate D_H by using the value of G_H from Figure 13.17 or from (13-42b). Thus

$$D_H = \frac{b}{\lambda} \frac{G_h}{\sqrt{\frac{50}{\rho_h/\lambda}}} \tag{13-42c}$$

This is the actual directivity of the horn.

INTEL-1045
U.S. Patent 7,151,430

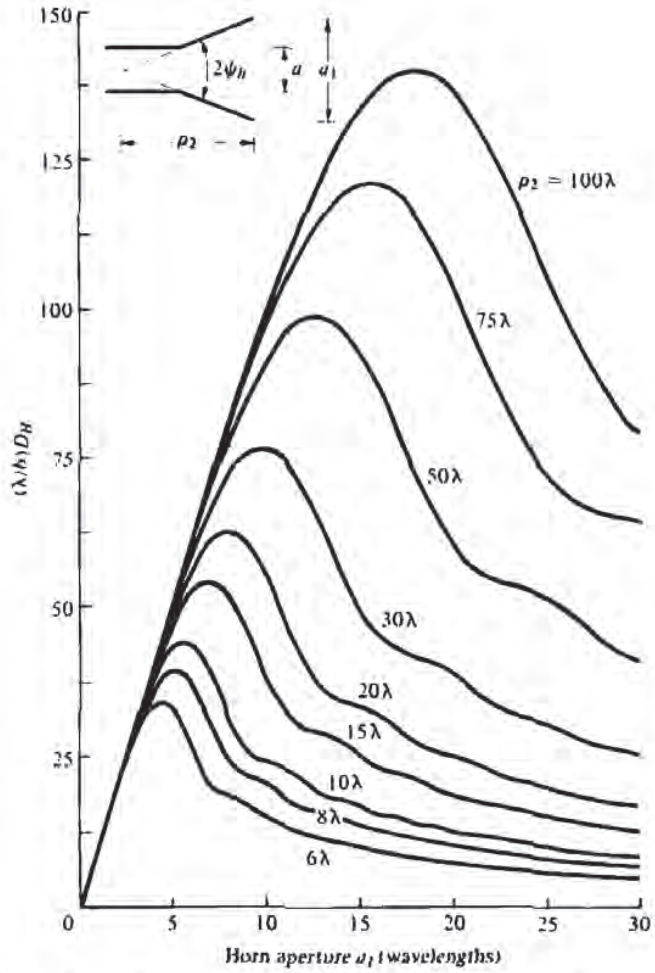


Figure 13.16 Normalized directivity of H-plane sectoral horn as a function of aperture size and for different lengths.

Example 13.4

An H-plane sectoral horn has dimensions of $a = 0.5\lambda$, $b = 0.25\lambda$, $a_1 = 5.5\lambda$, and $\rho_2 = 6\lambda$. Compute the directivity using (13-41) and (13-42c). Compare the answers.

SOLUTION

For this horn

$$u = \frac{1}{\sqrt{2}}\left(\frac{\sqrt{6}}{5.5} + \frac{5.5}{\sqrt{6}}\right) = 1.9$$

$$v = \frac{1}{\sqrt{2}}\left(\frac{\sqrt{6}}{5.5} - \frac{5.5}{\sqrt{6}}\right) = -1.273$$

INTEL-1045
U.S. Patent 7,151,430

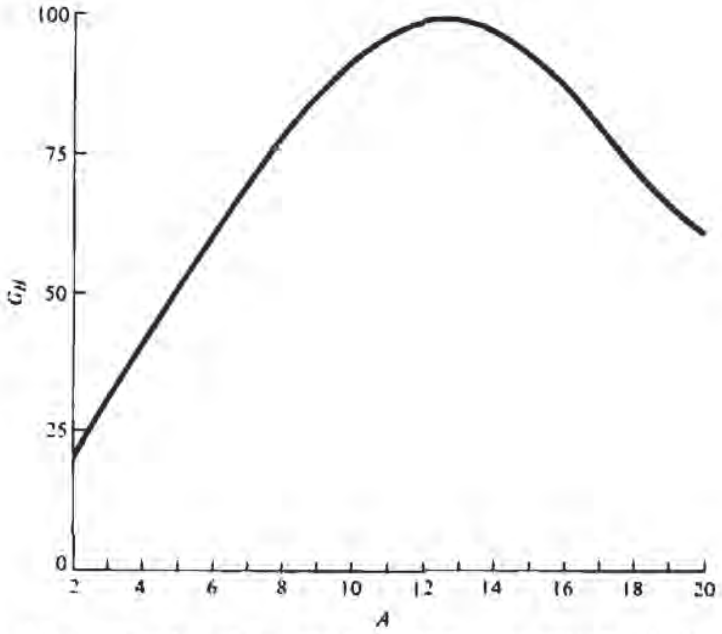


Figure 13.17 G_H as a function of A. (SOURCE: Adopted from data by E. H. Braun, "Some Data for the Design of Electromagnetic Horns," *IRE Trans. Antennas Propagat.*, Vol. AP-4, No. 1, January 1956. © (1956) IEEE)

Therefore (from Appendix IV)

$$C(1.9) = 0.394$$
$$C(-1.273) = -C(1.273) = -0.659$$
$$S(1.9) = 0.373$$
$$S(-1.273) = -S(1.273) = -0.669$$

Using (13-41)

$$D_H = \frac{4\pi(0.25)6}{5.5}[(0.394 + 0.659)^2 + (0.373 + 0.669)^2]$$
$$D_H = 7.52 = 8.763 \text{ dB}$$

To compute the directivity using (13-42c), the following parameters are computed:

$$\rho_h = \lambda\sqrt{(6)^2 + (5.5/2)^2} = 6.6\lambda$$
$$\sqrt{\frac{50}{\rho_h/\lambda}} = \sqrt{\frac{50}{6.6}} = 2.7524$$
$$A = 5.5(2.7524) = 15.14$$

For $A = 15.14$, $G_H = 91.8$ from Figure 13.17. Thus, using (13-42c)

$$D_H = \frac{0.25(91.8)}{2.7524} = 8.338 = 9.21 \text{ dB}$$

INTEL-1045
U.S. Patent 7,151,430

Although there is a good agreement between the results of (13-41) and (13-42c), they do not compare as well as those of Example 13.3.

13.4 PYRAMIDAL HORN

The most widely used horn is the one which is flared in both directions, as shown in Figure 13.18. It is widely referred to as a pyramidal horn, and its radiation characteristics are essentially a combination of the E- and H-plane sectoral horns.

13.4.1 Aperture Fields, Equivalent, and Radiated Fields

To simplify the analysis and to maintain a modeling that leads to computations that have been shown to correlate well with experimental data, the tangential components of the E- and H-fields over the aperture of the horn are approximated by

$$E_y'(x', y') = E_0 \cos\left(\frac{\pi}{a_1} x'\right) e^{-j[k(x'^2/\rho_2 + y'^2/\rho_1)/2]} \tag{13-43a}$$

$$H_x'(x', y') = -\frac{E_0}{\eta} \cos\left(\frac{\pi}{a_1} x'\right) e^{-j[k(x'^2/\rho_2 + y'^2/\rho_1)/2]} \tag{13-43b}$$

and the equivalent current densities by

$$J_y(x', y') = -\frac{E_0}{\eta} \cos\left(\frac{\pi}{a_1} x'\right) e^{-j[k(x'^2/\rho_2 + y'^2/\rho_1)/2]} \tag{13-44a}$$

$$M_x(x', y') = E_0 \cos\left(\frac{\pi}{a_1} x'\right) e^{-j[k(x'^2/\rho_2 + y'^2/\rho_1)/2]} \tag{13-44b}$$

The above expressions contain a cosinusoidal amplitude distribution in the x' direction and quadratic phase variations in both the x' and y' directions, similar to those of the sectoral E- and H-plane horns.

The N_θ, N_ϕ, L_θ and L_ϕ can now be formulated as before, and it can be shown that they are given by

$$N_\theta = -\frac{E_0}{\eta} \cos\theta \sin\phi I_1 I_2 \tag{13-45a}$$

$$N_\phi = -\frac{E_0}{\eta} \cos\phi I_1 I_2 \tag{13-45b}$$

$$L_\theta = E_0 \cos\theta \cos\phi I_1 I_2 \tag{13-45c}$$

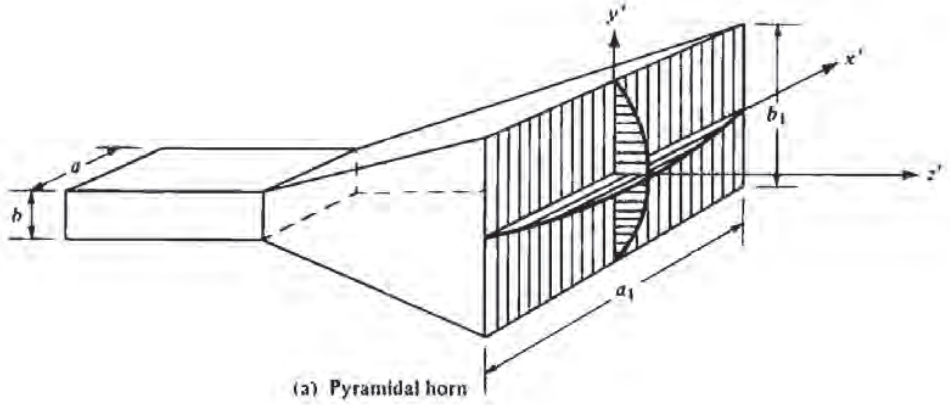
$$L_\phi = -E_0 \sin\phi I_1 I_2 \tag{13-45d}$$

where

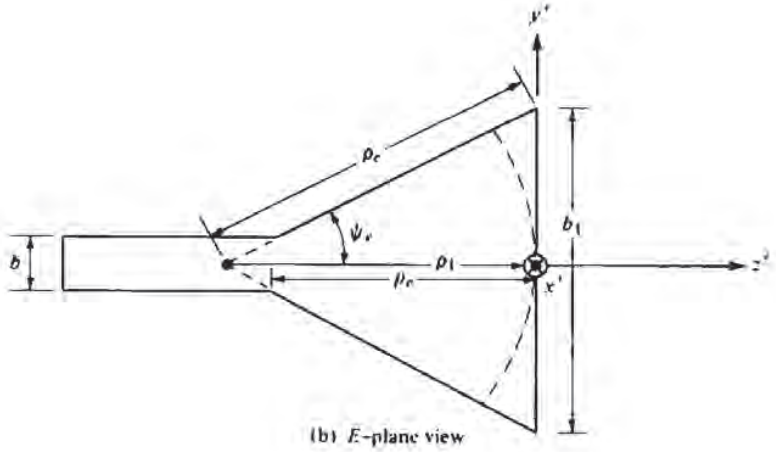
$$I_1 = \int_{-a_1/2}^{+a_1/2} \cos\left(\frac{\pi}{a} x'\right) e^{-jk[x'^2/(2\rho_1) - x'\sin\theta\cos\phi]} dx' \tag{13-45e}$$

$$I_2 = \int_{-b_1/2}^{+b_1/2} e^{-jk[y'^2/(2\rho_1) - y'\sin\theta\sin\phi]} dy' \tag{13-45f}$$

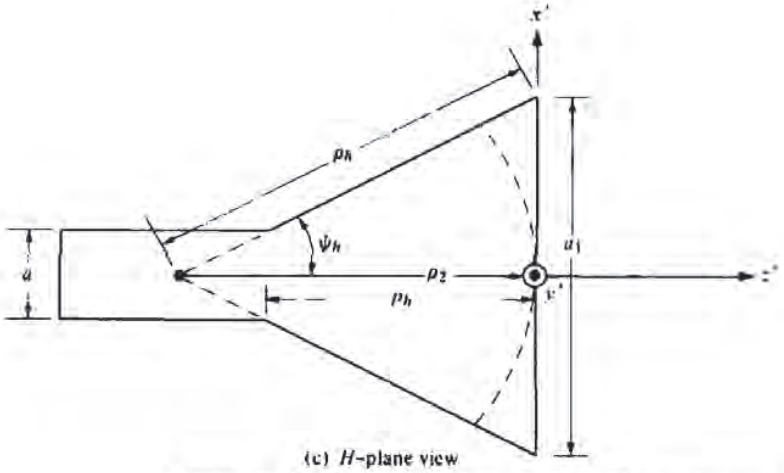
INTEL-1045
U.S. Patent 7,151,430



(a) Pyramidal horn



(b) *E*-plane view



(c) *H*-plane view

Figure 13.18 Pyramidal horn and coordinate system.

INTEL-1045
U.S. Patent 7,151,430

Using (13-23b), (13-25), (13-26), and (13-27), (13-45e) can be expressed as

$$I_1 = \frac{1}{2}\sqrt{\frac{\pi\rho_2}{k}}\left\{e^{j(k_x'^2\rho_2/2k)}\{[C(t_2') - C(t_1')] - j[S(t_2') - S(t_1')]\} + e^{j(k_x''^2\rho_2/2k)}\{[C(t_2'') - C(t_1'')] - j[S(t_2'') - S(t_1'')]\}\right\} \tag{13-46}$$

where t_1', t_2', k_x', t_1'', t_2'', and k_x'' are given by (13-26a)–(13-26c) and (13-27a)–(13-27c). Similarly, using (13-5)–(13-8d), I_2 of (13-45f) can be written as

$$I_2 = \sqrt{\frac{\pi\rho_1}{k}}\, e^{j(k_x^2\rho_1/2k)}\{[C(t_2) - C(t_1)] - j[S(t_2) - S(t_1)]\} \tag{13-47}$$

where k_x, t_1, and t_2 are given by (13-5a), (13-8a), and (13-8b).

Combining (13-45a)–(13-45d), the far-zone **E**- and **H**-field components of (12-10a)–(12-10c) reduce to

$$E_r = 0 \tag{13-48a}$$

$$E_\theta = -j\frac{ke^{jkr}}{4\pi r}[L_\phi + \eta N_\theta] = j\frac{kE_0e^{-jkr}}{4\pi r}[\sin\phi(1 + \cos\theta)\, I_1I_2] \tag{13-48b}$$

$$E_\phi = +j\frac{ke^{-jkr}}{4\pi r}[L_\theta - \eta N_\phi] = j\frac{kE_0e^{-jkr}}{4\pi r}[\cos\phi(\cos\theta + 1)\, I_1I_2] \tag{13-48c}$$

where I_1 and I_2 are given by (13-46) and (13-47), respectively.

The fields radiated by a pyramidal horn, as given by (13-48a)–(13-48c), are valid for all angles of observation. An examination of these equations reveals that the principal E-plane pattern ($\phi = \pi/2$) of a pyramidal horn, aside from a normalization factor, is identical to the E-plane pattern of an E-plane sectoral horn. Similarly the H-plane ($\phi = 0$) is identical to that of an H-plane sectoral horn. Therefore the pattern of a pyramidal horn is very narrow in both principal planes and, in fact, in all planes. This is illustrated in Figure 13.19. The corresponding E-plane pattern is shown in Figure 13.4 and the H-plane pattern in Figure 13.12.

To demonstrate that the maximum radiation for a pyramidal horn is not necessarily directed along its axis, the three-dimensional field pattern for a horn with $\rho_1 = \rho_2 = 6\lambda$, $a_1 = 12\lambda$, $b_1 = 6\lambda$, $a = 0.50\lambda$ and $b = 0.25\lambda$ is displayed in Figure 13.20. The corresponding two-dimensional E- and H-plane patterns are shown in Figure 13.21. The maximum does not occur on axis because the phase error taper at the aperture is such that the rays emanating from the different parts of the aperture toward the axis are not in phase and do not add constructively.

To physically construct a pyramidal horn, the dimension p_e of Figure 13.18(b) given by

$$p_e = (b_1 - b)\left[\left(\frac{\rho_e}{b_1}\right)^2 - \frac{1}{4}\right]^{1/2} \tag{13-49a}$$

INTEL-1045
U.S. Patent 7,151,430

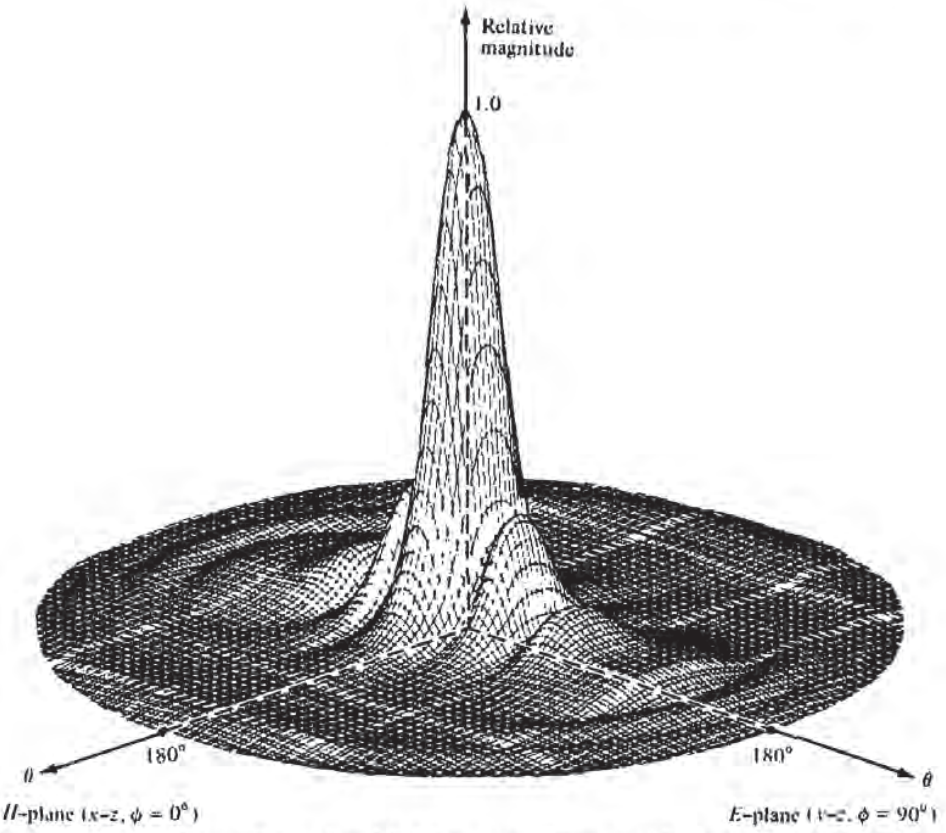


Figure 13.19 Three-dimensional field pattern of a pyramidal horn ($\rho_1 = \rho_2 = 6\lambda$, $a_1 = 5.5\lambda$, $b_1 = 2.75\lambda$, $a = 0.5\lambda$, $b = 0.25\lambda$).

should be equal to the dimension ρ_h of Figure 13.18(c) given by

$$\rho_h = (a_1 - a)\left[\left(\frac{\rho_h}{a_1}\right)^2 - \frac{1}{4}\right]^{1/2} \tag{13-49b}$$

The dimensions chosen for Figures 13.19 and 13.20 do satisfy these requirements. For the horn of Figure 13.19, $\rho_e = 6.1555\lambda$, $\rho_h = 6.6\lambda$, and $\rho_e = \rho_h = 5.4544\lambda$, whereas for that of Figure 13.20, $\rho_e = 6.7082\lambda$, $\rho_h = 8.4853\lambda$, and $\rho_e = \rho_h = 5.75\lambda$. The fields of (13-48a)–(13-48c) provide accurate patterns for angular regions near the main lobe and its closest minor lobes. To accurately predict the field intensity of the pyramidal and other horns, especially in the minor lobes, diffraction techniques can be utilized [15]–[18]. These methods take into account diffractions that occur near the aperture edges of the horn. The diffraction contributions become more dominant in regions where the radiation of (13-48a)–(13-48c) is of very low intensity.

In addition to the previous methods, the horn antenna has been examined using full-wave analyses, such as the Method of Moments (MoM) [8] and the Finite-Difference Time-Domain (FDTD) [19]. These methods yield more accurate results in all regions, and they are able to include many of the other features of the horn, such as its wall thickness, etc. Predicted patterns based on these methods compare extremely well with measurements, even in regions of very low intensity (such as the back lobes). An example of such a comparison is made in Figure 13.22 (a,b) for the E- and

INTEL-1045
U.S. Patent 7,151,430

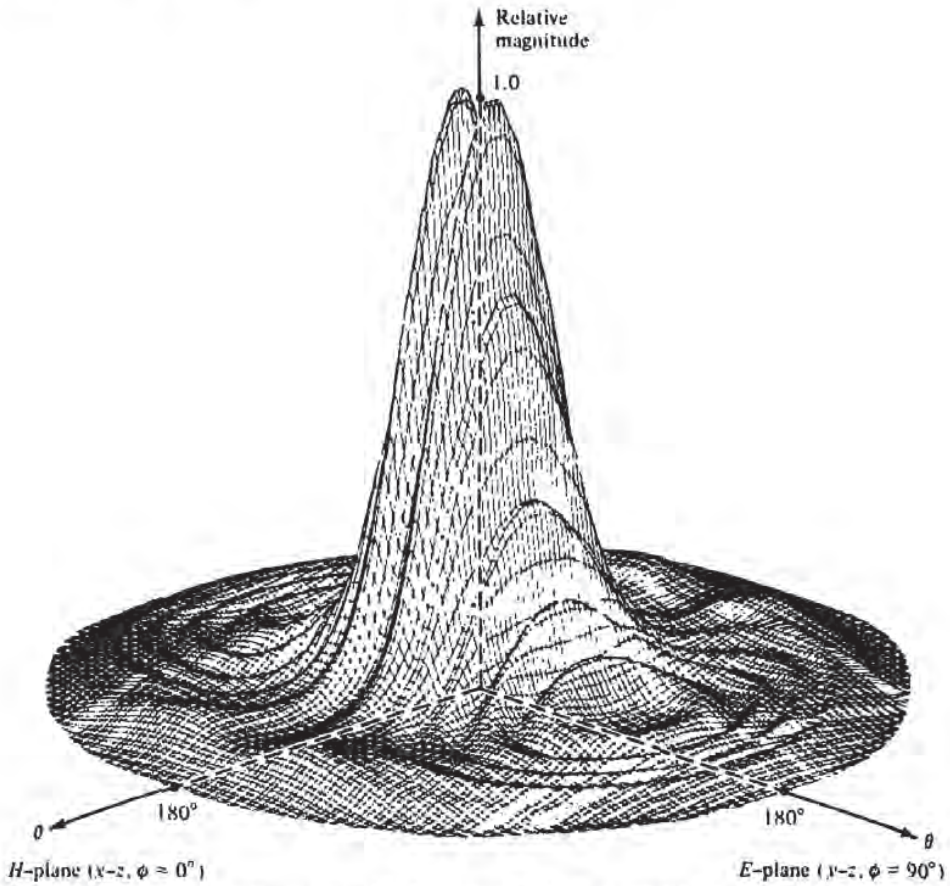


Figure 13.20 Three-dimensional field pattern of a pyramidal horn with maximum not on axis ($\rho_1 = \rho_2 = 6\lambda$, $a_1 = 12\lambda$, $b_1 = 6\lambda$, $a = 0.5\lambda$, $b = 0.25\lambda$).

H-plane patterns of a 20-dB standard gain horn whose Method of Moment predicted values are compared with measured patterns and with predicted values based on (13-48a) and (13-48c), which in Figure 13.22 are labeled as *approximate*. It is apparent that the MoM predicted patterns compare extremely well with the measured data.

All of the patterns presented previously represent the main polarization of the field radiated by the antenna (referred to as *co-polarized* or *co-pol*). If the horn is symmetrical and it is excited in the dominant mode, ideally there should be no field component radiated by the antenna which is orthogonal to the main polarization (referred to as *cross-polarization* or *cross-pol*), especially in the principal planes. However, in practice, either because of nonsymmetries, defects in construction and/or excitation of higher order modes, all antennas exhibit cross-polarized components. These cross-pol components are usually of very low intensity compared to those of the primarily polarization. For good designs, these should be 30 or more dB below the co-polarized fields and are difficult to measure accurately or be symmetrical, as they should be in some cases.

13.4.2 Directivity

As for the *E*- and *H*-plane sectoral horns, the directivity of the pyramidal configuration is vital to the antenna designer. The maximum radiation of the pyramidal horn is

INTEL-1045
U.S. Patent 7,151,430

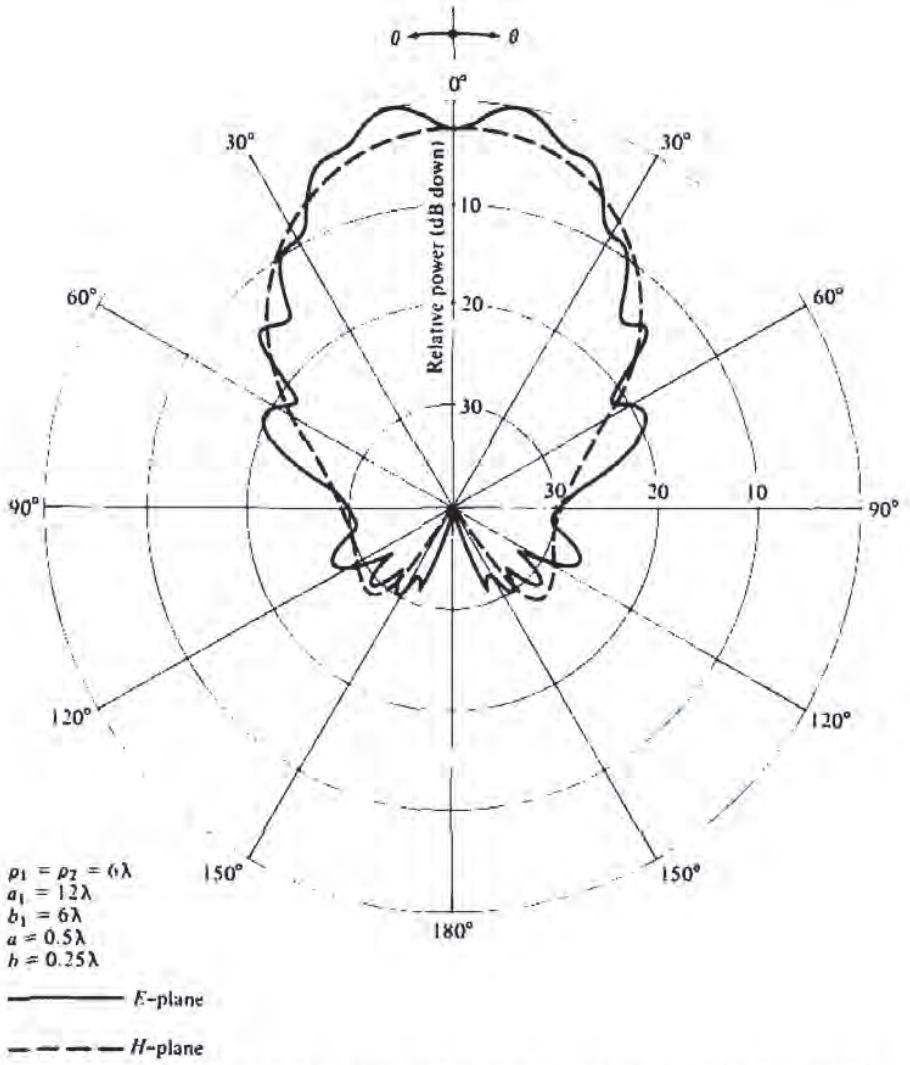


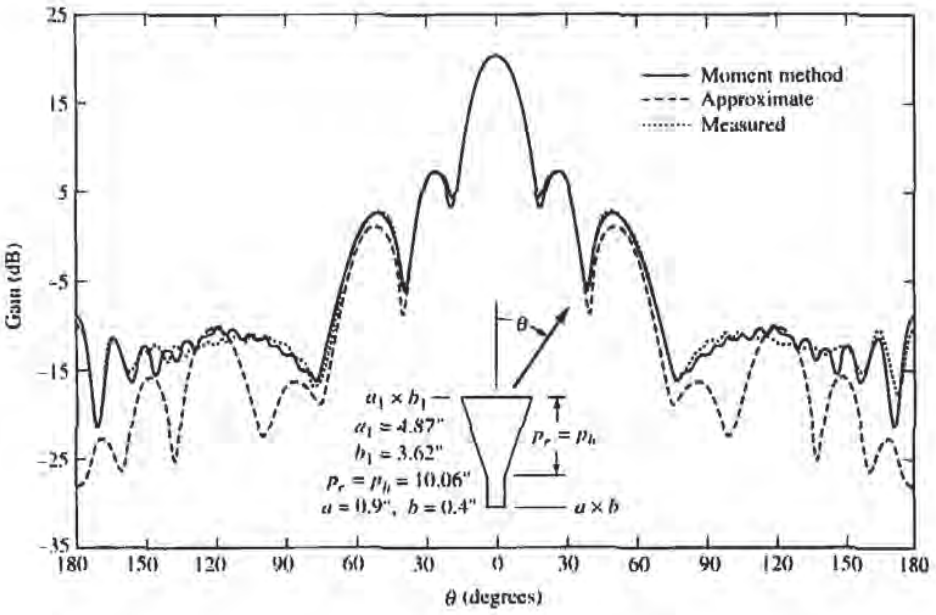
Figure 13.21 *E*- and *H*-plane amplitude patterns of a pyramidal horn with maximum not on-axis.

directed nearly along the z-axis ($\theta = 0°$). It is a very simple exercise to show that $|E_\theta|_{\max}$, $|E_\phi|_{\max}$, and in turn $U_{\max}$ can be written, using (13-48b) and (13-48c), as

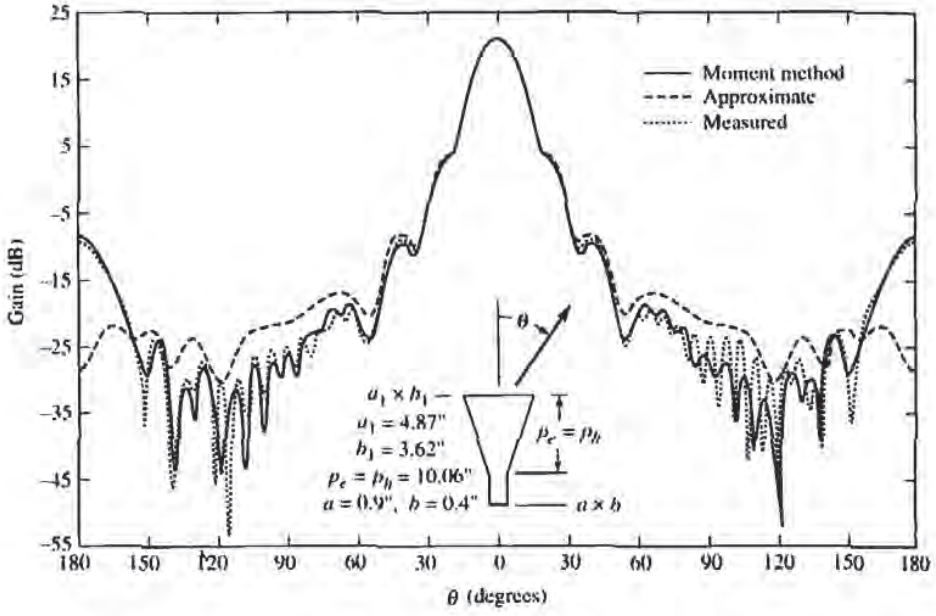
$$|E_\theta|_{\max} = |E_0 \sin\phi| \frac{\sqrt{\rho_1\rho_2}}{r} \{[C(u) - C(v)]^2 + [S(u) - S(v)]^2\}^{1/2} \times \left\{ C^2\left(\frac{b_1}{\sqrt{2\lambda\rho_1}}\right) + S^2\left(\frac{b_1}{\sqrt{2\lambda\rho_1}}\right)\right\}^{1/2} \tag{13-50a}$$

$$|E_\phi|_{\max} = |E_0 \cos\phi| \frac{\sqrt{\rho_1\rho_2}}{r} \{[C(u) - C(v)]^2 + [S(u) - S(v)]^2\}^{1/2} \times \left\{ C^2\left(\frac{b_1}{\sqrt{2\lambda\rho_1}}\right) + S^2\left(\frac{b_1}{\sqrt{2\lambda\rho_1}}\right)\right\}^{1/2} \tag{13-50b}$$

INTEL-1045
U.S. Patent 7,151,430



(a) E-plane



(b) H-plane

Figure 13.22 Comparison of E- and H-plane patterns for 20-dB standard-gain horn at 10 GHz.

$$U_{\max} = \frac{r^2}{2\eta}|\mathbf{E}|^2_{\max} = |E_0|^2 \frac{\rho_1\rho_2}{2\eta}\{[C(u) - C(v)]^2 + [S(u) - S(v)]^2\} \times \left\{C^2\left(\frac{b_1}{\sqrt{2\lambda\rho_1}}\right) + S^2\left(\frac{b_1}{\sqrt{2\lambda\rho_1}}\right)\right\} \tag{13-50c}$$

where u and v are defined by (13-41a) and (13-41b).

INTEL-1045
U.S. Patent 7,151,430

Since

$$P_{\text{rad}} = |E_0|^2 \frac{a_1 b_1}{4\eta} \tag{13-51}$$

the directivity of the pyramidal horn can be written as

$$D_p = \frac{4\pi U_{\max}}{P_{\text{rad}}} = \frac{8\pi\rho_1\rho_2}{a_1 b_1}\{[C(u) - C(v)]^2 + [S(u) - S(v)]^2\} \times \left\{C^2\left(\frac{b_1}{\sqrt{2\lambda\rho_1}}\right) + S^2\left(\frac{b_1}{\sqrt{2\lambda\rho_1}}\right)\right\} \tag{13-52}$$

which reduces to

$$D_p = \frac{\pi\lambda^2}{32ab} D_E D_H \tag{13-52a}$$

where D_E and D_H are the directivities of the E- and H-plane sectoral horns as given by (13-19) and (13-41), respectively. This is a well-known relationship and has been used extensively in the design of pyramidal horns.

The directivity (in dB) of a pyramidal horn, over isotropic, can also be approximated by

$$D_p(\text{dB}) = 10\left[1.008 + \log_{10}\left(\frac{a_1 b_1}{\lambda^2}\right)\right] - (L_e + L_h) \tag{13-53}$$

where L_e and L_h represent, respectively, the losses (in dB) due to phase errors in the E- and H-planes of the horn which are found plotted in Figure 13.23.

The directivity of a pyramidal horn can also be calculated by doing the following [14].

1. Calculate

$$A = \frac{a_1}{\lambda}\sqrt{\frac{50}{\rho_h/\lambda}} \tag{13-54a}$$

$$B = \frac{b_1}{\lambda}\sqrt{\frac{50}{\rho_e/\lambda}} \tag{13-54b}$$

2. Using A and B, find G_H and G_E, respectively, from Figures 13.17 and 13.9. If the values of either A or B or both are smaller than 2, then calculate G_E and/or G_H by

$$G_E = \frac{32}{\pi} B \tag{13-54c}$$

$$G_H = \frac{32}{\pi} A \tag{13-54d}$$

3. Calculate D_p by using the values of G_E and G_H from Figures 13.9 and 13.17 or from (13-54c) and (13-54d). Thus

INTEL-1045
U.S. Patent 7,151,430

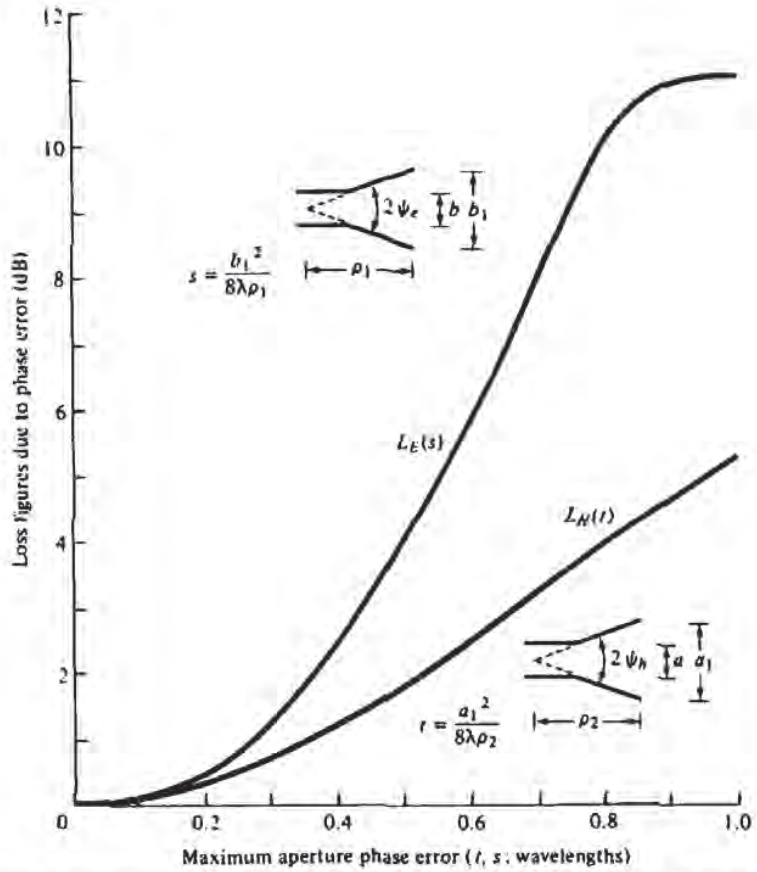


Figure 13.23 Loss figures for E- and H-planes due to phase errors. (SOURCE: W. C. Jakes, in H. Jasik (ed.), *Antenna Engineering Handbook*, McGraw-Hill, New York, 1961)

$$D_p = \frac{G_E G_H}{\frac{32}{\pi}\sqrt{\frac{50}{\rho_e/\lambda}}\sqrt{\frac{50}{\rho_h/\lambda}}} = \frac{G_E G_H}{10.1859\sqrt{\frac{50}{\rho_e/\lambda}}\sqrt{\frac{50}{\rho_h/\lambda}}} = \frac{\lambda^2\pi}{32ab} D_E D_H \tag{13-54e}$$

where D_E and D_H are, respectively, the directivities of (13-20c) and (13-42c). This is the actual directivity of the horn. The above procedure has led to results accurate to within 0.01 dB for a horn with $\rho_e = \rho_h = 50\lambda$.

A commercial X-band (8.2–12.4 GHz) horn is that shown in Figure 13.24. It is a lightweight precision horn antenna, which is usually cast of aluminum, and it can be used as a

1. standard for calibrating other antennas
2. feed for reflectors and lenses
3. pickup (probe) horn for sampling power
4. receiving and/or transmitting antenna

INTEL-1045
U.S. Patent 7,151,430

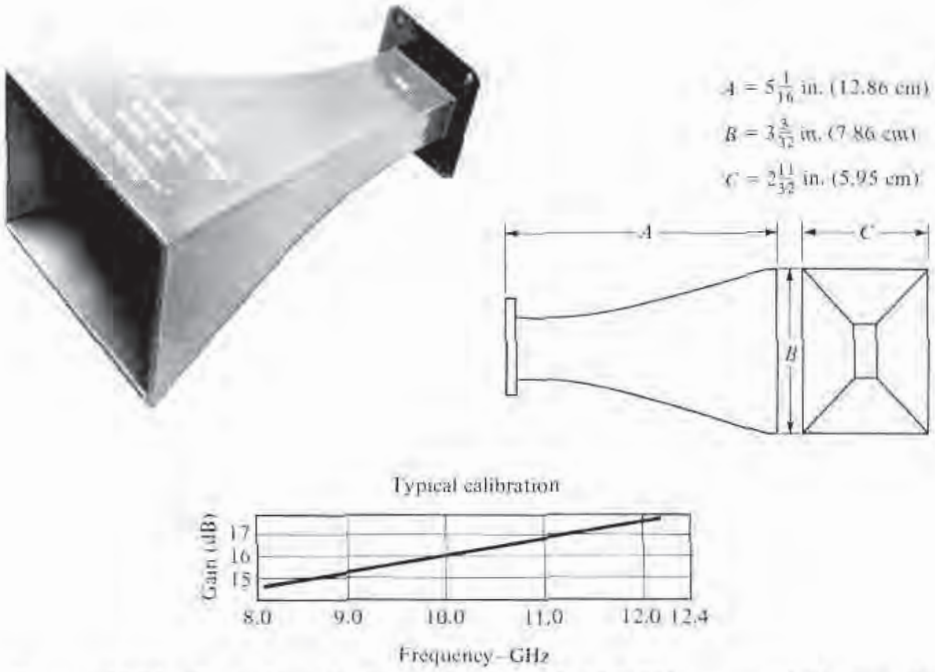


Figure 13.24 Typical standard gain *X*-band (8.2–12.4 GHz) pyramidal horn and its gain characteristics (courtesy of The NARDA Microwave Corporation).

It possesses an exponential taper, and its dimensions and typical gain characteristics are indicated in the figure. The half-power beamwidth in both the *E*- and *H*-planes is about 28° while the side lobes in the *E*- and *H*-planes are, respectively, about 13 and 20 dB down.

Gains of the horn antenna which were measured, predicted and provided by the manufacturer, whose amplitude patterns are shown in Figure 13.22, are displayed in Figure 13.25. A very good agreement amongst all three sets is indicated.

Example 13.5

A pyramidal horn has dimensions of $\rho_1 = \rho_2 = 6\lambda$, $a_1 = 5.5\lambda$, $b_1 = 2.75\lambda$, $a = 0.5\lambda$, and $b = 0.25\lambda$.

(a) Check to see if such a horn can be constructed physically.

(b) Compute the directivity using (13-52a), (13-53), and (13-54e).

SOLUTION

From Examples 13.3 and 13.4,

$$\rho_e = 6.1555\lambda$$
$$\rho_h = 6.6\lambda$$

INTEL-1045
U.S. Patent 7,151,430

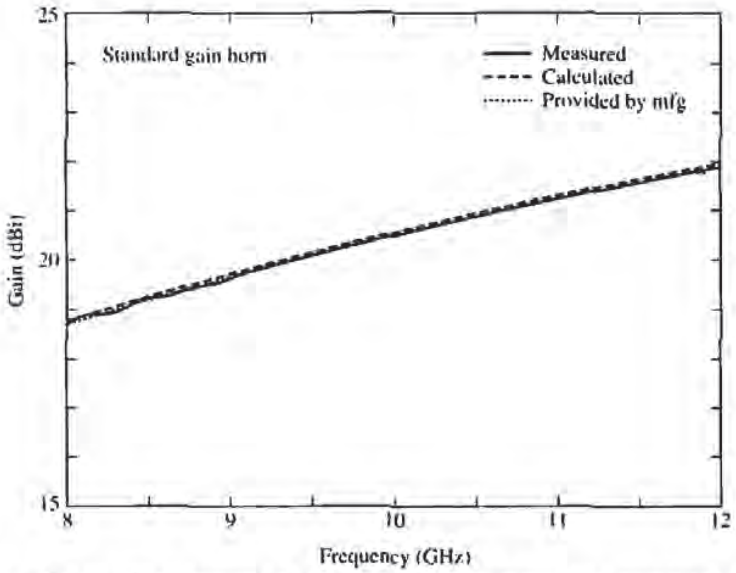


Figure 13.25 Gains of the pyramidal horn which were measured, computed and provided by the manufacturer. The amplitude patterns of the horn are shown in Figure 13.22.

Thus

$$p_e = (2.75 - 0.25)\lambda \sqrt{\left(\frac{6.1555}{2.75}\right)^2 - \frac{1}{4}} = 5.454\lambda$$

$$p_h = (5.5 - 0.5)\lambda \sqrt{\left(\frac{6}{5.5}\right)^2 - \frac{1}{4}} = 5.454\lambda$$

Therefore the horn can be constructed physically.

The directivity can be computed by utilizing the results of Examples 13.3 and 13.4. Using (13-52a) with the values of D_E and D_H computed using, respectively, (13-19) and (13-41) gives

$$D_0 = \frac{\pi\lambda^2}{32ab} D_E D_H = \frac{\pi}{32(0.5)(0.25)} (12.79)(7.52) = 75.54 = 18.78 \text{ dB}$$

Utilizing the values of D_E and D_H computed using, respectively, (13-20c) and (13-42c), the directivity of (13-54e) is equal to

$$D_0 = \frac{\pi\lambda^2}{32ab} D_E D_H = \frac{\pi}{32(0.5)0.25} (12.89)(8.338) = 84.41 = 19.26 \text{ dB}$$

For this horn

$$s = \frac{b_1^2}{8\lambda\rho_1} = \frac{(2.75)^2}{8(6)} \approx 0.1575$$

$$t = \frac{a_1^2}{8\lambda\rho_2} = \frac{(5.5)^2}{8(6)} = 0.63$$

INTEL-1045
U.S. Patent 7,151,430

For these values of s and t

$$L_E = 0.20 \text{ dB}$$
$$L_H = 2.75 \text{ dB}$$

from Figure 13.23. Using (13-53)

$$D_0 = 10\{1.008 + \log_{10}[5.5(2.75)]\} - (0.20 + 2.75) = 18.93 \text{ dB}$$

The agreement is best between the directivities of (13-52a) and (13-53).

A computer program entitled PYRAMIDAL HORN-ANALYSIS has been developed to analyze the radiation characteristics of a pyramidal horn and the directivities of the corresponding E- and H-plane sectoral horns. The program is found at the end of this chapter.

13.4.3 Design Procedure

The pyramidal horn is widely used as a standard to make gain measurements of other antennas (see Section 16.4, Chapter 16), and as such it is often referred to as a *standard gain horn*. To design a pyramidal horn, one usually knows the desired gain G_0 and the dimensions a, b of the rectangular feed waveguide. The objective of the design is to determine the remaining dimensions (a_1, b_1, ρ_e, ρ_h, p_e, and p_h) that will lead to an optimum gain. The procedure that follows can be used to accomplish this [2], [3].

The design equations are derived by first selecting values of b_1 and a_1 that lead, respectively, to optimum directivities for the E- and H-plane sectoral horns using (13-19a) and (13-41c). Since the overall efficiency (including both the antenna and aperture efficiencies) of a horn antenna is about 50% [2], [3], the gain of the antenna can be related to its physical area. Thus it can be written using (12-39c), (12-40), and (13-19a), (13-41c) as

$$G_0 = \frac{1}{2}\frac{4\pi}{\lambda^2}(a_1 b_1) = \frac{2\pi}{\lambda^2}\sqrt{3\lambda\rho_2}\sqrt{2\lambda\rho_1} \simeq \frac{2\pi}{\lambda^2}\sqrt{3\lambda\rho_h}\sqrt{2\lambda\rho_e} \quad (13\text{-}55)$$

since for long horns $\rho_2 \simeq \rho_h$ and $\rho_1 \simeq \rho_e$. For a pyramidal horn to be physically realizable, p_e and p_h of (13-49a) and (13-49b) must be equal. Using this equality, it can be shown that (13-55) reduces to

$$\boxed{\left(\sqrt{2\chi} - \frac{b}{\lambda}\right)^2 (2\chi - 1) = \left(\frac{G_0}{2\pi}\sqrt{\frac{3}{2\pi}}\frac{1}{\sqrt{\chi}} - \frac{a}{\lambda}\right)^2 \left(\frac{G_0^2}{6\pi^3}\frac{1}{\chi} - 1\right)} \quad (13\text{-}56)$$

where

$$\boxed{\frac{\rho_e}{\lambda} = \chi} \quad (13\text{-}56a)$$

$$\boxed{\frac{\rho_h}{\lambda} = \frac{G_0^2}{8\pi^3}\left(\frac{1}{\chi}\right)} \quad (13\text{-}56b)$$

INTEL-1045
U.S. Patent 7,151,430

Equation (13-56) is the horn design equation.

1. As a first step of the design, find the value of χ which satisfies (13-56) for a desired gain G_0 (dimensionless). Use an iterative technique and begin with a trial value of

$$\chi\,(\text{trial}) = \chi_1 = \frac{G_0}{2\pi\sqrt{2\pi}} \tag{13-57}$$

2. Once the correct χ has been found, determine ρ_e and ρ_h using (13-56a) and (13-56b), respectively.
3. Find the corresponding values of a_1 and b_1 using (13-19a) and (13-41c) or

$$a_1 = \sqrt{3\lambda\rho_2} \simeq \sqrt{3\lambda\rho_h} = \frac{G_0}{2\pi}\sqrt{\frac{3}{2\pi\chi}}\,\lambda \tag{13-58a}$$

$$b_1 = \sqrt{2\lambda\rho_1} \simeq \sqrt{2\lambda\rho_e} = \sqrt{2\chi}\lambda \tag{13-58b}$$

4. The values of p_e and p_h can be found using (13-49a) and (13-49b).

A computer program entitled PYRAMIDAL HORN-DESIGN has been developed to accomplish this, and it is found at the end of this chapter.

Example 13.6

Design an optimum gain X-band (8.2–12.4 GHz) pyramidal horn so that its gain (above isotropic) at $f = 11$ GHz is 22.6 dB. The horn is fed by a WR 90 rectangular waveguide with inner dimensions of $a = 0.9$ in. (2.286 cm) and $b = 0.4$ in. (1.016 cm).

SOLUTION

Convert the gain G_0 from dB to a dimensionless quantity. Thus

$$G_0\,(\text{dB}) = 22.6 = 10\log_{10}G_0 \Rightarrow G_0 = 10^{2.26} = 181.97$$

Since $f = 11$ GHz, $\lambda = 2.7273$ cm and

$$a = 0.8382\lambda$$
$$b = 0.3725\lambda$$

1. The initial value of χ is taken, using (13-57), as

$$\chi_1 = \frac{181.97}{2\pi\sqrt{2\pi}} = 11.5539$$

which does not satisfy (13-56) for the desired design specifications. After a few iterations, a more accurate value is $\chi = 11.1157$.

2. *Using (13-56a) and (13-56b)*

$$\rho_e = 11.1157\lambda = 30.316\text{ cm} = 11.935\text{ in.}$$
$$\rho_h = 12.0094\lambda = 32.753\text{ cm} = 12.895\text{ in.}$$

INTEL-1045
U.S. Patent 7,151,430

3. The corresponding values of a_1 and b_1 are

$$a_1 = 6.002\lambda = 16.370 \text{ cm} = 6.445 \text{ in.}$$
$$b_1 = 4.715\lambda = 12.859 \text{ cm} = 5.063 \text{ in.}$$

4. The values of p_e and p_h are equal to

$$p_e = p_h = 10.005\lambda = 27.286 \text{ cm} = 10.743 \text{ in.}$$

The same values are obtained using the computer program at the end of this chapter.

The derived design parameters agree closely with those of a commercial gain horn available in the market. As a check, the gain of the designed horn was computed using (13-52a) and (13-53), assuming an antenna efficiency e_t of 100%, and (13-55). The values were

$$G_0 \simeq D_0 \simeq 22.4 \text{ dB} \quad \text{for (13-52a)}$$
$$G_0 \simeq D_0 = 22.1 \text{ dB} \quad \text{for (13-53)}$$
$$G_0 = 22.5 \text{ dB} \quad \text{for (13-55)}$$

All three computed values agree closely with the designed value of 22.6 dB.

13.5 CONICAL HORN

Another very practical microwave antenna is the conical horn shown in Figure 13.26. While the pyramidal, E-, and H-plane sectoral horns are usually fed by a rectangular waveguide, the feed of a conical horn is often a circular waveguide.

The first rigorous treatment of the fields radiated by a conical horn is that of Schorr and Beck [20]. The modes within the horn are found by introducing a spherical coordinate system and are in terms of spherical Bessel functions and Legendre polynomials. The analysis is too involved and will not be attempted here. However data, in the form of curves [21], will be presented which give a qualitative description of the performance of a conical horn.

Referring to Figure 13.27, it is apparent that the behavior of a conical horn is similar to that of a pyramidal or a sectoral horn. As the flare angle increases, the directivity for a given length horn increases until it reaches a maximum beyond which it begins to decrease. The decrease is a result of the dominance of the quadratic phase error at the aperture. In the same figure, an optimum directivity line is indicated.

The results of Figure 13.27 behave as those of Figures 13.8 and 13.16. When the horn aperture (d_m) is held constant and its length (L) is allowed to vary, the maximum directivity is obtained when the flare angle is zero ($\psi_f = 0$ or $L = \infty$). This is equivalent to a circular waveguide of diameter d_m. As for the pyramidal and sectoral horns, a lens is usually placed at the aperture of the conical horn to compensate for its quadratic phase error. The result is a narrower pattern as its flare increases.

The directivity (in dB) of a conical horn, with an aperture efficiency of ϵ_{ap} and aperture circumference C, can be computed using

$$D_c \text{ (dB)} = 10\log_{10}\left[\epsilon_{ap}\frac{4\pi}{\lambda^2}(\pi a^2)\right] = 10\log_{10}\left(\frac{C}{\lambda}\right)^2 - L(s) \tag{13-59}$$

INTEL-1045
U.S. Patent 7,151,430

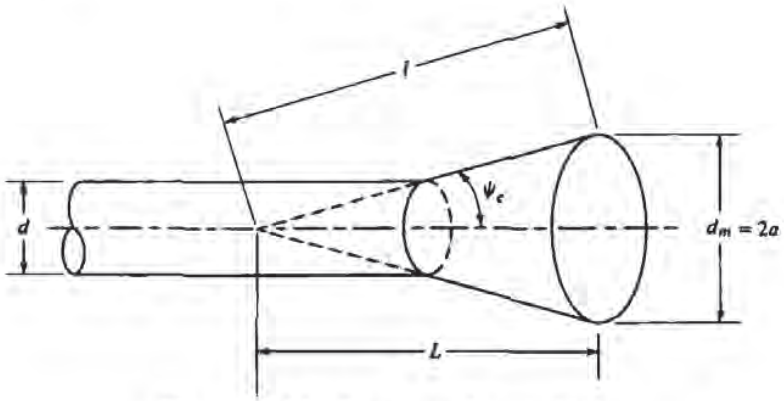


Figure 13.26 Geometry of conical horn.

where a is the radius of horn at the aperture and

$$\boxed{L(s) = -10\log_{10}(\epsilon_{ap})} \tag{13-59a}$$

The first term in (13-59) represents the directivity of a uniform circular aperture whereas the second term, represented by (13-59a), is a correction figure to account for the loss in directivity due to the aperture efficiency. Usually the term in (13-59a) is referred to as *loss figure* which can be computed (in decibels) using [2], [3]

$$L(s) \simeq (0.8 - 1.71s + 26.25s^2 - 17.79s^3) \tag{13-59b}$$

where s is the maximum phase deviation (in number of wavelengths), and it is given by

$$s = \frac{d_m^2}{8\lambda l} \tag{13-59c}$$

The directivity of a conical horn is optimum when its diameter is equal to

$$\boxed{d_m \simeq \sqrt{3l\lambda}} \tag{13-60}$$

which corresponds to a maximum aperture phase deviation of $s = 3/8$ (wavelengths) and a loss figure of about 2.9 dB (or an aperture efficiency of about 51%).

13.6 CORRUGATED HORN

The large emphasis placed on horn antenna research in the 1960s was inspired by the need to reduce spillover efficiency and cross-polarization losses and increase aperture efficiencies of large reflectors used in radio astronomy and satellite communications. In the 1970s high-efficiency and rotationally symmetric antennas were needed in microwave radiometry. Using conventional feeds, aperture efficiencies of 50–60% were obtained. However, efficiencies of the order of 75–80% can be obtained with improved feed systems utilizing corrugated horns.

The aperture techniques introduced in Chapter 12 can be used to compute the pattern of a horn antenna and would yield accurate results only around the main lobe and the first few minor lobes. The antenna pattern structure in the back lobe region is strongly influenced by diffractions from the edges, especially from those that are perpendicular to the E-field at the horn aperture. The diffractions lead to undesirable

INTEL-1045
U.S. Patent 7,151,430

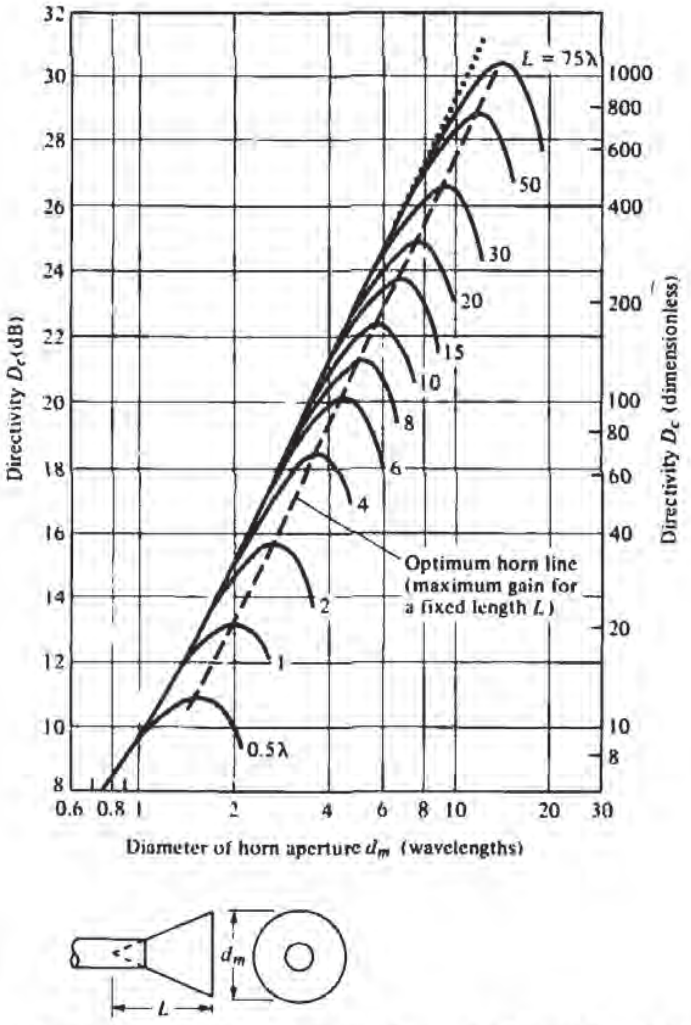
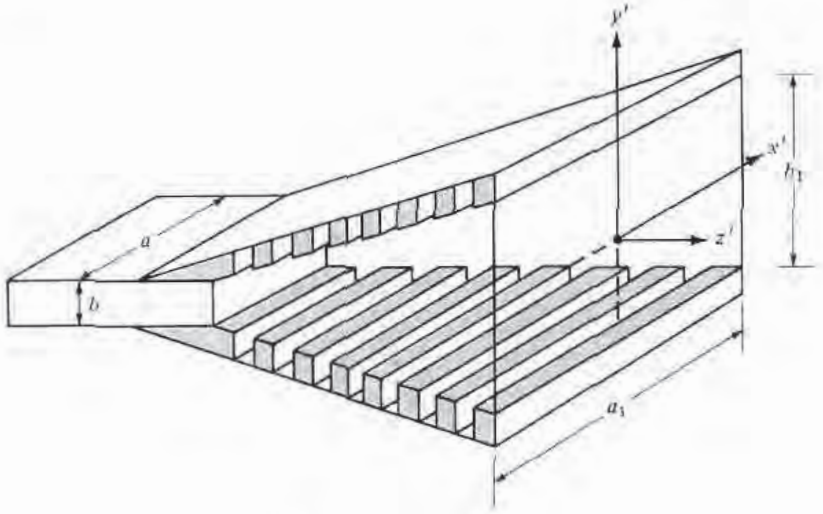


Figure 13.27 Directivity of a conical horn as a function of aperture diameter and for different axial horn lengths. (SOURCE: A. P. King, "The Radiation Characteristics of Conical Horn Antennas," *Proc. IRE*, Vol. 38, pp. 249–251, March 1950. © (1950) IEEE)

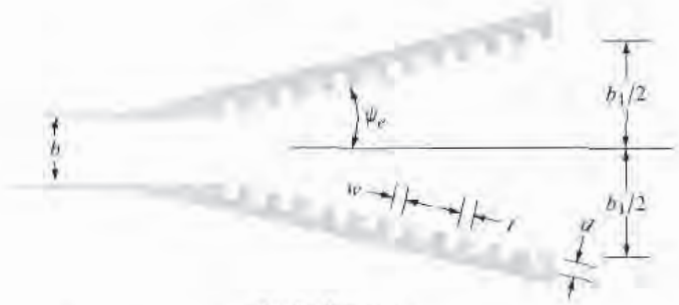
radiation not only in the back lobes but also in the main lobe and in the minor lobes. However, they dominate only in low-intensity regions.

In 1964 Kay [22] realized that grooves on the walls of a horn antenna would present the same boundary conditions to all polarizations and would taper the field distribution at the aperture in all the planes. The creation of the same boundary conditions on all four walls would eliminate the spurious diffractions at the edges of the aperture. For a square aperture, this would lead to an almost rotationally symmetric pattern with equal E- and H-plane beamwidths. A *corrugated (grooved)* pyramidal horn, with corrugations in the E-plane walls, is shown in Figure 13.28(a) with a side view in Figure 13.28(b). Since diffractions at the edges of the aperture in the H-plane are minimal, corrugations are usually not placed on the walls of that plane. Corrugations can also be placed in a conical horn forming a *conical corrugated* horn, also referred to in [22] as *scalar horn*. However, instead of the corrugations being formed as shown in Figure 13.29(a), practically it is much easier to machine them to have the profile shown in Figure 13.29(b).

INTEL-1045
U.S. Patent 7,151,430



(a) Corrugated horn



(b) *E*-plane view

Figure 13.28 Pyramidal horn with corrugations in the *E*-plane.

To form an effective corrugated surface, it usually requires 10 or more slots (corrugations) per wavelength [23]. To simplify the analysis of an infinite corrugated surface, the following assumptions are usually required:

1. The teeth of the corrugations are vanishingly thin.
2. Reflections from the base of the slot are only those of a TEM mode.

The second assumption is satisfied provided the width of the corrugation (w) is small compared to the free-space wavelength (λ_0) and the slot depth (d) (usually $w < \lambda_0/10$). For a corrugated surface satisfying the above assumptions, its approximate surface reactance is given by [24]

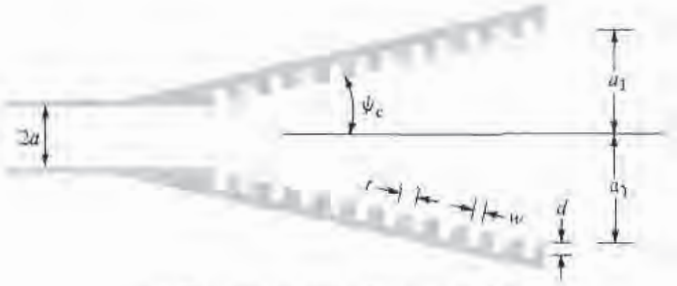
$$X = \frac{w}{w + t}\sqrt{\frac{\mu_0}{\epsilon_0}}\tan(k_0 d) \tag{13-61}$$

when

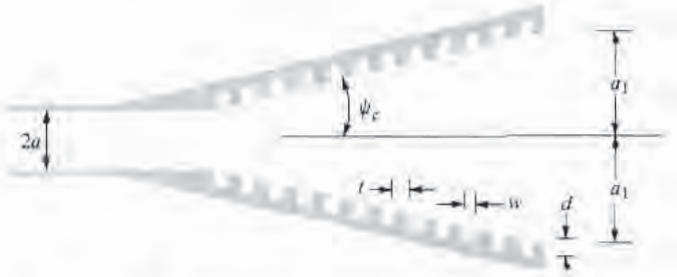
$$\frac{w}{w + t} \simeq 1 \tag{13-61a}$$

which can be satisfied provided $t \leq w/10$.

INTEL-1045
U.S. Patent 7,151,430



(a) Corrugations perpendicular to surface



(b) Corrugations perpendicular to axis

Figure 13.29 Side view profiles of conical corrugated horns.

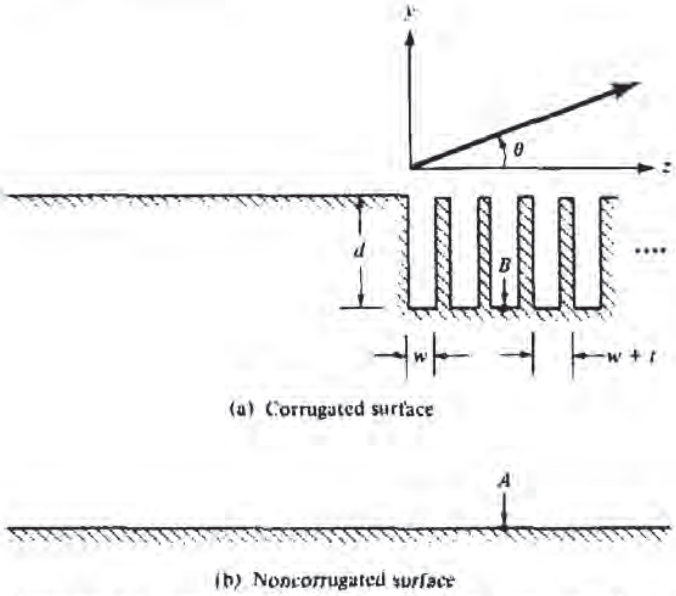
The surface reactance of a corrugated surface, used on the walls of a horn, must be capacitive in order for the surface to force to zero the tangential magnetic field parallel to the edge at the wall. Thus the surface will not support surface waves, will prevent illumination of the *E*-plane edges, and will diminish diffractions. This can be accomplished, according to (13-61), if $\lambda_0/4 < d < \lambda_0/2$ or more generally when $(2n + 1)\lambda_0/4 < d < (n + 1)\lambda_0/2$. Even though the cutoff depth is also a function of the slot width w, its influence is negligible if $w < \lambda_0/10$ and $\lambda_0/4 < d < \lambda_0/2$.

To study the performance of a corrugated surface, an analytical model was developed and parametric studies were performed [25]. Although the details are numerous, only the results will be presented here. In Figure 13.30(a) a corrugated surface is sketched and in Figure 13.30(b) its corresponding uncorrugated counterpart is shown.

For a free-space wavelength of $\lambda_0 = 8$ cm, the following have been plotted for point B in Figure 13.30(a) relative to point A in Figure 13.30(b):

1. In Figure 13.31(a) the surface current density decay at B relative to that at $A[J_s(B)/J_s(A)]$ as a function of corrugation number (for 20 total corrugations) due to energy being forced away from the corrugations. As expected, no decay occurs for $d = 0.5\lambda_0$ and the most rapid decay is obtained for $d = 0.25\lambda_0$.
2. In Figure 13.31(b) the surface current density decay at B relative to that in $A[J_s(B)/J_s(A)]$ as a function of the distance z from the onset of the corrugations for four and eight corrugations per wavelength. The results indicate an almost independence of current density decay as a function of corrugation density for the cases considered.
3. In Figure 13.31(c) the surface current density decay at B relative to that in $A[J_s(B)/J_s(A)]$ as a function of the distance z from the onset of the corrugations

INTEL-1045
U.S. Patent 7,151,430



(a) Corrugated surface

(b) Noncorrugated surface

Figure 13.30 Geometry of corrugated and plane surfaces. (SOURCE: C. A. Mentzer and L. Peters, Jr., "Properties of Cutoff Corrugated Surfaces for Corrugated Horn Design," *IEEE Trans. Antennas Propagat.*, Vol. AP-22, No. 2, March 1974. © (1974) IEEE)

for $w/(w + t)$ ratios ranging from 0.5 to 0.9. For $z < 4$ cm $\approx \lambda_0/2$, thinner corrugations [larger $w/(w + t)$ ratios] exhibit larger rates of decay. Beyond that point, the rate of decay is approximately constant. This would indicate that in a practical design thinner corrugations can be used at the onset followed by thicker ones, which are easier to construct.

The effect of the corrugations on the walls of a horn is to modify the electric field distribution in the E-plane from uniform (at the waveguide-horn junction) to cosine (at the aperture). Through measurements, it has been shown that the transition from uniform to cosine distribution takes place almost at the onset of the corrugations. For a horn of about 45 corrugations, the cosine distribution has been established by the fifth corrugation (from the onset) and the spherical phase front by the fifteenth [26]. The E- and H-plane amplitude and phase distributions at the aperture of the horn with 45 corrugations are shown in Figure 13.32(a,b). It is clear that the cosine distribution is well established.

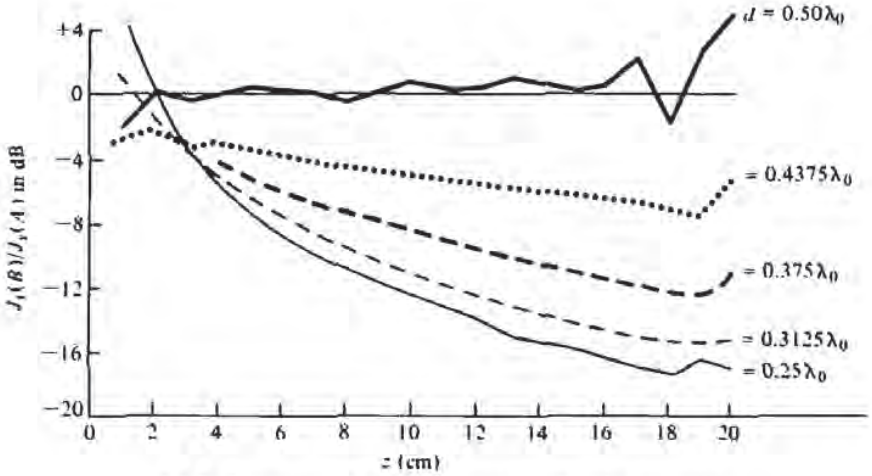
Referring to Figure 13.28(a), the field distribution at the aperture can be written as

$$E_y'(x', y') = E_0 \cos\left(\frac{\pi}{a_1}x'\right)\cos\left(\frac{\pi}{b_1}y'\right)e^{-j[k(x'^2/\rho_2 + y'^2/\rho_1)/2]} \tag{13-62a}$$

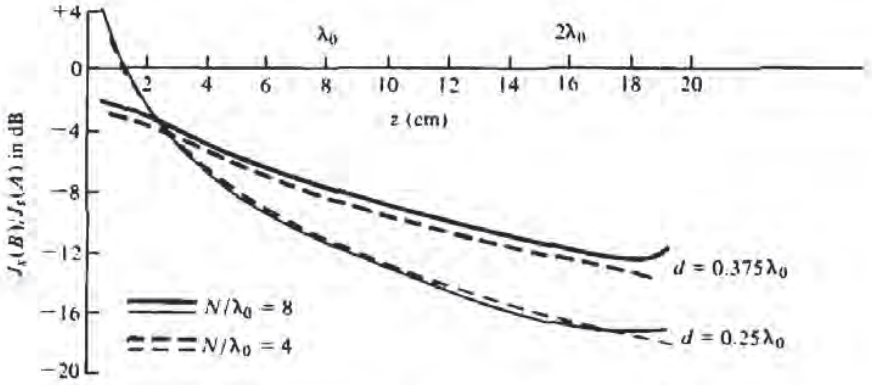
$$H_x'(x', y') = -\frac{E_0}{\eta}\cos\left(\frac{\pi}{a_1}x'\right)\cos\left(\frac{\pi}{b_1}y'\right)e^{-j[k(x'^2/\rho_2 + y'^2/\rho_1)/2]} \tag{13-62b}$$

corresponding to (13-43a) and (13-43b) of the uncorrugated pyramidal horn. Using the above distributions, the fields radiated by the horn can be computed in a manner analogous to that of the pyramidal horn of Section 13.4. Patterns have been computed and compare very well with measurements [26].

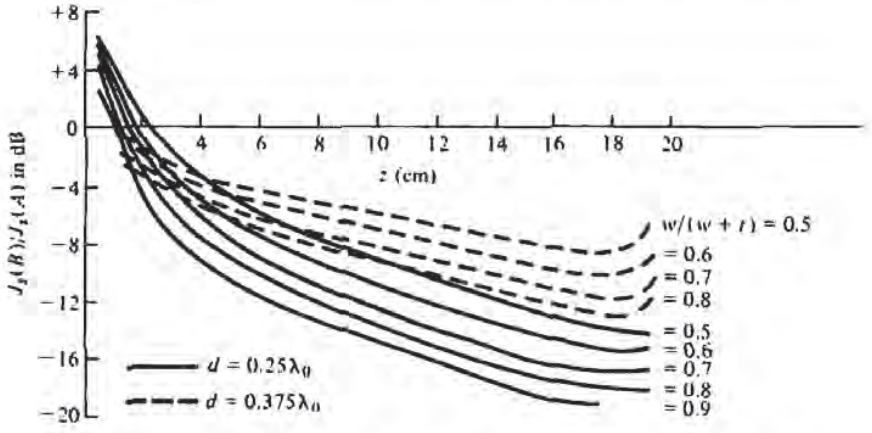
INTEL-1045
U.S. Patent 7,151,430



(a) Surface current decay on corrugated surface due to energy forced away from corrugations.



(b) Surface current decay on corrugations as a function of corrugation density.



(c) Surface current decay on corrugations as a function of corrugation shape.

Figure 13.31 Surface current decays on corrugated surface. (SOURCE: C. A. Mentzer and L. Peters, Jr., "Properties of Cutoff Corrugated Surfaces for Corrugated Horn Design," *IEEE Trans. Antennas Propagat.*, Vol. AP-22, No. 2, March 1974. © (1974) IEEE)

INTEL-1045
U.S. Patent 7,151,430

Figure 13.32 Amplitude and phase distributions in *H*- and *E*-planes. (SOURCE: C. A. Mentzer and L. Peters, Jr., "Pattern Analysis of Corrugated Horn Antennas," *IEEE Trans. Antennas Propagat.*, Vol. AP-24, No. 3, May 1976. © (1976) IEEE)

INTEL-1045
U.S. Patent 7,151,430

In Figure 13.33(a) the measured E-plane patterns of an uncorrugated square pyramidal horn (*referred to as the control horn*) and a corrugated square pyramidal horn are shown. The aperture size on each side was 3.5 in. (2.96λ at 10 GHz) and the total flare angle in each plane was 50°. It is evident that the levels of the minor lobes and back lobes are much lower for the corrugated horn than those of the control horn. However the corrugated horn also exhibits a wider main beam for small angles; thus a larger 3-dB beamwidth (HPBW) but a lower 10-dB beamwidth. This is attributed to the absence of the diffracted fields from the edges of the corrugated horn which, for nearly on-axis observations, add to the direct wave contribution because of their in-phase relationship. The fact that the on-axis far-fields of the direct and diffracted fields are nearly in-phase is also evident from the pronounced on-axis maximum of the control horn. The E- and H-plane patterns of the corrugated horn are almost identical to those of Figure 13.33(a) over the frequency range from 8 to 14 GHz. These suggest that the main beam in the E-plane can be obtained from known H-plane patterns of horn antennas.

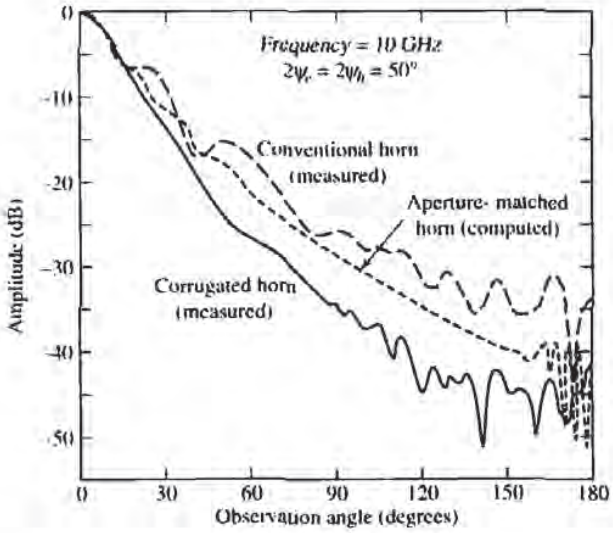
In Figure 13.33(b) the measured E-plane patterns of larger control and corrugated square pyramidal horns, having an aperture of 9.7 in. on each side (8.2λ at 10 GHz) and included angles of 34° and 31° in the E- and H-planes, respectively, are shown. For this geometry, the pattern of the corrugated horn is narrower and its minor and back lobes are much lower than those of the corresponding control horn. The saddle formed on the main lobe of the control horn is attributed to the out-of-phase relations between the direct and diffracted rays. The diffracted rays are nearly absent from the corrugated horn and the minimum on-axis field is eliminated. The control horn is a thick-edged horn which has the same interior dimensions as the corrugated horn. The H-plane pattern of the corrugated horn is almost identical to the H-plane pattern of the corresponding control horn.

In Figures 13.33(c) and 13.33(d) the back lobe level and the 3-dB beamwidth for the smaller size control and corrugated horns, whose E-plane patterns are shown in Figure 13.33(a), are plotted as a function of frequency. All the observations made previously for that horn are well evident in these figures.

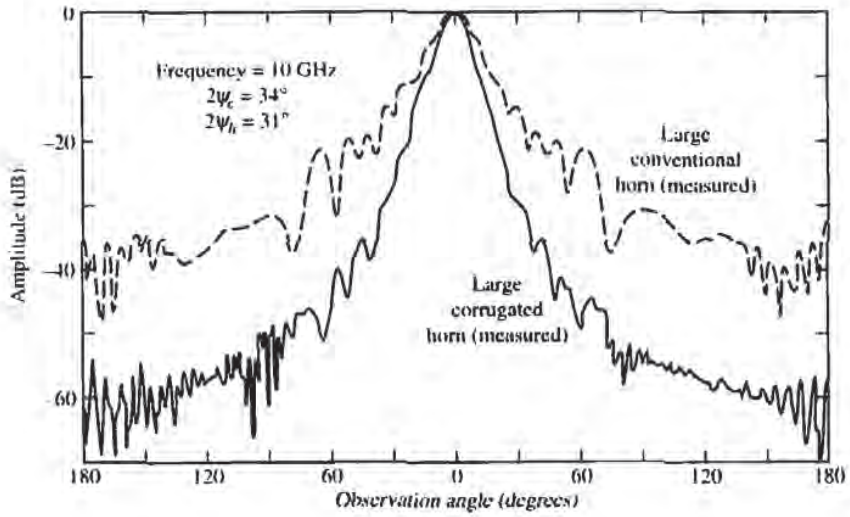
The presence of the corrugations, especially near the waveguide-horn junction, can affect the impedance and VSWR of the antenna. The usual practice is to begin the corrugations at a small distance away from the junction. This leads to low VSWR's over a broad band. Previously it was indicated that the width w of the corrugations must be small (usually $w < \lambda_0/10$) to approximate a corrugated surface. This would cause corona and other breakdown phenomena. However the large corrugated horn, whose E-plane pattern is shown in Figure 13.33(b), has been used in a system whose peak power was 20 kW at 10 GHz with no evidence of any breakdown phenomena.

The design concepts of the pyramidal corrugated horn can be extended to include circumferentially corrugated conical horns, as shown in Figure 13.29. Several designs of conical corrugated horns were investigated in terms of pattern symmetry, low cross polarization, low side lobe levels, circular polarization, axial ratio, and phase center [27]–[36]. For small flare angles (ψ_c less than about 20° to 25°) the slots can be machined perpendicular to the axis of the horn, as shown in Figure 13.29(b), and the grooves can be considered sections of parallel-plate TEM-mode waveguides of depth d. For large flare angles, however, the slots should be constructed perpendicular to the surface of the horn, as shown in Figure 13.29(a). The groove arrangement of Figure 13.29(b) is usually preferred because it is easier to fabricate.

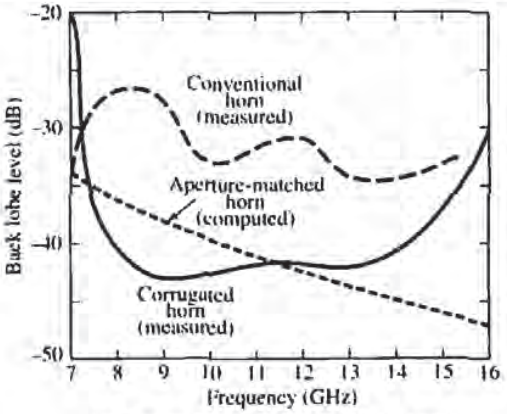
INTEL-1045
U.S. Patent 7,151,430



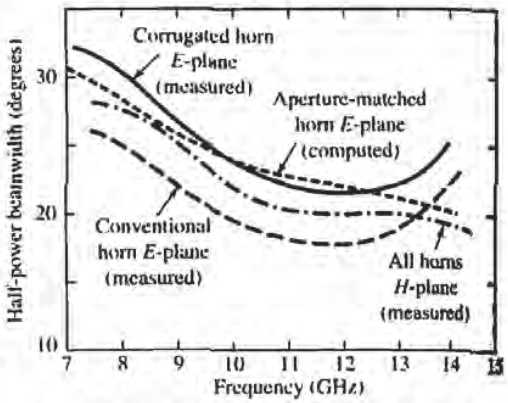
(a) E-plane ($2.96\lambda \times 2.96\lambda$)



(b) E-plane ($8.2\lambda \times 8.2\lambda$)



(c) E-plane back lobe level ($2.96\lambda \times 2.96\lambda$)



(d) E-plane half-power beamwidth ($2.96\lambda \times 2.96\lambda$)

Figure 13.33 Radiation characteristics of conventional (control), corrugated, and aperture-matched pyramidal horns. (SOURCE: (a), (c), (d). W. D. Burnside and C. W. Chuang, "An Aperture-Matched Horn Design," *IEEE Trans. Antennas Propagat.*, Vol. AP-30, No. 4, pp. 790–796, July 1982. © (1982) IEEE. (b) R. E. Laurie and L. Peters, Jr., "Modifications of Horn Antennas for Low Side Lobe Levels," *IEEE Trans. Antennas Propagat.*, Vol. AP-14, No. 5, pp. 605–610, September 1966. © (1966) IEEE)

INTEL-1045
U.S. Patent 7,151,430

13.7 APERTURE-MATCHED HORNS

A horn which provides significantly better performance than an ordinary horn (in terms of pattern, impedance, and frequency characteristics) is that shown in Figure 13.34(a), which is referred to as an *aperture-matched* horn [37]. The main modification to the ordinary (conventional) horn, which we refer to here as the *control* horn, consists of the attachment of curved surface sections to the outside of the aperture edges, which reduces the diffractions that occur at the sharp edges of the aperture and provides smooth matching sections between the horn modes and the free-space radiation.

In contrast to the corrugated horn, which is complex and costly and reduces the diffractions at the edges of the aperture by minimizing the incident field, the aperture-matched horn reduces the diffractions by modifying the structure (without sacrificing size, weight, bandwidth, and cost) so that the diffraction coefficient is minimized. The basic concepts were originally investigated using elliptic cylinder sections, as shown in Figure 13.34(b); however, other convex curved surfaces, which smoothly blend to the ordinary horn geometry at the attachment point, will lead to similar improvements. This modification in geometry can be used in a wide variety of horns, and includes E-plane, H-plane, pyramidal, and conical horns. Bandwidths of 2:1 can be attained easily with aperture-matched horns having elliptical, circular, or other curved surfaces. The radii of curvature of the curved surfaces used in experimental models [37] ranged over $1.69\lambda \leq a \leq 8.47\lambda$ with $a = b$ and $b = 2a$. Good results can be obtained by using circular cylindrical surfaces with $2.5\lambda \leq a \leq 5\lambda$.

The basic radiation mechanism of such a horn is shown in Figure 13.34(c). The introduction of the curved sections at the edges does not eliminate diffractions; instead it substitutes edge diffractions by curved-surface diffractions which have a tendency to provide an essentially undisturbed energy flow across the junction, around the curved surface, and into free space. Compared with conventional horns, this radiation mechanism leads to smoother patterns with greatly reduced black lobes and negligible reflections back into the horn. The size, weight, and construction costs of the aperture-matched horn are usually somewhat larger and can be held to a minimum if half (one-half sections of an ellipse) or quadrant (one-fourth sections of an ellipse) sections are used instead of the complete closed surfaces.

To illustrate the improvements provided by the aperture-matched horns, the E-plane pattern, back lobe level, and half-power beamwidth of a pyramidal $2.96\lambda \times 2.96\lambda$ horn were computed and compared with the measured data of corresponding control and corrugated horns. The data are shown in Figures 13.33 (a, c, d). It is evident by examining the patterns of Figure 13.33(a) that the aperture-matched horn provides a smoother pattern and lower back lobe level than conventional horns (referred to here as control horn); however, it does not provide, for the wide minor lobes, the same reduction as the corrugated horn. To achieve nearly the same E-plane pattern for all three horns, the overall horn size must be increased. If the modifications for the aperture-matched and corrugated horns were only made in the E-plane edges, the H-plane patterns for all three horns would be virtually the same except that the back lobe level of the aperture-matched and corrugated horns would be greatly reduced.

The back lobe level of the same three horns (control, corrugated, and aperture-matched) are shown in Figure 13.33(c). The corrugated horn has lower back lobe intensity at the lower end of the frequency band, while the aperture-matched horn exhibits superior performance at the high end. However, both the corrugated and aperture-matched horns exhibit superior back lobe level characteristics to the control

INTEL-1045
U.S. Patent 7,151,430

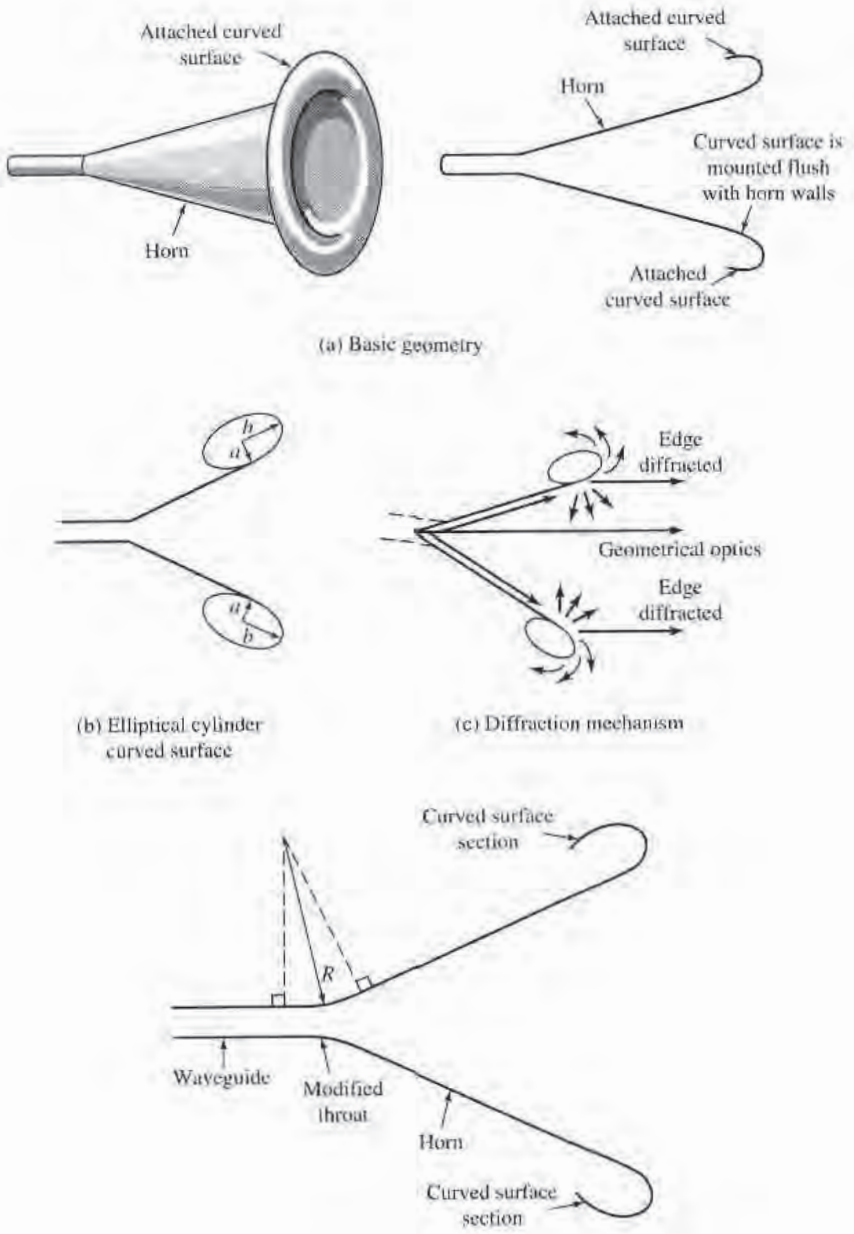


Figure 13.34 Geometry and diffraction mechanism of an aperture-matched horn. (SOURCE: W. D. Burnside and C. W. Chuang, "An Aperture-Matched Horn Design," *IEEE Trans. Antennas Propagat.*, Vol. AP-30, No. 4, pp. 790–796, July 1982. © (1982) IEEE)

(conventional) horn throughout almost the entire frequency band. The half-power beamwidth characteristics of the same three horns are displayed in Figure 13.33(d). Because the control (conventional) horn has uniform distribution across the complete aperture plane, compared with the tapered distributions for the corrugated and aperture-matched horns, it possesses the smallest beamwidth almost over the entire frequency band.

INTEL-1045
U.S. Patent 7,151,430

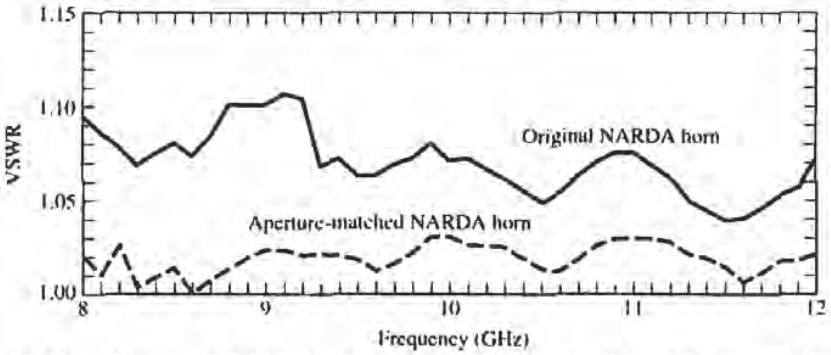


Figure 13.35 Measured VSWR for exponentially tapered pyramidal horns (conventional and aperture-matched). (SOURCE: W. D. Burnside and C. W. Chuang, "An Aperture-Matched Horn Design," *IEEE Trans. Antennas Propagat.*, Vol. AP-30, No. 4, pp. 790–796, July 1982. © (1982) IEEE)

In a conventional horn the VSWR and antenna impedance are primarily influenced by the throat and aperture reflections. Using the aperture-matched horn geometry of Figure 13.34(a), the aperture reflections toward the inside of the horn are greatly reduced. Therefore the only remaining dominant factors are the throat reflections. To reduce the throat reflections it has been suggested that a smooth curved surface be used to connect the waveguide and horn walls, as shown in Figure 13.34(d). Such a transition has been applied in the design and construction of a commerical *X*-band (8.2–12.4 GHz) pyramidal horn (see Fig. 13.24), whose tapering is of an exponential nature. The VSWR's measured in the 8-12 GHz frequency band using the conventional exponential *X*-band horn (shown in Figure 13.24), with and without curved sections at its aperture, are shown in Figure 13.35.

The matched sections used to create the aperture-matched horn were small cylinder sections. The VSWR's for the conventional horn are very small (less than 1.1) throughout the frequency band because the throat reflections are negligible compared with the aperture reflections. It is evident, however, that the VSWR's of the corresponding aperture-matched horn are much superior to those of the conventional horn because both the throat and aperture reflections are very minimal.

The basic design of the aperture-matched horn can be extended to include corrugations on its inside surface [29]. This type of design enjoys the advantages presented by both the aperture-matched and corrugated horns with cross-polarized components of less than -45 dB over a significant part of the bandwidth. Because of its excellent cross-polarization characteristics, this horn is recommended for use as a reference and for frequency reuse applications in both satellite and terrestrial applications.

13.8 MULTIMODE HORNS

Over the years there has been a need in many applications for horn antennas which provide symmetric patterns in all planes, phase center coincidence for the electric and magnetic planes, and side lobe suppression. All of these are attractive features for designs of optimum reflector systems and monopulse radar systems. Side lobe reduction is a desired attribute for horn radiators utilized in antenna range, anechoic cham-

INTEL-1045
U.S. Patent 7,151,430

ber, and standard gain applications, while pattern plane symmetry is a valuable feature for polarization diversity.

Pyramidal horns have traditionally been used over the years, with good success, in many of these applications. Such radiators, however, possess nonsymmetric beamwidths and undesirable side lobe levels, especially in the *E*-plane. Conical horns, operating in the dominant TE_{11} mode, have a tapered aperture distribution in the *E*-plane. Thus, they exhibit more symmetric electric- and magnetic-plane beamwidths and reduced side lobes than do the pyramidal horns. One of the main drawbacks of a conical horn is its relative incompatibility with rectangular waveguides.

To remove some of the deficiencies of pyramidal and conical horns and further improve some of their attractive characteristics, corrugations were introduced on the interior walls of the waveguides, which lead to the corrugated horns that were discussed in a previous section of this chapter. In some other cases designs were suggested to improve the beamwidth equalization in all planes and reduce side lobe levels by utilizing horn structures with multiple-mode excitations. These have been designated as *multimode* horns, and some of the designs will be discussed briefly here. For more information the reader should refer to the cited references.

One design of a multimode horn is the "diagonal" horn [38], shown in Figure 13.36, all of whose cross sections are square and whose internal fields consist of a superposition of TE_{10} and TE_{01} modes in a square waveguide. For small flare angles, the field structure within the horn is such that the **E**-field vector is parallel to one of the diagonals. Although it is not a multimode horn in the true sense of the word, because it does not make use of higher-order TE and TM modes, it does possess the desirable attributes of the usual multimode horns, such as equal beamwidths and suppressed beamwidths and side lobes in the *E*- and *H*-planes which are nearly equal to those in the principal planes. These attractive features are accomplished, however, at the expense of pairs of cross-polarized lobes in the intercardinal planes which make such a horn unattractive for applications where a high degree of polarization purity is required.

Diagonal horns have been designed, built, and tested [38] such that the 3-, 10-, and 30-dB beamwidths are nearly equal not only in the principal *E*- and *H*-planes, but also in the 45° and 135° planes. Although the theoretical limit of the side lobe level in the principal planes is 31.5 dB down, side lobes of at least 30 dB down have been observed in those planes. Despite a theoretically predicted level of -19.2 dB in the $\pm 45°$ planes, side lobes with level of -23 to -27 dB have been observed. The principal deficiency in the side lobe structure appears in the $\pm 45°$-plane cross-polarized lobes whose intensity is only 16 dB down; despite this, the overall horn efficiency remains high. Compared with diagonal horns, conventional pyramidal square horns have *H*-plane beamwidths which are about 35% wider than those in the *E*-plane, and side lobe levels in the *E*-plane which are only 12 to 13 dB down (although those in the *H*-plane are usually acceptable).

For applications which require optimum performance with narrow beamwidths, lenses are usually recommended for use in conjunction with diagonal horns. Diagonal horns can also be converted to radiate circular polarization by inserting a differential phase shifter inside the feed guide whose cross section is circular and adjusted so that it produces phase quadrature between the two orthogonal modes.

Another multimode horn which exhibits suppressed side lobes, equal beamwidths, and reduces cross-polarization is the *dual-mode* conical horn [39]. Basically this horn is designed so that diffractions at the aperture edges of the horn, especially those in the *E*-plane, are minimized by reducing the fields incident on the aperture edges and consequently the associated diffractions. This is accomplished by utilizing a conical

INTEL-1045
U.S. Patent 7,151,430

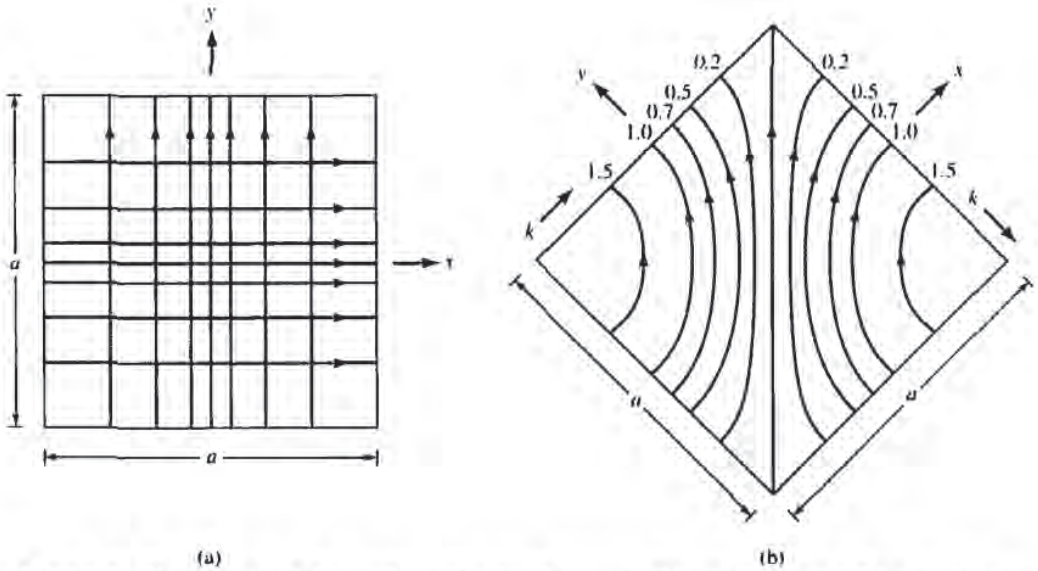


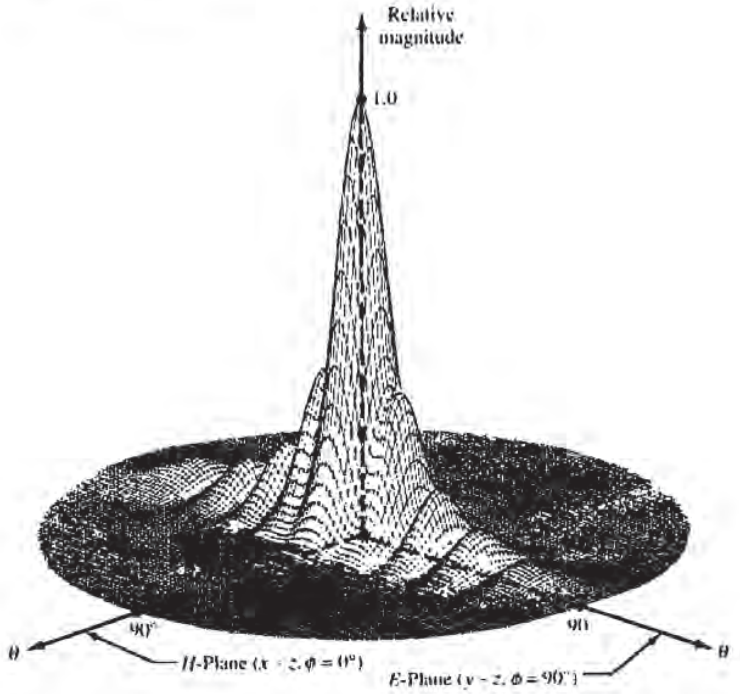
Figure 13.36 Electric-field configuration inside square diagonal horn. (*a*) Two coexisting equal orthogonal modes. (*b*) Result of combining the two modes shown in (*a*). (*After Love* [38] *reprinted with permission of* Microwave Journal, Vol. V, No. 3, March 1962)

horn which at its throat region is excited in both the dominant TE_{11} and higher-order TM_{11} mode. A discontinuity is introduced at a position within the horn where two modes exist. The horn length is adjusted so that the superposition of the relative amplitudes of the two modes at the edges of the aperture is very small compared with the maximum aperture field magnitude. In addition, the dimensions of the horn are controlled so that the total phase at the aperture is such that, in conjunction with the desired amplitude distribution, it leads to side lobe suppression, beamwidth equalization, and phase center coincidence.

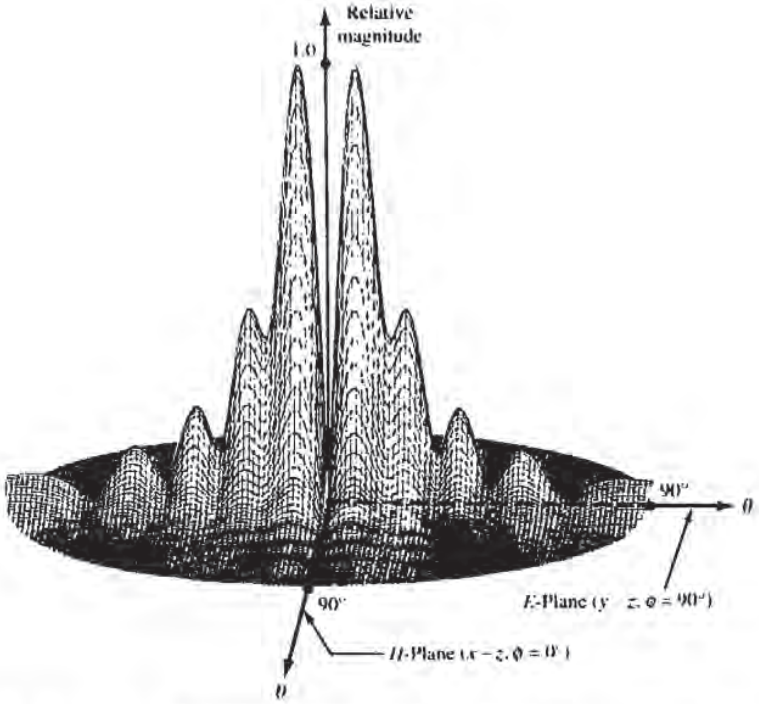
Qualitatively the pattern formation of a dual-mode conical horn operating in the TE_{11} and TM_{11} modes is accomplished by utilizing a pair of modes which have radiation functions with the same argument. However, one of the modes, in this case the TM_{11} mode, contains an additional envelope factor which varies very rapidly in the main beam region and remains relatively constant at large angles. Thus, it is possible to control the two modes in such a way that their fields cancel in all directions except within the main beam. The TM_{11} mode exhibits a null in its far-field pattern. Therefore a dual-mode conical horn possesses less axial gain than a conventional dominant-mode conical horn of the same aperture size. Because of that, dual-mode horns render better characteristics and are more attractive for applications where pattern plane symmetry and side lobe reduction are more important than maximum aperture efficiency. A most important application of a dual-mode horn is as a feed of Cassegrain reflector systems.

Dual-mode conical horns have been designed, built, and tested [39] with relatively good success in their performance. Generally, however, diagonal horns would be good competitors for the dual-mode horns if it were not for the undesirable characteristics (especially the cross-polarized components) that they exhibit in the very important 45° and 135° planes. Improved performance can be obtained from dual-mode horns if additional higher-order modes (such as the TE_{12}, TE_{13} and TM_{12}) are excited [40] and if their relative amplitudes and phases can be properly controlled. Computed

INTEL-1045
U.S. Patent 7,151,430



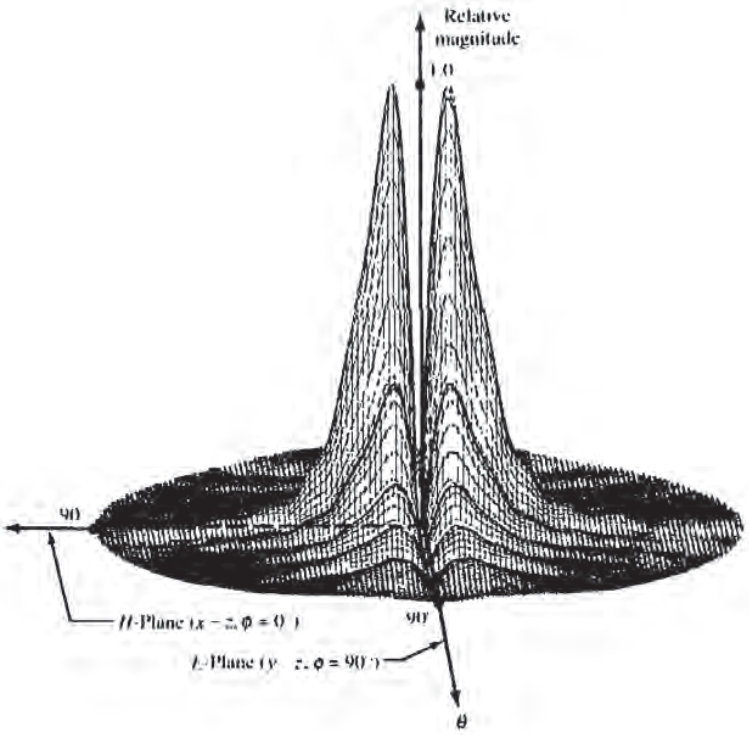
(a) Sum (TE_{10} + TE_{30} modes)



(b) E-plane difference (TE_{11} + TM_{11} modes)

Figure 13.37 Three-dimensional sum and difference (E- and H-planes) field patterns of a monopulse pyramidal horn. (C. A. Balanis, "Horn Antennas," in *Antenna Handbook* (Y. T. Lo and S. W. Lee, eds.). © 1988, Van Nostrand Reinhold Co., Inc.)

INTEL-1045
U.S. Patent 7,151,430



(c) *H*-plane difference (TE_{20} mode)

Figure 13.37 (Continued)

maximum aperture efficiencies of paraboloidal reflectors, using such horns as feeds, have reached 90% contrasted with efficiencies of about 76% for reflector systems using conventional dominant-mode horn feeds. In practice the actual maximum efficiency achieved is determined by the number of modes that can be excited and the degree to which their relative amplitudes and phases can be controlled.

The techniques of the dual-mode and multimode conical horns can be extended to the design of horns with rectangular cross sections. In fact a multimode pyramidal horn has been designed, built, and tested to be used as a feed in a low-noise Cassegrain monopulse system [41]. This rectangular pyramidal horn utilizes additional higher-order modes to provide monopulse capability, side lobe suppression in both the *E*- and *H*-planes, and beamwidth equalization. Specifically the various pattern modes for the monopulse system are formed in a single horn as follows:

(a) *Sum:* Utilizes $TE_{10} + TE_{30}$ instead of only TE_{10}. When the relative amplitude and phase excitations of the higher-order TE_{30} mode are properly adjusted, they provide side lobe cancellation at the second minor lobe of the TE_{10}-mode pattern

(b) *E-Plane Difference:* Utilizes $TE_{11} + TM_{11}$ modes

(c) *H-Plane Difference:* Utilizes TE_{20} mode

In its input the horn of [41] contained a four-guide monopulse bridge circuitry, a multimode matching section, a difference mode phasing section, and a sum mode excitation and control section. To illustrate the general concept, in Figure 13.37(a–c) are plots of three-dimensional patterns of the sum, *E*-plane difference, and *H*-plane difference modes which utilize, respectively, the $TE_{10} + TE_{30}$, $TE_{11} + TM_{11}$, and TE_{20}

INTEL-1045
U.S. Patent 7,151,430

modes. The relative excitation between the modes has been controlled so that each pattern utilizing multiple modes in its formation displays its most attractive features for its function.

13.9 DIELECTRIC-LOADED HORNS

Over the years much effort has been devoted in enhancing the antenna and aperture efficiencies of aperture antennas, especially for those that serve as feeds for reflectors (such as the horn). One technique that was proposed and then investigated was to use dielectric guiding structures, referred to as *Dielguides* [42], between the primary feed and the reflector (or subreflector). The technique is simple and inexpensive to implement and provides broadband, highly efficient, and low-noise antenna feeds. The method negates the compromise between taper and spillover efficiencies, and it is based on the principle of internal reflections, which has been utilized frequently in optics. Its role bears a very close resemblance to that of a lens, and it is an extension of the classical parabolic-shaped lens to other geometrical shapes.

Another method that has been used to control the radiation pattern of electromagnetic horns is to insert totally within them various shapes of dielectric material (wedges, slabs, etc.) [43]–[51] to control in a predictable manner not only the phase distribution over the aperture, as is usually done by using the classical parabolic lenses, but also to change the power (amplitude) distribution over the aperture. The control of the amplitude and phase distributions over the aperture are very essential in the design of very low side lobe antenna patterns.

Symmetrical loading of the H-plane walls has also been utilized, by proper parameter selection, to create a dominant longitudinal section electric (LSE) mode and to enhance the aperture efficiency and pattern-shaping capabilities of symmetrically loaded horns [43]. The method is simple and inexpensive, and it can also be utilized to realize high efficiency from small horns which can be used in limited scan arrays. Aperture efficiencies on the order of 92 to 96% have been attained, in contrast to values of 81% for unloaded horns.

A similar technique has been suggested to symmetrically load the E-plane walls of rectangular horns [45]–[51] and eventually to line all four of its walls with dielectric slabs. Other similar techniques have been suggested, and a summary of these and other classical papers dealing with dielectric-loaded horns can be found in [1].

13.10 PHASE CENTER

Each far-zone field component radiated by an antenna can be written, in general, as

$$\mathbf{E}_u = \hat{\mathbf{u}} E(\theta, \phi) e^{j\psi(\theta,\phi)} \frac{e^{-jkr}}{r} \tag{13-63}$$

where $\hat{\mathbf{u}}$ is a unit vector. The terms $E(\theta, \phi)$ and $\psi(\theta, \phi)$ represent, respectively, the (θ, ϕ) variations of the amplitude and phase.

In navigation, tracking, homing, landing, and other aircraft and aerospace systems it is usually desirable to assign to the antenna a reference point such that for a given frequency, $\psi(\theta, \phi)$ of (13-63) is independent of θ and ϕ (i.e., $\psi(\theta, \phi) =$ constant). The reference point which makes $\psi(\theta, \phi)$ independent of θ and ϕ is known as the *phase center* of the antenna [52]–[56]. When referenced to the phase center, the fields radiated by the antenna are spherical waves with ideal spherical wave fronts or

INTEL-1045
U.S. Patent 7,151,430

equiphase surfaces. Therefore a phase center is a reference point from which radiation is said to emanate, and radiated fields measured on the surface of a sphere whose center coincides with the phase center have the same phase.

For practical antennas such as arrays, reflectors, and others, a single unique phase center valid for all values of θ and ϕ does not exist; for most, however, their phase center moves along a surface, and its position depends on the observation point. However, in many antenna systems a reference point can be found such that $\psi(\theta, \phi) =$ constant, or nearly so, over most of the angular space, especially over the main lobe. When the phase center position variation is sufficiently small, that point is usually referred to as the *apparent phase center.*

The need for the phase center can best be explained by examining the radiation characteristics of a paraboloidal reflector (parabola of revolution). Plane waves incident on a paraboloidal reflector focus at a single point which is known as the *focal point.* Conversely, spherical waves emanating from the focal point are reflected by the paraboloidal surface and form plane waves. Thus in the receiving mode all the energy is collected at a single point. In the transmitting mode, ideal plane waves are formed if the radiated waves have spherical wavefronts and emanate from a single point.

In practice, no antenna is a point source with ideal spherical equiphases. Many of them, however, contain a point from which their radiation, over most of the angular space, seems to have spherical wavefronts. When such an antenna is used as a feed for a reflector, its phase center must be placed at the focal point. Deviations of the feed from the focal point of the reflector lead to phase errors which result in significant gain reductions of the antenna, as illustrated in Section 15.4.1(G) of Chapter 15.

The analytical formulations for locating the phase center of an antenna are usually very laborious and exist only for a limited number of configurations [52]–[54]. Experimental techniques [55], [56] are available to locate the phase center of an antenna. The one reported in [55] is also discussed in some detail in [2], and it will not be repeated here. The interested reader is referred to [2] and [55].

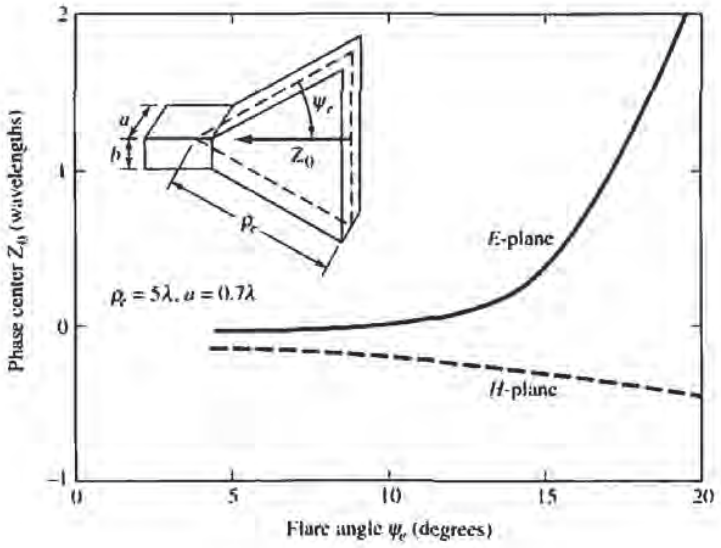
The horn is a microwave antenna that is widely used as a feed for reflectors [57]. To perform as an efficient feed for reflectors, it is imperative that its phase center is known and it is located at the focal point of the reflector. Instead of presenting analytical formulations for the phase center of a horn, graphical data will be included to illustrate typical phase centers.

Usually the phase center of a horn is not located at its mouth (throat) or at its aperture but mostly between its imaginary apex point and its aperture. The exact location depends on the dimensions of the horn, especially on its flare angle. For large flare angles the phase center is closer to the apex. As the flare angle of the horn becomes smaller, the phase center moves toward the aperture of the horn.

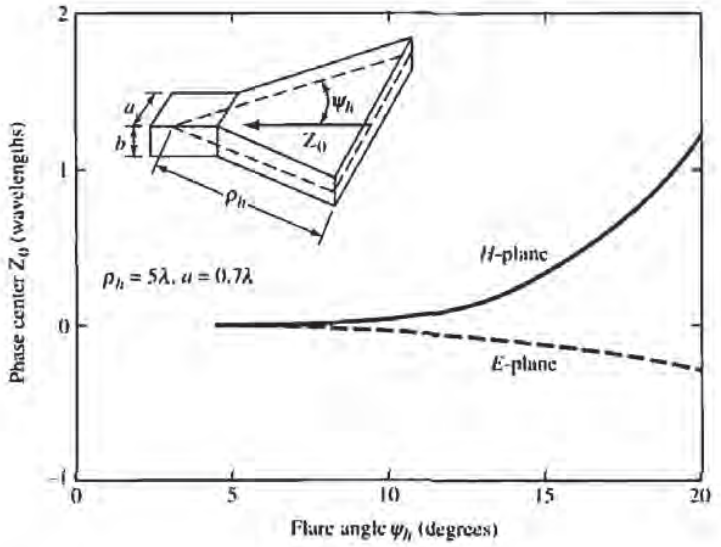
Computed phase centers for an E-plane and an H-plane sectoral horn are displayed in Figure 13.38(a,b). It is apparent that for small flare angles the E- and H-plane phase centers are identical. Although each specific design has its own phase center, the data of Figure 13.38(a,b) are typical. If the E- and H-plane phase centers of a pyramidal horn are not identical, its phase center can be taken to be the average of the two.

Phase center nomographs for conical corrugated and uncorrugated (TE_{11}-mode) horns are available [54], and they can be found in [2] and [54]. The procedure to use these in order to locate a phase center is documented in [2] and [54], and it is not repeated here. The interested reader is referred to [2] where examples are also illustrated.

INTEL-1045
U.S. Patent 7,151,430



(a) E-plane



(b) H-plane

Figure 13.38 Phase center location, as a function of flare angle, for E- and H-plane sectoral horns. (*Adapted from Hu* [52])

References

1. A. W. Love, *Electromagnetic Horn Antennas*, IEEE Press, New York, 1976.
2. C. A. Balanis, "Horn Antennas," Chapter 8 in *Antenna Handbook: Theory, Applications and Design* (Y. T. Lo and S. W. Lee, eds.), Van Nostrand Reinhold Co., New York, 1988.
3. A. W. Love, "Horn Antennas," Chapter 15 in *Antenna Engineering Handbook* (R. C. Johnson and H. Jasik, eds.), New York, 1984.
4. R. F. Harrington, *Time-Harmonic Electromagnetic Fields*, McGraw-Hill, New York, 1961, pp. 208–213.

INTEL-1045
U.S. Patent 7,151,430

5. S. Silver (ed.), *Microwave Antenna Theory and Design*, MIT Radiation Laboratory Series, Vol. 12, McGraw-Hill, New York, 1949, pp. 349–376.
6. C. A. Balanis, *Advanced Engineering Electromagnetics*, John Wiley and Sons, New York, 1989.
7. M. J. Maybell and P. S. Simon, "Pyramidal Horn Gain Calculation with Improved Accuracy," *IEEE Trans. Antennas Propagat.*, Vol. 41, No. 7, pp. 884–889, July 1993.
8. K. Liu, C. A. Balanis, C. R. Birtcher and G. C. Barber, "Analysis of Pyramidal Horn Antennas Using Moment Method," *IEEE Trans. Antennas Propagat.*, Vol. 41, No. 10, pp. 1379–1389, October 1993.
9. M. Abramowitz and I. A. Stegun (eds.), *Handbook of Mathematical Functions*, National Bureau of Standards, United States Dept. of Commerce, June 1964.
10. J. Boersma, "Computation of Fresnel Integrals," *Math. Comp.*, Vol. 14, p. 380, 1960.
11. Y.-B. Cheng, "Analysis of Aircraft Antenna Radiation for Microwave Landing System Using Geometrical Theory of Diffraction," MSEE Thesis, Dept. of Electrical Engineering, West Virginia University, pp. 208–211, 1976.
12. E. V. Jull, "Gain of an E-Plane Sectoral Horn–A Failure of the Kirchoff Theory and a New Proposal," *IEEE Trans. Antennas Propagat.*, Vol. AP-22, No. 2, pp. 221–226, March 1974.
13. E. V. Jull, *Aperture Antennas and Diffraction Theory*, Peter Peregrinus Ltd., London, United Kingdom, pp. 55–65, 1981.
14. E. H. Braun, "Some Data for the Design of Electromagnetic Horns," *IRE Trans. Antennas Propagat.*, Vol. AP-4, No. 1, pp. 29–31, January 1956.
15. P. M. Russo, R. C. Rudduck, and L. Peters, Jr., "A Method for Computing *E*-Plane Patterns of Horn Antennas," *IEEE Trans. Antennas Propagat.*, Vol. AP-13, No. 2, pp. 219–224, March 1965.
16. J. S. Yu, R. C. Rudduck, and L. Peters, Jr., "Comprehensive Analysis for *E*-Plane of Horn Antennas by Edge Diffraction Theory," *IEEE Trans. Antennas Propagat.*, Vol. AP-14, No. 2, pp. 138–149, March 1966.
17. M. A. K. Hamid, "Diffraction by a Conical Horn," *IEEE Trans. Antennas Propagat.*, Vol. AP-16, No. 5, pp. 520–528, September 1966.
18. M. S. Narasimhan and M. S. Shehadri, "GTD Analysis of the Radiation Patterns of Conical Horns," *IEEE Trans. Antennas Propagat.*, Vol. AP-26, No. 6, pp. 774–778, November 1978.
19. P. A. Tirkas and C. A. Balanis, "Contour Path FDTD Method for Analysis of Pyramidal Horns with Composite Inner E-Plane Walls," *IEEE Trans. Antennas Propagat.*, Vol. AP-42, No. 11, pp. 1476–1483, November 1994.
20. M. G. Schorr and F. J. Beck, Jr., "Electromagnetic Field of a Conical Horn," *J. Appl. Phys.*, Vol. 21, pp. 795–801, August 1950.
21. A. P. King, "The Radiation Characteristics of Conical Horn Antennas," *Proc. IRE*, Vol. 38, pp. 249–251, March 1950.
22. A. F. Kay, "The Scalar Feed," AFCRL Rep. 64-347, AD601609, March 1964.
23. R. E. Lawrie and L. Peters, Jr., "Modifications of Horn Antennas for Low Side Lobe Levels," *IEEE Trans. Antennas Propagat.*, Vol. AP-14, No. 5, pp. 605–610, September 1966.
24. R. S. Elliott, "On the Theory of Corrugated Plane Surfaces," *IRE Trans. Antennas Propagat.*, Vol. AP-2, No. 2, pp. 71–81, April 1954.
25. C. A. Mentzer and L. Peters, Jr., "Properties of Cutoff Corrugated Surfaces for Corrugated Horn Design," *IEEE Trans. Antennas Propagat.*, Vol. AP-22, No. 2, pp. 191–196, March 1974.
26. C. A. Mentzer and L. Peters, Jr., "Pattern Analysis of Corrugated Horn Antennas," *IEEE Trans. Antennas Propagat.*, Vol. AP-24, No. 3, pp. 304–309, May 1976.
27. M. J. Al-Hakkak and Y. T. Lo, "Circular Waveguides and Horns with Anisotropic and Corrugated Boundaries," *Antenna Laboratory Report No. 73-3*, Department of Electrical Engineering, University of Illinois, Urbana, January 1973.

INTEL-1045
U.S. Patent 7,151,430

28. B. MacA. Thomas, G. L. James and K. J. Greene, "Design of Wide-Band Corrugated Conical Horns for Cassegrain Antennas," *IEEE Trans. Antennas Propagat.*, Vol. AP-34, No. 6, pp. 750–757, June 1986.
29. B. MacA. Thomas, "Design of Corrugated Conical Horns," *IEEE Trans. Antennas Propagat.*, Vol. AP-26, No. 2, pp. 367–372, March 1978.
30. B. MacA. Thomas and K. J. Greene, "A Curved-Aperture Corrugated Horn Having Very Low Cross-Polar Performance," *IEEE Trans. Antennas Propagat.*, Vol. AP-30, No. 6, pp. 1068–1072, November 1982.
31. G. L. James, "TE_{11}-to-HE_{11} Mode Converters for Small-Angle Corrugated Horns," *IEEE Trans. Antennas Propagat.*, Vol. AP-30, No. 6, pp. 1057–1062, November 1982.
32. K. Tomiyasu, "Conversion of TE_{11} mode by a Large-Diameter Conical Junction," *IEEE Trans. Microwave Theory Tech.*, Vol. MTT-17, No. 5, pp. 277–279, May 1969.
33. B. MacA. Thomas, "Mode Conversion Using Circumferentially Corrugated Cylindrical Waveguide," *Electronic Letters*, Vol. 8, pp. 394–396, 1972.
34. J. K. M. Jansen and M. E. J. Jeuken, "Surface Waves in Corrugated Conical Horn," *Electronic Letters*, Vol. 8, pp. 342–344, 1972.
35. Y. Tacheichi, T. Hashimoto, and F. Takeda, "The Ring-Loaded Corrugated Waveguide," *IEEE Trans. Microwave Theory Tech.*, Vol. MTT-19, No. 12, pp. 947–950, December 1971.
36. F. Takeda and T. Hashimoto, "Broadbanding of Corrugated Conical Horns by Means of the Ring-Loaded Corrugated Waveguide Structure," *IEEE Trans. Antennas Propagat.*, Vol. AP-24, No. 6, pp. 786–792, November 1976.
37. W. D. Burnside and C. W. Chuang, "An Aperture-Matched Horn Design," *IEEE Trans. Antennas Propagat.*, Vol. AP-30, No. 4, pp. 790–796, July 1982.
38. A. W. Love, "The Diagonal Horn Antenna," *Microwave Journal*, Vol. V, pp. 117–122, March 1962.
39. P. D. Potter, "A New Horn Antenna with Suppressed Side Lobes and Equal Beamwidths," *Microwave Journal*, pp. 71–78, June 1963.
40. P. D. Potter and A. C. Ludwig, "Beamshaping by Use of Higher-Order Modes in Conical Horns," *Northeast Electron. Res. and Eng. Mtg.*, pp. 92–93, November 1963.
41. P. A. Jensen, "A Low-Noise Multimode Cassegrain Monopulse with Polarization Diversity," *Northeast Electron. Res. and Eng. Mtg.*, pp. 94–95, November 1963.
42. H. E. Bartlett and R. E. Moseley, "Dielguides—Highly Efficient Low-Noise Antenna Feeds," *Microwave Journal*, Vol. 9, pp. 53–58, December 1966.
43. L. L. Oh, S. Y. Peng, and C. D. Lunden, "Effects of Dielectrics on the Radiation Patterns of an Electromagnetic Horn," *IEEE Trans. Antennas Propagat.*, Vol. AP-18, No. 4, pp. 553–556, July 1970.
44. G. N. Tsandoulas and W. D. Fitzgerald, "Aperture Efficiency Enhancement in Dielectrically Loaded Horns," *IEEE Trans. Antennas Propagat.*, Vol. AP-20, No. 1, pp. 69–74, January 1972.
45. R. Baldwin and P. A. McInnes, "Radiation Patterns of Dielectric Loaded Rectangular Horns," *IEEE Trans. Antennas Propagat.*, Vol. AP-21, No. 3, pp. 375–376, May 1973.
46. C. M. Knop, Y. B. Cheng, and E. L. Osterlag, "On the Fields in a Conical Horn Having an Arbitrary Wall Impedance," *IEEE Trans. Antennas Propagat.*, Vol. AP-34, No. 9, pp. 1092–1098, September 1986.
47. J. J. H. Wang, V. K. Tripp, and R. P. Zimmer, "Magnetically Coated Horn for Low Sidelobes and Low Cross-Polarization," *IEE Proceedings*, Vol. 136, pp. 132–138, April 1989.
48. J. J. H. Wang, V. K. Tripp, and J. E. Tehan, "The Magnetically Coated Conducting Surface as a Dual Conductor and Its Application to Antennas and Microwaves," *IEEE Trans. Antennas Propagat.*, Vol. AP-38, No. 7, pp. 1069–1077, July 1990.
49. K. Liu and C. A. Balanis, "Analysis of Horn Antennas with Impedance Walls," *1990 IEEE Antennas and Propagatation Symposium Digest*, Vol. 1, pp. 1184–1187, May 7–11, 1990, Dallas, TX.

INTEL-1045
U.S. Patent 7,151,430

50. K. Liu and C. A. Balanis, "Low-Loss Material Coating for Horn Antenna Beam Shaping," *1991 IEEE Antennas and Propagatation Symposium Digest*, Vol. 3, pp. 1664–1667, June 24–28, 1991, London, Ontario, Canada.
51. P. A. Tirkas, "Finite-Difference Time-Domain for Aperture Antenna Radiation," PhD Dissertation, Dept. of Electrical Engineering, Arizona State University, December 1993.
52. Y. Y. Hu, "A Method of Determining Phase Centers and Its Applications to Electromagnetic Horns," *Journal of the Franklin Institute*, Vol. 271, pp. 31–39, January 1961.
53. E. R. Nagelberg, "Fresnel Region Phase Centers of Circular Aperture Antennas," *IEEE Trans. Antennas Propagat.*, Vol. AP-13, No. 3, pp. 479–480, May 1965.
54. I. Ohtera and H. Ujiie, "Nomographs for Phase Centers of Conical Corrugated and TE_{11} Mode Horns," *IEEE Trans. Antennas Propagat.*, Vol. AP-23, No. 6, pp. 858–859, November 1975.
55. J. D. Dyson, "Determination of the Phase Center and Phase Patterns of Antennas," in *Radio Antennas for Aircraft and Aerospace Vehicles*, W. T. Blackband (ed.), AGARD Conference Proceedings, No. 15, Slough, England Technivision Services, 1967.
56. M. Teichman, "Precision Phase Center Measurements of Horn Antennas," *IEEE Trans. Antennas Propagat.*, Vol. AP-18, No. 5, pp. 689–690, September 1970.
57. W. M. Truman and C. A. Balanis, "Optimum Design of Horn Feeds for Reflector Antennas," *IEEE Trans. Antennas Propagat.*, Vol. AP-22, No. 4, pp. 585–586, July 1974.

PROBLEMS

13.1. Derive (13-1a)–(13-1c) by treating the E-plane horn as a radial waveguide.

13.2. Design an E-plane horn such that the maximum phase difference between two points at the aperture, one at the center and the other at the edge, is 120°. Assuming that the maximum length along its wall (ρ_ℓ), measured from the aperture to its apex, is 10λ, find the
(a) maximum total flare angle of the horn
(b) largest dimension of the horn at the aperture
(c) directivity of the horn (dimensionless and in dB)
(d) gain of the antenna (in dB) when the reflection coefficient within the waveguide feeding the horn is 0.2. Assume only mismatch losses. The waveguide feeding the horn has dimensions of 0.5λ and 0.25λ

13.3. For an E-plane horn with $\rho_1 = 6\lambda$, $b_1 = 3.47\lambda$, and $a = 0.5\lambda$,
(a) compute (in dB) its pattern at $\theta = 0°$, 10°, and 20° using the results of Figure 13.6. Show all the steps for one angle.
(b) compute its directivity using (13-19) and (13-20c). Compare the answers.

13.4. Repeat Problem 13.3 for $\rho_1 = 6\lambda$, $b_1 = 6\lambda$, and $a = 0.5\lambda$.

13.5. For an E-plane sectoral horn, plot b_1 (in λ) versus ρ_1 (in λ) using (13-19a). Verify, using the data of Figure 13.8, that the maximum directivities occur when (13-19a) is satisfied.

13.6. For an E-plane sectoral horn with $\rho_1 = 20\lambda$, $a = 0.5\lambda$
(a) find its optimum aperture dimensions for maximum normalized directivity
(b) compute the total flare angle of the horn
(c) compute its directivity, using (13-19), and compare it with the graphical answer
(d) find its half-power beamwidth (in degrees)
(e) compute the directivity using (13-20c)

13.7. An E-plane horn is fed by an X-band WR 90 rectangular waveguide with inner dimensions of 0.9 in. (2.286 cm) and $b = 0.4$ in. (1.016 cm). Design the horn so that its maximum directivity at $f = 11$ GHz is 30 (14.77 dB).

13.8. Design an optimum directivity E-plane sectoral horn whose axial length is $\rho_1 = 10\lambda$. The horn is operating at X-band with a desired center frequency equal to $f = 10$ GHz.

INTEL-1045
U.S. Patent 7,151,430

The dimensions of the feed waveguide are $a = 0.9$ in. (2.286 cm) and $b = 0.4$ in. (1.016 cm). Assuming an 100% efficient horn ($e_t = 1$), find the
(a) horn aperture dimensions b_1 and ρ_e (in wavelengths), and flare half-angle ψ_e (in degrees)
(b) directivity D_E (in dB) using (13-20c)
(c) aperture efficiency
(d) largest phase difference (in degrees) between center of horn at the aperture and any point on the horn aperture along the principal E-plane

13.9. Derive (13-21a)–(13-21e) by treating the H-plane horn as a radial waveguide.

13.10. For an H-plane sectoral horn with $\rho_2 = 6\lambda$, $a_1 = 6\lambda$, and $b = 0.25\lambda$ compute the
(a) directivity (in dB) using (13-41), (13-42c) and compare the answers
(b) normalized field strength (in dB) at $\theta = 30°$, 45°, and 90°. Approximate it using linear interpolation

13.11. For an H-plane sectoral horn, plot a_1 (in λ) versus ρ_2 (in λ) using (13-41c). Verify, using the data of Figure 13.16, that the maximum directivities occur when (13-41c) is satisfied.

13.12. An H-plane sectoral horn is fed by an X-band WR 90 rectangular waveguide with dimensions of $a = 0.9$ in. (2.286 cm) and $b = 0.4$ in. (1.016 cm). Design the horn so that its maximum directivity at $f = 11$ GHz is 16.3 (12.12 dB).

13.13. Repeat the design of Problem 13.8 for an H-plane sectoral horn where axial length is also $\rho_2 = 10\lambda$. The feed waveguide dimensions and center frequency of operation are the same as in Problem 13.8. Assuming an 100% efficient horn ($e_t = 1$), find the
(a) horn aperture dimensions a_1 and ρ_h (in wavelengths), and the flare half-angle ψ_h (in degrees)
(b) directiviy D_H (in dB) using (13-42c)
(c) aperture efficiency
(d) largest phase difference (in degrees) between center of horn at the aperture and any point on the horn aperture along the principal H-plane

13.14. Show that (13-49a) and (13-49b) must be satisfied in order for a pyramidal horn to be physically realizable.

13.15. A standard gain X-band (8.2–12.4 GHz) pyramidal horn has dimensions of $\rho_1 \approx 13.5$ *in. (34.29 cm)*, $\rho_2 \approx 14.2$ *in. (36.07 cm)*, $a_1 = 7.65$ *in. (19.43 cm)*, $b_1 = 5.65$ *in.* (14.35 cm), $a = 0.9$ in. (2.286 cm), and $b = 0.4$ in. (1.016 cm).
(a) Check to see if such a horn can be constructed physically.
(b) Compute the directivity (in dB) at $f = 8.2$, 10.3, 12.4 GHz using for each (13-52a), (13-53), and (13-54e). Compare the answers. Verify with the computer program PYRAMIDAL HORN-ANALYSIS at the end of this chapter.

13.16. A standard gain X-band (8.2–12.4 GHz) pyramidal horn has dimensions of $\rho_1 = 5.3$ in. (13.46 cm), $\rho_2 = 6.2$ in. (15.75 cm), $a_1 = 3.09$ in. (7.85 cm), $b_1 = 2.34$ in. (5.94 cm), $a = 0.9$ in. (2.286 cm), and $b = 0.4$ in. (1.016 cm).
(a) Check to see if such a horn can be constructed physically.
(b) Compute the directivity (in dB) at $f = 8.2$, 10.3, 12.4 GHz using for each (13-52a), (13-53), and (13-54e). Compare the computed answers with the gains of Figure 13.24. Verify with the computer program PYRAMIDAL HORN-ANALYSIS at the end of this chapter.

13.17. Repeat the design of the optimum X-band pyramidal horn of Example 13.6 so that the gain at $f = 11$ GHz is 17.05 dB.

13.18. Design a pyramidal horn antenna with optimum gain at a frequency of 10 GHz. The overall length of the antenna from the imaginary vertex of the horn to the center of the aperture is 10λ and is nearly the same in both planes. Determine the
(a) Aperture dimension of the horn (in cm).
(b) Gain of the antenna (in dB)
(c) Aperture efficiency of the antenna (in %). Assume the reflection, conduction and dielectric losses of the antenna are negligible.

INTEL-1045
U.S. Patent 7,151,430

(d) Power delivered to a matched load when the incident power density is 10μ watts/m^2.

13.19. Design an optimum gain C-band (3.95–5.85 GHz) pyramidal horn so that its gain at $f = 4.90$ GHz is 20.0 dBi. The horn is fed by a WR 187 rectangular waveguide with inner dimensions of $a = 1.872$ in. (4.755 cm) and $b = 0.872$ in. (2.215 cm). Refer to Figure 13.18 for the horn geometry. Determine in cm. the remaining dimensions of the horn: ρ_e, ρ_h, a_1, b_1, ρ_e, and ρ_h. Verify using the computer program PYRAMIDAL HORN-DESIGN at the end of this chapter.

13.20. For a conical horn, plot d_m (in λ) versus l (in λ) using (13-60). Verify, using the data of Figure 13.27, that the maximum directivities occur when (13-60) is satisfied.

13.21. A conical horn has dimensions of $L = 19.5$ in. (49.53 cm), $d_m = 15$ in. (38.10 cm), and $d = 2.875$ in. (7.3025 cm).
(a) Find the frequency (in GHz) which will result in maximum directivity for this horn. What is that directivity (in dB)?
(b) Find the directivity (in dB) at 2.5 and 5 GHz.
(c) Compute the cutoff frequency (in GHz) of the TE_{11}-mode which can exist inside the circular waveguide that is used to feed the horn.

13.22. Design an optimum directivity conical horn, using (13-59)–(13-60), so that its directivity (above isotropic) at $f = 11$ GHz is 22.6 dB. Check your design with the data in Figure 13.27. Compare the design dimensions with those of the pyramidal horn of Example 13.6.

13.23. Design an optimum directivity conical horn so that its directivity at 10 GHz (above a standard gain horn of 15 dB directivity) is 5 dB. Determine the horn diameter (in cm) and its flare angle (in degrees).

13.24. As part of a 10-GHz microwave communication system, you purchase a horn antenna that is said to have a directivity of 75. The conduction and dielectric losses of the antenna are negligible, and the horn is polarization matched to the incoming signal. A standing wave meter indicates a voltage reflection coefficient of 0.1 at the antenna-waveguide junction.
(a) Calculate the maximum effective aperture of the horn.
(b) If an impinging wave with a uniform power density of 1 μ watts/m^2 is incident upon the horn, what is the maximum power delivered to a load which is connected and matched to the lossless waveguide?

13.25. For an X-band pyramidal corrugated horn operating at 10.3 GHz, find the
(a) smallest lower and upper limits of the corrugation depths (in cm)
(b) width w of each corrugation (in cm)
(c) width t of each corrugation tooth (in cm)

13.26. Find the E- and H-plane phase centers (in λ) of
(a) an E-plane ($\rho_e = 5\lambda$, $a = 0.7\lambda$)
(b) an H-plane ($\rho_h = 5\lambda$, $a = 0.7\lambda$)
sectoral horn with a total included angle of 30°.

INTEL-1045
U.S. Patent 7,151,430

COMPUTER PROGRAM - PYRAMIDAL HORN: ANALYSIS

```
C*****************************************************************
C THIS IS A FORTRAN PROGRAM THAT COMPUTES FOR A PYRAMIDAL
C HORN THE:
C
C     I.   FAR-ZONE E- AND H-PLANE AMPLITUDE PATTERNS
C          BASED ON THE THEORY OF SECTION 13.4,
C          EQUATIONS (13-46) - (13-48c)
C     II.  DIRECTIVITY (in dB) BASED ON EQUATION (13-52)
C     III. DIRECTIVITY (in dB) OF THE CORRESPONDING E-PLANE
C          SECTORAL HORN BASED ON EQUATION (13-19)
C     IV.  DIRECTIVITY (in dB) OF THE CORRESPONDING H-PLANE
C          SECTORAL HORN BASED ON EQUATION (13-41)
C
C TO COMPUTE THE DESIRED HORN RADIATION CHARACTERISTICS:
C
C       **INPUT PARAMETERS
C       1. ρ1 =  RHO1 (in λ)
C       2. ρ2 =  RHO2 (in λ)
C       3. a & b    =  WAVEGUIDE DIMENSIONS (in λ)
C       4. a1 & b1  =  HORN APERTURE DIMENSIONS (in λ)
C
C       **NOTES
C       1. REFER TO FIGURE 13.18 FOR THE GEOMETRY
C       2. THE E- AND H-PLANE AMPLITUDE PATTERNS ARE STORED IN TW
C          DATA FILES; NAMELY, E-theta.dat AND E-phi.dat, RESPECTIVELY.
C
C*****************************************************************
```


INTEL-1045
U.S. Patent 7,151,430

COMPUTER PROGRAM - PYRAMIDAL HORN: DESIGN

```
C*****************************************************************
C
C THIS IS A FORTRAN PROGRAM THAT DESIGNS AN OPTIMUM GAIN
C PYRAMIDAL HORN BASED ON THE FORMULATION OF SECTION 13.4.3,
C EQUATIONS (13-55) - (13-58b).
C
C THE PROGRAM COMPUTES THE:
C
C     I.  HORN DIMENSIONS a1, b1, RHOE ρe, RHOH ρh, pe and
C         ph (in cm)
C     II. HORN FLARE ANGLES PSIE ψe AND PSIH ψh (in degrees)
C
C TO DESIGN THE HORN:
C
C       **INPUT PARAMETERS
C       1. Go    =  DESIRED GAIN (in dB)
C       2. F     =  FREQUENCY (in GHz)
C       3. a & b =  FEED RECTANGULAR WAVEGUIDE DIMENSIONS (in cm)
C
C       **NOTES
C       1. REFER TO FIGURE 13.18 FOR THE GEOMETRY
C       2. THIS PROGRAM USES A BISECTION METHOD ROUTINE TO FIND
C          THE ROOT OF THE DESIGN EQUATION (see NUMERICAL RECIPES
C          IN FORTRAN, SECOND EDITION, PAGE 347)
C
C*****************************************************************
```


INTEL-1045
U.S. Patent 7,151,430

CHAPTER 14

MICROSTRIP ANTENNAS

14.1 INTRODUCTION

In high-performance aircraft, spacecraft, satellite and missile applications, where size, weight, cost, performance, ease of installation, and aerodynamic profile are constraints, low profile antennas may be required. Presently there are many other government and commercial applications, such as mobile radio and wireless communications, that have similar specifications. To meet these requirements, microstrip antennas [1]–[38] can be used. These antennas are low-profile, conformable to planar and nonplanar surfaces, simple and inexpensive to manufacture using modern printed-circuit technology, mechanically robust when mounted on rigid surfaces, compatible with MMIC designs, and when the particular patch shape and mode are selected they are very versatile in terms of resonant frequency, polarization, pattern and impedance. In addition, by adding loads between the patch and the ground plane, such as pins and varactor diodes, adaptive elements with variable resonant frequency, impedance, polarization and pattern can be designed [18], [39]–[44].

Major operational disadvantages of microstrip antennas are their low efficiency, low power, high Q (sometimes in excess of 100), poor polarization purity, poor scan performance, spurious feed radiation and very narrow frequency bandwidth, which is typically only a fraction of a percent or at most a few percent. In some applications, such as in government security systems, narrow bandwidths are desirable. However, there are methods, such by increasing the height of the substrate, that can be used to extend the efficiency (as large as 90 percent if surface waves are not included) and bandwidth (up to about 35 percent) [38]. However, as the height increases, surface waves are introduced which usually are not desirable because they extract power from the total available for direct radiation (space waves). The surface waves travel within the substrate and they are scattered at bends and surface discontinuities, such as the truncation of the dielectric and ground plane [45]–[49], and degrade the antenna pattern and polarization characteristics. Surface waves can be eliminated, while maintaining large bandwidths, by using cavities [50], [51]. Stacking, as well as other methods, of microstrip elements can also be used to increase the bandwidth [13], [52]–[62]. In addition, microstrip antennas also exhibit large electromagnetic signature at certain frequencies outside the operating band, are rather large physically at VHF and possibly UHF frequencies, and in large arrays there is a tradeoff between bandwidth and scan volume [63]–[65].

INTEL-1045
U.S. Patent 7,151,430

14.1.1 Basic Characteristics

Microstrip antennas received considerable attention starting in the 1970s, although the idea of a microstrip antenna can be traced to 1953 [1] and a patent in 1955 [2]. Microstrip antennas, as shown in Figure 14.1(a), consist of a very thin ($t \ll \lambda_0$ where λ_0 is the free-space wavelength) metallic strip (patch) placed a small fraction of a wavelength ($h \ll \lambda_0$, usually $0.003\lambda_0 \leq h \leq 0.05\lambda_0$) above a ground plane. The microstrip patch is designed so its pattern maximum is normal to the patch (broadside radiator). This is accomplished by properly choosing the mode (field configuration) of excitation beneath the patch. End-fire radiation can also be accomplished by judicious mode selection. For a rectangular patch, the length L of the element is usually $\lambda_0/3 < L < \lambda_0/2$. The strip (patch) and the ground plane are separated by a dielectric sheet (referred to as the substrate), as shown in Figure 14.1(a).

There are numerous substrates that can be used for the design of microstrip antennas, and their dielectric constants are usually in the range of $2.2 \leq \epsilon_r \leq 12$. The ones that are most desirable for antenna performance are thick substrates whose dielectric constant is in the lower end of the range because they provide better efficiency, larger bandwidth, loosely bound fields for radiation into space, but at the expense of larger element size [38]. Thin substrates with higher dielectric constants are desirable for microwave circuitry because they require tightly bound fields to minimize undesired radiation and coupling, and lead to smaller element sizes; however, because of their greater losses, they are less efficient and have relatively smaller bandwidths [38]. Since microstrip antennas are often integrated with other microwave circuitry, a compromise has to be reached between good antenna performance and circuit design.

Often microstrip antennas are also referred to as *patch* antennas. The radiating elements and the feed lines are usually photoetched on the dielectric substrate. The radiating patch may be square, rectangular, thin strip (dipole), circular, elliptical, triangular or any other configuration. These and others are illustrated in Figure 14.2.

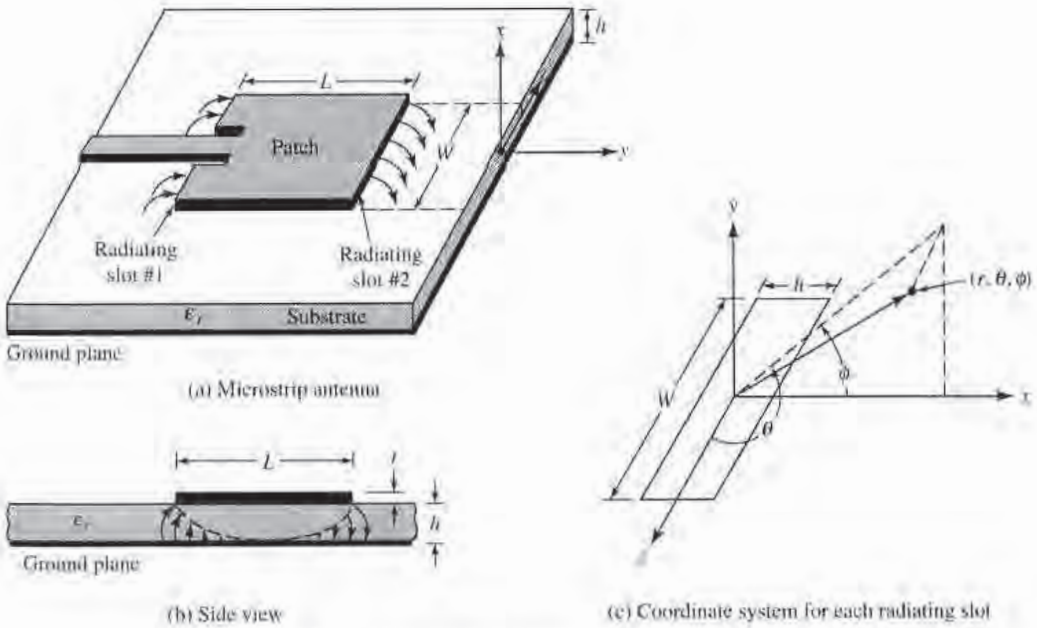


Figure 14.1 Microstrip antenna and coordinate system.

INTEL-1045
U.S. Patent 7,151,430

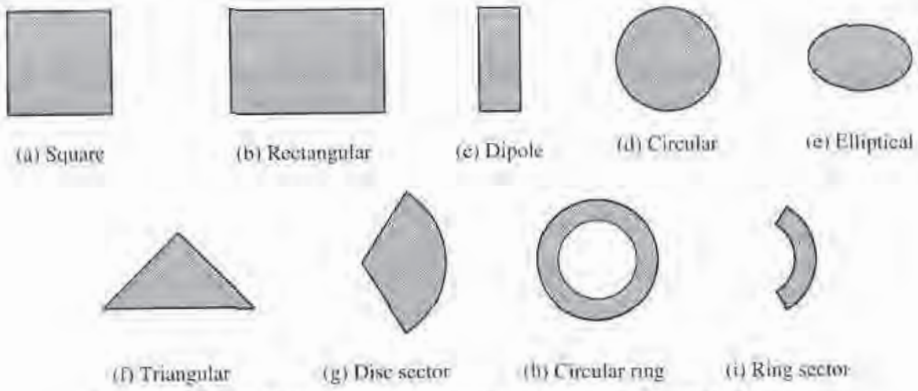


Figure 14.2 Representative shapes of microstrip patch elements.

Square, rectangular, dipole (strip), and circular are the most common because of ease of analysis and fabrication, and their attractive radiation characteristics, especially low cross-polarization radiation. Microstrip dipoles are attractive because they inherently possess a large bandwidth and occupy less space, which makes them attractive for arrays [14], [22], [30], [31]. Linear and circular polarizations can be achieved with either single elements or arrays of microstrip antennas. Arrays of microstrip elements, with single or multiple feeds, may also be used to introduce scanning capabilities and achieve greater directivities. These will be discussed in later sections.

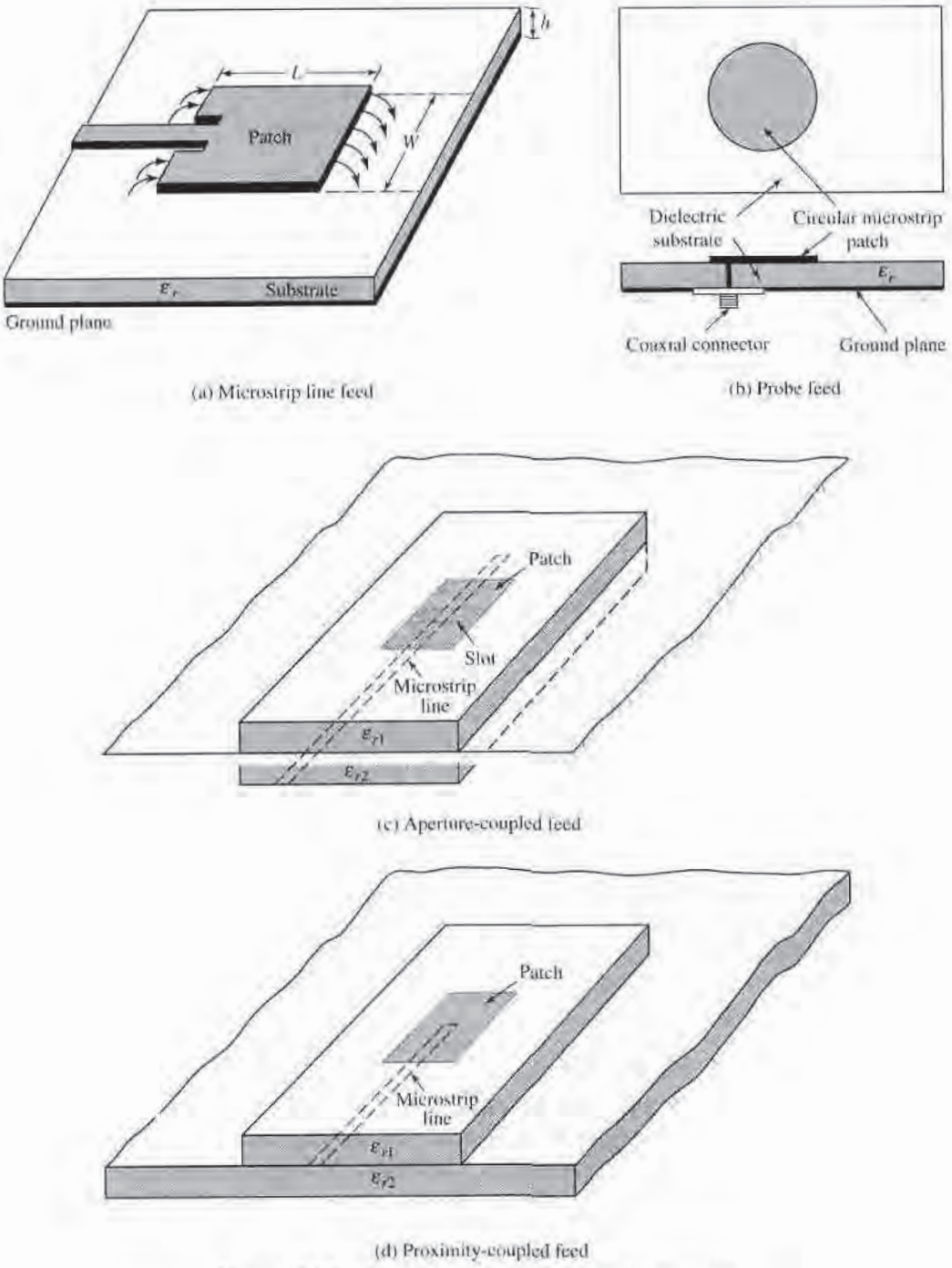
14.1.2 Feeding Methods

There are many configurations that can be used to feed microstrip antennas. The four most popular are the microstrip line, coaxial probe, aperture coupling and proximity coupling [15], [16], [30], [35], [38], [66]–[68]. These are displayed in Figure 14.3. One set of equivalent circuits for each one of these is shown in Figure 14.4. The microstrip feed line is also a conducting strip, usually of much smaller width compared to the patch. The microstrip line feed is easy to fabricate, simple to match by controlling the inset position and rather simple to model. However as the substrate thickness increases surface waves and spurious feed radiation increase, which for practical designs limit the bandwidth (typically 2–5%).

Coaxial-line feeds, where the inner conductor of the coax is attached to the radiation patch while the outer conductor is connected to the ground plane, are also widely used. The coaxial probe feed is also easy to fabricate and match, and it has low spurious radiation. However, it also has narrow bandwidth and it is more difficult to model, especially for thick substrates ($h > 0.02\lambda_0$).

Both the microstrip feed line and the probe possess inherent asymmetries which generate higher order modes which produce cross-polarized radiation. To overcome some of these problems, noncontacting aperture coupling feeds, as shown in Figures 14.3(c,d), have been introduced. The aperture coupling of Figure 14.3(c) is the most difficult of all four to fabricate and it also has narrow bandwidth. However, it is somewhat easier to model and has moderate spurious radiation. The aperture coupling consists of two substrates separated by a ground plane. On the bottom side of the lower substrate there is a microstrip feed line whose energy is coupled to the patch through a slot on the ground plane separating the two substrates. This arrangement allows independent optimization of the feed mechanism and the radiating element. Typically a high dielectric material is used for the bottom substrate, and thick low

INTEL-1045
U.S. Patent 7,151,430



(a) Microstrip line feed

(b) Probe feed

(c) Aperture-coupled feed

(d) Proximity-coupled feed

Figure 14.3 Typical feeds for microstrip antennas.

dielectric constant material for the top substrate. The ground plane between the substrates also isolates the feed from the radiating element and minimizes interference of spurious radiation for pattern formation and polarization purity. For this design, the substrate electrical parameters, feed line width, and slot size and position can be used to optimize the design [38]. Typically matching is performed by controlling the width of the feed line and the length of the slot. The coupling through the slot can be modeled using the theory of Bethe [69], which is also used to account for coupling

INTEL-1045
U.S. Patent 7,151,430

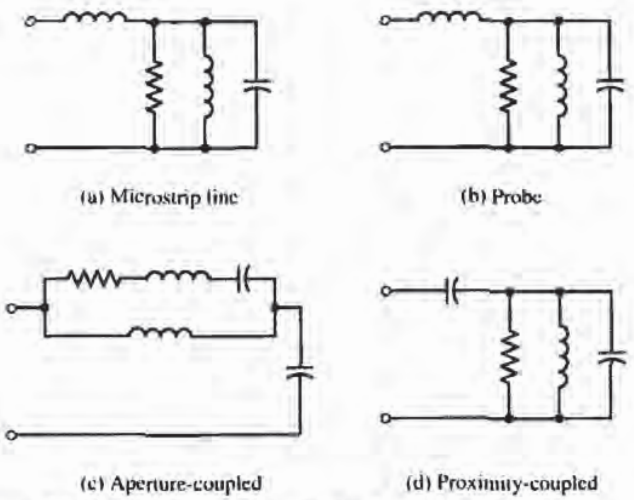


Figure 14.4 Equivalent circuits for typical feeds of Figure 14.3.

through a small aperture in a conducting plane. This theory has been successfully used to analyze waveguide couplers using coupling through holes [70]. In this theory the slot is represented by an equivalent normal electric dipole to account for the normal component (to the slot) of the electric field and an equivalent horizontal magnetic dipole to account for the tangential component (to the slot) magnetic field. If the slot is centered below the patch, where ideally for the dominant mode the electric field is zero while the magnetic field is maximum, the magnetic coupling will dominate. Doing this also leads to good polarization purity and no cross-polarized radiation in the principal planes [38]. Of the four feeds described here, the proximity coupling has the largest bandwidth (as high as 13 percent), is somewhat easy to model and has low spurious radiation. However its fabrication is somewhat more difficult. The length of the feeding stub and the width-to-line ratio of the patch can be used to control the match [61].

14.1.3. Methods of Analysis

There are many methods of analysis for microstrip antennas. The most popular models are the *transmission-line* [16], [35], *cavity* [12], [16], [18], [35], and *full-wave* (which include primarily integral equations/Moment Method) [22], [26], [71]–[74]. The transmission-line model is the easiest of all, it gives good physical insight, but is less accurate and it is more difficult to model coupling [75]. Compared to the transmission-line model, the cavity model is more accurate but at the same time more complex. However, it also gives good physical insight and is rather difficult to model coupling, although it has been used successfully [8], [76], [77]. In general when applied properly, the full-wave models are very accurate, very versatile, and can treat single elements, finite and infinite arrays, stacked elements, arbitrary shaped elements, and coupling. However they are the most complex models and usually give less physical insight. In this chapter we will cover the transmission-line and cavity models only. However results and design curves from full-wave models will also be included. Since they are the most popular and practical, in this chapter the only two patch configurations that will be considered are the rectangular and circular. Representative radiation characteristics of some other configurations will be included.

INTEL-1045
U.S. Patent 7,151,430

14.2 RECTANGULAR PATCH

The rectangular patch is by far the most widely used configuration. It is very easy to analyze using both the transmission-line and cavity models, which are most accurate for thin substrates [78]. We begin with the transmission-line model because it is easier to illustrate.

14.2.1 Transmission-Line Model

It was indicated earlier that the transmission-line model is the easiest of all but it yields the least accurate results and it lacks the versatility. However, it does shed some physical insight. As it will be demonstrated in Section 14.2.2 using the cavity model, a rectangular microstrip antenna can be represented as an array of two *radiating* narrow apertures (slots), each of width W and height h, separated by a distance L. Basically the transmission line model represents the microstrip antenna by two slots, separated by a low-impedance Z_c transmission line of length L.

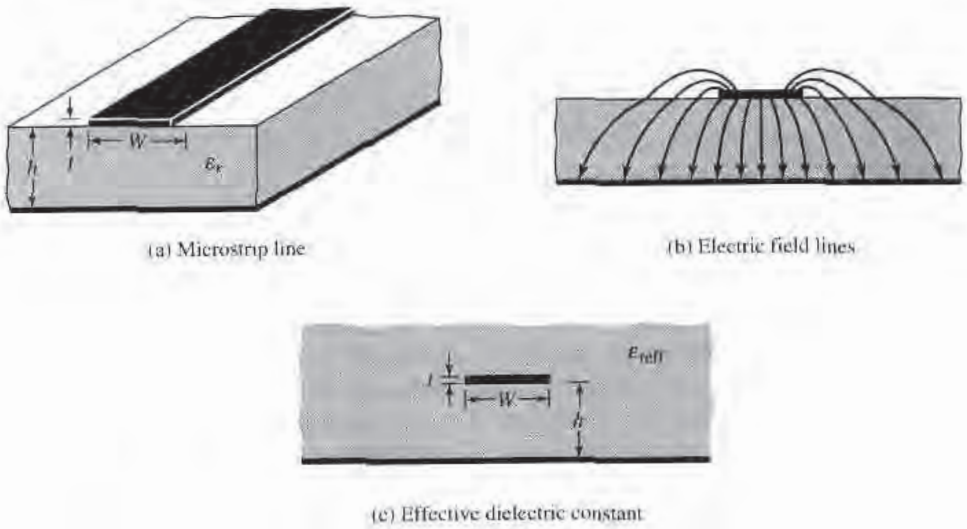
A. Fringing Effects

Because the dimensions of the patch are finite along the length and width, the fields at the edges of the patch undergo fringing. This is illustrated along the length in Figures 14.1(a,b) for the two radiating slots of the microstrip antenna. The same applies along the width. The amount of fringing is a function of the dimensions of the patch and the height of the substrate. For the principal E-plane (xy-plane) fringing is a function of the ratio of the length of the patch L to the height h of the substrate (L/h) and the dielectric constant ϵ_r of the substrate. Since for microstrip antennas $L/h \gg 1$, fringing is reduced; however, it must be taken into account because it influences the resonant frequency of the antenna. The same applies for the width.

For a microstrip line shown in Figure 14.5(a), typical electric field lines are shown in Figure 14.5(b). This is a nonhomogeneous line of two dielectrics: typically the substrate and air. As can be seen, most of the electric field lines reside in the substrate and parts of some lines exist in air. As $W/h \gg 1$ and $\epsilon_r \gg 1$, the electric field lines concentrate mostly in the substrate. Fringing in this case makes the microstrip line look wider electrically compared to its physical dimensions. Since some of the waves travel in the substrate and some in air, an *effective dielectric constant* ϵ_{reff} is introduced to account for fringing and the wave propagation in the line.

To introduce the effective dielectric constant, let us assume that the center conductor of the microstrip line with its original dimensions and height above the ground plane is embedded into one dielectric, as shown in Figure 14.5(c). The effective dielectric constant is defined *as the dielectric constant of the uniform dielectric material so that the line of Figure 14.5(c) has identical electrical characteristics, particularly propagation constant, as the actual line of Figure 14.5(a).* For a line with air above the substrate, the effective dielectric constant has values in the range of $1 < \epsilon_{reff} < \epsilon_r$. For most applications where the dielectric constant of the substrate is much greater than unity ($\epsilon_r \gg 1$), the value of ϵ_{reff} will be closer to the value of the actual dielectric constant ϵ_r of the substrate. The effective dielectric constant is also a function of frequency. As the frequency of operation increases, most of the electric field lines concentrate in the substrate. Therefore the microstrip line behaves more like a homogeneous line of one dielectric (only the substrate), and the effective dielectric constant approaches the value of the dielectric constant of the substrate. Typical variations, as a function of frequency, of the effective dielectric constant for a microstrip line with three different substrates are shown in Figure 14.6.

INTEL-1045
U.S. Patent 7,151,430



(a) Microstrip line (b) Electric field lines

(c) Effective dielectric constant

Figure 14.5 Microstrip line and its electric field lines, and effective dielectric constant geometry.

For low frequencies the effective dielectric constant is essentially constant. At intermediate frequencies its values begin to monotonically increase and eventually approach the values of the dielectric constant of the substrate. The initial values (at low frequencies) of the effective dielectric constant are referred to as the *static values*, and they are given by [79]

$$W/h > 1$$

$$\epsilon_{reff} = \frac{\epsilon_r + 1}{2} + \frac{\epsilon_r - 1}{2}\left[1 + 12\frac{h}{W}\right]^{-1/2} \tag{14-1}$$

B. Effective Length, Resonant Frequency, and Effective Width

Because of the fringing effects, electrically the patch of the microstrip antenna looks greater than its physical dimensions. For the principal *E*-plane (*xy*-plane), this is

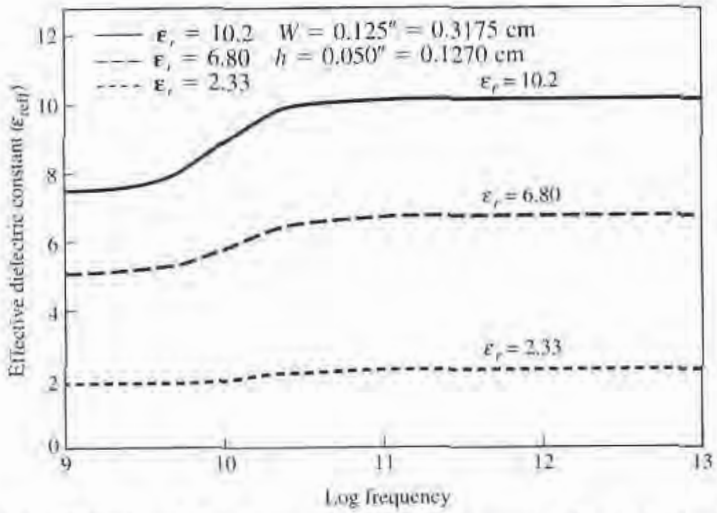


Figure 14.6 Effective dielectric constant versus frequency for typical substrates.

INTEL-1045
U.S. Patent 7,151,430

demonstrated in Figure 14.7 where the dimensions of the patch along its length have been extended on each end by a distance ΔL, which is a function of the effective dielectric constant ϵ_{reff} and the width-to-height ratio (W/h). A very popular and practical approximate relation for the normalized extension of the length is [80]

$$\frac{\Delta L}{h} = 0.412 \frac{(\epsilon_{reff} + 0.3)\left(\frac{W}{h} + 0.264\right)}{(\epsilon_{reff} - 0.258)\left(\frac{W}{h} + 0.8\right)} \tag{14-2}$$

Since the length of the patch has been extended by ΔL on each side, the effective length of the patch is now ($L = \lambda/2$ for dominant TM_{010} mode with no fringing)

$$L_{eff} = L + 2\Delta L \tag{14-3}$$

For the dominant TM_{010} mode, the resonant frequency of the microstrip antenna is a function of its length. Usually it is given by

$$(f_r)_{010} = \frac{1}{2L\sqrt{\epsilon_r}\sqrt{\mu_0\epsilon_0}} = \frac{v_0}{2L\sqrt{\epsilon_r}} \tag{14-4}$$

where v_0 is the speed of light in free space. Since (14-4) does not account for fringing, it must be modified to include edge effects and should be computed using

$$\begin{aligned}(f_{rc})_{010} &= \frac{1}{2L_{eff}\sqrt{\epsilon_{reff}}\sqrt{\mu_0\epsilon_0}} = \frac{1}{2(L + 2\Delta L)\sqrt{\epsilon_{reff}}\sqrt{\mu_0\epsilon_0}} \\ &= q\frac{1}{2L\sqrt{\epsilon_r}\sqrt{\mu_0\epsilon_0}} = q\frac{v_0}{2L\sqrt{\epsilon_r}}\end{aligned} \tag{14-5}$$

where

$$q = \frac{(f_{rc})_{010}}{(f_r)_{010}} \tag{14-5a}$$

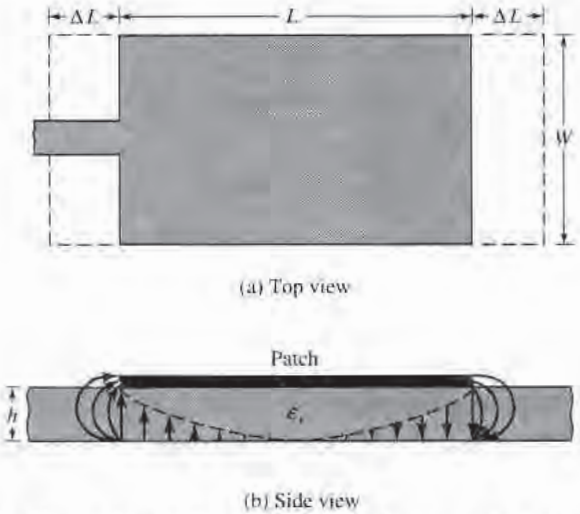


Figure 14.7 Physical and effective lengths of rectangular microstrip patch.

INTEL-1045
U.S. Patent 7,151,430

The q factor is referred to as the *fringe factor* (length reduction factor). As the substrate height increases, fringing also increases and leads to larger separations between the radiating edges and lower resonant frequencies.

C. Design

Based on the simplified formulation that has been described, a design procedure is outlined which leads to practical designs of rectangular microstrip antennas. The procedure assumes that the specified information includes the dielectric constant of the substrate (ϵ_r), the resonant frequency (f_r), and the height of the substrate h. The procedure is as follows:

Specify:

$$\epsilon_r, f_r \text{ (in Hz)}, \text{ and } h$$

Determine:

$$W, L$$

Design procedure:

1. For an efficient radiator, a practical width that leads to good radiation efficiencies is [15]

$$W = \frac{1}{2f_r\sqrt{\mu_0\epsilon_0}}\sqrt{\frac{2}{\epsilon_r + 1}} = \frac{v_0}{2f_r}\sqrt{\frac{2}{\epsilon_r + 1}} \tag{14-6}$$

   where v_0 is the free-space velocity of light.

2. Determine the effective dielectric constant of the microstrip antenna using (14-1).
3. Once W is found using (14-6), determine the extension of the length ΔL using (14-2).
4. The actual length of the patch can now be determined by solving (14-5) for L, or

$$L = \frac{1}{2f_r\sqrt{\epsilon_{reff}}\sqrt{\mu_0\epsilon_0}} - 2\Delta L \tag{14-7}$$

Example 14.1

Design a rectangular microstrip antenna using a substrate (RT/duroid 5880) with dielectric constant of 2.2, $h = 0.1588$ cm (0.0625 inches) so as to resonate at 10 GHz.

SOLUTION

Using (14-6), the width W of the patch is

$$W = \frac{30}{2(10)}\sqrt{\frac{2}{2.2 + 1}} = 1.186 \text{ cm } (0.467 \text{ in})$$

INTEL-1045
U.S. Patent 7,151,430

The effective dielectric constant of the patch is found using (14-1), or

$$\epsilon_{reff} = \frac{2.2 + 1}{2} + \frac{2.2 - 1}{2}\left(1 + 12\frac{0.1588}{1.186}\right)^{-1/2} = 1.972$$

The extended incremental length of the patch ΔL is, using (14-2)

$$\Delta L = 0.1588(0.412)\frac{(1.972 + 0.3)\left(\frac{1.186}{0.1588} + 0.264\right)}{(1.972 - 0.258)\left(\frac{1.186}{0.1588} + 0.8\right)}$$

$$= 0.081 \text{ cm } (0.032 \text{ in})$$

The actual length L of the patch is found using (14-3), or

$$L = \frac{\lambda}{2} - 2\Delta L = \frac{30}{2(10)\sqrt{1.972}} - 2(0.081) = 0.906 \text{ cm } (0.357 \text{ in})$$

Finally the effective length is

$$L_e = L + 2\Delta L = \frac{\lambda}{2} = 1.068 \text{ cm } (0.421 \text{ in})$$

D. Conductance

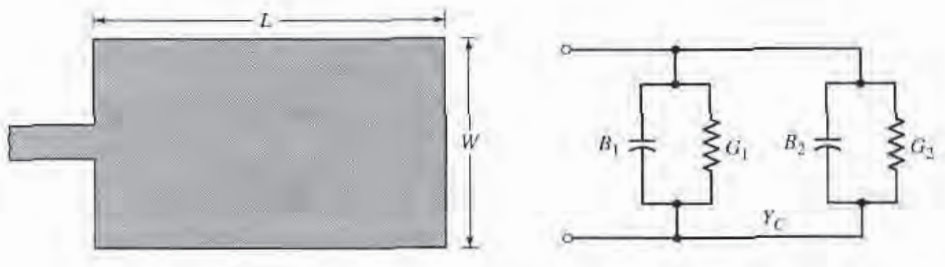
Each radiating slot is represented by a parallel equivalent admittance Y (with conductance G and susceptance B). This is shown in Figure 14.8. The slots are labeled as #1 and #2. The equivalent admittance of slot #1, based on an infinitely wide, uniform slot, is derived in Example 12.8 of Chapter 12, and it is given by [81]

$$Y_1 = G_1 + jB_1 \tag{14-8}$$

where for a slot of finite width W

$$G_1 = \frac{W}{120\lambda_0}\left[1 - \frac{1}{24}(k_0 h)^2\right] \qquad \frac{h}{\lambda_0} < \frac{1}{10} \tag{14-8a}$$

$$B_1 = \frac{W}{120\lambda_0}[1 - 0.636 \ln (k_0 h)] \qquad \frac{h}{\lambda_0} < \frac{1}{10} \tag{14-8b}$$



(a) Rectangular patch (b) Transmission model equivalent

Figure 14.8 Rectangular microstrip patch and its equivalent circuit transmission model.

INTEL-1045
U.S. Patent 7,151,430

Since slot #2 is identical to slot #1, its equivalent admittance is

$$Y_2 = Y_1, \qquad G_2 = G_1, \qquad B_2 = B_1 \tag{14-9}$$

The conductance of a single slot can also be obtained by using the field expression derived by the cavity model. In general, the conductance is defined as

$$G_1 = \frac{2P_{\text{rad}}}{|V_0|^2} \tag{14-10}$$

Using the electric field of (14-41), the radiated power is written as

$$P_{\text{rad}} = \frac{|V_0|^2}{2\pi\eta_0}\int_0^{\pi}\left[\frac{\sin\left(\frac{k_0W}{2}\cos\theta\right)}{\cos\theta}\right]^2\sin^3\theta\,d\theta \tag{14-11}$$

Therefore the conductance of (14-10) can be expressed as

$$G_1 = \frac{I_1}{120\pi^2} \tag{14-12}$$

where

$$I_1 = \int_0^{\pi}\left[\frac{\sin\left(\frac{k_0W}{2}\cos\theta\right)}{\cos\theta}\right]^2\sin^3\theta\,d\theta$$

$$= -2 + \cos(X) + XS_i(X) + \frac{\sin(X)}{X} \tag{14-12a}$$

$$X = k_0W \tag{14-12b}$$

Asymptotic values of (14-12) and (14-12a) are

$$G_1 = \begin{cases} \dfrac{1}{90}\left(\dfrac{W}{\lambda_0}\right)^2 & W \ll \lambda_0 \\ \dfrac{1}{120}\left(\dfrac{W}{\lambda_0}\right) & W \gg \lambda_0 \end{cases} \tag{14-13}$$

The values of (14-13) for $W \gg \lambda_0$ are identical to those given by (14-8a) for $h \ll \lambda_0$. A plot of G as a function of W/λ_0 is shown in Figure 14.9.

E. Resonant Input Resistance

The total admittance at slot #1 (input admittance) is obtained by transferring the admittance of slot #2 from the output terminals to input terminals using the admittance transformation equation of transmission lines [16], [70], [79]. Ideally the two slots should be separated by $\lambda/2$ where λ is the wavelength in the dielectic (substrate). However, because of fringing the length of the patch is electrically longer than the actual length. Therefore the actual separation of the two slots is slightly less than $\lambda/2$. If the reduction of the length is properly chosen using (14-2) (typically $0.48\lambda < L < 0.49\lambda$), the transformed admittance of slot #2 becomes

$$\tilde{Y}_2 = \tilde{G}_2 + j\tilde{B}_2 = G_1 - jB_1 \tag{14-14}$$

INTEL-1045
U.S. Patent 7,151,430

or

$$\tilde{G}_2 = G_1 \tag{14-14a}$$

$$\tilde{B}_2 = -B_1 \tag{14-14b}$$

Therefore the total resonant input admittance is real and is given by

$$Y_{in} = Y_1 + \tilde{Y}_2 = 2G_1 \tag{14-15}$$

Since the total input admittance is real, the resonant input impedance is also real, or

$$Z_{in} = \frac{1}{Y_{in}} = R_{in} = \frac{1}{2G_1}. \tag{14-16}$$

The resonant input resistance, as given by (14-16), does not take into account mutual effects between the slots. This can be accomplished by modifying (14-16) to [8]

$$R_{in} = \frac{1}{2(G_1 \pm G_{12})} \tag{14-17}$$

where the plus (+) sign is used for modes with odd (antisymmetric) resonant voltage distribution beneath the patch and between the slots while the minus (−) sign is used for modes with even (symmetric) resonant voltage distribution. The mutual conductance is defined, in terms of the far-zone fields, as

$$G_{12} = \frac{1}{|V_0|^2} \text{Re} \iint_S \mathbf{E}_1 \times \mathbf{H}_2^* \cdot d\mathbf{s} \tag{14-18}$$

where $\mathbf{E}_1$ is the electric field radiated by slot #1, $\mathbf{H}_2$ is the magnetic field radiated by slot #2, V_0 is the voltage across the slot, and the integration is performed over a sphere of large radius. It can be shown that G_{12} can be calculated using [8], [34]

$$G_{12} = \frac{1}{120\pi^2} \int_0^{\pi} \left[\frac{\sin\left(\frac{k_0 W}{2} \cos\theta\right)}{\cos\theta} \right]^2 J_0(k_0 L \sin\theta) \sin^3\theta \, d\theta \tag{14-18a}$$

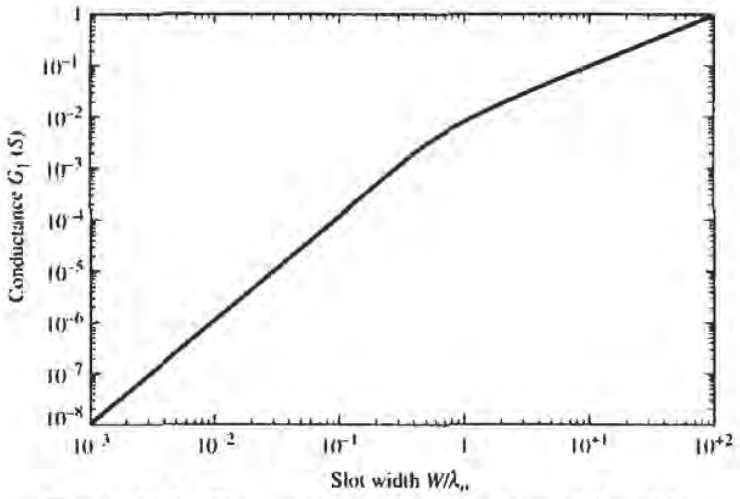


Figure 14.9 Slot conductance as a function of slot width.

INTEL-1045
U.S. Patent 7,151,430

where J_0 is the Bessel function of the first kind of order zero. For typical microstrip antennas, the mutual conductance obtained using (14-18a) is small compared to the self conductance G_1 of (14-8a) or (14-12).

As shown by (14-8a) and (14-17), the input resistance is not strongly dependent upon the substrate height h. In fact for very small values of h, such that $k_0 h \ll 1$, the input resistance is not dependent on h. Modal-expansion analysis also reveals that the input resistance is not strongly influenced by the substrate height h. It is apparent from (14-8a) and (14-17) that the resonant input resistance can be decreased by increasing the width W of the patch. This is acceptable as long as the ratio of W/L does not exceed 2 because the aperture efficiency of a single patch begins to drop, as W/L increases beyond 2.

The resonant input resistance, as calculated by (14-17), is referenced at slot #1. However, it has been shown that the resonant input resistance can be changed by using an inset feed, recessed a distance y_0 from slot #1, as shown in Figure 14.10(a). This technique can be used effectively to match the patch antenna using a microstrip-line feed whose characteristic impedance is given by [79]

$$Z_c = \begin{cases} \dfrac{60}{\sqrt{\epsilon_{reff}}} \ln\left[\dfrac{8h}{W_0} + \dfrac{W_0}{4h}\right], & \dfrac{W_0}{h} \le 1 \quad (14\text{-}19a) \\ \dfrac{120\pi}{\sqrt{\epsilon_{reff}}\left[\dfrac{W_0}{h} + 1.393 + 0.667 \ln\left(\dfrac{W_0}{h} + 1.444\right)\right]}, & \dfrac{W_0}{h} > 1 \quad (14\text{-}19b) \end{cases}$$

where W_0 is the width of the microstrip line, as shown in Figure 14.10. Using modal-expansion analysis, the input resistance for the inset-feed is given approximately by [8], [16]

$$R_{in}(y = y_0) = \frac{1}{2(G_1 \pm G_{12})}\left[\cos^2\left(\frac{\pi}{L}y_0\right) + \frac{G_1^2 + B_1^2}{Y_c^2}\sin^2\left(\frac{\pi}{L}y_0\right) - \frac{B_1}{Y_c}\sin\left(\frac{2\pi}{L}y_0\right)\right] \quad (14\text{-}20)$$

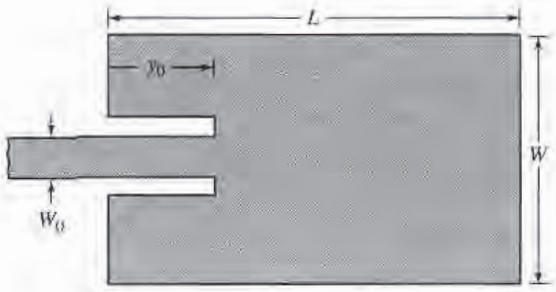
where $Y_c = 1/Z_c$. Since for most typical microstrips $G_1/Y_c \ll 1$ and $B_1/Y_c \ll 1$, (14-20) reduces to

$$R_{in}(y = y_0) = \frac{1}{2(G_1 \pm G_{12})}\cos^2\left(\frac{\pi}{L}y_0\right) = R_{in}(y = 0)\cos^2\left(\frac{\pi}{L}y_0\right) \quad (14\text{-}20a)$$

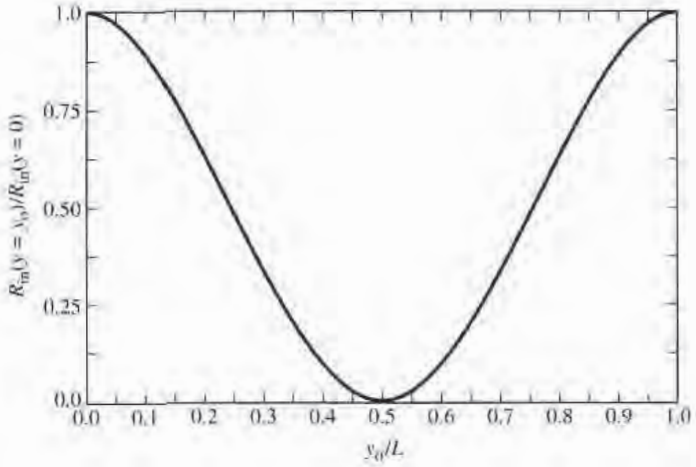
A plot of the normalized value of (14-20a) is shown in Figure 14.10(b).

The values obtained using (14-20) agree fairly well with experimental data. However, the inset feed introduces a physical notch, which in turn introduces a junction capacitance. The physical notch and its corresponding junction capacitance influence slightly the resonance frequency, which typically may vary by about 1%. It is apparent from (14-20a) and Figure 14.10(b) that the maximum value occurs at the edge of the slot ($y_0 = 0$) where the voltage is maximum and the current is minimum; typical values are in the 150–300 ohms. The minimum value (zero) occurs at the

INTEL-1045
U.S. Patent 7,151,430



(a) Recessed microstrip-line feed



(b) Normalized input resistance

Figure 14.10 Recessed microstrip-line feed and variation of normalized input resistance.

center of the patch ($y_0 = L/2$) where the voltage is zero and the current is maximum. As the inset feed-point moves from the edge toward the center of the patch the resonant input impedance decreases monotonically and reaches zero at the center. When the value of the inset feed-point approaches the center of the patch ($y_0 = L/2$), the $\cos^2(\pi y_0/L)$ function varies very rapidly; therefore the input resistance also changes rapidly with the position of the feed point. To maintain very accurate values, a close tolerance must be preserved.

Example 14.2

A microstrip antenna with overall dimensions of $L = 0.906$ cm (0.357 inches) and $W = 1.186$ cm (0.467 inches), substrate with height $h = 0.1588$ cm (0.0625 inches) and dielectric constant of $\epsilon_r = 2.2$, is operating at 10 GHz. Find:

a. The input impedance.

b. The position of the inset feed-point where the input impedance is 50 ohms.

INTEL-1045
U.S. Patent 7,151,430

SOLUTION

$$\lambda_0 = \frac{30}{10} \approx 3 \text{ cm}$$

Using (14-12) and (14-12a)

$$G_1 = 0.00157 \text{ siemens}$$

which compares with $G_1 = 0.00328$ using (14-8a). Using (14-18a)

$$G_{12} = 6.1683 \times 10^{-4}$$

Using (14-17) with the (+) sign because of the odd field distribution between the radiating slots for the dominant TM_{010} mode

$$R_{in} = 228.3508 \text{ ohms.}$$

Since the input impedance at the leading radiating edge of the patch is 228.3508 ohms while the desired impedance is 50 ohms, the inset feet-point distance y_0 is obtained using (14-20a). Thus

$$50 = 228.3508 \cos^2\left(\frac{\pi}{L} y_0\right)$$

or

$$y_0 = 0.3126 \text{ cm (0.123 inches)}$$

14.2.2 Cavity Model

Microstrip antennas resemble dielectric loaded cavities, and they exhibit higher order resonances. The normalized fields within the dielectric substrate (between the patch and the ground plane) can be found more accurately by treating that region as a cavity bounded by electric conductors (above and below it) and by magnetic walls (to simulate an open circuit) along the perimeter of the patch. This is an approximate model, which in principle leads to a reactive input impedance (of zero or infinite value of resonance), and it does not radiate any power. However, assuming that the actual fields are approximate to those generated by such a model, the computed pattern, input admittance, and resonant frequencies compare well with measurements [12], [16], [18]. This is an accepted approach, and it is similar to the perturbation methods which have been very successful in the analysis of waveguides, cavities, and radiators [81].

To shed some insight into the cavity model, let us attempt to present a physical interpretation into the formation of the fields within the cavity and radiation through its side walls. When the microstrip patch is energized, a charge distribution is established on the upper and lower surfaces of the patch, as well as on the surface of the ground plane, as shown in Figure 14.11. The charge distribution is controlled by two mechanisms; an *attractive* and a *repulsive* mechanism [34]. The *attractive* mechanism is between the corresponding opposite charges on the bottom side of the patch and the ground plane, which tends to maintain the charge concentration on the bottom of the patch. The *repulsive* mechanism is between like charges on the bottom surface of the patch, which tends to push some charges from the bottom of the patch, around its

INTEL-1045
U.S. Patent 7,151,430

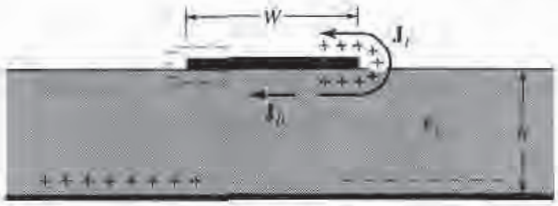


Figure 14.11 Charge distribution and current density creation on microstrip patch.

edges, to its top surface. The movement of these charges creates corresponding current densities $\mathbf{J}_b$ and $\mathbf{J}_t$, at the bottom and top surfaces of the patch, respectively, as shown in Figure 14.11. Since for most practical microstrips the height-to-width ratio is very small, the attractive mechanism dominates and most of the charge concentration and current flow remain underneath the patch. A small amount of current flows around the edges of the patch to its top surface. However, this current flow decreases as the height-to-width ratio decreases. In the limit, the current flow to the top would be zero, which ideally would not create any tangential magnetic field components to the edges of the patch. This would allow the four side walls to be modelled by perfect magnetic conducting surfaces which ideally would not disturb the magnetic field and, in turn, the electric field distributions beneath the patch. Since in practice there is a finite height-to-width ratio, although small, the tangential magnetic fields at the edges would not be exactly zero. However, since they will be small, a good approximation to the cavity model is to treat the side walls as perfectly magnetic conducting. This model produces good normalized electric and magnetic field distributions (modes) beneath the patch.

If the microstrip antenna were treated only as a cavity, it would not be sufficient to find the absolute amplitudes of the electric and magnetic fields. In fact by treating the walls of the cavity, as well as the material within it as lossless, the cavity would not radiate and its input impedance would be purely reactive. Also the function representing the impedance would only have real poles. To account for radiation, a loss mechanism has to be introduced. In Figure 2.21 of Chapter 2, this was taken into account by the radiation resistance R_r and loss resistance R_L. These two resistances allow the input impedance to be complex and for its function to have complex poles; the imaginary poles representing, through R_r and R_L, the radiation and conduction-dielectric losses. To make the microstrip lossy using the cavity model, which would then represent an antenna, the loss is taken into account by introducing an effective loss tangent δ_{eff}. The effective loss tangent is chosen appropriately to represent the loss mechanism of the cavity, which now behaves as an antenna and is taken as the reciprocal of the antenna quality factor Q ($\delta_{\text{eff}} = 1/Q$).

Because the thickness of the microstrip is usually very small, the waves generated within the dielectric substrate (between the patch and the ground plane) undergo considerable reflections when they arrive at the edge of the patch. Therefore only a small fraction of the incident energy is radiated; thus the antenna is considered to be very inefficient. The fields beneath the patch form standing waves that can be represented by cosinusoidal wave functions. Since the height of the substrate is very small ($h \ll \lambda$ where λ is the wavelength within the dielectric), the field variations along the height will be considered constant. In addition, because of the very small substrate height, the fringing of the fields along the edges of the patch are also very small whereby the electric field is nearly normal to the surface of the patch. Therefore only TM^z field configurations will be considered within the cavity. While the top and

INTEL-1045
U.S. Patent 7,151,430

bottom walls of the cavity are perfectly electric conducting, the four side walls will be modeled as perfectly conducting magnetic walls (tangential magnetic fields vanish along those four walls).

A. Field Configurations (modes)—TM^z

The field configurations within the cavity can be found using the vector potential approach described in detail in Chapter 8 of [79]. Referring to Figure 14.12, the volume beneath the patch can be treated as a rectangular cavity loaded with a dielectric material with dielectric constant ϵ_r. The dielectric material of the substrate is assumed to be truncated and not extended beyond the edges of the patch. The vector potential A_z must satisfy the homogeneous wave equation of

$$\nabla^2 A_z + k^2 A_z = 0 \tag{14-21}$$

whose solution is written in general, using the separation of variables, as [79]

$$\begin{aligned} A_z = {} & [A_1 \cos(k_x x) + B_1 \sin(k_x x)][A_2 \cos(k_y y) + B_2 \sin(k_y y)] \\ & \cdot [A_3 \cos(k_z z) + B_3 \sin(k_z z)] \end{aligned} \tag{14-22}$$

where k_x, k_y and k_z are the wavenumbers along the x, y and z directions, respectively. These will be determined subject to the boundary conditions. The electric and magnetic fields within the cavity are related to the vector potential A_z by [79]

$$\begin{aligned} E_x &= -j\frac{1}{\omega\mu\epsilon}\left(\frac{\partial^2}{\partial x^2} + k^2\right)A_z & H_x &= 0 \\ E_y &= -j\frac{1}{\omega\mu\epsilon}\frac{\partial^2 A_z}{\partial x \partial y} & H_y &= \frac{1}{\mu}\frac{\partial A_z}{\partial z} \\ E_z &= -j\frac{1}{\omega\mu\epsilon}\frac{\partial^2 A_z}{\partial x \partial z} & H_z &= -\frac{1}{\mu}\frac{\partial A_z}{\partial y} \end{aligned} \tag{14-23}$$

subject to the boundary conditions of

$$\begin{aligned} & E_y(x' = 0,\ 0 \le y' \le L,\ 0 \le z' \le W) \\ & \quad = E_y(x' = h,\ 0 \le y' \le L,\ 0 \le z' \le W) = 0 \\ & H_y(0 \le x' \le h,\ 0 \le y' \le L,\ z' = 0) \\ & \quad = H_y(0 \le x' \le h,\ 0 \le y' \le L,\ z' = W) = 0 \\ & H_z(0 \le x' \le h,\ y' = 0,\ 0 \le z' \le W) \\ & \quad = H_z(0 \le x' \le h,\ y' = L,\ 0 \le z' \le W) = 0 \end{aligned} \tag{14-24}$$

The primed coordinates x', y', z' are used to represent the fields within the cavity.

Applying the boundary conditions $E_y(x' = 0,\ 0 \le y' \le L,\ 0 \le z' \le W) = 0$ and $E_y(x' = h,\ 0 \le y' \le L,\ 0 \le z' \le W) = 0$, it can be shown that $B_1 = 0$ and

$$k_x = \frac{m\pi}{h}, \qquad m = 0, 1, 2, \ldots \tag{14-25}$$

Similarly, applying the boundary conditions $H_y(0 \le x' \le h,\ 0 \le y' \le L,\ z' = 0) = 0$ and $H_y(0 \le x' \le h,\ 0 \le y' \le L,\ z' = W) = 0$, it can be shown that $B_3 = 0$ and

$$k_z = \frac{p\pi}{W}, \qquad p = 0, 1, 2, \ldots \tag{14-26}$$

INTEL-1045
U.S. Patent 7,151,430

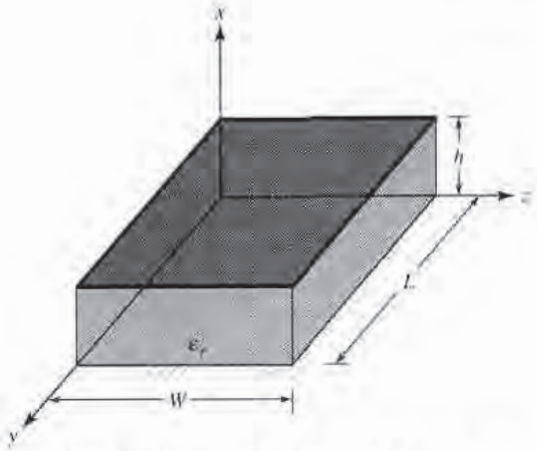


Figure 14.12 Rectangular microstrip patch geometry.

Finally, applying the boundary conditions $H_z(0 \le x' \le h,\ y' = 0,\ 0 \le z' \le W) = 0$ and $H_z(0 \le x' \le h,\ y' = L,\ 0 \le z' \le W) = 0$, it can be shown that $B_2 = 0$ and

$$k_y = \frac{n\pi}{L}, \qquad n = 0, 1, 2, \ldots \tag{14-27}$$

Thus the final form for the vector potential A_x within the cavity is

$$A_x = A_{mnp} \cos(k_x x') \cos(k_y y') \cos(k_z z') \tag{14-28}$$

where A_{mnp} represents the amplitude coefficients of each mnp mode. The wavenumbers k_x, k_y, k_z are equal to

$$\left.\begin{aligned} k_x &= \left(\frac{m\pi}{h}\right), \quad m = 0, 1, 2, \ldots \\ k_y &= \left(\frac{n\pi}{L}\right), \quad n = 0, 1, 2, \ldots \\ k_z &= \left(\frac{p\pi}{W}\right), \quad p = 0, 1, 2, \ldots \end{aligned}\right\} m = n = p \neq 0 \tag{14-29}$$

where m, n, p represent, respectively, the number of half-cycle field variations along the x, y, z directions.

Since the wavenumbers k_x, k_y, and k_z are subject to the constraint equation

$$k_x^2 + k_y^2 + k_z^2 = \left(\frac{m\pi}{h}\right)^2 + \left(\frac{n\pi}{L}\right)^2 + \left(\frac{p\pi}{W}\right)^2 = k_r^2 = \omega_r^2 \mu\epsilon \tag{14-30}$$

the resonant frequencies for the cavity are given by

$$(f_r)_{mnp} = \frac{1}{2\pi\sqrt{\mu\epsilon}} \sqrt{\left(\frac{m\pi}{h}\right)^2 + \left(\frac{n\pi}{L}\right)^2 + \left(\frac{p\pi}{W}\right)^2} \tag{14-31}$$

INTEL-1045
U.S. Patent 7,151,430

Substituting (14-28) into (14-23), the electric and magnetic fields within the cavity are written as

$$
\begin{aligned}
E_x &= -j\frac{(k^2 - k_x^2)}{\omega\mu\epsilon} A_{mnp} \cos(k_x x') \cos(k_y y') \cos(k_z z') \\
E_y &= -j\frac{k_x k_y}{\omega\mu\epsilon} A_{mnp} \sin(k_x x') \sin(k_y y') \cos(k_z z') \\
E_z &= -j\frac{k_x k_z}{\omega\mu\epsilon} A_{mnp} \sin(k_x x') \cos(k_y y') \sin(k_z z') \\
H_x &= 0 \\
H_y &= -\frac{k_z}{\mu} A_{mnp} \cos(k_x x') \cos(k_y y') \sin(k_z z') \\
H_z &= \frac{k_y}{\mu} A_{mnp} \cos(k_x x') \sin(k_y y') \cos(k_z z')
\end{aligned}
\tag{14-32}
$$

To determine the dominant mode with the lowest resonance, we need to examine the resonant frequencies. The mode with the lowest order resonant frequency is referred to as the *dominant* mode. Placing the resonant frequencies in ascending order determines the order of the modes of operation. For all microstrip antennas $h \ll L$ and $h \ll W$. If $L > W > h$, the mode with the lowest frequency (dominant mode) is the TM^x_{010} whose resonant frequency is given by

$$
(f_r)_{010} = \frac{1}{2L\sqrt{\mu\epsilon}} = \frac{v_0}{2L\sqrt{\epsilon_r}} \tag{14-33}
$$

where v_0 is the speed of light in free space. If in addition $L > W > L/2 > h$, the next higher order (second) mode is the TM^x_{001} whose resonant frequency is given by

$$
(f_r)_{001} = \frac{1}{2W\sqrt{\mu\epsilon}} = \frac{v_0}{2W\sqrt{\epsilon_r}} \tag{14-34}
$$

If, however, $L > L/2 > W > h$, the second order mode is the TM^x_{020}, instead of the TM^x_{001}, whose resonant frequency is given by

$$
(f_r)_{020} = \frac{1}{L\sqrt{\mu\epsilon}} = \frac{v_0}{L\sqrt{\epsilon_r}} \tag{14-35}
$$

If $W > L > h$, the dominant mode is the TM^x_{001} whose resonant frequency is given by (14-34) while if $W > W/2 > L > h$ the second order mode is the TM^x_{002}. Based upon (14-32), the distribution of the tangential electric field along the side walls of the cavity for the TM^x_{010}, TM^x_{001}, TM^x_{020} and TM^x_{002} is as shown, respectively, in Figure 14.13.

In all of the preceding discussion, it was assumed that there is no fringing of the fields along the edges of the cavity. This is not totally valid, but it is a good assumption. However, fringing effects and their influence were discussed previously, and they should be taken into account in determining the resonant frequency. This was done in (14-5) for the dominant TM^x_{010} mode.

INTEL-1045
U.S. Patent 7,151,430

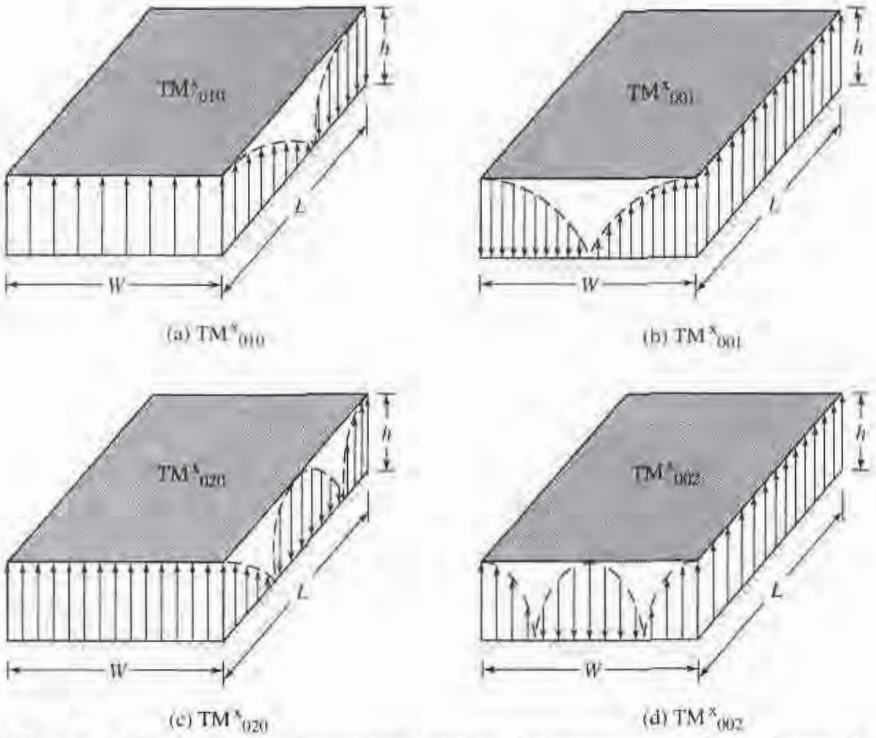


Figure 14.13 Field configurations (modes) for rectangular microstrip patch.

B. Equivalent Current Densities

It has been shown using the cavity model that the microstrip antenna can be modeled reasonably well by a dielectric-loaded cavity with two perfectly conducting electric walls (top and bottom), and four perfectly conducting magnetic walls (sidewalls). It is assumed that the material of the substrate is truncated and does not extend beyond the edges of the patch. The four sidewalls represent four narrow apertures (slots) through which radiation takes place. Using the Field Equivalence Principle (Huygens' Principle) of Section 12.2 of Chapter 12, the microstrip patch is represented by an equivalent electric current density $\mathbf{J}_t$ at the top surface of the patch to account for the presence of the patch (there is also a current density $\mathbf{J}_b$ at the bottom of the patch which is not needed for this model). The four side slots are represented by the equivalent electric current density $\mathbf{J}_s$ and equivalent magnetic current density $\mathbf{M}_s$, as shown in Figure 14.14(a), each represented by

$$\mathbf{J}_s = \hat{\mathbf{n}} \times \mathbf{H}_a \tag{14-36}$$

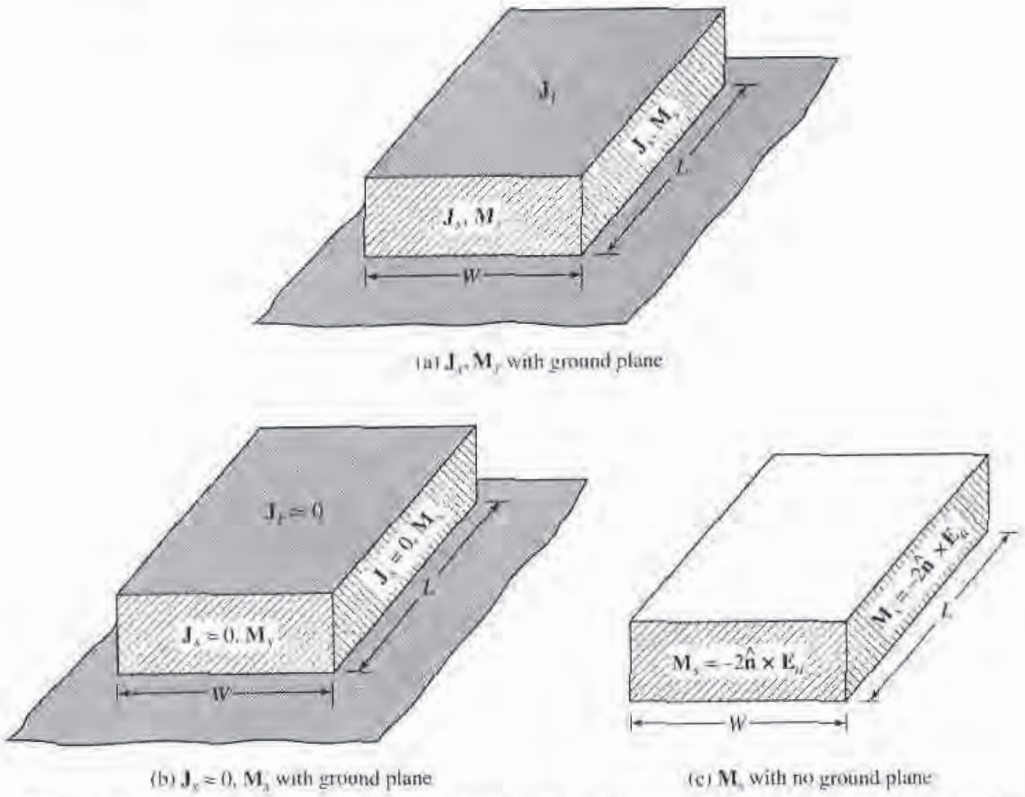
and

$$\mathbf{M}_s = -\hat{\mathbf{n}} \times \mathbf{E}_a \tag{14-37}$$

where $\mathbf{E}_a$ and $\mathbf{H}_a$ represent, respectively, the electric and magnetic fields at the slots.

Because it was shown that for microstrip antennas with very small height-to-width ratio the current density $\mathbf{J}_t$ at the top of the patch is much smaller than the current density $\mathbf{J}_b$ at the bottom of the patch, it will be assumed it is negligible here and it will be set to zero. Also it was argued that the tangential magnetic fields along the edges of the patch are very small, ideally zero. Therefore the corresponding equivalent electric current density $\mathbf{J}_s$ will be very small (ideally zero), and it will be

INTEL-1045
U.S. Patent 7,151,430



(a) $\mathbf{J}_s, \mathbf{M}_y$ with ground plane

(b) $\mathbf{J}_s = 0, \mathbf{M}_s$ with ground plane

(c) $\mathbf{M}_s$ with no ground plane

Figure 14.14 Equivalent current densities on four sides of rectangular microstrip patch.

set to zero here. Thus the only nonzero current density is the equivalent magnetic current density $\mathbf{M}_s$ of (14-37) along the side periphery of the cavity radiating in the presence of the ground plane, as shown in Figure 14.14(b). The presence of the ground plane can be taken into account by image theory which will double the equivalent magnetic current density of (14-37). Therefore the final equivalent is a magnetic current density of twice (14-37) or

$$\mathbf{M}_s = -2\hat{\mathbf{n}} \times \mathbf{E}_a \tag{14-38}$$

around the side periphery of the patch radiating into free space, as shown in Figure 14.14(c).

It was shown, using the transmission-line model, that the microstrip antenna can be represented by two radiating slots along the length of the patch (each of width W and height h). Similarly it will be shown here also that while there are a total of four slots representing the microstrip antenna, only two (the radiating slots) account for most of the radiation; the fields radiated by the other two, which are separated by the width W of the patch, cancel along the principal planes. Therefore the same two slots, separated by the length of the patch, are referred to here also as *radiating* slots. The slots are separated by a very low impedance parallel-plate transmission line of length L, which acts as a transformer. The length of the transmission line is approximately $\lambda/2$, where λ is the guide wavelength in the substrate, in order for the fields at the aperture of the two slots to have opposite polarization. This is illustrated in Figures 14.1(a) and 14.13(a). The two slots form a two-element array with a spacing of $\lambda/2$ between the elements. It will be shown here that in a direction perpendicular to the

INTEL-1045
U.S. Patent 7,151,430

ground plane the components of the field add in phase and give a maximum radiation normal to the patch: thus broadside antenna.

Assuming that the dominant mode within the cavity is the TM^x_{010} mode, the electric and magnetic field components reduce from (14-32) to

$$E_x = E_0 \cos\left(\frac{\pi}{L}y'\right)$$
$$H_z = H_0 \sin\left(\frac{\pi}{L}y'\right) \tag{14-39}$$
$$E_y = E_z = H_x = H_y = 0$$

where $E_0 = -j\omega A_{010}$ and $H_0 = (\pi/\mu L) A_{010}$. The electric field structure within the substrate and between the radiating element and the ground plane is sketched in Figures 14.1(a,b) and 14.13(a). It undergoes a phase reversal along the length but it is uniform along its width. The phase reversal along the length is necessary for the antenna to have broadside radiation characteristics.

Using the equivalence principle of Section 12.3, each slot radiates the same fields as a magnetic dipole with current density $\mathbf{M}_s$ equal to (14-38). By referring to Figures 14.15 the equivalent magnetic current densities along the two slots, each of width W and height h, are both of the same magnitude and of the same phase. Therefore these two slots form a two-element array with the sources (current densities) of the same magnitude and phase, and separated by L. Thus these two sources will add in a direction normal to the patch and ground plane forming a broadside pattern. This is illustrated in Figures 14.16(a) where the normalized radiation pattern of each slot in the principal E-plane is sketched individually along with the total pattern of the two. In the H-plane, the normalized pattern of each slot and of the two together is the same, as shown in Figure 14.16(b).

The equivalent current densities for the other two slots, each of length L and height h, are shown in Figure 14.17. Since the current densities on each wall are of the same magnitude but of opposite direction, the fields radiated by these two slots cancel each other in the principal H-plane. Also since corresponding slots on opposite walls are 180° out of phase, the corresponding radiations cancel each other in the principal E-plane. This will be shown analytically. The radiation from these two side walls in nonprincipal planes is small compared to the other two side walls. Therefore these two slots are usually referred to as *nonradiating* slots.

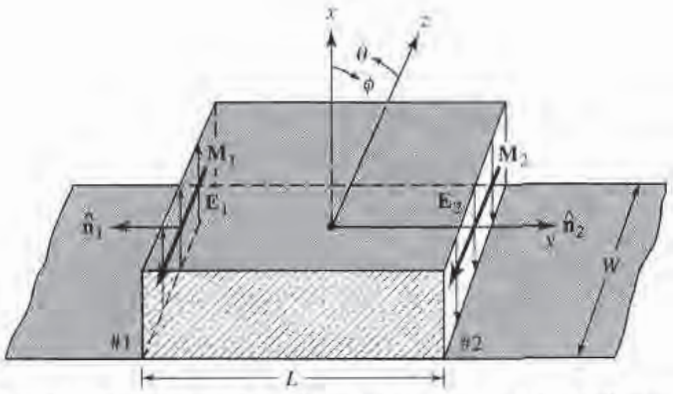
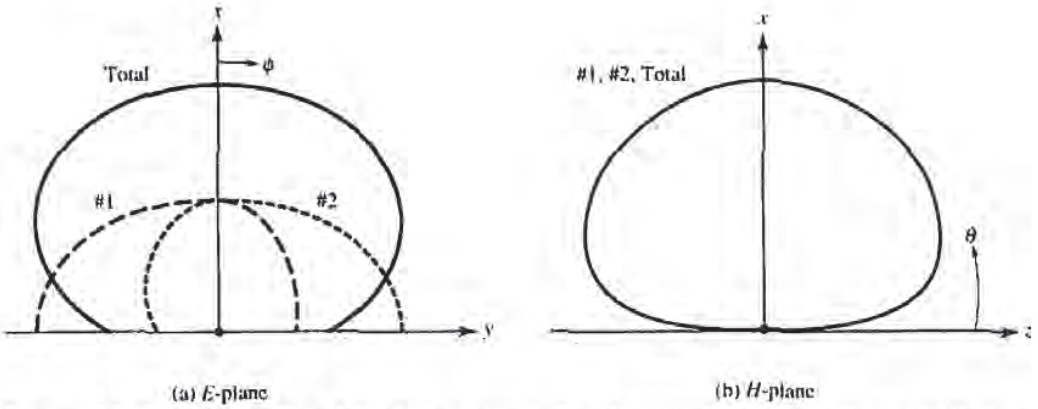


Figure 14.15 Rectangular microstrip patch radiating slots and equivalent magnetic current densities.

INTEL-1045
U.S. Patent 7,151,430



(a) E-plane (b) H-plane

Figure 14.16 Typical E- and H-plane patterns of each microstrip patch slot, and of the two together.

C. Fields Radiated—TM^{z}_{010} Mode

To find the fields radiated by each slot, we follow a procedure similar to that used to analyze the aperture in Section 12.5.1. The total field is the sum of the two-element array with each element representing one of the slots. Since the slots are identical, this is accomplished by using an array factor for the two slots.

Radiating Slots Following a procedure similar to that used to analyze the aperture in Section 12.5.1, the far-zone electric fields radiated by each slot, using the equivalent current densities of (14-38), are written as

$$E_r = E_\theta \simeq 0 \tag{14-40a}$$

$$E_\phi = +j\frac{k_0 hW E_0 e^{-jk_0 r}}{2\pi r}\left\{\sin\theta \frac{\sin(X)}{X}\frac{\sin(Z)}{Z}\right\} \tag{14-40b}$$

where

$$X = \frac{k_0 h}{2}\sin\theta\cos\phi \tag{14-40c}$$

$$Z = \frac{k_0 W}{2}\cos\theta \tag{14-40d}$$

For very small heights ($k_0 h \ll 1$), (14-40b) reduces to

$$E_\phi \simeq +j\frac{V_0 e^{-jk_0 r}}{\pi r}\left\{\sin\theta \frac{\sin\left(\frac{k_0 W}{2}\cos\theta\right)}{\cos\theta}\right\} \tag{14-41}$$

where $V_0 = hE_0$.

According to the theory of Chapter 6, the array factor for the two elements, of the same magnitude and phase, separated by a distance L_e along the y direction is

$$(AF)_y = 2\cos\left(\frac{k_0 L_e}{2}\sin\theta\sin\phi\right) \tag{14-42}$$

where L_e is the effective length of (14-3). Thus, the total electric field for the two slots (also for the microstrip antenna) is

INTEL-1045
U.S. Patent 7,151,430

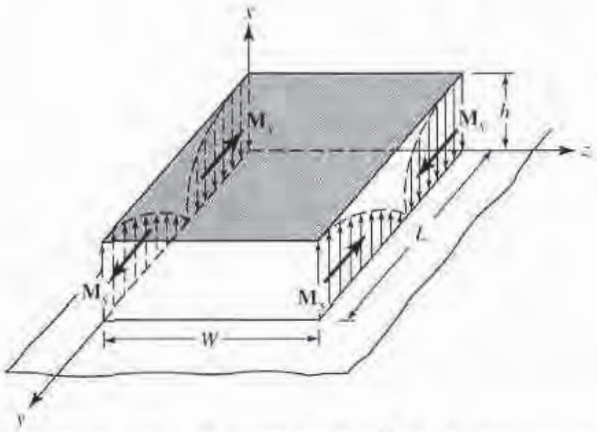


Figure 14.17 Current densities on nonradiating slots of rectangular microstrip patch.

$$E_\phi^I = +j\frac{k_0 hW\,E_0 e^{-jk_0 r}}{\pi r}\left\{\sin\theta\,\frac{\sin(X)}{X}\,\frac{\sin(Z)}{Z}\right\} \times \cos\left(\frac{k_0 L_e}{2}\sin\theta\sin\phi\right) \tag{14-43}$$

where

$$X = \frac{k_0 h}{2}\sin\theta\cos\phi \tag{14-43a}$$

$$Z = \frac{k_0 W}{2}\cos\theta \tag{14-43b}$$

For small values of h ($k_0 h \ll 1$), (14-43) reduces to

$$E_\phi^I \simeq +j\frac{2V_0 e^{-jk_0 r}}{\pi r}\left\{\sin\theta\,\frac{\sin\left(\frac{k_0 W}{2}\cos\theta\right)}{\cos\theta}\right\}\cos\left(\frac{k_0 L_e}{2}\sin\theta\sin\phi\right) \tag{14-44}$$

where $V_0 = hE_0$ is the voltage across the slot.

***E*-Plane ($\theta = 90°$, $0° \le \phi \le 90°$ and $270° \le \phi \le 360°$)**

For the microstrip antenna, the x-y plane ($\theta = 90°$, $0° \le \phi \le 90°$ and $270° \le \phi \le 360°$) is the principal E-plane. For this plane, the expressions for the radiated fields of (14-43)–(14-43b) reduce to

$$E_\phi^I = +j\frac{k_0 WV_0 e^{-jk_0 r}}{\pi r}\left\{\frac{\sin\left(\frac{k_0 h}{2}\cos\phi\right)}{\frac{k_0 h}{2}\cos\phi}\right\}\cos\left(\frac{k_0 L_e}{2}\sin\phi\right) \tag{14-45}$$

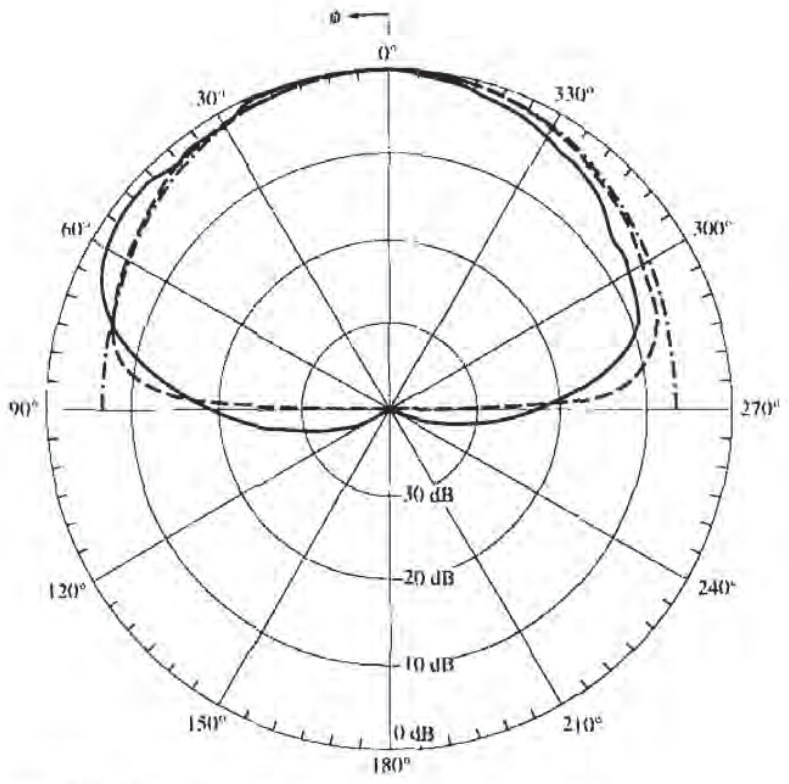
***H*-Plane ($\phi = 0°$, $0° \le \theta \le 180°$)**

The principal H-plane of the microstrip antenna is the x-z plane ($\phi = 0°$, $0° \le \theta \le 180°$), and the expressions for the fields radiated of (14-43)–(14-43b) reduce to

INTEL-1045
U.S. Patent 7,151,430

$$E_\phi^I \simeq +j\frac{k_0 W V_0 e^{-jk_0 r}}{\pi r}\left\{\sin\theta \frac{\sin\left(\frac{k_0 h}{2}\sin\theta\right)}{\frac{k_0 h}{2}\sin\theta}\frac{\sin\left(\frac{k_0 W}{2}\cos\theta\right)}{\frac{k_0 W}{2}\cos\theta}\right\} \quad (14\text{-}46)$$

To illustrate the modeling of the microstrip using the cavity model, the principal E- and H-plane patterns have been computed at $f_0 = 10$ GHz for the rectangular microstrip of Example 14.1 with $\epsilon_r = 2.2$, $h = 0.1588$ cm, $L = 0.906$ cm and $L_e = 1.068$ cm. These are displayed in Figure 14.18(a) for the E-plane and Figure 14.18(b) for the H-plane where they are compared with measurements. A good agreement is indicated. However there are some differences in the E-plane primarily near grazing and in the region below the ground plane. The differences near grazing in the E-plane are primarily because the theory assumes the dielectric material of the substrate is truncated and does not cover the ground plane beyond the edges of the patch while those in the back region are because the theory assumes an infinite ground plane. The shape of the H-plane patterns are not affected significantly by the dielectric cover or the edges. Edge effects can be taken into account using diffraction theory [48], [79].



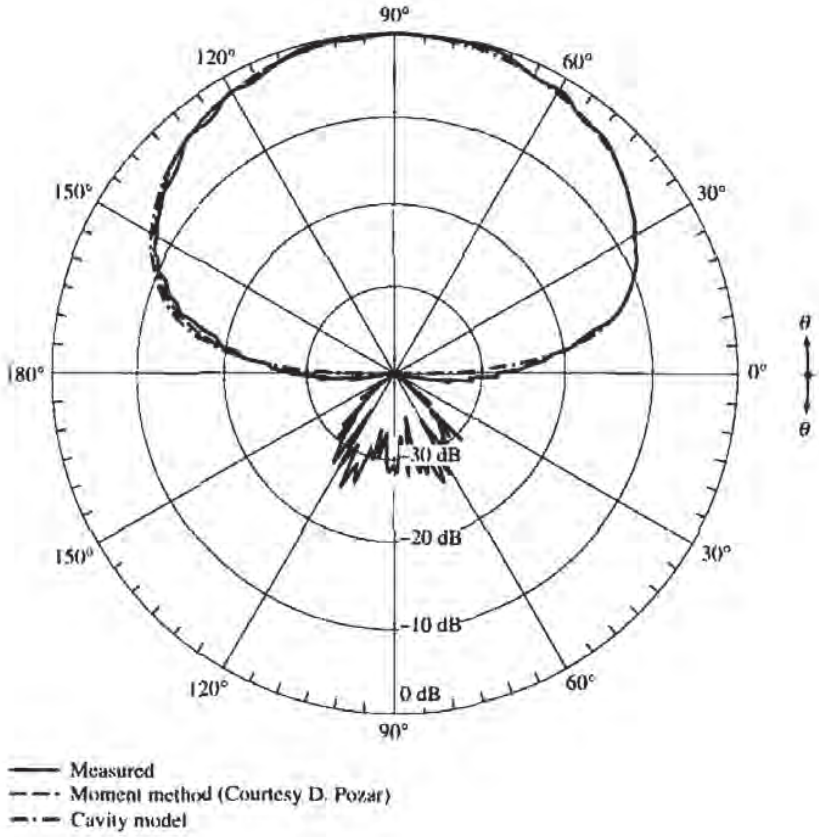
(a) E-plane ($\theta = 90°$)

Figure 14.18 Predicted and measured E- and H-plane patterns of rectangular microstrip patch ($L = 0.906$ cm, $W = 1.186$ cm, $h = 0.1588$ cm, $y_0 = 0.3126$ cm, $\epsilon_r = 2.2$, $f_0 = 10$ GHz).

INTEL-1045
U.S. Patent 7,151,430

The noted asymmetry in the measured and Moment Method computed patterns is due to the feed which is not symmetrically positioned along the E-plane. The Moment Method analysis accounts for the position of the feed, while the cavity model does not account for it. The pattern for $0° \leq \phi \leq 180°$ [left half in Figure 14.18(a)] corresponds to observation angles which lie on the same side of the patch as does the feed probe.

The presence of the dielectric-covered ground plane modifies the reflection coefficient, which influences the magnitude and phase of the image. This is similar to the ground effects discussed in Section 4.8 of Chapter 4. To account for the dielectric, the reflection coefficient for vertical polarization of $+1$ must be replaced by the reflection coefficient of (4-125) while the reflection coefficient for horizontal polarization of -1 must be replaced by the reflection coefficient of (4-129). Basically the introduction of the reflection coefficients of (4-125) and (4-129) to account for the dielectric cover of the ground plane is to modify the boundary conditions of the perfect conductor to one with an impedance surface. The result is for (4-125) to modify the shape of the pattern in the E-plane of the microstrip antenna, primarily for observation angles near grazing (near the ground plane), as was done in Figure 4.28 for the lossy earth. Similar changes are expected for the microstrip antenna. The changes in the pattern near grazing come from the fact that for the perfect conductor the reflection coefficient for vertical polarization is $+1$ for all observation angles.



(b) H-plane ($\phi = 0°$)

Figure 14.18 (Continued)

INTEL-1045
U.S. Patent 7,151,430

However for the dielectric-covered ground plane (impedance surface), the reflection coefficient of (4-129) is nearly $+1$ for observation angles far away from grazing but begins to change very rapidly near grazing and becomes -1 at grazing [79]; thus the formation of an ideal null at grazing.

Similarly the reflection coefficient of (4-129) should basically control the pattern primarily in the H-plane. However, because the reflection coefficient for horizontal polarization for a perfect conductor is -1 for all observation angles while that of (4-129) for the dielectric covered ground plane is nearly -1 for all observation angles, the shape of the pattern in the H-plane is basically unaltered by the presence of the dielectric cover [79]. This is illustrated in Figure 4.30 for the earth. The pattern also exhibits a null along the ground plane. Similar changes are expected for the microstrip antenna.

Nonradiating Slots The fields radiated by the so-called nonradiating slots, each of effective length L_e and height h, are found using the same procedure as for the two radiating slots. Using the fields of (14-39), the equivalent magnetic current density of one of the nonradiating slots facing the $+z$ axis is

$$\mathbf{M}_s = -2\hat{\mathbf{n}} \times \mathbf{E}_a = \hat{\mathbf{a}}_y 2E_0 \cos\left(\frac{\pi}{L_e}y'\right) \tag{14-47}$$

and it is sketched in Figure 14.17. A similar one is facing the $-z$ axis. Using the same procedure as for the radiating slots, the normalized far-zone electric field components radiated by each slot are given by

$$E_\theta = -\frac{k_0 h L_e E_0 e^{-jk_0 r}}{2\pi r}\left\{Y\cos\phi\frac{\sin X}{X}\frac{\cos Y}{(Y)^2-(\pi/2)^2}\right\}e^{j(X+Y)} \tag{14-48a}$$

$$E_\phi = \frac{k_0 h L_e E_0 e^{-jk_0 r}}{2\pi r}\left\{Y\cos\theta\sin\phi\frac{\sin X}{X}\frac{\cos Y}{(Y)^2-(\pi/2)^2}\right\}e^{j(X+Y)} \tag{14-48b}$$

where

$$X = \frac{k_0 h}{2}\sin\theta\cos\phi \tag{14-48c}$$

$$Y = \frac{k_0 L_e}{2}\sin\theta\sin\phi \tag{14-48d}$$

Since the two nonradiating slots form an array of two elements, of the same magnitude but of opposite phase, separated along the z axis by a distance W, the array factor is

$$(AF)_z = 2j\sin\left(\frac{k_0 W}{2}\cos\theta\right) \tag{14-49}$$

Therefore the total far-zone electric field is given by the product of each of (14-48a) and (14-48b) with the array factor of (14-49).

In the H-plane ($\phi = 0°$, $0° \le \theta \le 180°$), (14-48a) and (14-48b) are zero because the fields radiated by each quarter cycle of each slot are cancelled by the fields radiated by the other quarter. Similarly in the E-plane ($\theta = 90°$, $0° \le \phi \le 90°$ and $270° \le \phi \le 360°$) the total fields are also zero because (14-49) vanishes. This implies that the fields radiated by each slot are cancelled by the fields radiated by the other. The nonradiation in the principal planes by these two slots was discussed earlier and demonstrated by the current densities in Figure 14.17. However, these two slots do radiate away from the principal planes, but their field intensity in these other planes

INTEL-1045
U.S. Patent 7,151,430

is small compared to that radiated by the two radiating slots such that it is usually neglected. Therefore they are referred to as *nonradiating* slots.

14.2.3 Directivity

As for every other antenna, the directivity is one of the most important figures-of-merit whose definition is given by (2-16a) or

$$D_0 = \frac{U_{\max}}{U_0} = \frac{4\pi U_{\max}}{P_{\text{rad}}} \tag{14-50}$$

Single Slot ($k_0 h \ll 1$) Using the electric field of (14-41), the maximum radiation intensity and radiated power can be written, respectively, as

$$U_{\max} = \frac{|V_0|^2}{2\eta_0 \pi^2}\left(\frac{\pi W}{\lambda_0}\right)^2 \tag{14-51}$$

$$P_{\text{rad}} = \frac{|V_0|^2}{2\eta_0 \pi}\int_0^{\pi}\left[\frac{\sin\left(\frac{k_0 W}{2}\cos\theta\right)}{\cos\theta}\right]^2 \sin^3\theta\, d\theta \tag{14-52}$$

Therefore, the directivity of a single slot can be expressed as

$$D_0 = \left(\frac{2\pi W}{\lambda_0}\right)^2 \frac{1}{I_1} \tag{14-53}$$

where

$$I_1 = \int_0^{\pi}\left[\frac{\sin\left(\frac{k_0 W}{2}\cos\theta\right)}{\cos\theta}\right]^2 \sin^3\theta\, d\theta$$

$$= \left[-2 + \cos(X) + XS_i(X) + \frac{\sin(X)}{X}\right] \tag{14-53a}$$

$$X = k_0 W \tag{14-53b}$$

Asymptotically the values of (14-53) vary as

$$D_0 = \begin{cases} 3.3 \text{ (dimensionless)} = 5.2 \text{ dB} & W \ll \lambda_0 \\ 4\left(\dfrac{W}{\lambda_0}\right) & W \gg \lambda_0 \end{cases} \tag{14-54}$$

The directivity of a single slot can be computed using (14-53) and (14-53a). In addition, it can also be computed using (14-41) and the computer program DIRECTIVITY at the end of Chapter 2. Since both are based on the same formulas, they should give the same results. Plots of the directivity of a single slot for $h = 0.01\lambda_0$ and $0.05\lambda_0$ as a function of the width of the slot are shown in Figure 14.19. It is evident that the directivity of a single slot is not influenced strongly by the height of the substrate, as long as it is maintained electrically small.

Two Slots ($k_0 h \ll 1$) For two slots, using (14-44), the directivity can be written as

$$D_2 = \left(\frac{2\pi W}{\lambda_0}\right)^2 \frac{\pi}{I_2} = \frac{2}{15 G_{\text{rad}}}\left(\frac{W}{\lambda_0}\right)^2 \tag{14-55}$$

INTEL-1045
U.S. Patent 7,151,430

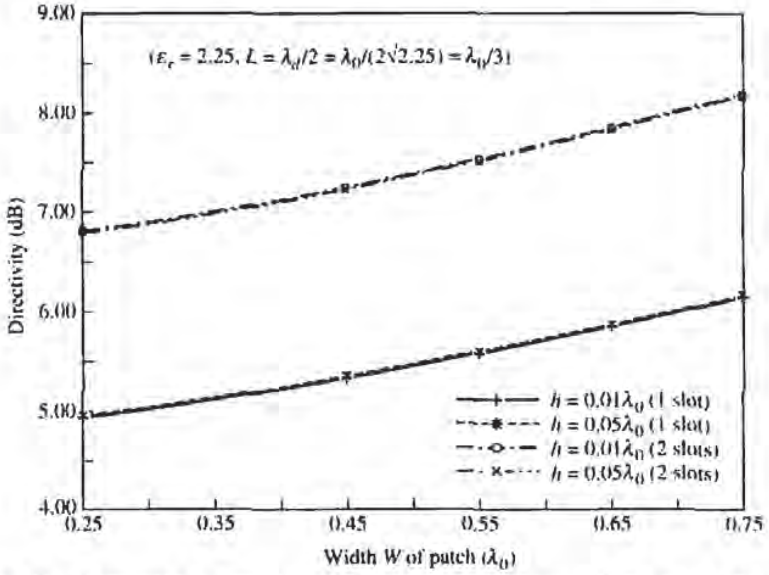


Figure 14.19 Computed directivity of one and two slots as a function of the slot width.

where G_{rad} is the radiation conductance and

$$I_2 = \int_0^{\pi}\int_0^{\pi}\left[\frac{\sin\left(\frac{k_0 W}{2}\cos\theta\right)}{\cos\theta}\right]^2 \sin^3\theta\cos^2\left(\frac{k_0 L_e}{2}\sin\theta\sin\phi\right)d\theta\,d\phi \qquad (14\text{-}55a)$$

The total broadside directivity D_2 for the two radiating slots, separated by the dominant TM^x_{010} mode field (antisymmetric voltage distribution), can also be written as [8], [82]

$$D_2 = D_0 D_{AF} = D_0\frac{2}{1+g_{12}} \qquad (14\text{-}56)$$

$$D_{AF} = \frac{2}{1+g_{12}} \overset{g_{12}\ll 1}{\simeq} 2 \qquad (14\text{-}56a)$$

where

D_0 = directivity of single slot [as given by (14-53) and (14-53a)]

D_{AF} = directivity of array factor AF

$$\left[AF = \cos\left(\frac{k_0 L_e}{2}\sin\theta\sin\phi\right)\right]$$

g_{12} = normalized mutual conductance = G_{12}/G_1

This can also be justified using the array theory of Chapter 6. The normalized mutual conductance g_{12} can be obtained using (14-12), (14-12a), and (14-18a). Computed values based on (14-18a) show that usually $g_{12} \ll 1$; thus (14-56a) is usually a good approximation to (14-56).

INTEL-1045
U.S. Patent 7,151,430

Asymptotically the directivity of two slots (microstrip antenna) can be expressed as

$$D_2 = \begin{cases} 6.6 \text{ (dimensionless)} = 8.2 \text{ dB} & W \ll \lambda_0 \\ 8\left(\dfrac{W}{\lambda_0}\right) & W \gg \lambda_0 \end{cases} \tag{14-57}$$

The directivity of the microstrip antenna can now be computed using (14-55) and (14-55a). In addition, it can also be computed using (14-44) and the computer program DIRECTIVITY at the end of Chapter 2. Since they are based on the same formulas, they should give the same results. Plots of directivity of a microstrip antenna, modeled by two slots, for $h = 0.01\lambda_0$ and $0.05\lambda_0$ are shown plotted as a function of the width of the patch (W/λ_0) in Figure 14.19. It is evident that the directivity is not a strong function of the height, as long as the height is maintained electrically small. A typical plot of the directivity of a patch for a fixed resonant frequency as a function of the substrate height (h/λ_0), for two different dielectrics, is shown in Figure 14.20.

The directivity of the slots also can be approximated by Kraus's, (2-26), and Tai & Pereira's, (2-30a), formulas in terms of the E- and H-plane beamwidths, which can be approximated by [36]

$$\Theta_E \simeq 2\cos^{-1}\sqrt{\frac{7.03\lambda_0^2}{4(3L_e^2 + h^2)\pi^2}} \tag{14-58}$$

$$\Theta_H \simeq 2\cos^{-1}\sqrt{\frac{1}{2 + k_0 W}} \tag{14-59}$$

The values of the directivities obtained using (14-58) and (14-59) along with either (2-26) or (2-30a) will not be very accurate since the beamwidths, especially in the E-plane, are very large. However, they can serve as guidelines.

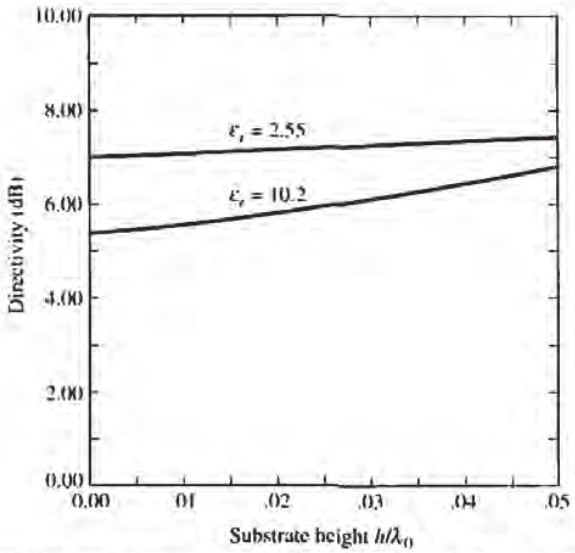


Figure 14.20 Directivity variations as a function of substrate height for a square microstrip patch antenna. (Courtesy of D. M. Pozar)

INTEL-1045
U.S. Patent 7,151,430

Example 14.3

For the rectangular microstrip antenna of Examples 14.1 and 14.2, with overall dimensions of $L = 0.906$ cm and $W = 1.186$ cm, substrate height $h = 0.1588$ cm, and dielectric constant of $\epsilon_r = 2.2$, center frequency of 10 GHz, find the directivity based on (14-56) and (14-56a). Compare with the values obtained using (14-55) and (14-55a).

SOLUTION

From the solution of Example 14.2

$$G_1 = 0.00157 \text{ Siemens}$$

$$G_{12} = 6.1683 \times 10^{-4} \text{ Siemens}$$

$$g_{12} = G_{12}/G_1 = 0.3921$$

Using (14-56a)

$$D_{AF} = \frac{2}{1 + g_{12}} = \frac{2}{1 + 0.3921} = 1.4367 = 1.5736 \text{ dB}$$

Using (14-53) and (14-53a)

$$I_1 = 1.863$$

$$D_0 = \left(\frac{2\pi W}{\lambda_0}\right)^2 \frac{1}{I_1} = 3.312 = 5.201 \text{ dB}$$

According to (14-56)

$$D_2 = D_0 D_{AF} = 3.312(1.4367) = 4.7584 = 6.7746 \text{ dB}$$

Using (14-55a)

$$I_2 = 3.59801$$

Finally, using (14-55)

$$D_2 = \left(\frac{2\pi W}{\lambda_0}\right)^2 \frac{\pi}{I_2} = 5.3873 = 7.314 \text{ dB}$$

14.3 CIRCULAR PATCH

Other than the rectangular patch, the next most popular configuration is the circular patch or disk, as shown in Figure 14.21. It also has received a lot of attention not only as a single element [6], [10], [13], [46], [47], [51], but also in arrays [65] and [74]. The modes supported by the circular patch antenna can be found by treating the patch, ground plane, and the material between the two as a circular cavity. As with the rectangular patch, the modes that are supported primarily by a circular microstrip antenna whose substrate height is small ($h \ll \lambda$) are TM^z where z is taken perpendicular to the patch. As far as the dimensions of the patch, there are two degrees of freedom to control (length and width) for the rectangular microstrip antenna. Therefore the order of the modes can be changed by changing the relative dimensions of the width and length of the patch (width-to-length ratio). However, for the circular patch

INTEL-1045
U.S. Patent 7,151,430

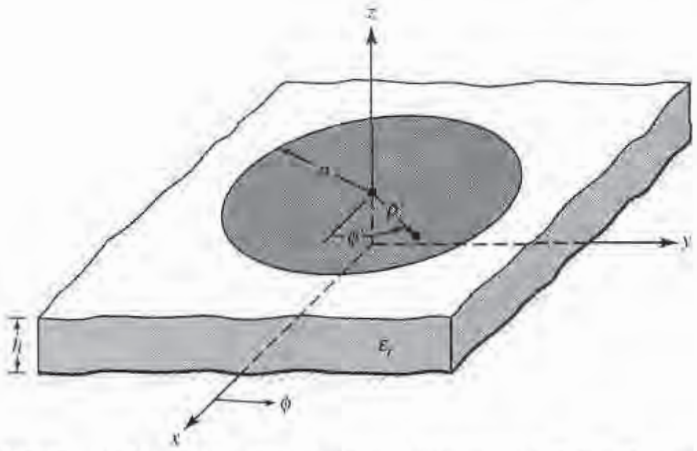


Figure 14.21 Geometry of circular microstrip patch antenna.

there is only one degree of freedom to control (radius of the patch). Doing this does not change the order of the modes; however, it does change the absolute value of the resonant frequency of each [79].

Other than using full-wave analysis [51], [65], [74], the circular patch antenna can only be analyzed conveniently using the cavity model [10], [46], [47]. This can be accomplished using a procedure similar to that for the rectangular patch but now using cylindrical coordinates [79]. The cavity is composed of two perfect electric conductors at the top and bottom to represent the patch and the ground plane, and by a cylindrical perfect magnetic conductor around the circular periphery of the cavity. The dielectric material of the substrate is assumed to be truncated beyond the extent of the patch.

14.3.1 Electric and Magnetic Fields—TM^z_{mnp}

To find the fields within the cavity, we use the vector potential approach. For TM^z we need to first find the magnetic vector potential A_z, which must satisfy, in cylindrical coordinates, the homogeneous wave equation of

$$\nabla^2 A_z(\rho, \phi, z) + k^2 A_z(\rho, \phi, z) = 0. \tag{14-60}$$

It can be shown that for TM^z modes, whose electric and magnetic fields are related to the vector potential A_z by [79]

$$\begin{aligned} E_\rho &= -j\frac{1}{\omega\mu\epsilon}\frac{\partial^2 A_z}{\partial\rho\partial z} & H_\rho &= \frac{1}{\mu}\frac{1}{\rho}\frac{\partial A_z}{\partial\phi} \\ E_\phi &= -j\frac{1}{\omega\mu\epsilon}\frac{1}{\rho}\frac{\partial^2 A_z}{\partial\phi\partial z} & H_\phi &= -\frac{1}{\mu}\frac{\partial A_z}{\partial\rho} \\ E_z &= -j\frac{1}{\omega\mu\epsilon}\left(\frac{\partial^2}{\partial z^2}+k^2\right)A_z & H_z &= 0 \end{aligned} \tag{14-61}$$

subject to the boundary conditions of

$$\begin{aligned} E_\rho(0 \le \rho' \le a, 0 \le \phi' \le 2\pi, z' = 0) &= 0 \\ E_\rho(0 \le \rho' \le a, 0 \le \phi' \le 2\pi, z' = h) &= 0 \\ H_\phi(\rho' = a, 0 \le \phi' \le 2\pi, 0 \le z' \le h) &= 0 \end{aligned} \tag{14-62}$$

INTEL-1045
U.S. Patent 7,151,430

the magnetic vector potential A_z reduces to [79]

$$A_z = B_{mnp} J_m(k_\rho \rho')[A_2 \cos(m\phi') + B_2 \sin(m\phi')] \cos(k_z z') \tag{14-63}$$

with the constraint equation of

$$(k_\rho)^2 + (k_z)^2 = k_r^2 = \omega_r^2 \mu\epsilon \tag{14-63a}$$

The primed cylindrical coordinates ρ', ϕ', z' are used to represent the fields within the cavity while $J_m(x)$ is the Bessel function of the first kind of order m, and

$$k_\rho = \chi'_{mn}/a \tag{14-63b}$$

$$k_z = \frac{p\pi}{h} \tag{14-63c}$$

$$m = 0, 1, 2, \ldots \tag{14-63d}$$

$$n = 1, 2, 3, \ldots \tag{14-63e}$$

$$p = 0, 1, 2, \ldots \tag{14-63f}$$

In (14-63b) χ'_{mn} represents the zeroes of the derivative of the Bessel function $J_m(x)$, and they determine the order of the resonant frequencies. The first four values of χ'_{mn}, in ascending order, are

$$\begin{aligned} \chi'_{11} &= 1.8412 \\ \chi'_{21} &= 3.0542 \\ \chi'_{01} &= 3.8318 \\ \chi'_{31} &= 4.2012 \end{aligned} \tag{14-64}$$

14.3.2 Resonant Frequencies

The resonant frequencies of the cavity, and thus of the microstrip antenna, are found using (14-63a)–(14-63f). Since for most typical microstrip antennas the substrate height h is very small (typically $h < 0.05\lambda_0$), the fields along z are essentially constant and are presented in (14-63f) by $p = 0$ and in (14-63c) by $k_z = 0$. Therefore the resonant frequencies for the TM^z_{mn0} modes can be written using (14-63a) as

$$(f_r)_{mn0} = \frac{1}{2\pi\sqrt{\mu\epsilon}} \left(\frac{\chi'_{mn}}{a}\right) \tag{14-65}$$

Based on the values of (14-64), the first four modes, in ascending order, are TM^z_{110}, TM^z_{210}, TM^z_{010}, and TM^z_{310}. The dominant mode is the TM^z_{110} whose resonant frequency is

$$(f_r)_{110} = \frac{1.8412}{2\pi a\sqrt{\mu\epsilon}} = \frac{1.8412 v_0}{2\pi a\sqrt{\epsilon_r}} \tag{14-66}$$

where v_0 is the speed of light in free space.

The resonant frequency of (14-66) does not take into account fringing. As was shown for the rectangular patch, and illustrated in Figure 14.7, fringing makes the patch look electrically larger and it was taken into account by introducing a length correction factor given by (14-2). Similarly for the circular patch a correction is

INTEL-1045
U.S. Patent 7,151,430

introduced by using an effective radius a_e, to replace the actual radius a, given by [6]

$$a_e = a\left\{1 + \frac{2h}{\pi a \epsilon_r}\left[\ln\left(\frac{\pi a}{2h}\right) + 1.7726\right]\right\}^{1/2} \tag{14-67}$$

Therefore the resonant frequency of (14-66) for the dominant TM_{110}^z should be modified by using (14-67) and expressed as

$$(f_r)_{110} = \frac{1.8412 v_0}{2\pi a_e \sqrt{\epsilon_r}} \tag{14-68}$$

14.3.3 Design

Based on the cavity model formulation, a design procedure is outlined which leads to practical designs of circular microstrip antennas for the dominant TM_{110}^z mode. The procedure assumes that the specified information includes the dielectric constant of the substrate (ϵ_r), the resonant frequency (f_r) and the height of the substrate h. The procedure is as follows:

Specify

$$\epsilon_r, f_r \text{(in Hz)}, \text{ and } h \text{ (in cm)}$$

Determine The actual radius a of the patch.

Design Procedure A first-order approximation to the solution of (14-67) for a is to find a_e using (14-68) and to substitute that into (14-67) for a_e and for a in the logarithmic function. Doing this leads to

$$a = \frac{F}{\left\{1 + \frac{2h}{\pi \epsilon_r F}\left[\ln\left(\frac{\pi F}{2h}\right) + 1.7726\right]\right\}^{1/2}} \tag{14-69}$$

where

$$F = \frac{8.791 \times 10^9}{f_r \sqrt{\epsilon_r}} \tag{14-69a}$$

Remember that h *in (14-69) must be in cm.*

Example 14.4

Design a circular microstrip antenna using a substrate (RT/duroid 5880) with a dielectric constant of 2.2, $h = 0.1588$ cm (0.0625 in.) so as to resonate at 10 GHz.

SOLUTION

Using (14-69a)

$$F = \frac{8.791 \times 10^9}{10 \times 10^9 \sqrt{2.2}} = 0.593$$

INTEL-1045
U.S. Patent 7,151,430

Therefore using (14-69)

$$a = \frac{F}{\left\{1 + \dfrac{2h}{\pi\epsilon_r F}\left[\ln\left(\dfrac{\pi F}{2h}\right) + 1.7726\right]\right\}^{1/2}} = 0.525 \text{ cm } (0.207 \text{ in.})$$

14.3.4 Equivalent Current Densities and Fields Radiated

As was done for the rectangular patch using the cavity model, the fields radiated by the circular patch can be found by using the Equivalence Principle whereby the circumferential wall of the cavity is replaced by an equivalent magnetic current density of (14-38) as shown in Figure 14.22. Based on (14-61)–(14-63) and assuming a TM^z_{110} mode field distribution beneath the patch, the normalized electric and magnetic fields within the cavity for the cosine azimuthal variations can be written as

$$E_\rho = E_\phi = H_z = 0 \tag{14-70a}$$

$$E_z = E_0 J_1(k\rho') \cos\phi' \tag{14-70b}$$

$$H_\rho = j\frac{E_0}{\omega\mu_0}\frac{1}{\rho} J_1(k\rho') \sin\phi' \tag{14-70c}$$

$$H_\phi = j\frac{E_0}{\omega\mu_0} J_1'(k\rho') \cos\phi' \tag{14-70d}$$

where $' = \partial/\partial\rho$ and ϕ' is the azimuthal angle along the perimeter of the patch.

Based on (14-70b) evaluated at the electrical equivalent edge of the disk ($\rho' = a_e$), the magnetic current density of (14-38) can be written as

$$\mathbf{M}_s = -2\hat{\mathbf{n}} \times \mathbf{E}_a|_{\rho'=a_e} = \hat{\mathbf{a}}_\phi 2E_0 J_1(ka_e) \cos\phi' \tag{14-71}$$

Since the height of the substrate is very small and the current density of (14-71) is uniform along the z direction, we can approximate (14-71) by a filamentary magnetic current of

$$\mathbf{I}_m = h\mathbf{M}_s = \hat{\mathbf{a}}_\phi 2hE_0 J_1(ka_e) \cos\phi' = \hat{\mathbf{a}}_\phi 2V_0 \cos\phi' \tag{14-71a}$$

where $V_0 = hE_0 J_1(ka_e)$ at $\phi' = 0$.

Using (14-71a) the microstrip antenna can be treated as a circular loop. Referring to Chapter 5 for the loop and using the radiation equations of Sections 12.3 and 12.6, we can write that [10], [83]

$$E_r = 0 \tag{14-72a}$$

$$E_\theta = -j\frac{k_0 a_e V_0 e^{-jk_0 r}}{2r}\{\cos\phi J_{02}'\} \tag{14-72b}$$

$$E_\phi = j\frac{k_0 a_e V_0 e^{-jk_0 r}}{2r}\{\cos\theta \sin\phi J_{02}\} \tag{14-72c}$$

$$J_{02}' = J_0(k_0 a_e \sin\theta) - J_2(k_0 a_e \sin\theta) \tag{14-72d}$$

$$J_{02} = J_0(k_0 a_e \sin\theta) + J_2(k_0 a_e \sin\theta) \tag{14-72e}$$

INTEL-1045
U.S. Patent 7,151,430

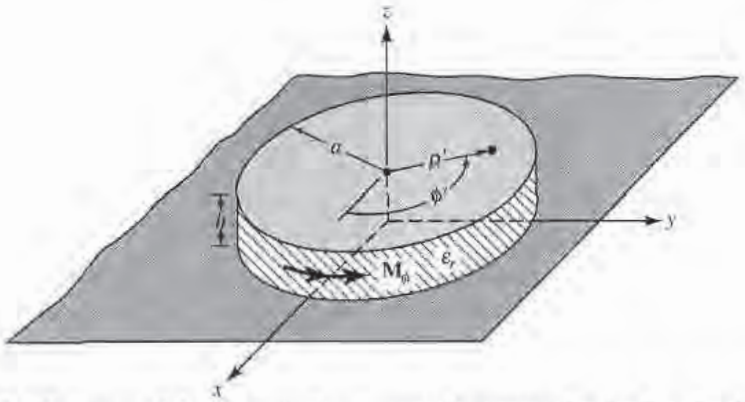


Figure 14.22 Cavity model and equivalent magnetic current density for circular microstrip patch antenna.

where a_e is the effective radius as given by (14-67). The fields in the principal planes reduce to:

E-plane ($\phi = 0°, 180°, 0° \leq \theta \leq 90°$)

$$E_\theta = j\frac{k_0 a_e V_0 e^{-jk_0 r}}{2r}[J'_{02}] \tag{14-73a}$$

$$E_\phi = 0 \tag{14-73b}$$

H-plane ($\phi = 90°, 270°, 0° \leq \theta \leq 90°$)

$$E_\theta = 0 \tag{14-74a}$$

$$E_\phi = j\frac{k_0 a_e V_0 e^{-jk_0 r}}{2r}[\cos\theta\, J_{02}] \tag{14-74b}$$

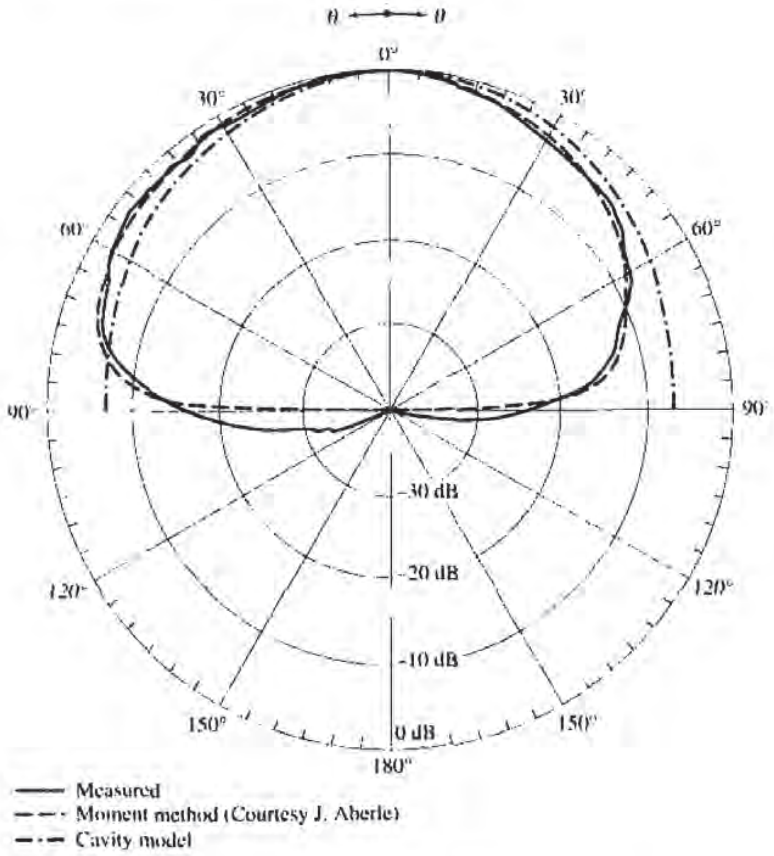
Patterns have been computed for the circular patch of Example 14.4 based on (14-73a)–(14-74b), and they are shown in Figure 14.23 where they are compared with measurements and Moment Method computed patterns. The noted asymmetry in the measured and Moment Method computed patterns is due to the feed which is not symmetrically positioned along the E-plane. The Moment Method analysis accounts for the position of the feed, while the cavity model does not account for it. The pattern for the left half of Figure 14.23(a) corresponds to observation angles which lie on the same side of the patch as does the feed probe.

14.3.5 Conductance and Directivity

The conductance due to the radiated power and directivity of the circular microstrip patch antenna can be computed using their respective definitions of (14-10) and (14-50). For each we need the radiated power, which based on the fields of (14-72b) and (14-72c) of the cavity model can be expressed as

$$P_{\text{rad}} = |V_0|^2 \frac{(k_0 a_e)^2}{960}\int_0^{\pi/2}[J'^2_{02} + \cos^2\theta\, J^2_{02}]\sin\theta\, d\theta \tag{14-75}$$

INTEL-1045
U.S. Patent 7,151,430



(a) E-plane ($\phi = 0°, 180°$)

Figure 14.23 Measured and computed (based on moment method and cavity models) E- and H-plane patterns of circular microstrip patch antenna ($a = 0.525$ cm, $a_e = 0.598$ cm, $\rho_i = 0.1$ cm, $\epsilon_r = 2.2$, $h = 0.1588$ cm, $f_0 = 10$ GHz, $\lambda_0 = 3$ cm).

Therefore the conductance across the gap between the patch and the ground plane at $\phi' = 0°$ based on (14-10) and (14-75) can be written as

$$G_{\text{rad}} = \frac{(k_0 a_e)^2}{480} \int_0^{\pi/2} [J_{02}'^2 + \cos^2\theta J_{02}^2] \sin\theta \, d\theta \tag{14-76}$$

A plot of the conductance of (14-76) for the TM_{110}^z mode is shown in Figure 14.24. While the conductance of (14-76) accounts for the losses due to radiation, it does not take into account losses due to conduction (ohmic) and dielectric losses, which each can be expressed as [10]

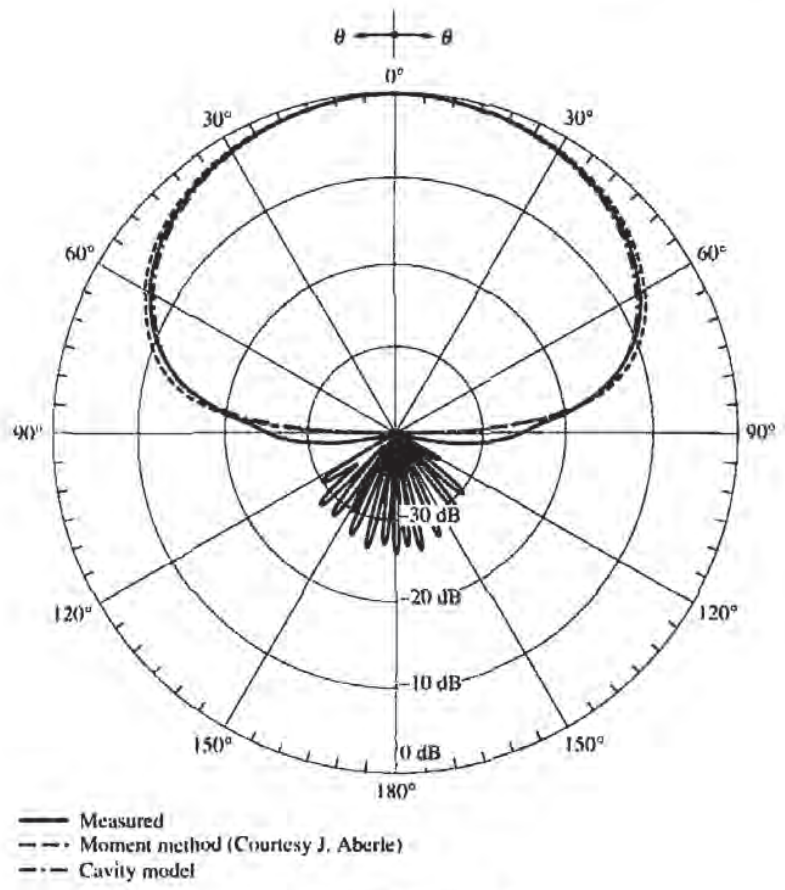
$$G_c = \frac{\epsilon_{m0}\pi(\pi\mu_0 f_r)^{-3/2}}{4h^2\sqrt{\sigma}}[(ka_e)^2 - m^2] \tag{14-77}$$

$$G_d = \frac{\epsilon_{m0}\tan\delta}{4\mu_0 h f_r}[(ka_e)^2 - m^2] \tag{14-78}$$

where $\epsilon_{m0} = 2$ for $m = 0$, $\epsilon_{m0} = 1$ for $m \neq 0$, and f_r represents the resonant frequency of the $mn0$ mode. Thus, the total conductance can be written as

$$G_t = G_{\text{rad}} + G_c + G_d \tag{14-79}$$

INTEL-1045
U.S. Patent 7,151,430



(a) H-plane ($\phi = 90°, 270°$)

Figure 14.23 (continued)

Based on (14-50), (14-72b), (14-72c), (14-75) and (14-76), the directivity for the slot at $\theta = 0°$ can be expressed as

$$D_0 = \frac{(k_0 a_e)^2}{120 G_{\text{rad}}} \tag{14-80}$$

A plot of the directivity of the dominant TM_{10}^{z} mode as a function of the radius of the disk is shown plotted in Figure 14.25. For very small values of the radius the directivity approaches 3 (4.8 dB), which is equivalent of that of a slot above a ground plane and it agrees with the value of (14-54) for $W \ll \lambda_0$.

14.3.6 Resonant Input Resistance

As was the case for the rectangular patch antenna, the input impedance of a circular patch at resonance is real. The input power is independent of the feed point position along the circumference. Taken the reference of the feed at $\phi' = 0°$, the input resistance at any radial distance $\rho' = \rho_0$ from the center of the patch can be written as

$$R_{\text{in}}(\rho' = \rho_0) = \frac{1}{G_t} \frac{J_m^2(k\rho_0)}{J_m^2(ka_e)} \tag{14-81}$$

INTEL-1045
U.S. Patent 7,151,430

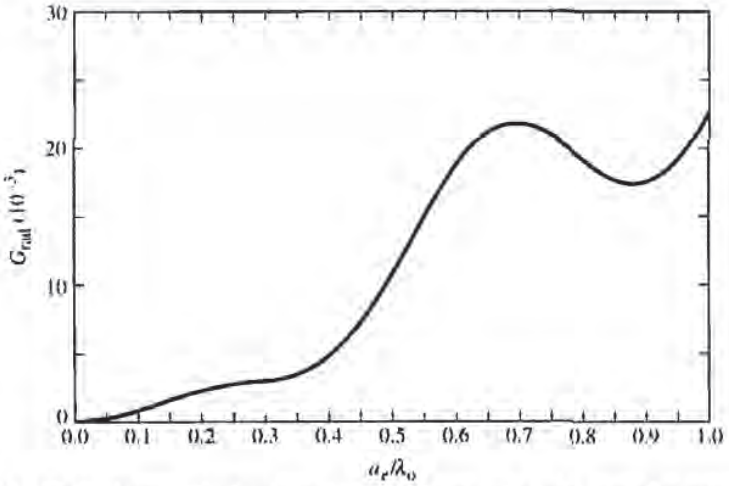


Figure 14.24 Radiation conductance versus effective radius for circular microstrip patch operating in dominant TM_{110}^{z} mode.

where G_t is the total conductance due to radiation, conduction (ohmic) and dielectric losses, as given by (14-79). As was the case with the rectangular patch, the resonant input resistance of a circular patch with an inset feed, which is usually a probe, can be written as

$$R_{in}(\rho' = \rho_0) = R_{in}(\rho' = a_e)\frac{J_m^2(k\rho_0)}{J_m^2(ka_e)} \tag{14-82}$$

where

$$R_{in}(\rho' = a_e) = \frac{1}{G_t} \tag{14-82a}$$

This is analogous to (14-20a) for the rectangular patch.

14.4 QUALITY FACTOR, BANDWIDTH AND EFFICIENCY

The quality factor, bandwidth, and efficiency are antenna figures-of-merit, which are interrelated, and there is no complete freedom to independently optimize each one. Therefore there is always a tradeoff between them in arriving at an optimum antenna performance. Often, however, there is a desire to optimize one of them while reducing the performance of the other.

The quality factor is a figure-of-merit that is representative of the antenna losses. Typically there are radiation, conduction (ohmic), dielectric and surface wave losses. Therefore the total quality factor Q_t is influenced by all of these losses and is, in general, written as [16]

$$\frac{1}{Q_t} = \frac{1}{Q_{rad}} + \frac{1}{Q_c} + \frac{1}{Q_d} + \frac{1}{Q_{sw}} \tag{14-83}$$

where

Q_t = total quality factor

Q_{rad} = quality factor due to radiation (space wave) losses

INTEL-1045
U.S. Patent 7,151,430

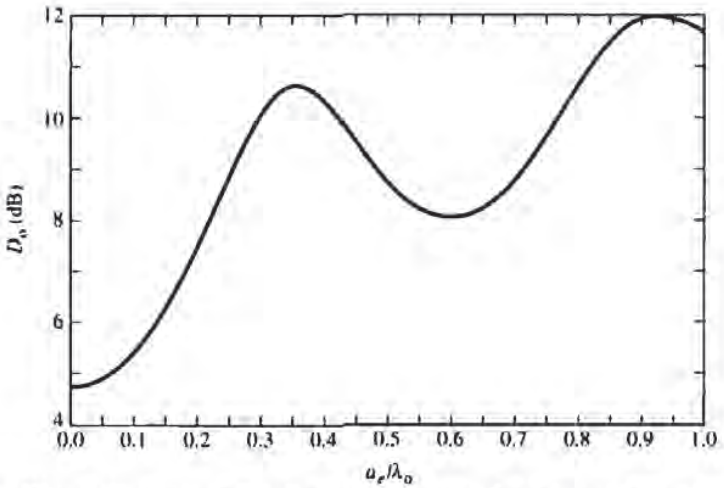


Figure 14.25 Directivity versus effective radius for circular microstrip patch antenna operating in dominant TM_{110}^{z} mode.

Q_c = quality factor due to conduction (ohmic) losses

Q_d = quality factor due to dielectric losses

Q_{sw} = quality factor due to surface waves

For very thin substrates, the losses due to surface waves are very small and can be neglected. However, for thicker substrates they need to be taken into account [84]. These losses can also be eliminated by using cavities [50] and [51].

For very thin substrates ($h \ll \lambda_0$) of arbitrary shapes (including rectangular and circular), there are approximate formulas to represent the quality factors of the various losses [16], [85]. These can be expressed as

$$Q_c = h\sqrt{\pi f \mu \sigma} \tag{14-84}$$

$$Q_d = \frac{1}{\tan \delta} \tag{14-85}$$

$$Q_{\text{rad}} = \frac{2\omega\epsilon_r}{hG_t/l} K \tag{14-86}$$

where $\tan \delta$ is the loss tangent of the substrate material, σ is the conductivity of the conductors associated with the patch and ground plane, G_t/l is the total conductance per unit length of the radiating aperture and

$$K = \frac{\iint_{\text{area}} |E|^2 \, dA}{\oint_{\text{perimeter}} |E|^2 \, dl} \tag{14-86a}$$

For a rectangular aperture operating in the dominant TM_{010}^{x} mode

$$K = \frac{L}{4} \tag{14-87a}$$

$$G_t/l = \frac{G_{\text{rad}}}{W} \tag{14-87b}$$

The Q_{rad} as represented by (14-86) is inversely proportional to the height of the substrate, and for very thin substrates is usually the dominant factor.

INTEL-1045
U.S. Patent 7,151,430

The fractional bandwidth of the antenna is inversely proportional to the Q_t of the antenna, and it is defined by (11-36) or

$$\frac{\Delta f}{f_0} = \frac{1}{Q_t} \tag{14-88}$$

However, (14-88) may not be as useful because it does not take into account impedance matching at the input terminals of the antenna. A more meaningful definition of the fractional bandwidth is over a band of frequencies where the VSWR at the input terminals is equal to or less than a desired maximum value, assuming that the VSWR is unity at the design frequency. A modified form of (14-88) that takes into account the impedance matching is [16]

$$\frac{\Delta f}{f_0} = \frac{\text{VSWR} - 1}{Q_t\sqrt{\text{VSWR}}} \tag{14-88a}$$

In general it is proportional to the volume, which for a rectangular microstrip antenna at a constant resonant frequency can be expressed as

$$\text{BW} \sim \text{volume} = \text{area} \cdot \text{height} = \text{length} \cdot \text{width} \cdot \text{height}$$

$$\sim \frac{1}{\sqrt{\epsilon_r}} \frac{1}{\sqrt{\epsilon_r}} \sqrt{\epsilon_r} = \frac{1}{\sqrt{\epsilon_r}} \tag{14-89}$$

Therefore the bandwidth is inversely proportional to the square root of the dielectric constant of the substrate. A typical variation of the bandwidth for a microstrip antenna as a function of the normalized height of the substrate, for two different substrates, is shown in Figure 14.26. It is evident that the bandwidth increases as the substrate height increases.

The radiation efficiency of an antenna is expressed by (2-90), and it is defined as the power radiated over the input power. It can also be expressed in terms of the quality factors, which for a microstrip antenna can be written as

$$e_{cdsw} = \frac{1/Q_{\text{rad}}}{1/Q_t} = \frac{Q_t}{Q_{\text{rad}}} \tag{14-90}$$

where Q_t is given by (14-83). Typical variations of the efficiency as a function of the substrate height for a microstrip antenna, with two different substrates, are shown in Figure 14.26.

14.5 INPUT IMPEDANCE

In the previous sections of this chapter, we derived approximate expressions for the resonant input resistance for both rectangular and circular microstrip antennas. Also, approximate expressions were stated which describe the variation of the resonant input resistance as a function of the inset feed position, which can be used effectively to match the antenna element to the input transmission line. In general, the input impedance is complex and it includes both a resonant and a nonresonant part which is usually reactive. Both the real and imaginary parts of the impedance vary as a function of frequency, and a typical variation is shown in Figure 14.27. Ideally both the resistance and reactance exhibit symmetry about the resonant frequency, and the reactance at resonance is equal to the average of sum of its maximum value (which is positive) and its minimum value (which is negative).

INTEL-1045
U.S. Patent 7,151,430

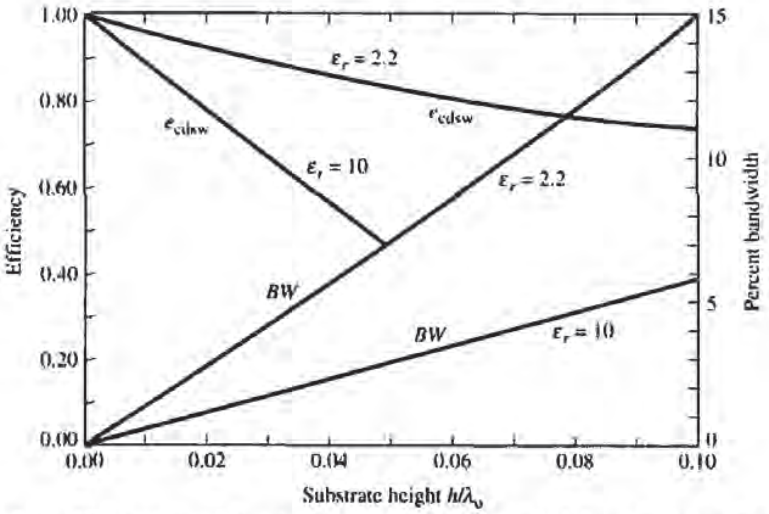


Figure 14.26 Efficiency and bandwidth versus substrate height at constant resonant frequency for rectangular microstrip patch for two different substrates (SOURCE: D. M. Pozar, "Microstrip Antennas," *Proc. IEEE*, Vol. 80, No. 1, January 1992, © 1992 IEEE).

Typically the feed reactance is very small, compared to the resonant resistance, for very thin substrates. However, for thick elements the reactance may be significant and needs to be taken into account in impedance matching and in determining the resonant frequency of a loaded element [34]. The variations of the feed reactance as a function of position can be intuitively explained by considering the cavity model for a rectangular patch with its four side perfect magnetic conducting walls [34], [85].

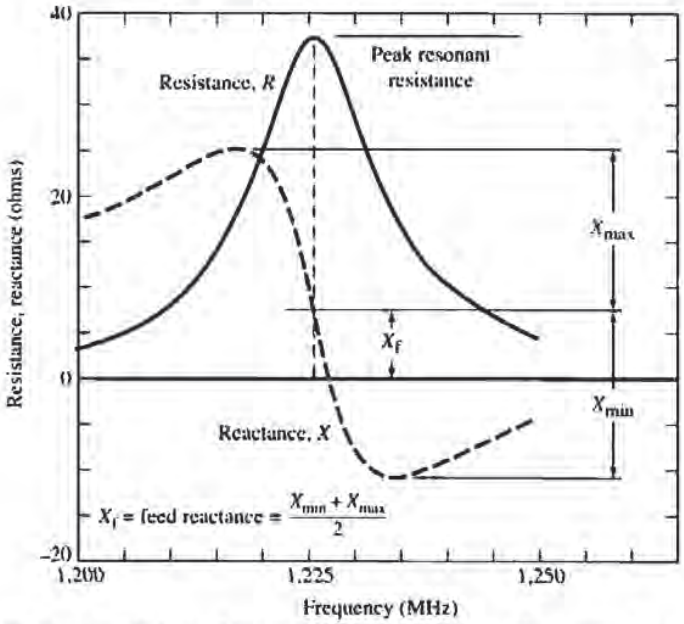


Figure 14.27 Typical variation of resistance and reactance of rectangular microstrip antenna versus frequency (*Electromagnetics*, Vol. 3, Nos. 3 and 4, p. 33, W. F. Richards, J. R. Zinecker, and R. D. Clark, Taylor & Francis, Washington, D.C. Reproduced by permission. All rights reserved).

INTEL-1045
U.S. Patent 7,151,430

As far as the impedance is concerned, the magnetic walls can be taken into account by introducing multiple images with current flow in the same direction as the actual feed. When the feed point is far away from one of the edges, the magnetic field associated with the images and that of the actual feed do not overlap strongly. Therefore the inductance associated with the magnetic energy density stored within a small testing volume near the feed will be primarily due to the current of the actual feed. However, when the feed is at one of the edges, the feed and one of the images, which accounts for the magnetic wall at that edge, coincide. Thus, the associated magnetic field stored energy of the equivalent circuit doubles while the respective stored magnetic energy density quadruples. However, because the volume in the testing region of the patch is only half from that when the feed was far removed from the edge, the net stored magnetic density is only double of that of the feed alone. Thus, the associated inductance and reactance, when the feed is at the edge, is twice that when the feed is far removed from the edge. When the feed is at a corner, there will be three images in the testing volume of the patch, in addition to the actual feed, to take into account the edges that form the corner. Using the same argument as above, the associated inductance and reactance for a feed at a corner is four times that when the feed is removed from an edge or a corner. Thus, the largest reactance (about a factor of four larger) is when the feed is at or near a corner while the smallest is when the feed is far removed from an edge or a corner.

Although such an argument predicts the relative variations (trends) of the reactance as a function of position, they do predict very accurately the absolute values especially when the feed is at or very near an edge. In fact it overestimates the values for feeds right on the edge; the actual values predicted by the cavity model with perfect magnetic conducting walls are smaller [34]. A formula that has been suggested to approximate the feed reactance, which does not take into account any images, is

$$x_f \simeq -\frac{\eta k h}{2\pi}\left[\ln\left(\frac{kd}{4}\right) + 0.577\right] \tag{14-91}$$

where d is the diameter of the feed probe. More accurate predictions of the input impedance, based on full wave models, have been made for circular patches where an attachment current mode is introduced to match the current distribution of the probe to that of the patch [74].

14.6 COUPLING

The coupling between two or more microstrip antenna elements can be taken into account easily using full-wave analyses. However, it is more difficult to do using the transmission-line and cavity models, although successful attempts have been made using the transmission-line model [75] and the cavity model [76], [77]. It can be shown that coupling between two patches, as is coupling between two aperture or two wire antennas, is a function of the position of one element relative to the other. This has been demonstrated in Figures 4.20 for a vertical half-wavelength dipole above a ground plane and in Figure 4.27 for a horizontal half-wavelength dipole above a ground plane. From these two, the ground effects are more pronounced for the horizontal dipole. Also, mutual effects have been discussed in Chapter 8 for the three different arrangements of dipoles, as shown in Figure 8.20 whose side-by-side arrangement exhibits the largest variations of mutual impedance.

For two rectangular microstrip patches the coupling for two side-by-side elements is a function of the relative alignment. When the elements are positioned collinearly

INTEL-1045
U.S. Patent 7,151,430

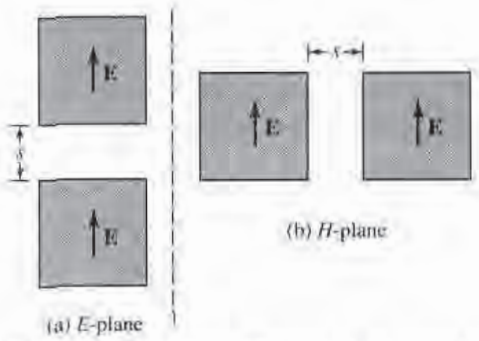


Figure 14.28 *E*- and *H*-plane arrangements of microstrip patch antennas.

along the *E*-plane, this arrangement is referred to as the *E-plane*, as shown in Figure 14.28(a); when the elements are positioned collinearly along the *H*-plane, this arrangement is referred to as the *H-plane*, as shown in Figure 14.28(b). For an edge-to-edge separation of s, the *E*-plane exhibits the smallest coupling isolation for very small spacing (typically $s < 0.10\lambda_0$) while the *H*-plane exhibits the smallest coupling for large spacing (typically $s > 0.10\lambda_0$). The spacing at which one plane coupling overtakes the other one depends on the electrical properties and geometrical dimensions of the microstrip antenna. Typical variations are shown in Figure 14.29.

In general, mutual coupling is primarily attributed to the fields that exist along the air-dielectric interface. The fields can be decomposed to space waves (with $1/\rho$ radial variations), higher order waves (with $1/\rho^2$ radial variations), surface waves (with $1/\rho^{1/2}$ radial variations), and leaky waves [with $\exp(-\lambda\rho)/\rho^{1/2}$ radial variations] [23], [86]. Because of the spherical radial variation, space ($1/\rho$) and higher order waves ($1/\rho^2$) are most dominant for very small spacing while surface waves, because

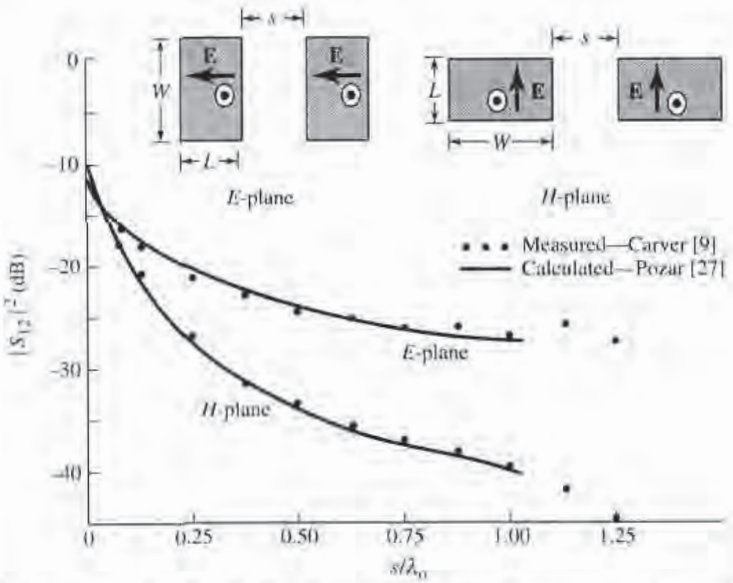


Figure 14.29 Measured and calculated mutual coupling between two coax-fed microstrip antennas, for both *E*-plane and *H*-plane coupling. ($W = 10.57$ cm, $L = 6.55$ cm, $h = 0.1588$ cm, $\epsilon_r = 2.55$, $f_r = 1{,}410$ MHz). (SOURCE: D. M. Pozar, "Input Impedance and Mutual Coupling of Rectangular Microstrip Antennas," *IEEE Trans. Antennas Propagat.*, Vol. AP-30, No. 6, November 1982. © 1982 IEEE)

INTEL-1045
U.S. Patent 7,151,430

of their $1/\rho^{1/2}$ radial variations are dominant for large separations. Surface waves exist and propagate within the dielectric, and their excitation is a function of the thickness of the substrate [79]. In a given direction, the lowest order (dominant) surface wave mode is TM(odd) with zero cutoff frequency followed by a TE(even), and alternatively by TM(odd) and TE(even) modes. For a rectangular microstrip patch, the fields are TM in a direction of progagation along the E-plane and TE in a direction of propagation along the H-plane. Since for the E-plane arrangement of Figure 14.28(a) the elements are placed collinearly along the E-plane where the fields in the space between the elements are primarily TM, there is a stronger surface wave excitation (based on a single dominant surface wave mode) between the elements, and the coupling is larger. However for the H-plane arrangement of Figure 14.28(b), the fields in the space between the elements are primarily TE and there is not as a strong dominant mode surface wave excitation; therefore there is less coupling between the elements. This does change as the thickness of the substrate increases which allows higher order TE surface wave excitation.

The mutual conductance between two rectangular microstrip patches has also been found using the basic definition of conductance given by (14-18), the far fields based on the cavity model, and the array theory of Chapter 6. For the E-plane arrangement of Figure 14.28(a) and for the odd mode field distribution beneath the patch, which is representative of the dominant mode, the mutual conductance is [8]

$$G_{12} = \frac{1}{\pi}\sqrt{\frac{\epsilon}{\mu}}\int_0^{\pi}\left[\frac{\sin\left(\frac{k_0 W}{2}\cos\theta\right)}{\cos\theta}\right]^2 \sin^3\theta\left\{2J_0\left(\frac{Y}{\lambda_0}2\pi\sin\theta\right)\right.$$
$$\left. + J_0\left(\frac{Y+L}{\lambda_0}2\pi\sin\theta\right) + J_0\left(\frac{Y-L}{\lambda_0}2\pi\sin\theta\right)\right\}d\theta \qquad (14\text{-}92)$$

where Y is the center-to-center separation between the slots and J_0 is the Bessel function of the first kind of order zero. The first term in (14-92) represents the mutual conductance of two slots separated by a distance X along the E-plane while the second and third terms represent, respectively, the conductances of two slots separated along the E-plane by distances $Y + L$ and $Y - L$. Typical normalized results are shown by the solid curve in Figure 14.30.

For the H-plane arrangement of Figure 14.28(b) and for the odd mode field distribution beneath the patch, which is representative of the dominant mode, the mutual conductance is [8]

$$G_{12} = \frac{2}{\pi}\sqrt{\frac{\epsilon}{\mu}}\int_0^{\pi}\left[\frac{\sin\left(\frac{k_0 W}{2}\cos\theta\right)}{\cos\theta}\right]^2 \sin^3\theta\cos\left(\frac{Z}{\lambda_0}2\pi\cos\theta\right)$$
$$\cdot\left\{1 + J_0\left(\frac{L}{\lambda_0}2\pi\sin\theta\right)\right\}d\theta \qquad (14\text{-}93)$$

where Z is the center-to-center separation between the slots and J_0 is the Bessel function of the first kind of order zero. The first term in (14-93) represents twice the mutual conductance of two slots separated along the H-plane by a distance Z while the second term represents twice the conductance between two slots separated along the E-plane by a distance L and along the H-plane by a distance Z. Typical normalized results are shown by the dotted curve in Figure 14.30. By comparing the results of Figures 14.30 it is clear that the mutual conductance for the H-plane arrangement, as expected, decreases with distance faster than that of the E-plane. Also it is observed

INTEL-1045
U.S. Patent 7,151,430

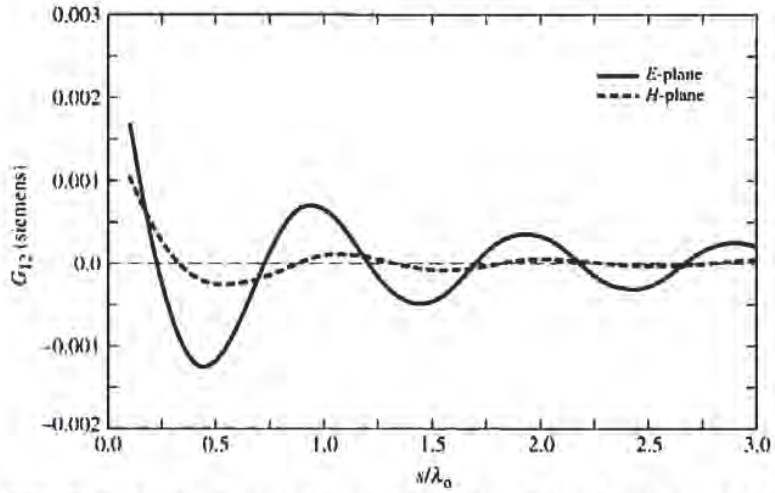


Figure 14.30 *E*- and *H*-plane mutual conductance versus patch separation for rectangular microstrip patch antennas ($W = 1.186$ cm, $L = 0.906$ cm, $\epsilon_r = 2.2$, $\lambda_0 = 3$ cm).

that the mutual conductance for the *E*-plane arrangement is higher for wider elements while it is lower for wider elements for the *H*-plane arrangement.

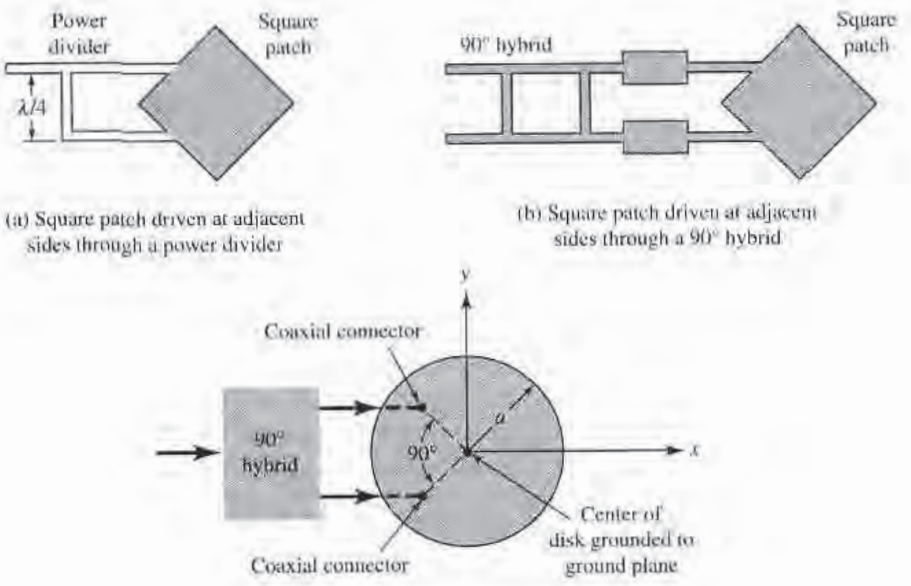
14.7 CIRCULAR POLARIZATION

The patch elements that we discussed so far, both the rectangular and the circular, radiate primarily linearly polarized waves if conventional feeds are used with no modifications. However, circular and elliptical polarizations can be obtained using various feed arrangements or slight modifications made to the elements. We will discuss here some of these arrangements.

Circular polarization can be obtained if two orthogonal modes are excited with a 90° time-phase difference between them. This can be accomplished by adjusting the physical dimensions of the patch and using either single, or two or more feeds. There have been some suggestions made and reported in the literature using single patches. For a square patch element, the easiest way to excite ideally circular polarization is to feed the element at two adjacent edges, as shown in Figures 14.31(a,b), to excite the two orthogonal modes; the TM^z_{010} with the feed at one edge and the TM^z_{001} with the feed at the other edge. The quadrature phase difference is obtained by feeding the element with a 90° power divider or 90° hybrid. Examples of arrays of linear elements that generate circular polarization are discussed in [87].

For a circular patch, circular polarization for the TM^z_{110} mode is achieved by using two feeds with proper angular separation. An example is shown in Figure 14.31(c) using two coax feeds separated by 90° which generate fields that are orthogonal to each other under the patch, as well as outside the patch. Also with this two-probe arrangement, each probe is always positioned at a point where the field generated by the other probe exhibits a null; therefore there is very little mutual coupling between the two probes. To achieve circular polarization, it is also required that the two feeds are fed in such a manner that there is 90° time-phase difference between the fields of the two; this is achieved through the use of a 90° hybrid, as shown in Figure 14.31(c). The shorting pin is placed at the center of the patch to ground the patch to the ground plane which is not necessary for circular polarization but is used

INTEL-1045
U.S. Patent 7,151,430



(a) Square patch driven at adjacent sides through a power divider

(b) Square patch driven at adjacent sides through a 90° hybrid

(c) Circular patch fed with coax

(d) Circular patch feed arrangements for $TM_{\tilde{1}10}$ and higher order modes

(Source: J. Huang, "Circularly Polarized Conical Patterns from Circular Microstrip Antennas," IEEE Trans. Antennas Propagat., Vol. AP-32, No. 9, Sept. 1984, © 1984 IEEE.)

Figure 14.31 Rectangular and circular patch arrangements for circular polarization.

to suppress modes with no ϕ variations and also may improve the quality of circular polarization.

For higher order modes, the spacing between the two feeds to achieve circular polarization is different. This is illustrated in Figure 14.31(d) and tabulated in Table 14.1, for the $TM_{\tilde{1}10}$ [same as in Figure 14.31(c)], $TM_{\tilde{2}10}$, $TM_{\tilde{3}10}$, and $TM_{\tilde{4}10}$ modes [88]. However to preserve symmetry and minimize cross polarization, especially for relatively thick substrates, two additional feed probes located diametrically opposite of the original poles are usually recommended. The additional probes are used to suppress the neighboring (adjacent) modes which usually have the next highest magnitudes [88]. For the even modes ($TM_{\tilde{2}10}$ and $TM_{\tilde{4}10}$), the four feed probes should have phases of 0°, 90°, 0° and 90° while the odd modes ($TM_{\tilde{1}10}$ and $TM_{\tilde{3}10}$) should have phases of 0°, 90°, 180° and 270°, as shown in Figure 14.31(d) [88].

To overcome the complexities inherent in dual-feed arrangements, circular polarization can also be achieved with a single feed. One way to accomplish this is to feed the patch at a single point to excite two orthogonal degenerate modes (of some resonant frequency) of ideally equal amplitudes. By introducing then a proper asymmetry in the cavity, the degeneracy can be removed with one mode increasing with

INTEL-1045
U.S. Patent 7,151,430

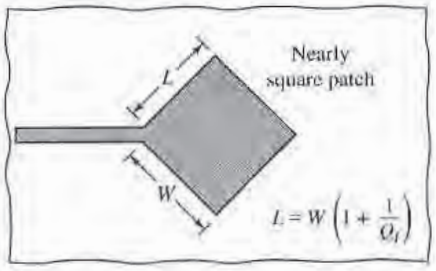
Table 14.1 FEED PROBE ANGULAR SPACING OF DIFFERENT MODES FOR CIRCULAR POLARIZATION (after [88])

	TM_{110}	TM_{210}	TM_{310}	TM_{410}	TM_{510}	TM_{610}
α	90°	45° or 135°	30° or 90°	22.5° or 67.5°	18°, 54° or 90°	15°, 45° or 75°

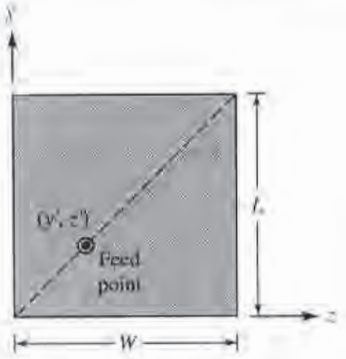
frequency while the orthogonal mode will be decreasing with frequency by the same amount. Since the two modes will have slightly different frequencies, by proper design the field of one mode can lead by 45° while that of the other can lag by 45° resulting in a 90° phase difference necessary for circular polarization [16]. To achieve this, several arrangements have been suggested.

To illustrate the procedure, let us consider a square patch, as shown in Figure 14.32(a) [34]. Initially assume that the dimensions L and W are nearly the same such that the resonant frequencies of the TM^x_{010} and TM^x_{001} overlap significantly. In the broadside direction to the patch, the TM^x_{010} mode produces an electric far-field E_y which is linearly polarized in the y direction while the TM^x_{001} mode produces an electric far-field E_z which is linearly polarized in the z direction. These fields can be expressed as

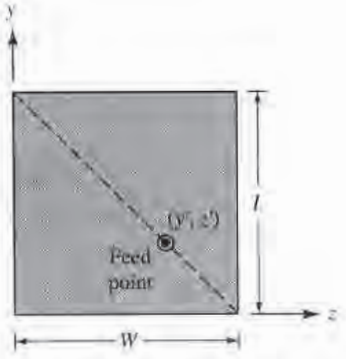
$$E_y = c\frac{\sin\left(\frac{\pi}{L}y'\right)}{k^2(1 - j/Q_t) - (k_y)^2} \tag{14-94a}$$



(a) Nearly square patch



(b) Left-hand circular (LHC)



(c) Right-hand circular (RHC)

Figure 14.32 Single-feed arrangements for circular polarization of rectangular microstrip patches.

INTEL-1045
U.S. Patent 7,151,430

$$E_z = c\frac{\sin\left(\frac{\pi}{W}z'\right)}{k^2(1 - j/Q_t) - (k_z)^2} \tag{14-94b}$$

$$k_y = \frac{\pi}{L} \tag{14-94c}$$

$$k_z = \frac{\pi}{W} \tag{14-94d}$$

where c (a proportionality constant) and Q_t ($Q_t = 1/\tan\delta_{\text{eff}}$) are identical in the broadside direction for both polarizations. If the feed point (y', z') is selected along the diagonal so that

$$\frac{y'}{L} = \frac{z'}{W} \tag{14-95}$$

then the axial ratio at broadside of the E_y to the E_z field can be expressed as

$$\frac{E_y}{E_z} \simeq \frac{k(1 - j/2Q_t) - k_y}{k(1 - j/2Q_t) - k_z} \tag{14-96}$$

To achieve circular polarization, the magnitude of the axial ratio must be unity while the phase must be $\pm 90°$. This is achieved when the two phasors representing the numerator and denominator are of equal magnitude and 90° out of phase. This can occur when [34]

$$k_y - k_z = \frac{k}{Q_t} \tag{14-97}$$

and the operating frequency is selected at the midpoint between the resonant frequencies of the TM^x_{010} and TM^x_{001} modes. The condition of (14-97) is satisfied when

$$L = W\left(1 + \frac{1}{Q_t}\right) \tag{14-98}$$

Based on (14-98) the resonant frequencies f_1 and f_2 of the bandwidth of (14-88a) associated with the two lengths L and W of a rectangular microstrip are [89]

$$f_1 = \frac{f_0}{\sqrt{1 + 1/Q_t}} \tag{14-99a}$$

$$f_2 = f_0\sqrt{1 + 1/Q_t} \tag{14-99b}$$

where f_0 is the center frequency.

Feeding the element along the diagonal starting at the lower left corner toward the upper right corner, shown dashed in Figure 14.32(b), yields ideally left-hand circular polarization at broadside. Right-hand circular polarization can be achieved by feeding along the opposite diagonal, which starts at the lower right corner and proceeds toward the upper left corner, shown dashed in Figure 14.32(c). Instead of moving the feed point each time to change the modes in order to change the type of circular polarization, varactor diodes can be used to adjust the capacitance and bias, which effectively shifts by electrical means the apparent physical location of the feed point.

This type of a feed to achieve circular polarization at broadside has been shown

INTEL-1045
U.S. Patent 7,151,430

experimentally to extend to a larger angular region [18]. However, the bandwidth over which circular polarization is maintained, even at broadside, is very narrow. An empirical formula of the percent bandwidth is [34]

$$\text{BW (percent)} = 12\frac{AR}{Q_t} \tag{14-100}$$

where the axial ratio is specified in dB. The design formulas of (14-98) and (14-100) yield good results for Q values as low as 10. Better designs are achieved for values of Q much greater than 10.

Circular polarization can also be achieved by feeding the element off the main diagonals. This can be accomplished if the dimensions of the rectangular patch are related by

$$L = W\left(1 + \frac{A + \dfrac{1}{A}}{2Q_t}\right) \tag{14-101}$$

where

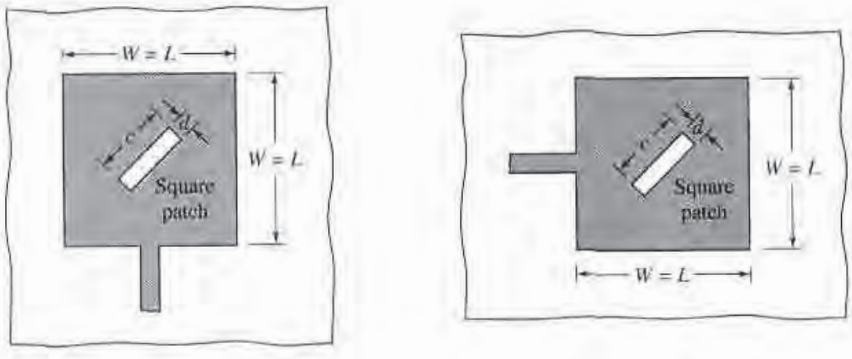
$$A = \frac{\cos\left(\pi\dfrac{y'}{L}\right)}{\cos\left(\pi\dfrac{z'}{W}\right)} \tag{14-101a}$$

There are some other practical ways of achieving nearly circular polarization. For a square patch, this can be accomplished by cutting very thin slots as shown in Figures 14.33(a,b) with dimensions

$$c = \frac{L}{2.72} = \frac{W}{2.72} \tag{14-102a}$$

$$d = \frac{c}{10} = \frac{L}{27.2} = \frac{W}{27.2} \tag{14-102b}$$

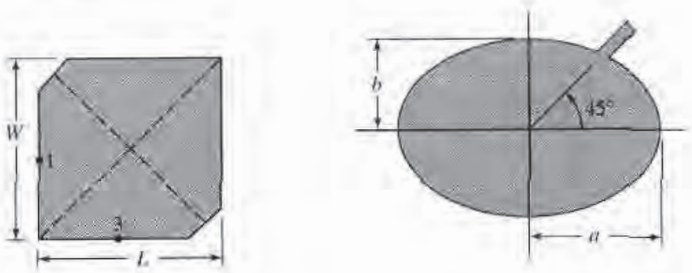
An alternative way is to trim the ends of two opposite corners of a square patch and feed at points 1 or 3, as shown in Figure 14.34(a). Circular polarization can also be



(a) Right-hand (b) Left-hand

Figure 14.33 Circular polarization for square patch with thin slots on patch ($c = W/2.72 = L/2.72$, $d = c/10 = W/27.2 = L/27.2$).

INTEL-1045
U.S. Patent 7,151,430



(a) Trimmed square ($L = W$) (b) Elliptical with tabs

Figure 14.34 Circular polarization by trimming opposite corners of a square patch and by making circular-patch slightly elliptical and adding tabs.

achieved with a circular patch by making it slightly elliptical or by adding tabs, as shown in Figure 14.34(b).

Example 14.5

The fractional bandwidth at a center frequency of 10 GHz of a rectangular patch antenna whose substrate is RT/duroid 5880 ($\epsilon_r = 2.2$) with height $h = 0.1588$ cm is about 5% for a VSWR of 2:1. Within that bandwidth, find resonant frequencies associated with the two lengths of the rectangular patch antenna, and the relative ratio of the two lengths.

SOLUTION

The total quality factor Q_t of the patch antenna is found using (14-88a) or

$$Q_t = \frac{1}{0.05\sqrt{2}} = 14.14$$

Using (14-99a) and (14-99b)

$$f_1 = \frac{10 \times 10^9}{\sqrt{1 + 1/14.14}} = 9.664 \text{ GHz}$$

$$f_2 = 10 \times 10^9 \sqrt{1 + 1/14.14} = 10.348 \text{ GHz}$$

The relative ratio of the two lengths according to (14-98) is

$$\frac{L}{W} = 1 + \frac{1}{Q_t} = 1 + \frac{1}{14.14} = 1.07$$

which makes the patch nearly square.

14.8 ARRAYS AND FEED NETWORKS

Microstrip antennas are used not only as single elements but are very popular in arrays [17], [23], [30], [31], [50], [51], [54], [63]–[65], and [74]–[77]. As discussed in

INTEL-1045
U.S. Patent 7,151,430

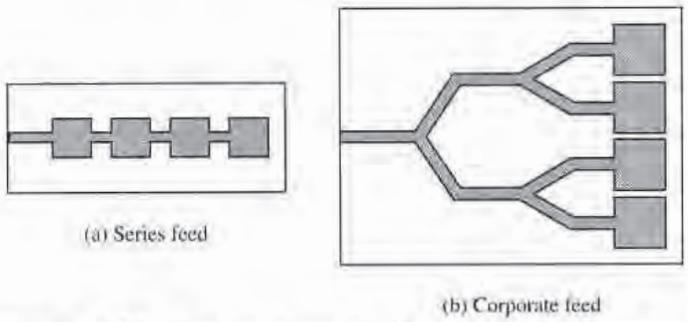
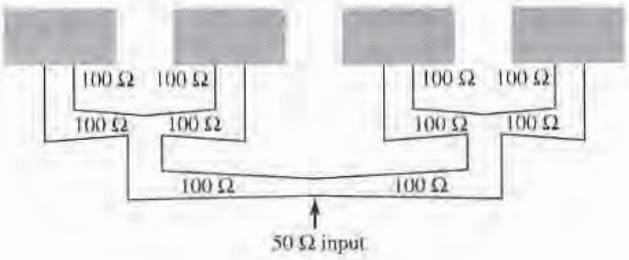


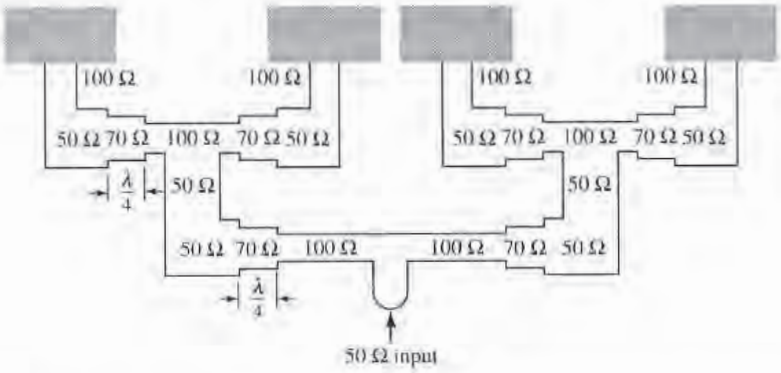
Figure 14.35 Feed arrangements for microstrip patch arrays.

Chapter 6. arrays are very versatile and are used, among other things, to synthesize a required pattern that cannot be achieved with a single element. In addition, they are used to scan the beam of an antenna system, increase the directivity, and perform various other functions which would be difficult with any one single element. The elements can be fed by a single line, as shown in Figure 14.35(a), or by multiple lines in a feed network arrangement, as shown in Figure 14.35(b). The first is referred to as a *series-feed network* while the second is referred to as a *corporate-feed network*.

The corporate-feed network is used to provide power splits of 2^n (i.e., n = 2, 4, 8, 16, 32, etc.). This is accomplished by using either tapered lines, as shown in Figure 14.36(a), to match 100-ohm patch elements to a 50-ohm input or using quarter-wavelength impedance transformers, as shown in Figure 14.36(b) [3]. The design of



(a) Tapered lines



(b) λ/4 transformers

Figure 14.36 Tapered and λ/4 impedance transformer lines to match 100-ohm patches to a 50-ohm line. (SOURCE: R. E. Munson, "Conformal Microstrip Antennas and Microstrip Phased Arrays," *IEEE Trans. Antennas Propagat.*, Vol. AP-22, No. 1, January 1974. © 1974 IEEE)

INTEL-1045
U.S. Patent 7,151,430

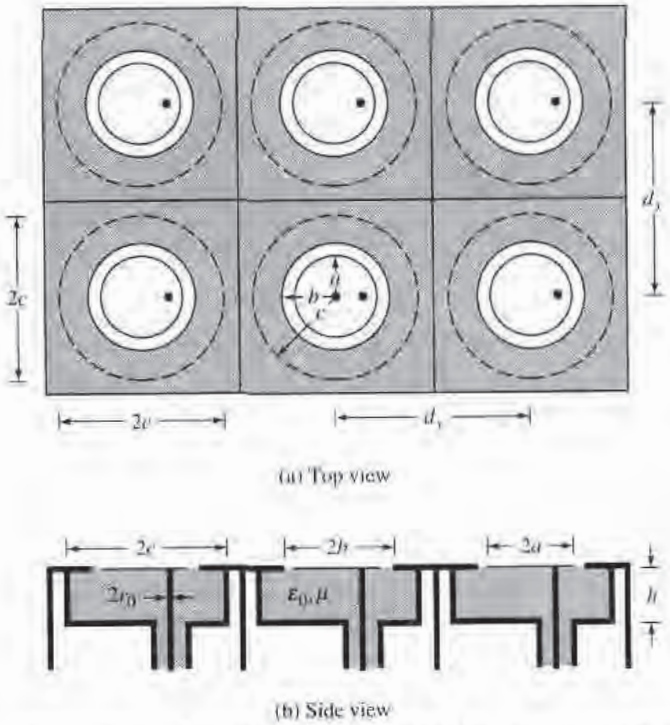


Figure 14.37 Infinite array of circular patches backed by circular cavities. (Courtesy J. T. Aberle and F. Zavosh)

single- and multiple-section quarter-wavelength impedance transformers is discussed in Section 9.8.

Series-fed arrays can be conveniently fabricated using photolithography for both the radiating elements and the feed network. However, this technique is limited to arrays with a fixed beam or those which are scanned by varying the frequency, but it can be applied to linear and planar arrays with single or dual polarization. Also any changes in one of the elements or feed lines affects the performance of the others. Therefore in a design it is important to be able to take into account these and other effects, such as mutual coupling, and internal reflections.

Corporate-fed arrays are general and versatile. With this method the designer has more control of the feed of each element (amplitude and phase) and it is ideal for scanning phased arrays, multibeam arrays, or shaped-beam arrays. As discussed in Chapter 6, the phase of each element can be controlled using phase shifters while the amplitude can be adjusted using either amplifiers or attenuators.

Those who have been designing and testing microstrip arrays indicate that radiation from the feed line, using either a series or corporate feed network, is a serious problem that limits the cross-polarization and side lobe level of the arrays [38]. Both cross-polarization and side lobe levels can be improved by isolating the feed network from the radiating face of the array. This can be accomplished using either probe feeds or aperture coupling.

Arrays can be analyzed using the theory of Chapter 6. However, such an approach does not take into account mutual coupling effects, which for microstrip patches can be significant. Therefore for more accurate results, full-wave solutions must be performed. In microstrip arrays [63], as in any other array [90], mutual coupling between

INTEL-1045
U.S. Patent 7,151,430

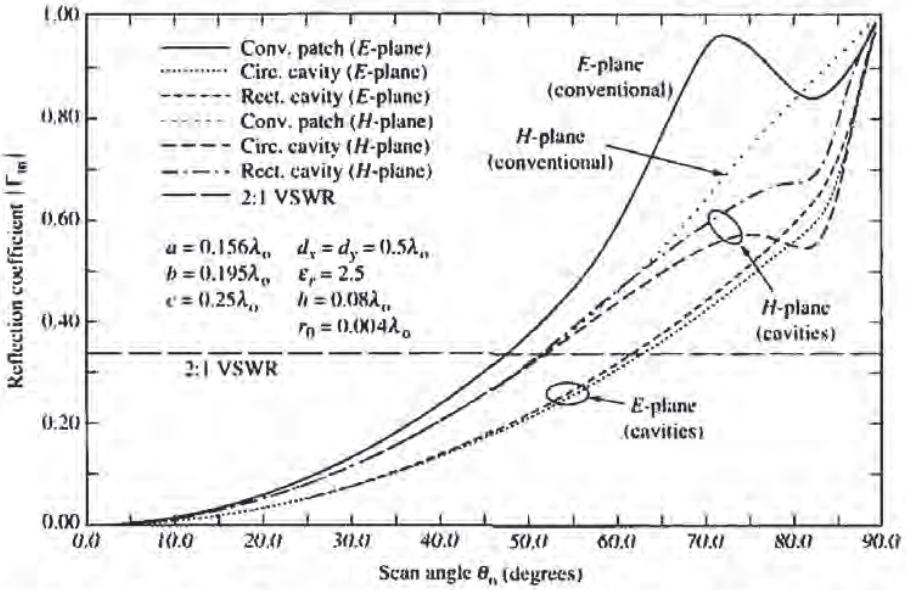


Figure 14.38 *E*- and *H*-plane broadside-matched input reflection coefficient versus scan angle for infinite array of circular microstrip patches with and without cavities. (Courtesy J. T. Aberle and F. Zavosh)

elements can introduce *scan blindness* which limits, for a certain maximum reflection coefficient, the angular volume over which the arrays can be scanned. For microstrip antennas, this scan limitation is strongly influenced by surface waves within the substrate. This scan angular volume can be extended by eliminating surface waves. One way to do this is to use cavities in conjunction with microstrip elements [50], [51]. Figure 14.37 shows an array of circular patches backed by either circular or rectangular cavities. It has been shown that the presence of cavities, either circular or rectangular, can have a pronounced enhancement in the *E*-plane scan volume, especially for thicker substrates [51]. The *H*-plane scan volume is not strongly enhanced. However the shape of the cavity, circular or rectangular, does not strongly influence the results. Typical results for broadside-matched reflection coefficient infinite array of circular patches, with a substrate $0.08\lambda_0$ thick and backed by circular and rectangular cavities, are shown in Figure 14.38 for the *E*-plane and *H*-plane. The broadside-matched reflection coefficient $\Gamma(\theta, \phi)$ is defined as

$$\Gamma(\theta, \phi) = \frac{Z_{in}(\theta, \phi) - Z_{in}(0, 0)}{Z_{in}(\theta, \phi) + Z_{in}^{*}(0, 0)} \tag{14-103}$$

where $Z_{in}(\theta, \phi)$ is the input impedance when the main beam is scanned toward an angle (θ, ϕ). The results are compared with those of a conventional cavity (noncavity backed). It is apparent that there is a significant scan enhancement for the *E*-plane, especially for a VSWR of about 2:1. *H*-plane enhancement occurs for reflection coefficients greater than about 0.60. For the conventional array, the *E*-plane response exhibits a large reflection coefficient, which approaches unity, near a scan angle of $\theta_0 = 72.5°$. This is evidence of scan blindness which ideally occurs when the reflection coefficient is unity, and it is attributed to the coupling between the array elements due to leaky waves [63]. Scan blindness occurs for both the *E*- and *H*-planes at grazing incidence ($\theta_0 = 90°$).

INTEL-1045
U.S. Patent 7,151,430

References

1. G. A. Deschamps, "Microstrip Microwave Antennas," presented at the Third USAF Symposium on Antennas, 1953.
2. H. Gutton and G. Baissinot, "Flat Aerial for Ultra High Frequencies," French Patent No. 703 113, 1955.
3. R. E. Munson, "Conformal Microstrip Antennas and Microstrip Phased Arrays," *IEEE Trans. Antennas Propagat.*, Vol. AP-22, No. 1, pp. 74–78, January 1974.
4. J. W. Howell, "Microstrip Antennas," *IEEE Trans. Antennas Propagat.*, Vol. AP-23, No. 1, pp. 90–93, January 1975.
5. A. G. Derneryd, "Linearly Polarized Microstrip Antennas," *IEEE Trans. Antennas Propagat.*, Vol. AP-24, No. 6, pp. 846–851, November 1976.
6. L. C. Shen, S. A. Long, M. R. Allerding, and M. D. Walton, "Resonant Frequency of a Circular Disc, Printed-Circuit Antenna," *IEEE Trans. Antennas Propagat.*, Vol. AP-25, No. 4, pp. 595–596, July 1977.
7. P. K. Agrawal and M. C. Bailey, "An Analysis Technique for Microstrip Antennas," *IEEE Trans. Antennas Propagat.*, Vol. AP-25, No. 6, pp. 756–759, November 1977.
8. A. G. Derneryd, "A Theoretical Investigation of the Rectangular Microstrip Antenna Element," *IEEE Trans. Antennas Propagat.*, Vol. AP-26, No. 4, pp. 532–535, July 1978.
9. *Proc. of the Workshop on Printed-Circuit Antenna Technology*, October 17–19, 1979, New Mexico State Univ., Las Cruces, NM.
10. A. G. Derneryd, "Analysis of the Microstrip Disk Antenna Element," *IEEE Trans. Antennas Propagat.*, Vol. AP-27, No. 5, pp. 660–664, September 1979.
11. A. G. Derneryd, "Extended Analysis of Rectangular Microstrip Resonator Antennas," *IEEE Trans. Antennas Propagat.*, Vol. AP-27, No. 6, pp. 846–849, November 1979.
12. Y. T. Lo, D. Solomon, and W. F. Richards, "Theory and Experiment on Microstrip Antennas," *IEEE Trans. Antennas Propagat.*, Vol. AP-27, No. 2, pp. 137–145, March 1979.
13. S. A. Long and M. D. Walton, "A Dual-Frequency Stacked Circular-Disc Antenna," *IEEE Trans. Antennas Propagat.*, Vol. AP-27, No. 2, pp. 270–273, March 1979.
14. N. K. Uzunoglu, N. G. Alexopoulos, and J. G. Fikioris, "Radiation Properties of Microstrip Dipoles," *IEEE Trans. Antennas Propagat.*, Vol. AP-27, No. 6, pp. 853–858, November 1979.
15. I. J. Bahl and P. Bhartia, *Microstrip Antennas*, Artech House, Dedham, MA, 1980.
16. K. R. Carver and J. W. Mink, "Microstrip Antenna Technology," *IEEE Trans. Antennas Propagat.*, Vol. AP-29, No. 1, pp. 2–24, January 1981.
17. R. J. Mailloux, J. F. McIlvenna, and N. P. Kernweis, "Microstrip Array Technology," *IEEE Trans. Antennas Propagat.*, Vol. AP-29, No. 1, pp. 25–27, January 1981.
18. W. F. Richards, Y. T. Lo, and D. D. Harrison, "An Improved Theory of Microstrip Antennas with Applications," *IEEE Trans. Antennas Propagat.*, Vol. AP-29, No. 1, pp. 38–46, January 1981.
19. E. H. Newman and P. Tylyathan, "Analysis of Microstrip Antennas Using Moment Methods," *IEEE Trans. Antennas Propagat.*, Vol. AP-29, No. 1, pp. 47–53, January 1981.
20. D. C. Chang, "Analytical Theory of an Unloaded Rectangular Microstrip Patch," *IEEE Trans. Antennas Propagat.*, Vol. AP-29, No. 1, pp. 54–62, January 1981.
21. T. Itoh and W. Menzel, "A Full-Wave Analysis Method for Open Microstrip Structures," *IEEE Trans. Antennas Propagat.*, Vol. AP-29, No. 1, pp. 63–68, January 1981.
22. I. E. Rana and N. G. Alexopoulos, "Current Distribution and Input Impedance of Printed Dipoles," *IEEE Trans. Antennas Propagat.*, Vol. AP-29, No. 1, pp. 99–105, January 1981.
23. N. G. Alexopoulos and I. E. Rana, "Mutual Impedance Computation Between Printed Dipoles," *IEEE Trans. Antennas Propagat.*, Vol. AP-29, No. 1, pp. 106–111, January 1981.

INTEL-1045
U.S. Patent 7,151,430

24. J. R. James, P. S. Hall, C. Wood, and A. Henderson, "Some Recent Developments in Microstrip Antenna Design," *IEEE Trans. Antennas Propagat.*, Vol. AP-29, No. 1, pp. 124–128, January 1981.
25. M. D. Deshpande and M. C. Bailey, "Input Impedance of Microstrip Antennas," *IEEE Trans. Antennas Propagat.*, Vol. AP-30, No. 4, pp. 645–650, July 1982.
26. M. C. Bailey and M. D. Deshpande, "Integral Equation Formulation of Microstrip Antennas," *IEEE Trans. Antennas Propagat.*, Vol. AP-30, No. 4, pp. 651–656, July 1982.
27. D. M. Pozar, "Input Impedance and Mutual Coupling of Rectangular Microstrip Antenna," *IEEE Trans. Antennas Propagat.*, Vol. AP-30, No. 6, pp. 1191–1196, November 1982.
28. D. M. Pozar, "Considerations for Millimeter-Wave Printed Antennas," *IEEE Trans. Antennas Propagat.*, Vol. AP-31, No. 5, pp. 740–747, September 1983.
29. E. F. Kuester and D. C. Chang, "A Geometrical Theory for the Resonant Frequencies and Q- Factors of Some Triangular Microstrip Patch Antennas," *IEEE Trans. Antennas Propagat.*, Vol. AP-31, No. 1, pp. 27–34, January 1983.
30. P. B. Katehi and N. G. Alexopoulos, "On the Modeling of Electromagnetically Coupled Microstrip Antennas-The Printed Strip Dipole," *IEEE Trans. Antennas Propagat.*, Vol. AP-32, No. 11, pp. 1179–1186, November 1984.
31. D. M. Pozar, "Analysis of Finite Phased Arrays of Printed Dipoles," *IEEE Trans. Antennas Propagat.*, Vol. AP-33, No. 10, pp. 1045–1053, October 1985.
32. J. R. James, P. S. Hall, and C. Wood, *Microstrip Antenna Theory and Design*, Peter Peregrinus, 1981, London, UK, 1981.
33. R. E. Munson, "Microstrip Antennas," Chapter 7 in *Antenna Engineering Handbook* (R. C. Johnson and H. Jasik, eds.), McGraw-Hill Book Co., New York, 1984.
34. W. F. Richards, "Microstrip Antennas," Chapter 10 in *Antenna Handbook: Theory, Applications and Design* (Y. T. Lo and S. W. Lee, eds.), Van Nostrand Reinhold Co., New York, 1988.
35. J. R. James, and P. S. Hall, *Handbook of Microstrip Antennas*, Vols. 1 and 2, Peter Peregrinus, London, UK, 1989.
36. P. Bhartia, K. V. S. Rao, and R. S. Tomar, *Millimeter-Wave Microstrip and Printed Circuit Antennas*, Artech House, Boston, MA, 1991.
37. J. R. James, "What's New in Antennas," *IEEE Antennas and Propagation Magazine*, Vol. 32, No. 1, pp. 6–18, February 1990.
38. D. M. Pozar, "Microstrip Antennas," *Proc. IEEE*, Vol. 80, No. 1, pp. 79–81, January 1992.
39. D. H. Schaubert, F. G. Farrar, A. Sindoris, and S. T. Hayes, "Microstrip Antennas with Frequency Agility and Polarization Diversity," *IEEE Trans. Antennas Propagat.*, Vol. AP-29, No. 1, pp. 118–123, January 1981.
40. P. Bhartia and I. J. Bahl, "Frequency Agile Microstrip Antennas," *Microwave Journal*, pp. 67–70, October 1982.
41. W. F. Richards and Y. T. Lo, "Theoretical and Experimental Investigation of a Microstrip Radiator with Multiple Lumped Linear Loads," *Electromagnetics*, Vol. 3, No. 3–4, pp. 371–385, July–December 1983.
42. W. F. Richards and S. A. Long, "Impedance Control of Microstrip Antennas Utilizing Reactive Loading," *Proc. Intl. Telemetering Conf.*, pp. 285–290, Las Vegas, 1986.
43. W. F. Richards and S. A. Long, "Adaptive Pattern Control of a Reactively Loaded, Dual-Mode Microstrip Antenna," *Proc. Intl. Telemetering Conf.*, pp. 291–296, Las Vegas, 1986.
44. M. P. Purchine and J. T. Aberle, "A Tunable L-Band Circular Microstrip Patch Antenna," *Microwave Journal*, pp. 80, 84, 87, and 88, October 1994.
45. C. M. Krowne, "Cylindrical-Rectangular Microstrip Antenna," *IEEE Trans. Antennas Propagat.*, Vol. AP-31, No. 1, pp. 194–199, January 1983.
46. S. B. De Assis Fonseca and A. J. Giarola, "Microstrip Disk Antennas, Part I: Efficiency of Space Wave Launching," *IEEE Trans. Antennas Propagat.*, Vol. AP-32, No. 6, pp. 561–567, June 1984.

INTEL-1045
U.S. Patent 7,151,430

47. S. B. De Assis Fonseca and A. J. Giarola, "Microstrip Disk Antennas, Part II: the Problem of Surface Wave Radiation by Dielectric Truncation," *IEEE Trans. Antennas Propagat.*, Vol. AP-32, No. 6, pp. 568–573, June 1984.
48. J. Huang, "The Finite Ground Plane Effect on the Microstrip Antenna Radiation Patterns," *IEEE Trans. Antennas Propagat.*, Vol. AP-31, No. 7, pp. 649–653, July 1983.
49. I. Lier and K. R. Jakobsen, "Rectangular Microstrip Patch Antennas with Infinite and Finite Ground-Plane Dimensions," *IEEE Trans. Antennas Propagat.*, Vol. AP-31, No. 6, pp. 978–984, November 1983.
50. R. J. Mailloux, "On the Use of Metallized Cavities in Printed Slot Arrays with Dielectric Substrates," *IEEE Trans. Antennas Propagat.*, Vol. AP-35, No. 5, pp. 477–487, May 1987.
51. J. T. Aberle and F. Zavosh, "Analysis of Probe-Fed Circular Microstrip Patches Backed by Circular Cavities," *Electromagnetics*, Vol. 14, pp. 239–258, 1994.
52. A. Henderson, J. R. James, and C. M. Hall, "Bandwidth Extension Techniques in Printed Conformal Antennas," *Military Microwaves*, MM 86, pp. 329–334, 1986.
53. H. F. Pues and A. R. Van de Capelle, "An Impedance Matching Technique for Increasing the Bandwidth of Microstrip Antennas," *IEEE Trans. Antennas Propagat.*, Vol. AP-37, No. 11, pp. 1345–1354, November 1989.
54. J. J. Schuss, J. D. Hanfling, and R. L. Bauer, "Design of Wideband Patch Radiator Phased Arrays," *IEEE Antennas Propagat. Symp. Dig.*, pp. 1220–1223, 1989.
55. C. H. Tsao, Y. M. Hwang, F. Kilburg, and F. Dietrich, "Aperture-Coupled Patch Antennas with Wide-Bandwidth and Dual Polarization Capabilities," *IEEE Antennas Propagat. Symp. Dig.*, pp. 936–939, 1988.
56. A. Ittipiboon, B. Clarke, and M. Cuhaci, "Slot-Coupled Stacked Microstrip Antennas," *IEEE Antennas Propagat. Symp. Dig.*, pp. 1108–1111, 1990.
57. S. Sabban, "A New Broadband Stacked Two-Layer Microstrip Antenna," *IEEE Antennas Propagat. Symp. Dig.*, pp. 63–66, 1983.
58. C. H. Chen, A. Tulintseff, and M. Sorbello, "Broadband Two-Layer Microstrip Antenna," *IEEE Antennas Propagat. Symp. Dig.*, pp. 251–254, 1984.
59. R. W. Lee, K. F. Lee, and J. Bobinchak, "Characteristics of a Two-Layer Electromagnetically Coupled Rectangular Patch Antenna," *Electronic Letters*, Vol. 23, pp. 1070–1072, September 1987.
60. W. F. Richards, S. Davidson, and S. A. Long, "Dual-Band, Reactively Loaded Microstrip Antennas," *IEEE Trans. Antennas Propagat.*, Vol. AP-33, No. 5, pp. 556–561, May 1985.
61. D. M. Pozar and B. Kaufman, "Increasing the Bandwidth of a Microstrip Antenna by Proximity Coupling," *Electronic Letters*, Vol. 23, pp. 368–369, April 1987.
62. N. W. Montgomery, "Triple-Frequency Stacked Microstrip Element," *IEEE Antennas Propagat. Symp. Dig.*, pp. 255–258, Boston, MA, 1984.
63. D. M. Pozar and D. H. Schaubert, "Scan Blindness in Infinite Phased Arrays of Printed Dipoles," *IEEE Trans. Antennas Propagat.*, Vol. AP-32, No. 6, pp. 602–610, June 1984.
64. D. M. Pozar, "Finite Phased Arrays of Rectangular Microstrip Antennas," *IEEE Trans. Antennas Propagat.*, Vol. AP-34, No. 5, pp. 658–665, May 1986.
65. F. Zavosh and J. T. Aberle, "Infinite Phased Arrays of Cavity-Backed Patches," Vol. AP-42, No. 3, pp. 390–398, March 1994.
66. H. G. Oltman and D. A. Huebner, "Electromagnetically Coupled Microstrip Dipoles," *IEEE Trans. Antennas Propagat.*, Vol. AP-29, No. 1, pp. 151–157, January 1981.
67. D. M. Pozar, "A Microstrip Antenna Aperture Coupled to a Microstrip Line," *Electronic Letters*, Vol. 21, pp. 49–50, January 1985.
68. G. Gronau and I. Wolff, "Aperture-Coupling of a Rectangular Microstrip Resonator," *Electronic Letters*, Vol. 22, pp. 554–556, May 1986.
69. H. A. Bethe, "Theory of Diffractions by Small Holes," *Physical Review*, Vol. 66, pp. 163–182, 1944.
70. R. E. Collin, *Foundations for Microwave Engineering*, Chapter 6, McGraw-Hill Book Co., New York, 1992.

INTEL-1045
U.S. Patent 7,151,430

71. J. R. Mosig and F. E. Gardiol, "General Integral Equation Formulation for Microstrip Antennas and Scatterers," *Proc. Inst. Elect. Eng.*, pt. H, Vol. 132, pp. 424–432, 1985.
72. N. G. Alexopoulos and D. R. Jackson, "Fundamental Superstrate (Cover) Effects on Printed Circuit Antennas," *IEEE Trans. Antennas Propagat.*, Vol. AP-32, No. 8, pp. 807–816, August 1984.
73. C. C. Liu, A. Hessel, and J. Shmoys, "Performance of Probe-Fed Rectangular Microstrip Patch Element Phased Arrays," *IEEE Trans. Antennas Propagat.*, Vol. AP-36, No. 11, pp. 1501–1509, November 1988.
74. J. T. Aberle and D. M. Pozar, "Analysis of Infinite Arrays of One- and Two-Probe-Fed Circular Patches," *IEEE Trans. Antennas Propagat.*, Vol. AP-38, No. 4, pp. 421–432, April 1990.
75. E. H. Van Lil and A. R. Van de Capelle, "Transmission-Line Model for Mutual Coupling Between Microstrip Antennas," *IEEE Trans. Antennas Propagat.*, Vol. AP-32, No. 8, pp. 816–821, August 1984.
76. K. Malkomes, "Mutual Coupling Between Microstrip Patch Antennas," *Electronic Letters*, Vol. 18, No. 122, pp. 520–522, June 1982.
77. E. Penard and J.-P. Daniel, "Mutual Coupling Between Microstrip Antennas," *Electronic Letters*, Vol. 18, No. 4, pp. 605–607, July 1982.
78. D. H. Schaubert, D. M. Pozar, and A. Adrian, "Effect of Microstrip Antenna Substrate Thickness and Permittivity: Comparison of Theories and Experiment," *IEEE Trans. Antennas Propagat.*, Vol. AP-37, No. 6, pp. 677–682, June 1989.
79. C. A. Balanis, *Advanced Engineering Electromagnetics*, John Wiley & Sons, New York, 1989.
80. E. O. Hammerstad, "Equations for Microstrip Circuit Design," *Proc. Fifth European Microwave Conf.*, pp. 268–272, September 1975.
81. R. F. Harrington, *Time-Harmonic Electromagnetic Fields*, McGraw-Hill Book Co., p. 183, 1961.
82. R. E. Collin and F. J. Zucker, *Antenna Theory*, Part I, Chapter 5, McGraw-Hill Book Co., New York, 1969.
83. E. J. Martin, "Radiation Fields of Circular Loop Antennas by a Direct Integration Process," *IRE Trans. Antennas Propagat.*, Vol. AP-8, pp. 105–107, January 1960.
84. R. J. Collier and P. D. White, "Surface Waves in Microstrip Circuits," *Proc. 6th European Microwave Conference*, 1976, pp. 632–636.
85. W. F. Richards, J. R. Zinecker, R. D. Clark, and S. A. Long, "Experimental and Theoretical Investigation of the Inductance Associated with a Microstrip Antenna Feed," *Electromagnetics*, Vol. 3, No. 3–4, pp. 327–346, July–December 1983.
86. L. B. Felsen and N. Marcuvitz, *Radiation and Scattering of Waves*, Prentice-Hall, Englewood Cliffs, NJ, 1973.
87. J. Huang, "A Technique for an Array to Generate Circular Polarization with Linearly Polarized Elements," *IEEE Trans. Antennas Propagat.*, Vol. AP-34, No. 9, pp. 1113–1124, September 1986.
88. J. Huang, "Circularly Polarized Conical Patterns from Circular Microstrip Antennas," *IEEE Trans. Antennas Propagat.*, Vol. AP-32, No. 9, pp. 991–994, September 1984.
89. T. A. Milligan, *Modern Antenna Design*, McGraw-Hill Book Co., New York, 1985.
90. R. J. Mailloux, "Phase Array Theory and Technology," *Proc. IEEE*, Vol. 70, No. 3, pp. 246–291, March 1982.

PROBLEMS

14.1. A microstrip line is used as a feed line to a microstrip patch. The substrate of the line is alumina ($\epsilon_r \simeq 10$) while the dimensions of the line are $w/h = 1.2$ and $t/h = 0$. Determine the effective dielectric constant and characteristic impedance of the line. Compare the computed characteristic impedance to that of a 50-ohm line.

14.2. A microstrip transmission line of beryllium oxide ($\epsilon_r \simeq 6.8$) has a width-to-height ratio of $w/h = 1.5$. Assuming that the thickness-to-height ratio is $t/h = 0$, determine:

INTEL-1045
U.S. Patent 7,151,430

(a) effective dielectric constant
(b) characteristic impedance of the line

14.3. Cellular and mobile telephony, using earth-based repeaters, has received wide acceptance and has become an essential means of communication for business, even for the household. Cellular telephony by satellites is the wave of the future and communication systems are being designed for that purpose. The present allocated frequency band for satellites is at L-band (= 1.6 GHz). Various antennas are being examined for that purpose; one candidate is the microstrip patch antenna. Design a rectangular microstrip patch antenna, based on the dominant mode, that can be mounted on the roof of a car to be used for satellite cellular telephone. The designed center frequency is 1.6 GHz, the dielectric constant of the substrate is 10.2 (i.e., RT/duroid), and the thickness of the substrate is 0.127 cm. Determine the
(a) dimensions of the rectangular patch (in cm)
(b) resonant input impedance, assuming no coupling between the two radiating slots
(c) mutual conductance between the two radiating slots of the patch
(d) resonant input impedance, taking into account coupling
(e) *position of the feed to match the antenna patch to a 75-ohm line*

14.4. Repeat the design of Problem 14.3 using a substrate with a dielectric constant of 2.2 (i.e., RT/duroid 5880) and with a height of 0.1575 cm. Are the new dimensions of the patch realistic for the roof of a personal car?

14.5. Design a rectangular microstrip patch with dimensions W and L, over a single substrate, whose center frequency is 10 GHz. The dielectric constant of the substrate is 10.2 and the height of the substrate is 0.127 cm (0.050 in.). Determine the physical dimensions W and L (in cm) of the patch, taking into account field fringing.

14.6. Using the transmission line model of Figure 14.8(b), derive (14-14)–(14-15).

14.7. To take into account coupling between the two radiating slots of a rectangular microstrip patch, the resonant input resistance is represented by (14-17). Justify, explain, and/or show why the plus (+) sign is used for modes with odd (antisymmetric) resonant voltage distribution beneath the patch while the minus (−) sign is used for modes with even (symmetric) resonant voltage distribution.

14.8. Show that for typical rectangular microstrip patches $G_1/Y_c \ll 1$ and $B_1/Y_c \ll 1$ so that (14-20) reduces to (14-20a).

14.9. A rectangular microstrip patch antenna operating at 10 GHz with a substrate with dimensions of length $L = 0.4097$ cm, width $W = 0.634$ cm, and substrate height $h = 0.127$ cm. It is desired to feed the patch using a probe feed. Neglecting mutual coupling calculate:
(a) What is the input impedance of the patch at one of the radiating edges based on the transmission-line model?
(b) At what distance y_0 (in cm) from one of the radiating edges should the coax feed be placed so that the input impedance is 50 ohms?

14.10. A rectangular microstrip patch antenna, whose input impedance is 152.44 ohms at its leading radiating edge, is fed by a microstrip line as shown in Figure 14.10. Assuming the width of the feeding line is $W_0 = 0.2984$ cm, the height of the substrate is 0.1575 cm and the dielectric constant of the substrate is 2.2, at what distance y_0 should the microstrip patch antenna be fed so as to have a perfect match between the line and the radiating element? The overall microstrip patch element length is 0.9068 cm.

14.11. The rectangular microstrip patch of Example 14.2 is fed by a microstrip transmission line of Figure 14.5. In order to reduce reflections at the inset feed point between the line and the patch element, design the microstrip line that its characteristic impedance matches that of the radiating element.

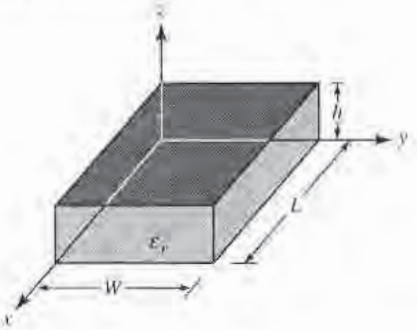
14.12. *Repeat the design of Example 14.2 so that the input impedance of the radiating patch* at the feed point is:
(a) 75 ohms
(b) 100 ohms

INTEL-1045
U.S. Patent 7,151,430

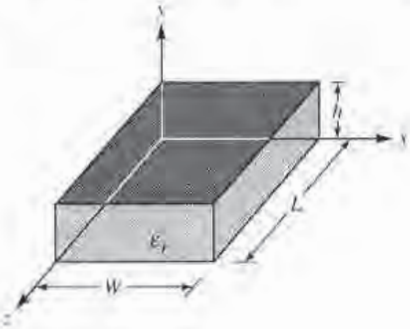
Then, assuming the feed line is a microstrip line, determine the dimensions of the line so that its characteristic impedance matches that of the radiating patch.

14.13. A rectangular microstrip patch antenna has dimensions of $L = 0.906$ cm, $W = 1.186$ cm, and $h = 0.1575$ cm. The dielectric constant of the substrate is $\epsilon_r = 2.2$. Using the geometry of Figure 14.12 and assuming no fringing, determine the resonant frequency of the first 4 TM^z_{0mp} modes, in order of ascending resonant frequency.

14.14. Derive the TM^z_{mnp} field configurations (modes) for the rectangular microstrip patch based on the geometry of Figure P14.14. Determine the:
(a) eigenvalues
(b) resonant frequency $(f_r)_{mnp}$ for the mnp mode.
(c) dominant mode if $L > W > h$
(d) resonant frequency of the dominant mode.



14.15. Repeat Problem 14.14 for the TM^y_{mnp} modes based on the geometry of Figure P14.15.



14.16. Derive the array factor of (14-42).

14.17. Assuming the coordinate system for the rectangular microstrip patch is that of Problem 14.14 (Fig. P14.14), derive based on the cavity model the
(a) far-zone electric field radiated by one of the radiating slots of the patch
(b) array factor for the two radiating slots of the patch
(c) far-zone total electric field radiated by both of the radiating slots

14.18. Repeat Problem 14.17 for the rectangular patch geometry of Problem 14.15 (Fig. P14.15).

14.19. Determine the directivity (in dB) of the rectangular microstrip patch of Example 14.3 using
(a) Kraus' approximate formula
(b) Tai & Pereira's approximate formula

14.20. Derive the directivity (in dB) of the rectangular microstrip patch of Problem 14.3.

14.21. Derive the directivity (in dB) of the rectangular microstrip patch of Problem 14.4.

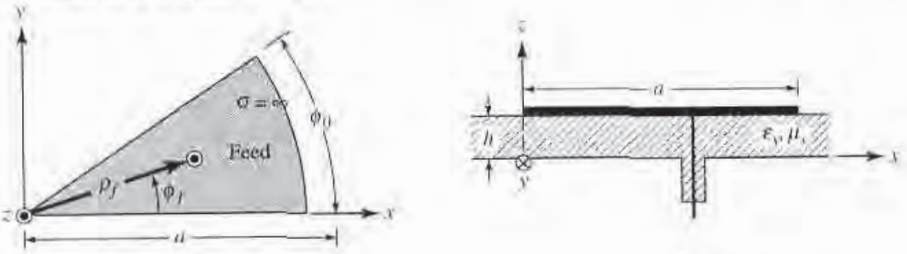
14.22. For a circular microstrip patch antenna operating in the dominant TM^z_{110} mode, derive the far-zone electric fields radiated by the patch based on the cavity model.

14.23. Using the cavity model, derive the TM^z_{mnp} resonant frequencies for a microstrip patch whose shape is that of a half of a circular patch (semicircle).

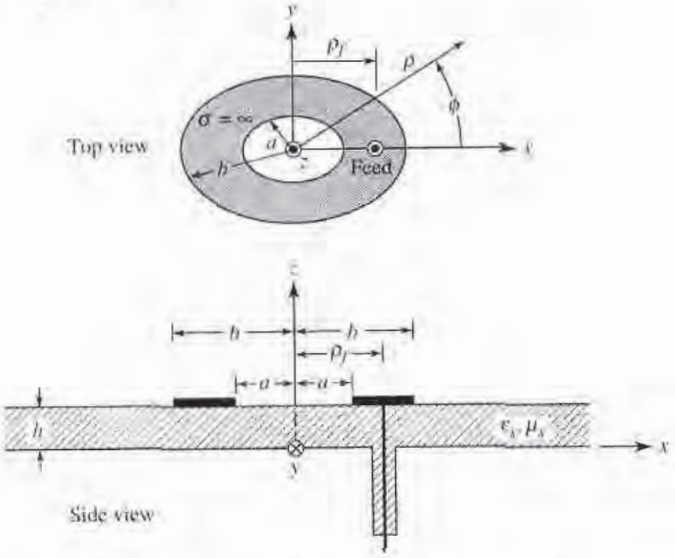
INTEL-1045
U.S. Patent 7,151,430

14.24. Repeat Problem 14.23 for a 90° circular disc (angular sector of 90°) microstrip patch.

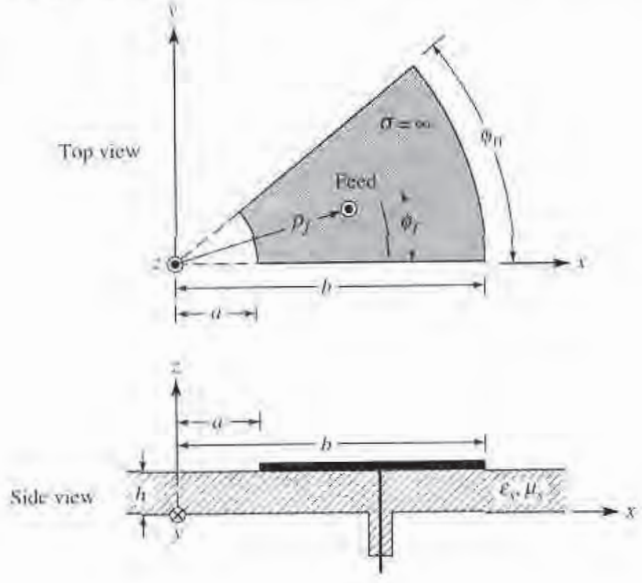
14.25. Repeat Problem 14.23 for the circular sector microstrip patch antenna whose geometry is shown in Figure P14.25.



14.26. Repeat Problem 14.23 for the annular microstrip patch antenna whose geometry is shown in Figure P14.26.



14.27. Repeat Problem 14.23 for the annular sector microstrip patch antenna whose geometry is shown in Figure P14.27.



INTEL-1045
U.S. Patent 7,151,430

14.28. Repeat the design of Problem 14.3 for a circular microstrip patch antenna operating in the dominant TM^z_{110} mode.

14.29. Repeat the design of Problem 14.4 for a circular microstrip patch antenna operating in the dominant TM^z_{110} mode.

14.30. For ground-based cellular telephony, the desired pattern coverage is omnidirectional and similar to that of a monopole (with a null toward zenith). This can be accomplished using circular microstrip patch antennas operating in higher order modes, such as the TM^z_{210}, TM^z_{310}, TM^z_{410}, etc. Assuming that the desired resonant frequency is 900 MHz, design a circular microstrip patch antenna operating in the TM^z_{210} mode. Assuming a substrate with a dielectric constant of 10.2 and a height of 0.127 cm:
(a) Derive an expression for the resonant frequency.
(b) Determine the radius of the circular patch. Neglect fringing.
(c) Derive expressions for the far-zone radiated fields.
(d) Plot the normalized E- and H-plane amplitude patterns (in dB).
(e) Plot the normalized azimuthal (xy plane) amplitude pattern (in dB).
(f) Determine the directivity (in dB) using the DIRECTIVITY computer program at the end of Chapter 2.

14.31. Repeat Problem 14.30 for the TM^z_{310} mode.

14.32. Repeat Problem 14.30 for the TM^z_{410} mode.

14.33. The diameter of a typical probe feed for a microstrip patch antenna is $d = 0.1$ cm. At $f = 10$ GHz, determine the feed reactance assuming a substrate with a dielectric constant of 2.2 and height of 0.1575 cm.

14.34. Determine the impedance of a single-section quarter-wavelength impedance transformer to match a 100-ohm patch element to a 50-ohm microstrip line. Determine the dimensions of the line assuming a substrate with a dielectric constant of 2.2 and a height of 0.1575 cm.

14.35. Repeat the design of Problem 14.34 using a two-section binomial transformer. Determine the dimensions of each section of the transformer.

14.36. Repeat the design of Problem 14.34 using a two-section Tschebyscheff transformer. Determine the dimensions of each section of the transformer.

INTEL-1045
U.S. Patent 7,151,430

COMPUTER PROGRAM - MICROSTRIP ANTENNAS

```
C*****************************************************************
C
C THIS IS A FORTRAN PROGRAM THAT DESIGNS AND COMPUTES THE
C ANTENNA RADIATION CHARACTERISTICS OF:
C
C     I.  RECTANGULAR
C     II. CIRCULAR
C
C MICROSTRIP PATCH ANTENNAS BASED ON THE CAVITY MODEL AND
C DOMINANT MODE OPERATION FOR EACH. THAT IS:
C
C     A. TM010 MODE FOR THE RECTANGULAR PATCH
C     B. TM110 MODE FOR THE CIRCULAR PATCH
C
C
C       **INPUT PARAMETERS
C       1. FREQ   = RESONANT FREQUENCY fr (in GHz)
C       2. EPSR   = DIELECTRIC CONSTANT OF THE SUBSTRATE εr
C       3. HEIGHT = HEIGHT OF THE SUBSTRATE h (in cm)
C       4. Y0     = POSITION OF RECESSED FEED POINT yo (in cm)
C                   RELATIVE TO LEADING RADIATING EDGE OF
C                   RECTANGULAR PATCH.
C                   NOT NECESSARY FOR CIRCULAR PATCH
C
C       **OUTPUT PARAMETERS
C
C       A. RECTANGULAR PATCH:
C
C            1. PHYSICAL WIDTH OF PATCH W (in cm)
C            2. EFFECTIVE LENGTH OF PATCH Le (in cm)
C            3. PHYSICAL LENGTH OF PATCH L (in cm)
C            4. NORMALIZED E-PLANE AMPLITUDE PATTERN (in dB)
C            5. NORMALIZED H-PLANE AMPLITUDE PATTERN (in dB)
C            6. E-PLANE HALF-POWER BEAMWIDTH (in degrees)
C            7. H-PLANE HALF-POWER BEAMWIDTH (in degrees)
C            8. DIRECTIVITY (dimensionless and in dB)
C            9. RESONANT INPUT RESISTANCE (in ohms)
C               a. AT LEADING RADIATING EDGE (y = 0)
C               b. AT RECESSED FEED POINT FROM LEADING
C                  RADIATING EDGE (y = yo)
C
C       B. CIRCULAR PATCH:
C
C            1. PHYSICAL RADIUS OF THE PATCH a (in cm)
C            2. EFFECTIVE RADIUS OF THE PATCH ae (in cm)
C            3. NORMALIZED E-PLANE AMPLITUDE PATTERN (in dB)
C            4. NORMALIZED H-PLANE AMPLITUDE PATTERN (in dB)
C            5. E-PLANE HALF-POWER BEAMWIDTH (in degrees)
C            6. H-PLANE HALF-POWER BEAMWIDTH (in degrees)
C            7. DIRECTIVITY (dimensionless and in dB)
C*****************************************************************
```


INTEL-1045
U.S. Patent 7,151,430

CHAPTER

15

REFLECTOR ANTENNAS

15.1 INTRODUCTION

Reflector antennas, in one form or another, have been in use since the discovery of electromagnetic wave propagation in 1888 by Hertz. However the fine art of analyzing and designing reflectors of many various geometrical shapes did not forge ahead until the days of World War II when numerous radar applications evolved. Subsequent demands of reflectors for use in radio astronomy, microwave communication, and satellite tracking resulted in spectacular progress in the development of sophisticated analytical and experimental techniques in shaping the reflector surfaces and optimizing illumination over their apertures so as to maximize the gain. The use of reflector antennas for deep space communication, such as in the space program and especially their deployment on the surface of the moon, resulted in establishing the reflector antenna almost as a household word during the 1960s. Although reflector antennas take many geometrical configurations, some of the most popular shapes are the plane, corner, and curved reflectors (especially the paraboloid), as shown in Figure 15.1, each of which will be discussed in this chapter. Many articles on various phases of the analysis and design of curved reflectors have been published and some of the most referenced can be found in a book of reprinted papers [1].

15.2 PLANE REFLECTOR

The simplest type of reflector is a plane reflector introduced to direct energy in a desired direction. The arrangement is that shown in Figure 15.1(a) which has been extensively analyzed in Section 4.7 when the radiating source is a vertical or horizontal linear element. It has been clearly demonstrated that the polarization of the radiating source and its position relative to the reflecting surface can be used to control the radiating properties (pattern, impedance, directivity) of the overall system. Image theory has been used to analyze the radiating characteristics of such a system. Although the infinite dimensions of the plane reflector are idealized, the results can be used as approximations for electrically large surfaces. The perturbations introduced by keeping the dimensions finite can be accounted for by using special methods such as the Geometrical Theory of Diffraction [2]–[5] which was introduced in Section 12.10.

INTEL-1045
U.S. Patent 7,151,430

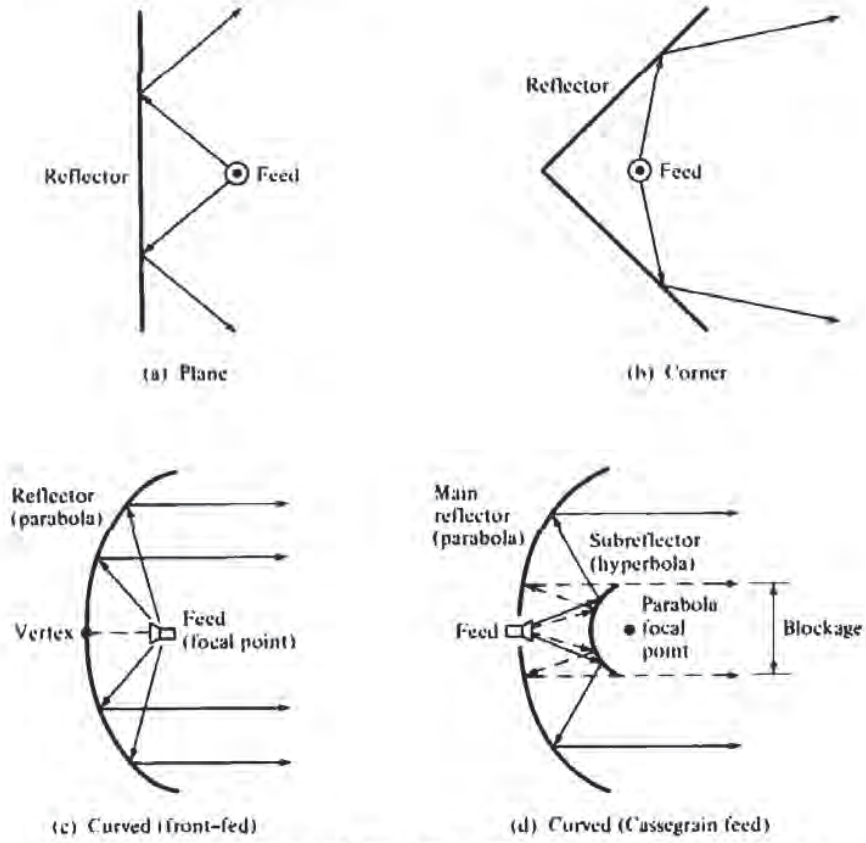


Figure 15.1 Geometrical configuration for some reflector systems.

15.3 CORNER REFLECTOR

To better collimate the energy in the forward direction, the geometrical shape of the plane reflector itself must be changed so as to prohibit radiation in the back and side directions. One arrangement which accomplishes that consists of two plane reflectors joined so as to form a corner, as shown in Figures 15.1(b) and in 15.2(a). This is known as the corner reflector. Because of its simplicity in construction, it has many unique applications. For example, if the reflector is used as a passive target for radar or communication applications, it will return the signal exactly in the same direction as it received it when its included angle is 90°. This is illustrated geometrically in Figure 15.2(b). Because of this unique feature, military ships and vehicles are designed with minimum sharp corners to reduce their detection by enemy radar. Corner reflectors are also widely used as receiving elements for home television.

In most practical applications, the included angle formed by the plates is usually 90°; however other angles are sometimes used. To maintain a given system efficiency, the spacing between the vertex and the feed element must increase as the included angle of the reflector decreases, and vice-versa. For reflectors with infinite sides, the gain increases as the included angle between the planes decreases. This, however, may not be true for finite size plates. For simplicity, in this chapter it will be assumed that the plates themselves are infinite in extent ($l = \infty$). However, since in practice the dimensions must be finite, guidelines on the size of the aperture (D_a), length (l), and height (h) will be given.

The feed element for a corner reflector is almost always a dipole or an array of

INTEL-1045
U.S. Patent 7,151,430

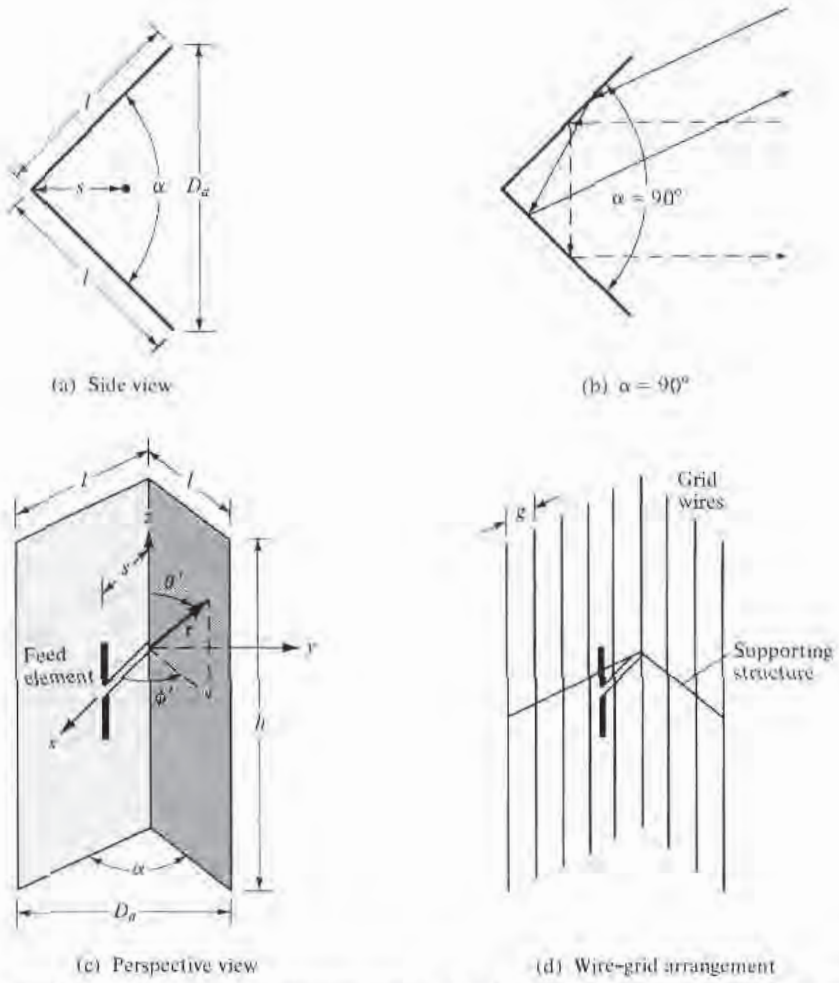


Figure 15.2 Side and perspective views of solid and wire-grid corner reflectors.

collinear dipoles placed parallel to the vertex a distance s away, as shown in a perspective view in Figure 15.2(c). Greater bandwidth is obtained when the feed elements are cylindrical or biconical dipoles instead of thin wires. In many applications, especially when the wavelength is large compared to tolerable physical dimensions, the surfaces of the corner reflector are frequently made of grid wires rather than solid sheet metal, as shown in Figure 15.2(d). One of the reasons for doing that is to reduce wind resistance and overall system weight. The spacing (g) between wires is made a small fraction of a wavelength (usually $g \leq \lambda/10$). For wires that are parallel to the length of the dipole, as is the case for the arrangement of Figure 15.2(d), the reflectivity of the grid-wire surface is as good as that of a solid surface.

In practice, the aperture of the corner reflector (D_a) is usually made between one and two wavelengths ($\lambda < D_a < 2\lambda$). The length of the sides of a 90° corner reflector is most commonly taken to be about twice the distance from the vertex to the feed ($l \simeq 2s$). For reflectors with smaller included angles, the sides are made larger. The feed-to-vertex distance (s) is usually taken to be between $\lambda/3$ and $2\lambda/3$ ($\lambda/3 < s < 2\lambda/3$). For each reflector, there is an optimum feed-to-vertex spacing. If the spacing becomes too small, the radiation resistance decreases and becomes comparable to the loss resistance of the system which leads to an inefficient antenna. For very large spacing, the system produces undesirable multiple lobes, and it loses its directional

INTEL-1045
U.S. Patent 7,151,430

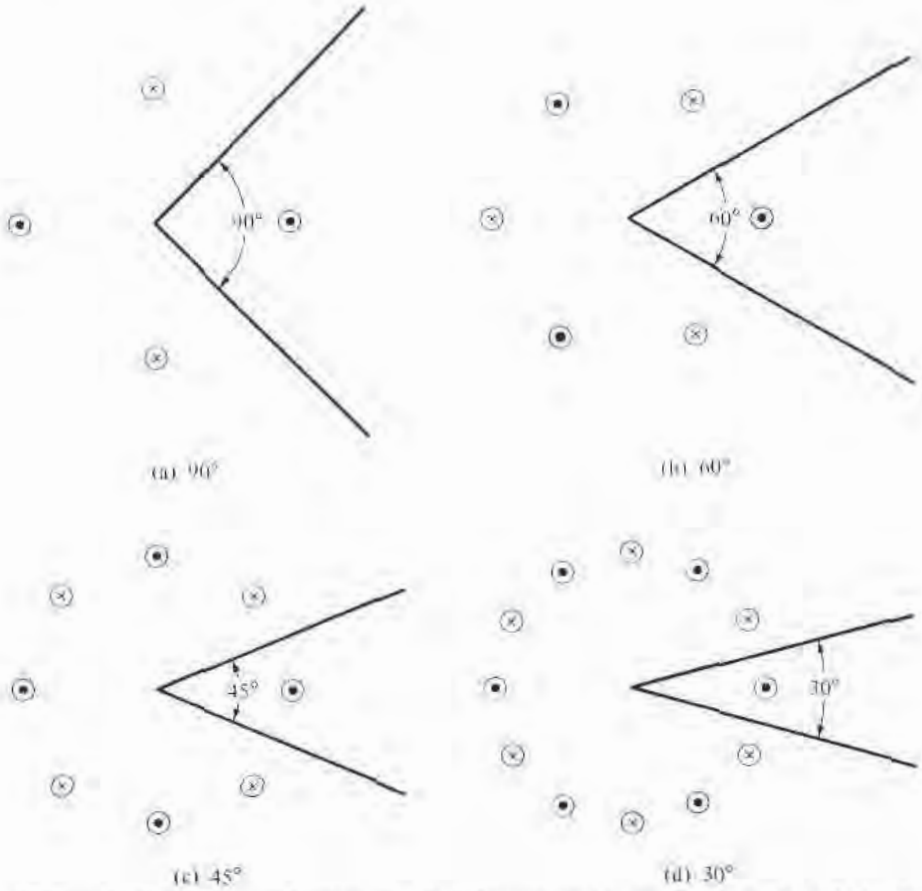
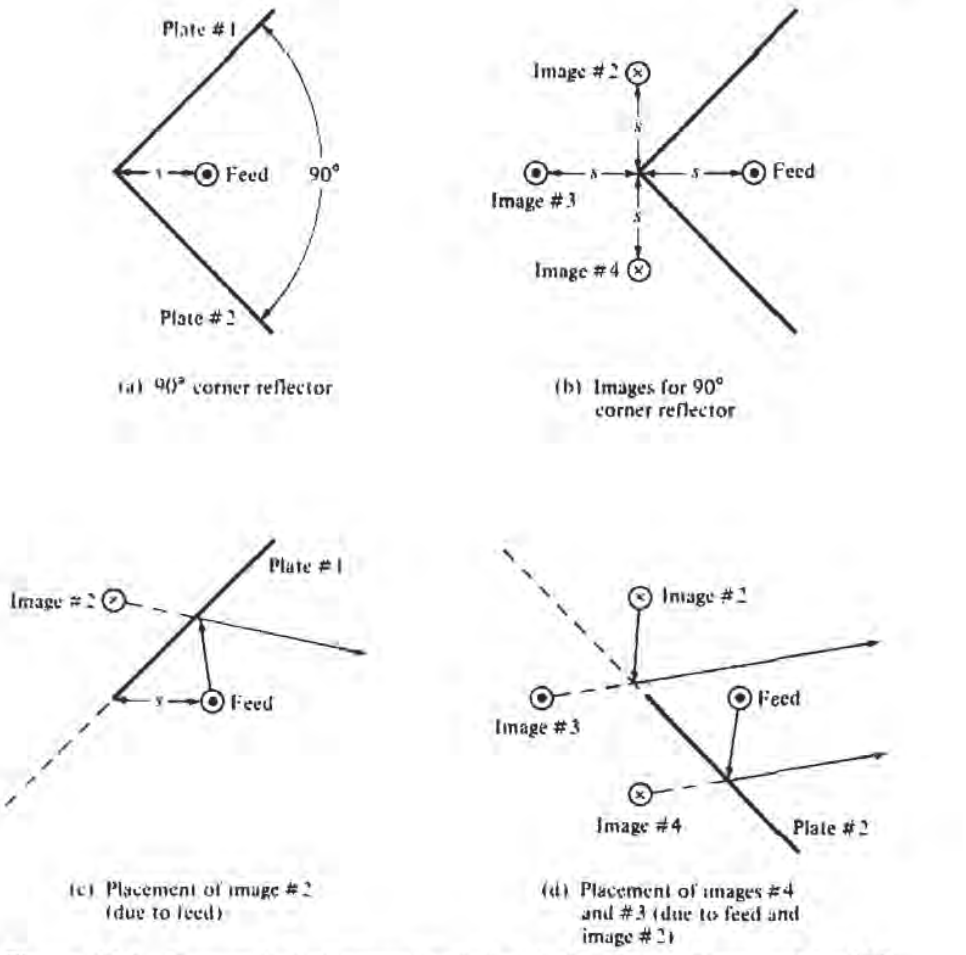


Figure 15.3 Corner reflectors and their images (with perpendicularly polarized feeds) for angles of 90°, 60°, 45°, and 30°.

characteristics. It has been experimentally observed that increasing the size of the sides does not greatly affect the beamwidth and directivity, but it increases the bandwidth and radiation resistance. The main lobe is somewhat broader for reflectors with finite sides compared to that of infinite dimensions. The height (h) of the reflector is usually taken to be about 1.2 to 1.5 times greater than the total length of the feed element, in order to reduce radiation toward the back region from the ends.

The analysis for the field radiated by a source in the presence of a corner reflector is facilitated when the included angle (α) of the reflector is $\alpha = \pi/n$, where n is an integer ($\alpha = \pi, \pi/2, \pi/3, \pi/4$, etc.). For those cases ($\alpha = 180°, 90°, 60°, 45°$, etc.) it is possible to find a system of images, which when properly placed in the absence of the reflector plates, form an array that yields the same field within the space formed by the reflector plates as the actual system. The number of images, polarity, and position of each is controlled by the included angle of the corner reflector and the polarization of the feed element. In Figure 15.3 we display the geometrical and electrical arrangement of the images for corner reflectors with included angles of 90°, 60°, 45°, and 30° and a feed with perpendicular polarization. The procedure for finding the number, location, and polarity of the images is demonstrated graphically in Figure 15.4 for a corner reflector with a 90° included angle. It is assumed that the feed element is a linear dipole placed parallel to the vertex. A similar procedure can be followed for all other reflectors with an included angle of $\alpha = 180°/n$, where n is an integer.

INTEL-1045
U.S. Patent 7,151,430



(a) 90° corner reflector

(b) Images for 90° corner reflector

(c) Placement of image #2 (due to feed)

(d) Placement of images #4 and #3 (due to feed and image #2)

Figure 15.4 Geometrical placement and electrical polarity of images for a 90° corner reflector with a parallel polarized feed.

15.3.1 90° Corner Reflector

The first corner reflector to be analyzed is the one with an included angle of 90°. Because its radiation characteristics are the most attractive, it has become the most popular.

Referring to the reflector of Figure 15.2(c) with its images in Figure 15.4(b), the total field of the system can be derived by summing the contributions from the feed and its images. Thus

$$\mathbf{E}(r, \theta, \phi) = \mathbf{E}_1(r_1, \theta, \phi) + \mathbf{E}_2(r_2, \theta, \phi) + \mathbf{E}_3(r_3, \theta, \phi) + \mathbf{E}_4(r_4, \theta, \phi) \quad (15\text{-}1)$$

In the far-zone, the normalized scalar field can be written as

$$E(r, \theta, \phi) = f(\theta, \phi)\frac{e^{-jkr_1}}{r_1} - f(\theta, \phi)\frac{e^{-jkr_2}}{r_2} + f(\theta, \phi)\frac{e^{-jkr_3}}{r_3} - f(\theta, \phi)\frac{e^{-jkr_4}}{r_4}$$

$$E(r, \theta, \phi) = [e^{+jks\cos\psi_1} - e^{+jks\cos\psi_2} + e^{+jks\cos\psi_3} - e^{+jks\cos\psi_4}]\, f(\theta, \phi)\frac{e^{-jkr}}{r} \quad (15\text{-}2)$$

INTEL-1045
U.S. Patent 7,151,430

where

$$\cos\psi_1 = \hat{\mathbf{a}}_x \cdot \hat{\mathbf{a}}_r = \sin\theta\cos\phi \tag{15-2a}$$

$$\cos\psi_2 = \hat{\mathbf{a}}_y \cdot \hat{\mathbf{a}}_r = \sin\theta\sin\phi \tag{15-2b}$$

$$\cos\psi_3 = -\hat{\mathbf{a}}_x \cdot \hat{\mathbf{a}}_r = -\sin\theta\cos\phi \tag{15-2c}$$

$$\cos\psi_4 = -\hat{\mathbf{a}}_y \cdot \hat{\mathbf{a}}_r = -\sin\theta\sin\phi \tag{15-2d}$$

since $\hat{\mathbf{a}}_r = \hat{\mathbf{a}}_x \sin\theta\cos\phi + \hat{\mathbf{a}}_y \sin\theta\sin\phi + \hat{\mathbf{a}}_z \cos\theta$. Equation (15-2) can also be written, using (15-2a)–(15-2d), as

$$E(r, \theta, \phi) = 2[\cos(ks\sin\theta\cos\phi) - \cos(ks\sin\theta\sin\phi)]\, f(\theta, \phi)\frac{e^{-jkr}}{r} \tag{15-3}$$

where for $\alpha = \pi/2 = 90°$

$$0 \le \theta \le \pi, \qquad \begin{matrix} 0 \le \phi \le \alpha/2 \\ 2\pi - \alpha/2 \le \phi \le 2\pi \end{matrix} \tag{15-3a}$$

Letting the field of a single isolated (radiating in free-space) element to be

$$E_0 = f(\theta, \phi)\frac{e^{-jkr}}{r} \tag{15-4}$$

(15-3) can be rewritten as

$$\boxed{\frac{E}{E_0} = \mathrm{AF}(\theta, \phi) = 2[\cos(ks\sin\theta\cos\phi) - \cos(ks\sin\theta\sin\phi)]} \tag{15-5}$$

Equation (15-5) represents not only the ratio of the total field to that of an isolated element at the origin but also the array factor of the entire reflector system. In the *azimuthal plane* ($\theta = \pi/2$), *(15-5) reduces to*

$$\frac{E}{E_0} = AF(\theta = \pi/2, \phi) = 2[\cos(ks\cos\phi) - \cos(ks\sin\phi)] \tag{15-6}$$

To gain some insight into the performance of a corner reflector, in Figure 15.5 we display the normalized patterns for an $\alpha = 90°$ corner reflector for spacings of $s = 0.1\lambda$, 0.7λ, 0.8λ, 0.9λ, and 1.0λ. It is evident that for the small spacings the pattern consists of a single major lobe whereas multiple lobes appear for the larger spacings ($s > 0.7\lambda$). For $s = \lambda$ the pattern exhibits two lobes separated by a null along the $\phi = 0°$ axis.

Another parameter of performance for the corner reflector is the field strength along the symmetry axis ($\theta = 90°$, $\phi = 0°$) as a function of feed-to-vertex distance s [6]. The normalized (relative to the field of a single isolated element) absolute field strength $|E/E_0|$ as a function of s/λ ($0 \le s \le 10\lambda$) for $\alpha = 90°$ is shown plotted in Figure 15.6. It is apparent that the first field strength peak is achieved when $s = 0.5\lambda$, and it is equal to 4. The field is also periodic with a period of $\Delta s/\lambda = 1$.

15.3.2 Other Corner Reflectors

A similar procedure can be used to derive the array factors and total fields for all other corner reflectors with included angles of $\alpha = 180°/n$. Referring to Figure 15.3, it can be shown that the array factors for $\alpha = 60°$, 45°, and 30° can be written as

INTEL-1045
U.S. Patent 7,151,430

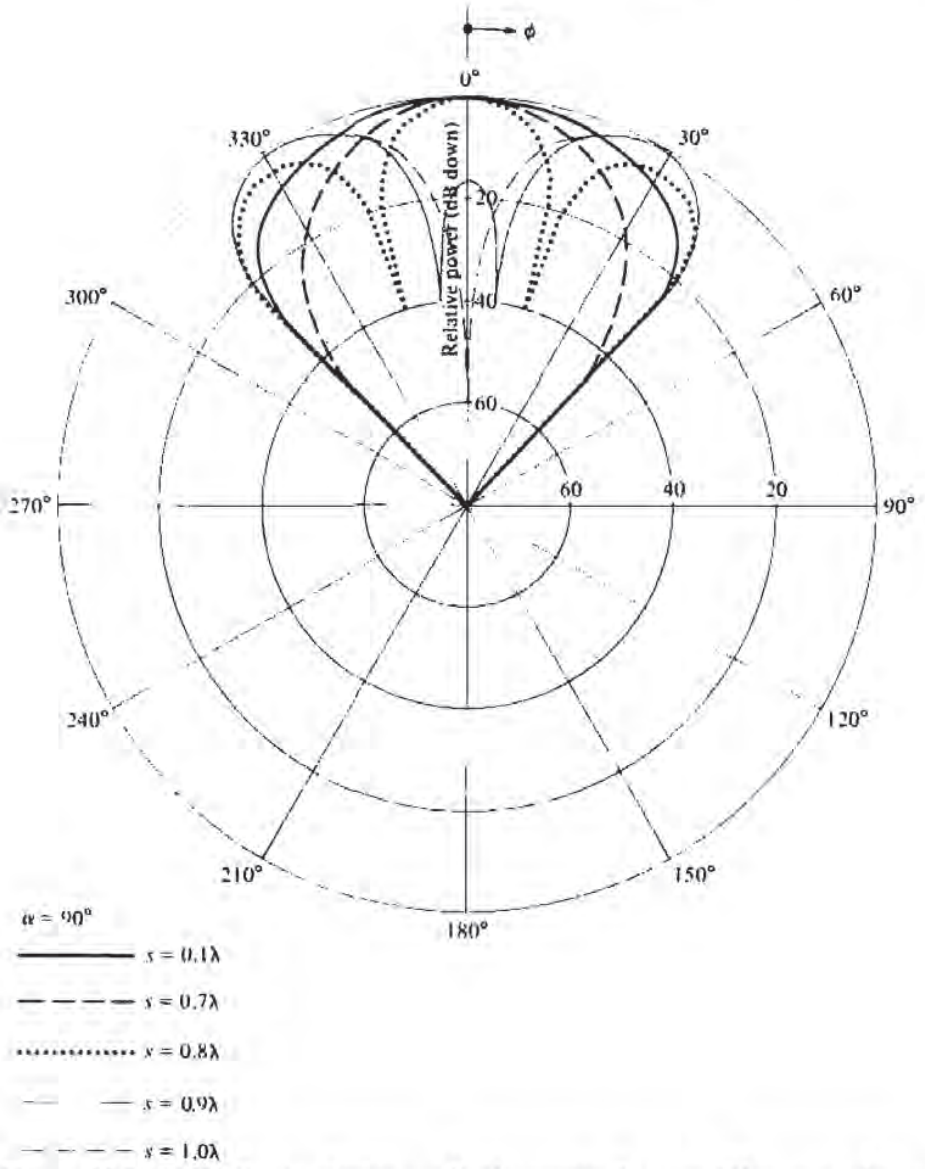


Figure 15.5 Normalized radiation amplitude patterns for $\alpha = 90°$ corner reflector.

$$\underline{\alpha = 60°}$$

$$\mathrm{AF}(\theta, \phi) = 4 \sin\left(\frac{X}{2}\right)\left[\cos\left(\frac{X}{2}\right) - \cos\left(\sqrt{3}\,\frac{Y}{2}\right)\right] \tag{15-7}$$

$$\underline{\alpha = 45°}$$

$$\mathrm{AF}(\theta, \phi) = 2\left[\cos(X) + \cos(Y) - 2\cos\left(\frac{X}{\sqrt{2}}\right)\cos\left(\frac{Y}{\sqrt{2}}\right)\right] \tag{15-8}$$

INTEL-1045
U.S. Patent 7,151,430

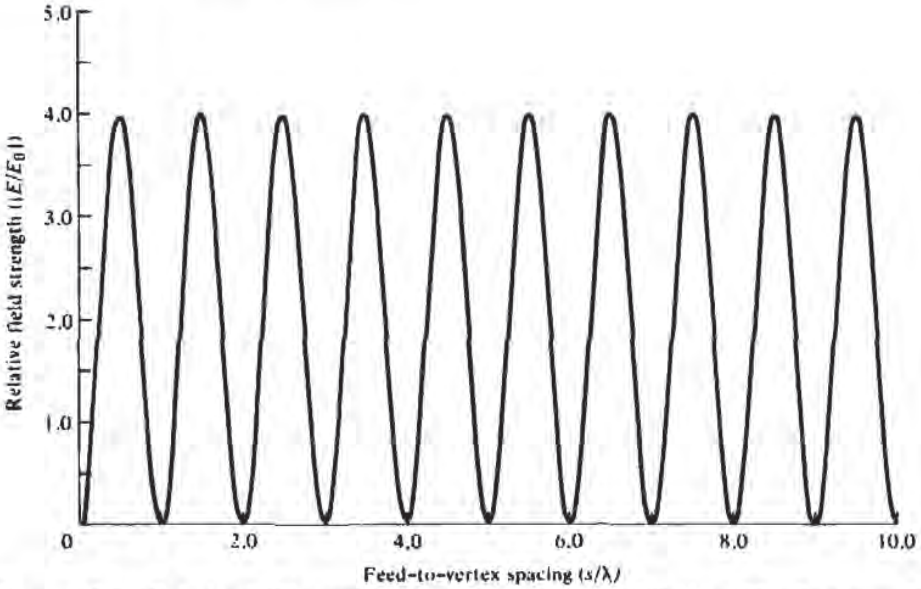


Figure 15.6 Relative field strength along the axis ($\theta = 90°$, $\phi = 0°$) of an $\alpha = 90°$ corner reflector as a function of feed-to-vertex spacing.

$$\underline{\alpha = 30°}$$

$$\mathrm{AF}(\theta, \phi) = 2\left[\cos(X) - 2\cos\left(\frac{\sqrt{3}}{2}X\right)\cos\left(\frac{Y}{2}\right) - \cos(Y) + 2\cos\left(\frac{X}{2}\right)\cos\left(\frac{\sqrt{3}}{2}Y\right)\right] \tag{15-9}$$

where

$$X = ks\sin\theta\cos\phi \tag{15-9a}$$

$$Y = ks\sin\theta\sin\phi \tag{15-9b}$$

These are assigned, at the end of the chapter, as exercises to the reader (Problem 15.2).

For a corner reflector with an included angle of $\alpha = 180°/n$, $n = 1, 2, 3, \ldots$, the number of images is equal to $N = (360/\alpha) - 1 \approx 2n - 1$.

It has also been shown [7] by using long filament wires as feeds, that the azimuthal plane ($\theta = \pi/2$) array factor for corner reflectors with $\alpha = 180°/n$, where n is an integer, can also be written as

n = even (n = 2, 4, 6, . . .)

$$\mathrm{AF}(\phi) = 4n(-1)^{n/2}[J_n(ks)\cos(n\phi) + J_{3n}(ks)\cos(3n\phi) + J_{5n}(ks)\cos(5n\phi) + \cdots] \tag{15-10a}$$

INTEL-1045
U.S. Patent 7,151,430

n = odd $(n = 1, 3, 5, \ldots)$

$$\mathrm{AF}(\phi) = 4nj(-1)^{(n-1)/2}[J_n(ks)\cos(n\phi) - J_{3n}(ks)\cos(3n\phi) + J_{5n}(ks)\cos(5n\phi) + \cdots] \quad (15\text{-}10b)$$

where $J_m(x)$ is the Bessel function of the first kind of order m (see Appendix V).

When n is not an integer, the field must be found by retaining a sufficient number of terms of the infinite series. It has also been shown [7] that for all values of $n = m$ (integral or fractional) that the field can be written as

$$\mathrm{AF}(\phi) = 4m[e^{jm\pi/2}J_m(ks)\cos(m\phi) + e^{j3m\pi/2}J_{3m}(ks)\cos(3m\phi) + \cdots] \quad (15\text{-}11)$$

The array factor for a corner reflector, as given by (15-10a)–(15-11), has a form that is similar to the array factor for a uniform circular array, as given by (6-121). This should be expected since the feed sources and their images in Figure 15.3 form a circular array. The number of images increase as the included angle of the corner reflector decreases.

Patterns have been computed for corner reflectors with included angles of 60°, 45°, and 30°. It has been found that these corner reflectors have also single-lobed patterns for the smaller values of s, and they become narrower as the included angle decreases. Multiple lobes begin to appear when

$$s \simeq 0.95\lambda \quad \text{for} \quad \alpha = 60°$$
$$s \simeq 1.2\lambda \quad \text{for} \quad \alpha = 45°$$
$$s \simeq 2.5\lambda \quad \text{for} \quad \alpha = 30°$$

The field strength along the axis of symmetry ($\theta = 90°$, $\phi = 0°$) as a function of the feed-to-vertex distance s, has been computed for reflectors with included angles of $\alpha = 60°$, 45°, and 30°. The results for $\alpha = 45°$ are shown in Figure 15.7 for $0 \le s \le 10\lambda$.

For reflectors with $\alpha = 90°$ and 60°, the normalized field strength is periodic with periods of λ and 2λ, respectively. However, for the 45° and 30° reflectors the normalized field is not periodic but rather "*almost periodic*" or "*pseudoperiodic*" [8]. For the 45° and 30° reflectors the arguments of the trigonometric functions representing the arrays factors, and given by (15-8)–(15-9b), are related by irrational numbers and therefore the arrays factors do not repeat. However, when plotted they look very similar. Therefore when examined only graphically, the observer erroneously may conclude that the patterns are periodic (because they look so much the same). However, when the array factors are examined analytically it is concluded that the functions are not periodic but rather nearly periodic. The field variations are "nearly similar" in form in the range $\Delta s = 16.69\lambda$ for the $\alpha = 45°$ and $\Delta s = 30\lambda$ for the $\alpha = 30°$. Therefore the array factors of (15-8) and (15-9) belong to the class of *nearly periodic functions* [8].

It has also been found that the maximum field strength increases as the included angle of the reflector decreases. This is expected since a smaller angle reflector exhibits better directional characteristics because of the narrowness of its angle. The maximum values of $|E/E_0|$ for $\alpha = 60°$, 45°, and 30° are approximately 5.2, 8, and 9, respectively. The first field strength peak, but not necessarily the ultimate maximum, is achieved when

$$s \simeq 0.65\lambda \quad \text{for} \quad \alpha = 60°$$
$$s \simeq 0.85\lambda \quad \text{for} \quad \alpha = 45°$$
$$s \simeq 1.20\lambda \quad \text{for} \quad \alpha = 30°$$

INTEL-1045
U.S. Patent 7,151,430

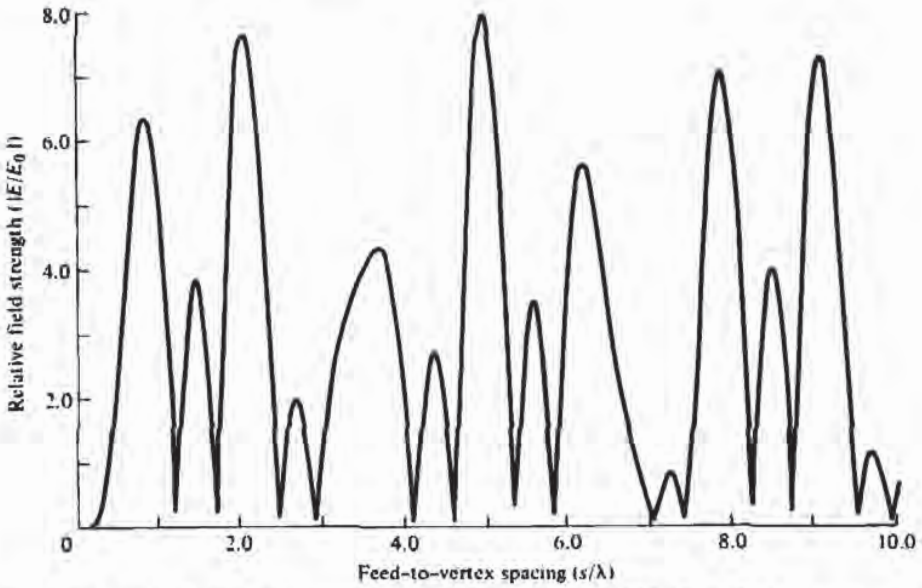


Figure 15.7 Relative field strength along the axis ($\theta = 90°$, $\phi = 0°$) for an $\alpha = 45°$ corner reflector as a function of feed-to-vertex spacing.

15.4 PARABOLIC REFLECTOR

The overall radiation characteristics (antenna pattern, antenna efficiency, polarization discrimination, etc.) of a reflector can be improved if the structural configuration of its surface is upgraded. It has been shown by geometrical optics that if a beam of parallel rays is incident upon a reflector whose geometrical shape is a parabola, the radiation will converge (focus) at a spot which is known as the *focal point*. In the same manner, if a point source is placed at the focal point, the rays reflected by a parabolic reflector will emerge as a parallel beam. This is one form of the principle of reciprocity, and it is demonstrated geometrically in Figure 15.1(c). The symmetrical point on the parabolic surface is known as the *vertex*. Rays that emerge in a parallel formation are usually said to be *collimated*. In practice, collimation is often used to describe the highly directional characteristics of an antenna even though the emanating rays are not exactly parallel. Since the transmitter (receiver) is placed at the focal point of the parabola, the configuration is usually known as *front fed*.

The disadvantage of the front-fed arrangement is that the transmission line from the feed must usually be long enough to reach the transmitting or the receiving equipment, which is usually placed behind or below the reflector. This may necessitate the use of long transmission lines whose losses may not be tolerable in many applications, especially in low-noise receiving systems. In some applications, the transmitting or receiving equipment is placed at the focal point to avoid the need for long transmission lines. However, in some of these applications, especially for transmission that may require large amplifiers and for low-noise receiving systems where cooling and weatherproofing may be necessary, the equipment may be too heavy and bulky and will provide undesirable blockage.

Another arrangement that avoids placing the feed (transmitter and/or receiver) at the focal point is that shown in Figure 15.1(d), and it is known as the *Cassegrain feed*. Through geometrical optics, Cassegrain, a famous astronomer (hence its name), showed that incident parallel rays can be focused to a point by utilizing two reflectors.

INTEL-1045
U.S. Patent 7,151,430

To accomplish this, the main (primary) reflector must be a parabola, the secondary reflector (subreflector) a hyperbola, and the feed placed along the axis of the parabola usually at or near the vertex. Cassegrain used this scheme to construct optical telescopes, and then its design was copied for use in radio frequency systems. For this arrangement, the rays that emanate from the feed illuminate the subreflector and are reflected by it in the direction of the primary reflector, as if they originated at the focal point of the parabola (primary reflector). The rays are then reflected by the primary reflector and are converted to parallel rays, provided the primary reflector is a parabola and the subreflector is a hyperbola. Diffractions occur at the edges of the subreflector and primary reflector, and they must be taken into account to accurately predict the overall system pattern, especially in regions of low intensity [9]–[11]. Even in regions of high intensity, diffractions must be included if an accurate formation of the fine ripple structure of the pattern is desired. With the Cassegrain-feed arrangement, the transmitting and/or receiving equipment can be placed behind the primary reflector. This scheme makes the system relatively more accessible for servicing and adjustments.

A parabolic reflector can take two different forms. One configuration is that of the parabolic right cylinder, shown in Figure 15.8(a), whose energy is collimated at a line that is parallel to the axis of the cylinder through the focal point of the reflector. The most widely used feed for this type of a reflector is a linear dipole, a linear array, or a slotted waveguide. The other reflector configuration is that of Figure 15.8(b) which is formed by rotating the parabola around its axis, and it is referred to as a *paraboloid* (parabola of revolution). A pyramidal or a conical horn has been widely utilized as a feed for this arrangement.

There are many other types of reflectors whose analysis is widely documented in the literature [12]–[14]. The spherical reflector, for example, has been utilized for radioastronomy and small earth station applications, because its beam can be efficiently scanned by moving its feed. An example of that is the 1,000-ft (305-m) diameter spherical reflector at Arecibo, Puerto Rico [12] whose primary surface is built into the ground and scanning of the beam is accomplished by movement of the feed. For spherical reflectors a substantial blockage may be provided by the feed leading to unacceptable minor lobe levels, in addition to the inherent reduction in gain and less favorable cross-polarization discrimination.

To eliminate some of the deficiencies of the symmetric configurations, offset-parabolic reflector designs have been developed for single- and dual-reflector systems

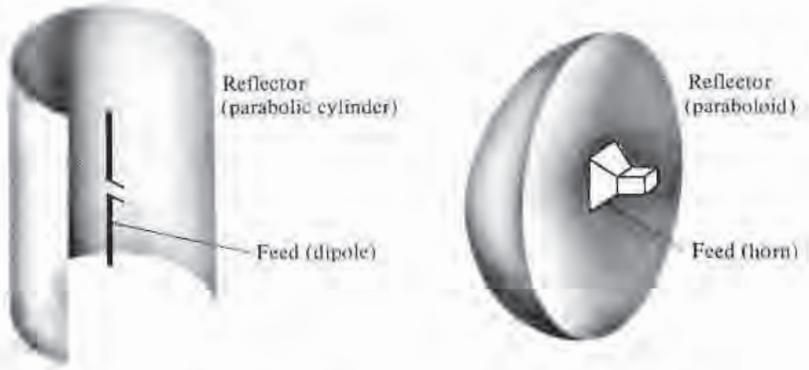


Figure 15.8 Parabolic right cylinder and paraboloid.

INTEL-1045
U.S. Patent 7,151,430

[13]. Because of the asymmetry of the system, the analysis is more complex. However the advent and advances of the computer technology have made the modeling and optimization of the offset reflector designs available and convenient. Offset reflector designs reduce aperture blocking and VSWR. In addition, they lead to the use of larger f/d ratios while maintaining acceptable structural rigidity, which provide an opportunity for improved feed-pattern shaping and better suppression of cross-polarized radiation emanating from the feed. However, offset-reflector configurations generate cross-polarized antenna radiation when illuminated by a linearly polarized primary-feed. Circularly polarized feeds eliminate depolarization, but they lead to squinting of the main beam from boresight. In addition, the structural asymmetry of the system is usually considered a major drawback.

Paraboloidal reflectors are the most widely used large aperture ground-based antennas [14]. At the time of its construction, the world's largest fully steerable reflector was the 100-m diameter radio telescope [15] of the Max Planck Institute for Radioastronomy at Effelsberg, West Germany, while the largest in the United States was the 64-m diameter [16] reflector at Goldstone, California built primarily for deep-space applications. When fed efficiently from the focal point, paraboloidal reflectors produce a high gain pencil beam with low side lobes and good cross-polarization discrimination characteristics. This type of an antenna is widely used for low-noise applications, such as in radioastronomy, and it is considered as a good compromise between performance and cost. To build a large reflector requires not only a large financial budget but also a difficult structural undertaking, because it must withstand severe weather conditions.

Cassegrain designs, employing dual reflector surfaces, are used in applications where pattern control is essential, such as in satellite ground-based systems, and have efficiencies of 65–80%. They supersede the performance of the single-reflector front-fed arrangement by about 10%. Using geometrical optics, the classical Cassegrain configuration, consisting of a paraboloid and a hyperboloid, is designed to achieve a uniform phase front in the aperture of the paraboloid. By employing good feed designs, this arrangement can achieve lower spillover and more uniform illumination of the main reflector. In addition, slight shaping of one or both of the dual-reflector's surfaces can lead to an aperture with almost uniform amplitude and phase with a substantial enhancement in gain [14]. These are referred to as *shaped* reflectors. Shaping techniques have been employed in dual-reflectors used in earth station applications. An example is the 10-m earth station dual-reflector antenna, shown in Figure 15.9, whose main reflector and subreflector are shaped.

For many years horns or waveguides, operating in a single mode, were used as feeds for reflector antennas. However because of radioastronomy and earth-station applications, considerable efforts have been placed in designing more efficient feeds to illuminate either the main reflector or the subreflector. It has been found that corrugated horns that support hybrid mode fields (combination of TE and TM modes) can be used as desirable feeds. Such feed elements match efficiently the fields of the feeds with the desired focal distribution produced by the reflector, and they can reduce cross-polarization. Dielectric cylinders and cones are other antenna structures that support hybrid modes [14]. Their structural configuration can also be used to support the subreflector and to provide attractive performance figures.

There are primarily two techniques that can be used to analyze the performance of a reflector system [17]. One technique is the *aperture distribution method* and the other the *current distribution method*. Both techniques will be introduced to show the similarities and differences.

INTEL-1045
U.S. Patent 7,151,430



Figure 15.9 Shaped 10-m earth station dual-reflector antenna (courtesy Andrew Corp.).

15.4.1 Front-Fed Parabolic Reflector

Parabolic cylinders have widely been used as high-gain apertures fed by line sources. The analysis of a parabolic cylinder (single curved) reflector is similar, but considerably simpler than that of a paraboloidal (double curved) reflector. The principal characteristics of aperture amplitude, phase, and polarization for a parabolic cylinder, as contrasted to those of a paraboloid, are as follows:

1. The amplitude taper, due to variations in distance from the feed to the surface of the reflector, is proportional to $1/\rho$ in a cylinder compared to $1/r^2$ in a paraboloid.
2. The focal region, where incident plane waves converge, is a line-source for a cylinder and a point source for a paraboloid.
3. When the fields of the feed are linearly polarized parallel to the axis of the cylinder, no cross-polarized components are produced by the parabolic cylinder. That is not the case for a paraboloid.

INTEL-1045
U.S. Patent 7,151,430

Generally, parabolic cylinders, as compared to paraboloids, (1) are mechanically simpler to build, (2) provide larger aperture blockage, and (3) do not possess the attractive characteristics of a paraboloid. In this chapter, only paraboloidal reflectors will be examined.

A. Surface Geometry

The surface of a paraboloidal reflector is formed by rotating a parabola about its axis. Its surface must be a paraboloid of revolution so that rays emanating from the focus of the reflector are transformed into plane waves. The design is based on optical techniques, and it does not take into account any deformations (diffractions) from the rim of the reflector. Referring to Figure 15.10 and choosing a plane perpendicular to the axis of the reflector through the focus, it follows that

$$OP + PQ = \text{constant} = 2f \tag{15-12}$$

Since

$$\begin{aligned} OP &= r' \\ PQ &= r' \cos\theta' \end{aligned} \tag{15-13}$$

(15-12) can be written as

$$r'(1 + \cos\theta') = 2f \tag{15-14}$$

or

$$\boxed{r' = \frac{2f}{1 + \cos\theta'} = f\sec^2\left(\frac{\theta'}{2}\right) \qquad \theta \le \theta_0} \tag{15-14a}$$

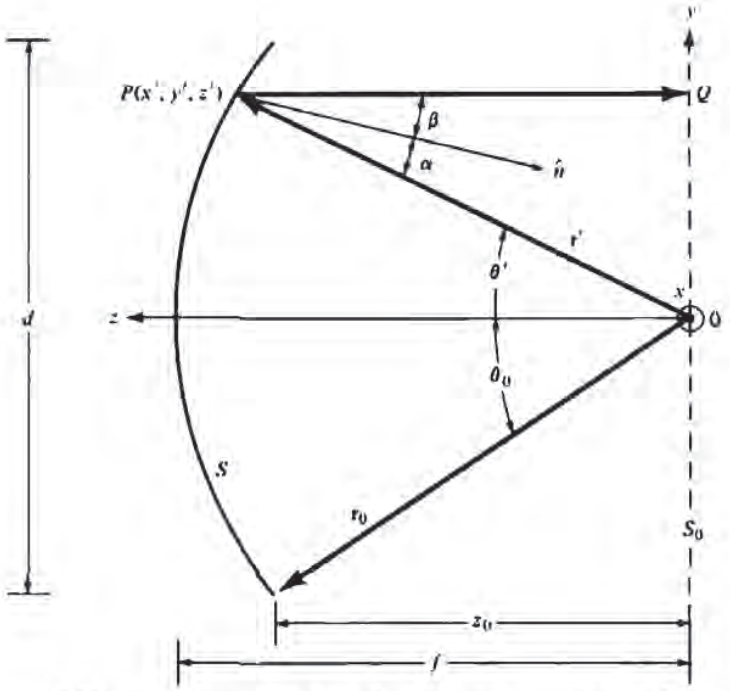


Figure 15.10 Two-dimensional configuration of a paraboloidal reflector.

INTEL-1045
U.S. Patent 7,151,430

Since a paraboloid is a parabola of revolution (about its axis), (15-14a) is also the equation of a paraboloid in terms of the spherical coordinates r', θ', ϕ'. Because of its rotational symmetry, there are no variations with respect to ϕ'.

Equation (15-14a) can also be written in terms of the rectangular coordinates x', y', z'. That is,

$$r' + r' \cos\theta' = \sqrt{(x')^2 + (y')^2 + (z')^2} + z' = 2f \tag{15-15}$$

or

$$(x')^2 + (y')^2 = 4f(f - z') \qquad \text{with } (x')^2 + (y')^2 \le (d/2)^2 \tag{15-15a}$$

In the analysis of parabolic reflectors, it is desirable to find a unit vector that is normal to the local tangent at the surface reflection point. To do this, (15-14a) is first expressed as

$$f - r' \cos^2\left(\frac{\theta'}{2}\right) = S = 0 \tag{15-16}$$

and then a gradient is taken to form a normal to the surface. That is,

$$\begin{aligned} \mathbf{N} = \nabla\left[f - r' \cos^2\left(\frac{\theta'}{2}\right)\right] &= \hat{\mathbf{a}}_{r'} \frac{\partial S}{\partial r'} + \hat{\mathbf{a}}_{\theta'} \frac{1}{r'} \frac{\partial S}{\partial \theta'} \\ &= -\hat{\mathbf{a}}_{r'} \cos^2\left(\frac{\theta'}{2}\right) + \hat{\mathbf{a}}_{\theta'} \cos\left(\frac{\theta'}{2}\right) \sin\left(\frac{\theta'}{2}\right) \end{aligned} \tag{15-17}$$

A unit vector, normal to S, is formed from (15-17) as

$$\hat{\mathbf{n}} = \frac{\mathbf{N}}{|\mathbf{N}|} = -\hat{\mathbf{a}}_{r'} \cos\left(\frac{\theta'}{2}\right) + \hat{\mathbf{a}}_{\theta'} \sin\left(\frac{\theta'}{2}\right) \tag{15-18}$$

To find the angle between the unit vector $\hat{\mathbf{n}}$ which is normal to the surface at the reflection point, and a vector directed from the focus to the reflection point, we form

$$\boxed{\begin{aligned} \cos\alpha = -\hat{\mathbf{a}}_{r'} \cdot \hat{\mathbf{n}} &= -\hat{\mathbf{a}}_{r'} \cdot \left[-\hat{\mathbf{a}}_{r'} \cos\left(\frac{\theta'}{2}\right) + \hat{\mathbf{a}}_{\theta'} \sin\left(\frac{\theta'}{2}\right)\right] \\ &= \cos\left(\frac{\theta'}{2}\right) \end{aligned}} \tag{15-19}$$

In a similar manner we can find the angle between the unit vector $\hat{\mathbf{n}}$ and the z-axis. That is,

$$\cos\beta = -\hat{\mathbf{a}}_z \cdot \hat{\mathbf{n}} = -\hat{\mathbf{a}}_z \cdot \left[-\hat{\mathbf{a}}_{r'} \cos\left(\frac{\theta'}{2}\right) + \hat{\mathbf{a}}_{\theta'} \sin\left(\frac{\theta'}{2}\right)\right] \tag{15-20}$$

Using the transformation of (4-5), (15-20) can be written as

$$\boxed{\begin{aligned} \cos\beta &= -(\hat{\mathbf{a}}_{r'} \cos\theta' - \hat{\mathbf{a}}_{\theta'} \sin\theta') \cdot \left[-\hat{\mathbf{a}}_{r'} \cos\left(\frac{\theta'}{2}\right) + \hat{\mathbf{a}}_{\theta'} \sin\left(\frac{\theta'}{2}\right)\right] \\ &= \cos\left(\frac{\theta'}{2}\right) \end{aligned}} \tag{15-21}$$

INTEL-1045
U.S. Patent 7,151,430

which is identical to α of (15-19). This is nothing more than a verification of Snell's law of reflection at each differential area of the surface, which has been assumed to be flat locally.

Another expression that is usually very prominent in the analysis of reflectors is that relating the subtended angle θ_0 to the f/d ratio. From the geometry of Figure 15.10

$$\theta_0 = \tan^{-1}\left(\frac{d/2}{z_0}\right) \tag{15-22}$$

where z_0 is the distance along the axis of the reflector from the focal point to the edge of the rim. From (15-15a)

$$z_0 = f - \frac{x_0^2 + y_0^2}{4f} = f - \frac{(d/2)^2}{4f} = f - \frac{d^2}{16f} \tag{15-23}$$

Substituting (15-23) into (15-22) reduces it to

$$\boxed{\theta_0 = \tan^{-1}\left|\frac{\frac{d}{2}}{f - \frac{d^2}{16f}}\right| = \tan^{-1}\left|\frac{\frac{1}{2}\left(\frac{f}{d}\right)}{\left(\frac{f}{d}\right)^2 - \frac{1}{16}}\right|} \tag{15-24}$$

It can also be shown that another form of (15-24) is

$$\boxed{f = \left(\frac{d}{4}\right)\cot\left(\frac{\theta_0}{2}\right)} \tag{15-25}$$

B. Induced Current Density

To determine the radiation characteristics (pattern, gain, efficiency, polarization, etc.) of a parabolic reflector, the current density induced on its surface must be known.

The current density $\mathbf{J}_s$ can be determined by using

$$\mathbf{J}_s = \hat{\mathbf{n}} \times \mathbf{H} = \hat{\mathbf{n}} \times (\mathbf{H}^i + \mathbf{H}^r) \tag{15-26}$$

where $\mathbf{H}^i$ and $\mathbf{H}^r$ represent, respectively, the incident and reflected magnetic field components evaluated at the surface of the conductor, and $\hat{\mathbf{n}}$ is a unit vector normal to the surface. If the reflecting surface can be approximated by an *infinite plane surface* (this condition is met locally for a parabola), then by the method of images

$$\hat{\mathbf{n}} \times \mathbf{H}^i = \hat{\mathbf{n}} \times \mathbf{H}^r \tag{15-27}$$

and (15-26) reduces to

$$\boxed{\mathbf{J}_s = \hat{\mathbf{n}} \times (\mathbf{H}^i + \mathbf{H}^r) = 2\hat{\mathbf{n}} \times \mathbf{H}^i = 2\hat{\mathbf{n}} \times \mathbf{H}^r} \tag{15-28}$$

The current density approximation of (15-28) is known as the *physical-optics* approximation, and it is valid when the transverse dimensions of the reflector, radius of curvature of the reflecting object, and the radius of curvature of the incident wave are large compared to a wavelength.

INTEL-1045
U.S. Patent 7,151,430

If the reflecting surface is in the far-field of the source generating the incident waves, then (15-28) can also be written as

$$\boxed{\mathbf{J}_s = 2\hat{\mathbf{n}} \times \mathbf{H}^i \simeq \frac{2}{\eta}[\hat{\mathbf{n}} \times (\hat{\mathbf{s}}_i \times \mathbf{E}^i)]} \tag{15-29}$$

or

$$\boxed{\mathbf{J}_s = 2\hat{\mathbf{n}} \times \mathbf{H}^r \simeq \frac{2}{\eta}[\hat{\mathbf{n}} \times (\hat{\mathbf{s}}_r \times \mathbf{E}^r)]} \tag{15-29a}$$

where η is the intrinsic impedance of the medium, $\hat{\mathbf{s}}_i$ and $\hat{\mathbf{s}}_r$ are radial unit vectors along the ray paths of the incident and reflected waves (as shown in Figure 15.11), and $\mathbf{E}^i$ and $\mathbf{E}^r$ are the incident and reflected electric fields.

C. Aperture Distribution Method

It was pointed out earlier that the two most commonly used techniques in analyzing the radiation characteristics of reflectors are the *aperture distribution* and the *current distribution* methods.

For the aperture distribution method, the field reflected by the surface of the paraboloid is first found over a plane which is normal to the axis of the reflector. Geometrical optics techniques (ray tracing) are usually employed to accomplish this. In most cases, the plane is taken through the focal point, and it is designated as the *aperture plane*, as shown in Figure 15.12. Equivalent sources are then formed over that plane. Usually it is assumed that the equivalent sources are zero outside the projected area of the reflector on the aperture plane. These equivalent sources are then used to compute the radiated fields utilizing the aperture techniques of Chapter 12.

For the *current distribution method*, the physical optics approximation of the induced current density $\mathbf{J}_s$ given by (15-28) ($\mathbf{J}_s = 2\hat{\mathbf{n}} \times \mathbf{H}^i$ where $\mathbf{H}^i$ is the incident magnetic field and $\hat{\mathbf{n}}$ is a unit vector normal to the reflector surface) is formulated over the illuminated side of the reflector (S_1) of Figure 15.11. This current density is then integrated over the surface of the reflector to yield the far-zone radiation fields.

For the reflector of Figure 15.11, approximations that are common to both methods are:

1. The current density is zero on the shadow side (S_2) of the reflector.
2. The discontinuity of the current density over the rim (Γ) of the reflector is neglected.
3. Direct radiation from the feed and aperture blockage by the feed are neglected.

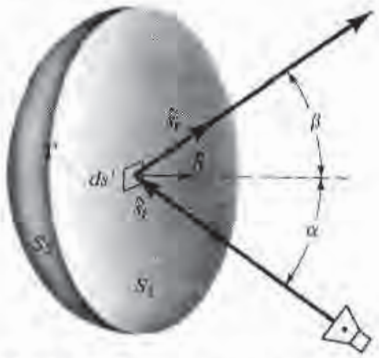


Figure 15.11 Reflecting surface with boundary Γ.

INTEL-1045
U.S. Patent 7,151,430

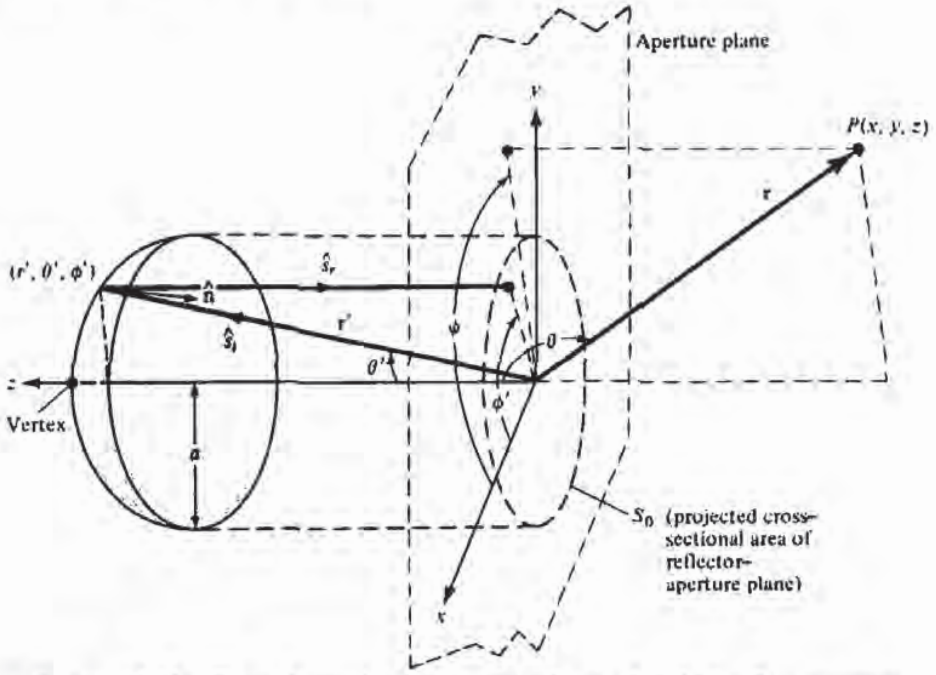


Figure 15.12 Three-dimensional geometry of a paraboloidal reflector system.

These approximations lead to accurate results, using either technique, for the radiated fields on the main beam and nearby minor lobes. To predict the pattern more accurately in all regions, especially the far minor lobes, geometrical diffraction techniques [9]–[11] can be applied. Because of the level of the material, it will not be included here. The interested reader can refer to the literature.

The advantage of the aperture distribution method is that the integration over the aperture plane can be performed with equal ease for any feed pattern or feed position [18]. The integration over the surface of the reflector as required for the current distribution method, becomes quite complex and time consuming when the feed pattern is asymmetrical and/or the feed is placed off-axis.

Let us assume that a y-polarized source with a gain function of $G_f(\theta', \phi')$ is placed at the focal point of a paraboloidal reflector. The radiation intensity of this source is given by

$$U(\theta', \phi') = \frac{P_t}{4\pi} G_f(\theta', \phi') \tag{15-30}$$

where P_t is the total radiated power. Referring to Figure 15.12, at a point r' in the far-zone of the source

$$U(\theta', \phi') = \frac{1}{2}\text{Re}[\mathbf{E}^{\circ}(\theta', \phi') \times \mathbf{H}^{\circ *}(\theta', \phi')] = \frac{1}{2\eta}|\mathbf{E}^{\circ}(\theta', \phi')|^2 \tag{15-31}$$

or

$$|\mathbf{E}^{\circ}(\theta', \phi')| = [2\eta\, U(\theta', \phi')]^{1/2} = \left[\eta \frac{P_t}{2\pi} G_f(\theta', \phi')\right]^{1/2} \tag{15-31a}$$

INTEL-1045
U.S. Patent 7,151,430

The incident field, with a direction perpendicular to the radial distance, can then be written as

$$\mathbf{E}^i(r', \theta', \phi') = \hat{\mathbf{e}}_i \left[\sqrt{\frac{\mu}{\epsilon}} \frac{P_t}{2\pi} G_f(\theta', \phi') \right]^{1/2} \frac{e^{-jkr'}}{r'} = \hat{\mathbf{e}}_i C_1 \sqrt{G_f(\theta', \phi')} \frac{e^{-jkr'}}{r'} \tag{15-32}$$

$$C_1 = \left(\frac{\mu}{\epsilon}\right)^{1/4} \left(\frac{P_t}{2\pi}\right)^{1/2} \tag{15-32a}$$

where $\hat{\mathbf{e}}_i$ is a unit vector perpendicular to $\hat{\mathbf{a}}_r'$ and parallel to the plane formed by $\hat{\mathbf{a}}_r'$ and $\hat{\mathbf{a}}_y$, as shown in Figure 15.13.

It can be shown [19] that on the surface of the reflector

$$\mathbf{J}_s = 2\sqrt{\frac{\epsilon}{\mu}} [\hat{\mathbf{n}} \times (\hat{\mathbf{s}}_i \times \mathbf{E}^i)] = 2\sqrt{\frac{\epsilon}{\mu}} C_1 \sqrt{G_f(\theta', \phi')} \frac{e^{-jkr'}}{r'} \mathbf{u} \tag{15-33}$$

where

$$\mathbf{u} = \hat{\mathbf{n}} \times (\hat{\mathbf{a}}_r' \times \hat{\mathbf{e}}_i) = (\hat{\mathbf{n}} \cdot \hat{\mathbf{e}}_i)\hat{\mathbf{a}}_r' - (\hat{\mathbf{n}} \cdot \hat{\mathbf{a}}_r')\hat{\mathbf{e}}_i \tag{15-33a}$$

which reduces to

$$\begin{aligned} \mathbf{u} = \Bigg[& - \hat{\mathbf{a}}_x \sin\theta' \sin\left(\frac{\theta'}{2}\right) \sin\phi' \cos\phi' \\ & + \hat{\mathbf{a}}_y \cos\left(\frac{\theta'}{2}\right) (\sin^2\phi' \cos\theta' + \cos^2\phi') \\ & - \hat{\mathbf{a}}_z \cos\theta' \sin\phi' \sin\left(\frac{\theta'}{2}\right) \Bigg] \Big/ \sqrt{1 - \sin^2\theta' \sin^2\phi'} \end{aligned} \tag{15-34}$$

To find the aperture field $\mathbf{E}_{ap}$ at the plane through the focal point, due to the reflector currents of (15-33), the reflected field $\mathbf{E}^r$ at r' (the reflection point) is first found. This is of the form

$$\mathbf{E}^r = \hat{\mathbf{e}}_r C_1 \sqrt{G_f(\theta', \phi')} \frac{e^{-jkr'}}{r'} \tag{15-35}$$

where $\hat{\mathbf{e}}_r$ is a unit vector depicting the polarization of the reflected field. From (15-29a)

$$\mathbf{J}_s = 2\sqrt{\frac{\epsilon}{\mu}} [\hat{\mathbf{n}} \times (\hat{\mathbf{s}}_r \times \mathbf{E}^r)] \tag{15-36}$$

Because $\hat{\mathbf{s}}_r = -\hat{\mathbf{a}}_z$, (15-36) can be written, using (15-35), as

$$\mathbf{J}_s = 2\sqrt{\frac{\epsilon}{\mu}} C_1 \sqrt{G_f(\theta', \phi')} \frac{e^{-jkr'}}{r'} \mathbf{u} \tag{15-37}$$

where

$$\mathbf{u} = \hat{\mathbf{n}} \times (-\hat{\mathbf{a}}_z \times \hat{\mathbf{e}}_r) = -\hat{\mathbf{a}}_z(\hat{\mathbf{n}} \cdot \hat{\mathbf{e}}_r) - \hat{\mathbf{e}}_r \cos\left(\frac{\theta'}{2}\right) \tag{15-37a}$$

INTEL-1045
U.S. Patent 7,151,430

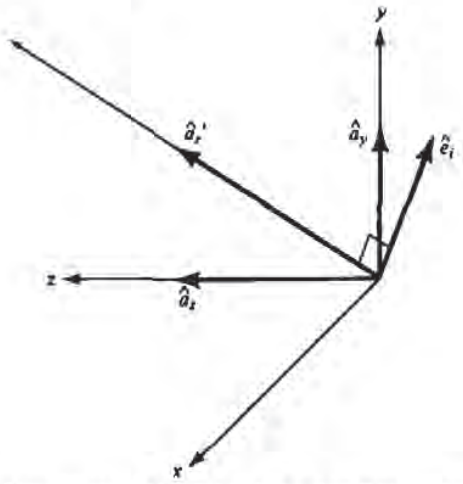


Figure 15.13 Unit vector alignment for a paraboloidal reflector system.

Since **u** in (15-37) and (15-37a) is the same as that of (15-33)–(15-34), it can be shown [19] through some extensive mathematical manipulations that

$$\hat{\mathbf{e}}_r = \frac{\hat{\mathbf{a}}_x \sin\phi' \cos\phi' (1 - \cos\theta') - \hat{\mathbf{a}}_y (\sin^2\phi' \cos\theta' + \cos^2\phi')}{\sqrt{1 - \sin^2\theta' \sin^2\phi'}} \tag{15-38}$$

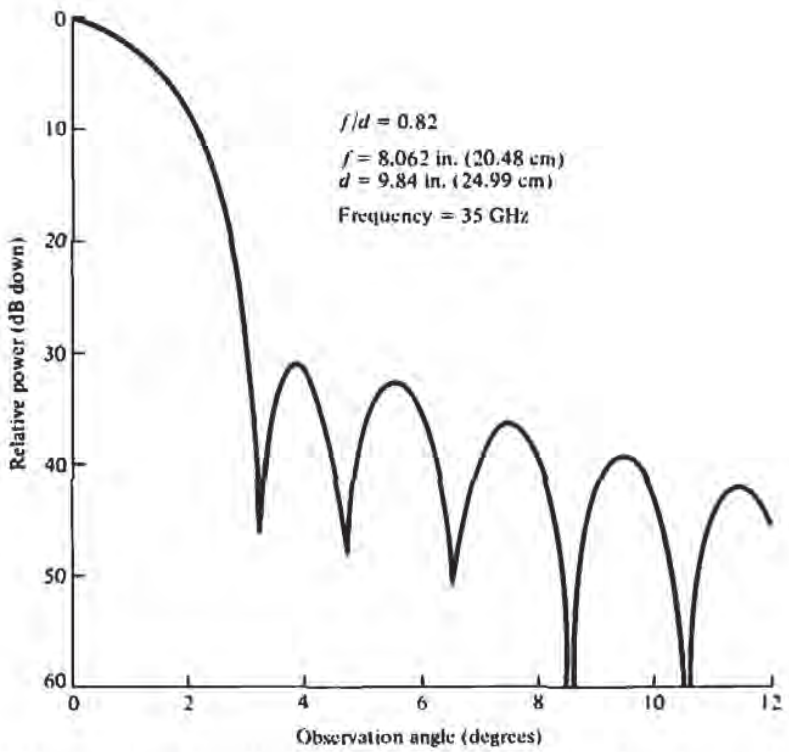


Figure 15.14 Principal *E*- or *H*-plane pattern of a symmetrical front-fed paraboloidal reflector (courtesy M. C. Bailey, NASA Langley Research Center).

INTEL-1045
U.S. Patent 7,151,430

Thus the field $\mathbf{E}^r$ at the point of reflection r' is given by (15-35) where $\hat{\mathbf{e}}_r$ is given by (15-38). At the plane passing through the focal point, the field is given by

$$\mathbf{E}_{ap} = \hat{\mathbf{e}}_r C_1 \sqrt{G_f(\theta', \phi')}\, \frac{e^{-jkr'(1+\cos\theta')}}{r'} = \hat{\mathbf{a}}_x E_{xa} + \hat{\mathbf{a}}_y E_{ya} \tag{15-39}$$

where E_{xa} and E_{ya} represent the x- and y-components of the reflected field over the aperture. Since the field from the reflector to the aperture plane is a plane wave, no correction in amplitude is needed to account for amplitude spreading.

Using the reflected electric field components (E_{xa} and E_{ya}) as given by (15-39), an equivalent is formed at the aperture plane. That is,

$$\mathbf{J}_s' = \hat{\mathbf{n}} \times \mathbf{H}_a = -\hat{\mathbf{a}}_z \times \left(\hat{\mathbf{a}}_x \frac{E_{ay}}{\eta} - \hat{\mathbf{a}}_y \frac{E_{ax}}{\eta}\right) = -\hat{\mathbf{a}}_x \frac{E_{ax}}{\eta} - \hat{\mathbf{a}}_y \frac{E_{ay}}{\eta} \tag{15-40a}$$

$$\mathbf{M}_s' = -\hat{\mathbf{n}} \times \mathbf{E}_a = +\hat{\mathbf{a}}_z \times (\hat{\mathbf{a}}_x E_{ax} + \hat{\mathbf{a}}_y E_{ay}) = -\hat{\mathbf{a}}_x E_{ay} + \hat{\mathbf{a}}_y E_{ax} \tag{15-40b}$$

The radiated field can be computed using the (15-40a), (15-40b), and the formulations of Section 12.3. The integration is restricted only over the projected cross-sectional area S_0 of the reflector at the aperture plane shown dashed in Figure 15.12. That is,

$$E_{\theta s} = \frac{jke^{-jkr}}{4\pi r}(1 + \cos\theta) \iint_{S_0} (-E_{ax}\cos\phi - E_{ay}\sin\phi) \times e^{jk(x'\sin\theta\cos\phi + y'\sin\theta\sin\phi)}\, dx'\, dy' \tag{15-41a}$$

$$E_{\phi s} = \frac{jke^{-jkr}}{4\pi r}(1 + \cos\theta) \iint_{S_0} (-E_{ax}\sin\phi + E_{ay}\cos\phi) \times e^{jk(x'\sin\theta\cos\phi + y'\sin\theta\sin\phi)}\, dx'\, dy' \tag{15-41b}$$

The aperture distribution method has been used to compute, using efficient numerical integration techniques, the radiation patterns of paraboloidal [18] and spherical [20] reflectors. The fields given by (15-41a) and (15-41b) represent only the secondary pattern due to scattering from the reflector. The total pattern of the system is represented by the sum of secondary pattern and the primary pattern of the feed element. For most feeds (such as horns), the primary pattern in the boresight (forward) direction of the reflector is of very low intensity and usually can be neglected.

To demonstrate the utility of the techniques, the principal E- and H-plane secondary patterns of a 35 GHz reflector, with an $f/d = 0.82$ [$f = 8.062$ in. (20.48 cm), $d = 9.84$ in. (24.99 cm)] and fed by a conical dual-mode horn, were computed and they are displayed in Figure 15.14. Since the feed horn has identical E- and H-plane patterns and the reflector is fed symmetrically, the reflector E- and H-plane patterns are also identical and do not possess any cross-polarized components.

To simultaneously display the field intensity associated with each point in the aperture plane of the reflector, a computer generated plot was developed [20]. The field point locations, showing quantized contours of constant amplitude in the aperture plane, are illustrated in Figure 15.15. The reflector system has an $f/d = 0.82$ with the same physical dimensions [$f = 8.062$ in. (20.48 cm), $d = 9.84$ in. (24.99 cm)] and the same feed as the principal pattern of Figure 15.14. One symbol is used to represent the amplitude level of each 3-dB region. The field intensity within the bounds of the reflector aperture plane is within the 0–15 dB range.

INTEL-1045
U.S. Patent 7,151,430

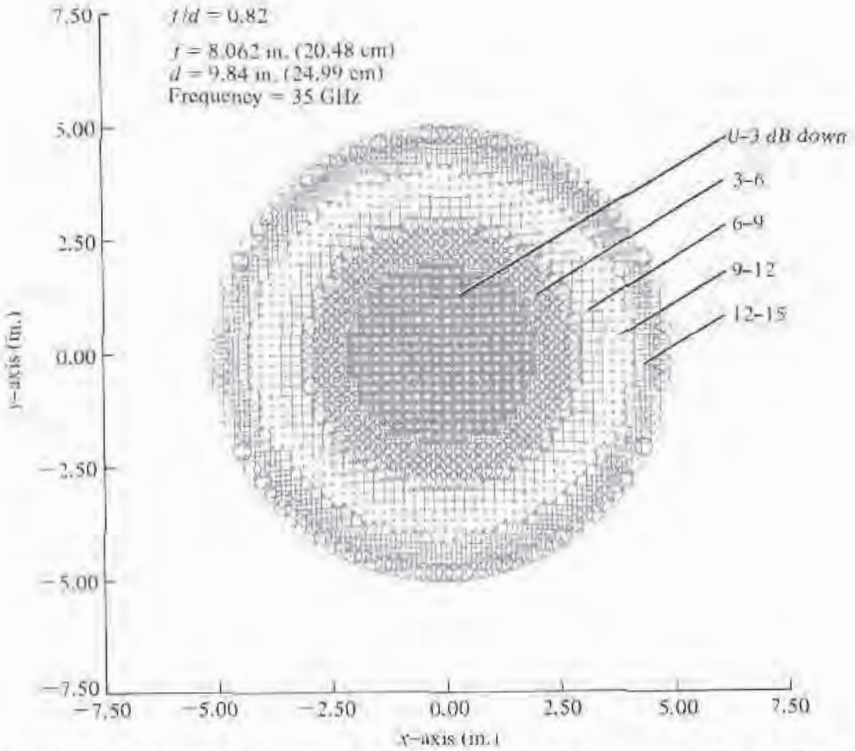


Figure 15.15 Field point locations of constant amplitude contours in the aperture plane of a symmetrical front-fed paraboloidal reflector (courtesy M. C. Bailey, NASA Langley Research Center).

D. Cross-Polarization

The field reflected by the paraboloid, as represented by (15-35) and (15-38) of the aperture distribution method, contains x- and y-polarized components when the incident field is y-polarized. The y-component is designated as the *principal polarization* and the x-component as the *cross-polarization*. This is illustrated in Figure 15.16. It is also evident that symmetrical (with respect to the principal planes) cross-polarized components are 180° out of phase with one another. However for very narrow beam reflectors or for angles near the boresight axis ($\theta' = 0°$), the cross-polarized x-component diminishes and it vanishes on axis ($\theta' = 0°$). A similar procedure can be used to show that for an incident x-polarized field, the reflecting surface decomposes the wave to a y-polarized field, in addition to its x-polarized component.

An interesting observation about the polarization phenomenon of a parabolic reflector can be made if we first assume that the feed element is an infinitesimal electric dipole ($l \ll \lambda$) with its length along the y-axis. For that feed, the field reflected by the reflector is given by (15-35) where from (4-114)

$$C_1\sqrt{G_f(\theta', \phi')} = j\eta\frac{kI_0l}{4\pi}\sin\psi = j\eta\frac{kI_0l}{4\pi}\sqrt{1-\cos^2\psi} \qquad (15\text{-}42)$$
$$= j\eta\frac{kI_0l}{4\pi}\sqrt{1-\sin^2\theta'\sin^2\phi'}$$

The angle ψ is measured from the y-axis toward the observation point.

INTEL-1045
U.S. Patent 7,151,430

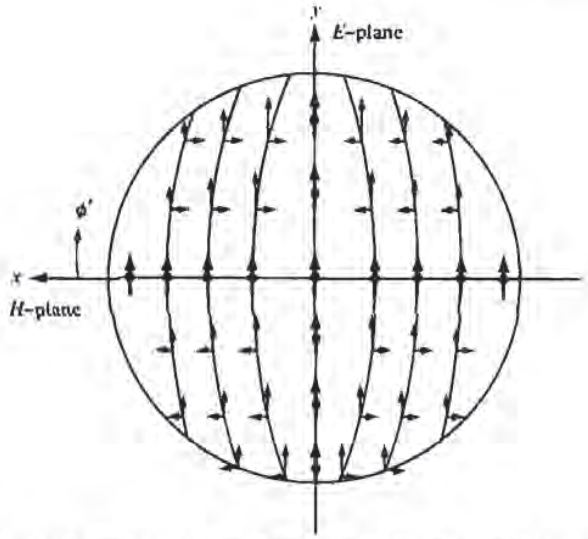


Figure 15.16 Principal (y-direction) and cross-polarization (x-direction) components of a paraboloidal reflector. (SOURCE: S. Silver (ed.), *Microwave Antenna Theory and Design* (MIT Radiation Lab. Series, Vol. 12), McGraw-Hill, New York, 1949)

When (15-42) is inserted in (15-35), we can write with the aid of (15-38) that

$$\mathbf{E}^r = [\hat{\mathbf{a}}_x \sin\phi' \cos\phi'(1 - \cos\theta') - \hat{\mathbf{a}}_y(\sin^2\phi' \cos\theta' + \cos^2\phi')] \times j\eta \frac{kI_0 l}{4\pi} \frac{e^{-jkr'}}{r'} \tag{15-43}$$

Now let us assume that an infinitesimal magnetic dipole, with its length along the x-axis (or a small loop with its area parallel to the y-z plane) and with a magnetic moment of $-\hat{\mathbf{a}}_x M$, is placed at the focal point and used as a feed. It can be shown [21]–[23] that the field reflected by the reflector has x- and y-components. However the x-component has a reverse sign to the x-component of the electric dipole feed. By adjusting the ratio of the electric to the magnetic dipole moments to be equal to $\sqrt{\mu/\epsilon}$, the two cross-polarized reflected components (x-components) can be made equal in magnitude and for their sum to vanish (because of reverse signs). Thus a cross electric and magnetic dipole combination located at the focal point of a paraboloid can be used to induce currents on the surface of the reflector which are parallel everywhere. This is illustrated graphically in Figure 15.17.

The direction of the induced current flow determines the far-field polarization of the antenna. Thus for the crossed electric and magnetic dipole combination feed, the far-field radiation is free of cross-polarization. This type of feed is "ideal" in that it does not require that the surface of the reflector be solid but can be formed by closely spaced parallel conductors. Because of its ideal characteristics, it is usually referred to as a *Huygens' source.*

E. Current Distribution Method

The current distribution method was introduced as a technique that can be used to better approximate, as compared to the geometrical-optics (ray-tracing) method, the field scattered from a surface. Usually the main difficulty in applying this method is the approximation of the current density over the surface of the scatterer.

INTEL-1045
U.S. Patent 7,151,430

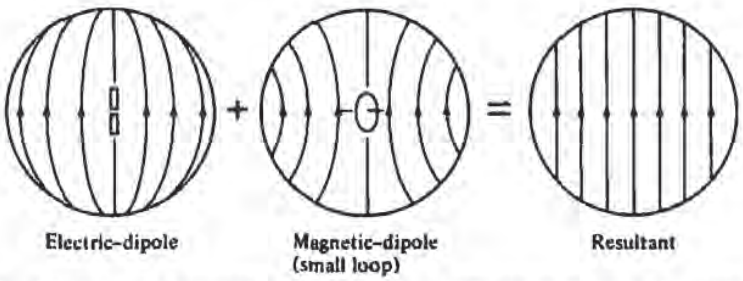


Figure 15.17 Electric and magnetic dipole fields combined to form a Huygens' source with ideal feed polarization for reflector. (SOURCE: A. W. Love, "Some Highlights in Reflector Antenna Development," *Radio Science*, Vol. 11, Nos. 8, 9, August–September 1976)

To analyze the reflector using this technique, we refer to the radiation integrals and auxiliary potential functions formulations of Chapter 3. While the two-step procedure of Figure 3.1 often simplifies the solution of most problems, the one-step formulation of Figure 3.1 is most convenient for the reflectors.

Using the potential function methods outlined in Chapter 3, and referring to the coordinate system of Figure 12.2(a), it can be shown [17] that the **E**- and **H**-fields radiated by the sources **J** and **M** can be written as

$$\mathbf{E} = \mathbf{E}_A + \mathbf{E}_F = -j\frac{1}{4\pi\omega\epsilon}\int_V [(\mathbf{J}\cdot\nabla)\nabla + k^2\mathbf{J} + j\omega\epsilon\mathbf{M}\times\nabla]\frac{e^{-jkR}}{R}dv' \tag{15-44a}$$

$$\mathbf{H} = \mathbf{H}_A + \mathbf{H}_F = -j\frac{1}{4\pi\omega\mu}\int_V [(\mathbf{M}\cdot\nabla)\nabla + k^2\mathbf{M} - j\omega\mu\mathbf{J}\times\nabla]\frac{e^{-jkR}}{R}dv' \tag{15-44b}$$

which for far-field observations reduce, according to the coordinate system of Figure 12.2(b), to

$$\mathbf{E} \simeq -j\frac{\omega\mu}{4\pi r}e^{-jkr}\int_V \left[\mathbf{J} - (\mathbf{J}\cdot\hat{\mathbf{a}}_r)\hat{\mathbf{a}}_r + \sqrt{\frac{\epsilon}{\mu}}\mathbf{M}\times\hat{\mathbf{a}}_r\right]e^{+jk\mathbf{r}'\cdot\hat{\mathbf{a}}_r}dv' \tag{15-45a}$$

$$\mathbf{H} \simeq -j\frac{\omega\epsilon}{4\pi r}e^{-jkr}\int_V \left[\mathbf{M} - (\mathbf{M}\cdot\hat{\mathbf{a}}_r)\hat{\mathbf{a}}_r - \sqrt{\frac{\mu}{\epsilon}}\mathbf{J}\times\hat{\mathbf{a}}_r\right]e^{+jk\mathbf{r}'\cdot\hat{\mathbf{a}}_r}dv' \tag{15-45b}$$

If the current distributions are induced by electric and magnetic fields incident on a perfect electric conducting ($\sigma = \infty$) surface shown in Figure 15.18, the fields created by these currents are referred to as *scattered fields*. If the conducting surface is closed, the far-zone fields are obtained from (15-45a) and (15-45b) by letting $\mathbf{M} = 0$ and reducing the volume integral to a surface integral with the surface current density **J** replaced by the linear current density $\mathbf{J}_s$. Thus

$$\mathbf{E}_s = -j\frac{\omega\mu}{4\pi r}e^{-jkr}\iint_S [\mathbf{J}_s - (\mathbf{J}_s\cdot\hat{\mathbf{a}}_r)\hat{\mathbf{a}}_r]e^{+jk\mathbf{r}'\cdot\hat{\mathbf{a}}_r}ds' \tag{15-46a}$$

$$\mathbf{H}_s = +j\frac{\omega\sqrt{\mu\epsilon}}{4\pi r}e^{-jkr}\iint_S [\mathbf{J}_s\times\hat{\mathbf{a}}_r]e^{+jk\mathbf{r}'\cdot\hat{\mathbf{a}}_r}ds' \tag{15-46b}$$

INTEL-1045
U.S. Patent 7,151,430

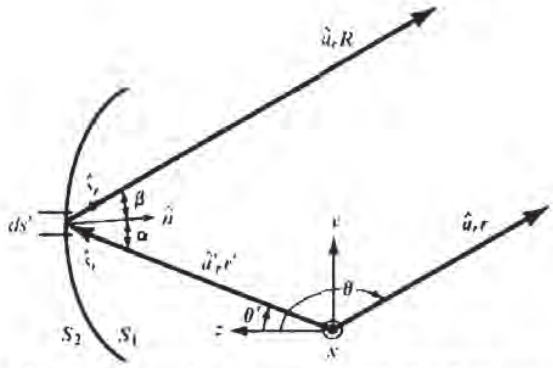


Figure 15.18 Geometrical arrangement of reflecting surface.

The electric and magnetic fields scattered by the closed surface of the reflector of Figure 15.11, and given by (15-46a) and (15-46b), are valid provided the source-density functions (current and charge) satisfy the equation of continuity. This would be satisfied if the scattering object is a smooth closed surface. For the geometry of Figure 15.11, the current distribution is discontinuous across the boundary Γ (being zero over the shadow area S_2) which divides the illuminated (S_1) and shadow (S_2) areas. It can be shown [17] that the equation of continuity can be satisfied if an appropriate line source distribution of charge is introduced along the boundary Γ. Therefore the total scattered field would be the sum of the (1) surface currents over the illuminated area, (2) surface charges over the illuminated area, and (3) line charge distribution over the boundary Γ.

The contributions from the surface charge density are taken into account by the current distribution through the equation of continuity. However it can be shown [17] that in the far-zone the contribution due to line-charge distribution cancels out the longitudinal component introduced by the surface current and charge distributions. Since in the far-zone the field components are predominantly transverse, the contribution due to the line-charge distribution need not be included and (15-46a)–(15-46b) can be applied to an open surface.

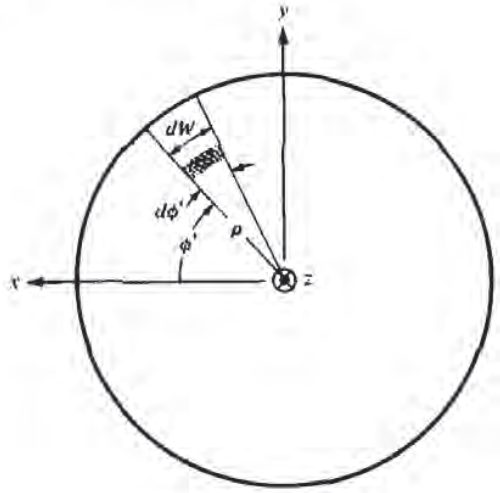
In this section, (15-46a) and (15-46b) will be used to calculate the field scattered from the surface of a parabolic reflector. Generally the field radiated by the currents on the shadow region of the reflector is very small compared to the total field, and the currents and field can be set equal to zero. The field scattered by the illuminated (concave) side of the parabolic reflector can be formulated, using the current distribution method, by (15-46a) and (15-46b) when the integration is restricted over the illuminated area.

The total field of the system can be obtained by a superposition of the radiation from the primary source in directions greater than θ_0 ($\theta > \theta_0$) and that scattered by the surface as obtained by using either the aperture distribution or the current distribution method.

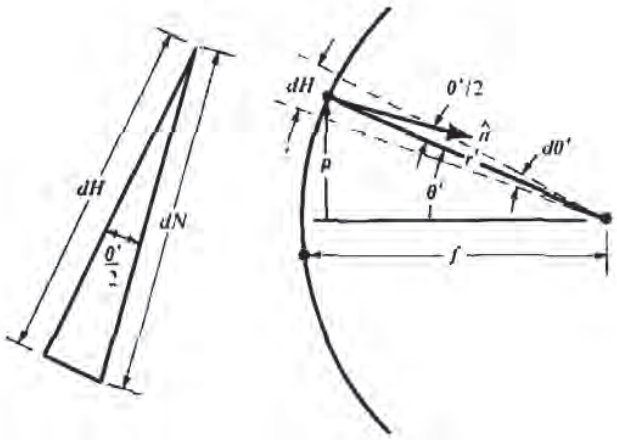
Generally edge effects are neglected. However the inclusion of diffracted fields [9]–[11] from the rim of the reflector not only introduce fields in the shadow region of the reflector, but also modify those present in the transition and lit regions. Any discontinuities introduced by geometrical optics methods along the transition region (between lit and shadow regions) are removed by the diffracted components.

The far-zone electric field of a parabolic reflector, neglecting the direct radiation, is given by (15-46a). When expanded, (15-46a) reduces, by referring to the geometry of Figure 15.18, to the two components of

INTEL-1045
U.S. Patent 7,151,430



(a) Projected cross section



(b) Side-view

Figure 15.19 Projected cross section and side view of reflector.

$$E_\theta = -j\frac{\omega\mu}{4\pi r}e^{-jkr}\iint_{S_1}\hat{\mathbf{a}}_\theta \cdot \mathbf{J}_s e^{+jkr'\cdot\hat{\mathbf{a}}_{r'}}\,ds' \tag{15-47a}$$

$$E_\phi = -j\frac{\omega\mu}{4\pi r}e^{-jkr}\iint_{S_1}\hat{\mathbf{a}}_\phi \cdot \mathbf{J}_s e^{+jkr'\cdot\hat{\mathbf{a}}_{r'}}\,ds' \tag{15-47b}$$

According to the geometry of Figure 15.19

$$ds' = dW\,dN = (r'\sin\theta'\,d\phi')\left[r'\sec\left(\frac{\theta'}{2}\right)d\theta'\right]$$

$$= (r')^2\sin\theta'\sec\left(\frac{\theta'}{2}\right)d\theta'\,d\phi' \tag{15-48}$$

INTEL-1045
U.S. Patent 7,151,430

since

$$dW = r' \sin\theta'\, d\phi' \tag{15-48a}$$

$$dH = -\hat{\mathbf{a}}_r' \cdot d\mathbf{N} = -\hat{\mathbf{a}}_r' \cdot \hat{\mathbf{n}}\, dN$$

$$= -\hat{\mathbf{a}}_r' \cdot \left[-\hat{\mathbf{a}}_r' \cos\left(\frac{\theta'}{2}\right) + \hat{\mathbf{a}}_\theta' \sin\left(\frac{\theta'}{2}\right)\right] dN = \cos\left(\frac{\theta'}{2}\right) dN \tag{15-48b}$$

$$dN = \sec\left(\frac{\theta'}{2}\right) dH = \sec\left(\frac{\theta'}{2}\right) r'\, d\theta' = r' \sec\left(\frac{\theta'}{2}\right) d\theta' \tag{15-48c}$$

Therefore, it can be shown that (15-47a) and (15-47b) can be expressed, with the aid of (15-37), (15-37a), and (15-48), as

$$\begin{bmatrix} E_\theta \\ E_\phi \end{bmatrix} = -j\frac{\omega\mu}{2\pi r}\sqrt{\frac{\epsilon}{\mu}}\, C_1 e^{-jkr} \begin{bmatrix} \hat{\mathbf{a}}_\theta \cdot \mathbf{I} \\ \hat{\mathbf{a}}_\phi \cdot \mathbf{I} \end{bmatrix}$$

$$= -j\frac{\omega\mu e^{-jkr}}{2\pi r}\left[\sqrt{\frac{\epsilon}{\mu}}\frac{P_t}{2\pi}\right]^{1/2} \begin{bmatrix} \hat{\mathbf{a}}_\theta \cdot \mathbf{I} \\ \hat{\mathbf{a}}_\phi \cdot \mathbf{I} \end{bmatrix} \tag{15-49}$$

where

$$\mathbf{I} = \mathbf{I}_t + \mathbf{I}_z \tag{15-49a}$$

$$\mathbf{I}_t = -\int_0^{2\pi}\int_0^{\theta_0} \hat{\mathbf{e}}_r \cos\left(\frac{\theta'}{2}\right) \frac{\sqrt{G_f(\theta', \phi')}}{r'} e^{-jkr'[1 - \sin\theta'\sin\theta\cos(\phi' - \phi) - \cos\theta'\cos\theta]}$$

$$\times (r')^2 \sin\theta' \sec\left(\frac{\theta'}{2}\right) d\theta'\, d\phi' \tag{15-49b}$$

$$\mathbf{I}_z = -\hat{\mathbf{a}}_z \int_0^{2\pi}\int_0^{\theta_0} (\hat{\mathbf{n}} \cdot \hat{\mathbf{e}}_r) \frac{\sqrt{G_f(\theta', \phi')}}{r'} e^{-jkr'[1 - \sin\theta'\sin\theta\cos(\phi' - \phi) - \cos\theta'\cos\theta]}$$

$$\times (r')^2 \sin\theta' \sec\left(\frac{\theta'}{2}\right) d\theta'\, d\phi' \tag{15-49c}$$

By comparing (15-49) with (15-35), the radiated field components formulated by the aperture distribution and current distribution methods lead to similar results provided the $\mathbf{I}_z$ contribution of (15-49c) is neglected. As the ratio of the aperture diameter to wavelength (d/λ) increases, the current distribution method results reduce to those of the aperture distribution and the angular pattern becomes more narrow.

For variations near the $\theta = \pi$ region, the $\mathbf{I}_z$ contribution becomes negligible because

$$\hat{\mathbf{a}}_\theta \cdot [-\hat{\mathbf{a}}_z(\hat{\mathbf{n}} \cdot \hat{\mathbf{e}}_r)] = [\hat{\mathbf{a}}_x \sin\theta\cos\phi + \hat{\mathbf{a}}_y \cos\theta\sin\phi - \hat{\mathbf{a}}_z \sin\theta]$$

$$\cdot [-\hat{\mathbf{a}}_z(\hat{\mathbf{n}} \cdot \hat{\mathbf{e}}_r)] = (\hat{\mathbf{n}} \cdot \hat{\mathbf{e}}_r)\sin\theta \tag{15-50a}$$

$$\hat{\mathbf{a}}_\phi \cdot [-\hat{\mathbf{a}}_z(\hat{\mathbf{n}} \cdot \hat{\mathbf{e}}_r)] = [-\hat{\mathbf{a}}_x \sin\phi + \hat{\mathbf{a}}_y \cos\phi] \cdot [-\hat{\mathbf{a}}_z(\hat{\mathbf{n}} \cdot \hat{\mathbf{e}}_r)] = 0 \tag{15-50b}$$

F. Directivity and Aperture Efficiency

In the design of antennas, the directivity is a very important figure-of-merit. The purpose of this section will be to examine the dependence of the directivity and aperture efficiency on the primary-feed pattern $G_f(\theta', \phi')$ and f/d ratio (or the included angle $2\theta_0$) of the reflector. To simplify the analysis, it will be assumed that the feed

INTEL-1045
U.S. Patent 7,151,430

pattern $G_f(\theta', \phi')$ is circularly symmetric (not a function of ϕ') and that $G_f(\theta') \approx 0$ for $\theta' > 90°$.

The secondary pattern (formed by the surface of the reflector) is given by (15-49). Approximating the **I** of (15-49a) by $\mathbf{I}_t$, the total **E**-field in the $\theta = \pi$ direction is given by either E_θ or E_ϕ of (15-49). Assuming the feed is circularly symmetric, linearly polarized in the y-direction, and by neglecting cross-polarized contributions, it can be shown with the aid of (15-14a) that (15-49) reduces to

$$E(r, \theta = \pi) = -j\frac{2\omega\mu f}{r}\left[\sqrt{\frac{\epsilon}{\mu}}\frac{P_t}{2\pi}\right]^{1/2} e^{-jk(r+2f)} \int_0^{\theta_0} \sqrt{G_f(\theta')}\tan\left(\frac{\theta'}{2}\right) d\theta' \tag{15-51}$$

The power intensity (power/unit solid angle) in the forward direction $U(\theta = \pi)$ is given by

$$U(\theta = \pi) = \frac{1}{2} r^2 \sqrt{\frac{\epsilon}{\mu}} |\mathbf{E}(r, \theta = \pi)|^2 \tag{15-52}$$

which by using (15-51) reduces to

$$U(\theta = \pi) = \frac{16\pi^2}{\lambda^2} f^2 \frac{P_t}{4\pi}\left|\int_0^{\theta_0} \sqrt{G_f(\theta')}\tan\left(\frac{\theta'}{2}\right) d\theta'\right|^2 \tag{15-52a}$$

The antenna directivity in the forward direction can be written, using (15-52a), as

$$D_0 = \frac{4\pi U(\theta = \pi)}{P_t} = \frac{U(\theta = \pi)}{P_t/4\pi} = \frac{16\pi^2}{\lambda^2} f^2 \left|\int_0^{\theta_0} \sqrt{G_f(\theta')}\tan\left(\frac{\theta'}{2}\right) d\theta'\right|^2 \tag{15-53}$$

The focal length is related to the angular spectrum and aperture diameter d by (15-25). Thus (15-53) reduces to

$$\boxed{D_0 = \left(\frac{\pi d}{\lambda}\right)^2 \left\{\cot^2\left(\frac{\theta_0}{2}\right)\left|\int_0^{\theta_0} \sqrt{G_f(\theta')}\tan\left(\frac{\theta'}{2}\right) d\theta'\right|^2\right\}} \tag{15-54}$$

The factor $(\pi d/\lambda)^2$ is the directivity of a uniformly illuminated constant phase aperture; the remaining part is the aperture efficiency defined as

$$\boxed{\epsilon_{ap} = \cot^2\left(\frac{\theta_0}{2}\right)\left|\int_0^{\theta_0} \sqrt{G_f(\theta')}\tan\left(\frac{\theta'}{2}\right) d\theta'\right|^2} \tag{15-55}$$

It is apparent by examining (15-55) that the aperture efficiency is a function of the subtended angle (θ_0) and the feed pattern $G_f(\theta')$ of the reflector. Thus for a given feed pattern, all paraboloids with the same *f/d* ratio have identical aperture efficiency.

To illustrate the variation of the aperture efficiency as a function of the feed pattern and the angular extent of the reflector, Silver [17] considered a class of feeds whose patterns are defined by

$$G_f(\theta') = \begin{cases} G_0^{(n)} \cos^n(\theta') & 0 \le \theta' \le \pi/2 \\ 0 & \pi/2 < \theta' \le \pi \end{cases} \tag{15-56}$$

where $G_0^{(n)}$ is a constant for a given value of n. Although idealistic, these patterns were chosen because (1) closed form solutions can be obtained, and (2) they often

INTEL-1045
U.S. Patent 7,151,430

are used to represent a major part of the main lobe of many practical antennas. The intensity in the back region ($\pi/2 < \theta' \leq \pi$) was assumed to be zero in order to avoid interference between the direct radiation from the feed and scattered radiation from the reflector.

The constant $G_0^{(n)}$ can be determined from the relation

$$\oiint_S G_f(\theta')\, d\Omega = \oiint_S G_f(\theta') \sin\theta'\, d\theta'\, d\phi' = 4\pi \tag{15-57}$$

which for (15-56) becomes

$$G_0^{(n)} \int_0^{\pi/2} \cos^n\theta' \sin\theta'\, d\theta' = 2 \Rightarrow G_0^{(n)} = 2(n+1) \tag{15-58}$$

Substituting (15-56) and (15-58) into (15-55) leads, for the even values of $n = 2$ through $n = 8$, to

$$\epsilon_{ap}(n=2) = 24\left\{\sin^2\left(\frac{\theta_0}{2}\right) + \ln\left[\cos\left(\frac{\theta_0}{2}\right)\right]\right\}^2 \cot^2\left(\frac{\theta_0}{2}\right) \tag{15-59a}$$

$$\epsilon_{ap}(n=4) = 40\left\{\sin^4\left(\frac{\theta_0}{2}\right) + \ln\left[\cos\left(\frac{\theta_0}{2}\right)\right]\right\}^2 \cot^2\left(\frac{\theta_0}{2}\right) \tag{15-59b}$$

$$\epsilon_{ap}(n=6) = 14\left\{2\ln\left[\cos\left(\frac{\theta_0}{2}\right)\right] + \frac{[1-\cos(\theta_0)]^3}{3} + \frac{1}{2}\sin^2(\theta_0)\right\}^2 \cot^2\left(\frac{\theta_0}{2}\right) \tag{15-59c}$$

$$\epsilon_{ap}(n=8) = 18\left\{\frac{1-\cos^4(\theta_0)}{4} - 2\ln\left[\cos\left(\frac{\theta_0}{2}\right)\right] - \frac{[1-\cos(\theta_0)]^3}{3} - \frac{1}{2}\sin^2(\theta_0)\right\}^2 \cot^2\left(\frac{\theta_0}{2}\right) \tag{15-59d}$$

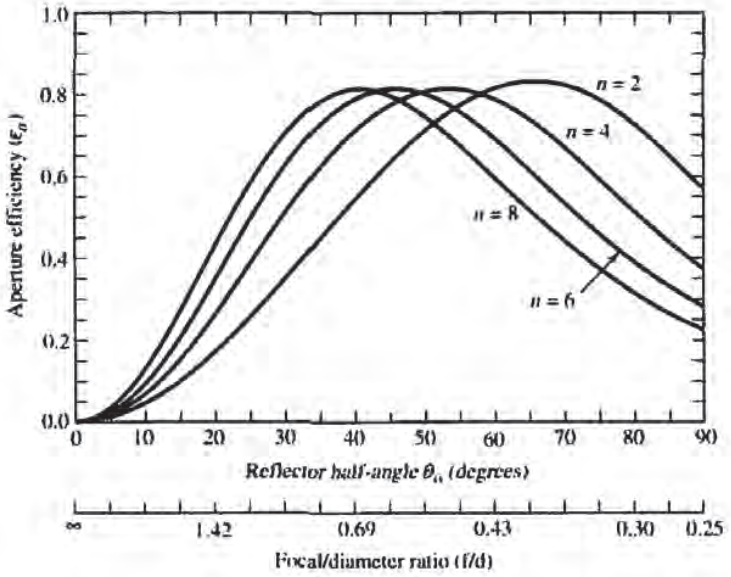
The variations of (15-59a)–(15-59d), as a function of the angular aperture of the reflector θ_0 or the *f/d* ratio, are shown plotted in Figure 15.20. It is apparent, from the graphical illustration, that for a given feed pattern (n = constant)

1. There is only one reflector with a given angular aperture or *f/d* ratio which leads to a maximum aperture efficiency.
2. Each maximum aperture efficiency is in the neighborhood of 82–83%.
3. Each maximum aperture efficiency, for any one of the given patterns, is almost the same as that of any of the others.
4. As the feed pattern becomes more directive (n increases), the angular aperture of the reflector that leads to the maximum efficiency is smaller.

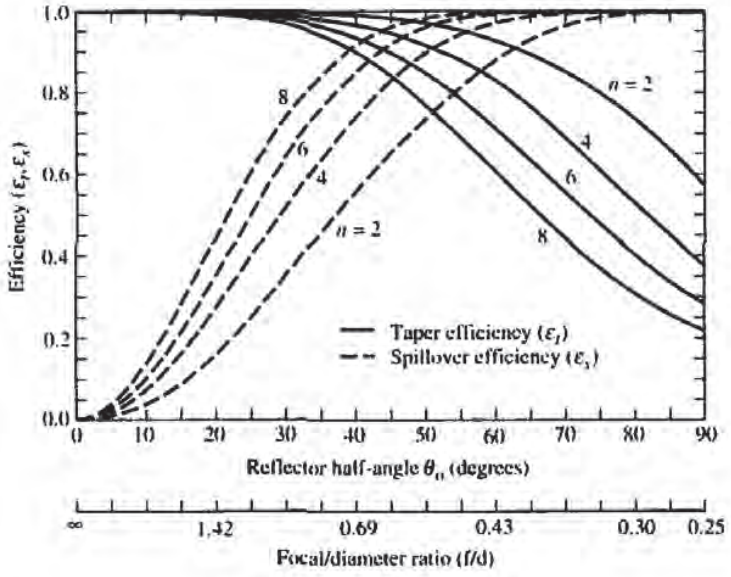
The aperture efficiency is generally the product of the

1. fraction of the total power that is radiated by the feed, intercepted, and collimated by the reflecting surface (generally known as *spillover efficiency* ϵ_s)
2. uniformity of the amplitude distribution of the feed pattern over the surface of the reflector (generally known as *taper efficiency* ϵ_t)
3. phase uniformity of the field over the aperture plane (generally known as *phase efficiency* ϵ_p)

INTEL-1045
U.S. Patent 7,151,430



(a) Aperture efficiency



(b) Taper and spillover efficiencies

Figure 15.20 Aperture, and taper and spillover efficiencies as a function of the reflector half-angle θ_0 (or *f/d* ratio) for different feed patterns.

4. polarization uniformity of the field over the aperture plane (generally known as *polarization efficiency* ϵ_x)
5. *blockage efficiency* ϵ_b
6. *random error efficiency* ϵ_r over the reflector surface

Thus in general

$$\epsilon_{ap} \approx \epsilon_s \epsilon_t \epsilon_p \epsilon_x \epsilon_b \epsilon_r \tag{15-60}$$

INTEL-1045
U.S. Patent 7,151,430

For feeds with symmetrical patterns

$$\epsilon_s = \frac{\int_0^{\theta_0} G_f(\theta') \sin \theta' \, d\theta'}{\int_0^{\pi} G_f(\theta') \sin \theta' \, d\theta'} \tag{15-61}$$

$$\epsilon_t = 2 \cot^2\left(\frac{\theta_0}{2}\right) \frac{\left| \int_0^{\theta_0} \sqrt{G_f(\theta')} \tan\left(\frac{\theta'}{2}\right) d\theta' \right|^2}{\int_0^{\theta_0} G_f(\theta') \sin \theta' \, d\theta'} \tag{15-62}$$

which by using (15-25) can also be written as

$$\epsilon_t = 32 \left(\frac{f}{d}\right)^2 \frac{\left| \int_0^{\theta_0} \sqrt{G_f(\theta')} \tan\left(\frac{\theta'}{2}\right) d\theta' \right|^2}{\int_0^{\theta_0} G_f(\theta') \sin \theta' \, d\theta'} \tag{15-62a}$$

Thus

1. $100(1 - \epsilon_s)$ = percent power loss due to energy from feed spilling past the main reflector.
2. $100(1 - \epsilon_t)$ = percent power loss due to nonuniform amplitude distribution over the reflector surface.
3. $100(1 - \epsilon_p)$ = percent power loss if the field over the aperture plane is not in phase everywhere.
4. $100(1 - \epsilon_c)$ = percent power loss if there are cross-polarized fields over the antenna aperture plane.
5. $100(1 - \epsilon_b)$ = percent power loss due to blockage provided by the feed or supporting struts (also by subreflector for a dual reflector).
6. $100(1 - \epsilon_r)$ = percent power loss due to random errors over the reflector surface.

An additional factor that reduces the antenna gain is the attenuation in the antenna feed and associated transmission line.

For feeds with

1. symmetrical patterns
2. aligned phase centers
3. no cross-polarized field components
4. no blockage
5. no random surface error

the two main factors that contribute to the aperture efficiency are the spillover and nonuniform amplitude distribution losses. Because these losses depend primarily on the feed pattern, a compromise between spillover and taper efficiency must emerge. Very high spillover efficiency can be achieved by a narrow beam pattern with low

INTEL-1045
U.S. Patent 7,151,430

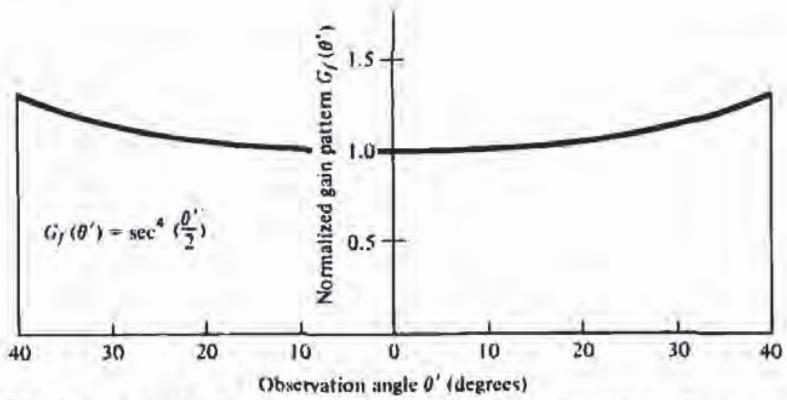


Figure 15.21 Normalized gain pattern of feed for uniform amplitude illumination of paraboloidal reflector with a total subtended angle of 80°.

minor lobes at the expense of a very low taper efficiency. Uniform illumination and ideal taper efficiency can be obtained when the feed power pattern is

$$G_f(\theta') = \begin{cases} \sec^4\left(\dfrac{\theta'}{2}\right) & 0 \le \theta' \le \theta_0 \\ 0 & \theta' > \theta_0 \end{cases} \tag{15-63}$$

which is shown plotted in Figure 15.21. Although such a pattern is "ideal" and impractical to achieve, much effort has been devoted to develop feed designs which attempt to approximate it [14].

To develop guidelines for designing practical feeds which result in high aperture efficiencies, it is instructive to examine the relative field strength at the edges of the reflector's bounds ($\theta' = \theta_0$) for patterns that lead to optimum efficiencies. For the patterns of (15-56), when used with reflectors that result in optimum efficiencies as demonstrated graphically in Figure 15.20, the relative field strength at the edges of their angular bounds ($\theta' = \theta_0$) is shown plotted in Figure 15.22. Thus for $n = 2$ the field strength of the pattern at $\theta' = \theta_0$ is 8 dB down from the maximum. As the pattern becomes more narrow (n increases), the relative field strength at the edges for maximum efficiency is further reduced as illustrated in Figure 15.20. Since for $n = 2$ through $n = 10$ the field strength is between 8 to 10.5 dB down, for most practical feeds the figure used is 9–10 dB.

Another parameter to examine for the patterns of (15-56), when used with reflectors that lead to optimum efficiency, is the amplitude taper or illumination of the main aperture of the reflector which is defined as *the ratio of the field strength at the edge of the reflector surface to that at the vertex*. The aperture illumination is a function of the feed pattern and the f/d ratio of the reflector. To obtain that, the ratio of the angular variation of the pattern toward the two points $[G_f(\theta' = 0)/G_f(\theta' = \theta_0)]$ is multiplied by the space attenuation factor $(r_0/f)^2$, where f is the focal distance of the reflector and r_0 is the distance from the focal point to the edge of the reflector. For each of the patterns, the reflector edge illumination for maximum efficiency is 11 dB down from that at the vertex.

The results obtained with the idealized patterns of (15-56) should only be taken as typical, because it was assumed that

1. the field intensity for $\theta' > 90°$ was zero
2. the feed was placed at the phase center of the system

INTEL-1045
U.S. Patent 7,151,430

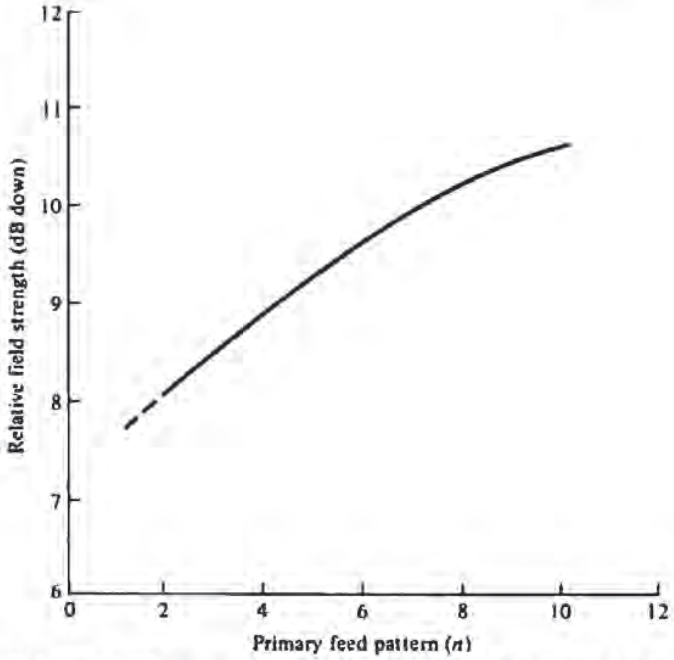


Figure 15.22 Relative field strength of feed pattern along reflector edge bounds as a function of primary feed pattern number ($\cos^n\theta$). (SOURCE: S. Silver (ed.), *Microwave Antenna Theory and Design* (MIT Radiation Lab. Series, Vol. 12), McGraw-Hill, New York, 1949)

3. the patterns were symmetrical
4. there were no cross-polarized field components
5. there was no blockage
6. there were no random errors at the surface of the reflector

Each factor can have a significant effect on the efficiency, and each has received much attention which is well documented in the open literature [1].

In practice, maximum reflector efficiencies are in the 65–80% range. To demonstrate that, paraboloidal reflector efficiencies for square corrugated horns feeds were computed, and they are shown plotted in Figure 15.23. The corresponding amplitude taper and spillover efficiencies for the aperture efficiencies of Figures 15.20(a) and 15.23 are displayed, respectively, in Figures 15.20(b) and 15.24. For the data of Figures 15.23 and 15.24, each horn had aperture dimensions of $8\lambda \times 8\lambda$, their patterns were assumed to be symmetrical (by averaging the *E*- and *H*-planes), and they were computed using the techniques of Section 13.6. From the plotted data, it is apparent that the maximum aperture efficiency for each feed pattern is in the range of 74–79%, and that the product of the taper and spillover efficiencies is approximately equal to the total aperture efficiency.

We would be remiss if we left the discussion of this section without reporting the gain of some of the largest reflectors that exist around the world [23]. The gains are shown in Figure 15.25 and include the 1,000-ft (305-m) diameter spherical reflector [12] at Arecibo, Puerto Rico, the 100-m radio telescope [15] at Effelsberg, West Germany, the 64-m reflector [16] at Goldstone, California, the 22-m reflector at Krim, USSR, and the 12-m telescope at Kitt Peak, Arizona. The dashed portions of the curves indicate extrapolated values. For the Arecibo reflector, two curves are shown.

INTEL-1045
U.S. Patent 7,151,430

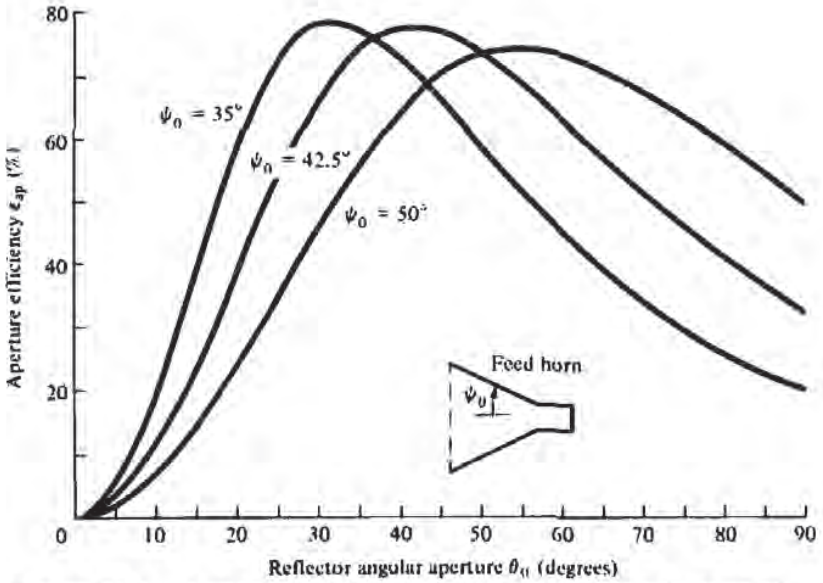


Figure 15.23 Parabolic reflector aperture efficiency as a function of angular aperture for $8\lambda \times 8\lambda$ square corrugated horn feed with total flare angles of $2\psi_0 = 70°$, 85°, and 100°.

The 215-m diameter curve is for a reduced aperture of the large reflector (305-m) for which a line feed at 1,415 MHz was designed [12].

G. Phase Errors

Any departure of the phase, over the aperture of the antenna, from uniform can lead to a significant diminution of its directivity [24]. For a paraboloidal reflector system, phase errors result from [17]

1. displacement (defocusing) of the feed phase center from the focal point
2. deviation of the reflector surface from a parabolic shape or random errors at the surface of the reflector
3. departure of the feed wave fronts from spherical shape

The defocusing effect can be reduced by first locating the phase center of the feed antenna and then placing it at the focal point of the reflector. In Chapter 13 (Section 13.10) it was shown that the phase center for horn antennas, which are widely utilized as feeds for reflectors, is located between the aperture of the horn and the apex formed by the intersection of the inclined walls of the horn [25].

Very simple expressions have been derived [24] to predict the loss in directivity for rectangular and circular apertures when the peak values of the aperture phase deviation is known. When the phase errors are assumed to be relatively small, it is not necessary to know the exact amplitude or phase distribution function over the aperture.

Assuming the maximum radiation occurs along the axis of the reflector, and that the maximum phase deviation over the aperture of the reflector can be represented by

$$|\Delta\phi(\rho)| = |\phi(\rho) - \overline{\phi(\rho)}| \leq m, \qquad \rho \leq a \tag{15-64}$$

where $\phi(\rho)$ is the aperture phase function and $\overline{\phi(\rho)}$ is its average value, then the ratio of the directivity with (D) and without (D_0) phase errors can be written as [24]

INTEL-1045
U.S. Patent 7,151,430

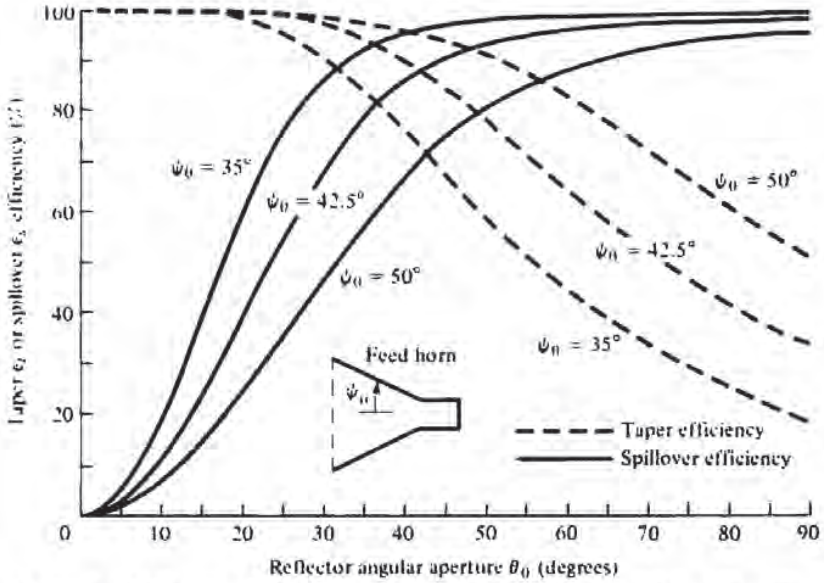


Figure 15.24 Parabolic reflector taper and spillover efficiencies as a function of reflector aperture for different corrugated horn feeds.

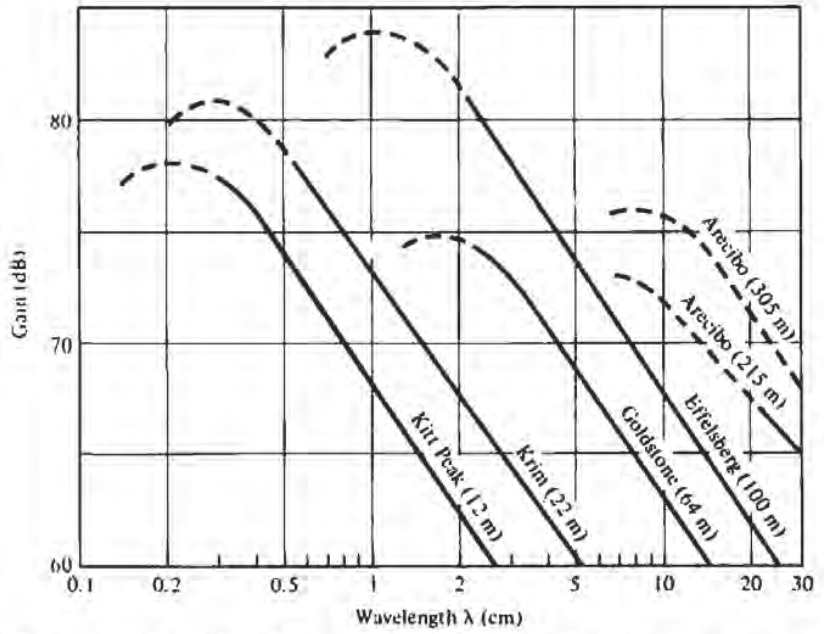


Figure 15.25 Gains of some worldwide large reflector antennas. (SOURCE: A. W. Love, Some Highlights in Reflector Antenna Development," *Radio Science*, Vol. 11, Nos. 8, 9, August–September 1976)

$$\boxed{\frac{D}{D_0} = \frac{\text{directivity with phase error}}{\text{directivity without phase error}} \geq \left(1 - \frac{m^2}{2}\right)^2} \tag{15-65}$$

and the maximum fractional reduction in directivity as

$$\frac{\Delta D}{D_0} = \frac{D_0 - D}{D_0} \leq m^2\left(1 - \frac{m^2}{4}\right) \tag{15-66}$$

Relatively simple expressions have also been derived [24] to compute the maximum possible change in half-power beamwidth.

Example 15.1

A 10-m diameter reflector, with an f/d ratio of 0.5, is operating at $f = 3$ GHz. The reflector is fed with an antenna whose primary pattern is symmetrical and which can be approximated by $G_f(\theta') = 6\cos^2\theta'$. Find its

(a) aperture efficiency
(b) overall directivity
(c) spillover and taper efficiencies
(d) directivity when the maximum aperture phase deviation is $\pi/8$ rad

SOLUTION

Using (15-24), half of the subtended angle of the reflector is equal to

$$\theta_0 = \tan^{-1}\left[\frac{0.5(0.5)}{(0.5)^2 - \dfrac{1}{16}}\right] = 53.13^\circ$$

(a) The aperture efficiency is obtained using (15-59a). Thus

$$\epsilon_{ap} = 24\{\sin^2(26.57^\circ) + \ln[\cos(26.57^\circ)]\}^2 \cot^2(26.57^\circ)$$
$$= 0.75 = 75\%$$

which agrees with the data of Figure 15.20.

(b) The overall directivity is obtained by (15-54), or

$$D = 0.75[\pi(100)]^2 = 74{,}022.03 = 48.69 \text{ dB}$$

(c) The spillover efficiency is computed using (15-61) where the upper limit of the integral in the denominator has been replaced by $\pi/2$. Thus

$$\epsilon_s = \frac{\displaystyle\int_0^{53.13^\circ} \cos^2\theta' \sin\theta'\, d\theta'}{\displaystyle\int_0^{90^\circ} \cos^2\theta' \sin\theta'\, d\theta'} = \frac{2\cos^3\theta'\big|_0^{53.13^\circ}}{2\cos^3\theta'\big|_0^{90^\circ}} = 0.784 = 78.4\%$$

In a similar manner, the taper efficiency is computed using (15-62). Since the numerator in (15-62) is identical in form to the aperture efficiency of (15-55), the taper efficiency can be found by multiplying (15-59a) by 2 and dividing by the denominator of (15-62). Thus

INTEL-1045
U.S. Patent 7,151,430

$$\epsilon_t = \frac{2(0.75)}{1.568} = 0.9566 = 95.66\%$$

The product of ϵ_s and ϵ_t is equal to

$$\epsilon_s \epsilon_t = 0.784(0.9566) = 0.75$$

and it is identical to the total aperture efficiency computed above.

(d) The directivity for a maximum phase error of $m = \pi/8 = 0.3927$ rad can be computed using (15-65). Thus

$$\frac{D}{D_0} \geq \left(1 - \frac{m^2}{2}\right)^2 = \left[1 - \frac{(0.3927)^2}{2}\right]^2 = 0.8517 = -0.69 \text{ dB}$$

or $D \geq 0.8517 D_0 = 0.8517(74,022.03) = 63,046.94 = 48.0$ dB

Surface roughness effects on the directivity of the antenna were first examined by Ruze [26] where he indicated that for any reflector antenna there is a wavelength (λ_{max}) at which the directivity reaches a maximum. This wavelength depends on the RMS deviation (σ) of the reflector surface from an ideal paraboloid. For a random roughness of Gaussian distribution, with correlation interval large compared to the wavelength, they are related by

$$\lambda_{max} = 4\pi\sigma \tag{15-67}$$

Thus the directivity of the antenna, given by (15-54), is modified to include surface roughness and can be written as

$$D = \left(\frac{\pi d}{\lambda}\right)^2 \epsilon_{ap} e^{-(4\pi\sigma/\lambda)^2} \tag{15-68}$$

Using (15-67), the maximum directivity of (15-68) can be written as

$$\boxed{D_{max} = 10^{2q} \epsilon_{ap} \left(\frac{e^{-1}}{16}\right)} \tag{15-69}$$

where q is the index of smoothness defined by

$$\frac{d}{\sigma} = 10^{+q} \tag{15-70}$$

In decibels, (15-69) reduces to

$$\boxed{D_{max}(\text{dB}) = 20q - 16.38 + 10\log_{10}(\epsilon_{ap})} \tag{15-71}$$

For an aperture efficiency of unity ($\epsilon_{ap} = 1$), the directivity of (15-68) is plotted in Figure 15.26, as a function of (d/λ), for values of $q = 3.5$, 4.0, and 4.5. It is apparent that for each value of q and a given reflector diameter d, there is a maximum wavelength where the directivity reaches a maximum value. This maximum wavelength is given by (15-67).

H. Feed Design

The widespread use of paraboloidal reflectors has stimulated interest in the development of feeds to improve the aperture efficiency and to provide greater discrimination

INTEL-1045
U.S. Patent 7,151,430

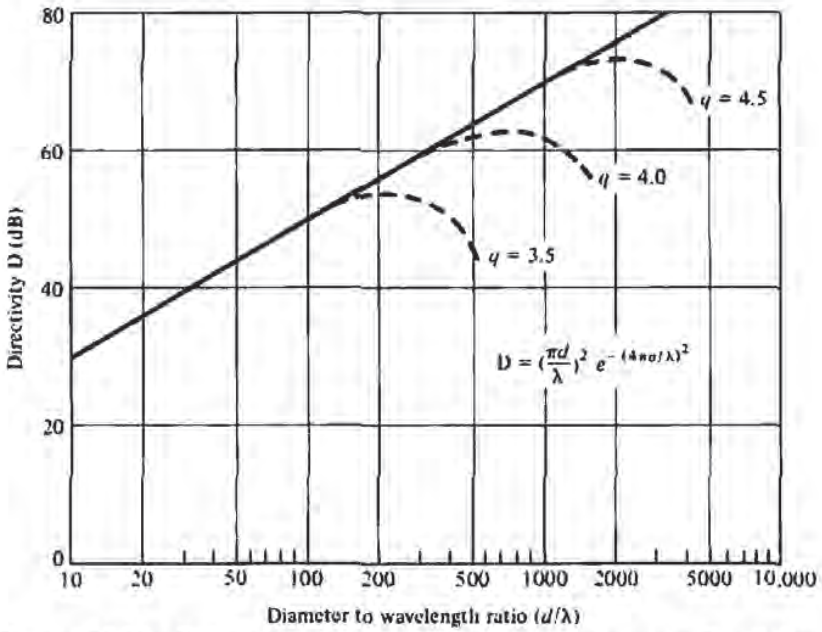


Figure 15.26 Reflector surface roughness effects on antenna directivity. (SOURCE: A. W. Love, "Some Highlights in Reflector Antenna Development," *Radio Science*, Vol. 11, Nos 8, 9, August–September 1976)

against noise radiation from the ground. This can be accomplished by developing design techniques that permit the synthesis of feed patterns with any desired distribution over the bounds of the reflector, rapid cutoff at its edges, and very low minor lobes in all the other space. In recent years, the two main problems that concerned feed designers were aperture efficiency and low cross-polarization.

In the receiving mode, an ideal feed and a matched load would be one that would absorb all the energy intercepted by the aperture when uniform and linearly polarized plane waves are normally incident upon it. The feed field structure must be made to match the focal region field structure formed by the reflecting, scattering, and diffracting characteristics of the reflector. By reciprocity, an ideal feed in the transmitting mode would be one that radiates only within the solid angle of the aperture and establishes within it an identical outward traveling wave. For this ideal feed system, the transmitting and receiving mode field structures within the focal region are identical with only the direction of propagation reversed.

An optical analysis indicates that the focal region fields, formed by the reflection of linearly polarized plane waves incident normally on an axially symmetric reflector, are represented by the well-known Airy rings described mathematically by the amplitude distribution intensity of $[2J_1(u)/u]^2$. This description is incomplete, because it is a scalar solution, and it does not take into account polarization effects. In addition, it is valid only for reflectors with large f/d ratios, which are commonly used in optical systems, and it would be significantly in error for reflectors with f/d ratios of 0.25 to 0.5, which are commonly used in microwave applications.

A vector solution has been developed [27] which indicates that the fields near the focal region can be expressed by hybrid TE and TM modes propagating along the axis of the reflector. This representation provides a clear physical picture for the understanding of the focal region field formation. The boundary conditions of the hybrid modes indicate that these field structures can be represented by a spectrum of

INTEL-1045
U.S. Patent 7,151,430

hybrid waves that are linear combinations of TE_{1n} and TM_{1n} modes of circular waveguides.

A single hollow pipe cannot simultaneously satisfy both the TE and TM modes because of the different radial periodicities. However, it has been shown that $\lambda/4$ deep annular slots on the inner surface of a circular pipe force the boundary conditions on **E** and **H** to be the same and provide a single anisotropic reactance surface which satisfies the boundary conditions on both TE and TM modes. This provided the genesis of hybrid mode waveguide radiators [28] and corrugated horns [29]. Corrugated horns, whose aperture size and flare angle are such that at least 180° phase error over their aperture is assured, are known as "scalar" horns [30]. Design data for uncorrugated horns that can be used to maximize the aperture efficiency or to produce maximum power transmission to the feed have been calculated [31] and are shown in graphical form in Figure 15.27.

A software package for computer-aided analysis and design of reflector antennas has been developed [32]. The program computes the radiation of parabolic and spherical reflectors. In addition it provides spatial and spectral methods to compute radiation due to an aperture distribution. The software package can also be used to investigate the directivity, beamwidth, sidelobe level, polarization, and near-to-far-zone fields. The program can be obtained through CAEME. Center of Excellence for Multimedia.

15.4.2 Cassegrain Reflectors

To improve the performance of large ground-based microwave reflector antennas for satellite tracking and communication, it has been proposed that a two-reflector system

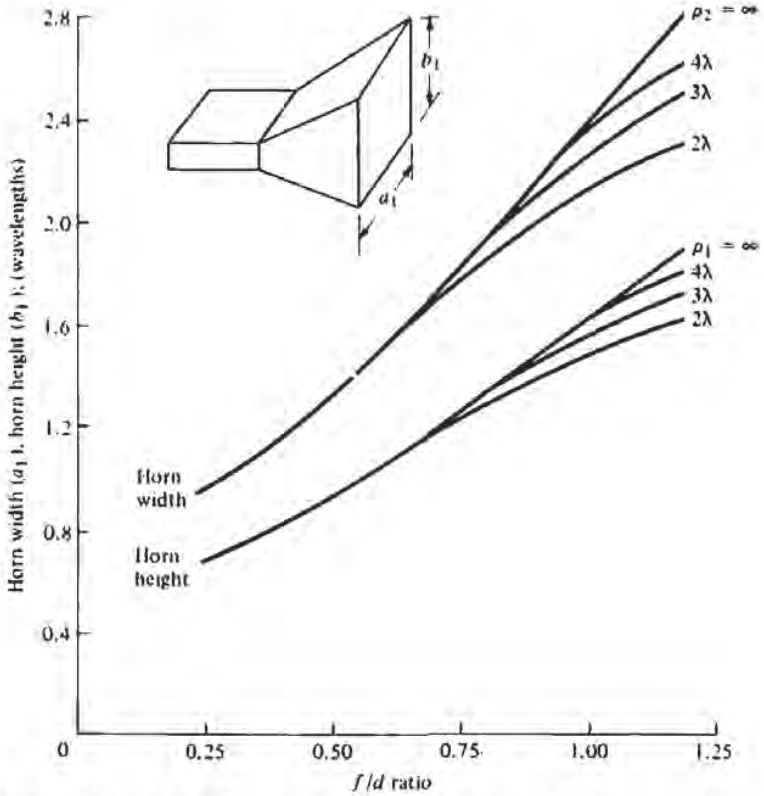


Figure 15.27 Optimum pyramidal horn dimensions versus *f/d* ratio for various horn lengths.

INTEL-1045
U.S. Patent 7,151,430

be utilized. The arrangement suggested was the Cassegrain dual-reflector system [33] of Figure 15.1(d), which was often utilized in the design of optical telescopes and it was named after its inventor. To achieve the desired collimation characteristics, the larger (main) reflector must be a paraboloid and the smaller (secondary) a hyperboloid. The use of a second reflector, which is usually referred to as the subreflector or subdish, gives an additional degree of freedom for achieving good performance in a number of different applications. For an accurate description of its performance, diffraction techniques must be used to take into account diffractions from the edges of the subreflector, especially when its diameter is small [34].

In general, the Cassegrain arrangement provides a variety of benefits, such as the

1. ability to place the feed in a convenient location
2. reduction of spillover and minor lobe radiation
3. ability to obtain an equivalent focal length much greater than the physical length
4. capability for scanning and/or broadening of the beam by moving one of the reflecting surfaces

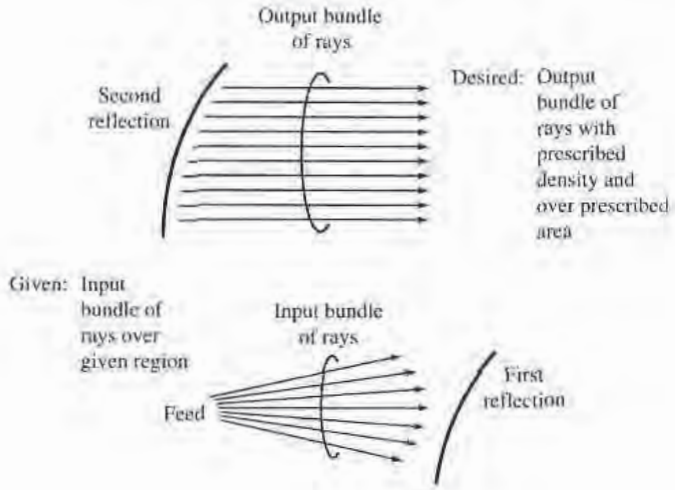
To achieve good radiation characteristics, the subreflector or subdish must be several, at least a few, wavelengths in diameter. However, its presence introduces shadowing which is the principal limitation of its use as a microwave antenna. The shadowing can significantly degrade the gain of the system, unless the main reflector is several wavelengths in diameter. Therefore the Cassegrain is usually attractive for applications that require gains of 40 dB or greater. There are, however, a variety of techniques that can be used to minimize aperture blocking by the subreflector. Some of them are [33] (1) minimum blocking with simple Cassegrain, and (2) twisting Cassegrains for least blocking.

The first comprehensive published analysis of the Cassegrain arrangement as a microwave antenna is that by Hannan [33]. He uses geometrical optics to derive the geometrical shape of the reflecting surfaces, and he introduces the equivalence concepts of the virtual feed and the equivalent parabola. Although his analysis does not predict fine details, it does give reasonably good results. Refinements to his analysis have been introduced [34]–[36].

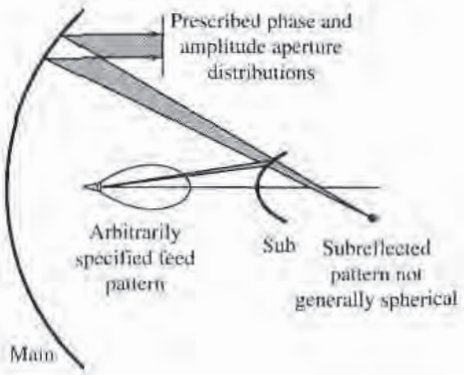
To improve the aperture efficiency, suitable modifications to the geometrical shape of the reflecting surfaces have been suggested [37]–[39]. The reshaping of the reflecting surfaces is used to generate desirable amplitude and phase distributions over one or both of the reflectors. The resultant system is usually referred to as *shaped* dual-reflector. The reflector antenna of Figure 15.9 is such a system. Shaped reflector surfaces, generated using analytical models, are illustrated in [39]. It also has been suggested [35] that a flange is placed around the subreflector to improve the aperture efficiency.

Since many reflectors have dimensions and radii of curvature large compared to the operating wavelength, they were traditionally designed based on geometrical optics (GO) [39]. Both the single- and double-reflector (Cassegrain) systems were designed to convert a spherical wave at the source (focal point) into a plane wave. Therefore the reflecting surfaces of both reflector systems were primarily selected to convert the phase of the wavefront from spherical to planar. However, because of the variable radius of curvature at each point of reflection, the magnitude of the reflected field is also changed due to spatial attenuation or amplitude spreading factor [40] or divergence factor (4-131) of Section 4.8.3, which are functions of the radius of curvature of the surface at the point of reflection. This ultimately leads to amplitude taper of

INTEL-1045
U.S. Patent 7,151,430



(a) Input and output bundle of rays.



(b) Specified feed and prescribed output.

Figure 15.28 Geometrical optics for the reshaping and synthesis of the reflectors of a Cassegrain system. (SOURCE: R. Mittra and V. Galindo-Israel "Shaped Dual Reflector Synthesis," *IEEE Antennas and Propagation Society Newsletter*, Vol. 22, No. 4, pp. 5–9, August 1980. © (1980) IEEE)

the wavefront at the aperture plane. This is usually undesirable, and it can sometimes be compensated to some extent by the design of the pattern of the feed element or of the reflecting surface.

For a shaped-dual reflector system, there are two surfaces or degrees of freedom that can be utilized to compensate for any variations in the phase and amplitude of the field at the aperture plane. To determine how each surface may be reshaped to control the phase and/or amplitude of the field at the aperture plane, let us use geometrical optics and assume that the field radiated by the feed (pattern) is represented, both in amplitude and phase, by a bundle of rays which has a well-defined periphery. This bundle of rays is initially intecepted by the subreflector and then by the main reflector. Ultimately the output, after two reflections, is also a bundle of rays with prescribed phase and amplitude distributions, and a prescribed periphery, as shown in Figure 15.28(a) [41]. It has been shown in [42] that for a two-reflector

INTEL-1045
U.S. Patent 7,151,430

system with high magnification (i.e., large ratio of main reflector diameter to subreflector diameter) that over the aperture plane the

(a) amplitude distribution is controlled largely by the subreflector curvature.
(b) phase distribution is controlled largely by the curvature of the main reflector.

Therefore in a Cassegrain two-reflector system the reshaping of the paraboloid main reflector can be used to optimize the phase distribution while the reshaping of the hyperboloid subreflector can be used to control the amplitude distribution. This was used effectively in [42] to design a shaped two-reflector system whose field reflected by the subreflector had a nonspherical phase but a $\csc^4(\theta/2)$ amplitude pattern. However, the output from the main reflector had a perfect plane wave phase front and a very good approximate uniform amplitude distribution, as shown in Figure 15.28(b).

Because a comprehensive treatment of this arrangement can be very lengthy, only a brief introduction of the system will be presented here. The interested reader is referred to the referenced literature.

A. Classical Cassegrain Form

The operation of the Cassegrain arrangement can be introduced by referring to Figure 15.1(d) and assuming the system is operating in the receiving or transmitting mode. To illustrate the principle, a receiving mode is adopted.

Let us assume that energy, in the form of parallel rays, is incident upon the reflector system. Energy intercepted by the main reflector, which has a large concave surface, is reflected toward the subreflector. Energy collected by the convex surface of the subdish is reflected by it, and it is directed toward the vertex of the main dish. If the incident rays are parallel, the main reflector is a paraboloid, and the subreflector is a hyperboloid, then the collected bundle of rays is focused at a single point. The receiver is then placed at this focusing point.

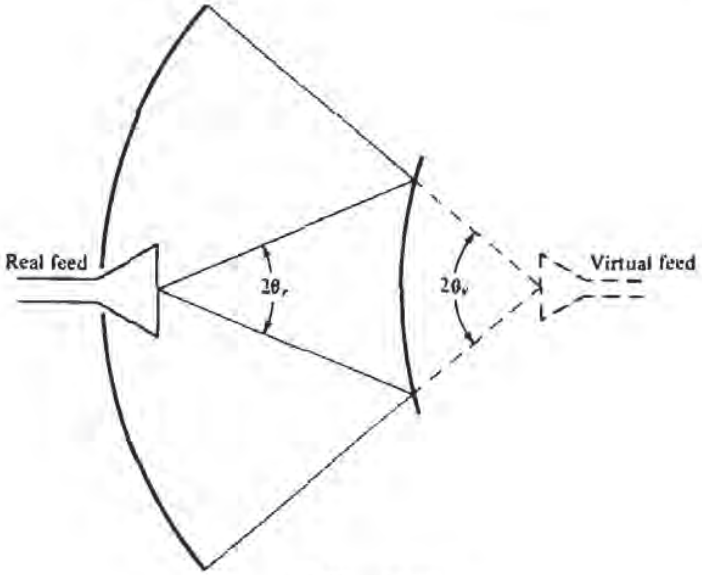
A similar procedure can be used to describe the system in the transmitting mode. The feed is placed at the focusing point, and it is usually sufficiently small so that the subdish is located in its far-field region. In addition, the subreflector is large enough that it intercepts most of the radiation from the feed. Using the geometrical arrangement of the paraboloid and the hyperboloid, the rays reflected by the main dish will be parallel. The amplitude taper of the emerging rays is determined by the feed pattern and the tapering effect of the geometry.

The geometry of the classical Cassegrain system, employing a concave paraboloid as the main dish and a convex hyperboloid as the subreflector, is simple and it can be described completely by only four independent parameters (two for each reflector). The analytical details can be found in [33].

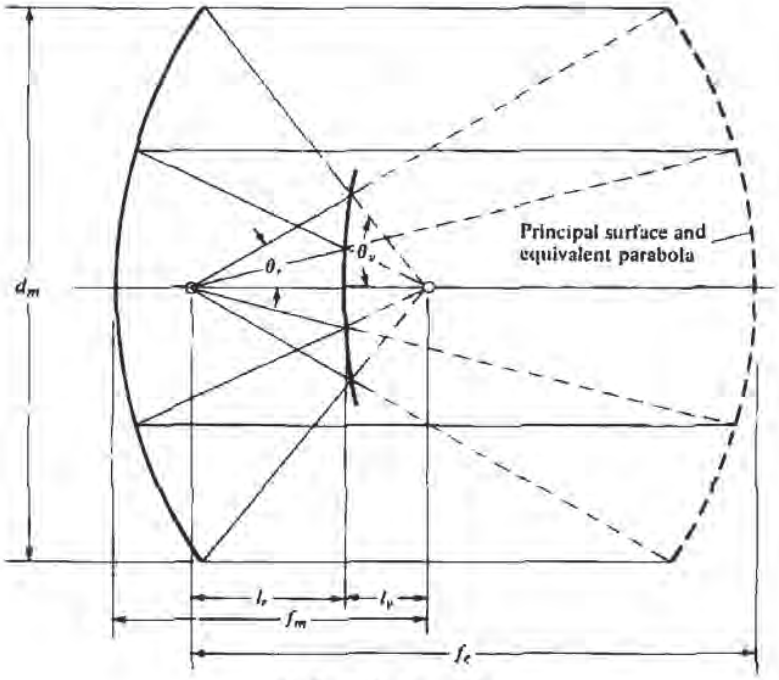
To aid in the understanding and in predicting the essential performance of a Cassegrain, the concept of *virtual feed* [33] is useful. By this principle, the real feed and the subreflector are replaced by an equivalent system which consists of a virtual feed located at the focal point of the main reflector, as shown by the dashed lines of Figure 15.29(a). For analysis purposes then, the new system is a single-reflector arrangement with the original main dish, a different feed, and no subreflector.

The configuration of the virtual feed can be determined by finding the optical image of the real feed. This technique is only accurate when examining the effective aperture of the feed and when the dimensions of the real and virtual feeds are larger than a wavelength. In fact, for the classical Cassegrain arrangement of Figure 15.29(a), the virtual feed has a smaller effective aperture, and a corresponding broader beamwidth, than the real feed. The increase in beamwidth is a result of the convex curvature

INTEL-1045
U.S. Patent 7,151,430



(a) Virtual-feed



(b) Equivalent-parabola

Figure 15.29 Virtual-feed and equivalent parabola concepts. (SOURCE: P. W. Hannan, "Microwave Antennas Derived from the Cassegrain Telescope." *IRE Trans. Antennas Propagat.* Vol. AP-9, No. 2, March 1961, © (1961) IEEE)

of the subreflector, and it can be determined by equating the ratio of the virtual to real-feed beamwidths to the ratio of the angles θ_v/θ_r.

The ability to obtain a different effective aperture for the virtual feed as compared to that of the real feed is useful in many applications such as in a monopulse antenna [33]. To maintain efficient and wideband performance and effective utilization of the

INTEL-1045
U.S. Patent 7,151,430

main aperture, this system requires a large feed aperture, a corresponding long focal length, and a large antenna structure. The antenna dimensions can be maintained relatively small by employing the Cassegrain configuration which utilizes a large feed and a short focal length for the main reflector.

Although the concept of virtual feed can furnish useful qualitative information for a Cassegrain system, it is not convenient for an accurate quantitative analysis. Some of the limitations of the virtual feed concept can be overcome by the concept of the *equivalent parabola* [33].

By the technique of the equivalent parabola, the main dish and the subreflector are replaced by an equivalent focusing surface at a certain distance from the real focal point. This surface is shown dashed in Figure 15.29(b), and it is defined as [33] "the locus of intersection of incoming rays parallel to the antenna axis with the extension of the corresponding rays converging toward the real focal point." Based on simple geometrical optics ray tracing, the equivalent focusing surface for a Cassegrain configuration is a paraboloid whose focal length equals the distance from its vertex to the real focal point. This equivalent system also reduces to a single-reflector arrangement, which has the same feed but a different main reflector, and it is accurate when the subreflector is only a few wavelengths in diameter. More accurate results can be obtained by including diffraction patterns. It also has the capability to focus toward the real focal point an incoming plane wave, incident from the opposite direction, in exactly the same manner as the actual main dish and the subreflector.

B. Cassegrain and Gregorian Forms

In addition to the classical Cassegrain forms, there are other configurations that employ a variety of main reflector and subreflector surfaces and include concave, convex, and flat shapes [33]. In one form, the main dish is held invariant while its feed beamwidth progressively increases and the axial dimensions of the antenna progressively decrease. In another form, the feed beamwidth is held invariant while the main reflector becomes progressively flatter and the axial dimensions progressively increase.

A series of configurations in which the feed beamwidth is progressively increased, while the overall antenna dimensions are held fixed, are shown in Figure 15.30. The first five are referred to as Cassegrain forms while the last two are Gregorian forms, whose configurations are similar to the Gregorian telescope. A number of parameter ranges, along with distinguishing characteristics, are indicated alongside each configuration sketch. The main dish for the fourth configuration has degenerated to a flat contour, the subreflector to a parabolic contour, and they can be separated by distances where the ray-tracing approximation is valid. For the fifth configuration, the subreflector has degenerated to a ridiculous extreme concave elliptical contour and the main dish to a convex parabolic form, with the former being larger than the latter.

For the last two configurations, which are referred to as Gregorian forms, the focal point of the main dish has moved to the region between the two dishes and the subreflector has attained a concave elliptical contour. When the overall size and the feed beamwidth of the classical Gregorian are identical to those of the classical Cassegrain, the Gregorian form requires a shorter focal length for the main dish. The feed for the second of the Gregorian forms has moved to a location between the focus of the main dish and the subreflector while the main dish has kept the same dimensions as the first form. In general, this configuration has several major disadvantages that make it unattractive for many antenna applications.

From the data in Figure 15.30, the relative sizes of the effective apertures of the virtual and real feeds can be inferred. When the subreflector is flat, the real and virtual feeds are identical. The virtual feeds of the Cassegrain configurations, which have a

INTEL-1045
U.S. Patent 7,151,430

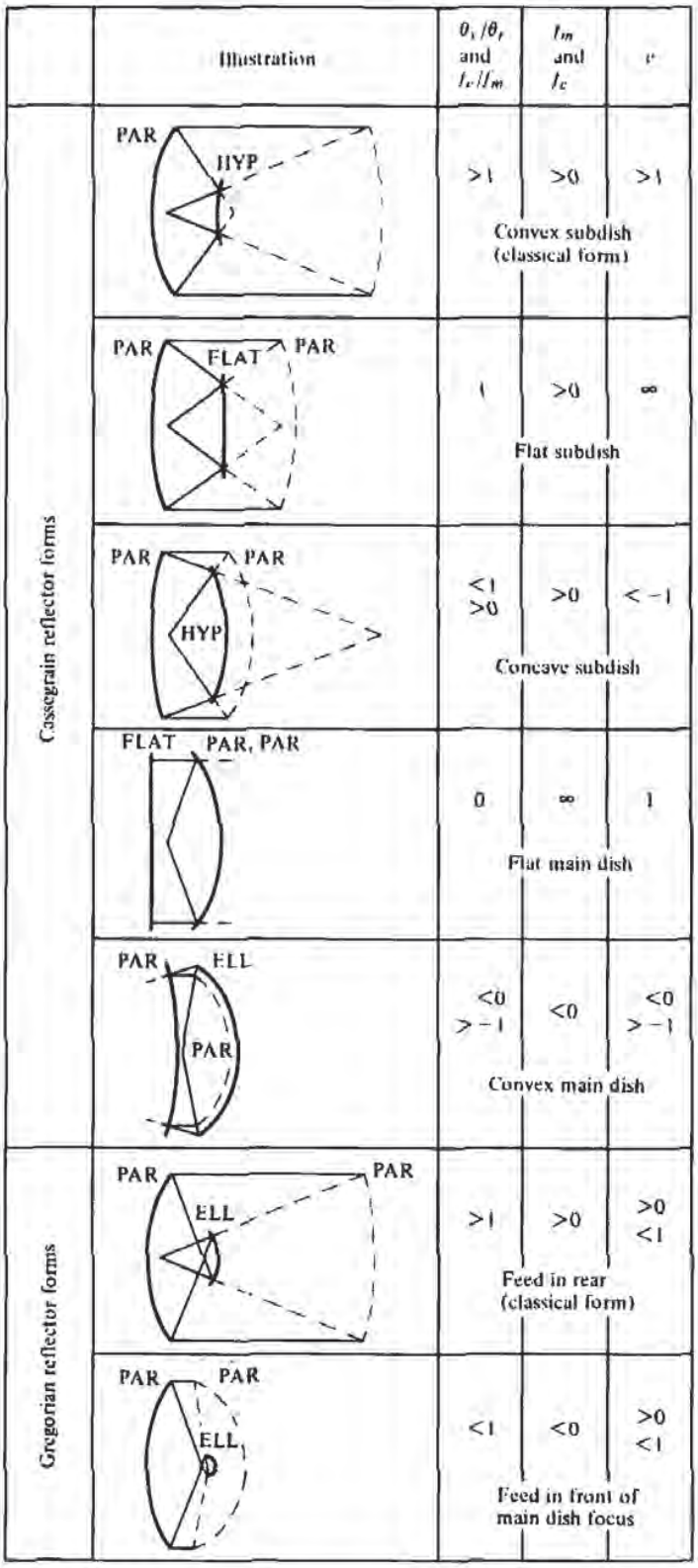


Figure 15.30 Series of Cassegrain and Gregorian reflector forms. (SOURCE: P. W. Hannan, "Microwave Antennas Derived from the Cassegrain Telescope," *IRE Trans. Antennas Propagat.*, Vol. AP-9, No. 2, March 1961. © (1961) IEEE)

INTEL-1045
U.S. Patent 7,151,430

concave subreflector, possess smaller beamwidths and larger effective apertures than their corresponding real feeds. However, the virtual feed of the classical Gregorian configuration, which also has a concave subreflector, possesses an effective aperture which is smaller than that of the real feed.

The equivalent parabola concept is applicable to all the Cassegrain and Gregorian forms, and they are shown dashed in Figure 15.30. The classical Cassegrain and Gregorian configurations have equivalent focal lengths which are greater than the focal lengths of the corresponding main dishes. For the Cassegrain arrangement with the flat subreflector, the equivalent focal length is equal to the focal length of the main dish. In general, the equivalent focal lengths of the Cassegrain configurations which have a concave subreflector are shorter than the focal lengths of their corresponding main dishes. For the configuration with the flat main dish, the equivalent parabola is identical with the subreflector.

The equivalent parabola concept can also be used to determine the amplitude taper across the aperture of a Cassegrain arrangement. As for the front-fed configuration, the amplitude taper or aperture illumination is determined by the radiation pattern of the feed modified by the space attenuation factor of the reflector. The amplitude taper of a Cassegrain configuration is identical to that of a front-fed arrangement whose feed is the actual feed and whose focal length is the equivalent focal length. In other words, the process is identical to that of a front-fed configuration except that the equivalent f_e/d ratio is used.

15.5 SPHERICAL REFLECTOR

The discussion and results presented in the previous sections illustrate that a paraboloidal reflector is an ideal collimating device. However, despite all of its advantages and many applications it is severely handicapped in angular scanning. Although scanning can be accomplished by (1) mechanical rotation of the entire structure, and (2) displacement of the feed alone, it is thwarted by the large mechanical moment of inertia in the first case and by the large coma and astigmatism in the second. By contrast, the spherical reflector can make an ideal wide-angle scanner because of its perfectly symmetrical geometrical configuration. However, it is plagued by poor inherent collimating properties. If, for example, a point source is placed at the focus of the sphere, it does not produce plane waves. The departure of the reflected wavefront from a plane wave is known as *spherical aberration*, and it depends on the diameter and focal length of the sphere. By reciprocity, plane waves incident on a spherical reflector surface parallel to its axis do not coverge at the focal point. However a spherical reflector has the capability of focusing plane waves incident at various angles by translating and orientating the feed and by illuminating different parts of the structural geometry. The 1,000-ft diameter reflector [12] at Arecibo, Puerto Rico is a spherical reflector whose surface is built into the earth and the scanning is accomplished by movement of the feed.

The focusing characteristics of a typical spherical reflector is illustrated in Figure 15.31 for three rays. The point F in the figure is the paraxial focus, and it is equal to one-half the radius of the sphere. The caustic* surface is an epicycloid and is generated

*A caustic is a point, a line, or a surface through which all the rays in a bundle pass and where the intensity is infinite. The caustic also represents the geometrical loci of all the centers of curvature of the wave surfaces. Examples of it include the focal line for cylindrical parabolic reflector and the focal point of a paraboloidal reflector.

INTEL-1045
U.S. Patent 7,151,430

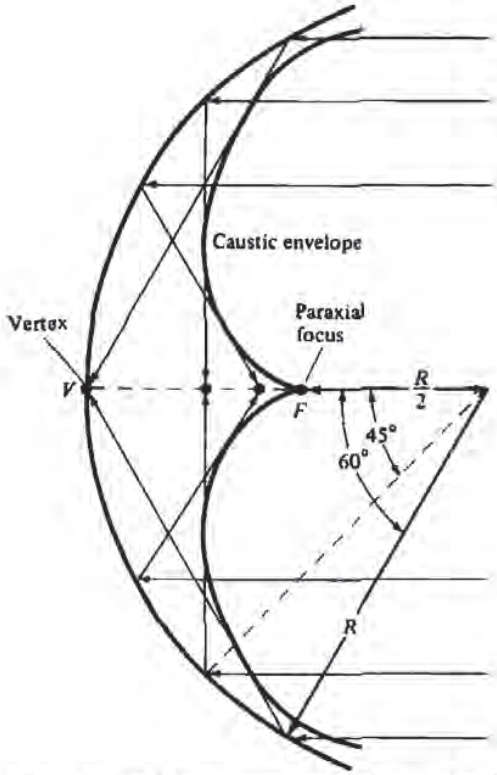


Figure 15.31 Spherical reflector geometry and rays that form a caustic.

by the reflection of parallel rays. A degenerate line FV of this caustic is parallel to the incident rays and extends from the paraxial focus to the vertex of the reflector. If one draws a ray diagram of plane waves incident within a 120° cone, it will be shown that all energy must pass through the line FV. Thus, the line FV can be used for the placement of the feed for the interception of plane waves incident parallel to the axial line. It can thus be said that a spherical reflector possesses a line focus instead of a point. However, amplitude and phase corrections must be made in order to realize maximum antenna efficiency.

Ashmead and Pippard [43] proposed to reduce spherical aberration and to minimize path error by placing a point source feed not at the paraxial focus F (half radius of the sphere), as taught in optics, but displaced slightly toward the reflector. For an aperture of diameter d, the correct location for placing a point source is a distance f_0 from the vertex such that the maximum path error value is [43]

$$\Delta_{max} \simeq \frac{d^4}{2000 f_0^3} \tag{15-72}$$

and the maximum phase error does not differ from a paraboloid by more than one-eighth of a wavelength. This, however, leads to large f/d and to poor area utilization. A similar result was obtained by Li [44]. He stated that the total phase error (sum of maximum absolute values of positive and negative phase errors) over an aperture of radius a is least when the phase error at the edge of the aperture is zero. Thus the optimum focal length is

INTEL-1045
U.S. Patent 7,151,430

$$\boxed{f_{op} = \frac{1}{4}(R + \sqrt{R^2 - a^2})} \tag{15-73}$$

where

R = radius of the spherical reflector

a = radius of the utilized aperture

Thus when $R = 2a$, the optimum focal length is $0.4665R$ and the corresponding total phase error, using the formula found in [44], is $0.02643(R/\lambda)$ rad. Even though the optimum focal length leads to minimum total phase error over a prescribed aperture, it does not yield the best radiation pattern when the illumination is not uniform. For a tapered amplitude distribution, the focal length that yields the best radiation pattern will be somewhat longer, and in practice, it is usually determined by experiment. Thus for a given maximum aperture size there exists a maximum value of total allowable phase error, and it is given by [44]

$$\left(\frac{a}{R}\right)^4_{\max} = 14.7\frac{(\Delta/\lambda)_{\text{total}}}{(R/\lambda)} \tag{15-74}$$

where (Δ/λ) is the total phase error in wavelengths.

Example 15.2

A spherical reflector has a 10-ft diameter. If at 11.2 GHz the maximum allowable phase error is $\lambda/16$, find the maximum permissible aperture.

SOLUTION

At $f = 11.2$ GHz

$$\lambda = 0.08788 \text{ ft}$$

$$\left(\frac{a}{R}\right)^4_{\max} = 14.7\left(\frac{1/16}{56.8957}\right) = 0.01615$$

$$a^4 \simeq 10.09$$

$$a = 1.78 \text{ ft}$$

To overcome the shortcoming of a point feed and minimize spherical aberration, Spencer, Sletten, and Walsh [45] were the first to propose the use of a line source feed. Instead of a continuous line source, a set of discrete feed elements can be used to reduce spherical aberration when they are properly placed along the axis in the vicinity of the paraxial focus. The number of elements, their position, and the portion of the reflector surface which they illuminate is dictated by the allowable wavefront distortion, size, and curvature of the reflector. This is shown in Figure 15.32 [46]. A single feed located near the paraxial focus will illuminate the central portion of the reflector. If the reflector is large, additional feed elements along the axis toward the

INTEL-1045
U.S. Patent 7,151,430

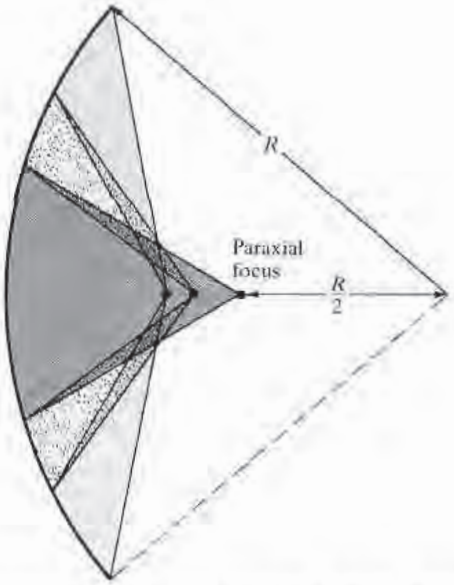


Figure 15.32 Reflector illumination by feed sections placed between paraxial focus and vertex. (SOURCE: A. C. Schell, "The Diffraction Theory of Large-Aperture Spherical Reflector Antennas," *IRE Trans. Antennas Propagat.*, Vol. AP-11, No. 4, July 1963, © (1963) IEEE)

vertex will be needed to minimize the phase errors in the aperture. The ultimate feed design will be a compromise between a single element and a line-source distribution.

An extensive effort has been placed on the analysis and experiment of spherical reflectors, and most of it can be found well documented in a book of reprinted papers [1]. In addition, a number of two-dimensional patterns and aperture plane constant amplitude contours, for symmetrical and offset feeds, have been computed [20].

References

1. A. W. Love (ed.), *Reflector Antennas*, IEEE Press, New York, 1978.
2. Y. Obha, "On the Radiation of a Corner Reflector Finite in Width," *IEEE Trans. Antennas Propagat.*, Vol. AP-11, No. 2, pp. 127–132, March 1963.
3. C. A. Balanis and L. Peters, Jr., "Equatorial Plane Pattern of an Axial-TEM Slot on a Finite Size Ground Plane," *IEEE Trans. Antennas Propagat.*, Vol. AP-17, No. 3, pp. 351–353, May 1969.
4. C. A. Balanis, "Pattern Distortion Due to Edge Diffractions," *IEEE Trans. Antennas Propagat.*, Vol. AP-18, No. 4, pp. 551–563, July 1970.
5. C. A. Balanis, "Analysis of an Array of Line Sources Above a Finite Ground Plane," *IEEE Trans. Antennas Propagat.*, Vol. AP-19, No. 2, pp. 181–185, March 1971.
6. D. Proctor, "Graphs Simplify Corner Reflector Antenna Design," *Microwaves*, Vol. 14, No. 7, pp. 48, 52, July 1975.
7. E. B. Moullin, *Radio Aerials*, Oxford University Press, 1949, Chapters 1 and 3.
8. R. E. Paley and N. Wiener, *Fourier Transforms in the Complex Domain*, American Mathematical Society, Providence, R. I., p. 116, 1934.
9. P. A. J. Ratnasiri, R. G. Kouyoumjian, and P. H. Pathak, "The Wide Angle Side Lobes of Reflector Antennas," ElectroScience Laboratory, The Ohio State University, Technical Report 2183-1, March 23, 1970.
10. G. L. James and V. Kerdemelidis, "Reflector Antenna Radiation Pattern Analysis by

INTEL-1045
U.S. Patent 7,151,430

Equivalent Edge Currents," *IEEE Trans. Antennas Propagat.*, Vol. AP-21, No. 1, pp. 19–24, January 1973.

11. C. A. Mentzer and L. Peters, Jr., "A GTD Analysis of the Far-out Side Lobes of Cassegrain Antennas," *IEEE Trans. Antennas Propagat.*, Vol. AP-23, No. 5, pp. 702–709, September 1975.
12. L. M. LaLonde and D. E. Harris, "A High Performance Line Source Feed for the AIO Spherical Reflector," *IEEE Trans. Antennas Propagat.*, Vol. AP-18, No. 1, pp. 41–48, January 1970.
13. A. W. Rudge, "Offset-Parabolic-Reflector Anennas: A Review," *Proc. IEEE*, Vol. 66, No. 12, pp. 1592–1618, December 1978.
14. P. J. B. Clarricoats and G. T. Poulton, "High-Efficiency Microwave Reflector Antennas—A Review," *Proc. IEEE*, Vol. 65, No. 10, pp. 1470–1502, October 1977.
15. O. Hachenberg, B. H. Grahl, and R. Wielebinski, "The 100-Meter Radio Telescope at Effelsberg," *Proc. IEEE*, Vol. 69, No. 9, pp. 1288–1295, 1973.
16. P. D. Potter, W. D. Merrick, and A. C. Ludwig, "Big Antenna Systems for Deep-Space Communications," *Astronautics and Aeronautics*, pp. 84–95, October 1966.
17. S. Silver (ed.), *Microwave Antenna Theory and Design*, McGraw-Hill, New York, 1949 (MIT Radiation Lab. Series, Vol. 12).
18. J. F. Kauffman, W. F. Croswell, and L. J. Jowers, "Analysis of the Radiation Patterns of Reflector Antennas," *IEEE Trans. Antennas Propagat.*, Vol. AP-24, No. 1, pp. 53–65, January 1976.
19. R. E. Collin and F. J. Zucker (eds.), *Antenna Theory Part II*, McGraw-Hill, New York, 1969, pp. 36–48.
20. P. K. Agrawal, J. F. Kauffman, and W. F. Croswell, "Calculated Scan Characteristics of a Large Spherical Reflector Antenna," *IEEE Trans. Antennas Propagat.*, Vol. AP-27, No. 3, pp. 430–431, May 1979.
21. E. M. T. Jones, "Paraboloid Reflector and Hyperboloid Lens Antennas," *IRE Trans. Antennas Propagat.*, Vol. AP-2, No. 3, pp. 119–127, July 1954.
22. I. Koffman, "Feed Polarization for Parallel Currents in Reflectors Generated by Conic Sections," *IEEE Trans. Antennas Propagat.*, Vol. AP-14, No. 1, pp. 37–40, January 1966.
23. A. W. Love, "Some Highlights in Reflector Antenna Development," *Radio Science*, Vol. 11, Nos. 8, 9, pp. 671–684, August–September 1976.
24. D. K. Cheng, "Effect of Arbitrary Phase Errors on the Gain and Beamwidth Characteristics of Radiation Pattern," *IRE Trans. Antennas Propagat.*, Vol. AP-3, No. 3, pp. 145–147, July 1955.
25. Y. Y. Hu, "A Method of Determining Phase Centers and Its Application to Electromagnetic Horns," *J. Franklin Inst.*, pp. 31–39, January 1961.
26. J. Ruze, "The Effect of Aperture Errors on the Antenna Radiation Pattern," *Nuevo Cimento Suppl.*, Vol. 9, No. 3, pp. 364–380, 1952.
27. H. C. Minnett and B. MacA. Thomas, "Fields in the Image Space of Symmetrical Focusing Reflectors," *Proc. IEE*, Vol. 115, pp. 1419–1430, October 1968.
28. G. F. Koch, "Coaxial Feeds for High Aperture Efficiency and Low Spillover of Paraboloidal Reflector Antennas," *IEEE Trans. Antennas Propagat.*, Vol. AP-21, No. 2, pp. 164–169, March 1973.
29. R. E. Lawrie and L. Peters, Jr., "Modifications of Horn Antennas for Low Side Lobe Levels," *IEEE Trans. Antennas Propagat.*, Vol. AP-14, No. 5, pp. 605–610, September 1966.
30. A. J. Simmons and A. F. Kay, "The Scalar Feed-A High Performance Feed for Large Paraboloid Reflectors," *Design and Construction of Large Steerable Aerials*, IEE Conf. Publ. 21, pp. 213–217, 1966.
31. W. M. Truman and C. A. Balanis, "Optimum Design of Horn Feeds for Reflector Antennas," *IEEE Trans. Antennas Propagat.*, Vol. AP-22, No. 4, pp. 585–586, July 1974.

INTEL-1045
U.S. Patent 7,151,430

32. B. Houshmand, B. Fu, and Y. Rahmat-Samii, "Reflector Antenna Analysis Software," Vol. II, Chapter 11, CAEME Center for Multimedia Education, University of Utah, pp. 447–465, 1995.
33. P. W. Hannan, "Microwave Antennas Derived from the Cassegrain Telescope," *IRE Trans. Antennas Propagat.*, Vol. AP-9, No. 2, pp. 140–153, March 1961.
34. W. V. T. Rusch, "Scattering from a Hyperboloidal Reflector in a Cassegrain Feed System," *IEEE Trans. Antennas Propagat.*, Vol. AP-11, No. 4, pp. 414–421, July 1963.
35. P. D. Potter, "Application of Spherical Wave Theory to Cassegrainian-Fed Paraboloids," *IEEE Trans. Antennas Propagat.*, Vol. AP-15, No. 6, pp. 727–736, November 1967.
36. W. C. Wong, "On the Equivalent Parabola Technique to Predict the Performance Characteristics of a Cassegrain System with an Offset Feed," *IEEE Trans. Antennas Propagat.*, Vol. AP-21, No. 3, pp. 335–339, May 1973.
37. V. Galindo, "Design of Dual-Reflector Antennas with Arbitrary Phase and Amplitude Distributions," *IEEE Trans. Antennas Propagat.*, Vol. AP-12, No. 4, pp. 403–408, July 1964.
38. W. F. Williams, "High Efficiency Antenna Reflector," *Microwave Journal*, Vol. 8, pp. 79–82, July 1965.
39. G. W. Collins, "Shaping of Subreflectors in Cassegrainian Antennas for Maximum Aperture Efficiency," *IEEE Trans. Antennas Propagat.*, Vol. AP-21, No. 3, pp. 309–313, May 1973.
40. C. A. Balanis, *Advanced Engineering Electromagnetics*, John Wiley & Sons, Inc., New York, pp. 744–764, 1989.
41. R. Mittra and V. Galindo-Israel, "Shaped Dual Reflector Synthesis," *IEEE Antennas and Propagation Society Newsletter*, Vol. 22, No. 4, pp. 5–9, August 1980.
42. K. A. Green, "Modified Cassegrain Antenna for Arbitrary Aperture Illumination," *IEEE Trans. Antennas Propagat.*, Vol. AP-11, No. 5, pp. 589–590, September 1963.
43. J. Ashmead and A. B. Pippard, "The Use of Spherical Reflectors as Microwave Scanning Aerials," *J. Inst. Elec. Eng.*, Vol. 93, Part III-A, pp. 627–632, 1946.
44. T. Li, "A Study of Spherical Reflectors as Wide-Angle Scanning Antennas," *IRE Trans. Antennas Propagat.*, Vol. AP-7, No. 3, pp. 223–226, July 1959.
45. R. C. Spencer, C. J. Sletten, and J. E. Walsh, "Correction of Spherical Aberration by a Phased Line Source," *Proceedings National Electronics Conference*, Vol. 5, pp. 320–333, 1949.
46. A. C. Schell, "The Diffraction Theory of Large-Aperture Spherical Reflector Antennas," *IEEE Trans. Antennas Propagat.*, Vol. AP-11, No. 4, pp. 428–432, July 1963.

PROBLEMS

15.1. An infinite line source, of constant electric current I_0, is placed a distance s above a flat and infinite electric ground plane. Derive the array factor.

15.2. For corner reflectors with included angles of $\alpha = 60°$, 45°, and 30°:
   (a) Derive the array factors of (15-7)–(15-9b).
   (b) Plot the field strength along the axis ($\theta = 90°$, $\phi = 0°$) as a function of the feed-to-vertex spacing, $0 \leq s/\lambda \leq 10$.

15.3. Consider a corner reflector with an included angle of $\alpha = 36°$.
   (a) Derive the array factor.
   (b) Plot the relative field strength along the axis ($\theta = 90°$, $\phi = 0°$) as a function of the feed-to-vertex spacing s, for $0 \leq s/\lambda \leq 10$.
   (c) Determine the spacing that yields the first maximum possible field strength along the axis. For this spacing, what is the ratio of the field strength of the corner reflector along the axis to the field strength of the feed element alone?
   (d) For the spacing in part c, plot the normalized power pattern in the azimuthal plane ($\theta = 90°$).

INTEL-1045
U.S. Patent 7,151,430

15.4. A 60° corner reflector, in conjunction with a $\lambda/2$ dipole feed, is used in a radar tracking system. One of the requirements for such a system is that the antenna, in one of its modes of operation, has a null along the forward symmetry axis. In order to accomplish this, what should be the feed spacing from the vertex (in wavelengths)? To get credit, give all the possible values of the feed-to-vertex spacing.

15.5. For a parabolic reflector, derive (15-25) which relates the f/d ratio to its subtended angle θ_0.

15.6. Show that for a parabolic reflector
(a) $0 \leq f/d \leq 0.25$ relates to $180° \geq \theta_0 \geq 90°$
(b) $0.25 \leq f/d \leq \infty$ relates to $90° \geq \theta_0 \geq 0°$

15.7. The diameter of a paraboloidal reflector antenna (dish), used for public television stations, is 10 meters. Find the far-zone distance if the antenna is used at 2 and 4 GHz.

15.8. Show that the directivity of a uniformly illuminated circular aperture of diameter d is equal to $(\pi d/\lambda)^2$.

15.9. Verify (15-33) and (15-33a).

15.10. The field radiated by a paraboloidal reflector with an f/d ratio of 0.5 is given by

$$\mathbf{E} = (\hat{\mathbf{a}}_x + \hat{\mathbf{a}}_y \sin\phi \cos\phi)\, f(r, \theta, \phi)$$

where the x-component is the co-pol and the y-component is the cross-pol.
(a) At what observation angle(s) (in degrees) ($0° - 180°$) is the cross-pol minimum? What is the minimum value?
(b) At what observation angle(s) (in degrees) ($0° - 180°$) is the cross-pol maximum? What is the maximum value?
(c) What is the polarization loss factor when the receiving antenna is linearly polarized in the x-direction.
(d) What is the polarization loss factor when the receiving antenna is linearly polarized in the y-direction.
(e) What should the polarization of the receiving antenna be in order to eliminate the losses due to polarization? Write an expression for the polarization of the receiving antenna to achieve this.

15.11. Verify (15-49) and (15-54).

15.12. A small parabolic reflector (dish) of revolution, referred to as a paraboloid, is now being advertised as a TV antenna for direct broadcast. Assuming the diameter of the reflector is 1 meter, determine at 3 GHz the directivity (in dB) of the antenna if the feed is such that
(a) the illumination over the aperture is uniform (ideal)
(b) the taper efficiency is 80% while the spillover efficiency is 85%. Assume no other losses. What is the total aperture efficiency of the antenna (in dB)?

15.13. The 140-ft (42.672-m) paraboloidal reflector at the National Radio Astronomy Observatory, Green Bank, W. Va, has an f/d ratio of 0.4284. Determine the
(a) subtended angle of the reflector
(b) aperture efficiency assuming the feed pattern is symmetrical and its gain pattern is given by $2\cos^2(\theta'/2)$, where θ' is measured from the axis of the reflector
(c) directivity of the entire system when the antenna is operating at 10 GHz, and it is illuminated by the feed pattern of part (b)
(d) directivity of the entire system at 10 GHz when the reflector is illuminated by the feed pattern of part (b) and the maximum aperture phase deviation is $\pi/16$ rad

15.14. A paraboloidal reflector has an f/d ratio of 0.38. Determine
(a) which $\cos^n \theta'$ symmetrical feed pattern will maximize its aperture efficiency
(b) the directivity of the reflector when the focal length is 10λ
(c) the value of the feed pattern in dB (relative to the main maximum) along the edges of the reflector

15.15. Verify that the ideal parabolic reflector feed pattern, for uniform amplitude taper and no spillover, is that represented by $\sec^4(\theta'/2)$.

INTEL-1045
U.S. Patent 7,151,430

15.16. The symmetrical feed pattern for a paraboloidal reflector is given by

$$G_f = \begin{cases} G_0 \cos^4\left(\dfrac{\theta'}{2}\right) & 0 \le \theta' \le \pi/2 \\ 0 & \text{elsewhere} \end{cases}$$

where G_0 is a constant.
(a) Evaluate the constant G_0.
(b) Derive an expression for the aperture efficiency.
(c) Find the subtended angle of the reflector that will maximize the aperture efficiency. What is the maximum aperture efficiency?

15.17. A paraboloidal reflector is operating at a frequency of 5 GHz. It is 8 meters in diameter, with an *f/d* ratio of 0.25. It is fed with an antenna whose primary pattern is symmetrical and which can be approximated by

$$G_f = \begin{cases} 10 \cos^4 \theta' & 0 \le \theta' \le \pi/2 \\ 0 & \text{elsewhere} \end{cases}$$

Find its
(a) aperture efficiency
(b) overall directivity
(c) spillover efficiency
(d) taper efficiency

15.18. A parabolic reflector has a diameter of 10 meters and has an included angle of $\theta_0 = 30°$. The directivity at the operating frequency of 25 GHz is 5,420,000. The phase efficiency, polarization efficiency, blockage efficiency, and random error efficiency are all 100%. The feed has a phi-symmetric pattern given by

$$G_f = \begin{cases} G_0 \cos^{10} \theta' & 0° \le \theta' \le 90° \\ 0 & \text{elsewhere} \end{cases}$$

Find the taper, spillover, and overall efficiencies.

15.19. A 10-meter diameter paraboloidal reflector is used as a TV satellite antenna. The focus-to-diameter ratio of the reflector is 0.536 and the pattern of the feed in the forward region can be approximated by $\cos^2(\theta')$. Over the area of the reflector, the incident power density from the satellite can be approximated by a uniform plane wave with a power density of 10 μ watts/m^2. At a center frequency of 9 GHz:
(a) What is the maximum directivity of the reflector (in dB)?
(b) Assuming no losses of any kind, what is the maximum power that can be delivered to a TV receiver connected to the reflector through a lossless transmission line?

15.20. A 3-meter diameter parabolic reflector is used as a receiving antenna for satellite television reception at 5 GHz. The reflector is connected to the television receiver through a 78-ohm coaxial cable. The aperture efficiency is approximately 75%. Assuming the maximum incident power density from the satellite is 10 microwatts/square meter and the incident wave is polarization-matched to the reflector antenna, what is the:
(a) Directivity of the antenna (in dB)
(b) Maximum power (in watts) that can be delivered to the receiving TV? Assume no losses.
(c) Power (in watts) delivered to the receiving TV if the reflection coefficient at the transmission line/receiving TV terminal junction is 0.2. Assume no other losses.

15.21. A reflector antenna with a total subtended angle of 120° is illuminated at 10 GHz with a specially designed feed so that its aperture efficiency is nearly unity. The focal distance of the reflector is 5 meters. Assuming the radiation pattern is nearly symmetric, determine the:

INTEL-1045
U.S. Patent 7,151,430

(a) Half-power beamwidth (in degrees).
(b) Sidelobe level (in dB).
(c) Directivity (in dB).
(d) Directivity (in dB) based on Kraus' formula and Tai & Pereira's formula.
(e) Loss in directivity (in dB) if the surface has rms random roughness of 0.64 mm.

15.22. A front-fed paraboloidal reflector with an f/d radio of 0.357, whose diameter is 10 meters and which operates at 10 GHz, is fed by an antenna whose power pattern is rotationally symmetric and it is represented by $\cos^2(\theta/2)$. All the power is radiated in the forward region ($0° \leq \theta' \leq 90°$) of the feed. Determine the
(a) spillover efficiency
(b) taper efficiency
(c) overall aperture efficiency
(d) directivity of the reflector (in dB)
(e) directivity of the reflector (in dB) if the RMS, reflector surface deviation from an ideal paraboloid is $\lambda/100$.

15.23. Design pyramidal horn antennas that will maximize the aperture efficiency or produce maximum power transmission to the feed, for paraboloidal reflectors with f/d ratios of
(a) 0.50
(b) 0.75
(c) 1.00

INTEL-1045
U.S. Patent 7,151,430

CHAPTER 16

ANTENNA MEASUREMENTS

16.1 INTRODUCTION

In the previous fifteen chapters, analytical methods have been outlined which can be used to analyze, synthesize, and numerically compute the radiation characteristics of antennas. Often many antennas, because of their complex structural configuration and excitation method, cannot be investigated analytically. Although the number of radiators that fall into this category has diminished, because special analytical methods (such as the GTD, Moment Method, Finite-Difference Time-Domain and Finite Element) have been developed during the past few years, there are still a fair number that have not been examined analytically. In addition, experimental results are often needed to validate theoretical data.

As was discussed in Chapter 3, Section 3.8.1, it is usually most convenient to perform antenna measurements with the test antenna in its receiving mode. If the test antenna is reciprocal, the receiving mode characteristics (gain, radiation pattern, etc.) are identical to those transmitted by the antenna. The ideal condition for measuring far-field radiation characteristics then, is the illumination of the test antenna by plane waves: uniform amplitude and phase. Although this ideal condition is not achievable, it can be approximated by separating the test antenna from the illumination source by a large distance on an outdoor range. At large radii, the curvature of the spherical phasefront produced by the source antenna is small over the test antenna aperture. If the separation distance is equal to the inner boundary of the far-field region, $2D^2/\lambda$, then the maximum phase error of the incident field from an ideal plane wave is about 22.5°, as shown in Figure 16.1. In addition to phasefront curvature due to finite separation distances, reflections from the ground and nearby objects are possible sources of degradation of the test antenna illumination.

Experimental investigations suffer from a number of drawbacks such as:

1. For pattern measurements, the distance to the far-field region ($r > 2D^2/\lambda$) is too long even for outside ranges. It also becomes difficult to keep unwanted reflections from the ground and the surrounding objects below acceptable levels.
2. In many cases, it may be impractical to move the antenna from the operating environment to the measuring site.
3. For some antennas, such as phased arrays, the time required to measure the necessary characteristics may be enormous.

INTEL-1045
U.S. Patent 7,151,430

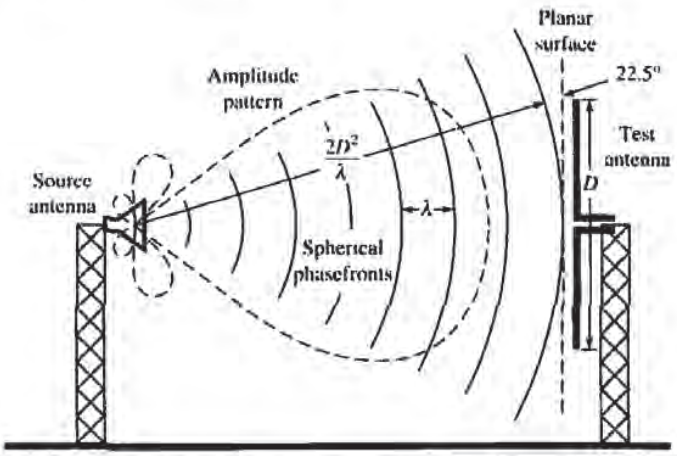


Figure 16.1 Phase error at the edges of a test antenna in the far-field when illuminated by a spherical wave.

4. Outside measuring systems provide an uncontrolled environment, and they do not possess an all-weather capability.
5. Enclosed measuring systems usually cannot accommodate large antenna systems (such as ships, aircraft, large spacecraft, etc.).
6. Measurement techniques, in general, are expensive.

Some of the above shortcomings can be overcome by using special techniques, such as indoor measurements, far-field pattern prediction from near-field measurements [1]–[4], scale model measurements, and automated commercial equipment specifically designed for antenna measurements and utilizing computer assisted techniques.

Because of the accelerated progress made in aerospace/defense related systems (with increasingly small design margins), more accurate measurement methods were necessary. To accommodate these requirements, improved instrumentation and measuring techniques were developed which include tapered anechoic chambers [5], compact and extrapolation ranges [2], near-field probing techniques [2]–[4], improved polarization techniques and swept-frequency measurements [6], indirect measurements of antenna characteristics, and automated test systems.

The parameters that often best describe an antenna system's performance are the pattern (amplitude and phase), gain, directivity, efficiency, impedance, current distribution, and polarization. Each of these topics will be addressed briefly in this chapter. A more extensive and exhaustive treatment of these and other topics can be found in the *IEEE Standard Test Procedures for Antennas* [7], in a summarized journal paper [8], and in a book on microwave antenna measurements [6]. Most of the material in this chapter is drawn from these three sources. The author recommends that the IEEE publication on test procedures for antennas becomes part of the library of every practicing antenna and microwave engineer.

16.2 ANTENNA RANGES

The testing and evaluation of antennas are performed in antenna ranges. Antenna facilities are categorized as *outdoor* and *indoor* ranges, and limitations are associated with both of them. Outdoor ranges are not protected from environmental conditions whereas indoor facilities are limited by space restrictions. Because some of the antenna characteristics are measured in the receiving mode and require far-field criteria, the

INTEL-1045
U.S. Patent 7,151,430

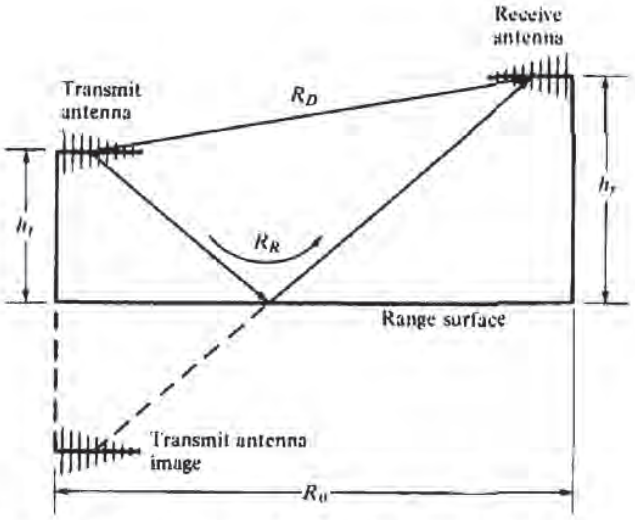


Figure 16.2 Geometrical arrangement for reflection range. (SOURCE: L. H. Hemming and R. A. Heaton, "Antenna Gain Calibration on a Ground Reflection Range," *IEEE Trans. Antennas Propagat.*, Vol. AP-21, No. 4, pp. 532–537, July 1973. © (1973) IEEE)

ideal field incident upon the test antenna should be a uniform plane wave. To meet this specification, a large space is usually required and it limits the value of indoor facilities.

16.2.1 Reflection Ranges

In general, there are two basic types of antenna ranges: the *reflection* and the *free-space* ranges. The reflection ranges, if judiciously designed [9], can create a constructive interference in the region of the test antenna which is referred to as the "quiet zone." This is accomplished by designing the ranges so that specular reflections from the ground, as shown in Figure 16.2, combine constructively with direct rays.

Usually it is desirable for the illuminating field to have a small and symmetric amplitude taper. This can be achieved by adjusting the transmitting antenna height while maintaining constant that of the receiving antenna. These ranges are of the outdoor type, where the ground is the reflecting surface, and they are usually employed in the UHF region for measurements of patterns of moderately broad antennas. They are also used for systems operating in the UHF to the 16-GHz frequency region.

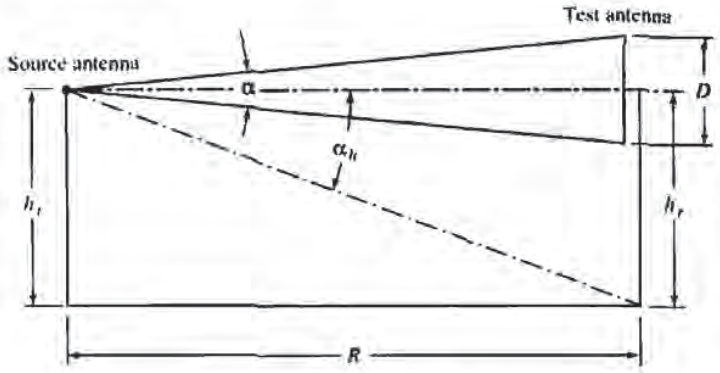
16.2.2 Free-Space Ranges

Free-space ranges are designed to suppress the contributions from the surrounding environment and include *elevated ranges*, *slant ranges* [10], *anechoic chambers*, *compact ranges* [2], and *near-field ranges* [4].

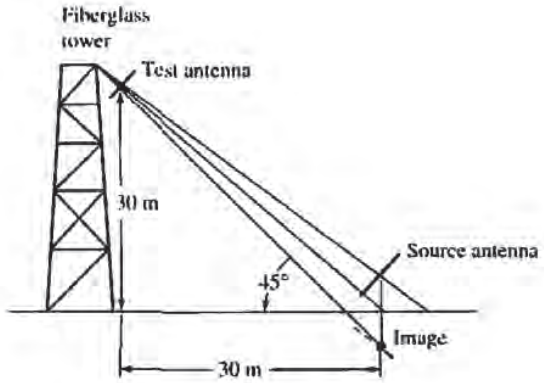
A. Elevated Ranges

Elevated ranges are usually designed to operate mostly over smooth terrains. The antennas are mounted on towers or roofs of adjacent buildings. These ranges are used to test physically large antennas. A geometrical configuration is shown in Figure 16.3(a). The contributions from the surrounding environment are usually reduced or eliminated by [7]

INTEL-1045
U.S. Patent 7,151,430



(a) Elevated (after [7])



(b) Slant (after P. W. Arnold [10])

Figure 16.3 Geometries of elevated and slant ranges. (SOURCES: *IEEE Standard Test Procedures for Antennas*, IEEE Std 149–1979, published by IEEE, Inc., 1979, distributed by Wiley; and P. W. Arnold, "The 'Slant' Antenna Range," *IEEE Trans. Antennas Propagat.*, Vol. AP-14, No. 5, pp. 658–659, Sept. 1966. © (1966) IEEE)

1. carefully selecting the directivity and side lobe level of the source antenna
2. clearing the line-of-sight between the antennas
3. redirecting or absorbing any energy that is reflected from the range surface and/or from any obstacles that cannot be removed
4. utilizing special signal processing techniques such as modulation tagging of the desired signal or by using short pulses

In some applications, such as between adjacent mountains or hilltops, the ground terrain may be irregular. For these cases, it is more difficult to locate the specular reflection points (points that reflect energy toward the test antenna). To take into account the irregular surface, scaled drawings of the vertical profile of the range are usually constructed from data obtained from the U.S. Geological Survey. The maps show ground contours [11], and they give sufficient details which can be used to locate the specular reflection points, determine the level of energy reflected toward the test antenna, and make corrections if it is excessive.

INTEL-1045
U.S. Patent 7,151,430

B. Slant Ranges

Slant ranges [10] are designed so that the test antenna, along with its positioner, are mounted at a fixed height on a nonconducting tower while the source (transmitting) antenna is placed near the ground, as shown in Figure 16.3(b). The source antenna is positioned so that the pattern maximum, of its free-space radiation, is oriented toward the center of the test antenna. The first null is usually directed toward the ground specular reflection point to suppress reflected signals. Slant ranges, in general, are more compact than elevated ranges in that they require less land.

C. Anechoic Chambers

To provide a controlled environment, an all-weather capability, and security, and to minimize electromagnetic interference, indoor anechoic chambers have been developed as an alternative to outdoor testing. By this method, the testing is performed inside a chamber having walls that are covered with RF absorbers. The availability of commercial high-quality RF absorbing material, with improved electrical characteristics, has provided the impetus for the development and proliferation of anechoic chambers. Anechoic chambers are mostly utilized in the microwave region, but materials have been developed [12] which provide a reflection coefficient of -40 dB at normal incidence at frequencies as low as 100 MHz. In general, as the operating frequency is lowered, the thickness of RF absorbing material must be increased to maintain a given level of reflectivity performance. An RF absorber that meets the minimum electrical requirements at the lower frequencies usually possesses improved performance at higher frequencies.

Presently there are two basic types of anechoic chamber designs: the *rectangular* and the *tapered chamber*. The design of each is based on geometrical optics techniques, and each attempts to reduce or to minimize specular reflections. The geometrical configuration of each, with specular reflection points depicted, is shown in Figures 16.4(a) and 16.4(b).

The rectangular chamber [13] is usually designed to simulate free-space conditions and maximize the volume of the quiet zone. The design takes into account the pattern and location of the source, the frequency of operation, and it assumes that the receiving antenna at the test point is isotropic. Reflected energy is minimized by the use of high-quality RF absorbers. Despite the use of RF absorbing material, significant specular reflections can occur, especially at large angles of incidence.

Tapered anechoic chambers [14] take the form of a pyramidal horn. They begin with a tapered chamber which leads to a rectangular configuration at the test region as shown in Figure 16.4(b). At the lower end of the frequency band at which the chamber is designed, the source is usually placed near the apex so that the reflections from the side walls, which contribute to the region of the test antenna, occur near the source antenna. For such paths, the phase difference between the direct radiation and that reflected from the walls near the source can be made very small by properly locating the source antenna near the apex. Thus the direct and reflected rays near the test antenna region add vectorially and provide a relatively smooth amplitude illumination taper. This can be illustrated by ray tracing techniques.

As the frequency of operation increases, it becomes increasingly difficult to place the source sufficiently close to the apex that the phase difference between the direct and specularly reflected rays can be maintained below an acceptable level. For such applications, reflections from the walls of the chamber are suppressed by using high-gain source antennas whose radiation toward the walls is minimal. In addition,

INTEL-1045
U.S. Patent 7,151,430

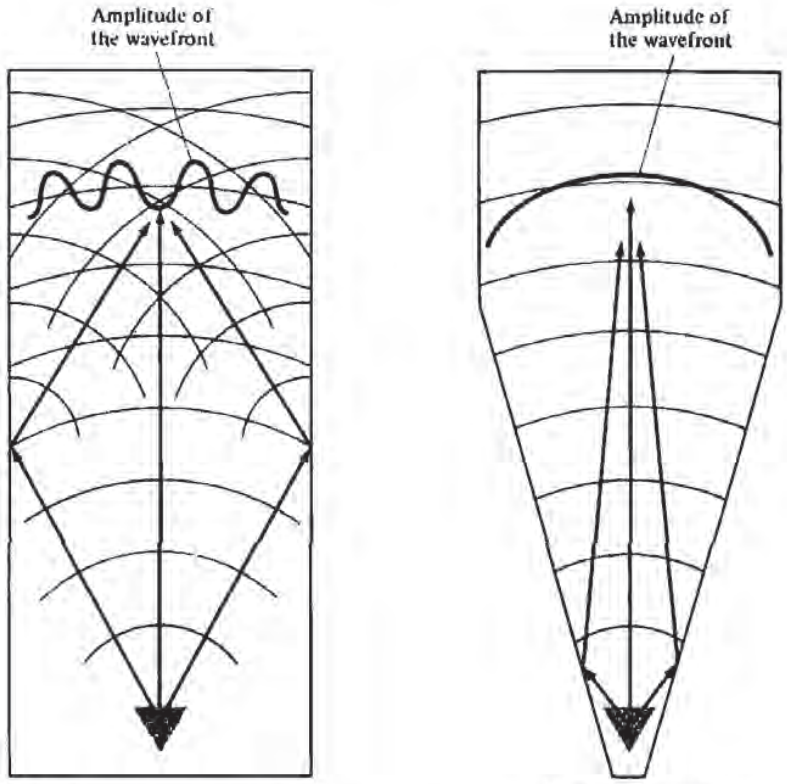


Figure 16.4 Rectangular and tapered anechoic chambers and the corresponding side-wall specular reflections. (SOURCE: W. H. Kummer and E. S. Gillespie, "Antenna Measurements—1978," *Proc. IEEE*, Vol. 66, No. 4, pp. 483–507, April 1978. © (1978) IEEE)

the source is moved away from the apex, and it is placed closer to the end of the tapering section so as to simulate a rectangular chamber.

16.2.3 Compact Ranges

Microwave antenna measurements require that the radiator under test be illuminated by a uniform plane wave. This is usually achieved only in the far-field region, which in many cases dictates very large distances. The requirement of an ideal plane wave illumination can be nearly achieved by utilizing a compact range.

A *C*ompact *A*ntenna *T*est *R*ange (CATR) is a collimating device which generates nearly planar wavefronts in a very short distance (typically 10–20 meters) compared to the $2D^2/\lambda$ (minimum) distance required to produce the same size test region using the standard system configuration of testing shown in Figure 16.1. Some attempts have been made to use dielectric lenses as collimators [15], but generally the name compact antenna test range refers to one or more curved metal reflectors which perform the collimating function. Compact antenna test ranges are essentially very large reflector antennas designed to optimize the planar characteristics of the fields in the near-field of the aperture. Compact range configurations are often designated according to their analogous reflector antenna configurations: parabolic, Cassegrain, Gregorian, and so forth.

One compact range configuration is that shown in Figure 16.5 where a source antenna is used as an offset feed that illuminates a paraboloidal reflector, which

INTEL-1045
U.S. Patent 7,151,430

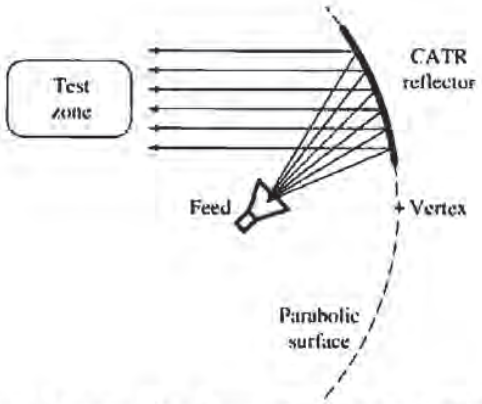


Figure 16.5 A Compact Antenna Test Range (CATR) synthesizes planar phasefronts by collimating spherical waves with a section of paraboloidal reflector.

converts the impinging spherical waves to plane waves [2]. Geometrical Optics (GO) is used in Figure 16.5 to illustrate general CATR operation. The rays from a feed antenna can, over the main beam, be viewed as emanating from a point at its phase center. When the phase center of the feed is located at the prime focus of a parabolic reflector, all rays that are reflected by the reflector and arrive at a plane transverse to the axis of the parabola have traveled an equal distance. See Chapter 15, Section 15.4 for details. Therefore, the field at the aperture of the reflector has a uniform phase; i.e., that of a plane wave. In addition to Geometrical Optics, analysis and design of CATRs have been performed with a number of other analytical methods. Compact range test zone fields have been predicted by the Method of Moments (MoM), but at high frequencies, the large electrical size of the CATR system makes the use of MoM, Finite-Difference Time-Domain (FDTD), and Finite Element Method (FEM) impractical. High-frequency techniques, however, are well suited for compact range analysis because the fields of interest are near the specular reflection direction, and the reflector is electrically large. The Geometrical Theory of Diffraction (GTD) is, in principle, an appropriate technique, but it is difficult to implement for serrated-edge reflectors due to the large number of diffracting edges. To date, Physical Optics (PO) is probably the most practical and efficient method of predicting the performance of CATRs [16], [17].

The major drawbacks of compact ranges are aperture blockage, direct radiation from the source to the test antenna, diffractions from the edges of the reflector and feed support, depolarization coupling between the two antennas, and wall reflections. The use of an offset feed eliminates aperture blockage and reduces diffractions. Direct radiation and diffractions can be reduced further if a reflector with a long focal length is chosen. With such a reflector, the feed can then be mounted below the test antenna and the depolarization effects associated with curved surfaces are reduced. Undesirable radiation toward the test antenna can also be minimized by the use of high-quality absorbing material. These and other concerns will be discussed briefly.

A. CATR Performance

A perfect plane wave would be produced by a CATR if the reflector has an ideal parabolic curvature, is infinite in size and is fed by a point source located at its focus. Of course CATR reflectors are of finite size, and their surfaces have imperfections; thus the test zone fields they produce can only approximate plane waves. Although

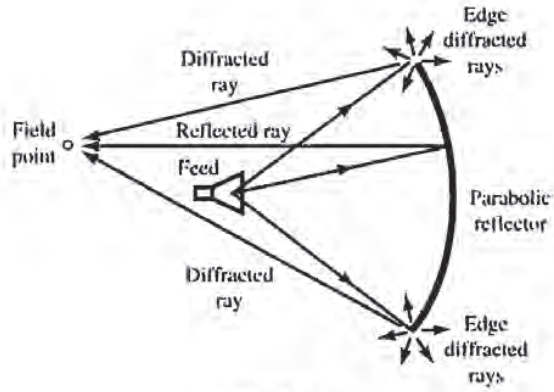
INTEL-1045
U.S. Patent 7,151,430

there are different configurations of CATR, their test zone fields have some common characteristics. The usable portion of the test zone consists of nearly planar wavefronts and is referred to as the "quiet zone." Outside the quiet zone, the amplitude of the fields decreases rapidly as a function of distance transverse to the range axis. The size of the quiet zone is typically about 50%–60% of the dimensions of the main reflector. Although the electromagnetic field in the quiet zone is often a very good approximation, it is not a "perfect" plane wave. The imperfections of the fields in the quiet zone from an ideal plane wave are usually represented by phase errors, and ripple and taper amplitude components. These discrepancies from an ideal plane wave, that occur over a specified test zone dimension, are the primary figures-of-merit of CATRs. For most applications phase deviations of less than 10°, peak-to-peak amplitude ripples of less than 1 dB, and amplitude tapers of less than 1 dB are considered adequate. More stringent quiet zone specifications may be required to measure, within acceptable error levels, low-side lobe antennas and low-observable scatterers. The sources of quiet zone taper and ripple are well known, but their minimization is a source of much debate.

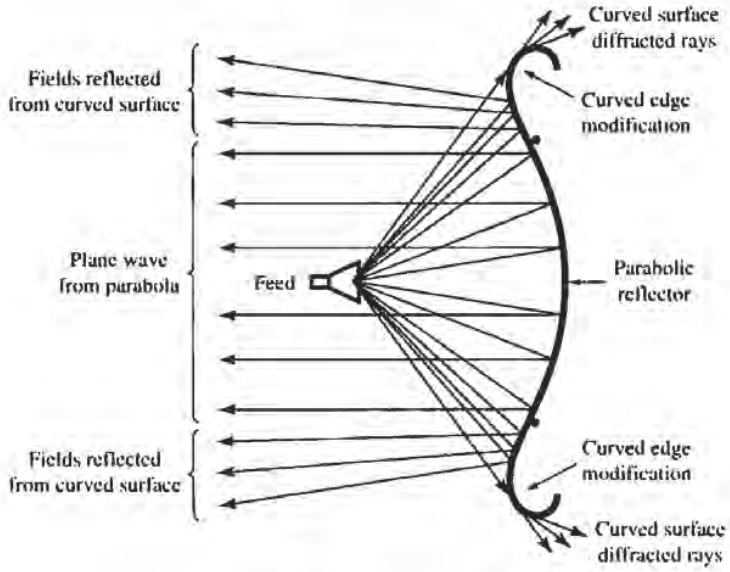
Amplitude taper across the quiet zone can be attributed to two sources: the feed pattern and space-attenuation. That portion of the radiation pattern of the feed antenna which illuminates the CATR reflector is directly mirrored into the quiet zone. For example, if the 3-dB beamwidth of the feed is equal to about 60% of the angle formed by lines from the reflector edges to the focal point, then the feed will contribute 3 dB of quiet zone amplitude taper. In general, as the directivity of the feed antenna increases, quiet zone amplitude taper increases. Usually, low-gain feed antennas are designed to add less than a few tenths of a dB of amplitude taper. The $1/r^2$ space-attenuation occurs with the spherical spreading of the uncollimated radiation from the feed. Although the total path from the feed to the quiet zone is a constant, the distance from the feed to the reflector varies. These differences in the propagation distances from the feed to various points across the reflector surface cause amplitude taper in the quiet zone due to space-attenuation. This taper is asymmetric in the plane of the feed offset.

Amplitude and phase ripple are primarily caused by diffractions from the edges of the reflector. The diffracted fields are spread in all directions which, along with the specular reflected signal, form constructive and destructive interference patterns in the quiet zone, as shown in Figure 16.6(a). Considerable research has been done on reflector edge terminations in an effort to minimize quiet zone ripple. Reflector edge *treatments are the physical analogues of windowing functions used in Fourier trans*forms. Edge treatments reduce the discontinuity of the reflector/free-space boundary, caused by the finite size of the reflector, by providing a gradually tapered transition. Common reflector edge treatments include serrations and rolled edges, as shown in Figure 16.7(a,b). The serrated edge of a reflector tapers the amplitude of the reflected fields near the edge. An alternate interpretation of the effects of serrations is based on edge diffraction. Serrations produce many low-amplitude diffractions as opposed to, for example, the large-amplitude diffractions that would be generated by the four straight edges and corners of a rectangular knife-edged reflector. These small diffractions are quasi-randomized in location and direction; hence, they are likely to have cancellations in the quiet zone. Although most serrated-edge CATRs have triangular serrations, curving the edges of each serration can result in improved performance at high frequencies [18]. A number of blended, rolled edge treatments have been suggested as alternatives to serrations, and have been implemented to gradually redirect energy away from the quiet zone, as shown in Figure 16.6(b) [19]–[21]. In

INTEL-1045
U.S. Patent 7,151,430



(a) Knife-edge

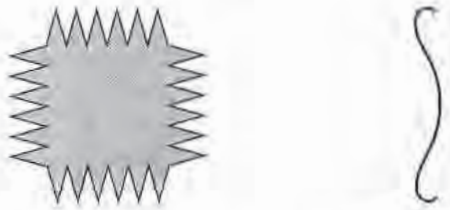


(b) Rolled-edge

Figure 16.6 Amplitude and phase ripple in the quiet zone fields produced by a compact antenna test range caused by the phasor sum of the reflected and diffracted rays from the reflector [SOURCE: W. D. Burnside, M. C. Gilreath, B. M. Kent and G. L. Clerici, "Curved Edge Modification of Compact Range Reflectors," *IEEE Trans. Antennas Propagat.*, Vol. AP-35, No. 2, pp. 176–182, February 1987. © (1987) IEEE)

these designs, the concave parabolic surface of the reflector is blended into a convex surface which wraps around the edges of the reflector and terminates behind it. The predicted quiet zone fields produced by a knife-edged reflector compared to those produced by a rolled-edged reflector are shown, respectively, in Figures 16.8(a,b) and demonstrate the effectiveness of this edge treatment. Another method of reducing quiet zone ripple is to taper the illumination amplitude near the reflector edges. This can be accomplished with a high-gain feed or the feed can consist of an array of small elements designed so that a null in the feed pattern occurs at the reflector edges [22]–[25]. Finally, the surface currents on the reflector can be terminated gradually at the edges by tapering the conductivity and/or the impedance of the reflector via the application of lossy material.

INTEL-1045
U.S. Patent 7,151,430



(a) Front view of a serrated-edge CATR reflector. (b) Side view of a rolled-edge CATR reflector.

Figure 16.7 Two common CATR reflector edge treatments that are used to reduce the diffracted fields in the quiet zone.

The frequency of operation of a CATR is determined by the size of the reflector and its surface accuracy. The low-frequency limit is usually encountered when the reflector is about 25 to 30 wavelengths in diameter [26]. Quiet zone ripple becomes large at the low-frequency limit. At high frequencies, reflector surface imperfections contribute to the quiet zone ripple. A rule of thumb used in the design of CATRs is that the surface must deviate less than about 0.007λ from that of a true paraboloid [27]. Since the effects of reflector surface imperfections are additive, dual reflector systems must maintain twice the surface precision of a single reflector system to operate at the same frequency. Many CATR systems operate typically from 1 GHz to 100 GHz.

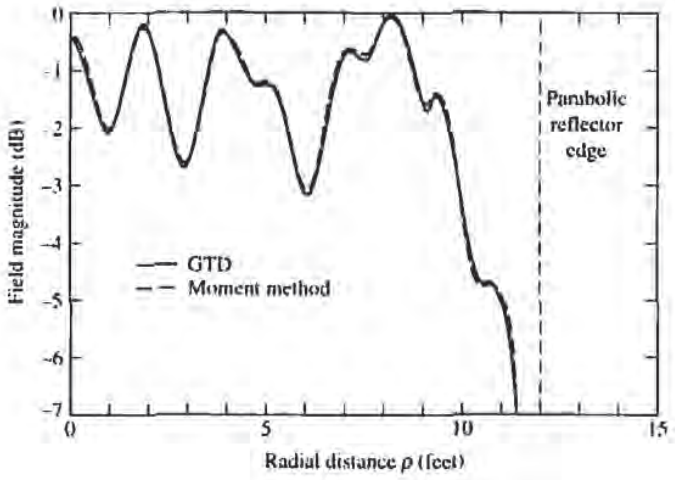
B. CATR Designs

Four reflector configurations that have been commercially developed will be briefly discussed: *the single paraboloid, the dual parabolic cylinder, the dual shaped-reflector,* and *the single parabolic cylinder systems.* The first three configurations are relatively common fully collimating compact ranges; the fourth is a hybrid approach which combines aspects of compact range technology with near-field/far-field (NF/FF) techniques.

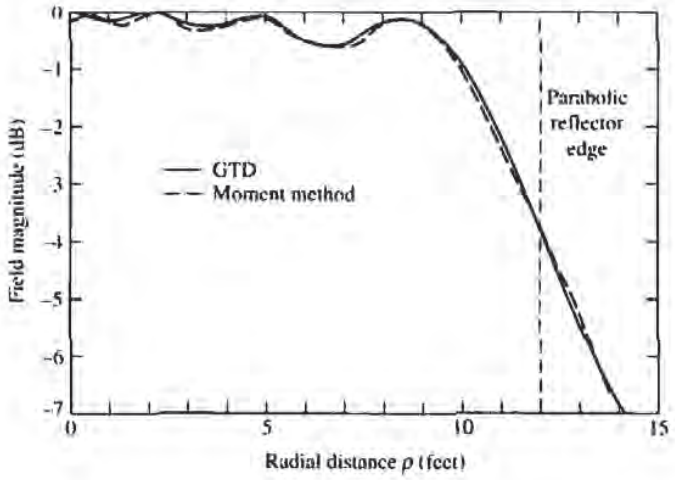
The single paraboloidal reflector CATR design was illustrated in Figure 16.5. As with all compact range designs, the feed antenna is offset by some angle from the propagation direction of the collimated energy. This is done to eliminate blockage and to reduce scattering of the collimated fields by the feed. To achieve this offset, the reflector is a sector of a paraboloid that does not include the vertex. This design is referred to as a *"virtual vertex"* compact range. With only one reflector, the paraboloidal CATR has a minimum number of surfaces and edges that can be sources of quiet-zone ripple. Feed spillover into the quiet zone is also low with this design since the feed antenna is pointed almost directly away from the test zone. On the other hand, it is more difficult and costly to produce a high-precision surface that is curved in two planes (three-dimensional) compared to producing a reflector that is curved in only one plane (two-dimensional). In addition, it has been reported that the single paraboloidal reflector design depolarizes the incident fields to a greater degree than other CATR designs. This is due to the relatively low *f/d* ratio needed to simultaneously maintain the feed antenna between the test zone and the reflector while keeping the test zone as close as possible to the reflector aperture [28].

The dual parabolic-cylinder reflector concept is illustrated in Figure 16.9, and it consists of two parabolic cylinders arranged so that one is curved in one plane (vertical or horizontal) while the other is curved in the orthogonal plane. The spherical phase-fronts radiated by the feed antenna are collimated first in the horizontal or vertical

INTEL-1045
U.S. Patent 7,151,430



(a) Knife-edge



(b) Rolled-edge

Figure 16.8 Predicted quiet zone field amplitude versus transverse distance for knife-edge and rolled-edge reflectors. (SOURCE: W. D. Burnside, M. C. Gilreath, B. M. Kent, and G. L. Clerici, "Curved Edge Modification of Compact Range Reflectors," *IEEE Trans. Antennas Propagat.*, Vol. AP-35, No. 2, pp. 176–182, February 1987. © (1987) IEEE)

plane by the first reflector, then are collimated in the orthogonal plane by the second reflector [29]. Because the boresight of the feed antenna is directed at almost 90° to the plane wave propagation direction, direct illumination of the test zone by the feed can be relatively high. In practice, quiet zone contamination from feed spillover is virtually eliminated through the use of range gating. Relatively low cross polarization is produced with this design because the doubly folded optics results in a long focal length main reflector.

The dual shaped-reflector CATR, shown schematically in Figure 16.10, is similar in design to a Cassegrain antenna, but the reflector surfaces are altered from the classical parabolic/hyperbolic shapes. An iterative design process is used to determine the shapes of the subreflector and main reflector needed to yield the desired quiet zone performance. The shape of the subreflector maps the high-gain feed pattern into

INTEL-1045
U.S. Patent 7,151,430

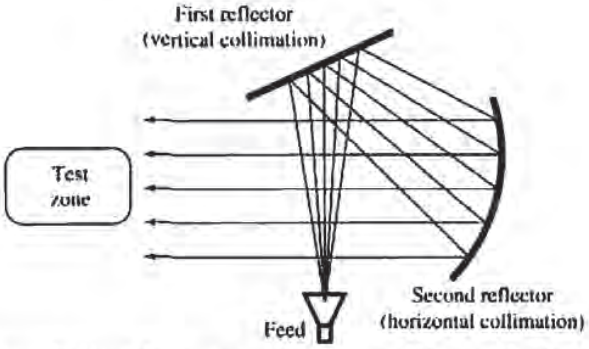


Figure 16.9 Dual parabolic-cylinder compact range collimates the fields in one plane with first reflector and then collimates the fields in the orthogonal plane with second reflector.

a nearly optimum illumination of the main reflector. An almost uniform energy density illuminates the central part of the main reflector while the amplitude tapers toward the reflector edges. This design results in a very high illumination efficiency (the power of the collimated quiet zone fields relative to the system input power) [30]. Two of the consequences of this high illumination efficiency are (1) the reduction of spillover into the chamber reduces range clutter, and (2) the increased RF power delivered to the target increases system sensitivity.

The single parabolic cylinder reflector system is essentially half of the dual parabolic-cylinder CATR. The reflector has a parabolic curvature in the vertical plane and is flat in the horizontal plane. This semicompact antenna test range collimates the fields only in the vertical plane, producing a quiet zone which consists of cylindrical waves, as shown in Figure 16.11 [31]–[33]. Such a compact range configuration is utilized in the ElectroMagnetic Anechoic Chamber (EMAC) at Arizona State University [32], [33].

This *Single-Plane Collimating Range* (SPCR) approach results in a number of advantages and compromises compared to conventional CATR systems and near-field/far-field (NF/FF) systems. For antennas that are small compared to the curvature of the cylindrical phasefront, far-field radiation patterns can be measured directly. Because of the folded optics, the radius of the cylindrical phasefront produced by the SPCR is larger than the radius of the spherical phasefront obtainable by separating the source antenna from the test antenna in a direct illumination configuration within the same anechoic chamber. Thus, with the SPCR it is possible to measure, directly, the far-field patterns of larger antennas compared to those directly measurable on an indoor far-field range. When the size of the antenna is significant relative to the curvature of the cylindrical phasefront, a NF/FF transformation is used to obtain the far-field pattern. However, because the fields are collimated in the vertical plane, only a one-dimensional transformation is required. This greatly simplifies the transforma-

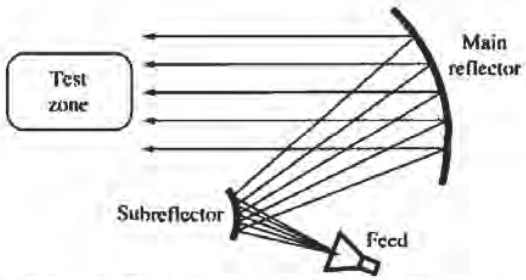


Figure 16.10 Dual shaped-reflector compact range analogous to a Cassegrain system.

INTEL-1045
U.S. Patent 7,151,430

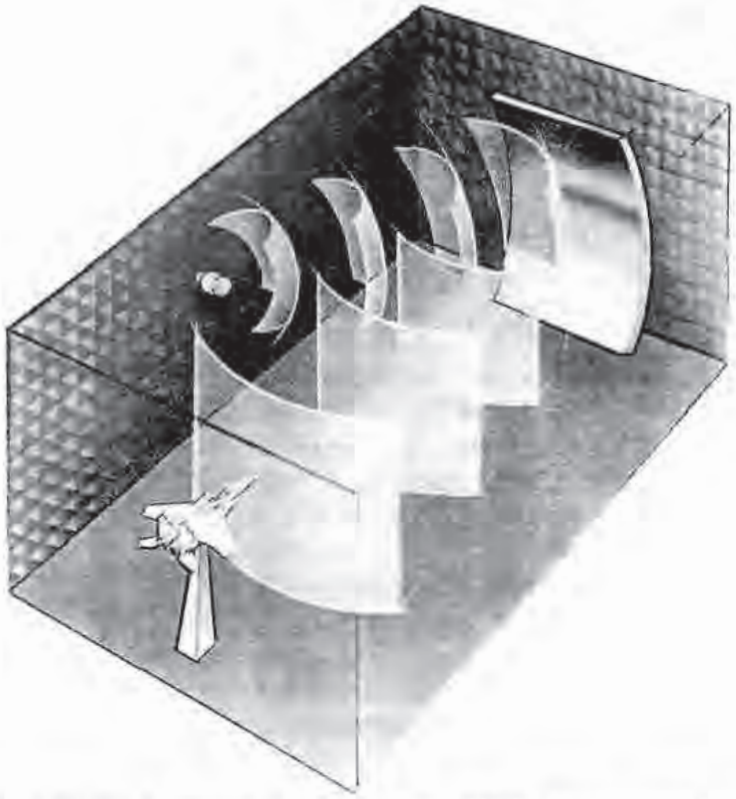


Figure 16.11 ASU Single-Plane Collimating Range (SPCR) produces a cylindrical wave in the quiet zone (artist rendering by Michael Hagelberg).

tion algorithm. Most importantly, there is a one-to-one correlation between a single azimuthal pattern cut measured in the near-field, and the predicted far-field pattern. The data acquisition time is identical to that of conventional CATRs, and the NF/FF calculation time is nearly negligible. Another advantage of the SPCR is the size of the quiet zone. In the vertical plane, the quiet zone dimension compared to the SPCR reflector is similar to that of conventional CATRs (about 50% to 60%). However, in the horizontal plane, the quiet zone is nearly 100% of the horizontal dimension of the reflector. For a given size anechoic chamber and reflector, targets having much larger horizontal dimensions (yaw patterns of aircraft, for example) can be measured using the SPCR than is possible using a conventional CATR. The SPCR system is relatively inexpensive; the manufacturer estimates that its cost is about 60% of conventional CATR systems.

In addition to the added complexity of NF/FF transformation considerations, this cylindrical wave approach has other disadvantages compared to conventional CATR designs. Because the quiet zone fields are expanding cylindrically as they propagate along the axis of the range, a large portion of the anechoic chamber is directly illuminated. This should be carefully considered in the design of the side walls of the anechoic chamber to control range clutter. Also, some measurement sensitivity is sacrificed for the same reason.

Compact antenna test ranges enable the measurement of full-sized antennas in very short distances, usually within the controlled environment of an anechoic chamber. A compact antenna test range can be used to accomplish any type of antenna testing (including radiation patterns, gain, efficiency, etc.) that can be performed on an outdoor facility.

INTEL-1045
U.S. Patent 7,151,430

16.2.4 Near-Field/Far-Field Methods

The dimensions of a conventional test range can be reduced by making measurements in the near-field, and then using analytical methods to transform the measured near-field data to compute the far-field radiation characteristics [2]–[4], [34]. These are referred to as *near-field to far-field (NF/FF) methods*. Such techniques are usually used to measure patterns, and they are often performed indoors. Therefore, they provide a controlled environment and an all-weather capability, the measuring system is time and cost effective, and the computed patterns are as accurate as those measured in a far-field range. However, such methods require more complex and expensive systems, more extensive calibration procedures, more sophisticated computer software, and the patterns are not obtained in real time.

The near-field measured data (usually amplitude and phase distributions) are measured by a scanning field probe over a preselected surface which may be a *plane*, a *cylinder*, or a *sphere*. The measured data are then transformed to the far-field using analytical Fourier transform methods. The complexity of the analytical transformation increases from the planar to the cylindrical, and from the cylindrical to the spherical surfaces. The choice is primarily determined by the antenna to be measured.

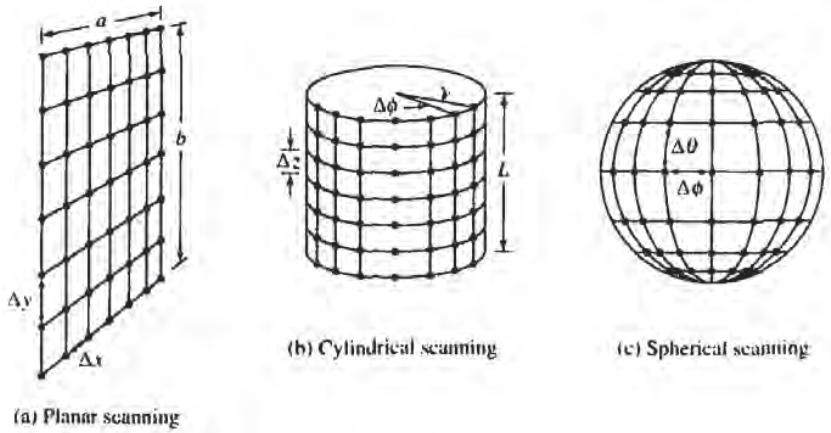
In general, the planar system is better suited for high-gain antennas, especially planar phased arrays, and it requires the least amount of computations and no movement of the antenna. Although the cylindrical system requires more computations than the planar, for many antennas its measuring, positioning, and probe equipment are the least expensive. The spherical system requires the most expensive computation, and antenna and probe positioning equipment, which can become quite significant for large antenna systems. This system is best suited for measurements of low-gain and omnidirectional antennas.

Generally, implementation of NF/FF transformation techniques begins with measuring the magnitude and phase of the tangential electric field components radiated by the test antenna at regular intervals over a well-defined surface in the near-field. By the principle of *modal expansion*, the sampled E-field data is used to determine the amplitude and phase of an angular spectrum of plane, cylindrical, or spherical waves. Expressing the total field of the test antenna in terms of a modal expansion, allows the calculation of the field at any distance from the antenna. Solving for the fields at an infinite distance results in the far-field pattern.

A consideration of the general case of scanning with ideal probes over an arbitrary surface [34] reveals that the choice of scanning surfaces is limited. Morse and Feshbach [35] show that derivation of the far-zone vector field from the near-field depends on vector wave functions that are orthogonal to that surface. Planar, circular cylindrical, spherical, elliptic cylindrical, parabolic cylindrical, and conical are the six coordinate systems that support orthogonal vector wave solutions. The first three coordinate systems are conducive to convenient data acquisition, but the last three require scanning on an elliptic cylinder, a parabolic cylinder, or a sphere in conical coordinates [34]. Thus, the three NF/FF techniques that have been developed and are widely used are based on *planar*, *cylindrical*, and *spherical* near-field scanning surfaces.

Acquisition of planar near-field data is usually conducted over a rectangular x-y grid, as shown in Figure 16.12(a), with a maximum near-field sample spacing of $\Delta x = \Delta y = \lambda/2$ [36]. It is also possible to acquire the near-field measurements on a plane-polar grid [37] or a bipolar grid [38]. The test antenna is held stationary while the probe (typically an open-ended waveguide or small horn) is moved to each grid location on the plane. As the probe location varies, its orientation relative to the test

INTEL-1045
U.S. Patent 7,151,430



(a) Planar scanning (b) Cylindrical scanning (c) Spherical scanning

Figure 16.12 Three near-field scanning surfaces that permit convenient data acquisition (planar, cylindrical, and spherical).

antenna changes, as illustrated in Figure 16.13. This directive property of the probe, as well as its polarization, must be taken into account using the technique of *probe compensation* [3], [4]. Probe compensation methods use the well-known Lorentz reciprocity theorem to couple the far-zone fields of the test antenna to those of the measuring probe.

The principal advantage of the planar near-field to far-field transformation, over the cylindrical and spherical techniques, is its mathematical simplicity. Furthermore, the planar transformation is suitable for applying the computationally efficient Fast Fourier Transform (FFT) algorithm [39]. Assuming that the number of near-field data points is 2^n (or artificially padded to that number with points of zero value) where n is a positive integer, the full planar far-field transformation can be computed in a time proportional to $(ka)^2 log_2(ka)$ where a is the radius of the smallest circle that inscribes the test antenna [34]. Planar NF/FF techniques are well suited for measuring antennas which have low backlobes. These include directional antennas such as horns, reflector antennas, planar arrays, and so forth. The primary disadvantage of probing the near-field on a planar surface to calculate the far-field is that the resulting far-field pattern is over a limited angular span. If the planar scanning surface is of infinite extent, one complete hemisphere of the far-field can be computed.

A complete set of near-field measurements over a *cylindrical* surface includes the information needed to compute complete azimuthal patterns for all elevation angles.

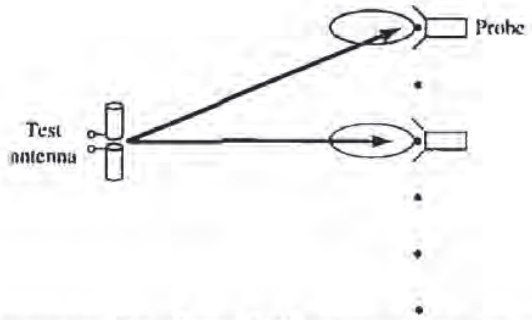


Figure 16.13 Probe compensation of near-field measurements due to nonisotropic radiation pattern of the probe.

INTEL-1045
U.S. Patent 7,151,430

excluding the conical regions at the top and bottom of the cylinder axis. Since the numerical integrations can be performed with the FFT, the cylindrical transformation exhibits numerical efficiencies and proportional computation times similar to those of the planar transformation. The angular modal expansion, however, is expressed in terms of Hankel functions, which can be more difficult to calculate, especially for large orders.

The cylindrical scanning grid is shown in Figure 16.12(b). The maximum angular and vertical sample spacing is

$$\Delta\phi = \frac{\lambda}{2(a + \lambda)} \tag{16-1}$$

and

$$\Delta z = \lambda/2 \tag{16-2}$$

where λ is the wavelength and a is the radius of the smallest cylinder that encloses the test antenna.

A typical cylindrical scanning system is illustrated in Figure 16.14(a). The azimuthal location of the antenna is held constant while the fields are probed at discrete locations in the vertical direction at some fixed distance from the antenna. At the completion of each vertical scan, the test antenna is rotated to the next angular position. The orientation of the probe with respect to the test antenna changes as the vertical location of the probe changes, thus a probe correction is generally required as in the planar case. In addition to directional antennas, the radiation patterns of antennas with narrow patterns along the vertical axis (horizontal fan beam antennas and vertical dipoles for example) can be predicted efficiently with the cylindrical NF/FF technique.

The information obtained by scanning the near-field radiation over a *spherical* surface enclosing a test antenna makes possible the most complete prediction of the far-field radiation pattern. The spherical scanning grid is illustrated in Figure 16.12(c). When sampled at the rate of

$$\Delta\theta = \frac{\lambda}{2(a + \lambda)} \tag{16-3}$$

and

$$\Delta\phi = \frac{\lambda}{2(a + \lambda)} \tag{16-4}$$

all of the spatial radiation characteristics of the test antenna are included in the transformation. Any far-field pattern cut can be computed from a complete near-field measurement with the spherical scanning scheme. Typically, a spherical scan is accomplished by fixing the location and orientation of the probe and varying the angular orientation of the test antenna with a dual-axis positioner, as shown in Figure 16.14(b). Since the probe is always pointed directly toward the test antenna, probe correction can be neglected for sufficiently large scan radii [34]. However, in general, probe correction is necessary.

The primary drawback of the spherical scanning technique lies in the mathematical transformation. A significant portion of the transformation cannot be accomplished via FFTs. Numerical integrations, matrix operations, and simultaneous solu-

INTEL-1045
U.S. Patent 7,151,430

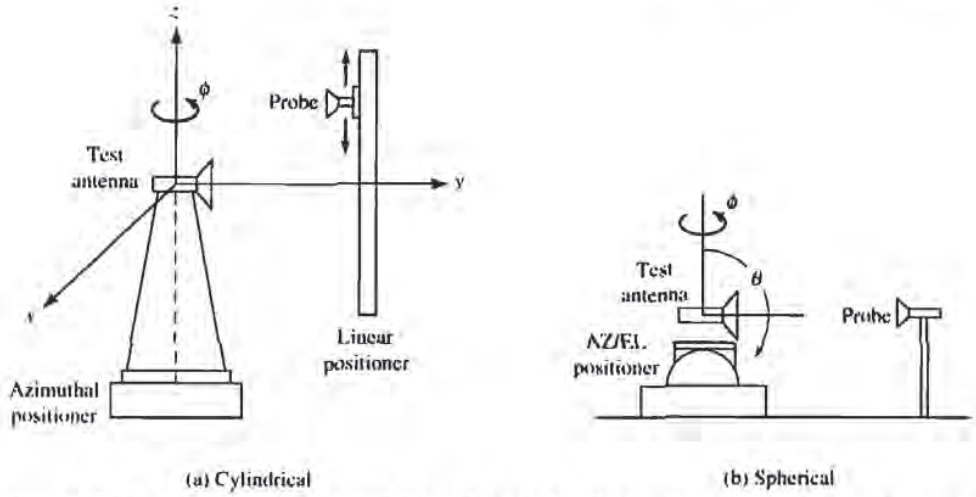


Figure 16.14 Schematic representation of typical cylindrical and spherical surface near-field positioning systems.

tion of equations are required. This increases the computational time and difficulty of the transformation considerably over those of the planar and cylindrical transformations.

A. Modal Expansion Method for Planar Systems

The mathematical formulations of the planar NF/FF system are based on the plane wave (modal) expansion using Fourier transform (spectral) techniques. Simply stated, any monochromatic, but otherwise arbitrary, wave can be represented as a superposition of plane waves traveling in different directions, with different amplitudes, but all of the same frequency. The objective of the plane wave expansion is to determine the unknown amplitudes and directions of propagation of the plane waves. The results comprise what is referred to as a *modal expansion* of the arbitrary wave. Similarly, cylindrical wave and spherical wave expansions are used to determine far-field patterns from fields measured in the near-field over cylindrical and spherical surfaces, respectively.

The relationships between the near-zone E-field measurements and the far-zone fields for planar systems follow from the transform (spectral) techniques of Chapter 12, Section 12.9, represented by (12-73)–(12-75), or

$$\mathbf{E}(x, y, z) = \frac{1}{4\pi^2}\int_{-\infty}^{\infty}\int_{-\infty}^{\infty}\mathbf{f}(k_x, k_y)e^{-j\mathbf{k}\cdot\mathbf{r}}\,dk_x dk_y \tag{16-5}$$

where

$$\mathbf{f}(k_x, k_y) = \hat{\mathbf{a}}_x f_x(k_x, k_y) + \hat{\mathbf{a}}_y f_y(k_x, k_y) + \hat{\mathbf{a}}_z f_z(k_x, k_y) \tag{16-5a}$$

$$\mathbf{k} = \hat{\mathbf{a}}_x k_x + \hat{\mathbf{a}}_y k_y + \hat{\mathbf{a}}_z k_z \tag{16-5b}$$

$$\mathbf{r} = \hat{\mathbf{a}}_x x + \hat{\mathbf{a}}_y y + \hat{\mathbf{a}}_z z \tag{16-5c}$$

where $\mathbf{f}(k_x, k_y)$ represents the plane wave spectrum of the field. The x and y components of the electric field measured over a plane surface ($z = 0$) from (16-5) are

$$E_{xa}(x, y, z = 0) = \frac{1}{4\pi^2}\int_{-\infty}^{\infty}\int_{-\infty}^{\infty}f_x(k_x, k_y)e^{-j(k_x x + k_y y)}\,dk_x dk_y \tag{16-6a}$$

INTEL-1045
U.S. Patent 7,151,430

$$E_{ya}(x, y, z = 0) = \frac{1}{4\pi^2}\int_{-\infty}^{\infty}\int_{-\infty}^{\infty} f_y(k_x, k_y)e^{-j(k_x x + k_y y)}\,dk_x dk_y \qquad (16\text{-}6b)$$

The x and y components of the *plane wave spectrum*, $f_x(k_x, k_y)$ and $f_y(k_x, k_y)$, are determined in terms of the near-zone electric field from the Fourier transforms of (16-6a) and (16-6b) as given by (12-85a), (12-85b), or

$$\boxed{f_x(k_x, k_y) \simeq \int_{-b/2}^{+b/2}\int_{-a/2}^{+a/2} E_{xa}(x', y', z' = 0)e^{+j(k_x x' + k_y y')}\,dx'\,dy'} \qquad (16\text{-}7a)$$

$$\boxed{f_y(k_x, k_y) \simeq \int_{-b/2}^{+b/2}\int_{-a/2}^{+a/2} E_{ya}(x', y', z' = 0)e^{+j(k_x x' + k_y y')}\,dx'\,dy'} \qquad (16\text{-}7b)$$

The far-field pattern of the antenna, in terms of the plane wave spectrum function $\mathbf{f}$, is then that of (12-107)

$$\boxed{\mathbf{E}(r, \theta, \phi) \simeq j\frac{ke^{-jkr}}{2\pi r}[\cos\theta\,\mathbf{f}(k_x, k_y)]} \qquad (16\text{-}8)$$

or (12-111)

$$\boxed{E_\theta(r, \theta, \phi) \simeq j\frac{ke^{-jkr}}{2\pi r}(f_x\cos\phi + f_y\sin\phi)} \qquad (16\text{-}9a)$$

$$\boxed{E_\phi(r, \theta, \phi) \simeq j\frac{ke^{-jkr}}{2\pi r}\cos\theta(-f_x\sin\phi + f_y\cos\phi)} \qquad (16\text{-}9b)$$

The procedure then to determine the far-zone field from near-field measurements is as follows:

1. Measure the electric field components $E_{xa}(x', y', z' = 0)$ and $E_{ya}(x', y', z' = 0)$ in the near-field.
2. Find the plane wave spectrum functions f_x and f_y using (16-7a) and (16-7b).
3. Determine the far-zone electric field using (16-8) or (16-9a) and (16-9b).

Similar procedures are used for cylindrical and spherical measuring systems except that the constant surfaces are, respectively, cylinders and spheres. However, their corresponding analytical expressions have different forms.

It is apparent once again, from another application problem, that if the tangential field components are known along a plane, the plane wave spectrum can be found, which in turn permits the evaluation of the field at any point. The computations become more convenient if the evaluation is restricted to the far-field region.

B. Measurements and Computations

The experimental procedure requires that a plane surface, a distance z_a from the test antenna, be selected where measurements are made as shown in Figure 16.12(a). The distance z_a should be at least two or three wavelengths away from the test antenna to be out of its reactive near-field region. The plane over which measurements are made is usually divided into a rectangular grid of M × N points spaced Δx and Δy apart and defined by the coordinates $(m\Delta x, n\Delta y, 0)$ where $-M/2 \le m \le M/2 - 1$ and

INTEL-1045
U.S. Patent 7,151,430

$-N/2 \le n \le N/2 - 1$. The values of M and N are determined by the linear dimensions of the sampling plane divided by the sampling space. To compute the far-field pattern, it requires that both polarization components of the near-field are measured. This can be accomplished by a simple rotation of a linear probe about the longitudinal axis or by the use of a dual-polarized probe. The probe used to make the measurements must not be circularly polarized, and it must not have nulls in the angular region of space over which the test antenna pattern is determined because the probe correction coefficients become infinite.

The measurements are carried out until the signal at the edges of the plane is of very low intensity, usually about 45 dB below the largest signal level within the measuring plane. Defining a and b the width and height, respectively, of the measuring plane, M and N are determined using

$$M = \frac{a}{\Delta x} + 1 \tag{16-10a}$$

$$N = \frac{b}{\Delta y} + 1 \tag{16-10b}$$

The sampling points on the measuring grid are chosen to be less than $\lambda/2$ in order to satisfy the Nyquist sampling criterion. If the plane $z = 0$ is located in the far-field of the source, the sample spacings can increase to their maximum value of $\lambda/2$. Usually the rectangular lattice points are separated by the grid spacings of

$$\Delta x = \frac{\pi}{k_{xo}} \tag{16-11a}$$

$$\Delta y = \frac{\pi}{k_{yo}} \tag{16-11b}$$

where k_{xo} and k_{yo} are real numbers and represent the largest magnitudes of k_x and k_y, respectively, such that $\mathbf{f}(k_x, k_y) = 0$ for $|k_x| > k_{xo}$ or $|k_y| > k_{yo}$.

At the grid sample points, the tangential electric field components, E_x and E_y, are recorded. The subscripts x and y represent, respectively, the two polarizations of the probe. The procedure for probe compensation is neglected here. A previously performed characterization of the probe is used to compensate for its directional effects in what is essentially an application of its "transfer function." The electric field components over the entire plane can be reconstructed from the samples taken at the grid points, and each is given by

$$E_{xa}(x, y, z = 0) = \sum_{n=-N/2}^{N/2-1} \sum_{m=-M/2}^{M/2-1} E_x(m\Delta x, n\Delta y, 0) \times \frac{\sin(k_{xo}x - m\pi)}{k_{xo}x - m\pi} \frac{\sin(k_{yo}y - n\pi)}{k_{yo}y - n\pi} \tag{16-12a}$$

$$E_{ya}(x, y, z = 0) = \sum_{n=-N/2}^{N/2-1} \sum_{m=-M/2}^{M/2-1} E_y(m\Delta x, n\Delta y, 0) \times \frac{\sin(k_{xo}x - m\pi)}{k_{xo}x - m\pi} \frac{\sin(k_{yo}y - n\pi)}{k_{yo}y - n\pi} \tag{16-12b}$$

INTEL-1045
U.S. Patent 7,151,430

Using (16-12a) and (16-12b), f_x and f_y of (16-7a) and (16-7b) can be evaluated, using a FFT algorithm, at the set of wavenumbers explicitly defined by the discrete Fourier transform and given by

$$k_x = \frac{2\pi m}{M\Delta x}, \qquad -\frac{M}{2} \le m \le \frac{M}{2} - 1 \tag{16-13a}$$

$$k_y = \frac{2\pi n}{N\Delta y}, \qquad -\frac{N}{2} \le n \le \frac{N}{2} - 1 \tag{16-13b}$$

The wavenumber spectrum points are equal to the number of points in the near-field distribution, and the maximum wavenumber coordinate of the wavenumber spectrum is inversely proportional to the near-field sampling spacing. While the maximum sampling spacing is $\lambda/2$, there is no minimum spacing restrictions. However, there are no advantages to increasing the near-field sample points by decreasing the sample spacing. The decreased sample spacing will increase the limits of the wavenumber spectrum points, which are in the large evanescent mode region, and do not contribute to increased resolution of the far-field pattern.

Increased resolution in the far-field power pattern can be obtained by adding artificial data sampling points (with zero value) at the outer extremities of the near-field distribution. This artificially increases the number of sample points without decreasing the sample spacing. Since the sample spacing remains fixed, the wavenumber limits also stay fixed. The additional wavenumber spectrum points are all within the original wavenumber limits and lead to increased resolution in the computed far-field patterns.

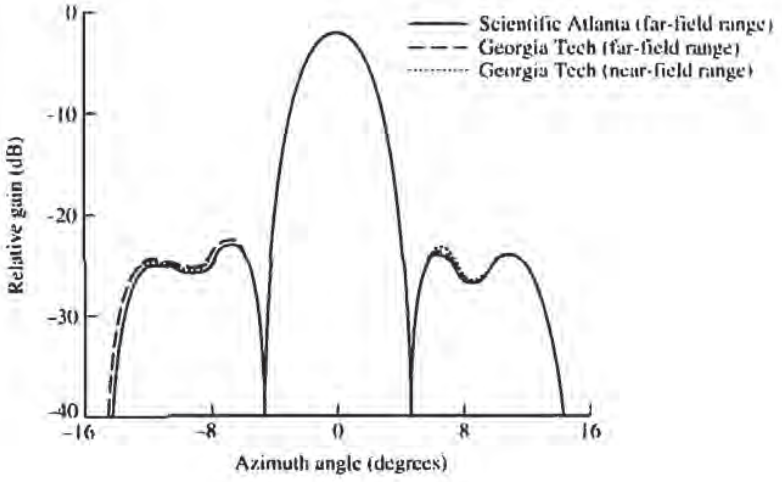
To validate the techniques, numerous comparisons between computed far-field patterns, from near-field measurements, and measured far-field patterns have been made. In Figure 16.15, the computed and measured sum and difference far-field azimuth plane patterns for a four-foot diameter parabolic reflector with a nominal gain of 30 dB are displayed [4]. Two measured far-field patterns were obtained on two different high-quality far-field ranges, one at the Georgia Institute of Technology and the other at Scientific-Atlanta. The third trace represents the computed far-field pattern from near-field measurements made at Georgia Tech. There are some minor discrepancies between the two measured far-field patterns which were probably caused by extraneous range reflections. The best agreement is between the computed far-field pattern and the one measured at Scientific Atlanta. Many other comparisons have been made with similar success. The limited results shown here, and the many others published in the literature [4], [40]–[42] clearly demonstrate the capability of the near-field technique.

The near-field technique provides the antenna designers information not previously available to them. For example, if a given far-field pattern does not meet required specifications, it is possible to use near-field data to pinpoint the cause [43]. Near-field measurements can be applied also to antenna analysis and diagnostic tasks [44], and it is most attractive when efficient near-field data collection and transformation methods are employed.

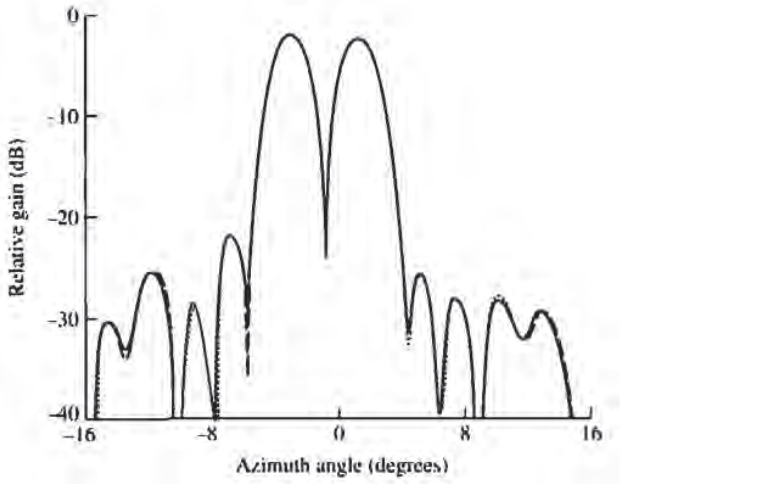
16.3 RADIATION PATTERNS

The radiation patterns (amplitude and phase), polarization, and gain of an antenna, which are used to characterize its radiation capabilities, are measured on the surface of a constant radius sphere. Any position on the sphere is identified using the standard spherical coordinate system of Figure 16.16. Since the radial distance is maintained

INTEL-1045
U.S. Patent 7,151,430



(a) Sum mode



(b) Difference mode

Figure 16.15 Measured and computed sum and difference mode principal plane far-field patterns for a four-foot parabolic reflector (SOURCE: E. D. Joy, W. M. Leach, Jr., G. P. Rodrique, and D. T. Paris, "Applications of Probe Compensated Near-Field Measurements," *IEEE Trans. Antennas Propagat.*, Vol. AP-26, No. 3, pp. 379–389, May 1978. © (1978) IEEE)

fixed, only the two angular coordinates (θ, ϕ) are needed for positional identification. A representation of the radiation characteristics of the radiator as a function of θ and ϕ for a constant radial distance and frequency, is defined as the *pattern* of the antenna.

In general, the pattern of an antenna is three-dimensional. Because it is impractical to measure a three-dimensional pattern, a number of two-dimensional patterns, as defined in Section 2.2, are measured. They are used to construct a three-dimensional pattern. The number of two-dimensional patterns needed to construct faithfully a three-dimensional graph is determined by the functional requirements of the description, and the available time and funds. The minimum number of two-dimensional patterns is two, and they are usually chosen to represent the orthogonal principal *E*- and *H*-plane patterns, as defined in Section 2.2.

INTEL-1045
U.S. Patent 7,151,430

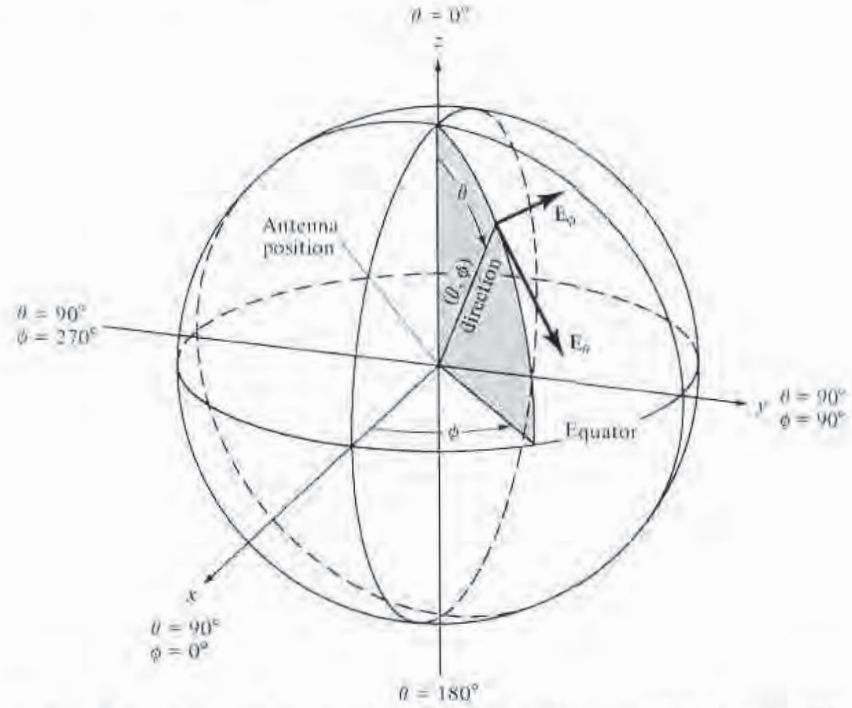


Figure 16.16 Spherical coordinate system geometry. (SOURCE: *IEEE Standard Test Procedures for Antennas*, IEEE Std 149-1979, published by IEEE, Inc., 1979, distributed by Wiley)

A two-dimensional pattern is also referred to as a *pattern cut*, and it is obtained by fixing one of the angles (θ or ϕ) while varying the other. For example, by referring to Figure 16.16, pattern cuts can be obtained by fixing ϕ_j ($0 \leq \phi_j \leq 2\pi$) and varying θ ($0 \leq \theta \leq 180°$). These are referred to as elevation patterns, and they are also displayed in Figure 2.15. Similarly θ can be maintained fixed ($0 \leq \theta_i \leq \pi$) while ϕ is varied ($0 \leq \phi \leq 2\pi$). These are designated as azimuthal patterns. Part ($0 \leq \phi \leq \pi/2$) of the $\theta_i = \pi/2$ azimuthal pattern is displayed in Figure 2.15.

The patterns of an antenna can be measured in the transmitting or receiving mode. The mode is dictated by the application. However, if the radiator is reciprocal, as is the case for most practical antennas, then either the transmitting or receiving mode can be utilized. For such cases, the receiving mode is selected. The analytical formulations upon which an amplitude pattern is based, along with the advantages and disadvantages for making measurements in the transmitting or receiving mode, are found in Section 3.8.1. The analytical basis of a phase pattern is discussed in Section 13.10. Unless otherwise specified, it will be assumed here that the measurements are performed in the receiving mode.

16.3.1 Instrumentation

The instrumentation required to accomplish a measuring task depends largely on the functional requirements of the design. An antenna range instrumentation must be designed to operate over a wide range of frequencies, and it usually can be classified into five categories [7]:

INTEL-1045
U.S. Patent 7,151,430

1. source antenna and transmitting system
2. receiving system
3. positioning system
4. recording system
5. data-processing system

A block diagram of a system that possesses these capabilities is shown in Figure 16.17.

The source antennas are usually log-periodic antennas for frequencies below 1 GHz, families of parabolas with broadband feeds for frequencies above 400 MHz, and even large horn antennas. The system must be capable of controlling the polarization. Continuous rotation of the polarization can be accomplished by mounting a linearly polarized source antenna on a polarization positioner. Antennas with circular polarization can also be designed, such as crossed log-periodic arrays, which are often used in measurements.

The transmitting RF source must be selected so that it has [7] frequency control, frequency stability, spectral purity, power level, and modulation. The receiving system could be as simple as a bolometer detector, followed possibly by an amplifier, and a recorder. More elaborate and expensive receiving systems that provide greater sensitivity, precision, and dynamic range can be designed. One such system is a heterodyne receiving system [7], which uses double conversion and phase locking, and it

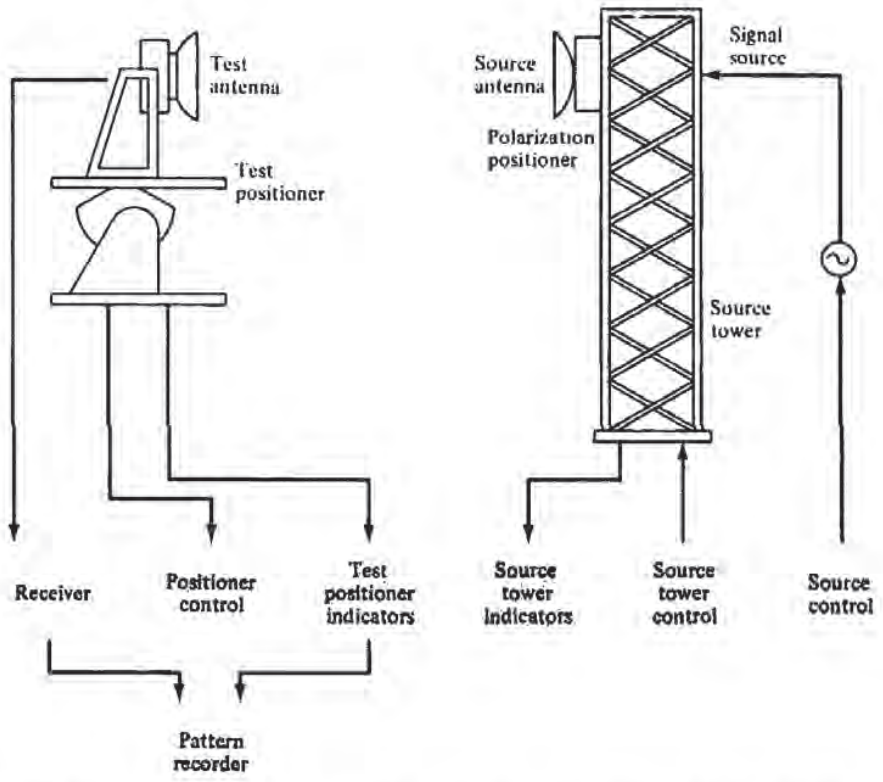
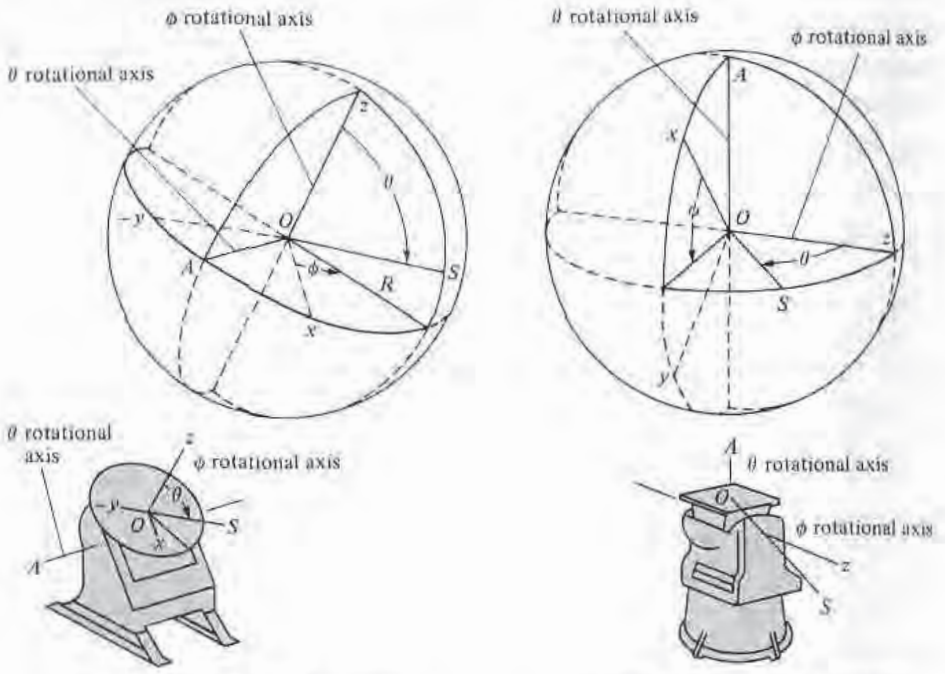


Figure 16.17 Instrumentation for typical antenna-range measuring system. (SOURCE: *IEEE Standard Test Procedures for Antennas*, IEEE Std 149-1979, published by IEEE, Inc., 1979, distributed by Wiley)

INTEL-1045
U.S. Patent 7,151,430



(a) Azimuth-over-elevation positioner (b) Elevation-over-azimuth positioner

Figure 16.18 Azimuth-over-elevation and elevation-over-azimuth rotational mounts. (SOURCE: *IEEE Standard Test Procedures for Antennas*, IEEE Std 149-1979, published by IEEE, Inc., 1979, distributed by Wiley)

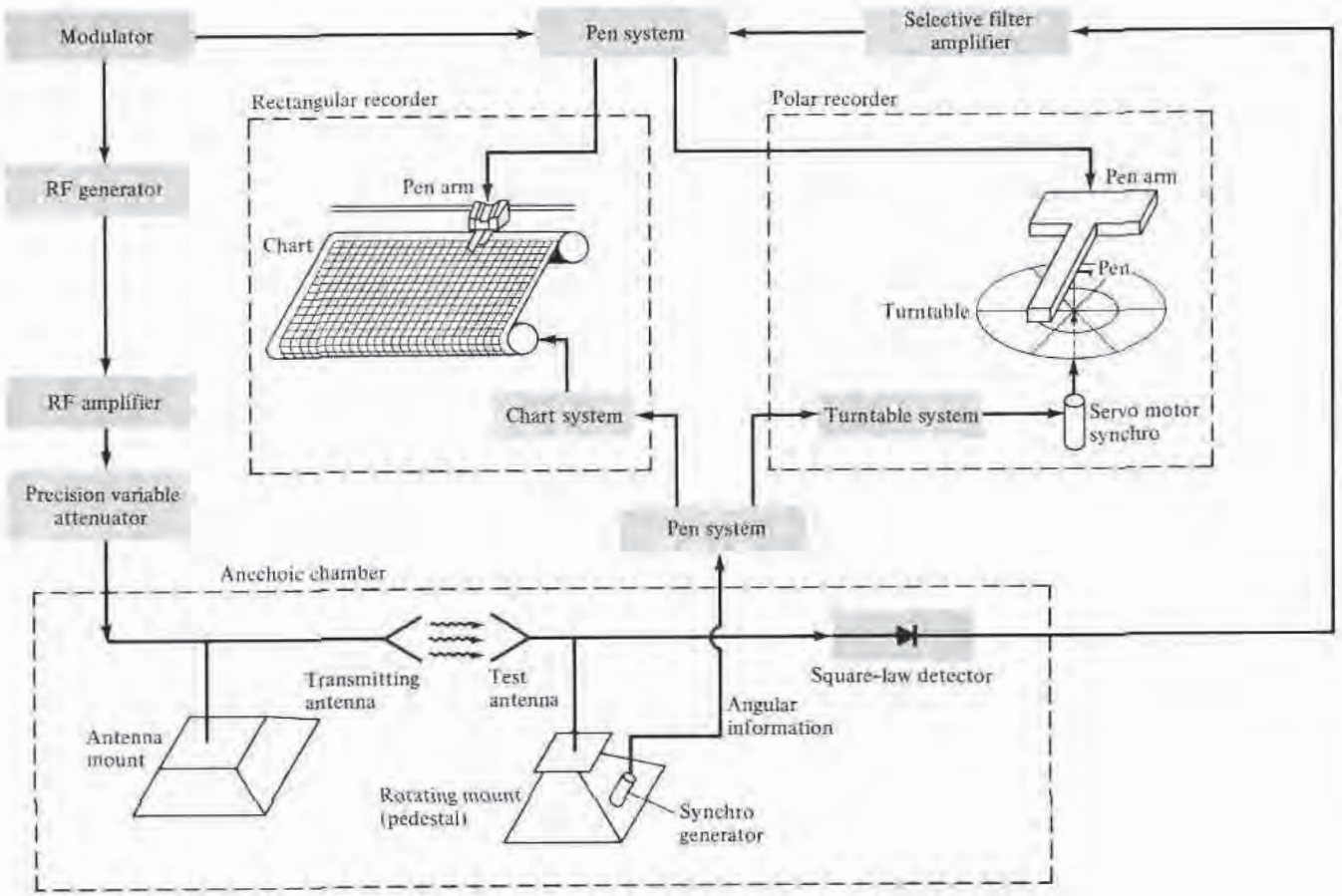
can be used for amplitude measurements. A dual-channel heterodyne system design is also available [7], and it can be used for phase measurements.

To achieve the desired plane cuts, the mounting structures of the system must have the capability to rotate in various planes. This can be accomplished by utilizing rotational mounts (pedestals), two of which are shown in Figure 16.18. Tower-model elevation-over-azimuth pedestals are also available [7].

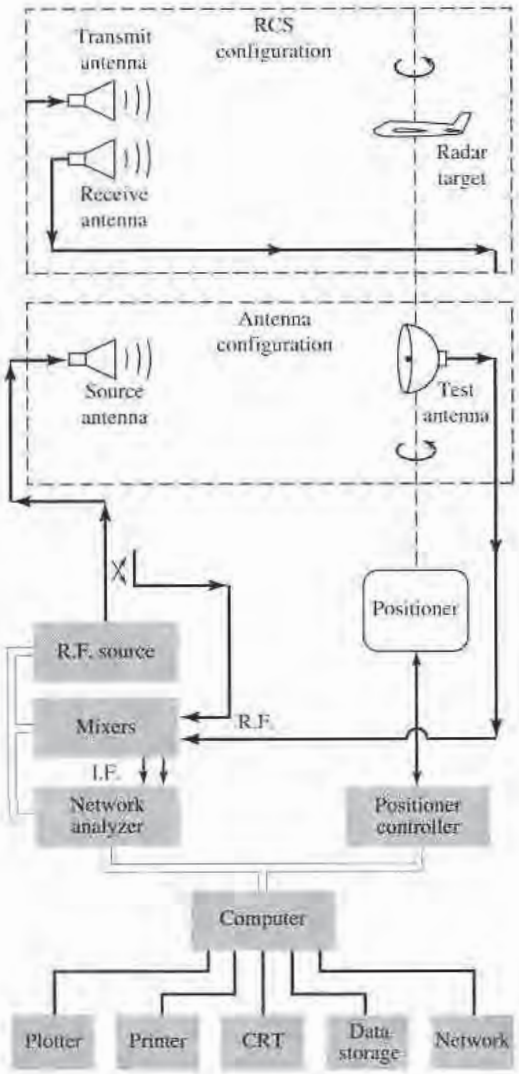
There are primarily two types of recorders; one that provides a linear (rectangular) plot and the other a polar plot. The polar plots are most popular because they provide a better visualization of the radiation distribution in space. Usually the recording equipment is designed to graph the relative pattern. Absolute patterns are obtained by making, in addition, gain measurements which will be discussed in the next section. The recording instrumentation is usually calibrated to record relative field or power patterns. Power pattern calibrations are in decibels with dynamic ranges of 0–60 dB. For most applications, a 40-dB dynamic range is usually adequate and it provides sufficient resolution to examine the pattern structure of the main lobe and the minor lobes.

In an indoor antenna range, the recording equipment is usually placed in a room that adjoins the anechoic chamber. To provide an interference free environment, the chamber is closed during measurements. To monitor the procedures, windows or closed-circuit TVs are utilized. In addition, the recording equipment is connected, through synchronous servo-amplifier systems, to the rotational mounts (pedestals) using the traditional system shown in Figure 16.19(a). The system can record rectangular or polar plots. Position references are recorded simultaneously with measurements, and they are used for angular positional identification. As the rotational mount

INTEL-1045
U.S. Patent 7,151,430



(a) Traditional system



(b) Computer automated system

Figure 16.19 Block diagrams of typical instrumentations for measuring rectangular and polar antenna and RCS patterns.

INTEL-1045
U.S. Patent 7,151,430

moves, the pattern is graphed simultaneously by the recorder on a moving chart. One of the axes of the chart is used to record the amplitude of the pattern while the other identifies the relative position of the radiator. A modern configuration to measure antenna and RCS patterns, using a network analyzer and being computer automated, is shown in Figure 16.19(b).

16.3.2 Amplitude Pattern

The total amplitude pattern of an antenna is described by the vector sum of the two orthogonally polarized radiated field components. The pattern on a conventional antenna range can be measured using the system of Figure 16.17 or Figure 16.19 with an appropriate detector. The receiver may be a simple bolometer (followed possibly by an amplifier), a double conversion phase-locking heterodyne system [7, Fig. 14], or any other design.

In many applications, the movement of the antenna to the antenna range can significantly alter the operational environment. Therefore, in some cases, antenna pattern measurements must be made *in situ* to preserve the environmental performance characteristics. A typical system arrangement that can be used to accomplish this is shown in Figure 16.20. The source is mounted on an airborne vehicle, which is maneuvered through space around the test antenna and in its far-field, to produce a plane wave and to provide the desired pattern cuts. The tracking device provides to the recording equipment the angular position data of the source relative to a reference direction. The measurements can be conducted either by a point-by-point or by a continuous method. Usually the continuous technique is preferred.

16.3.3 Phase Measurements

Phase measurements are based on the analytical formulations of Section 13.10. The phase pattern of the field, in the direction of the unit vector $\hat{\mathbf{u}}$, is given by the $\psi(\theta, \phi)$ phase function of (13-63). For linear polarization $\hat{\mathbf{u}}$ is real, and it may represent $\hat{\mathbf{a}}_\theta$ or $\hat{\mathbf{a}}_\phi$ in the direction of θ or ϕ.

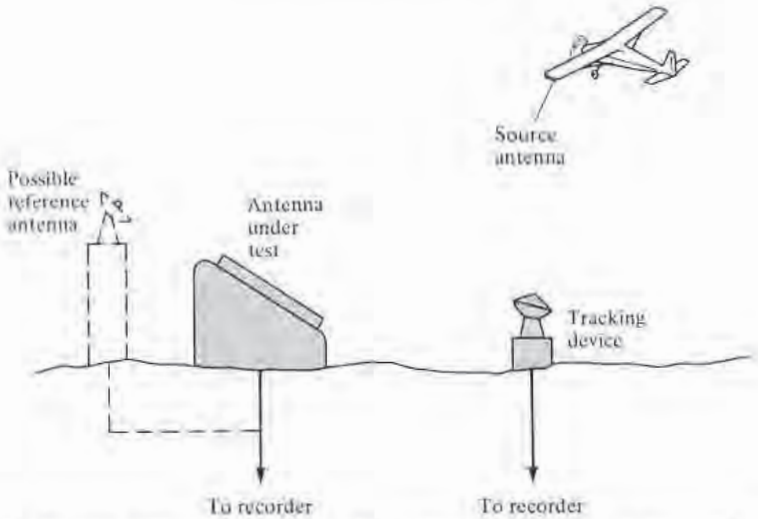


Figure 16.20 System arrangement for *in situ* antenna pattern measurements. (SOURCE: *IEEE Standard Test Procedures for Antennas*, IEEE Std 149-1979, published by IEEE, Inc., 1979, distributed by Wiley)

INTEL-1045
U.S. Patent 7,151,430

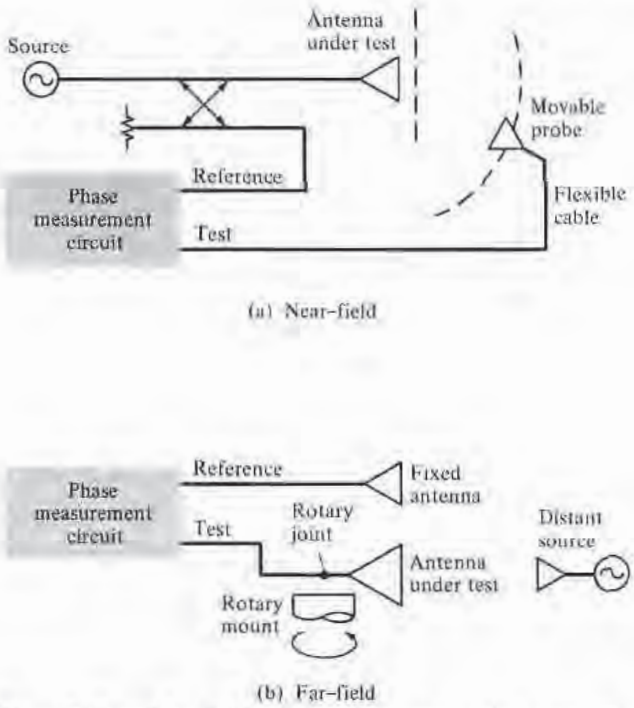


Figure 16.21 Near-field and far-field phase pattern measuring systems. (SOURCE: *IEEE Standard Test Procedures for Antennas*, IEEE Std 149-1979, published by IEEE, Inc., 1979, distributed by Wiley)

The phase of an antenna is periodic, and it is defined in multiples of 360°. In addition, the phase is a relative quantity, and a reference must be provided during measurements for comparison.

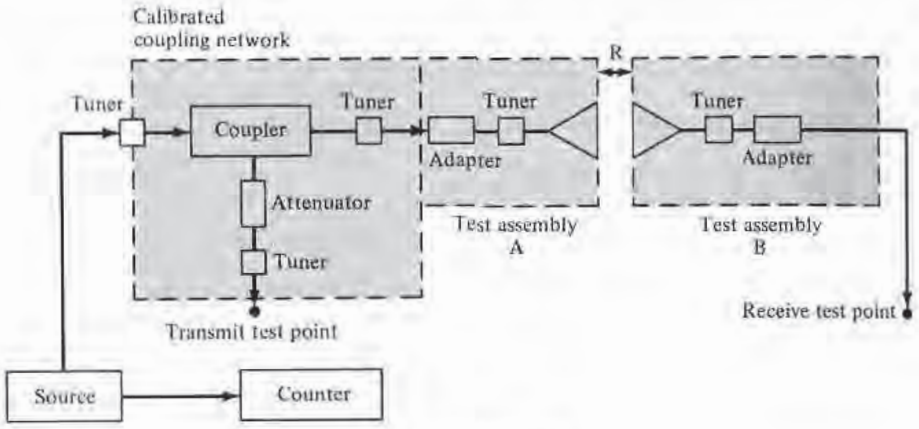
Two basic system techniques that can be used to measure phase patterns at short and long distances from the antenna are shown respectively, in Figures 16.21(a) and 16.21(b). For the design of Figure 16.21(a), a reference signal is coupled from the transmission line, and it is used to compare, in an appropriate network, the phase of the received signal. For large distances, this method does not permit a direct comparison between the reference and the received signal. In these cases, the arrangement of Figure 16.21(b) can be used in which the signal from the source antenna is received simultaneously by a fixed antenna and the antenna under test. The phase pattern is recorded as the antenna under test is rotated while the fixed antenna serves as a reference. The phase measuring circuit may be the dual-channel heterodyne system [7, Fig. 15].

16.4 GAIN MEASUREMENTS

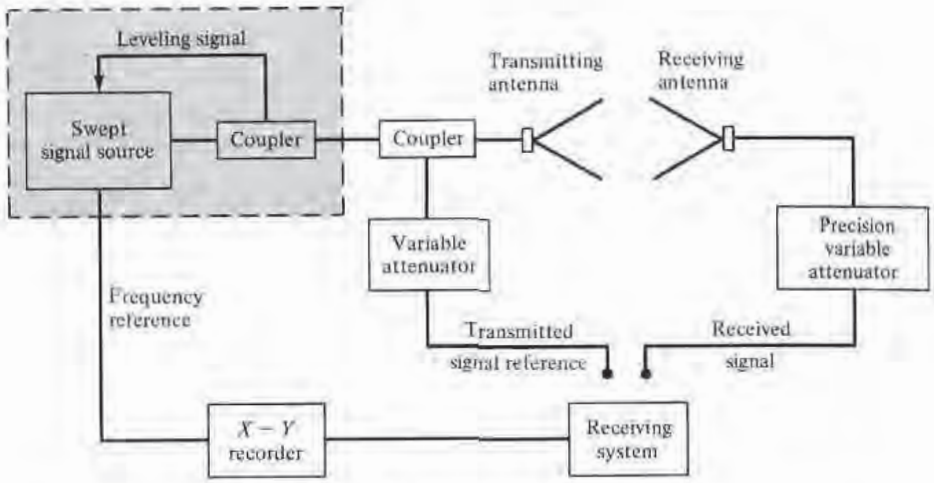
The most important figure-of-merit that describes the performance of a radiator is the gain. There are various techniques and antenna ranges that are used to measure the gain. The choice of either depends largely on the frequency of operation.

Usually free-space ranges are used to measure the gain above 1 GHz. In addition, microwave techniques, which utilize waveguide components, can be used. At lower frequencies, it is more difficult to simulate free-space conditions because of the longer wavelengths. Therefore between 0.1–1 GHz, ground-reflection ranges are utilized. Scale models can also be used in this frequency range. However, since the conductivity

INTEL-1045
U.S. Patent 7,151,430



(a) Single frequency



(b) Swept frequency

Figure 16.22 Typical two- and three-antenna measuring systems for single and swept frequency measurements. (SOURCE: J. S. Hollis, T. J. Lyon, and L. Clayton, Jr., *Microwave Antenna Measurements*, Scientific-Atlanta, Inc., Atlanta, Georgia, July 1970)

and loss factors of the structures cannot be scaled conveniently, the efficiency of the full scale model must be found by other methods to determine the gain of the antenna. This is accomplished by multiplying the directivity by the efficiency to result in the gain. Below 0.1 GHz, directive antennas are physically large and the ground effects become increasingly pronounced. Usually the gain at these frequencies is measured *in situ*. Antenna gains are not usually measured at frequencies below 1 MHz. Instead, measurements are conducted on the field strength of the ground wave radiated by the antenna.

Usually there are two basic methods that can be used to measure the gain of an electromagnetic radiator: *absolute-gain* and *gain-transfer* (or *gain-comparison*) measurements. The absolute-gain method is used to calibrate antennas that can then be used as standards for gain measurements, and it requires no *a priori* knowledge of the gains of the antennas. Gain-transfer methods must be used in conjunction with standard gain antennas to determine the absolute gain of the antenna under test.

INTEL-1045
U.S. Patent 7,151,430

The two antennas that are most widely used and universally accepted as gain standards are the resonant $\lambda/2$ dipole (with a gain of about 2.1 dB) and the pyramidal horn antenna (with a gain ranging from 12–25 dB). Both antennas possess linear polarizations. The dipole, in free-space, exhibits a high degree of polarization purity. However, because of its broad pattern, its polarization may be suspect in other than reflection-free environments. Pyramidal horns usually possess, in free-space, slightly elliptical polarization (axial ratio of about 40 to infinite dB). However, because of their very directive patterns, they are less affected by the surrounding environment.

16.4.1 Absolute-Gain Measurements

There are a number of techniques that can be employed to make absolute-gain measurements. A very brief review of each will be included here. More details can be found in [6]–[8]. All of these methods are based on Friis transmission formula [as given by (2-118)] which assumes that the measuring system employs, each time, two antennas (as shown in Figure 2.25). The antennas are separated by a distance R, and it must satisfy the far-field criterion of each antenna. For polarization matched antennas, aligned for maximum directional radiation, (2-118) reduces to (2-119).

A. Two-Antenna Method

Equation (2-119) can be written in a logarithmic decibel form as

$$(G_{0t})_{dB} + (G_{0r})_{dB} = 20 \log_{10}\left(\frac{4\pi R}{\lambda}\right) + 10 \log_{10}\left(\frac{P_r}{P_t}\right) \qquad (16\text{-}14)$$

where

$(G_{0t})_{dB}$ = gain of the transmitting antenna (dB)
$(G_{0r})_{dB}$ = gain of the receiving antenna (dB)
P_r = received power (W)
P_t = transmitted power (W)
R = antenna separation (m)
λ = operating wavelength (m)

If the transmitting and receiving antennas are identical ($G_{0t} = G_{0r}$), (16-14) reduces to

$$(G_{0t})_{dB} = (G_{0r})_{dB} = \frac{1}{2}\left[20 \log_{10}\left(\frac{4\pi R}{\lambda}\right) + 10 \log_{10}\left(\frac{P_r}{P_t}\right)\right] \qquad (16\text{-}15)$$

By measuring R, λ, and the ratio of P_r/P_t, the gain of the antenna can be found. At a given frequency, this can be accomplished using the system of Figure 16.22(a). The system is simple and the procedure straightforward. For continuous multifrequency measurements, such as for broadband antennas, the swept frequency instrumentation of Figure 16.22(b) can be utilized.

B. Three-Antenna Method

If the two antennas in the measuring system are not identical, three antennas (a, b, c) must be employed and three measurements must be made (using all combinations of the three) to determine the gain of each of the three. Three equations (one for each combination) can be written, and each takes the form of (16-14). Thus

INTEL-1045
U.S. Patent 7,151,430

(a-b Combination)

$$(G_a)_{\text{dB}} + (G_b)_{\text{dB}} = 20 \log_{10}\left(\frac{4\pi R}{\lambda}\right) + 10 \log_{10}\left(\frac{P_{rb}}{P_{ta}}\right) \qquad (16\text{-}16a)$$

(a-c Combination)

$$(G_a)_{\text{dB}} + (G_c)_{\text{dB}} = 20 \log_{10}\left(\frac{4\pi R}{\lambda}\right) + 10 \log_{10}\left(\frac{P_{rc}}{P_{ta}}\right) \qquad (16\text{-}16b)$$

(b-c Combination)

$$(G_b)_{\text{dB}} + (G_c)_{\text{dB}} = 20 \log_{10}\left(\frac{4\pi R}{\lambda}\right) + 10 \log_{10}\left(\frac{P_{rc}}{P_{tb}}\right) \qquad (16\text{-}16c)$$

From these three equations, the gains $(G_a)_{\text{dB}}$, $(G_b)_{\text{dB}}$, and $(G_c)_{\text{dB}}$ can be determined provided R, λ, and the ratios of P_{rb}/P_{ta}, P_{rc}/P_{ta}, and P_{rc}/P_{tb} are measured.

The two- and three-antenna methods are both subject to errors. Care must be utilized so

1. the system is frequency stable
2. the antennas meet the far-field criteria
3. the antennas are aligned for boresight radiation
4. all the components are impedance and polarization matched
5. there is a minimum of proximity effects and multipath interference

Impedance and polarization errors can be accounted for by measuring the appropriate complex reflection coefficients and polarizations and then correcting accordingly the measured power ratios. The details for these corrections can be found in [7], [8]. There are no rigorous methods to account for proximity effects and multipath interference. These, however, can be minimized by maintaining the antenna separation by at least a distance of $2D^2/\lambda$, as is required by the far-field criteria, and by utilizing RF absorbers to reduce unwanted reflections. The interference pattern that is created by the multiple reflections from the antennas themselves, especially at small separations, is more difficult to remove. It usually manifests itself as a cyclic variation in the measured antenna gain as a function of separation.

C. Extrapolation Method

The extrapolation method is an absolute-gain method, which can be used with the three-antenna method, and it was developed [15] to rigorously account for possible errors due to proximity, multipath, and nonidentical antennas. If none of the antennas used in the measurements are circularly polarized, the method yields the gains and polarizations of all three antennas. If only one antenna is circularly polarized, this method yields only the gain and polarization of the circularly polarized antenna. The method fails if two or more antennas are circularly polarized.

The method requires both amplitude and phase measurements when the gain and the polarization of the antennas is to be determined. For the determination of gains, amplitude measurements are sufficient. The details of this method can be found in [8], [45].

D. Ground-Reflection Range Method

A method that can be used to measure the gain of moderately broad beam antennas, usually for frequencies below 1 GHz, has been reported [46]. The method takes into account the specular reflections from the ground (using the system geometry of Figure

INTEL-1045
U.S. Patent 7,151,430

16.2), and it can be used with some restrictions and modifications with the two- or three-antenna methods. As described here, the method is applicable to linear antennas that couple only the electric field. Modifications must be made for loop radiators. Using this method, it is recommended that the linear vertical radiators be placed in a horizontal position when measurements are made. This is desired because the reflection coefficient of the earth, as a function of incidence angle, varies very rapidly for vertically polarized waves. Smoother variations are exhibited for horizontally polarized fields. Circularly and elliptically polarized antennas are excluded, because the earth exhibits different reflective properties for vertical and horizontal fields.

To make measurements using this technique, the system geometry of Figure 16.2 is utilized. Usually it is desirable that the height of the receiving antenna h_r be much smaller than the range R_0 ($h_r \ll R_0$). Also the height of the transmitting antenna is adjusted so that the field of the receiving antenna occurs at the first maximum nearest to the ground. Doing this, each of the gain equations of the two- or three-antenna methods take the form of

$$(G_a)_{dB} + (G_b)_{dB} = 20 \log_{10}\left(\frac{4\pi R_D}{\lambda}\right) + 10 \log_{10}\left(\frac{P_r}{P_t}\right) - 20 \log_{10}\left(\sqrt{D_A D_B} + \frac{rR_D}{R_R}\right) \tag{16-17}$$

D_A and D_B are the directivities (relative to their respective maximum values) along R_D, and they can be determined from amplitude patterns measured prior to the gain measurements. R_D, R_R, λ, and P_r/P_t are also measured. The only quantity that needs to be determined is the factor r which is a function of the radiation patterns of the antennas, the frequency of operation, and the electrical and geometrical properties of the antenna range.

The factor r can be found by first repeating the above measurements but with the transmitting antenna height adjusted so that the field at the receiving antenna is minimum. The quantities measured with this geometry are designated by the same letters as before but with a prime (′) to distinguish them from those of the previous measurement.

By measuring or determining the parameters

1. R_R, R_D, P_r, D_A, and D_B at a height of the transmitting antenna such that the receiving antenna is at the first maximum of the pattern
2. R'_R, R'_D, P'_r, D'_A, and D'_B at a height of the transmitting antenna such that the receiving antenna is at a field minimum

it can be shown [46] that r can be determined from

$$r = \left(\frac{R_R R'_R}{R_D R'_D}\right)\left[\frac{\sqrt{(P_r/P'_r)(D'_A D'_B)}\, R_D - \sqrt{D_A D_B} R'_D}{\sqrt{(P_r/P'_r)}\, R_R + R'_R}\right] \tag{16-18}$$

Now all parameters included in (16-17) can either be measured or computed from measurements. The free-space range system of Figure 16.22(a) can be used to perform these measurements.

16.4.2 Gain-Transfer (Gain-Comparison) Measurements

The method most commonly used to measure the gain of an antenna is the gain-transfer method. This technique utilizes a gain standard (with a known gain) to

INTEL-1045
U.S. Patent 7,151,430

determine absolute gains. Initially relative gain measurements are performed, which when compared with the known gain of the standard antenna, yield absolute values. The method can be used with free-space and reflection ranges, and for *in situ* measurements.

The procedure requires two sets of measurements. In one set, using the test antenna as the receiving antenna, the received power (P_T) into a matched load is recorded. In the other set, the test antenna is replaced by the standard gain antenna and the received power (P_S) into a matched load is recorded. In both sets, the geometrical arrangement is maintained intact (other than replacing the receiving antennas), and the input power is maintained the same.

Writing two equations of the form of (16-14) or (16-17), for free-space or reflection ranges, it can be shown that they reduce to [7]

$$(G_T)_{\text{dB}} = (G_S)_{\text{dB}} + 10 \log_{10}\left(\frac{P_T}{P_S}\right) \tag{16-19}$$

where $(G_T)_{\text{dB}}$ and $(G_S)_{\text{dB}}$ are the gains (in dB) of the test and standard gain antennas.

System disturbance during replacement of the receiving antennas can be minimized by mounting the two receiving antennas back-to-back on either side of the axis of an azimuth positioner and connecting both of them to the load through a common switch. One antenna can replace the other by a simple, but very precise, 180° rotation of the positioner. Connection to the load can be interchanged by proper movement of the switch.

If the test antenna is not too dissimilar from the standard gain antenna, this method is less affected by proximity effects and multipath interference. Impedance and polarization mismatches can be corrected by making proper complex reflection coefficient and polarization measurements [8].

If the test antenna is circularly or elliptically polarized, gain measurements using the gain-transfer method can be accomplished by at least two different methods. One way would be to design a standard gain antenna that possesses circular or elliptical polarization. This approach would be attractive in mass productions of power-gain measurements of circularly or elliptically polarized antennas.

The other approach would be to measure the gain with two orthogonal linearly polarized standard gain antennas. Since circularly and elliptically polarized waves can be decomposed to linear (vertical and horizontal) components, the total power of the wave can be separated into two orthogonal linearly polarized components. Thus the total gain of the circularly or elliptically polarized test antenna can be written as

$$(G_T)_{\text{dB}} = 10 \log_{10}(G_{TV} + G_{TH}) \tag{16-20}$$

G_{TV} and G_{TH} are, respectively, the partial power gains with respect to vertical-linear and horizontal-linear polarizations.

G_{TV} is obtained, using (16-19), by performing a gain-transfer measurement with the standard gain antenna possessing vertical polarization. The measurements are repeated with the standard gain antenna oriented for horizontal polarization. This allows the determination of G_{TH}. Usually a single linearly polarized standard gain antenna (a linear $\lambda/2$ resonant dipole or a pyramidal horn) can be used, by rotating it by 90°, to provide both vertical and horizontal polarizations. This approach is very convenient, especially if the antenna possesses good polarization purity in the two orthogonal planes.

The techniques outlined above yield good results provided the transmitting and standard gain antennas exhibit good linear polarization purity. Errors will be intro-

INTEL-1045
U.S. Patent 7,151,430

duced if either one of them possesses a polarization with a finite axial ratio. In addition, these techniques are accurate if the tests can be performed in a free-space, a ground-reflection, or an extrapolation range. These requirements place a low-frequency limit of 50 MHz.

Below 50 MHz, the ground has a large effect on the radiation characteristics of the antenna, and it must be taken into account. It usually requires that the measurements are performed on full scale models and *in situ*. Techniques that can be used to measure the gain of large HF antennas have been devised [47]–[49].

16.5 DIRECTIVITY MEASUREMENTS

If the directivity of the antenna cannot be found using solely analytical techniques, it can be computed using measurements of its radiation pattern. One of the methods is based on the approximate expressions of (2-27) by Kraus or (2-30b) by Tai and Pereira, whereas the other relies on the numerical techniques that were developed in Section 2.6. The computations can be performed very efficiently and economically with modern computational facilities and numerical techniques.

The simplest, but least accurate method, requires that the following procedure is adopted:

1. Measure the two principal E- and H-plane patterns of the test antenna.
2. Determine the half-power beamwidths (in degrees) of the E- and H-plane patterns.
3. Compute the directivity using either (2-27) or (2-30b).

The method is usually employed to obtain rough estimates of directivity. It is more accurate when the pattern exhibits only one major lobe, and its minor lobes are negligible.

The other method requires that the directivity be computed using (2-35) where P_{rad} is evaluated numerically using (2-43). The $F(\theta_i, \phi_j)$ function represents the radiation intensity or radiation pattern, as defined by (2-42), and it will be obtained by measurements. U_{max} in (2-35) represents the maximum radiation intensity of $F(\theta, \phi)$ in all space, as obtained by the measurements.

The radiation pattern is measured by sampling the field over a sphere of radius r. The pattern is measured in two-dimensional plane cuts with ϕ_j constant ($0 \leq \phi_j \leq 2\pi$) and θ variable ($0 \leq \theta \leq \pi$), as shown in Figure 2.15, or with θ_i fixed ($0 \leq \theta_i \leq \pi$) and ϕ variable ($0 \leq \phi \leq 2\pi$). The first are referred to as elevation or great-circle cuts, whereas the second represent azimuthal or conical cuts. Either measuring method can be used. Equation (2-43) is written in a form that is most convenient for elevation or great-circle cuts. However, it can be rewritten to accommodate azimuthal or conical cuts.

The spacing between measuring points is largely controlled by the directive properties of the antenna and the desired accuracy. The method is most accurate for broad beam antennas. However, with the computer facilities and the numerical methods now available, this method is very attractive even for highly directional antennas. To maintain a given accuracy, the number of sampling points must increase as the pattern becomes more directional. The pattern data is recorded digitally on tape, and it can be entered to a computer at a later time. If on-line computer facilities are available, the measurements can be automated to provide essentially real-time computations.

The above discussion assumes that all the radiated power is contained in a single polarization, and the measuring probe possesses that polarization. If the antenna is

INTEL-1045
U.S. Patent 7,151,430

polarized such that the field is represented by both θ and ϕ components, the *partial directivities* $D_\theta(\theta, \phi)$ and $D_\phi(\theta, \phi)$ of (2-17)–(2-17b) must each be found. This is accomplished from pattern measurements with the probe positioned, respectively, to sample the θ and ϕ components. The *total directivity* is then given by (2-17)–(2-17b), or

$$D_0 = D_\theta + D_\phi \tag{16-21}$$

where

$$D_\theta = \frac{4\pi U_\theta}{(P_{\text{rad}})_\theta + (P_{\text{rad}})_\phi} \tag{16-21a}$$

$$D_\phi = \frac{4\pi U_\phi}{(P_{\text{rad}})_\theta + (P_{\text{rad}})_\phi} \tag{16-21b}$$

U_θ, $(P_{\text{rad}})_\theta$ and U_ϕ, $(P_{\text{rad}})_\phi$ represent the radiation intensity and radiated power as contained in the two orthogonal θ and ϕ field components, respectively.

The same technique can be used to measure the field intensity and to compute the directivity of any antenna that possess two orthogonal polarizations. Many antennas have only one polarization (θ or ϕ). This is usually accomplished by design and/or proper selection of the coordinate system. In this case, the desired polarization is defined as the *primary polarization*. Ideally, the other polarization should be zero. However, in practice, it is non-vanishing, but it is very small. Usually it is referred to as the *cross-polarization*, and for good designs it is usually below -40 dB.

The directivity of circularly or elliptically polarized antennas can also be measured. Precautions must be taken [7] as to which component represents the primary polarization and which the cross-polarization contribution.

16.6 RADIATION EFFICIENCY

The radiation efficiency is defined as the ratio of the total power radiated by the antenna to the total power accepted by the antenna at its input terminals during radiation. System factors, such as impedance and/or polarization mismatches, do not contribute to the radiation efficiency because it is an inherent property of the antenna.

The radiation efficiency can also be defined, using the direction of maximum radiation as reference, as

$$\text{radiation efficiency} = \frac{\text{gain}}{\text{directivity}} \tag{16-22}$$

where directivity and gain, as defined in Sections 2.5 and 2.7, imply that they are measured or computed in the direction of maximum radiation. Using techniques that were outlined in Sections 16.4 and 16.5 for the measurements of the gain and directivity, the radiation efficiency can then be computed using (16-22).

If the antenna is very small and simple, it can be represented as a series network as shown in Figures 2.21(b) or 2.22(b). For antennas that can be represented by such a series network, the radiation efficiency can also be defined by (2-90) and it can be computed by another method [50]. For these antennas, the real part of the input impedance is equal to the total antenna resistance which consists of the radiation resistance and the loss resistance.

The radiation resistance accounts for the radiated power. For many simple antennas (dipoles, loops, etc.), it can be found by analytically or numerically integrating

INTEL-1045
U.S. Patent 7,151,430

the pattern, relating it to the radiated power and to the radiation resistance by a relation similar to (4-18). The loss resistance accounts for the dissipated power, and it is found by measuring the input impedance (input resistance − radiation resistance = loss resistance).

Because the loss resistance of antennas coated with lossy dielectrics or antennas over lossy ground cannot be represented in series with the radiation resistance, this method cannot be used to determine their radiation efficiency. The details of this method can be found in [50].

16.7 IMPEDANCE MEASUREMENTS

Associated with an antenna there are two types of impedances: a *self* and a *mutual* impedance. When the antenna is radiating into an unbounded medium and there is no coupling between it and other antennas or surrounding obstacles, the self-impedance is also the driving-point impedance of the antenna. If there is coupling between the antenna under test and other sources or obstacles, the driving-point impedance is a function of its self-impedance and the mutual impedances between it and the other sources or obstacles. In practice, the driving-point impedance is usually referred to as the input impedance. The definitions and the analytical formulations that underlie the self, mutual, and input impedances are presented in Chapter 8.

To attain maximum power transfer between a source or a source-transmission line and an antenna (or between an antenna and a receiver or transmission line-receiver), a conjugate match is usually desired. In some applications, this may not be the most ideal match. For example, in some receiving systems, minimum noise is attained if the antenna impedance is lower than the load impedance. However, in some transmitting systems, maximum power transfer is attained if the antenna impedance is greater than the load impedance. If conjugate matching does not exist, the power lost can be computed [7] using

$$\frac{P_{\text{lost}}}{P_{\text{available}}} = \left| \frac{Z_{\text{ant}} - Z_{\text{cct}}^*}{Z_{\text{ant}} + Z_{\text{cct}}} \right|^2 \tag{16-23}$$

where

Z_{ant} = input impedance of the antenna

Z_{cct} = input impedance of the circuits which are connected to the antenna at its input terminals

When a transmission line is associated with the system, as is usually the case, the matching can be performed at either end of the line. In practice, however, the matching is performed near the antenna terminals, because it usually minimizes line losses and voltage peaks in the line and maximizes the useful bandwidth of the system.

In a mismatched system, the degree of mismatch determines the amount of incident or available power which is reflected at the input antenna terminals into the line. The degree of mismatch is a function of the antenna input impedance and the characteristic impedance of the line. These are related to the input reflection coefficient and the input VSWR at the antenna input terminals by the standard transmission line relationships of

$$\frac{P_{\text{refl}}}{P_{\text{inc}}} = |\Gamma|^2 = \frac{|Z_{\text{ant}} - Z_c|^2}{|Z_{\text{ant}} + Z_c|^2} = \left| \frac{\text{VSWR} - 1}{\text{VSWR} + 1} \right|^2 \tag{16-24}$$

INTEL-1045
U.S. Patent 7,151,430

where

$\Gamma = |\Gamma|e^{j\gamma}$ = voltage reflection coefficient at the antenna input terminals
VSWR = voltage standing wave ratio at the antenna input terminals
Z_c = characteristic impedance of the transmission line

Equation (16-24) shows a direct relationship between the antenna input impedance (Z_{ant}) and the VSWR. In fact, if Z_{ant} is known, the VSWR can be computed using (16-24). In practice, however, that is not the case. What is usually measured is the VSWR, and it alone does not provide sufficient information to uniquely determine the complex input impedance. To overcome this, the usual procedure is to measure the VSWR, and to compute the magnitude of the reflection coefficient using (16-24). The phase of the reflection coefficient can be determined by locating a voltage maximum or a voltage minimum (from the antenna input terminals) in the transmission line. Since in practice the minima can be measured more accurately than the maxima, they are usually preferred. In addition, the first minimum is usually chosen unless the distance from it to the input terminals is too small to measure accurately. The phase γ of the reflection coefficient is then computed using [51]

$$\gamma = 2\beta x_n \pm (2n - 1)\pi = \frac{4\pi}{\lambda_g} x_n \pm (2n - 1)\pi, \qquad n = 1, 2, 3, \ldots \tag{16-25}$$

where

n = the voltage minimum from the input terminals (i.e., $n = 1$ is used to locate the first voltage minimum)
x_n = distance from the input terminals to the nth voltage minimum
λ_g = wavelength measured inside the input transmission line (it is twice the distance between two voltage minima or two voltage maxima)

Once the reflection coefficient is completely described by its magnitude and phase, it can be used to determine the antenna impedance by

$$Z_{ant} = Z_c \left[\frac{1 + \Gamma}{1 - \Gamma}\right] = Z_c \left[\frac{1 + |\Gamma|e^{j\gamma}}{1 - |\Gamma|e^{j\gamma}}\right] \tag{16-26}$$

Other methods, utilizing impedance bridges, slotted lines, and broadband swept-frequency network analyzers, can be utilized to determine the antenna impedance [51]–[53].

The input impedance is generally a function of frequency, geometry, method of excitation, and proximity to its surrounding objects. Because of its strong dependence on the environment, it should usually be measured *in situ* unless the antenna possesses very narrow beam characteristics.

Mutual impedances, which take into account interaction effects, are usually best described and measured by the cross-coupling coefficients S_{mn} of the device's (antenna's) scattering matrix. The coefficients of the scattering matrix can then be related to the coefficients of the impedance matrix [54].

16.8 CURRENT MEASUREMENTS

The current distribution along an antenna is another very important antenna parameter. A complete description of its amplitude and phase permit the calculation of the radiation pattern.

INTEL-1045
U.S. Patent 7,151,430

There are a number of techniques that can be used to measure the current distribution [55]–[58]. One of the simplest methods requires that a small sampling probe, usually a small loop, be placed near the radiator. On the sampling probe, a current is induced which is proportional to the current of the test antenna.

The indicating meter can be connected to the loop in many different ways [55]. If the wavelength is very long, the meter can be consolidated into one unit with the measuring loop. At smaller wavelengths, the meter can be connected to a crystal rectifier. In order not to disturb the field distribution near the radiator, the rectifier is attached to the meter using long leads. To reduce the interaction between the measuring instrumentation and the test antenna and to minimize induced currents on the leads, the wires are wound on a dielectric support rod to form a helical choke. Usually the diameter of each turn, and spacing between them, is about $\lambda/50$. The dielectric rod can also be used as a support for the loop. To prevent a dc short circuit on the crystal rectifier, a bypass capacitor is placed along the circumference of the loop.

There are many other methods, some of them more elaborate and accurate, and the interested reader can refer to the literature [55]–[58].

16.9 POLARIZATION MEASUREMENTS

The polarization of a wave was defined in Section 2.12 as *the curve traced by the instantaneous electric field, at a given frequency, in a plane perpendicular to the direction of wave travel.* The far-field polarization of an antenna is usually measured at distances where the field radiated by the antenna forms, in a small region, a plane wave that propagates in the outward radial direction.

In a similar manner, the polarization of the antenna is defined as *the curve traced by the instantaneous electric field radiated by the antenna in a plane perpendicular to the radial direction*, as shown in Figure 16.23(a). The locus is usually an ellipse. In a spherical coordinate system, which is usually adopted in antennas, the polarization ellipse is formed by the orthogonal electric field components of E_θ and E_ϕ. The sense of rotation, also referred to as the sense of polarization, is defined by the sense of rotation of the wave as it is observed along the direction of propagation [see Figure 16.23(b)].

The general polarization of an antenna is characterized by the axial ratio (AR), the sense of rotation (CW or CCW, RH or LH), and the tilt angle τ. The tilt angle is used to identify the spatial orientation of the ellipse, and it is usually measured clockwise from the reference direction. This is demonstrated in Figure 16.23(a) where τ is measured clockwise with respect to $\hat{\mathbf{a}}_\theta$, for a wave traveling in the outward radial direction.

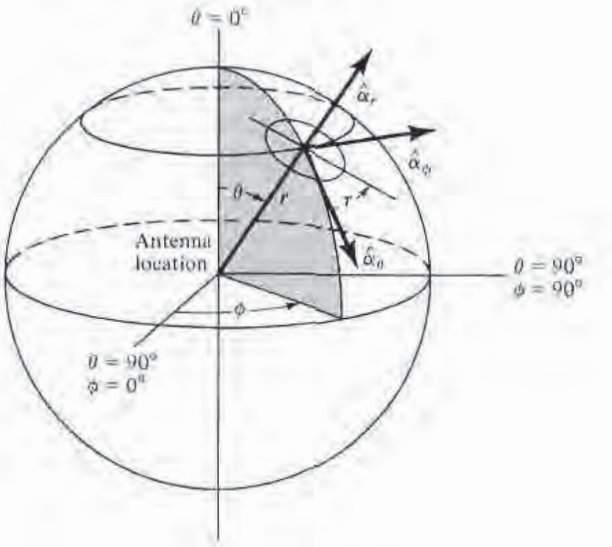
Care must be exercised in the characterization of the polarization of a receiving antenna. If the tilt angle of an incident wave that is polarization matched to the receiving antenna is τ_m, it is related to the tilt angle τ_t of a wave transmitted by the same antenna by

$$\tau_t = 180^\circ - \tau_m \tag{16-27}$$

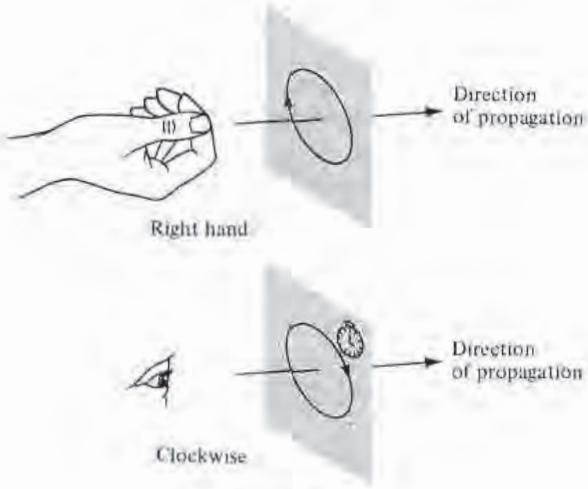
if a single coordinate system and one direction of view are used to characterize the polarization. If the receiving antenna has a polarization that is different from that of the incident wave, the polarization loss factor (PLF) of Section 2.12.2 can be used to account for the polarization mismatch losses.

The polarization of a wave and/or an antenna can best be displayed and visualized on the surface of a Poincaré sphere [59]. Each polarization occupies a unique point

INTEL-1045
U.S. Patent 7,151,430



(a) Polarization ellipse



(b) Sense of rotation

Figure 16.23 Polarization ellipse and sense of rotation for antenna coordinate system. (SOURCE: *IEEE Standard Test Procedures for Antennas*, IEEE Std 149-1979, published by IEEE, Inc., 1979, distributed by Wiley)

on the sphere, as shown in Figure 16.24. If one of the two points on the Poincaré sphere is used to define the polarization of the incident wave and the other the polarization of the receiving antenna, the angular separation can be used to determine the polarization losses. The procedure requires that the complex polarization ratios of each are determined, and they are used to compute the polarization efficiency in a number of different ways. The details of this procedure are well documented, and they can be found in [7], [8].

Practically it is very difficult to design radiators that maintain the same polarization state in all parts of their pattern. A complete description requires a number of

INTEL-1045
U.S. Patent 7,151,430

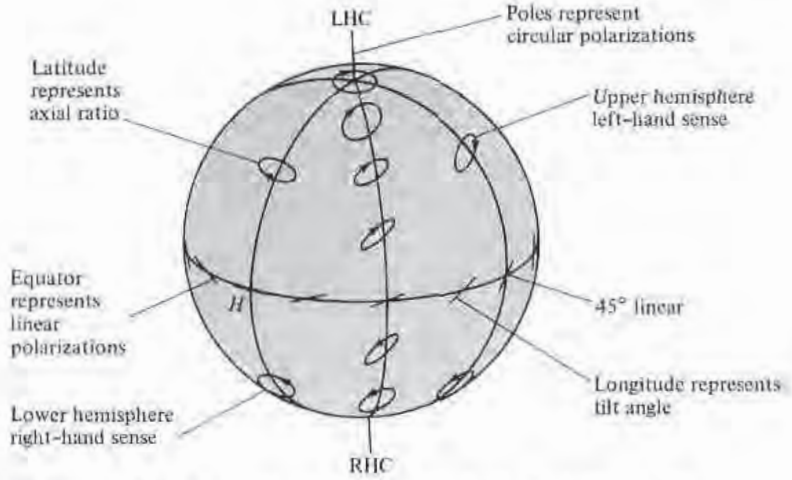


Figure 16.24 Polarization representation on Poincaré sphere. (SOURCE: W. H. Kummer and E. S. Gillespie, "Antenna Measurements—1978," *Proc. IEEE*, Vol. 66, No. 4, pp. 483–507, April 1978. © (1978) IEEE)

measurements in all parts of the pattern. The number of measurements is determined by the required degree of polarization description.

There are a number of techniques that can be used to measure the polarization state of a radiator [7], [8], and they can be classified into three main categories:

1. Those that yield partial polarization information. They do not yield a unique point on the Poincaré sphere.
2. Those that yield complete polarization information but require a polarization standard for comparison. They are referred to as *comparison methods*.
3. Those that yield complete polarization information and require no *a priori* polarization knowledge or no polarization standard. They are designated as *absolute methods*.

The method selected depends on such factors as the type of antenna, the required accuracy, and the time and funds available. A complete description requires not only the polarization ellipse (axial ratio and tilt angle), but also its sense of rotation (CW or CCW, RH or LH).

In this text, a method will be discussed which can be used to determine the polarization ellipse (axial ratio and tilt angle) of an antenna but not its sense of rotation. This technique is referred to as the *polarization-pattern method*. The sense of polarization or rotation can be found by performing auxiliary measurements or by using other methods [7].

To perform the measurements, the antenna under test can be used either in the transmitting or in the receiving mode. Usually the transmitting mode is adopted. The method requires that a linearly polarized antenna, usually a dipole, be used to probe the polarization in the plane that contains the direction of the desired polarization. The arrangement is shown in Figure 16.25(a). The dipole is rotated in the plane of the polarization, which is taken to be normal to the direction of the incident field, and the output voltage of the probe is recorded.

If the test antenna is linearly polarized, the output voltage response will be proportional to $\sin \psi$ (which is the far-zone field pattern of an infinitesimal dipole).

INTEL-1045
U.S. Patent 7,151,430

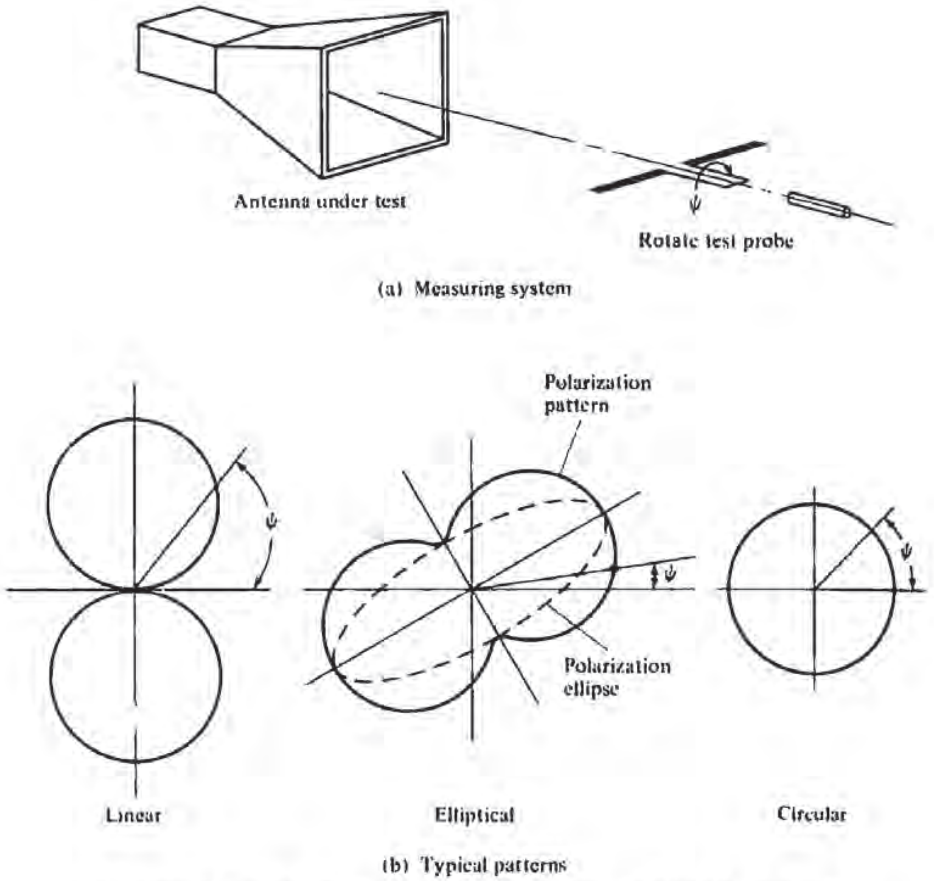


Figure 16.25 Polarization measuring system and typical patterns.

The pattern forms a figure-eight, as shown in Figure 16.25(b), where ψ is the rotation angle of the probe relative to a reference direction. For an elliptically polarized test antenna, the nulls of the figure-eight are filled and a dumbbell polarization curve (usually referred to as *polarization pattern*) is generated, as shown in Figure 16.25(b). The dashed curve represents the polarization ellipse.

The polarization ellipse is tangent to the polarization pattern, and it can be used to form the axial ratio and the tilt angle of the test antenna. The polarization pattern will be a circle, as shown in Figure 16.25(b), if the test antenna is circularly polarized. Ideally, this process must be repeated at every point of the antenna pattern. Usually it is performed at a number of points that describe sufficiently well the polarization of the antenna at the major and the minor lobes.

In some cases the polarization needs to be known over an entire plane. The axial ratio part of the polarization state can be measured using the arrangement of Figure 16.25(a) where the test probe antenna is used usually as a source while the polarization pattern of the test antenna is being recorded while the test antenna is rotated over the desired plane. This arrangement does not yield the tilt angle or sense of rotation of the polarization state. In order to obtain the desired polarization pattern, the rate of rotation of the linear probe antenna (usually a dipole) is much greater than the rotation rate of the positioner over which the test antenna is mounted and rotated to allow, ideally, the probe antenna to measure the polarization response of the test antenna at that direction before moving to another angle. When this is performed over an entire plane, a typical pattern recorded in decibels is shown in Figure 16.26 [60], and it is

INTEL-1045
U.S. Patent 7,151,430

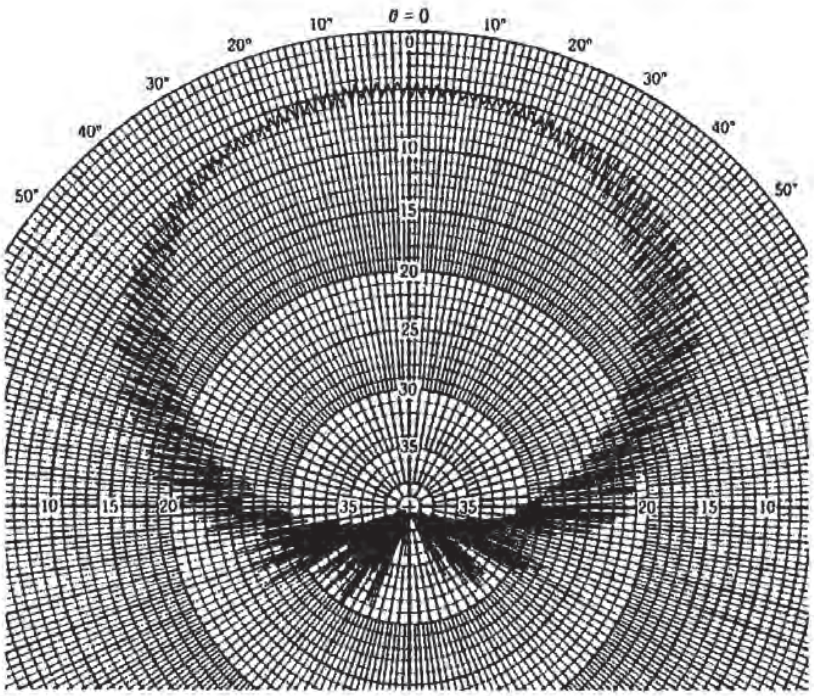


Figure 16.26 Pattern of a circularly polarized test antenna taken with a rotating, linearly polarized, source antenna [E. S. Gillespie, "Measurement of Antenna Radiation Characteristics on Far-Field Ranges," in *Antenna Handbook* (Y. T. Lo & S. W. Lee, eds.), 1988, © Van Nostrand Reinhold Co., Inc.]

referred as the *axial ratio pattern*. It is apparent that the axial ratio pattern can be inscribed by inner and outer envelopes. At any given angle, the ratio of the outer and inner envelope responses represent the axial ratio. If the pattern is recorded in decibels, the axial ratio is the difference between the outer and inner envelopes (in dB); zero dB difference represents circular polarization (axial ratio of unity). Therefore the polarization pattern of Figure 16.26 indicates that the test antenna it represents is nearly circularly polarized (within 1 dB; axial ratio less than 1.122) at and near $\theta = 0°$ and deviates from that almost monotonically at greater angles (typically by about 7 dB maximum; maximum axial ratio of about 2.24).

The sense of rotation can be determined by performing auxiliary measurements. One method requires that the responses of two circularly polarized antennas, one responsive to CW and the other to CCW rotation, be compared [55]. The sense of rotation corresponds to the sense of polarization of the antenna with the more intense response.

Another method would be to use a dual-polarized probe antenna, such as a dual-polarized horn, and to record simultaneously the amplitude polarization pattern and the relative phase between the two orthogonal polarizations. This is referred to as the *phase-amplitude* method, and it can be accomplished using the instrumentation of Figure 16.27. Double-conversion phase-locked receivers can be used to perform the amplitude and phase comparison measurements.

Another absolute polarization method, which can be used to completely describe the polarization of a test antenna, is referred to as the *three-antenna* method [7], [8]. As its name implies, it requires three antennas, two of which must not be circularly

INTEL-1045
U.S. Patent 7,151,430

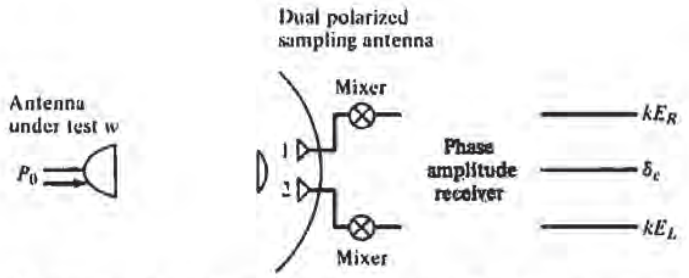


Figure 16.27 System configuration for measurements of polarization amplitude and phase. (SOURCE: W. H. Kummer and E. S. Gillespie, "Antenna Measurements—1978," *Proc. IEEE*, Vol. 66, No. 4, pp. 483–507, April 1978. © (1978) IEEE)

polarized. There are a number of transfer methods [7], [8], but they require calibration standards for complete description of the polarization state.

16.10 SCALE MODEL MEASUREMENTS

In many applications (such as with antennas on ships, aircraft, large spacecraft, etc.), the antenna and its supporting structure are so immense in weight and/or size that they cannot be moved or accommodated by the facilities of a measuring antenna range. In addition, a movement of the structure to an antenna range can eliminate or introduce environmental effects. To satisfy these system requirements, *in situ* measurements are usually executed.

A technique that can be used to perform antenna measurements associated with large structures is *geometrical scale modeling*. Geometrical modeling is employed to

1. physically accommodate, within small ranges or enclosures, measurements that can be related to large structures
2. provide experimental control over the measurements
3. minimize costs associated with large structures and corresponding experimental parametric studies

Geometrical scale modeling by a factor of n (n smaller or greater than unity) requires the scaling indicated in Table 16.1. The primed parameters represent the scaled model while the unprimed represent the full scale model. For a geometrical scale model, all the linear dimensions of the antenna and its associated structure are divided by n whereas the operating frequency and the conductivity of the antenna material and its structure are multiplied by n. In practice, the scaling factor n is usually chosen greater than unity.

Ideal scale modeling for antenna measurements requires exact replicas, both physically and electrically, of the full scale structures. In practice, however, this is closely approximated. The most difficult scaling is that of the conductivity. If the full scale model possesses excellent conductors, even better conductors will be required in the scaled models. At microwave and millimeter wave frequencies this can be accomplished by utilizing clean polished surfaces, free of films and other residues.

Geometrical scaling is often used for pattern measurements. However, it can also be employed to measure gain, directivity, radiation efficiency, input and mutual impedances, and so forth. For gain measurements, the inability to properly scale the conductivity can be overcome by measuring the directivity and the antenna efficiency

INTEL-1045
U.S. Patent 7,151,430

Table 16.1 GEOMETRICAL SCALE MODEL

Scaled Parameters		*Unchanged Parameters*	
Length:	$l' = l/n$	Permittivity:	$\epsilon' = \epsilon$
Time:	$t' = t/n$	Permeability:	$\mu' = \mu$
Wavelength:	$\lambda' = \lambda/n$	Velocity:	$v' = v$
Capacitance	$C' = C/n$	Impedance:	$Z' = Z$
Inductance:	$L' = L/n$	Antenna gain:	$G_0' = G_0$
Echo area:	$A_e' = A_e/n^2$		
Frequency:	$f' = nf$		
Conductivity:	$\sigma' = n\sigma$		

and multiplying the two to determine the gain. Scalings that permit additional parameter changes are available [61]. The changes must satisfy the *theorem of similitude*.

References

1. J. Brown and E. V. Jull, "The Prediction of Aerial Patterns from Near-Field Measurements," *IEE (London)*, Paper No. 3469E, pp. 635–644, November 1961.
2. R. C. Johnson, H. A. Ecker, and J. S. Hollis, "Determination of Far-Field Antenna Patterns from Near-Field Measurements," *Proc. IEEE*, Vol. 61, No. 12, pp. 1668–1694, December 1973.
3. D. T. Paris, W. M. Leach, Jr., and E. B. Joy, "Basic Theory of Probe-Compensated Near-Field Measurements," *IEEE Trans. Antennas Propagat.*, Vol. AP-26, No. 3, pp. 373–379, May 1978.
4. E. B. Joy, W. M. Leach, Jr., G. P. Rodrigue, and D. T. Paris, "Applications of Probe-Compensated Near-Field Measurements," *IEEE Trans. Antennas Propagat.*, Vol. AP-26, No. 3, pp. 379–389, May 1978.
5. E. F. Buckley, "Modern Microwave Absorbers and Applications," Emerson & Cuming, Inc., Canton, Mass.
6. J. S. Hollis, T. J. Lyon, and L. Clayton, Jr., *Microwave Antenna Measurements*, Scientific-Atlanta, Inc., Atlanta, Georgia, July 1970.
7. *IEEE Standard Test Procedures for Antennas*, IEEE Std 149-1979, published by IEEE, Inc., 1979, distributed by Wiley-Interscience.
8. W. H. Kummer and E. S. Gillespie, "Antenna Measurements—1978," *Proc. IEEE*, Vol. 66, No. 4, pp. 483–507, April 1978.
9. L. H. Hemming and R. A. Heaton, "Antenna Gain Calibration on a Ground Reflection Range," *IEEE Trans. Antennas Propagat.*, Vol. AP-21, No. 4, pp. 532–537, July 1973.
10. P. W. Arnold, "The 'Slant' Antenna Range," *IEEE Trans. Antennas Propagat.*, Vol. AP-14, No. 5, pp. 658–659, September 1966.
11. A. W. Moeller, "The Effect of Ground Reflections on Antenna Test Range Measurements," *Microwave Journal*, Vol. 9, pp. 47–54, March 1966.
12. W. H. Emerson, "Electromagnetic Wave Absorbers and Anechoic Chambers Through the Years," *IEEE Trans. Antennas Propagat.*, Vol. AP-21, No. 4, pp. 484–490, July 1973.
13. M. R. Gillette and P. R. Wu, "RF Anechoic Chamber Design Using Ray Tracing," *1977 Int. IEEE/AP-S Symp. Dig.*, pp. 246–252, June 1977.
14. W. H. Emerson and H. B. Sefton, "An Improved Design for Indoor Ranges," *Proc. IEEE*, Vol. 53, pp. 1079–1081, August 1965.
15. J. R. Mentzer, "The Use of Dielectric Lenses in Reflection Measurements," *Proc. IRE*, Vol. 41, pp. 252–256, February 1953.

INTEL-1045
U.S. Patent 7,151,430

16. P. A. Beeckman, "Prediction of the Fresnel Region Field of a Compact Antenna Test Range with Serrated Edges," *IEE Proc.*, Vol. 133, Pt. H, No. 2, pp. 108–114, April 1986.
17. H. F. Schluper, "Compact Antenna Test Range Analysis Using Physical Optics," *AMTA Proceedings*, pp. 309–312, Seattle, WA, October 1987.
18. H. F. Schluper, "Verification Method for the Serration Design of CATR Reflectors," *AMTA Proceedings*, pp. 10-9 to 10-14, Monterey, CA, October 1989.
19. W. D. Burnside, M. C. Gilreath, and B. Kent, "A Rolled Edge Modification of Compact Range Reflectors," presented at AMTA Conf., San Diego, CA, October 1984.
20. W. D. Burnside, M. C. Gilreath, B. M. Kent, and G. L. Clerici, "Curved Edge Modification of Compact Range Reflector," *IEEE Trans. Antennas Propagat.*, Vol. AP-35, No. 2, pp. 176–182, February 1987.
21. M. R. Hurst and P. E. Reed, "Hybrid Compact Radar Range Reflector," *AMTA Proceedings*, pp. 8-9 to 8-13, Monterey, CA, October 1989.
22. J. P. McKay and Y. Rahmat-Samii, "Multi-Ring Planar Array Feeds for Reducing Diffraction Effects in the Compact Range," *AMTA Proceedings*, pp. 7-3 to 7-8, Columbus, OH, October 1992.
23. J. P. McKay, Y. Rahmat-Samii, and F. M. Espiau, "Implementation Considerations for a Compact Range Array Feed," *AMTA Proceedings*, pp. 4-21 to 4-26, Columbus, OH, October 1992.
24. J. P. McKay and Y. Rahmat-Samii, "A Compact Range Array Feed: Tolerances and Error Analysis," *1993 Int. IEEE/AP-S Symp. Dig.*, Vol. 3, pp. 1800–1803, June 1993.
25. J. P. McKay, Y. Rahmat-Samii, T. J. De Vicente, and L. U. Brown, "An X-Band Array for Feeding a Compact Range Reflector," *AMTA Proceedings*, pp. 141–146, Dallas, TX, October 1993.
26. H. F. Schluper, J. Van Damme, and V. J. Vokurka, "Optimized Collimators—Theoretical Performance Limits," *AMTA Proceedings*, p. 313, Seattle, WA, October 1987.
27. J. D. Huff, J. H. Cook, Jr., and B. W. Smith, "Recent Developments in Large Compact Range Design," *AMTA Proceedings*, pp. 5-39 to 5-44, Columbus, OH, October 1992.
28. H. F. Schluper and V. J. Vokurka, "Troubleshooting Limitations in Indoor RCS Measurements," *Microwaves & RF*, pp. 154–163, May 1987.
29. V. J. Vokurka, "Seeing Double Improves Indoor Range," *Microwaves & RF*, pp. 71–76, 94, February 1985.
30. T. Harrison, "A New Approach to Radar Cross-Section Compact Range," *Microwave Journal*, pp. 137–145, June 1986.
31. K. W. Lam and V. J. Vokurka, "Hybrid Near-Field/Far-Field Antenna Measurement Techniques," *AMTA Proceedings*, pp. 9-29 to 9-34, Boulder, CO, October 1991.
32. C. R. Birtcher, C. A. Balanis, and V. J. Vokurka, "RCS Measurements, Transformations, and Comparisons Under Cylindrical and Plane Wave Illumination," *IEEE Trans. Antennas Propagat.*, Vol. AP-42, No. 3, pp. 329–334, March 1994.
33. C. R. Birtcher, C. A. Balanis, and V. J. Vokurka, "Quiet Zone Scan of the Single-Plane Collimating Range," *AMTA Proceedings*, pp. 4-37 to 4-42, Boulder, CO, October 1991.
34. A. D. Yaghjian, "An Overview of Near-Field Antenna Measurements," *IEEE Trans. Antennas Propagat.*, Vol. AP-34, pp. 30–45, January 1986.
35. P. M. Morse and H. Feshbach, *Methods of Theoretical Physics*, New York: McGraw-Hill, 1953, Chapter 13.
36. A. V. Oppenheim and R. W. Schaffer, *Digital Signal Processing*, Englewood Cliffs, NJ: Prentice-Hall, 1975, Chapter 3.
37. Y. Rahmat-Samii, V. Galindo, and R. Mittra, "A Plane-Polar Approach for Far-Field Construction from Near-Field Measurements," *IEEE Trans. Antennas Propagat.*, Vol. AP-28, No. 3, pp. 216–230, March 1980.
38. L. I. Williams and Y. Rahmat-Samii, "Novel Bi-Polar Planar Near-Field Measurement Scanner at UCLA," *1991 Int. IEEE/AP-S Symp. Dig.*, London, Ontario, Canada, June 1991.
39. G. D. Bergland, "A Guided Tour of the Fast Fourier Transform," *IEEE Spectrum*, pp. 41–52, July 1969.

INTEL-1045
U.S. Patent 7,151,430

40. W. M. Leach, Jr. and D. T. Paris, "Probe Compensated Near-Field Measurements on a Cylinder," *IEEE Trans. Antennas Propagat.*, Vol. AP-21, No. 4, pp. 435–445, July 1973.
41. C. F. Stubenrauch and A. C. Newell, "Some Recent Near-Field Antenna Measurements at NBS," *Microwave Journal*, pp. 37–42, November 1980.
42. J. Lemanczyk and F. H. Larsen, "Comparison of Near-Field Range Results," *IEEE Trans. Antennas Propagat.*, Vol. AP-36, No. 6, pp. 845–851, June 1988.
43. J. J. Lee, E. M. Ferren, D. P. Woollen, and K. M. Lee, "Near-Field Probe Used as a Diagnostic Tool to Locate Defective Elements in an Array Antenna," *IEEE Trans. Antennas Propagat.*, Vol. AP-36, No. 6, pp. 884–889, June 1988.
44. Y. Rahmat-Samii and J. Lemanczyk, "Application of Spherical Near-Field Measurements to Microwave Holographic Diagnosis of Antennas," *IEEE Trans. Antennas Propagat.*, Vol. AP-36, No. 6, pp. 869–878, June 1988.
45. A. C. Newell, R. C. Baird, and P. F. Wacker, "Accurate Measurement of Antenna Gain and Polarization at Reduced Distances by an Extrapolation Technique," *IEEE Trans. Antennas Propagat.*, Vol. AP-21, No. 4, pp. 418–431, July 1973.
46. L. H. Hemming and R. A. Heaton, "Antenna Gain Calibration on a Ground Reflection Range," *IEEE Trans. Antennas Propagat.*, Vol. AP-21, No. 4, pp. 532–537, July 1973.
47. R. G. FitzGerrell, "Gain Measurements of Vertically Polarized Antennas over Imperfect Ground," *IEEE Trans. Antennas Propagat.*, Vol. AP-15, No. 2, pp. 211–216, March 1967.
48. R. G. FitzGerrell, "The Gain of a Horizontal Half-Wave Dipole over Ground," *IEEE Trans. Antennas Propagat.*, Vol. AP-15, No. 4, pp. 569–571, July 1967.
49. R. G. FitzGerrell, "Limitations on Vertically Polarized Ground-Based Antennas as Gain Standards," *IEEE Trans. Antennas Propagat.*, Vol. AP-23, No. 2, pp. 284–286, March 1975.
50. E. H. Newman, P. Bohley, and C. H. Walter, "Two Methods for the Measurement of Antenna Efficiency," *IEEE Trans. Antennas Propagat.*, Vol. AP-23, No. 4, pp. 457–461, July 1975.
51. M. Sucher and J. Fox, *Handbook of Microwave Measurements*, Vol. I, Polytechnic Press of the Polytechnic Institute of Brooklyn, New York, 1963.
52. C. G. Montgomery, *Techniques of Microwave Measurements*, Vol. II, MIT Radiation Laboratory Series, Vol. 11, McGraw-Hill, New York, 1947, Chapter 8.
53. ANSI/IEEE Std 148-1959 (Reaff 1971).
54. R. E. Collin, *Foundations for Microwave Engineering*, McGraw-Hill, New York, 1992, pp. 248–257.
55. J. D. Kraus, *Antennas*, McGraw-Hill, New York, 1988.
56. G. Barzilai, "Experimental Determination of the Distribution of Current and Charge Along Cylindrical Antennas," *Proc. IRE* (Waves and Electrons Section), pp. 825–829, July 1949.
57. T. Morita, "Current Distributions on Transmitting and Receiving Antennas," *Proc. IRE*, pp. 898–904, August 1950.
58. A. F. Rashid, "Quasi-Near-Zone Field of a Monopole Antenna and the Current Distribution of an Antenna on a Finite Conductive Earth," *IEEE Trans. Antennas Propagat.*, Vol. AP-18, No. 1, pp. 22–28, January 1970.
59. H. G. Booker, V. H. Rumsey, G. A. Deschamps, M. I. Kales, and J. I. Bonhert, "Techniques for Handling Elliptically Polarized Waves with Special Reference to Antennas," *Proc. IRE*, Vol. 39, pp. 533–552, May 1951.
60. E. S. Gillespie, "Measurement of Antenna Radiation Characteristics on Far-Field Ranges," Chapter 32 in *Antenna Handbook* (Y. T. Lo and S. W. Lee, eds.), pp. 32-1 to 32-91, New York, Van Nostrand Reinhold Co., Inc., 1988.
61. G. Sinclair, "Theory of Models of Electromagnetic Systems," *Proc. IRE*, Vol. 36, pp. 1364–1370, November 1948.

INTEL-1045
U.S. Patent 7,151,430

APPENDIX

I

$$f(x) = \frac{\sin(x)}{x}$$

x	$\sin(x)/x$	x	$\sin(x)/x$	x	$\sin(x)/x$
0.0	1.00000	2.8	0.11964	5.6	−0.11273
0.1	0.99833	2.9	0.08250	5.7	−0.09661
0.2	0.99335	3.0	0.04704	5.8	−0.08010
0.3	0.98507	3.1	0.01341	5.9	−0.06337
0.4	0.97355	3.2	−0.01824	6.0	−0.04657
0.5	0.95885	3.3	−0.04780	6.1	−0.02986
0.6	0.94107	3.4	−0.07516	6.2	−0.01340
0.7	0.92031	3.5	−0.10022	6.3	0.00267
0.8	0.89670	3.6	−0.12292	6.4	0.01821
0.9	0.87036	3.7	−0.14320	6.5	0.03309
1.0	0.84147	3.8	−0.16101	6.6	0.04720
1.1	0.81019	3.9	−0.17635	6.7	0.06042
1.2	0.77670	4.0	−0.18920	6.8	0.07266
1.3	0.74120	4.1	−0.19958	6.9	0.08383
1.4	0.70389	4.2	−0.20752	7.0	0.09385
1.5	0.66500	4.3	−0.21306	7.1	0.10267
1.6	0.62473	4.4	−0.21627	7.2	0.11023
1.7	0.58333	4.5	−0.21723	7.3	0.11650
1.8	0.54103	4.6	−0.21602	7.4	0.12145
1.9	0.49805	4.7	−0.21275	7.5	0.12507
2.0	0.45465	4.8	−0.20753	7.6	0.12736
2.1	0.41105	4.9	−0.20050	7.7	0.12833
2.2	0.36750	5.0	−0.19179	7.8	0.12802
2.3	0.32422	5.1	−0.18153	7.9	0.12645
2.4	0.28144	5.2	−0.16990	8.0	0.12367
2.5	0.23939	5.3	−0.15703	8.1	0.11974
2.6	0.19827	5.4	−0.14310	8.2	0.11472
2.7	0.15829	5.5	−0.12828	8.3	0.10870

INTEL-1045
U.S. Patent 7,151,430

x	$\sin(x)/x$	x	$\sin(x)/x$	x	$\sin(x)/x$
8.4	0.10174	10.7	−0.08941	13.0	0.03232
8.5	0.09394	10.8	−0.09083	13.1	0.03883
8.6	0.08540	10.9	−0.09132	13.2	0.04485
8.7	0.07620	11.0	−0.09091	13.3	0.05034
8.8	0.06647	11.1	−0.08960	13.4	0.05525
8.9	0.05629	11.2	−0.08743	13.5	0.05954
9.0	0.04579	11.3	−0.08443	13.6	0.06317
9.1	0.03507	11.4	−0.08064	13.7	0.06613
9.2	0.02423	11.5	−0.07613	13.8	0.06838
9.3	0.01338	11.6	−0.07093	13.9	0.06993
9.4	0.00264	11.7	−0.06513	14.0	0.07076
9.5	−0.00791	11.8	−0.05877	14.1	0.07087
9.6	−0.01816	11.9	−0.05194	14.2	0.07028
9.7	−0.02802	12.0	−0.04471	14.3	0.06901
9.8	−0.03740	12.1	−0.03716	14.4	0.06706
9.9	−0.04622	12.2	−0.02936	14.5	0.06448
10.0	−0.05440	12.3	−0.02140	14.6	0.06129
10.1	−0.06189	12.4	−0.01336	14.7	0.05753
10.2	−0.06861	12.5	−0.00531	14.8	0.05326
10.3	−0.07453	12.6	0.00267	14.9	0.04852
10.4	−0.07960	12.7	0.01049	15.0	0.04335
10.5	−0.08378	12.8	0.01809		
10.6	−0.08705	12.9	0.02539		

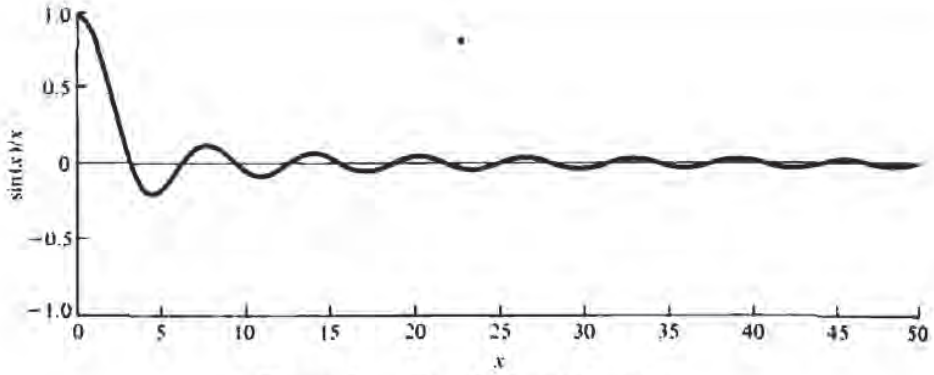


Figure 1.1 Plot of sin $(x)/x$ function.

INTEL-1045
U.S. Patent 7,151,430

APPENDIX

II

$$f_N(x) = \left| \frac{\sin(Nx)}{N \sin(x)} \right|$$

$$N = 1, 3, 5, 10, 20$$

x	$f_1(x)$	$f_3(x)$	$f_5(x)$	$f_{10}(x)$	$f_{20}(x)$
0.0	1.00000	1.00000	1.00000	1.00000	1.00000
0.1	1.00000	0.98671	0.96045	0.84287	0.45540
0.2	1.00000	0.94737	0.84711	0.45769	0.19047
0.3	1.00000	0.88356	0.67508	0.04775	0.04727
0.4	1.00000	0.79780	0.46700	0.19434	0.12703
0.5	1.00000	0.69353	0.24966	0.20001	0.05674
0.6	1.00000	0.57490	0.04998	0.04948	0.04751
0.7	1.00000	0.44664	0.10890	0.10198	0.07688
0.8	1.00000	0.31387	0.21100	0.13792	0.02007
0.9	1.00000	0.18186	0.24958	0.05261	0.04794
1.0	1.00000	0.05590	0.22792	0.06465	0.05425
1.1	1.00000	0.05900	0.15833	0.11221	0.00050
1.2	1.00000	0.15826	0.05996	0.05757	0.04858
1.3	1.00000	0.23793	0.04465	0.04361	0.03957
1.4	1.00000	0.29481	0.13334	0.10052	0.01375
1.5	1.00000	0.32666	0.18807	0.06519	0.04953
1.6	1.00000	0.33220	0.19796	0.02880	0.02758
1.7	1.00000	0.31120	0.16104	0.09695	0.02668
1.8	1.00000	0.26451	0.08464	0.07712	0.05092
1.9	1.00000	0.19398	0.01588	0.01584	0.01566
2.0	1.00000	0.10243	0.11966	0.10040	0.04097
2.1	1.00000	0.00649	0.20382	0.09692	0.05309
2.2	1.00000	0.12844	0.24737	0.00109	0.00109
2.3	1.00000	0.25856	0.23480	0.11348	0.06047
2.4	1.00000	0.39167	0.15888	0.13407	0.05687
2.5	1.00000	0.52244	0.02216	0.02211	0.02192
2.6	1.00000	0.64568	0.16301	0.14792	0.09570
2.7	1.00000	0.75646	0.37615	0.22378	0.06537
2.8	1.00000	0.85038	0.59143	0.08087	0.07785
2.9	1.00000	0.92368	0.78152	0.27738	0.20750
3.0	1.00000	0.97345	0.92161	0.70013	0.10799
3.1	1.00000	0.99769	0.99309	0.97172	0.88885
3.1415	1.00000	1.00000	1.00000	1.00000	1.00000

INTEL-1045
U.S. Patent 7,151,430

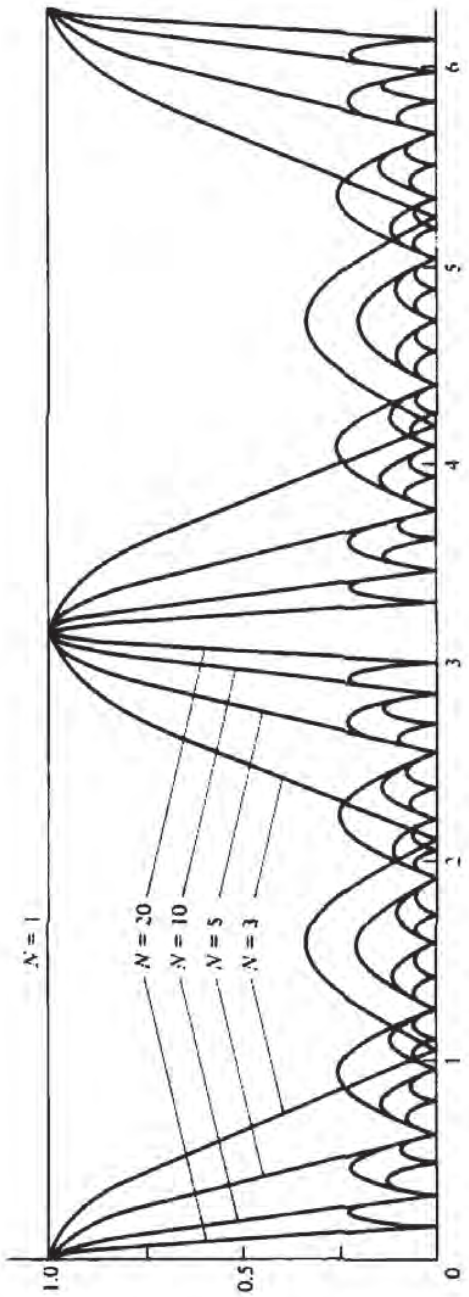


Figure II.1 Curves of $|\sin(Nx)/N\sin(x)|$ function.

INTEL-1045
U.S. Patent 7,151,430

APPENDIX

III

COSINE AND SINE INTEGRALS

$$S_i(x) = \int_0^x \frac{\sin(\tau)}{\tau}\, d\tau \tag{III-1}$$

$$C_i(x) = -\int_x^\infty \frac{\cos(\tau)}{\tau}\, d\tau = \int_\infty^x \frac{\cos(\tau)}{\tau}\, d\tau \tag{III-2}$$

$$C_{in}(x) = \int_0^x \frac{1 - \cos(\tau)}{\tau}\, d\tau \tag{III-3}$$

$$C_{in}(x) = \ln(\gamma x) - C_i(x) = \ln(\gamma) + \ln(x) - C_i(x)$$

$$C_{in}(x) = \ln(1.781) + \ln(x) - C_i(x) = 0.577215665 + \ln(x) - C_i(x) \tag{III-4}$$

Also

$$S_i(x) = \sum_{k=0}^{\infty} \frac{(-1)^k x^{2k+1}}{(2k+1)(2k+1)!}$$

$$C_i(x) = C + \ln(x) + \sum_{k=1}^{\infty} (-1)^k \frac{x^{2k}}{2k(2k)!}$$

$$C_{in}(x) = \sum_{k=1}^{\infty} (-1)^{k+1} \frac{x^{2k}}{2k(2k)!}$$

INTEL-1045
U.S. Patent 7,151,430

x	$S_i(x)$	$C_i(x)$	$C_{in}(x)$	x	$S_i(x)$	$C_i(x)$	$C_{in}(x)$
0.0	0.0	$-\infty$	0.00000	5.1	1.53125	−0.18348	2.38993
0.1	0.09994	−1.72787	0.00250	5.2	1.51367	−0.17525	2.40113
0.2	0.19956	−1.04221	0.00998	5.3	1.49732	−0.16551	2.41043
0.3	0.29850	−0.64917	0.02242	5.4	1.48230	−0.15439	2.41800
0.4	0.39646	−0.37881	0.03973	5.5	1.46872	−0.14205	2.42402
0.5	0.49311	−0.17778	0.06185	5.6	1.45667	−0.12867	2.42865
0.6	0.58813	−0.02227	0.08866	5.7	1.44620	−0.11441	2.43209
0.7	0.68122	0.10051	0.12003	5.8	1.43736	−0.09944	2.43451
0.8	0.77210	0.19828	0.15579	5.9	1.43018	−0.08393	2.43610
0.9	0.86047	0.27607	0.19579	6.0	1.42469	−0.06806	2.43703
1.0	0.94608	0.33740	0.23981	6.1	1.42087	−0.05198	2.43749
1.1	1.02869	0.38487	0.28765	6.2	1.41871	−0.03587	2.43764
1.2	1.10805	0.42046	0.33908	6.3	1.41817	−0.01989	2.43765
1.3	1.18396	0.44574	0.39384	6.4	1.41922	−0.00418	2.43770
1.4	1.25623	0.46201	0.45168	6.5	1.42179	0.01110	2.43792
1.5	1.32468	0.47036	0.51232	6.6	1.42582	0.02582	2.43846
1.6	1.38918	0.47173	0.57549	6.7	1.43121	0.03986	2.43947
1.7	1.44959	0.46697	0.64088	6.8	1.43787	0.05308	2.44106
1.8	1.50582	0.45681	0.70819	6.9	1.44570	0.06539	2.44334
1.9	1.55778	0.44194	0.77713	7.0	1.45460	0.07670	2.44643
2.0	1.60541	0.42298	0.84738	7.1	1.46443	0.08691	2.45040
2.1	1.64870	0.40051	0.91864	7.2	1.47509	0.09596	2.45534
2.2	1.68762	0.37507	0.99060	7.3	1.48644	0.10379	2.46130
2.3	1.72221	0.34718	1.06295	7.4	1.49834	0.11036	2.46834
2.4	1.75249	0.31729	1.13539	7.5	1.51068	0.11563	2.47649
2.5	1.77852	0.28587	1.20764	7.6	1.52331	0.11960	2.48577
2.6	1.80039	0.25334	1.27939	7.7	1.53611	0.12225	2.49619
2.7	1.81821	0.22008	1.35038	7.8	1.54894	0.12359	2.50775
2.8	1.83210	0.18649	1.42035	7.9	1.56167	0.12364	2.52044
2.9	1.84219	0.15290	1.48903	8.0	1.57419	0.12243	2.53422
3.0	1.84865	0.11963	1.55620	8.1	1.58637	0.12002	2.54906
3.1	1.85166	0.08699	1.62163	8.2	1.59810	0.11644	2.56491
3.2	1.85140	0.05526	1.68511	8.3	1.60928	0.11177	2.58170
3.3	1.84808	0.02468	1.74646	8.4	1.61981	0.10607	2.59938
3.4	1.84191	−0.00452	1.80551	8.5	1.62960	0.09943	2.61785
3.5	1.83313	−0.03213	1.86211	8.6	1.63857	0.09194	2.63704
3.6	1.82195	−0.05797	1.91612	8.7	1.64665	0.08368	2.65686
3.7	1.80862	−0.08190	1.96745	8.8	1.65379	0.07476	2.67721
3.8	1.79339	−0.10378	2.01599	8.9	1.65993	0.06528	2.69799
3.9	1.77650	−0.12350	2.06169	9.0	1.66504	0.05535	2.71909
4.0	1.75820	−0.14098	2.10449	9.1	1.66908	0.04507	2.74042
4.1	1.73874	−0.15617	2.14437	9.2	1.67205	0.03455	2.76186
4.2	1.71837	−0.16901	2.18131	9.3	1.67393	0.02391	2.78332
4.3	1.69732	−0.17951	2.21534	9.4	1.67473	0.01325	2.80467
4.4	1.67583	−0.18766	2.24648	9.5	1.67446	0.00268	2.82583
4.5	1.65414	−0.19349	2.27478	9.6	1.67316	−0.00771	2.84669
4.6	1.63246	−0.19705	2.30032	9.7	1.67084	−0.01780	2.86715
4.7	1.61101	−0.19839	2.32317	9.8	1.66757	−0.02752	2.88712
4.8	1.58998	−0.19760	2.34344	9.9	1.66338	−0.03676	2.90651
4.9	1.56956	−0.19478	2.36123	10.0	1.65835	−0.04546	2.92526
5.0	1.54993	−0.19003	2.37668	10.1	1.65253	−0.05352	2.94327

INTEL-1045
U.S. Patent 7,151,430

x	$S_i(x)$	$C_i(x)$	$C_{in}(x)$	x	$S_i(x)$	$C_i(x)$	$C_{in}(x)$
10.2	1.64600	−0.06089	2.96050	15.3	1.62865	0.02955	3.27552
10.3	1.63883	−0.06751	2.97687	15.4	1.63093	0.02345	3.28813
10.4	1.63112	−0.07332	2.99234	15.5	1.63258	0.01719	3.30086
10.5	1.62294	−0.07828	3.00687	15.6	1.63359	0.01084	3.31364
10.6	1.61439	−0.08237	3.02044	15.7	1.63396	0.00447	3.32641
10.7	1.60556	−0.08555	3.03301	15.8	1.63370	−0.00187	3.33910
10.8	1.59654	−0.08781	3.04457	15.9	1.63280	−0.00812	3.35165
10.9	1.58743	−0.08915	3.05513	16.0	1.63130	−0.01420	3.36400
11.0	1.57831	−0.08956	3.06467	16.1	1.62921	−0.02007	3.37610
11.1	1.56927	−0.08907	3.07323	16.2	1.62657	−0.02566	3.38789
11.2	1.56042	−0.08769	3.08082	16.3	1.62339	−0.03093	3.39931
11.3	1.55182	−0.08546	3.08748	16.4	1.61973	−0.03583	3.41033
11.4	1.54356	−0.08240	3.09323	16.5	1.61563	−0.04031	3.42088
11.5	1.53571	−0.07857	3.09813	16.6	1.61112	−0.04433	3.43095
11.6	1.52835	−0.07401	3.10224	16.7	1.60627	−0.04786	3.44049
11.7	1.52155	−0.06879	3.10560	16.8	1.60111	−0.05087	3.44947
11.8	1.51535	−0.06297	3.10828	16.9	1.59572	−0.05334	3.45787
11.9	1.50981	−0.05661	3.11036	17.0	1.59014	−0.05524	3.46567
12.0	1.50497	−0.04978	3.11190	17.1	1.58443	−0.05657	3.47287
12.1	1.50088	−0.04257	3.11299	17.2	1.57865	−0.05732	3.47945
12.2	1.49755	−0.03504	3.11369	17.3	1.57285	−0.05749	3.48541
12.3	1.49501	−0.02729	3.11410	17.4	1.56711	−0.05708	3.49076
12.4	1.49327	−0.01938	3.11429	17.5	1.56146	−0.05610	3.49552
12.5	1.49234	−0.01141	3.11435	17.6	1.55598	−0.05458	3.49969
12.6	1.49221	−0.00344	3.11436	17.7	1.55070	−0.05252	3.50330
12.7	1.49287	0.00443	3.11439	17.8	1.54568	−0.04997	3.50638
12.8	1.49430	0.01214	3.11452	17.9	1.54097	−0.04694	3.50895
12.9	1.49647	0.01961	3.11484	18.0	1.53661	−0.04348	3.51106
13.0	1.49936	0.02676	3.11540	18.1	1.53264	−0.03962	3.51274
13.1	1.50292	0.03355	3.11628	18.2	1.52909	−0.03540	3.51404
13.2	1.50711	0.03989	3.11754	18.3	1.52600	−0.03088	3.51500
13.3	1.51188	0.04574	3.11924	18.4	1.52339	−0.02610	3.51566
13.4	1.51716	0.05104	3.12143	18.5	1.52128	−0.02111	3.51609
13.5	1.52291	0.05576	3.12415	18.6	1.51969	−0.01596	3.51634
13.6	1.52905	0.05984	3.12744	18.7	1.51863	−0.01071	3.51644
13.7	1.53552	0.06327	3.13134	18.8	1.51810	−0.00540	3.51647
13.8	1.54225	0.06602	3.13587	18.9	1.51810	−0.00010	3.51648
13.9	1.54917	0.06806	3.14104	19.0	1.51863	0.00515	3.51650
14.0	1.55621	0.06940	3.14688	19.1	1.51967	0.01029	3.51661
14.1	1.56330	0.07002	3.15337	19.2	1.52122	0.01528	3.51685
14.2	1.57036	0.06993	3.16053	19.3	1.52324	0.02006	3.51726
14.3	1.57733	0.06914	3.16834	19.4	1.52572	0.02459	3.51790
14.4	1.58414	0.06767	3.17678	19.5	1.52863	0.02883	3.51880
14.5	1.59072	0.06554	3.18583	19.6	1.53192	0.03274	3.52000
14.6	1.59702	0.06278	3.19546	19.7	1.53557	0.03629	3.52155
14.7	1.60296	0.05943	3.20563	19.8	1.53954	0.03943	3.52347
14.8	1.60851	0.05554	3.21631	19.9	1.54378	0.04215	3.52579
14.9	1.61360	0.05113	3.22744	20.0	1.54824	0.04442	3.52853
15.0	1.61819	0.04628	3.23899				
15.1	1.62226	0.04102	3.25089				
15.2	1.62575	0.03543	3.26308				

INTEL-1045
U.S. Patent 7,151,430

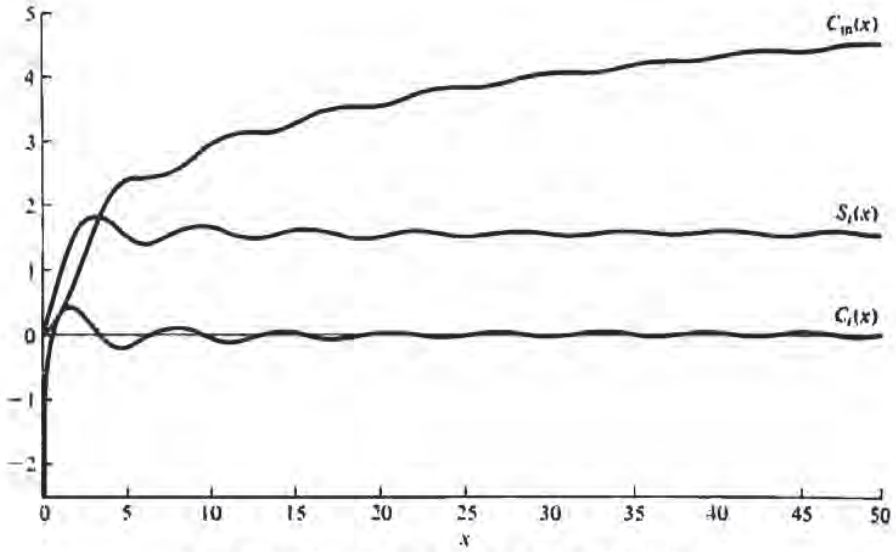


Figure III.1 Plots of sine and cosine integrals.

APPENDIX

IV

FRESNEL INTEGRALS

$$C_0(x) = \int_0^x \frac{\cos(\tau)}{\sqrt{2\pi\tau}}\, d\tau \tag{IV-1}$$

$$S_0(x) = \int_0^x \frac{\sin(\tau)}{\sqrt{2\pi\tau}}\, d\tau \tag{IV-2}$$

$$C(x) = \int_0^x \cos\left(\frac{\pi}{2}\tau^2\right) d\tau \tag{IV-3}$$

$$S(x) = \int_0^x \sin\left(\frac{\pi}{2}\tau^2\right) d\tau \tag{IV-4}$$

$$C_1(x) = \int_x^\infty \cos(\tau^2)\, d\tau \tag{IV-5}$$

$$S_1(x) = \int_x^\infty \sin(\tau^2)\, d\tau \tag{IV-6}$$

$$C(x) - jS(x) = \int_0^x e^{-j(\pi/2)\tau^2}\, d\tau = \int_0^{(\pi/2)x^2} \frac{e^{-j\tau}}{\sqrt{2\pi\tau}}\, d\tau$$

$$C(x) - jS(x) = C_0\left(\frac{\pi}{2}x^2\right) - jS_0\left(\frac{\pi}{2}x^2\right) \tag{IV-7}$$

$$C_1(x) - jS_1(x) = \int_x^\infty e^{-j\tau^2}\, d\tau = \sqrt{\frac{\pi}{2}} \int_{x^2}^\infty \frac{e^{-j\tau}}{\sqrt{2\pi\tau}}\, d\tau$$

$$C_1(x) - jS_1(x) = \sqrt{\frac{\pi}{2}} \left\{ \int_0^\infty \frac{e^{-j\tau}}{\sqrt{2\pi\tau}}\, d\tau - \int_0^{x^2} \frac{e^{-j\tau}}{\sqrt{2\pi\tau}}\, d\tau \right\}$$

$$C_1(x) - jS_1(x) = \sqrt{\frac{\pi}{2}} \left\{ \left[\frac{1}{2} - j\frac{1}{2} \right] - \left[C_0(x^2) - jS_0(x^2) \right] \right\}$$

$$C_1(x) - jS_1(x) = \sqrt{\frac{\pi}{2}} \left\{ \left[\frac{1}{2} - C_0(x^2) \right] - j\left[\frac{1}{2} - S_0(x^2) \right] \right\} \tag{IV-8}$$

INTEL-1045
U.S. Patent 7,151,430

x	$C_1(x)$	$S_1(x)$	$C(x)$	$S(x)$
0.0	0.62666	0.62666	0.0	0.0
0.1	0.52666	0.62632	0.10000	0.00052
0.2	0.42669	0.62399	0.19992	0.00419
0.3	0.32690	0.61766	0.29940	0.01412
0.4	0.22768	0.60536	0.39748	0.03336
0.5	0.12977	0.58518	0.49234	0.06473
0.6	0.03439	0.55532	0.58110	0.11054
0.7	−0.05672	0.51427	0.65965	0.17214
0.8	−0.14119	0.46092	0.72284	0.24934
0.9	−0.21606	0.39481	0.76482	0.33978
1.0	−0.27787	0.31639	0.77989	0.43826
1.1	−0.32285	0.22728	0.76381	0.53650
1.2	−0.34729	0.13054	0.71544	0.62340
1.3	−0.34803	0.03081	0.63855	0.68633
1.4	−0.32312	−0.06573	0.54310	0.71353
1.5	−0.27253	−0.15158	0.44526	0.69751
1.6	−0.19886	−0.21861	0.36546	0.63889
1.7	−0.10790	−0.25905	0.32383	0.54920
1.8	−0.00871	−0.26682	0.33363	0.45094
1.9	0.08680	−0.23918	0.39447	0.37335
2.0	0.16520	−0.17812	0.48825	0.34342
2.1	0.21359	−0.09141	0.58156	0.37427
2.2	0.22242	0.00743	0.63629	0.45570
2.3	0.18833	0.10054	0.62656	0.55315
2.4	0.11650	0.16879	0.55496	0.61969
2.5	0.02135	0.19614	0.45742	0.61918
2.6	−0.07518	0.17454	0.38894	0.54999
2.7	−0.14816	0.10789	0.39249	0.45292
2.8	−0.17646	0.01329	0.46749	0.39153
2.9	−0.15021	−0.08181	0.56237	0.41014
3.0	−0.07621	−0.14690	0.60572	0.49631
3.1	0.02152	−0.15883	0.56160	0.58181
3.2	0.10791	−0.11181	0.46632	0.59335
3.3	0.14907	−0.02260	0.40570	0.51929
3.4	0.12691	0.07301	0.43849	0.42965
3.5	0.04965	0.13335	0.53257	0.41525
3.6	−0.04819	0.12973	0.58795	0.49231
3.7	−0.11929	0.06258	0.54195	0.57498
3.8	−0.12649	−0.03483	0.44810	0.56562
3.9	−0.06469	−0.11030	0.42233	0.47521
4.0	0.03219	−0.12048	0.49842	0.42052
4.1	0.10690	−0.05815	0.57369	0.47580
4.2	0.11228	0.03885	0.54172	0.56320
4.3	0.04374	0.10751	0.44944	0.55400
4.4	−0.05287	0.10038	0.43833	0.46227
4.5	−0.10884	0.02149	0.52602	0.43427
4.6	−0.08188	−0.07126	0.56724	0.51619
4.7	0.00810	−0.10594	0.49143	0.56715
4.8	0.08905	−0.05381	0.43380	0.49675
4.9	0.09277	0.04224	0.50016	0.43507
5.0	0.01519	0.09874	0.56363	0.49919
5.1	−0.07411	0.06405	0.49979	0.56239
5.2	−0.09125	−0.03004	0.43889	0.49688

INTEL-1045
U.S. Patent 7,151,430

x	$C_1(x)$	$S_1(x)$	$C(x)$	$S(x)$
5.3	−0.01892	−0.09235	0.50778	0.44047
5.4	0.07063	−0.05976	0.55723	0.51403
5.5	0.08408	0.03440	0.47843	0.55369
5.6	0.00641	0.08900	0.45171	0.47004
5.7	−0.07642	0.04296	0.53846	0.45953
5.8	−0.06919	−0.05135	0.52984	0.54604
5.9	0.01998	−0.08231	0.44859	0.51633
6.0	0.08245	−0.01181	0.49953	0.44696
6.1	0.03946	0.07180	0.54950	0.51647
6.2	−0.05363	0.06018	0.46761	0.53982
6.3	−0.07284	−0.03144	0.47600	0.45555
6.4	0.00835	−0.07765	0.54960	0.49649
6.5	0.07574	−0.01326	0.48161	0.54538
6.6	0.03183	0.06872	0.46899	0.46307
6.7	−0.05828	0.04658	0.54674	0.49150
6.8	−0.05734	−0.04600	0.48307	0.54364
6.9	0.03317	−0.06440	0.47322	0.46244
7.0	0.06832	0.02077	0.54547	0.49970
7.1	−0.00944	0.06977	0.47332	0.53602
7.2	−0.06943	0.00041	0.48874	0.45725
7.3	−0.00864	−0.06793	0.53927	0.51894
7.4	0.06582	−0.01521	0.46010	0.51607
7.5	0.02018	0.06353	0.51601	0.46070
7.6	−0.06137	0.02367	0.51564	0.53885
7.7	−0.02580	−0.05958	0.46278	0.48202
7.8	0.05828	−0.02668	0.53947	0.48964
7.9	0.02638	0.05752	0.47598	0.53235
8.0	−0.05730	0.02494	0.49980	0.46021
8.1	−0.02238	−0.05752	0.52275	0.53204
8.2	0.05803	−0.01870	0.46384	0.48589
8.3	0.01387	0.05861	0.53775	0.49323
8.4	−0.05899	0.00789	0.47092	0.52429
8.5	−0.00080	−0.05881	0.51417	0.46534
8.6	0.05767	0.00729	0.50249	0.53693
8.7	−0.01616	0.05515	0.48274	0.46774
8.8	−0.05079	−0.02545	0.52797	0.52294
8.9	0.03461	−0.04425	0.46612	0.48856
9.0	0.03526	0.04293	0.53537	0.49985
9.1	−0.04951	0.02381	0.46661	0.51042
9.2	−0.01021	−0.05338	0.52914	0.48135
9.3	0.05354	0.00485	0.47628	0.52467
9.4	−0.02020	0.04920	0.51803	0.47134
9.5	−0.03995	−0.03426	0.48729	0.53100
9.6	0.04513	−0.02599	0.50813	0.46786
9.7	0.00837	0.05086	0.49549	0.53250
9.8	−0.04983	−0.01094	0.50192	0.46758
9.9	0.02916	−0.04124	0.49961	0.53215
10.0	0.02554	0.04298	0.49989	0.46817
10.1	−0.04927	0.00478	0.49961	0.53151
10.2	0.01738	−0.04583	0.50186	0.46885
10.3	0.03233	0.03621	0.49575	0.53061
10.4	−0.04681	0.01094	0.50751	0.47033
10.5	0.01360	−0.04563	0.48849	0.52804

INTEL-1045
U.S. Patent 7,151,430

x	$C_1(x)$	$S_1(x)$	$C(x)$	$S(x)$
10.6	0.03187	0.03477	0.51601	0.47460
10.7	−0.04595	0.00848	0.47936	0.52143
10.8	0.01789	−0.04270	0.52484	0.48413
10.9	0.02494	0.03850	0.47211	0.50867
11.0	−0.04541	−0.00202	0.52894	0.49991
11.1	0.02845	−0.03492	0.47284	0.49079
11.2	0.01008	0.04349	0.52195	0.51805
11.3	−0.03981	−0.01930	0.48675	0.47514
11.4	0.04005	−0.01789	0.50183	0.52786
11.5	−0.01282	0.04155	0.51052	0.47440
11.6	−0.02188	−0.03714	0.47890	0.51755
11.7	0.04164	0.00962	0.52679	0.49525
11.8	−0.03580	0.02267	0.47489	0.49013
11.9	0.00977	−0.04086	0.51544	0.52184
12.0	0.02059	0.03622	0.49993	0.47347
12.1	−0.03919	−0.01309	0.48426	0.52108
12.2	0.03792	−0.01555	0.52525	0.49345
12.3	−0.01914	0.03586	0.47673	0.48867
12.4	−0.00728	−0.03966	0.50951	0.52384
12.5	0.02960	0.02691	0.50969	0.47645
12.6	−0.03946	−0.00421	0.47653	0.50936
12.7	0.03445	−0.01906	0.52253	0.51097
12.8	−0.01783	0.03475	0.49376	0.47593
12.9	−0.00377	−0.03857	0.48523	0.51977
13.0	0.02325	0.03064	0.52449	0.49994
13.1	−0.03530	−0.01452	0.48598	0.48015
13.2	0.03760	−0.00459	0.49117	0.52244
13.3	−0.03075	0.02163	0.52357	0.49583
13.4	0.01744	−0.03299	0.48482	0.48173
13.5	−0.00129	0.03701	0.49103	0.52180
13.6	−0.01421	−0.03391	0.52336	0.49848
13.7	0.02639	0.02521	0.48908	0.47949
13.8	−0.03377	−0.01313	0.48534	0.51781
13.9	0.03597	−0.00002	0.52168	0.50737
14.0	−0.03352	0.01232	0.49996	0.47726
14.1	0.02749	−0.02240	0.47844	0.50668
14.2	−0.01916	0.02954	0.51205	0.51890
14.3	0.00979	−0.03357	0.51546	0.48398
14.4	−0.00043	0.03472	0.48131	0.48819
14.5	−0.00817	−0.03350	0.49164	0.52030
14.6	0.01553	0.03052	0.52113	0.50538
14.7	−0.02145	−0.02640	0.50301	0.47856
14.8	0.02591	0.02168	0.47853	0.49869
14.9	−0.02903	−0.01683	0.49971	0.52136
15.0	0.03103	0.01217	0.52122	0.49926

INTEL-1045
U.S. Patent 7,151,430

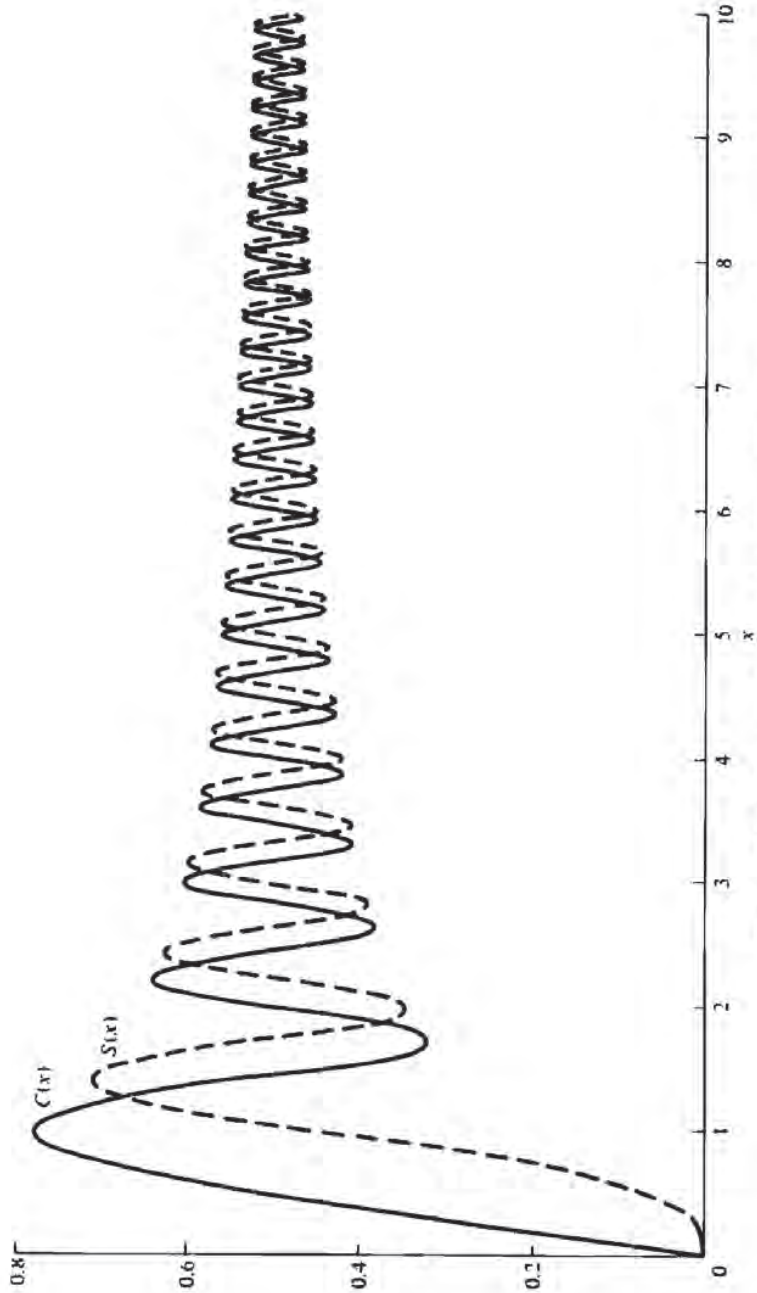


Figure IV.1 Plots of $C(x)$ and $S(x)$ Fresnel integrals.

INTEL-1045
U.S. Patent 7,151,430

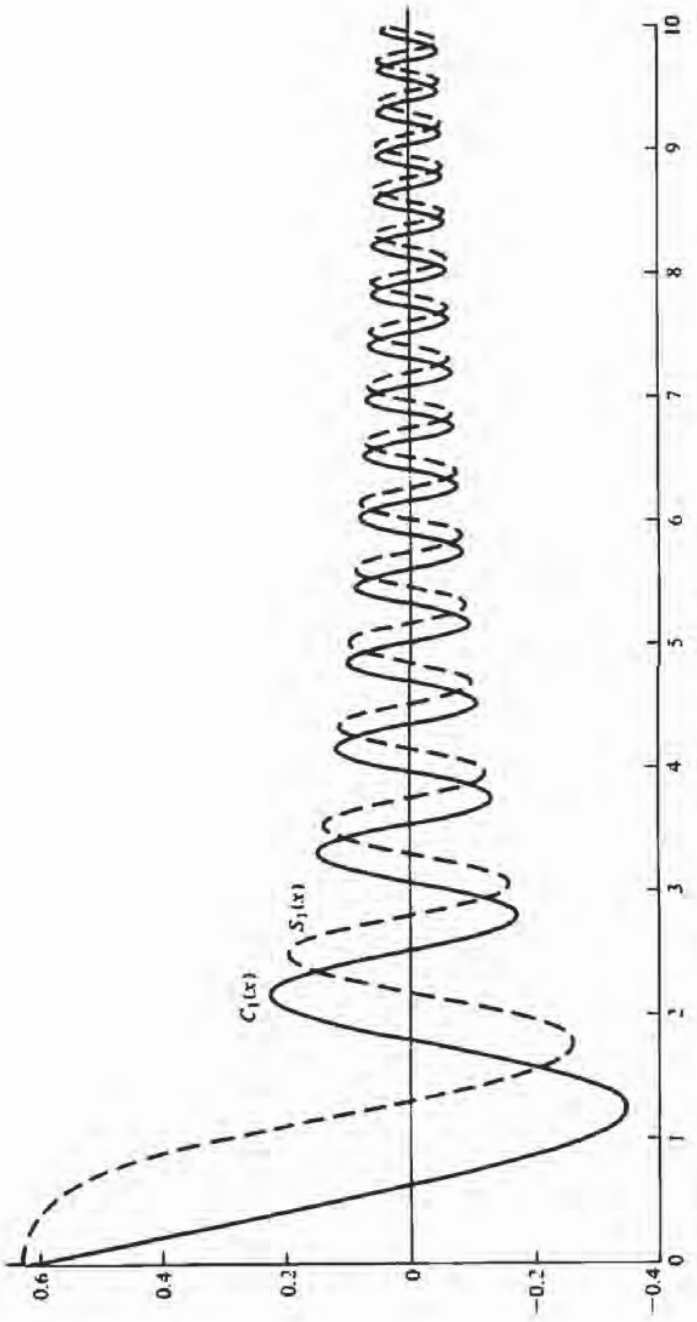


Figure IV.2 Plots of $C_1(x)$ and $S_1(x)$ Fresnel integrals.

INTEL-1045
U.S. Patent 7,151,430

APPENDIX

V

BESSEL FUNCTIONS

Bessel's equation can be written as

$$x^2\frac{d^2y}{dx^2} + x\frac{dy}{dx} + (x^2 - p^2)y = 0 \tag{V-1}$$

Using the method of Frobenius, we can write its solutions as

$$y(x) = A_1 J_p(x) + B_1 J_{-p}(x), \qquad p \neq 0 \text{ or integer} \tag{V-2}$$

or

$$y(x) = A_2 J_n(x) + B_2 Y_n(x), \qquad p = n = 0 \text{ or integer} \tag{V-3}$$

where

$$J_p(x) = \sum_{m=0}^{\infty} \frac{(-1)^m (x/2)^{2m+p}}{m!(m+p)!} \tag{V-4}$$

$$J_{-p}(x) = \sum_{m=0}^{\infty} \frac{(-1)^m (x/2)^{2m-p}}{m!(m-p)!} \tag{V-5}$$

$$Y_p(x) = \frac{J_p(x)\cos(p\pi) - J_{-p}(x)}{\sin(p\pi)} \tag{V-6}$$

$$m! = \Gamma(m+1) \tag{V-7}$$

$J_p(x)$ is referred to as the Bessel function of the first kind of order p, $Y_p(x)$ as the Bessel function of the second kind of order p, and $\Gamma(x)$ as the gamma function.

When $p = n =$ integer, using (V-5) and (V-7) it can be shown that

$$J_{-n}(x) = (-1)^n J_n(x) \tag{V-8}$$

and no longer are the two Bessel functions independent of each other. Therefore a second solution is required and it is given by (V-3). It can also be shown that

$$Y_n(x) = \lim_{p \to n} Y_p(x) = \lim_{p \to n} \frac{J_p(x)\cos(p\pi) - J_{-p}(x)}{\sin(p\pi)} \tag{V-9}$$

INTEL-1045
U.S. Patent 7,151,430

When the argument of the Bessel function is negative and $p = n$, using (V-4) leads to

$$J_n(-x) = (-1)^n J_n(x) \tag{V-10}$$

In many applications Bessel functions of small and large arguments are required. Using asymptotic methods, it can be shown that

$$\left.\begin{aligned} J_0(x) &\simeq 1 \\ Y_0(x) &\simeq \frac{2}{\pi}\ln\left(\frac{\gamma x}{2}\right) \\ \gamma &= 1.781 \end{aligned}\right\} x \to 0 \tag{V-11}$$

$$\left.\begin{aligned} J_p(x) &\simeq \frac{1}{p!}\left(\frac{x}{2}\right)^p \\ Y_p(x) &\simeq -\frac{(p-1)!}{\pi}\left(\frac{2}{x}\right)^p \end{aligned}\right\} \begin{aligned} x &\to 0 \\ p &> 0 \end{aligned} \tag{V-12}$$

and

$$\left.\begin{aligned} J_p(x) &\simeq \sqrt{\frac{2}{\pi x}}\cos\left(x - \frac{\pi}{4} - \frac{p\pi}{2}\right) \\ Y_p(x) &\simeq \sqrt{\frac{2}{\pi x}}\sin\left(x - \frac{\pi}{4} - \frac{p\pi}{2}\right) \end{aligned}\right\} x \to \infty \tag{V-13}$$

For wave propagation it is often convenient to introduce Hankel functions defined as

$$H_p^{(1)}(x) = J_p(x) + jY_p(x) \tag{V-14}$$

$$H_p^{(2)}(x) = J_p(x) - jY_p(x) \tag{V-15}$$

where $H_p^{(1)}(x)$ is the Hankel function of the first kind of order p and $H_p^{(2)}(x)$ is the Hankel function of the second kind of order p. For large arguments

$$H_p^{(1)}(x) \simeq \sqrt{\frac{2}{\pi x}}\, e^{j[x - p(\pi/2) - \pi/4]}, \qquad x \to \infty \tag{V-16}$$

$$H_p^{(2)}(x) \simeq \sqrt{\frac{2}{\pi x}}\, e^{-j[x - p(\pi/2) - \pi/4]}, \qquad x \to \infty \tag{V-17}$$

A derivative can be taken using either

$$\frac{d}{dx}[Z_p(\alpha x)] = \alpha Z_{p-1}(\alpha x) - \frac{p}{x}Z_p(\alpha x) \tag{V-18}$$

or

$$\frac{d}{dx}[Z_p(\alpha x)] = -\alpha Z_{p+1}(\alpha x) + \frac{p}{x}Z_p(\alpha x) \tag{V-19}$$

where Z_p can be a Bessel function (J_p, Y_p) or a Hankel function [$H_p^{(1)}$ or $H_p^{(2)}$].

INTEL-1045
U.S. Patent 7,151,430

A useful identity relating Bessel functions and their derivatives is given by

$$J_p(x)\,Y_p'(x) - Y_p(x)\,J_p'(x) = \frac{2}{\pi x} \tag{V-20}$$

and it is referred to as the Wronskian. The prime (') indicates a derivative. Also

$$J_p(x)\,J'_{-p}(x) - J_{-p}(x)\,J_p'(x) = -\frac{2}{\pi x}\sin(p\pi) \tag{V-21}$$

Some useful integrals of Bessel functions are

$$\int x^{p+1} J_p(\alpha x)\,dx = \frac{1}{\alpha} x^{p+1} J_{p+1}(\alpha x) + C \tag{V-22}$$

$$\int x^{1-p} J_p(\alpha x)\,dx = -\frac{1}{\alpha} x^{1-p} J_{p-1}(\alpha x) + C \tag{V-23}$$

$$\int x^3 J_0(x)\,dx = x^3 J_1(x) - 2x^2 J_2(x) + C \tag{V-24}$$

$$\int x^6 J_1(x)\,dx = x^6 J_2(x) - 4x^5 J_3(x) + 8x^4 J_4(x) + C \tag{V-25}$$

$$\int J_3(x)\,dx = -J_2(x) - \frac{2}{x} J_1(x) + C \tag{V-26}$$

$$\int x J_1(x)\,dx = -x J_0(x) + \int J_0(x)\,dx + C \tag{V-27}$$

$$\int x^{-1} J_1(x)\,dx = -J_1(x) + \int J_0(x)\,dx + C \tag{V-28}$$

$$\int J_2(x)\,dx = -2J_1(x) + \int J_0(x)\,dx + C \tag{V-29}$$

$$\int x^m J_n(x)\,dx = x^m J_{n+1}(x) - (m - n - 1)\int x^{m-1} J_{n+1}(x)\,dx \tag{V-30}$$

$$\int x^m J_n(x)\,dx = -x^m J_{n-1}(x) + (m + n - 1)\int x^{m-1} J_{n-1}(x)\,dx \tag{V-31}$$

$$J_1(x) = \frac{2}{\pi}\int_0^{\pi/2} \sin(x\sin\theta)\sin\theta\,d\theta \tag{V-32}$$

$$\frac{1}{x} J_1(x) = \frac{2}{\pi}\int_0^{\pi/2} \cos(x\sin\theta)\cos^2\theta\,d\theta \tag{V-33}$$

$$J_2(x) = \frac{2}{\pi}\int_0^{\pi/2} \cos(x\sin\theta)\cos 2\theta\,d\theta \tag{V-34}$$

$$J_n(x) = \frac{j^{-n}}{2\pi}\int_0^{2\pi} e^{jx\cos\phi} e^{jn\phi}\,d\phi \tag{V-35}$$

INTEL-1045
U.S. Patent 7,151,430

$$J_n(x) = \frac{j^{-n}}{\pi} \int_0^{\pi} \cos(n\phi)\, e^{jx\cos\phi}\, d\phi \tag{V-36}$$

$$J_n(x) = \frac{1}{\pi} \int_0^{\pi} \cos(x \sin \phi - n\phi)\, d\phi \tag{V-37}$$

$$J_{2n}(x) = \frac{2}{\pi} \int_0^{\pi/2} \cos(x \sin \phi) \cos(2n\phi)\, d\phi \tag{V-38}$$

$$J_{2n}(x) = (-1)^n \frac{2}{\pi} \int_0^{\pi/2} \cos(x \cos \phi) \cos(2n\phi)\, d\phi \tag{V-39}$$

The integrals

$$\int_0^x J_0(\tau)\, d\tau \quad \text{and} \quad \int_0^x Y_0(\tau)\, d\tau \tag{V-40}$$

often appear in solutions of problems but cannot be integrated in closed form. Graphs and tables for each, obtained using numerical techniques, are included.

INTEL-1045
U.S. Patent 7,151,430

x	$J_0(x)$	$J_1(x)$	$Y_0(x)$	$Y_1(x)$
0.0	1.00000	0.0	$-\infty$	$-\infty$
0.1	0.99750	0.04994	−1.53424	−6.45895
0.2	0.99003	0.09950	−1.08110	−3.32382
0.3	0.97763	0.14832	−0.80727	−2.29310
0.4	0.96040	0.19603	−0.60602	−1.78087
0.5	0.93847	0.24227	−0.44452	−1.47147
0.6	0.91201	0.28670	−0.30851	−1.26039
0.7	0.88120	0.32900	−0.19066	−1.10325
0.8	0.84629	0.36884	−0.08680	−0.97814
0.9	0.80752	0.40595	0.00563	−0.87313
1.0	0.76520	0.44005	0.08826	−0.78121
1.1	0.71962	0.47090	0.16216	−0.69812
1.2	0.67113	0.49829	0.22808	−0.62114
1.3	0.62009	0.52202	0.28654	−0.54852
1.4	0.56686	0.54195	0.33789	−0.47915
1.5	0.51183	0.55794	0.38245	−0.41231
1.6	0.45540	0.56990	0.42043	−0.34758
1.7	0.39799	0.57777	0.45203	−0.28473
1.8	0.33999	0.58152	0.47743	−0.22366
1.9	0.28182	0.58116	0.49682	−0.16441
2.0	0.22389	0.57673	0.51038	−0.10703
2.1	0.16661	0.56829	0.51829	−0.05168
2.2	0.11036	0.55596	0.52078	0.00149
2.3	0.05554	0.53987	0.51807	0.05228
2.4	0.00251	0.52019	0.51041	0.10049
2.5	−0.04838	0.49710	0.49807	0.14592
2.6	−0.09681	0.47082	0.48133	0.18836
2.7	−0.14245	0.44161	0.46050	0.22763
2.8	−0.18504	0.40972	0.43592	0.26354
2.9	−0.22432	0.37544	0.40791	0.29594
3.0	−0.26005	0.33906	0.37686	0.32467
3.1	−0.29206	0.30092	0.34310	0.34963
3.2	−0.32019	0.26134	0.30705	0.37071
3.3	−0.34430	0.22066	0.26909	0.38785
3.4	−0.36430	0.17923	0.22962	0.40101
3.5	−0.38013	0.13738	0.18902	0.41019
3.6	−0.39177	0.09547	0.14771	0.41539
3.7	−0.39923	0.05383	0.10607	0.41667
3.8	−0.40256	0.01282	0.06450	0.41411
3.9	−0.40183	−0.02724	0.02338	0.40782
4.0	−0.39715	−0.06604	−0.01694	0.39793
4.1	−0.38868	−0.10328	−0.05609	0.38459
4.2	−0.37657	−0.13865	−0.09375	0.36801
4.3	−0.36102	−0.17190	−0.12960	0.34839
4.4	−0.34226	−0.20278	−0.16334	0.32597
4.5	−0.32054	−0.23106	−0.19471	0.30100
4.6	−0.29614	−0.25655	−0.22346	0.27375
4.7	−0.26933	−0.27908	−0.24939	0.24450
4.8	−0.24043	−0.29850	−0.27230	0.21356
4.9	−0.20974	−0.31470	−0.29205	0.18125
5.0	−0.17760	−0.32758	−0.30852	0.14786

INTEL-1045
U.S. Patent 7,151,430

x	$J_0(x)$	$J_1(x)$	$Y_0(x)$	$Y_1(x)$
5.1	−0.14434	−0.33710	−0.32160	0.11374
5.2	−0.11029	−0.34322	−0.33125	0.07919
5.3	−0.07580	−0.34596	−0.33744	0.04455
5.4	−0.04121	−0.34534	−0.34017	0.01013
5.5	−0.00684	−0.34144	−0.33948	−0.02376
5.6	0.02697	−0.33433	−0.33544	−0.05681
5.7	0.05992	−0.32415	−0.32816	−0.08872
5.8	0.09170	−0.31103	−0.31775	−0.11923
5.9	0.12203	−0.29514	−0.30437	−0.14808
6.0	0.15065	−0.27668	−0.28819	−0.17501
6.1	0.17729	−0.25587	−0.26943	−0.19981
6.2	0.20175	−0.23292	−0.24831	−0.22228
6.3	0.22381	−0.20809	−0.22506	−0.24225
6.4	0.24331	−0.18164	−0.19995	−0.25956
6.5	0.26009	−0.15384	−0.17324	−0.27409
6.6	0.27404	−0.12498	−0.14523	−0.28575
6.7	0.28506	−0.09534	−0.11619	−0.29446
6.8	0.29310	−0.06522	−0.08643	−0.30019
6.9	0.29810	−0.03490	−0.05625	−0.30292
7.0	0.30008	−0.00468	−0.02595	−0.30267
7.1	0.29905	+0.02515	0.00418	−0.29948
7.2	0.29507	0.05433	0.03385	−0.29342
7.3	0.28822	0.08257	0.06277	−0.28459
7.4	0.27860	0.10962	0.09068	−0.27311
7.5	0.26634	0.13525	0.11731	−0.25913
7.6	0.25160	0.15921	0.14243	−0.24280
7.7	0.23456	0.18131	0.16580	−0.22432
7.8	0.21541	0.20136	0.18723	−0.20388
7.9	0.19436	0.21918	0.20652	−0.18172
8.0	0.17165	0.23464	0.22352	−0.15806
8.1	0.14752	0.24761	0.23809	−0.13315
8.2	0.12222	0.25800	0.25012	−0.10724
8.3	0.09601	0.26574	0.25951	−0.08060
8.4	0.06916	0.27079	0.26622	−0.05348
8.5	0.04194	0.27312	0.27021	−0.02617
8.6	0.01462	0.27276	0.27146	0.00108
8.7	−0.01252	0.26972	0.27000	0.02801
8.8	−0.03923	0.26407	0.26587	0.05436
8.9	−0.06525	0.25590	0.25916	0.07987
9.0	−0.09033	0.24531	0.24994	0.10431
9.1	−0.11424	0.23243	0.23834	0.12747
9.2	−0.13675	0.21741	0.22449	0.14911
9.3	−0.15765	0.20041	0.20857	0.16906
9.4	−0.17677	0.18163	0.19074	0.18714
9.5	−0.19393	0.16126	0.17121	0.20318
9.6	−0.20898	0.13952	0.15018	0.21706
9.7	−0.22180	0.11664	0.12787	0.22866
9.8	−0.23228	0.09284	0.10453	0.23789
9.9	−0.24034	0.06837	0.08038	0.24469
10.0	−0.24594	0.04347	0.05567	0.24902

INTEL-1045
U.S. Patent 7,151,430

x	$J_0(x)$	$J_1(x)$	$Y_0(x)$	$Y_1(x)$
10.1	−0.24903	0.01840	0.03066	0.25084
10.2	−0.24962	−0.00662	0.00558	0.25019
10.3	−0.24772	−0.03132	−0.01930	0.24707
10.4	−0.24337	−0.05547	−0.04375	0.24155
10.5	−0.23665	−0.07885	−0.06753	0.23370
10.6	−0.22764	−0.10123	−0.09042	0.22363
10.7	−0.21644	−0.12240	−0.11219	0.21144
10.8	−0.20320	−0.14217	−0.13264	0.19729
10.9	−0.18806	−0.16035	−0.15158	0.18132
11.0	−0.17119	−0.17679	−0.16885	0.16371
11.1	−0.15277	−0.19133	−0.18428	0.14464
11.2	−0.13299	−0.20385	−0.19773	0.12431
11.3	−0.11207	−0.21426	−0.20910	0.10294
11.4	−0.09021	−0.22245	−0.21829	0.08074
11.5	−0.06765	−0.22838	−0.22523	0.05794
11.6	−0.04462	−0.23200	−0.22987	0.03477
11.7	−0.02133	−0.23330	−0.23218	0.01145
11.8	0.00197	−0.23229	−0.23216	−0.01179
11.9	0.02505	−0.22898	−0.22983	−0.03471
12.0	0.04769	−0.22345	−0.22524	−0.05710
12.1	0.06967	−0.21575	−0.21844	−0.07874
12.2	0.09077	−0.20598	−0.20952	−0.09942
12.3	0.11080	−0.19426	−0.19859	−0.11895
12.4	0.12956	−0.18071	−0.18578	−0.13714
12.5	0.14689	−0.16549	−0.17121	−0.15384
12.6	0.16261	−0.14874	−0.15506	−0.16888
12.7	0.17659	−0.13066	−0.13750	−0.18213
12.8	0.18870	−0.11143	−0.11870	−0.19347
12.9	0.19885	−0.09125	−0.09887	−0.20282
13.0	0.20693	−0.07032	−0.07821	−0.21008
13.1	0.21289	−0.04885	−0.05692	−0.21521
13.2	0.21669	−0.02707	−0.03524	−0.21817
13.3	0.21830	−0.00518	−0.01336	−0.21895
13.4	0.21773	0.01660	0.00848	−0.21756
13.5	0.21499	0.03805	0.03008	−0.21402
13.6	0.21013	0.05896	0.05122	−0.20839
13.7	0.20322	0.07914	0.07169	−0.20074
13.8	0.19434	0.09839	0.09130	−0.19116
13.9	0.18358	0.11653	0.10986	−0.17975
14.0	0.17108	0.13338	0.12719	−0.16664
14.1	0.15695	0.14879	0.14314	−0.15198
14.2	0.14137	0.16261	0.15754	−0.13592
14.3	0.12449	0.17473	0.17028	−0.11862
14.4	0.10649	0.18503	0.18123	−0.10026
14.5	0.08755	0.19343	0.19030	−0.08104
14.6	0.06787	0.19986	0.19742	−0.06115
14.7	0.04764	0.20426	0.20252	−0.04079
14.8	0.02708	0.20660	0.20557	−0.02016
14.9	0.00639	0.20688	0.20655	0.00053
15.0	−0.01422	0.20511	0.20546	0.02107

INTEL-1045
U.S. Patent 7,151,430

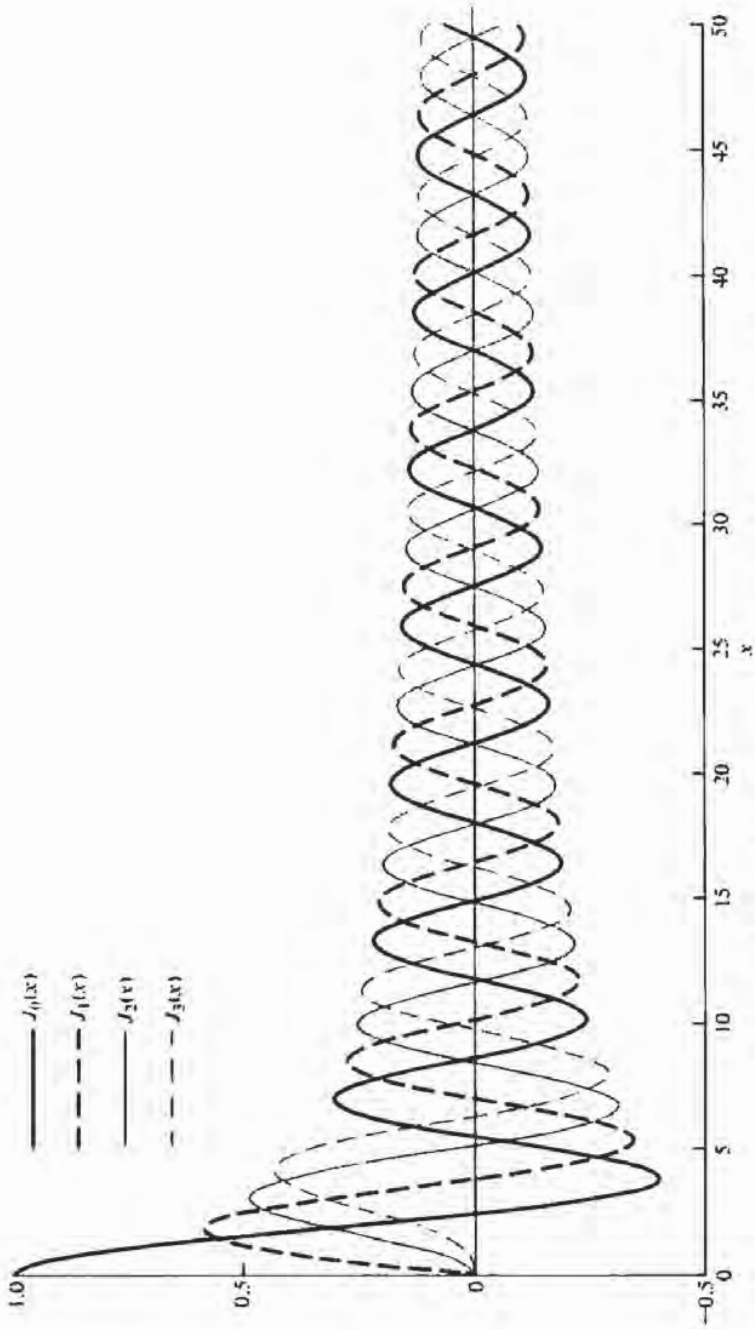


Figure V.1 Bessel functions of the first kind [$J_0(x)$, $J_1(x)$, $J_2(x)$, $J_3(x)$].

INTEL-1045
U.S. Patent 7,151,430

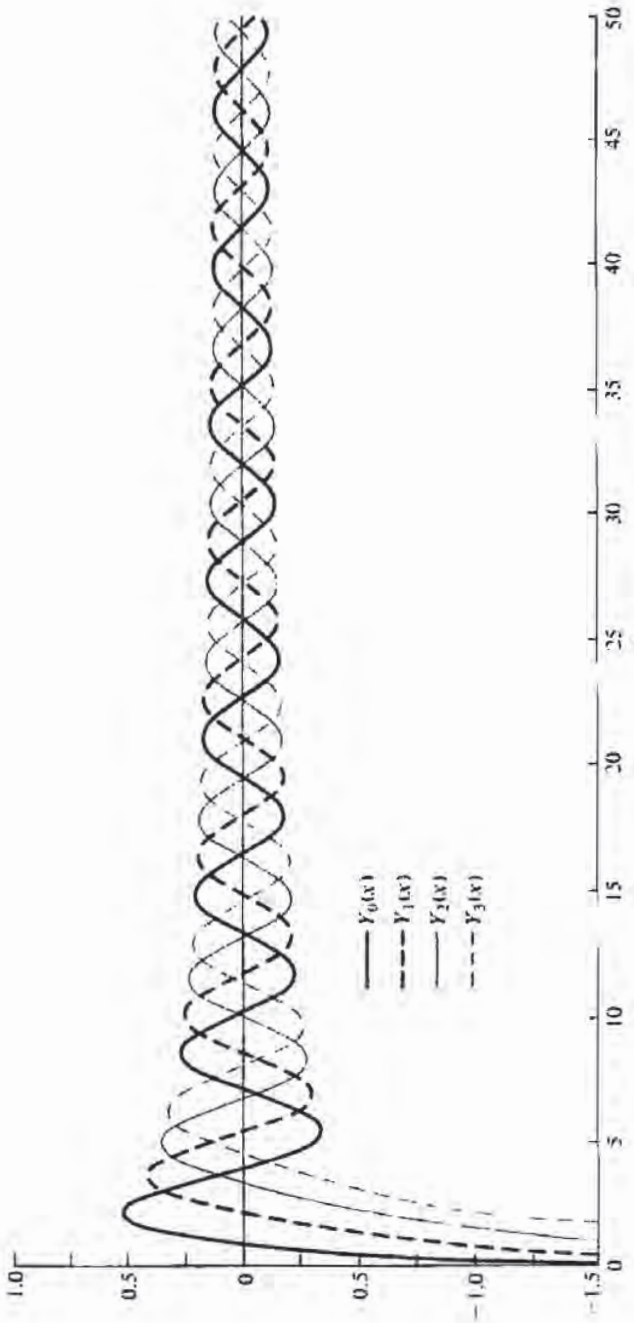


Figure V.2 Bessel functions of the second kind [$Y_0(x)$, $Y_1(x)$, $Y_2(x)$, $Y_3(x)$].

INTEL-1045
U.S. Patent 7,151,430

$J_1(x)/x$ FUNCTION

x	$J_1(x)/x$	x	$J_1(x)/x$	x	$J_1(x)/x$
0.0	0.50000	5.1	−0.06610	10.2	−0.00065
0.1	0.49938	5.2	−0.06600	10.3	−0.00304
0.2	0.49750	5.3	−0.06528	10.4	−0.00533
0.3	0.49440	5.4	−0.06395	10.5	−0.00751
0.4	0.49007	5.5	−0.06208	10.6	−0.00955
0.5	0.48454	5.6	−0.05970	10.7	−0.01144
0.6	0.47783	5.7	−0.05687	10.8	−0.01316
0.7	0.46999	5.8	−0.05363	10.9	−0.01471
0.8	0.46105	5.9	−0.05002	11.0	−0.01607
0.9	0.45105	6.0	−0.04611	11.1	−0.01724
1.0	0.44005	6.1	−0.04194	11.2	−0.01820
1.1	0.42809	6.2	−0.03757	11.3	−0.01896
1.2	0.41524	6.3	−0.03303	11.4	−0.01951
1.3	0.40156	6.4	−0.02838	11.5	−0.01986
1.4	0.38710	6.5	−0.02367	11.6	−0.02000
1.5	0.37196	6.6	−0.01894	11.7	−0.01994
1.6	0.35618	6.7	−0.01423	11.8	−0.01969
1.7	0.33986	6.8	−0.00959	11.9	−0.01924
1.8	0.32306	6.9	−0.00506	12.0	−0.01862
1.9	0.30587	7.0	−0.00067	12.1	−0.01783
2.0	0.28836	7.1	0.00354	12.2	−0.01688
2.1	0.27061	7.2	0.00755	12.3	−0.01579
2.2	0.25271	7.3	0.01131	12.4	−0.01457
2.3	0.23473	7.4	0.01481	12.5	−0.01324
2.4	0.21674	7.5	0.01803	12.6	−0.01180
2.5	0.19884	7.6	0.02095	12.7	−0.01029
2.6	0.18108	7.7	0.02355	12.8	−0.00871
2.7	0.16356	7.8	0.02582	12.9	−0.00707
2.8	0.14633	7.9	0.02774	13.0	−0.00541
2.9	0.12946	8.0	0.02933	13.1	−0.00373
3.0	0.11302	8.1	0.03057	13.2	−0.00205
3.1	0.09707	8.2	0.03146	13.3	−0.00039
3.2	0.08167	8.3	0.03202	13.4	0.00124
3.3	0.06687	8.4	0.03224	13.5	0.00282
3.4	0.05271	8.5	0.03213	13.6	0.00434
3.5	0.03925	8.6	0.03172	13.7	0.00578
3.6	0.02652	8.7	0.03100	13.8	0.00713
3.7	0.01455	8.8	0.03001	13.9	0.00838
3.8	0.00337	8.9	0.02875	14.0	0.00953
3.9	−0.00699	9.0	0.02726	14.1	0.01055
4.0	−0.01651	9.1	0.02554	14.2	0.01145
4.1	−0.02519	9.2	0.02363	14.3	0.01222
4.2	−0.03301	9.3	0.02155	14.4	0.01285
4.3	−0.03998	9.4	0.01932	14.5	0.01334
4.4	−0.04609	9.5	0.01697	14.6	0.01369
4.5	−0.05135	9.6	0.01453	14.7	0.01389
4.6	−0.05578	9.7	0.01202	14.8	0.01396
4.7	−0.05938	9.8	0.00947	14.9	0.01388
4.8	−0.06219	9.9	0.00691	15.0	0.01367
4.9	−0.06423	10.0	0.00435		
5.0	−0.06552	10.1	0.00182		

INTEL-1045
U.S. Patent 7,151,430

$\int_0^x J_0(\tau)\,d\tau$ AND $\int_0^x Y_0(\tau)\,d\tau$ FUNCTIONS

x	$\int_0^x J_0(\tau)\,d\tau$	$\int_0^x Y_0(\tau)\,d\tau$	x	$\int_0^x J_0(\tau)\,d\tau$	$\int_0^x Y_0(\tau)\,d\tau$
0.0	0.00000	0.00000	5.1	0.69920	0.16818
0.1	0.09991	−0.21743	5.2	0.68647	0.13551
0.2	0.19933	−0.34570	5.3	0.67716	0.10205
0.3	0.29775	−0.43928	5.4	0.67131	0.06814
0.4	0.39469	−0.50952	5.5	0.66891	0.03413
0.5	0.48968	−0.56179	5.6	0.66992	0.00035
0.6	0.58224	−0.59927	5.7	0.67427	−0.03284
0.7	0.67193	−0.62409	5.8	0.68187	−0.06517
0.8	0.75834	−0.63786	5.9	0.69257	−0.09630
0.9	0.84106	−0.64184	6.0	0.70622	−0.12595
1.0	0.91973	−0.63706	6.1	0.72263	−0.15385
1.1	0.99399	−0.62447	6.2	0.74160	−0.17975
1.2	1.06355	−0.60490	6.3	0.76290	−0.20344
1.3	1.12813	−0.57911	6.4	0.78628	−0.22470
1.4	1.18750	−0.54783	6.5	0.81147	−0.24338
1.5	1.24144	−0.51175	6.6	0.83820	−0.25931
1.6	1.28982	−0.47156	6.7	0.86618	−0.27239
1.7	1.33249	−0.42788	6.8	0.89512	−0.28252
1.8	1.36939	−0.38136	6.9	0.92470	−0.28966
1.9	1.40048	−0.33260	7.0	0.95464	−0.29377
2.0	1.42577	−0.28219	7.1	0.98462	−0.29486
2.1	1.44528	−0.23071	7.2	1.01435	−0.29295
2.2	1.45912	−0.17871	7.3	1.04354	−0.28811
2.3	1.46740	−0.12672	7.4	1.07190	−0.28043
2.4	1.47029	−0.07526	7.5	1.09917	−0.27002
2.5	1.46798	−0.02480	7.6	1.12508	−0.25702
2.6	1.46069	0.02420	7.7	1.14941	−0.24159
2.7	1.44871	0.07132	7.8	1.17192	−0.22392
2.8	1.43231	0.11617	7.9	1.19243	−0.20421
2.9	1.41181	0.15839	8.0	1.21074	−0.18269
3.0	1.38756	0.19765	8.1	1.22671	−0.15959
3.1	1.35992	0.23367	8.2	1.24021	−0.13516
3.2	1.32928	0.26620	8.3	1.25112	−0.10966
3.3	1.29602	0.29502	8.4	1.25939	−0.08335
3.4	1.26056	0.31996	8.5	1.26494	−0.05650
3.5	1.22330	0.34090	8.6	1.26777	−0.02940
3.6	1.18467	0.35775	8.7	1.26787	−0.00230
3.7	1.14509	0.37044	8.8	1.26528	0.02451
3.8	1.10496	0.37896	8.9	1.26005	0.05078
3.9	1.06471	0.38335	9.0	1.25226	0.07625
4.0	1.02473	0.38366	9.1	1.24202	0.10069
4.1	0.98541	0.38000	9.2	1.22946	0.12385
4.2	0.94712	0.37250	9.3	1.21473	0.14552
4.3	0.91021	0.36131	9.4	1.19799	0.16550
4.4	0.87502	0.34665	9.5	1.17944	0.18361
4.5	0.84186	0.32872	9.6	1.15927	0.19969
4.6	0.81100	0.30779	9.7	1.13772	0.21360
4.7	0.78271	0.28413	9.8	1.11499	0.22523
4.8	0.75721	0.25802	9.9	1.09134	0.23448
4.9	0.73468	0.22977	10.0	1.06701	0.24129
5.0	0.71531	0.19971			

INTEL-1045
U.S. Patent 7,151,430

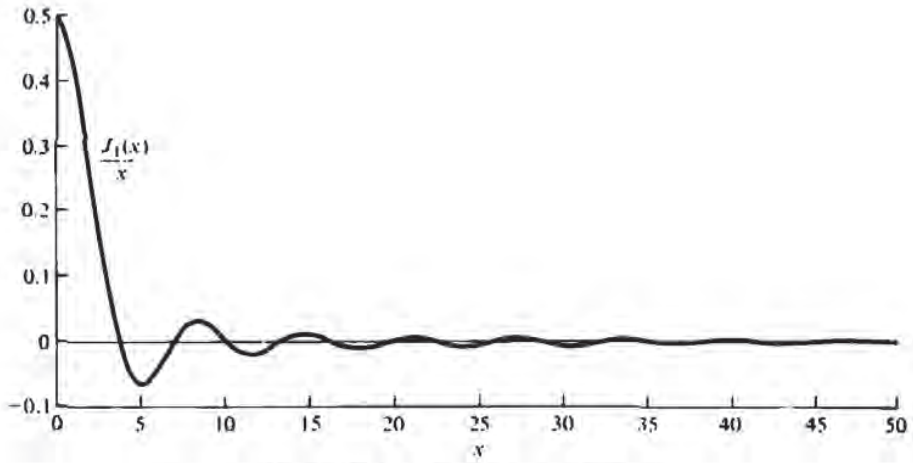


Figure V.3 Plot of $J_1(x)/x$ function.

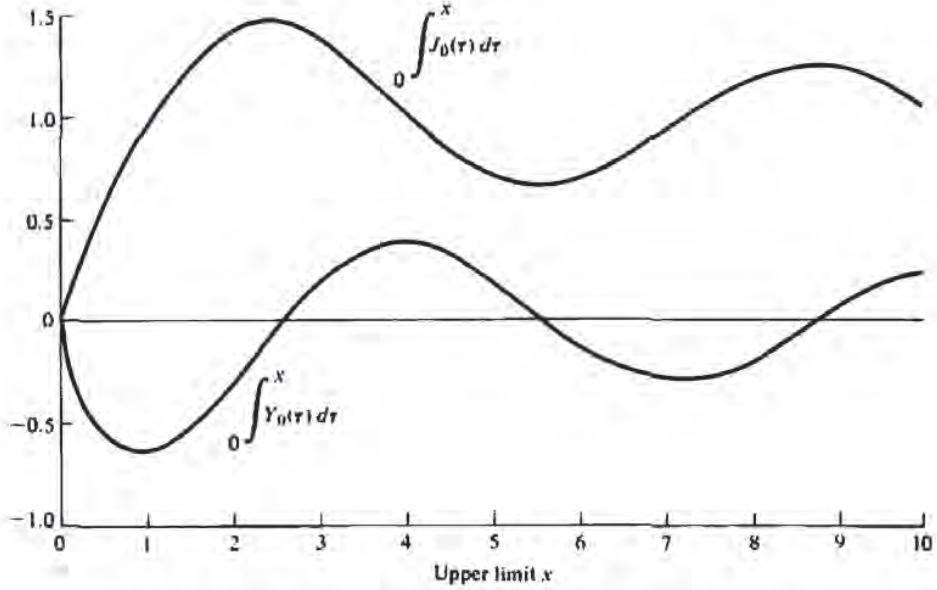


Figure V.4 Plots of $\int_0^x J_0(\tau)\,d\tau$ and $\int_0^x Y_0(\tau)\,d\tau$ functions.

INTEL-1045
U.S. Patent 7,151,430

APPENDIX

VI

IDENTITIES

VI.1 TRIGONOMETRIC

1. Sum or difference:
   - **a.** $\sin(x + y) = \sin x \cos y + \cos x \sin y$
   - **b.** $\sin(x - y) = \sin x \cos y - \cos x \sin y$
   - **c.** $\cos(x + y) = \cos x \cos y - \sin x \sin y$
   - **d.** $\cos(x - y) = \cos x \cos y + \sin x \sin y$
   - **e.** $\tan(x + y) = \dfrac{\tan x + \tan y}{1 - \tan x \tan y}$
   - **f.** $\tan(x - y) = \dfrac{\tan x - \tan y}{1 + \tan x \tan y}$
   - **g.** $\sin^2 x + \cos^2 x = 1$
   - **h.** $\tan^2 x - \sec^2 x = -1$
   - **i.** $\cot^2 x - \csc^2 x = -1$
2. Sum or difference into products:
   - **a.** $\sin x + \sin y = 2 \sin \frac{1}{2}(x + y) \cos \frac{1}{2}(x - y)$
   - **b.** $\sin x - \sin y = 2 \cos \frac{1}{2}(x + y) \sin \frac{1}{2}(x - y)$
   - **c.** $\cos x + \cos y = 2 \cos \frac{1}{2}(x + y) \cos \frac{1}{2}(x - y)$
   - **d.** $\cos x - \cos y = -2 \sin \frac{1}{2}(x + y) \sin \frac{1}{2}(x - y)$
3. Products into sum or difference:
   - **a.** $2 \sin x \cos y = \sin(x + y) + \sin(x - y)$
   - **b.** $2 \cos x \sin y = \sin(x + y) - \sin(x - y)$
   - **c.** $2 \cos x \cos y = \cos(x + y) + \cos(x - y)$
   - **d.** $2 \sin x \sin y = -\cos(x + y) + \cos(x - y)$
4. Double and half-angles:
   - **a.** $\sin 2x = 2 \sin x \cos x$
   - **b.** $\cos 2x = \cos^2 x - \sin^2 x = 2 \cos^2 x - 1 = 1 - 2 \sin^2 x$
   - **c.** $\tan 2x = \dfrac{2 \tan x}{1 - \tan^2 x}$
   - **d.** $\sin \dfrac{1}{2}x = \pm \sqrt{\dfrac{1 - \cos x}{2}}$ or $2 \sin^2 \theta = 1 - \cos 2\theta$

INTEL-1045
U.S. Patent 7,151,430

e. $\cos\frac{1}{2}x = \pm\sqrt{\frac{1+\cos x}{2}}$ or $2\cos^2\theta = 1 + \cos 2\theta$

f. $\tan\frac{1}{2}x = \pm\sqrt{\frac{1-\cos x}{1+\cos x}} = \frac{\sin x}{1+\cos x} = \frac{1-\cos x}{\sin x}$

5. Series:

a. $\sin x = \frac{e^{jx} - e^{-jx}}{2j} = x - \frac{x^3}{3!} + \frac{x^5}{5!} - \frac{x^7}{7!} + \cdots$

b. $\cos x = \frac{e^{jx} + e^{-jx}}{2} = 1 - \frac{x^2}{2!} + \frac{x^4}{4!} - \frac{x^6}{6!} + \cdots$

c. $\tan x = \frac{e^{jx} - e^{-jx}}{j(e^{jx} + e^{-jx})} = x + \frac{x^3}{3} + \frac{2x^5}{15} + \frac{17x^7}{315} + \cdots$

V1.2 HYPERBOLIC

1. Definitions:

a. Hyperbolic sine: $\sinh x = \frac{1}{2}(e^x - e^{-x})$

b. Hyperbolic cosine: $\cosh x = \frac{1}{2}(e^x + e^{-x})$

c. Hyperbolic tangent: $\tanh x = \frac{\sinh x}{\cosh x}$

d. *Hyperbolic cotangent:* $\coth x = \frac{1}{\tanh x} = \frac{\cosh x}{\sinh x}$

e. Hyperbolic secant: $\operatorname{sech} x = \frac{1}{\cosh x}$

f. Hyperbolic cosecant: $\operatorname{csch} x = \frac{1}{\sinh x}$

2. Sum or difference:

a. $\cosh(x + y) = \cosh x \cosh y + \sinh x \sinh y$

b. $\sinh(x - y) = \sinh x \cosh y - \cosh x \sinh y$

c. $\cosh(x - y) = \cosh x \cosh y - \sinh x \sinh y$

d. $\tanh(x + y) = \frac{\tanh x + \tanh y}{1 + \tanh x \tanh y}$

e. $\tanh(x - y) = \frac{\tanh x - \tanh y}{1 - \tanh x \tanh y}$

f. $\cosh^2 x - \sinh^2 x = 1$

g. $\tanh^2 x + \operatorname{sech}^2 x = 1$

h. $\coth^2 x - \operatorname{csch}^2 x = 1$

i. $\cosh(x \pm jy) = \cosh x \cos y \pm j \sinh x \sin y$

j. $\sinh(x \pm jy) = \sinh x \cos y \pm j \cosh x \sin y$

3. Series:

a. $\sinh x = \frac{e^x - e^{-x}}{2} = x + \frac{x^3}{3!} + \frac{x^5}{5!} + \frac{x^7}{7!} + \cdots$

b. $\cosh x = \frac{e^x + e^{-x}}{2} = 1 + \frac{x^2}{2!} + \frac{x^4}{4!} + \frac{x^6}{6!} + \cdots$

c. $e^x = 1 + x + \frac{x^2}{2!} + \frac{x^3}{3!} + \frac{x^4}{4!} + \cdots$

INTEL-1045
U.S. Patent 7,151,430

VI.3 LOGARITHMIC

1. $\log_b(MN) = \log_b M + \log_b N$
2. $\log_b(M/N) = \log_b M - \log_b N$
3. $\log_b(1/N) = -\log_b N$
4. $\log_b(M^n) = n \log_b M$
5. $\log_b(M^{1/n}) = \dfrac{1}{n} \log_b M$
6. $\log_a N = \log_b N \cdot \log_a b = \log_b N / \log_b a$
7. $\log_e N = \log_{10} N \cdot \log_e 10 = 2.302585 \log_{10} N$
8. $\log_{10} N = \log_e N \cdot \log_{10} e = 0.434294 \log_e N$

INTEL-1045
U.S. Patent 7,151,430

APPENDIX

VII

VECTOR ANALYSIS

VII.1 VECTOR TRANSFORMATIONS

In this appendix we present the vector transformations from rectangular-to-cylindrical (and vice-versa), from cylindrical-to-spherical (and vice-versa), and from rectangular-to-spherical (and vice-versa). The three coordinate systems are shown in Figure VII.1.

VII.1.1 Rectangular-to-Cylindrical (and Vice-Versa)

The coordinate transformation from rectangular (x, y, z) to cylindrical (ρ, ϕ, z) is given. referring to Figure VII.1(b)

$$\left.\begin{aligned} x &= \rho \cos \phi \\ y &= \rho \sin \phi \\ z &= z \end{aligned}\right\} \tag{VII-1}$$

In the rectangular coordinate system we express a vector $\mathbf{A}$ as

$$\mathbf{A} = \hat{\mathbf{a}}_x A_x + \hat{\mathbf{a}}_y A_y + \hat{\mathbf{a}}_z A_z \tag{VII-2}$$

where $\hat{\mathbf{a}}_x$, $\hat{\mathbf{a}}_y$, $\hat{\mathbf{a}}_z$ are the unit vectors and A_x, A_y, A_z are the components of the vector $\mathbf{A}$ in the rectangular coordinate system. We wish to write $\mathbf{A}$ as

$$\mathbf{A} = \hat{\mathbf{a}}_\rho A_\rho + \hat{\mathbf{a}}_\phi A_\phi + \hat{\mathbf{a}}_z A_z \tag{VII-3}$$

where $\hat{\mathbf{a}}_\rho$, $\hat{\mathbf{a}}_\phi$, $\hat{\mathbf{a}}_z$ are the unit vectors and A_ρ, A_ϕ, A_z are the vector components in the cylindrical coordinate system. The z-axis is common to both of them.

Referring to Figure VII.2. we can write

$$\left.\begin{aligned} \hat{\mathbf{a}}_x &= \hat{\mathbf{a}}_\rho \cos \phi - \hat{\mathbf{a}}_\phi \sin \phi \\ \hat{\mathbf{a}}_y &= \hat{\mathbf{a}}_\rho \sin \phi + \hat{\mathbf{a}}_\phi \cos \phi \\ \hat{\mathbf{a}}_z &= \hat{\mathbf{a}}_z \end{aligned}\right\} \tag{VII-4}$$

Using (VII-4) reduces (VII-2) to

$$\mathbf{A} = (\hat{\mathbf{a}}_\rho \cos \phi - \hat{\mathbf{a}}_\phi \sin \phi) A_x + (\hat{\mathbf{a}}_\rho \sin \phi + \hat{\mathbf{a}}_\phi \cos \phi) A_y + \hat{\mathbf{a}}_z A_z$$

$$\mathbf{A} = \hat{\mathbf{a}}_\rho (A_x \cos \phi + A_y \sin \phi) + \hat{\mathbf{a}}_\phi (-A_x \sin \phi + A_y \cos \phi) + \hat{\mathbf{a}}_z A_z \tag{VII-5}$$

INTEL-1045
U.S. Patent 7,151,430

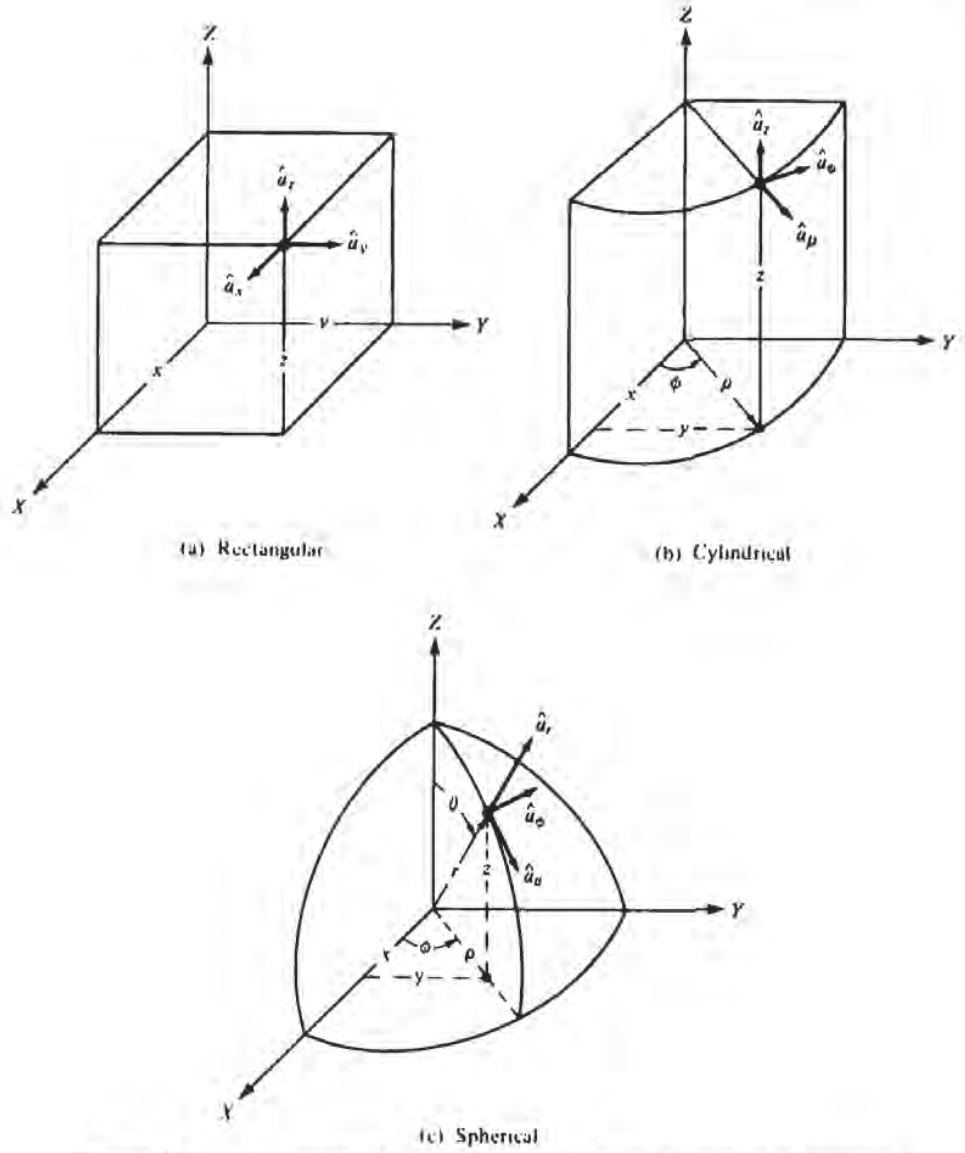


Figure VII.1 Rectangular, cylindrical, and spherical coordinate systems.

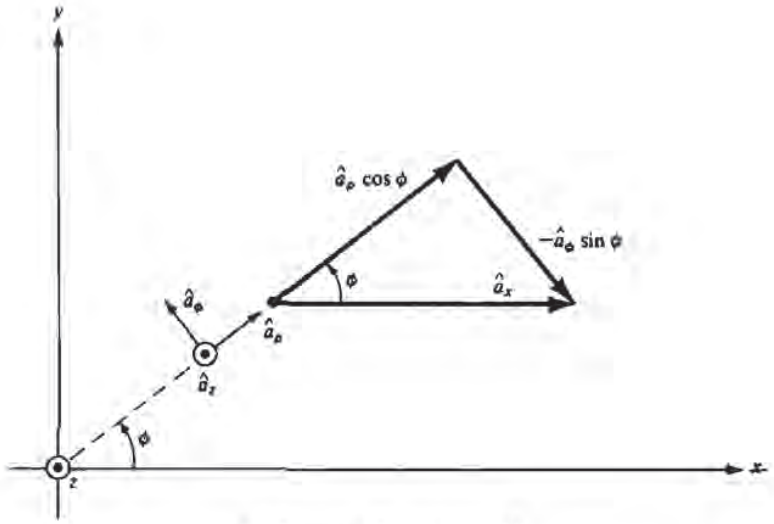
which when compared with (VII-3) leads to

$$\left.\begin{aligned} A_\rho &= A_x \cos\phi + A_y \sin\phi \\ A_\phi &= -A_x \sin\phi + A_y \cos\phi \\ A_z &= A_z \end{aligned}\right\} \tag{VII-6}$$

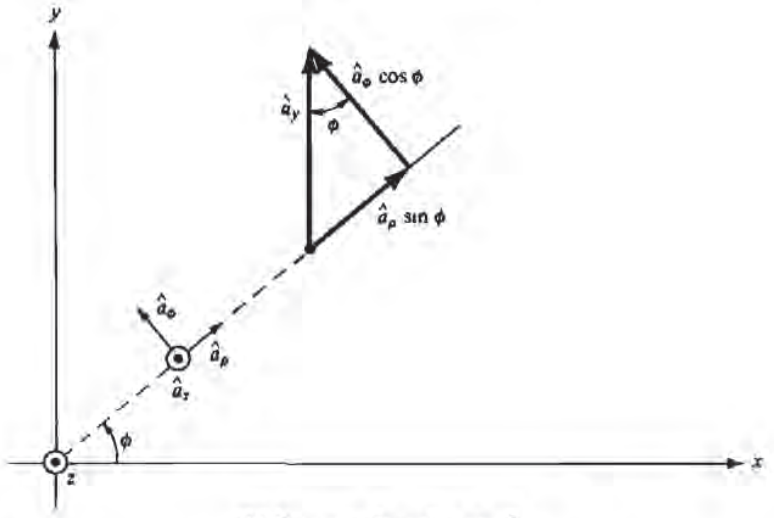
In matrix form, (VII-6) can be written as

$$\begin{pmatrix} A_\rho \\ A_\phi \\ A_z \end{pmatrix} = \begin{pmatrix} \cos\phi & \sin\phi & 0 \\ -\sin\phi & \cos\phi & 0 \\ 0 & 0 & 1 \end{pmatrix} \begin{pmatrix} A_x \\ A_y \\ A_z \end{pmatrix} \tag{VII-6a}$$

INTEL-1045
U.S. Patent 7,151,430



(a) Geometry for unit vector $\hat{a}_x$



(b) Geometry for unit vector $\hat{a}_y$

Figure VII.2 Geometrical representation of transformations between unit vectors of rectangular and cylindrical coordinate systems.

where

$$[A]_{rr} = \begin{bmatrix} \cos\phi & \sin\phi & 0 \\ -\sin\phi & \cos\phi & 0 \\ 0 & 0 & 1 \end{bmatrix} \tag{VII-6b}$$

is the transformation matrix for rectangular-to-cylindrical components.

Since $[A]_{rr}$ is an orthonormal matrix (its inverse is equal to its transpose), we can *write the transformation matrix for cylindrical-to-rectangular components as*

$$[A]_{cr} = [A]_{rc}^{-1} = [A]_{rc}^{t} = \begin{bmatrix} \cos\phi & -\sin\phi & 0 \\ \sin\phi & \cos\phi & 0 \\ 0 & 0 & 1 \end{bmatrix} \tag{VII-7}$$

INTEL-1045
U.S. Patent 7,151,430

or

$$\begin{pmatrix} A_x \\ A_y \\ A_z \end{pmatrix} = \begin{pmatrix} \cos\phi & -\sin\phi & 0 \\ \sin\phi & \cos\phi & 0 \\ 0 & 0 & 1 \end{pmatrix} \begin{pmatrix} A_\rho \\ A_\phi \\ A_z \end{pmatrix} \tag{VII-7a}$$

or

$$\left.\begin{aligned} A_x &= A_\rho \cos\phi - A_\phi \sin\phi \\ A_y &= A_\rho \sin\phi + A_\phi \cos\phi \\ A_z &= A_z \end{aligned}\right\} \tag{VII-7b}$$

VII.1.2 Cylindrical-to-Spherical (and Vice-Versa)

Referring to Figure VII.1(c), we can write that the cylindrical and spherical coordinates are related by

$$\left.\begin{aligned} \rho &= r\sin\theta \\ z &= r\cos\theta \end{aligned}\right\} \tag{VII-8}$$

In a geometrical approach similar to the one employed in the previous section, we can show that the cylindrical-to-spherical transformation of vector components is given by

$$\left.\begin{aligned} A_r &= A_\rho \sin\theta + A_z \cos\theta \\ A_\theta &= A_\rho \cos\theta - A_z \sin\theta \\ A_\phi &= A_\phi \end{aligned}\right\} \tag{VII-9}$$

or in matrix form by

$$\begin{pmatrix} A_r \\ A_\theta \\ A_\phi \end{pmatrix} = \begin{pmatrix} \sin\theta & 0 & \cos\theta \\ \cos\theta & 0 & -\sin\theta \\ 0 & 1 & 0 \end{pmatrix} \begin{pmatrix} A_\rho \\ A_\phi \\ A_z \end{pmatrix} \tag{VII-9a}$$

Thus the cylindrical-to-spherical transformation matrix can be written as

$$[A]_{cs} = \begin{bmatrix} \sin\theta & 0 & \cos\theta \\ \cos\theta & 0 & -\sin\theta \\ 0 & 1 & 0 \end{bmatrix} \tag{VII-9b}$$

The $[A]_{cs}$ matrix is also orthonormal so that its inverse is given by

$$[A]_{sc} = [A]_{cs}^{-1} = [A]_{cs}^{t} = \begin{bmatrix} \sin\theta & \cos\theta & 0 \\ 0 & 0 & 1 \\ \cos\theta & -\sin\theta & 0 \end{bmatrix} \tag{VII-10}$$

and the spherical-to-cylindrical transformation is accomplished by

$$\begin{pmatrix} A_\rho \\ A_\phi \\ A_z \end{pmatrix} = \begin{pmatrix} \sin\theta & \cos\theta & 0 \\ 0 & 0 & 1 \\ \cos\theta & -\sin\theta & 0 \end{pmatrix} \begin{pmatrix} A_r \\ A_\theta \\ A_\phi \end{pmatrix} \tag{VII-10a}$$

INTEL-1045
U.S. Patent 7,151,430

or

$$\left.\begin{aligned} A_\rho &= A_r \sin\theta + A_\theta \cos\theta \\ A_\phi &= A_\phi \\ A_z &= A_r \cos\theta - A_\theta \sin\theta \end{aligned}\right\} \qquad \text{(VII-10b)}$$

This time the component A_ϕ and coordinate ϕ are the same in both systems.

VII.1.3 Rectangular-to-Spherical (and Vice-Versa)

Many times it may be required that a transformation be performed directly from rectangular-to-spherical components. By referring to Figure VII.1, we can write that the rectangular and spherical coordinates are related by

$$\left.\begin{aligned} x &= r\sin\theta\cos\phi \\ y &= r\sin\theta\sin\phi \\ z &= r\cos\theta \end{aligned}\right\} \qquad \text{(VII-11)}$$

and the rectangular and spherical components by

$$\left.\begin{aligned} A_r &= A_x \sin\theta\cos\phi + A_y \sin\theta\sin\phi + A_z\cos\theta \\ A_\theta &= A_x\cos\theta\cos\phi + A_y\cos\theta\sin\phi - A_z\sin\theta \\ A_\phi &= -A_x\sin\phi + A_y\cos\phi \end{aligned}\right\} \qquad \text{(VII-12)}$$

which can also be obtained by substituting (VII-6) into (VII-9). In matrix form, (VII-12) can be written as

$$\begin{pmatrix} A_r \\ A_\theta \\ A_\phi \end{pmatrix} = \begin{pmatrix} \sin\theta\cos\phi & \sin\theta\sin\phi & \cos\theta \\ \cos\theta\cos\phi & \cos\theta\sin\phi & -\sin\theta \\ -\sin\phi & \cos\phi & 0 \end{pmatrix} \begin{pmatrix} A_x \\ A_y \\ A_z \end{pmatrix} \qquad \text{(VII-12a)}$$

with the rectangular-to-spherical transformation matrix being

$$[A]_{rs} = \begin{pmatrix} \sin\theta\cos\phi & \sin\theta\sin\phi & \cos\theta \\ \cos\theta\cos\phi & \cos\theta\sin\phi & -\sin\theta \\ -\sin\phi & \cos\phi & 0 \end{pmatrix} \qquad \text{(VII-12b)}$$

The transformation matrix of (VII-12b) is also orthonormal so that its inverse can be written as

$$[A]_{sr} = [A]_{rs}^{-1} = [A]_{rs}^{t} = \begin{pmatrix} \sin\theta\cos\phi & \cos\theta\cos\phi & -\sin\phi \\ \sin\theta\sin\phi & \cos\theta\sin\phi & \cos\phi \\ \cos\theta & -\sin\theta & 0 \end{pmatrix} \qquad \text{(VII-13)}$$

and the spherical-to-rectangular components related by

$$\begin{pmatrix} A_x \\ A_y \\ A_z \end{pmatrix} = \begin{pmatrix} \sin\theta\cos\phi & \cos\theta\cos\phi & -\sin\phi \\ \sin\theta\sin\phi & \cos\theta\sin\phi & \cos\phi \\ \cos\theta & -\sin\theta & 0 \end{pmatrix} \begin{pmatrix} A_r \\ A_\theta \\ A_\phi \end{pmatrix} \qquad \text{(VII-13a)}$$

or

$$\left.\begin{aligned} A_x &= A_r\sin\theta\cos\phi + A_\theta\cos\theta\cos\phi - A_\phi\sin\phi \\ A_y &= A_r\sin\theta\sin\phi + A_\theta\cos\theta\sin\phi + A_\phi\cos\phi \\ A_z &= A_r\cos\theta - A_\theta\sin\theta \end{aligned}\right\} \qquad \text{(VII-13b)}$$

INTEL-1045
U.S. Patent 7,151,430

VII.2 VECTOR DIFFERENTIAL OPERATORS

The differential operators of gradient of a scalar ($\nabla\psi$), divergence of a vector ($\nabla \cdot \mathbf{A}$), curl of a vector ($\nabla \times \mathbf{A}$), Laplacian of a scalar ($\nabla^2\psi$), and Laplacian of a vector ($\nabla^2\mathbf{A}$) frequently encountered in electromagnetic field analysis will be listed in the rectangular, cylindrical, and spherical coordinate systems.

VII.2.1 Rectangular Coordinates

$$\nabla\psi = \hat{\mathbf{a}}_x\frac{\partial\psi}{\partial x} + \hat{\mathbf{a}}_y\frac{\partial\psi}{\partial y} + \hat{\mathbf{a}}_z\frac{\partial\psi}{\partial z} \tag{VII-14}$$

$$\nabla\cdot\mathbf{A} = \frac{\partial A_x}{\partial x} + \frac{\partial A_y}{\partial y} + \frac{\partial A_z}{\partial z} \tag{VII-15}$$

$$\nabla\times\mathbf{A} = \hat{\mathbf{a}}_x\left(\frac{\partial A_z}{\partial y} - \frac{\partial A_y}{\partial z}\right) + \hat{\mathbf{a}}_y\left(\frac{\partial A_x}{\partial z} - \frac{\partial A_z}{\partial x}\right) + \hat{\mathbf{a}}_z\left(\frac{\partial A_y}{\partial x} - \frac{\partial A_x}{\partial y}\right) \tag{VII-16}$$

$$\nabla\cdot\nabla\psi = \nabla^2\psi = \frac{\partial^2\psi}{\partial x^2} + \frac{\partial^2\psi}{\partial y^2} + \frac{\partial^2\psi}{\partial z^2} \tag{VII-17}$$

$$\nabla^2\mathbf{A} = \hat{\mathbf{a}}_x\nabla^2A_x + \hat{\mathbf{a}}_y\nabla^2A_y + \hat{\mathbf{a}}_z\nabla^2A_z \tag{VII-18}$$

VII.2.2 Cylindrical Coordinates

$$\nabla\psi = \hat{\mathbf{a}}_\rho\frac{\partial\psi}{\partial\rho} + \hat{\mathbf{a}}_\phi\frac{1}{\rho}\frac{\partial\psi}{\partial\phi} + \hat{\mathbf{a}}_z\frac{\partial\psi}{\partial z} \tag{VII-19}$$

$$\nabla\cdot\mathbf{A} = \frac{1}{\rho}\frac{\partial}{\partial\rho}(\rho A_\rho) + \frac{1}{\rho}\frac{\partial A_\phi}{\partial\phi} + \frac{\partial A_z}{\partial z} \tag{VII-20}$$

$$\nabla\times\mathbf{A} = \hat{\mathbf{a}}_\rho\left(\frac{1}{\rho}\frac{\partial A_z}{\partial\phi} - \frac{\partial A_\phi}{\partial z}\right) + \hat{\mathbf{a}}_\phi\left(\frac{\partial A_\rho}{\partial z} - \frac{\partial A_z}{\partial\rho}\right) + \hat{\mathbf{a}}_z\left(\frac{1}{\rho}\frac{\partial(\rho A_\phi)}{\partial\rho} - \frac{1}{\rho}\frac{\partial A_\rho}{\partial\phi}\right) \tag{VII-21}$$

$$\nabla^2\psi = \frac{1}{\rho}\frac{\partial}{\partial\rho}\left(\rho\frac{\partial\psi}{\partial\rho}\right) + \frac{1}{\rho^2}\frac{\partial^2\psi}{\partial\phi^2} + \frac{\partial^2\psi}{\partial z^2} \tag{VII-22}$$

$$\nabla^2\mathbf{A} = \nabla(\nabla\cdot\mathbf{A}) - \nabla\times\nabla\times\mathbf{A} \tag{VII-23}$$

or in an expanded form

$$\begin{aligned}\nabla^2\mathbf{A} = {} & \hat{\mathbf{a}}_\rho\left(\frac{\partial^2A_\rho}{\partial\rho^2} + \frac{1}{\rho}\frac{\partial A_\rho}{\partial\rho} - \frac{A_\rho}{\rho^2} + \frac{1}{\rho^2}\frac{\partial^2A_\rho}{\partial\phi^2} - \frac{2}{\rho^2}\frac{\partial A_\phi}{\partial\phi} + \frac{\partial^2A_\rho}{\partial z^2}\right)\\ & + \hat{\mathbf{a}}_\phi\left(\frac{\partial^2A_\phi}{\partial\rho^2} + \frac{1}{\rho}\frac{\partial A_\phi}{\partial\rho} - \frac{A_\phi}{\rho^2} + \frac{1}{\rho^2}\frac{\partial^2A_\phi}{\partial\phi^2} + \frac{2}{\rho^2}\frac{\partial A_\rho}{\partial\phi} + \frac{\partial^2A_\phi}{\partial z^2}\right)\\ & + \hat{\mathbf{a}}_z\left(\frac{\partial^2A_z}{\partial\rho^2} + \frac{1}{\rho}\frac{\partial A_z}{\partial\rho} + \frac{1}{\rho^2}\frac{\partial^2A_z}{\partial\phi^2} + \frac{\partial^2A_z}{\partial z^2}\right)\end{aligned} \tag{VII-23a}$$

In the cylindrical coordinate system $\nabla^2\mathbf{A} \neq \hat{\mathbf{a}}_\rho\nabla^2A_\rho + \hat{\mathbf{a}}_\phi\nabla^2A_\phi + \hat{\mathbf{a}}_z\nabla^2A_z$ because the orientation of the unit vectors $\hat{\mathbf{a}}_\rho$ and $\hat{\mathbf{a}}_\phi$ varies with the ρ and ϕ coordinates.

INTEL-1045
U.S. Patent 7,151,430

VII.2.3 Spherical Coordinates

$$\nabla\psi = \hat{\mathbf{a}}_r \frac{\partial\psi}{\partial r} + \hat{\mathbf{a}}_\theta \frac{1}{r}\frac{\partial\psi}{\partial\theta} + \hat{\mathbf{a}}_\phi \frac{1}{r\sin\theta}\frac{\partial\psi}{\partial\phi} \tag{VII-24}$$

$$\nabla\cdot\mathbf{A} = \frac{1}{r^2}\frac{\partial}{\partial r}(r^2 A_r) + \frac{1}{r\sin\theta}\frac{\partial}{\partial\theta}(A_\theta \sin\theta) + \frac{1}{r\sin\theta}\frac{\partial A_\phi}{\partial\phi} \tag{VII-25}$$

$$\nabla\times\mathbf{A} = \frac{\hat{\mathbf{a}}_r}{r\sin\theta}\left[\frac{\partial}{\partial\theta}(A_\phi\sin\theta) - \frac{\partial A_\theta}{\partial\phi}\right] + \frac{\hat{\mathbf{a}}_\theta}{r}\left[\frac{1}{\sin\theta}\frac{\partial A_r}{\partial\phi} - \frac{\partial}{\partial r}(rA_\phi)\right] + \frac{\hat{\mathbf{a}}_\phi}{r}\left[\frac{\partial}{\partial r}(rA_\theta) - \frac{\partial A_r}{\partial\theta}\right] \tag{VII-26}$$

$$\nabla^2\psi = \frac{1}{r^2}\frac{\partial}{\partial r}\left(r^2\frac{\partial\psi}{\partial r}\right) + \frac{1}{r^2\sin\theta}\frac{\partial}{\partial\theta}\left(\sin\theta\frac{\partial\psi}{\partial\theta}\right) + \frac{1}{r^2\sin^2\theta}\frac{\partial^2\psi}{\partial\phi^2} \tag{VII-27}$$

$$\nabla^2\mathbf{A} = \nabla(\nabla\cdot\mathbf{A}) - \nabla\times\nabla\times\mathbf{A} \tag{VII-28}$$

or in an expanded form

$$\begin{aligned}\nabla^2\mathbf{A} = {} & \hat{\mathbf{a}}_r\left(\frac{\partial^2 A_r}{\partial r^2} + \frac{2}{r}\frac{\partial A_r}{\partial r} - \frac{2}{r^2}A_r + \frac{1}{r^2}\frac{\partial^2 A_r}{\partial\theta^2} + \frac{\cot\theta}{r^2}\frac{\partial A_r}{\partial\theta} + \frac{1}{r^2\sin^2\theta}\frac{\partial^2 A_r}{\partial\phi^2} - \frac{2}{r^2}\frac{\partial A_\theta}{\partial\theta} - \frac{2\cot\theta}{r^2}A_\theta - \frac{2}{r^2\sin\theta}\frac{\partial A_\phi}{\partial\phi}\right) \\ & + \hat{\mathbf{a}}_\theta\left(\frac{\partial^2 A_\theta}{\partial r^2} + \frac{2}{r}\frac{\partial A_\theta}{\partial r} - \frac{A_\theta}{r^2\sin^2\theta} + \frac{1}{r^2}\frac{\partial^2 A_\theta}{\partial\theta^2} + \frac{\cot\theta}{r^2}\frac{\partial A_\theta}{\partial\theta} + \frac{1}{r^2\sin^2\theta}\frac{\partial^2 A_\theta}{\partial\phi^2} + \frac{2}{r^2}\frac{\partial A_r}{\partial\theta} - \frac{2\cot\theta}{r^2\sin\theta}\frac{\partial A_\phi}{\partial\phi}\right) \\ & + \hat{\mathbf{a}}_\phi\left(\frac{\partial^2 A_\phi}{\partial r^2} + \frac{2}{r}\frac{\partial A_\phi}{\partial r} - \frac{1}{r^2\sin^2\theta}A_\phi + \frac{1}{r^2}\frac{\partial^2 A_\phi}{\partial\theta^2} + \frac{\cot\theta}{r^2}\frac{\partial A_\phi}{\partial\theta} + \frac{1}{r^2\sin^2\theta}\frac{\partial^2 A_\phi}{\partial\phi^2} + \frac{2}{r^2\sin\theta}\frac{\partial A_r}{\partial\phi} + \frac{2\cot\theta}{r^2\sin\theta}\frac{\partial A_\theta}{\partial\phi}\right)\end{aligned} \tag{VII-28a}$$

Again note that $\nabla^2\mathbf{A} \neq \hat{\mathbf{a}}_r\nabla^2 A_r + \hat{\mathbf{a}}_\theta\nabla^2 A_\theta + \hat{\mathbf{a}}_\phi\nabla^2 A_\phi$ since the orientation of the unit vectors $\hat{\mathbf{a}}_r$, $\hat{\mathbf{a}}_\theta$, and $\hat{\mathbf{a}}_\phi$ varies with the r, θ, and ϕ coordinates.

VII.3 VECTOR IDENTITIES

VII.3.1 Addition and Multiplication

$$\mathbf{A}\cdot\mathbf{A} = |\mathbf{A}|^2 \tag{VII-29}$$

$$\mathbf{A}\cdot\mathbf{A}^* = |\mathbf{A}|^2 \tag{VII-30}$$

$$\mathbf{A} + \mathbf{B} = \mathbf{B} + \mathbf{A} \tag{VII-31}$$

$$\mathbf{A}\cdot\mathbf{B} = \mathbf{B}\cdot\mathbf{A} \tag{VII-32}$$

$$\mathbf{A}\times\mathbf{B} = -\mathbf{B}\times\mathbf{A} \tag{VII-33}$$

$$(\mathbf{A} + \mathbf{B})\cdot\mathbf{C} = \mathbf{A}\cdot\mathbf{C} + \mathbf{B}\cdot\mathbf{C} \tag{VII-34}$$

$$(\mathbf{A} + \mathbf{B})\times\mathbf{C} = \mathbf{A}\times\mathbf{C} + \mathbf{B}\times\mathbf{C} \tag{VII-35}$$

INTEL-1045
U.S. Patent 7,151,430

$$\mathbf{A}\cdot\mathbf{B}\times\mathbf{C} = \mathbf{B}\cdot\mathbf{C}\times\mathbf{A} = \mathbf{C}\cdot\mathbf{A}\times\mathbf{B} \tag{VII-36}$$

$$\mathbf{A}\times(\mathbf{B}\times\mathbf{C}) = (\mathbf{A}\cdot\mathbf{C})\mathbf{B} - (\mathbf{A}\cdot\mathbf{B})\mathbf{C} \tag{VII-37}$$

$$\begin{aligned}(\mathbf{A}\times\mathbf{B})\cdot(\mathbf{C}\times\mathbf{D}) &= \mathbf{A}\cdot\mathbf{B}\times(\mathbf{C}\times\mathbf{D}) \\ &= \mathbf{A}\cdot(\mathbf{B}\cdot\mathbf{DC} - \mathbf{B}\cdot\mathbf{CD}) \\ &= (\mathbf{A}\cdot\mathbf{C})(\mathbf{B}\cdot\mathbf{D}) - (\mathbf{A}\cdot\mathbf{D})(\mathbf{B}\cdot\mathbf{C})\end{aligned} \tag{VII-38}$$

$$(\mathbf{A}\times\mathbf{B})\times(\mathbf{C}\times\mathbf{D}) = (\mathbf{A}\times\mathbf{B}\cdot\mathbf{D})\mathbf{C} - (\mathbf{A}\times\mathbf{B}\cdot\mathbf{C})\mathbf{D} \tag{VII-39}$$

VII.3.2 Differentiation

$$\nabla\cdot(\nabla\times\mathbf{A}) = 0 \tag{VII-40}$$

$$\nabla\times\nabla\psi = 0 \tag{VII-41}$$

$$\nabla(\phi+\psi) = \nabla\phi + \nabla\psi \tag{VII-42}$$

$$\nabla(\phi\psi) = \phi\nabla\psi + \psi\nabla\phi \tag{VII-43}$$

$$\nabla\cdot(\mathbf{A}+\mathbf{B}) = \nabla\cdot\mathbf{A} + \nabla\cdot\mathbf{B} \tag{VII-44}$$

$$\nabla\times(\mathbf{A}+\mathbf{B}) = \nabla\times\mathbf{A} + \nabla\times\mathbf{B} \tag{VII-45}$$

$$\nabla\cdot(\psi\mathbf{A}) = \mathbf{A}\cdot\nabla\psi + \psi\nabla\cdot\mathbf{A} \tag{VII-46}$$

$$\nabla\times(\psi\mathbf{A}) = \nabla\psi\times\mathbf{A} + \psi\nabla\times\mathbf{A} \tag{VII-47}$$

$$\nabla(\mathbf{A}\cdot\mathbf{B}) = (\mathbf{A}\cdot\nabla)\mathbf{B} + (\mathbf{B}\cdot\nabla)\mathbf{A} + \mathbf{A}\times(\nabla\times\mathbf{B}) + \mathbf{B}\times(\nabla\times\mathbf{A}) \tag{VII-48}$$

$$\nabla\cdot(\mathbf{A}\times\mathbf{B}) = \mathbf{B}\cdot\nabla\times\mathbf{A} - \mathbf{A}\cdot\nabla\times\mathbf{B} \tag{VII-49}$$

$$\nabla\times(\mathbf{A}\times\mathbf{B}) = \mathbf{A}\nabla\cdot\mathbf{B} - \mathbf{B}\nabla\cdot\mathbf{A} + (\mathbf{B}\cdot\nabla)\mathbf{A} - (\mathbf{A}\cdot\nabla)\mathbf{B} \tag{VII-50}$$

$$\nabla\times\nabla\times\mathbf{A} = \nabla(\nabla\cdot\mathbf{A}) - \nabla^2\mathbf{A} \tag{VII-51}$$

VII.3.3 Integration

$$\oint_C \mathbf{A}\cdot d\mathbf{l} = \iint_S (\nabla\times\mathbf{A})\cdot d\mathbf{s} \qquad \text{Stoke's theorem} \tag{VII-52}$$

$$\oiint_S \mathbf{A}\cdot d\mathbf{s} = \iiint_V (\nabla\cdot\mathbf{A})\,dv \qquad \text{Divergence theorem} \tag{VII-53}$$

$$\oiint_S (\hat{\mathbf{n}}\times\mathbf{A})\,ds = \iiint_V (\nabla\times\mathbf{A})\,dv \tag{VII-54}$$

$$\oiint_S \psi\,d\mathbf{s} = \iiint_V \nabla\psi\,dv \tag{VII-55}$$

$$\oint_C \psi\,d\mathbf{l} = \iint_S \hat{\mathbf{n}}\times\nabla\psi\,ds \tag{VII-56}$$

INTEL-1045
U.S. Patent 7,151,430

APPENDIX

VIII

METHOD OF STATIONARY PHASE

In many problems, the following integral is often encountered and in most cases cannot be integrated exactly:

$$I(k) = \int_a^b \int_c^d F(x, y) e^{jkf(x,y)}\, dx\, dy \qquad \text{(VIII-1)}$$

where

k = real

$f(x, y)$ = real, independent of k, and nonsingular

$F(x, y)$ = may be complex, independent of k, and nonsingular

Often, however, the above integral needs to be evaluated only for large values of k, but the task is still formidable. An approximate technique, known as the *Method of Stationary Phase*, exists that can be used to obtain an approximate asymptotic expression, for large values of k, for the above integral.

The method is justified by the asymptotic approximation of the single integral

$$I'(k) = \int_a^b F(x) e^{jkf(x)}\, dx \qquad \text{(VIII-2)}$$

where

k = real

$f(x, y)$ = real, independent of k, and nonsingular

$F(x, y)$ = may be complex, independent of k, and nonsingular

which can be extended to include double integrals.

The asymptotic evaluation of (VIII-1) for large k is based on the following: $f(x, y)$ is a well behaved function and its variation near the stationary points x_s, y_s determined by

$$\left.\frac{\partial f}{\partial x}\right|_{\substack{x=x_s \\ y=y_s}} \equiv f'_x(x_s, y_s) = 0 \qquad \text{(VIII-3a)}$$

INTEL-1045
U.S. Patent 7,151,430

$$\left.\frac{\partial f}{\partial y}\right|_{\substack{x=x_s\\y=y_s}} \equiv f'_y(x_s, y_s) = 0 \tag{VIII-3b}$$

is slow varying. Outside these regions, the function $f(x, y)$ varies faster such that the exponential factor $\exp[jkf(x, y)]$ of the integrand oscillates very rapidly between the values of $+1$ and -1, for large values of k. Assuming $F(x, y)$ is everywhere a slow varying function, the contributions to the integral outside the stationary points tend to cancel each other. Thus the only contributors to the integral, in an approximate sense, are the stationary points and their neighborhoods. Thus, we can write (VIII-1) approximately as

$$\begin{aligned} I(k) &\simeq \int_{-\infty}^{+\infty}\int_{-\infty}^{+\infty} F(x_s, y_s)e^{jkf(x,y)}\,dx\,dy \\ &= F(x_s, y_s)\int_{-\infty}^{+\infty}\int_{-\infty}^{+\infty} e^{jkf(x,y)}\,dx\,dy \end{aligned} \tag{VIII-4}$$

where the limits have been extended, for convenience, to infinity since the net contribution outside the stationary points and their near regions is negligible.

In the neighborhood of the stationary points, the function $f(x, y)$ can be approximated by a truncated Taylor series

$$\begin{aligned} f(x, y) = f(x_s, y_s) &+ \frac{1}{2}(x - x_s)^2 f''_{xx}(x_s, y_s) + \frac{1}{2}(y - y_s)^2 f''_{yy}(x_s, y_s) \\ &+ (x - x_s)(y - y_s)f''_{xy}(x_s, y_s) \end{aligned} \tag{VIII-5}$$

since

$$f'_x(x_s, y_s) = f'_y(x_s, y_s) = 0 \tag{VIII-6}$$

by (VIII-3a) and (VIII-3b). For convenience, we have adopted the notation

$$\left.\frac{\partial^2 f}{\partial x^2}\right|_{\substack{x=x_s\\y=y_s}} \equiv f''_{xx}(x_s, y_s) \tag{VIII-7a}$$

$$\left.\frac{\partial^2 f}{\partial y^2}\right|_{\substack{x=x_s\\y=y_s}} \equiv f''_{yy}(x_s, y_s) \tag{VIII-7b}$$

$$\left.\frac{\partial^2 f}{\partial x \partial y}\right|_{\substack{x=x_s\\y=y_s}} \equiv f''_{xy}(x_s, y_s) \tag{VIII-7c}$$

For brevity, we write (VIII-5) as

$$f(x, y) = f(x_s, y_s) + A\xi^2 + B\eta^2 + C\xi\eta \tag{VIII-8}$$

where

$$A = \frac{1}{2}f''_{xx}(x_s, y_s) \tag{VIII-8a}$$

$$B = \frac{1}{2}f''_{yy}(x_s, y_s) \tag{VIII-8b}$$

$$C = f''_{xy}(x_s, y_s) \tag{VIII-8c}$$

INTEL-1045
U.S. Patent 7,151,430

$$\xi = (x - x_s) \tag{VIII-8d}$$

$$\eta = (y - y_s) \tag{VIII-8e}$$

Using (VIII-8)–(VIII-8e) reduces (VIII-4) to

$$I(k) \simeq F(x_s, y_s)e^{jkf(x_s,y_s)} \int_{-\infty}^{+\infty}\int_{-\infty}^{+\infty} e^{jk(A\xi^2 + B\eta^2 + C\xi\eta)}\, d\xi\, d\eta \tag{VIII-9}$$

We now write the quadratic factor of the exponential, by a proper rotation of the coordinate axes ξ, η to μ, λ, in a diagonal form as

$$A\xi^2 + B\eta^2 + C\xi\eta \simeq A'\mu^2 + B'\lambda^2 \tag{VIII-10}$$

related to A, B, and C by

$$A' = \frac{1}{2}\left[(A + B) + \sqrt{(A + B)^2 - (4AB - C^2)}\right] \tag{VIII-10a}$$

$$B' = \frac{1}{2}\left[(A + B) - \sqrt{(A + B)^2 - (4AB - C^2)}\right] \tag{VIII-10b}$$

which are found by solving the secular determinant

$$\begin{vmatrix} (A - \zeta) & C/2 \\ C/2 & (B - \zeta) \end{vmatrix} = 0 \tag{VIII-11}$$

with $\zeta_1 = A'$ and $\zeta_2 = B'$. Substituting (VIII-10) into (VIII-9) we can write

$$I(k) \simeq F(x_s, y_s)e^{jkf(x_s,y_s)} \int_{-\infty}^{+\infty}\int_{-\infty}^{+\infty} e^{jk(A'\mu^2 + B'\lambda^2)}\, d\mu\, d\lambda$$

$$I(k) \simeq F(x_s, y_s)e^{jkf(x_s,y_s)} \int_{-\infty}^{+\infty} e^{\pm jk|A'|\mu^2}\, d\mu \int_{-\infty}^{+\infty} e^{\pm jk|B'|\lambda^2}\, d\lambda \tag{VIII-12}$$

where the signs in the exponents are determined by the signs of A' and B', which in turn depend upon A and B, as given in (VIII-10a) and (VIII-10b). The two integrals in (VIII-12) are of the same form and can be evaluated by examining the integral

$$I''(k) = \int_{-\infty}^{+\infty} e^{\pm jk|\alpha|t^2}\, dt = 2\int_0^{\infty} e^{\pm jk|\alpha|t^2}\, dt \tag{VIII-13}$$

where α can represent either A' or B' of (VIII-12). Making a change of variable by letting

$$k|\alpha|t^2 = \frac{\pi}{2}\tau^2 \tag{VIII-13a}$$

$$dt = \sqrt{\frac{\pi}{2k|\alpha|}}\, d\tau \tag{VIII-13b}$$

we can rewrite (VIII-13) as

$$I''(k) = 2\sqrt{\frac{\pi}{2k|\alpha|}} \int_0^{\infty} e^{\pm j\frac{\pi}{2}\tau^2}\, d\tau \tag{VIII-14}$$

The integral is recognized as being the complex Fresnel integral whose value is

$$\int_0^{\infty} e^{\pm j\frac{\pi}{2}\tau^2}\, d\tau = \frac{1}{2}(1 \pm j) = \frac{1}{\sqrt{2}} e^{\pm j\frac{\pi}{4}} \tag{VIII-15}$$

INTEL-1045
U.S. Patent 7,151,430

which can be used to write (VIII-14) as

$$I''(k) = 2\sqrt{\frac{\pi}{2k|\alpha|}}\int_0^\infty e^{\pm j\frac{\pi}{2}\tau^2}\,d\tau = \sqrt{\frac{\pi}{k|\alpha|}}\,e^{\pm j\frac{\pi}{4}} \qquad \text{(VIII-16)}$$

The result of (VIII-16) can be used to reduce (VIII-12) to

$$I(k) \simeq F(x_s, y_s)\,e^{jkf(x_s,y_s)}\,\frac{\pi}{k\sqrt{|A'||B'|}}\,e^{\mp j\frac{\pi}{4}}e^{\mp j\frac{\pi}{4}} \qquad \text{(VIII-17)}$$

If A' and B' are both positive, then $e^{\mp j\frac{\pi}{4}}e^{\mp j\frac{\pi}{4}} = e^{\mp j\frac{\pi}{2}} = +j$

If A' and B' are both negative, then $e^{\mp j\frac{\pi}{4}}e^{\mp j\frac{\pi}{4}} = e^{-j\frac{\pi}{2}} = -j$

If A' and B' have different signs, then $e^{\mp j\frac{\pi}{4}}e^{\mp j\frac{\pi}{4}} = 1$

Thus, (VIII-17) can be cast into the form

$$I(k) \simeq F(x_s, y_s)\,e^{jkf(x_s,y_s)}\,\frac{j\pi\delta}{k\sqrt{|A'||B'|}} \qquad \text{(VIII-18)}$$

where

$$\delta = \begin{cases} +1 & \text{if } A' \text{ and } B' \text{ are both positive} \\ -1 & \text{if } A' \text{ and } B' \text{ are both negative} \\ -j & \text{if } A' \text{ and } B' \text{ have different signs} \end{cases} \qquad \text{(VIII-18a)}$$

Examining (VIII-10a) and (VIII-10b), it is clear that

(a) A' and B' are real (because A, B, and C are real)

(b) $A' + B' = A + B$ (VIII-19)

(c) $A'B' = (4AB - C^2)/4$

Using the results of (VIII-19), we reduce (VIII-18) to

$$I(k) \simeq F(x_s, y_s)\,e^{jkf(x_s,y_s)}\,\frac{j2\pi\delta}{k\sqrt{|4AB - C^2|}}. \qquad \text{(VIII-20)}$$

To determine the signs of A' and B', let us refer to (VIII-19).

(a) If $4AB > C^2$, then A and B have the same sign and $A'B' > 0$. Thus, A' and B' have the same sign.
   1. If $A > 0$ then $B > 0$ and $A' > 0$, $B' > 0$
   2. If $A < 0$ then $B < 0$ and $A' < 0$, $B' < 0$

(b) If $4AB < C^2$, then $A'B' < 0$, and A' and B' have different signs. Summarizing the results we can write that
   1. If $4AB > C^2$ and $A > 0$, then A' and B' are both positive
   2. If $4AB > C^2$ and $A < 0$, then A' and B' are both negative
   3. If $4AB < C^2$, then A' and B' have different signs

Using the preceding deductions, we can write the sign information of (VIII-18a) as

$$\delta = \begin{cases} +1 & \text{if } 4AB > C^2 \text{ and } A > 0 \\ -1 & \text{if } 4AB > C^2 \text{ and } A < 0 \\ -j & \text{if } 4AB < C^2 \end{cases} \qquad \text{(VIII-21)}$$

INTEL-1045
U.S. Patent 7,151,430

in the evaluation of the integral in

$$I(k) = F(x_s, y_s)\, e^{jkf(x_s, y_s)} \int_{-\infty}^{+\infty} \int_{-\infty}^{+\infty} e^{jk(A\xi^2 + B\eta^2 - C\xi\eta)}\, d\xi\, d\eta$$

$$I(k) = F(x_s, y_s)\, e^{jkf(x_s, y_s)} \frac{j2\pi\delta}{k\sqrt{|4AB - C^2|}} \qquad \text{(VIII-22)}$$

INTEL-1045
U.S. Patent 7,151,430

APPENDIX

IX

TELEVISION, RADIO, TELEPHONE, AND RADAR FREQUENCY SPECTRUMS

IX.1 TELEVISION

IX.1.1 *Very High Frequency* (VHF) Channels

CHANNEL NUMBER	2 3 4	5 6	7 8 9 10 11 12 13
FREQUENCY (MHz)	54–60–66–72	76–82–88	174–180–186–192–198–204–210–216

IX.1.2 *Ultra High Frequency* (UHF) Channels*

CHANNEL NUMBER	14 15 16 17 18 19 20 ... 82 83
FREQUENCY (MHz)	470–476–482–488–494–500–506–512 ... 878–884–890

For both VHF and UHF channels, each channel has a 6-MHz bandwidth. For each channel, the carrier frequency for the video part is equal to the lower frequency of the bandwidth plus 1.25 MHz while the carrier frequency for the audio part is equal to the upper frequency of the bandwidth minus 0.25 MHz.

*In top ten urban areas in the United States, land mobile is allowed in the first seven UHF TV channels (470–512 MHz).

INTEL-1045
U.S. Patent 7,151,430

Examples: Channel 2 (VHF): f_0 (video) = 54 + 1.25 = 55.25 MHz
f_0 (audio) = 60 − 0.25 = 59.75 MHz

Channel 14 (UHF): f_0 (video) = 470 + 1.25 = 471.25 MHz
f_0 (audio) = 476 − 0.25 = 475.75 MHz

IX.2 RADIO

IX.2.1 *Amplitude Modulation* (AM) Radio

Number of channels: 107 (each with 10-kHz separation)
Frequency range: 535–1605 kHz

IX.2.2 *Frequency Modulation* (FM) Radio

Number of channels: 100 (each with 200-kHz separation)
Frequency range: 88–108 MHz

IX.3 AMATEUR BANDS

Band	Frequency (MHz)	Band	Frequency (MHz)
160-m	1.8–2.0	2-m	144.0–148.0
80-m	3.5–4.0	—	220–225
40-m	7.0–7.3	—	420–450
20-m	14.0–14.35	—	1215–1300
15-m	21.0–21.45	—	2300–2450
10-m	28.0–29.7	—	3300–3500
6-m	50.0–54.0	—	5650–5925

IX.4 CELLULAR TELEPHONE

IX.4.1 Land Mobile Systems

Uplink: MS to BS (mobile station to base station)

Downlink: BS to MS (base station to mobile station)

	UPLINK (MHz)	DOWNLINK (MHz)
United States of America (IS-54):	869–894	824–849
Europe–Asia (GSM): Global System for Mobile communications	890–915	935–960
Japan (NTT): Nippon Telegraph & Telephone Corporation	870–885	925–940

INTEL-1045
U.S. Patent 7,151,430

IX.4.2 Cordless Telephone

United States of America: 46–49 MHz
Digital European Cordless Telecommunications (DECT): 1.880–1.990 GHz

IX.5 RADAR IEEE BAND DESIGNATIONS

HF (High Frequency):	3–30	MHz
VHF (Very High Frequency):	30–300	MHz
UHF (Ultra High Frequency):	300–1,000	MHz
L-band:	1–2	GHz
S-band:	2–4	GHz
C-band:	4–8	GHz
X-band:	8–12	GHz
K_u-band:	12–18	GHz
K-band:	18–27	GHz
K_a-band:	27–40	GHz
Millimeter wave band:	40–300	GHz

INTEL-1045
U.S. Patent 7,151,430

Index

A
Absolute-gain measurements, 867–869
Active driving impedance, 424
Amateur band radio frequency spectrum, 928
Amplitude Modulation (AM) radio frequency spectrum, 928
Amplitude patterns
  antenna measurements, 864
  long wire antennas, 494–495
  3-D, thin dipoles, 155
Analysis methods, for antennas, 23, 116–126
  microstrip antennas, 726
  vector analysis: *See* Vector analysis
Anechoic chambers, 843–844
Antenna impedance, 73–77, 424
Antenna measurements, 839–883
  antenna ranges and, 840–858
    compact ranges, 844–851
    free-space ranges, 841–844
    near-field/far-field methods, 852–858
    reflection ranges, 841
  current, 874–875
  directivity, 871–872
  gain, 865–871
    absolute-gain, 867–869
    gain-transfer (gain-comparison), 869–871
  impedance, 873–874
  polarization, 875–880
  radiation efficiency, 872–873
  radiation patterns, 858–865
    amplitude pattern, 864
    instrumentation and, 860–864
    phase measurements, 864–865
  scale models and, 880–881
Antenna mode scattering, 92–93
Antenna patterns: *See also* Radiation patterns
  plotter for, 2-D, 113–114
Antenna ranges: *See* Antenna measurements
Antennas
  analysis methods, 23, 726
  aperture: *See* Aperture antennas
  circular: *See* Loop antennas
  defined, 1–2
  as directional device, 3
  elements for, 21–22
  frequency independent: *See* Frequency independent antennas
  future direction of, 23–24
  gain and: *See* Gain
  historical advancement of, 19–24
  linear: *See* Linear wire antennas
  loop: *See* Loop antennas
  for mobile communications systems, 175
  radiation efficiency of, 60–62, 78–79, 872–873
  thin wire: *See* Thin wire antennas
  as transitions device, 1–2
  traveling wave: *See* Traveling wave antennas
  types of, 3–7
Antenna synthesis, 339–378
  continuous sources and, 340–342
    apertures, 373–375
    discretization of, 341–342
    line source distributions, 340–341
  cosine distributions, 368–371
  cosine-squared distributions, 368–371
  Fourier transform method, 346–352
    line-source distribution, 347–349
    N-element linear arrays, 349–352
  line-source phase distributions, 371–373

INTEL-1045
U.S. Patent 7,151,430

Antenna synthesis *(Continued)*
Schelkunoff polynomial method, 342–346
Taylor line-source, 358–368
triangular distributions, 368–371
Woodward-Lawson method, 352–358
linear arrays and, 357–358
line-source distribution, 353–356
Aperture admittance, 631–638
Aperture antennas, 4, 575–650
Babinet's principle, 616–620
circular, 603–611
beam efficiency, 611
design considerations, 614–616
TE_{11}-mode distribution, 610–611
uniform distribution, 605–610
design considerations, 611–616
directivity, 584
field equivalence principle, 575–581
Fourier transforms and, 620–638
aperture admittance, 631–638
asymptotic evaluation of radiated field, 625–630
dielectric covered apertures, 630–631
radiated fields, 622–630
spectral domain, 621–622
geometrical theory of diffraction, 638–643
ground plane edge effects, 638–643
Huygens' principle, 575–581
radiation equations, 582–584
rectangular, 584–603
beam efficiency, 601–603
design considerations, 613–614
TE_{10}-mode distribution, 599–601
uniform distribution, 586–599
Aperture distribution method, 801–806
Aperture efficiency, 599–601, 811–818
Aperture fields
E-plane sectoral horns, 652–655
H-plane sectoral horns, 668–669
pyramidal horns, 682–686
Aperture-matched horns, 705–707
Array antennas, 56, 249–329
Array factor, 169, 250, 258–260
circular arrays, 324–328
Dolph-Tschebyscheff arrays, 294–296
N-element arrays, 289–290
planar arrays, 309–314
Arrays, 249–338
broadside, 316
circular, 324–328
and circular loop antennas, 229
computer programs for, *337–338*
design considerations, 282–283, 321–324
dipole, log-periodic antennas, 553–566
and feed networks, microstrip antennas, 772–775
infinite regular, 426–429
mutual coupling in: *See* Mutual coupling in arrays
N-element: *See* N-element arrays
performance of, mutual coupling and, 425
planar, 309–321
array factor, 309–314
beam width and, 314–318
computer programs for, 338
directivity, 318–321
rectangular-to-polar graphical solution, 287–288
superdirectivity, 306–309
designs with constraints, 307–309
efficiency and, 306–307
two-element, 250–257
Asymptotic evaluation of radiated field, aperture antennas, 625–630
Attractive mechanisms, 736–737

B
Babinet's principle, 616–620
Back lobes, 32
Backscattering radar cross section (RCS), 90
Baluns and transformers, 480–483
Bandwidth, 63–64, 449, 760–762
Basis functions, 387, 396–400
Bazooka balun, 480
Beam efficiency, 63, 601–603, 611
Beamwidths
broadside arrays, 265
circular aperture antennas, 607–609
Dolph-Tschebyscheff arrays, 302–304
half-power, 62
N-element binomial arrays, 302–304
ordinary end-fire arrays, 268
planar arrays, 314–318
rectangular aperture antennas, 589–592, 595–598, 599
Bessel functions, 899–910
Biconical antennas, 442–447
Binomial arrays, N-element, 290–294
Binomial matching transformers, 469–471
Bistatic radar cross section (RCS), 90
Bow-tie simulation, 447–449
Broadband antennas, 505–534
electric-magnetic dipoles, 512–513
helical antennas, 505–512
Yagi-Uda arrays, *513–534*
Broadband dipoles, 441–487

INTEL-1045
U.S. Patent 7,151,430

biconical antennas, 442–447
conical skirt monopoles, 462–464
cylindrical dipoles, 449–457
bandwidth, 449
dielectric coating, 454–457
equivalent radii, 454
input impedance, 449–451
radiation patterns, 453
resonance and ground plane simulation, 451–453
discone monopoles, 462–464
folded dipoles, 458–462
matching techniques: *See* Matching techniques
sleeve dipoles, 464–466
triangular sheet, bow-tie, and wire simulation, 447–449
Broadside arrays, 316
computer programs for, 337–338
N-element linear, 262–264, 276–279

C
Cassegrain parabolic reflectors: *See* Reflector antennas, parabolic
Cavity model, 736–749
Cellular telephone frequency spectrums, 928–929
Circular aperture antennas: *See* Aperture antennas
Circular aperture sources, 373–375
Circular arrays, 324–328
Circular loop antennas: *See* Loop antennas
Circular patch microstrip antennas: *See* Microstrip antennas
Circular polarization, 66–69, 767–772
Clockwise polarization, 66
Compact antenna test range (CATR), 844–851
Composing function, 353
Computer programs
arrays, 337–338, 573–574
2-D antenna pattern plotters, 113–114
dipole arrays, 573–574
directivity, 57–58, 115
linear dipoles, 202
maximum directivity, 115
microstrip antennas, 784
Moment Method (MM), 438
mutual impedance, 439–440
pyramidal horns, 720–721
radiated power, 115
self-impedance, 439–440
Yagi-Uda array, 521–525
Conductance, 731–732, 757–759
Conduction-dielectric efficiency, 78–79
Conical horns, 695–696
Conical skirt monopoles, 462–464
Conical spiral antennas, 549–550
Conjugate matching, 1
Continuous sources, 340–342, 373–375
Co-polarization, 66
Cordless cellular telephones, 928
Corner reflector antennas, 786–793
Corporate-feed network, 773
Corrugated horns, 696–704
Cosine distributions, 368–371
Cosine integrals, 889–893
Cosine-squared distributions, 368–371
Counterclockwise polarization, 66
Coupling
microstrip antennas, 764–767
mutual, in arrays: *See* Mutual coupling in arrays
Cross field, 140
Cross-polarization, 66, 806–807
Cubic phase distributions, 371–373
Current, measurement of, 874–875
Current distribution
finite length dipoles, 151
front-fed parabolic reflectors, 807–811
linear wire antennas, 151, 156
thin wire antenna, 17–19
Cylindrical coordinates, vector analysis and, 919
Cylindrical dipoles: *See* Broadband dipoles
Cylindrical-to-rectangular vector analysis, 914–917
Cylindrical-to-spherical vector analysis, 917–918

D
Density, radiation power, 35–37
Design procedures
aperture antennas, 611–616
arrays, 282–283, 321–324
circular loop antennas, 229–230
circular patch microstrip antennas, 755–756
with constraints, 307–309
Dolph-Tschebyscheff arrays, 296–302, 305–306
N-element binomial arrays, 292–294, 296–306
pyramidal horns, 693–695
rectangular patch microstrip antennas, 730–731

INTEL-1045
U.S. Patent 7,151,430

Design procedures *(Continued)*
Taylor line-source (Tschebyscheff error), 360–362
Dielectric coating, 454–457, 630–631
Dielectric-loaded horns, 712
Differentiation, vector identities and, 921
Dipole arrays, 553–566
computer programs for, 573–574
Dipole radiation mechanism, 14–16
Dipoles
broadband: *See* Broadband dipoles
electric-magnetic, 512–513
folded, 458–462
ground effects, 182–188
half-wavelength, 42–44
horizontal electric, 185–188
infinitesimal: *See* Linear wire antennas
near-field of, 405–408
sleeve, 464–466
small, 143–145
thin, 154, 155
vertical electric, 182–185
Directional device, antennas as, 3
Directional radiation patterns, 29, 45–49
Directive gain, 39
Directivity, 39–53: *See also* Radiation patterns
aperture antennas, 584
circular, 607–609
computer programs for, 57–58, 115, 202, 248
directional radiation patterns and, 45–49
E-plane sectoral horns, 663–668
front-fed parabolic reflectors, 811–818
of half-wavelength dipoles, 42–44
H-plane sectoral horns, 676–682
isotropic, 42–44
linear dipoles, 202
linear wire antennas, 142–143
finite length dipoles, 157–159
loop antennas, circular, 219–224, 248
maximum, 39–41, 49, 84–86
computer programs for, 202, 248
numerical techniques for, 53–58
measurement of, 871–872
N-element arrays, 276–282, 302–304
omnidirectional radiation patterns and, 49–53
partial, 40
patch microstrip antennas, circular, 757–759
planar arrays, 318–321
pyramidal horns, 686–693
rectangular aperture antennas, 593–594, 598–601
rectangular patch microstrip antennas, 749–752
small circular loop antennas, 213–214
superdirectivity, 306–309
Discone monopoles, 462–464
Dolph-Tschebyscheff arrays, 294–306
Driving-point impedance, 412
Duality theorem, 126–127
Dual parabolic-cylinder reflector, 848–850

E
Earth curvature effects, 188–194, 230–233
Effective area, maximum, 84–86
Effective length, 79–81, 728–730
Effective width, 728–730
Efficiency
antenna radiation, 60–62, 78–79
microstrip antennas, 760–762
polarization, 70–73
superdirectivity, 306–307
Electric and magnetic fields-TM^{z}_{mnp}, 753–754
Electric current sources, 117–119, 120–121
Electric field integral equation (EFIE), 387
Electric field lines, 12–15
Electric fields, 120–121
Electrostatic charge distribution, 381–387
Element factor, 151–153
Elements, used in antennas, 21–22
Elevated ranges, 841–843
Elliptical polarization, 66–69
EMF method, induced: *See* Induced EMF method
End-fire arrays
Hansen-Woodyard, N-element linear, 271–276, 281–282
ordinary, N-element linear, 264–266, 268, 279–280
Entire domain functions, 399–400
E-plane radiation patterns, 17, 27, 29, 30
E-plane sectoral horns: *See* Horns
Equiangular spiral antennas, 545–550
Equivalent areas, 81–84
Equivalent circuits, 214–217
Equivalent current densities, 741–744, 756–757
Equivalent magnetic ring current, 392
Equivalent radii, cylindrical dipoles, 454
Equivalents
antennas, 73–77
circular aperture antennas, 605–607

INTEL-1045
U.S. Patent 7,151,430

pyramidal horns, 682–686
rectangular aperture antennas, 587, 595, 599
Excitation coefficients, 290–292
Expansion functions, 387
Extrapolation method, 868

F
Far-field method, antenna ranges and, 852–858
Far-field pattern, Yagi-Uda array, 520–521
Far-field radiation, 125–126
Far-field region, 33–34
linear wire antennas, 138, 141–142
region separation and, 145, 146–149
and small circular loop antennas, 213
Feed design, 821–823
Feeding methods, 724–726
Feed networks, 772–775
Ferrite loop antennas, 240–241
Field configurations (modes)-TM^z, 738–741
Field equivalence principle, aperture antennas, 575–581
Field regions, in radiation patterns, 32–34
Fields radiated
circular patch microstrip antennas, 756–757
-TM $^z_{010}$ mode, 744–749
Finite cones, 447
Finite diameter wires, 388–395
Hallén's integral equation, 392
Pocklington's integral equation, 388–391
source modeling, 392–395
Finite-Difference Time-Domain (FD-TD) method, 16–17, 23
Finite feed gap, 161–162
Finite length dipoles: *See* Linear wire antennas
Finite straight wire, 381–385
Folded dipoles, 458–462
Formulas, linear wire antennas, 173–174
Fourier transforms
antenna synthesis, 346–352
aperture antennas and: *See* Aperture antennas
Fraunhofer region, 33–34
Free-space ranges, 841–844
Frequency independent antennas, 64, 542–574
conical spiral antennas, 549–550
equiangular spiral antennas, 545–550
limits of electrically small antennas, 566–570
log-periodic antennas, 551–566
dipole arrays, 553–566
planar and wire surfaces, 551–553
planar spiral antennas, 545–549
theory, 543–544
*F*requency *M*odulation (FM) radio frequency spectrum, 928
Fresnel integrals, 893–898
Fresnel region, 32–33
Friis transmission equation, 86–88
Fringing effects, 727–728
Front-fed parabolic reflector antennas: *See* Reflector antennas, parabolic

G
Gain, 58–60
measurements, 865–871
Galerkin's method, 401–402
Gamma match, 475–480
Geometrical theory of diffraction, 638–643
Grating lobes, 311–314, 429–434
Gregorian reflectors, 828–830
Ground effects
circular loop antennas, 230–233
linear wire antennas: *See* Linear wire antennas
Ground plane and resonance simulation, 451–453
Ground plane edge effects, 638–643
Ground-reflection method, 868–869

H
Half-power beamwidth, 62
Half-wavelength dipoles, 42–44, 162–164
Hallén's integral equation, 392
Hansen-Woodyard end-fire arrays, 271–276, 281–282
Helical antennas, 505–512
Hertz, Heinrich Rudolph, 19
Historical advancement, of antennas, 19–24
Horizontal electric dipoles, 175–181, 185–188
Horns, 651–721
aperture-matched, 705–707
conical, 695–696
corrugated, 696–704
dielectric-loaded, 712
E-plane sectoral, 651–668
aperture fields, 652–655
directivity, 663–668
radiated fields, 655–663
H-plane sectoral, 668–682
aperture fields, 668–669

INTEL-1045
U.S. Patent 7,151,430

Horns *(Continued)*
directivity, 676–682
radiated fields, 669–676
monopulse, 711
multimode, 707–712
phase center, 712–714
pyramidal, 682–695
aperture fields, 682–686
computer programs for, 720–721
design procedure, 693–695
directivity, 686–693
equivalents, 682–686
radiated fields, 682–686
H-plane radiation patterns, 29, 30
H-plane sectoral horns: *See* Horns
Huygens' principle, 575–581
Hyperbolic identities, 912

I
Identities, 911–913
Image theory, 164–165
Impedance
active driving, 424
antenna, 424
bandwidth of, 63–64
driving-point, 412
input: *See* Input impedance
measurement of, 873–874
mutual: *See* Mutual impedance
passive driving, 424
self-impedance: *See* Self-impedance
Incident electric field - $\mathbf{E}^i(\mathbf{r})$, 388–391
Induced current density, 800–801
Induced EMF method, 405–412, 416–422
Infinite cones, 445–447
Infinite line source radiation problem, 16–17
Infinite regular arrays, 426–429
Infinitesimal dipoles: *See also* Linear wire antennas
small circular loop antennas, 208
Input impedance, 73–77
biconical antennas, 445–447
cylindrical dipoles, 449–451
long wire antennas, 495–496
microstrip antennas, 762–764
Yagi-Uda array, 528–529
Input resistance, 159–161, 202
Instrumentation, radiation patterns and, 860–864
Integral equation method, 380–388: *See also* Moment Method (MM)
electrostatic charge distribution and, 381–387
bent wire, 385–387
finite straight wire, 381–385
integral equation, 387–388
mutual impedance, between linear elements, 414–416
Pocklington's, 388–391
self-impedance, 403–405
Yagi-Uda array, 516–520
Integration, vector identities and, 921
Intensity, radiation, 38–39
Intermediate-field region, 138, 140
Intermediate loop approximation, 222
Invisible region, 343–344
Isotropic radiation patterns, 29, 42–44

L
Land mobile cellular telephones, frequency spectrum, 928
Large loop approximation, 221–222
Lens antennas, 7, 9
Linear arrays: *See* N-element arrays
Linear dipoles, 202
Linear elements
near or on infinite perfect conductors: *See* Linear wire antennas
Yagi-Uda array of, 513–532
Linear phase distributions, 371–373
Linear polarization, 66–69
Linear wire antennas, 133–202
current distributions, 156
finite length dipoles, 151–162
current distribution, 151
directivity, 157–159
element factor, 151–153
finite feed gap, 161–162
input resistance and, 159–161
pattern multiplication, 151–153
power density, 153–157
radiated fields, 151–153
radiation intensity, 153–157
radiation resistance, 153–157
space factor, 151–153
ground effects, 181–194
earth curvature, 188–194
horizontal electric dipoles, 185–188
vertical electric dipoles, 182–185
half-wavelength dipoles, 162–164
infinitesimal dipoles, 133–143
directivity, 142–143
far-field region, 138, 141–142
intermediate-field region, 138, 140
near-field region, 138–140

INTEL-1045
U.S. Patent 7,151,430

power density and radiation resistance, 136–138
radian distance and radian sphere, 138–139
radiated fields and, 133–136
linear elements near or on infinite perfect conductors, 164–181
antennas for mobile communications systems, 175
formulas, rapid calculation and design, 173–174
horizontal electric dipoles, 175–181
image theory, 164–165
vertical electrical dipoles, 165–173
region separation and, 145–151
far-field (Fraunhofer) region, 145, 146–149
radiating near-field region (Fresnel), 145, 149–150
reactive near-field region, 145, 150–151
small dipole, 143–145
Line-source distributions
antenna synthesis, Woodward-Lawson method, 353–356
continuous sources and, 340–341
Fourier transform method, 347–349
Line-source-Gaussian pulse radiation problem, 27
Line-source phase distributions, 371–373
Lobes, of radiation patterns, 31–32
Logarithmic identities, 913
Log-periodic antennas: *See* Frequency independent antennas
Long wire antennas, 490–498
Loop antennas, 203–248
circular
computer programs for, 248
with constant current, 217–224
directivity, 219–224
earth curvature effects, 230–233
ground effects, 230–233
with nonuniform current, 224–230
power density, 219–224
radiated fields, 217–219
radiation intensity, 219–224
radiation resistance, 219224
ferrite, 240–241
ferrite loaded receiving loops, 241
radiation resistance, 240–241
mobile communications applications, 242
polygonal, 233–239
rectangular, 236–239
rhombic, 236–239
square loop, 233–236
triangular, 236–239
small circular, 204–217
directivity, 213–214
equivalent circuits for, 214–217
far-field region, 213
infinitesimal magnetic dipoles and, 208
near-field region, 212
power density and radiation resistance in, 208–212
radiated fields and, 204–208
radiation intensity, 213–214
Yagi-Uda array of, 533–534
Lorentz Reciprocity Theorem, 127–128
Loss factor, polarization (PLF), 69–73

M
Magnetic and electric current sources, 119–121
Magnetic and electric fields, -TM'_{amp}, 753–754
Magnetic field integral equation (MFIE), 387
Magnetic frill generator, 392–395
Major lobes, 32
Marconi, Guglielmo, 19–20
Matching techniques, 466–483
baluns and transformers, 480–483
binomial, 469–471
gamma match, 475–480
omega match, 480
quarter-wavelength transformers, 468–472
stub-matching, 466–468
T-match, 472–475
Tschebyscheff, 471–472
Yagi-Uda array, 528–529
MATLAB computer program, 16, 17
Maxima, long wire antennas, 494–495
Maximum directivity, 3941, 49, 84–86
computer programs for, 115, 202, 248
numerical techniques for, 53–58
Maximum effective area, 84–86
Maxwell, James Clerk, 19
Maxwell's Equations, 19
Method of stationary phase, 922–926
Microstrip antennas, 45, 722–784
analysis methods, 726
arrays and feed networks, 772–775
bandwidth, 760–762
circular patch, 752–760
conductance, 757–759
design, 755–756
directivity, 757–759

INTEL-1045
U.S. Patent 7,151,430

Microstrip antennas *(Continued)*
electric and magnetic fields-TM^z_{mnp}, 753–754
equivalent current densities, 756–757
fields radiated, 756–757
resonant frequencies, 754–755
resonant input resistance, 759–760
circular polarization, 767–772
computer programs for, 784
coupling, 764–767
efficiency, 760–762
feeding methods, 724–726
feed networks, arrays and, 772–775
input impedance, 762–764
quality factor, 760–762
rectangular patch, 727–752
cavity model, 736–749
conductance, 731–732
design procedure, 730–731
directivity, 749–752
effective length, 728–730
effective width, 728–730
equivalent current densities, 741–744
field configurations (modes)-TM^z, 738–741
fields radiated-TM^z_{010} mode, 744–749
fringing effects, 727–728
resonant frequency, 728–730
resonant input resistance, 732–736
transmission line model, 727–736
Miniaturization, 566–574
Mini-Numerical Electromagnetics Code (MININEC), 415
Minor lobes, 32
Mobile communications systems, 175, 242, 928–929
Modal expansion method, 855–856
Moment Method (MM): *See also* Integral equation method
computer programs for, 438
Galerkin's method, 401–402
solution for, 395–403
basis functions, 396–400
entire domain functions, 399–400
subdomain functions, 397–399
weighting (testing) functions, 400–403
Monopoles, 462–464
Monopulse horns, 710–711
E-plane, 710
H-plane, 711
sum, 710
Monostatic radar cross section (RCS), 90
Multimode horns, 707–712
Mutual coupling in arrays, 422–434
array performance, 425
grating lobes considerations, 429–434
infinite regular arrays, 426–429
in receiving mode, 425
in transmitting mode, 423–425
Mutual impedance
computer programs for, 439–440
between linear elements, 412–422
induced EMF method, 416–422
integral equation-moment method, 414–416
Mini-Numerical Electromagnetics Code (MININEC), 415
Numerical Electromagnetics Code (NEC), 415

N
Near-field/far-field methods, 852–858
Near-field of dipole, 405–408
Near-field region
linear wire antennas, 138–140
small circular loop antennas, 212
N-element arrays
linear
broadside arrays, 262–264, 276–279
computer programs for, 337
directivity, 276–282
Fourier transform method, 349–352
Hansen-Woodyard end-fire arrays, 271–276, 281–282
ordinary end-fire arrays, 264–266, 279–280
phased (scanning) arrays, 266–271
3-D characteristics, 283–286
uniform amplitude and spacing, 257–276
broadside arrays, 262–264
ordinary end-fire arrays, 264–266
Woodward-Lawson method, 357–358
X- or Y-axis, 284–286
Z-axis, 283–284
uniform spacing, nonuniform amplitude, 288–306
array factor, 289–290
binomial arrays, 290–294
Dolph-Tschebyscheff arrays, 294–306
90° corner reflector antennas, 789–790
Nonradiating slots, rectangular patch antennas, 748–749
Nulls, long wire antennas, 494–495
Numerical Electromagnetics Code (NEC), 415

INTEL-1045
U.S. Patent 7,151,430

Numerical techniques: *See also* Computer programs
for radiation patterns, 53–58

O
Omega match, 480
Omnidirectional radiation patterns, 29, 30, 49–53
One-parameter Taylor line-source antenna synthesis, 362–368
Optimization, Yagi-Uda array, 525–528
Ordinary end-fire arrays, 264–266, 279–280

P
Parabolic reflector antennas: *See* Reflector antennas
Partial directivity, 40
Passive driving impedance, 424
Patch antennas: *See* Microstrip antennas
Pattern bandwidth, 63–64
Pattern multiplication, 151–153, 169
PEC square cylinder, 17, 27
Phase center horns, 712–714
Phase errors
line sources, 371–373
reflectors, 818–821
Phase measurements, 864–865
Piecewise constant function, 397–398
Piecewise linear function, 398
Piecewise sinusoid function, 399
Planar and wire surfaces, 551–553
Planar arrays: *See* Arrays
Planar spiral antennas, 545–549
Plane reflector antennas, 785–786
Pocklington's integral equation, 388–391
Poincaré sphere, 65–68, 878
Polarization, 64–73
circular, microstrip antennas, 767–772
long wire antennas, 496–497
measurement of, 875–880
Poincaré sphere, 65–68, 878
Polarization efficiency, 70–73
Polarization loss factor (PLF), 69–73
Polygonal loop antennas: *See* Loop antennas
Power density, 35–36
circular loop antennas, 208–212, 219–224
linear wire antennas, 136–138, 153–157
radiation, 35–37
and radiation resistance, 136–138, 208–212
Power patterns, 28, 353
Principal radiation patterns, 29–31
Pyramidal horns: *See* Horns

Q
Quadratic phase distributions, 371–373
Quality factor, 760–762
Quarter-wavelength transformers, 468–472
Quasistationary fields, 212

R
Radar cross section (RCS), 90–98, 91
RADAR IEEE band designations, 929
Radar range equation, 88–90
Radian, 34–35, 138–139
Radiated fields
aperture antennas, 622–630
biconical antennas, 442–445
circular loop antennas, 204–208, 217–219
E-plane sectoral horns, 655–663
H-plane sectoral horns, 669–676
linear wire antennas, 133–136
finite length dipoles, 151–153
pyramidal horns, 682–686
rectangular aperture antennas, 587–589, 595, 599
Radiated power, 115
Radiated (transmitted) wave polarization, 64–65
Radiating near-field (Fresnel) region, 32–33, 145, 149–150
Radiating slots, rectangular patch microstrip antennas, 744–748
Radiation efficiency, 872–873
Radiation equations, 582–584
Radiation fields, 605–607
Radiation integrals and auxiliary potential functions, 116–132
duality theorem, 126–127
electric and magnetic fields, 120–121
far-field radiation, 125–126
reciprocity and reaction theorems, 127–132
for radiation patterns, 130–132
for two antennas, 129–130
vector potentials, 116
for electric current source, 117–119
for magnetic current source, 119–120
wave equation, 121–125
Radiation intensity, 38–39
circular loop antennas, 219–224
linear wire antennas, 153–157
small circular loop antennas, 213–214
Radiation mechanism, 717
Radiation patterns, 28–35: *See also* Directivity
antenna measurements and, 858–865

INTEL-1045
U.S. Patent 7,151,430

Radiation patterns *(Continued)*
cylindrical dipoles, 453
directional, 29
field regions, 32–34
isotropic, 29
lobes of, 31–32
numerical techniques for, 53–58
omnidirectional, 29
principal, 29–31
radian and steradian, 34–35
Radiation power density, 35–37
Radiation resistance, 1
circular loop antennas, 219–224, 248
computer programs for, 202, 248
and ferrite loop antennas, 240–241
linear wire antennas, finite length dipoles, 153–157
power density and, 136–138, 208–212
Radio frequency spectrums, 927–928
Reactive near-field region, 32, 145, 150–151
Received wave polarization, 64–65
Receiving mode
antenna equivalent, 76–77
circular loop, 216–217
coupling, 425
Reciprocity and reaction theorems, 127–132
Rectangular aperture antennas: *See* Aperture antennas
Rectangular aperture sources, 373
Rectangular coordinates, vector analysis and, 919
Rectangular loop antennas, 236–239
Rectangular patch microstrip antennas: *See* Microstrip antennas
Rectangular-to-cylindrical vector analysis, 914–917
Rectangular-to-polar graphical solution, 287–288
Rectangular-to-spherical vector analysis, 918
Reflection ranges, 841
Reflector antennas, 6, 785–838
corner, 786–793
parabolic, 794–830
Cassegrain, 823–830
classical form, 826–828
Gregorian form, 828–830
front-fed, 797–823
aperture distribution method, 801–806
aperture efficiency, 811–818
cross-polarization, 806–807
current distribution method, 807–811
directivity, 811–818
feed design, 821–823
induced current density, 800–801
phase errors, 818–821
surface geometry, 798–800
plane, 785–786
spherical, 830–833
Region separation, 145–151
Repulsive mechanism, for microstrip patches, 736–737
Resonance and ground plane simulation, cylindrical dipoles, 451–453
Resonant frequencies, 728–730, 754–755
Resonant input resistance, 732–736, 759–760
Resonant wires,
Rhombic antennas, 236–239, 502–505
Root-matching, for continuous source discretization, 341

S
Scale models, 880–881
Scattered electric field - $\mathbf{E}^s(\mathbf{r})$, 388–391
Schelkunoff polynomial method, 342–346
Self-impedance, 379, 403–412
computer programs for, 439–440
induced EMF method, 405–412
integral equation-moment method, 403–405
Series-feed network, 773
Side lobe levels, 592–599, 607–609
Sine function tables, 885–889
Sine integrals, 889–893
Single paraboloidal reflector, 848–850
Single-plane collimating range (SPCR), 850–851
Single wire radiation mechanism, 711
Slant ranges, 843
Sleeve dipoles, 464–466
Small circular loop antennas: *See* Loop antennas
Small dipoles, 143–145
Small loop approximation, 222–223
Source modeling, 392–395
delta gap, 393
magnetic frill generator, 393–394
Space factor, 151–153
Spectral domain, 621–622
Spherical coordinates, 920
Spherical reflectors, 830–833
Spherical-to-cylindrical vector analysis, 917–918
Spherical-to-rectangular vector analysis, 918
Square loop antennas, 233–236

INTEL-1045
U.S. Patent 7,151,430

Standing waves, 2
Stationary phase, method of, 922–926
Steradian, 34–35
Structural scattering, 93
Stub-matching, 466–468
Subdomain functions, 397–399
Superdirectivity, 306–309
Supergain, 306
Surface geometry, front-fed parabolic reflectors, 798–800
Synthesis: *See* Antenna synthesis

T
Taylor line-source, 321–322, 358–368
Television frequency spectrums, 927–928
TE_{11}-mode distribution, circular aperture, 610–611
TE_{10}-mode distribution, rectangular aperture, 599–601
Temperature, of antennas, 98–100
Thin dipoles, 154
Thin wire antennas
  on current distribution, 17–19
  linear: *See* Linear wire antennas
Three-antenna method, gain measurements, 867–868
Three-dimensional amplitude patterns, 155
Three-dimensional characteristics, 283–286
T-match, 472–475
Total electric field - $\mathbf{E}^t(\mathbf{r})$, 388–391
Transformers, baluns and, 480–483
Transmission line model, rectangular microstrip antennas, 727–736
Transmitting mode, 74–76, 215–216, 423–425
Traveling wave antennas, 488–505
  long wire, 490–
  rhombic antennas, 502–505
  V antennas, –502
Triangular distributions, 368–371
Triangular loop antennas, 236–239
Triangular sheet simulation, 447–449
Trigonometric identities, 911–912
Truncated cosine function, 399
Tschebyscheff error, Taylor line-source, 321–322, 358–362
Tschebyscheff matching transformers, 471–472
Two-antenna method, gain measurements, 867
Two-element arrays, 250–257
Two wire radiation mechanism, 1114

U
*U*ltra *H*igh *F*requency (UHF) channels, 927–928
Uniform distribution on an infinite ground plane, 586–594, 605–610
Unipoles, 447

V
V antennas, –502
Vector analysis, 914–921
Vector effective length, 79–81
Vector potentials: *see also* Radiation integrals and auxiliary potential functions
  wave equations and, 121–125
Vertical electric dipoles, 165–173, 182–185
*V*ery *H*igh *F*requency (VHF) channels, 927–928
Virtual feed, 826
Visible region, 343–344

W
Weighted residuals, 401
Weighting (testing) functions, 400–403
Wire antennas, 4
  linear: *See* Linear wire antennas
  thin wire: *See* Thin wire antennas
Wireless communication antennas, 175, 242, 928–929
Wire simulation, 447–449
Woodward-Lawson method, 352–358

Y
Yagi-Uda arrays
  computer programs for, 521–525, 541
  of linear elements, 513–532
  of loops, 533–534

INTEL-1045
U.S. Patent 7,151,430